Spring 2021

Electrocatalytic Oxygen Reduction using Molecular Iron Porphyrins: Detailing the Role of Electrostatics in Small Molecule Activation

Daniel James Martin
Yale University Graduate School of Arts and Sciences, danieljmartin93@gmail.com

Abstract

Electrocatalytic Oxygen Reduction using Molecular Iron Porphyrins:

Detailing the Role of Electrostatics in Small Molecule Activation

Daniel J. Martin

2021

Energy storage and conversion are key facets of sustainable energy science. Fuel cells, for instance, allow us to convert chemical and electrical energies while minimizing energy loss in the form of heat. The oxygen reduction reaction—which involves combining O_2, protons, and electrons to make water—is one such reaction common to many types of fuel cells but is hard to perform both rapidly and efficiently. Typically there are trade-offs, and faster catalysis is only achieved at lower efficiencies. Overcoming these tradeoffs is a long withstanding goal in electrocatalysis and would be broadly impactful for the optimization of energy-relevant reactions. The atomistic insight obtained from homogeneous (electro)catalysts can help realize this goal, for instance by identifying kinetic/thermodynamic relationships or key structure-function properties in catalyst design.

This thesis describes a series of related stories in which homogeneous, molecular iron porphyrins are used as i) (electro)catalysts for the oxygen reduction reaction (ORR) and ii) electrostatic models for small molecule activation.

Chapters 1-3 begin this thesis with the derivation, utility, and application of molecular "scaling relationships," the tradeoffs described above, for iron porphyrin catalyzed ORR. Chapter 1 starts this narrative with a summary of the kinetic and thermodynamic studies required to derive and apply the scaling relationships. Chapter 2 details a complete mechanistic study of O_2 reduction by iron tetraphenylporphyrin in nonaqueous solvents and identifies key intermediates, energies, and steps involved during turnover. Using an iron porphyrin bearing four *ortho*-trimethylanilinium groups and buffered carboxylic acids in acetonitrile, Chapter 3 demonstrates that molecular scaling relationships can be additive and that a cooperative scaling approach is a powerful way to improve multistep electrocatalytic processes. Together, these studies demonstrate the power of

kinetic/thermodynamic scaling relationships and show that cooperative, or “tandem” scaling is an untapped method for optimization of energy-relevant reactions.

Chapter 4 is a turning point in this thesis, wherein the focus pivots from molecular scaling relationships to intramolecular electrostatic effects. Using iron(III) αβαβ-tetra(*o*-*N*,*N*,*N*-trimethylanilinium)porphyrin pentatriflate—an atropisomerically-pure form of the catalyst used in Chapter 3—this Chapter details how the charged *o*-$[N(CH_3)_3]^+$ groups on the iron porphyrin affect acetate, O_2, and CO_2 binding, various pre-equilibria that are invoked in the molecular electrocatalysis literature. The results of this study highlight how electrostatic, secondary sphere motifs affect specific small molecule binding in nonaqueous media and underscore their utility in catalyst design.

Chapters 5 details the synthesis and characterization of all four atropisomers (αβαβ, ααββ, αααβ, and αααα) of the polycationic catalyst used in Chapters 3 and 4 and identifies the role of electrostatic effects in both solution and solid-state data. Chapter 6 takes advantage of the molecules prepared in Chapter 5 and reports both O_2 reduction and CO_2 reduction using the set of charged isomers. Together, Chapters 5-6 offer a first-of-a-kind look at the role of charge orientation on the behavior of molecular electrocatalysts and small molecule activation. Chapter 7 closes this thesis and reports the synthesis and prior misidentification of 4-*tert*-butyl-2,6-dinitrobenzaldehyde. This small molecule is a common precursor for bis-picket fence porphyrins and is potential starting point for the synthesis of new, highly charged iron porphyrin complexes.

Taken together, the results and conclusions presented in this thesis have direct, immediate ramifications for ORR and CO_2RR electrocatalysis and are broadly relevant for many other chemical-to-electrical energy processes. I hope that readers are inspired by some of the ideas presented herein and can find takeaways that aid in their own scientific pursuits.

Electrocatalytic Oxygen Reduction using Molecular Iron Porphyrins: Detailing the Role of Electrostatics in Small Molecule Activation

A Dissertation

Presented to the Faculty of the Graduate School

Of

Yale University

In Candidacy for the Degree of

Doctor of Philosophy

by

Daniel J. Martin

Dissertation Director: James M. Mayer

June 2021

Table of Contents

List of Figures

List of Schemes

List of Tables

Acknowledgments

A lot of people struggle during graduate school. Be it a test of confidence or compassion, a journey of self-discovery, or finding intellectual cairns in the dark – graduate school is a challenge. It is also an opportunity and a place to grow, if provided the right setting and help along the way. While at Yale, I was fortunate to be in the right place at the right time and surrounded by the right people. I cannot name them all, but I would like to name a few.

To Jim. While many students celebrate achievement and shout "I made it!" or perhaps "I survived!", I find this moment truly bittersweet. I am so lucky to have made many friends these past five years. People who have taught me lessons, treated me with kindness and compassion, and have helped me grow into the person I am today. You are among the closest of those friends, Jim. Not only have you pushed me as a scientist, but you have shown me compassion and friendship and support – kindnesses that will stick with me far longer than any of the science. You are a good boss, a great person, and an excellent friend. I am infinitely grateful that we crossed paths.

To Pat Holland and Nilay Hazari. Thank you both for curating an environment and a culture that was warm and welcoming these past five years. One of the simplest and most profound questions that I was asked during graduate school was "Are you happy? Are students happy here?" While I can only speak for myself, I offer an emphatic 'Yes.' Some of that credit is due to the quality of the science, but much more is due to the quality of the people. You both are role models to many and set the precedent for that sort of environment, and for that I am truly grateful.

To the Mayer Group. You all are some of the strangest and kindest folk that I have had the good fortune of befriending. Despite the change of guard these past few years—and Jim's ceaseless commentary on turnover—the group really has not changed all that much. Some new faces and some old, but you all are still the same goofy, brilliant, and contagiously passionate people that I have come to admire. I am going to miss the lot of you.

To Catherine Wise, Brian Koronkiewicz, Stephanie Laga, and Rishi Agarwal. You all are dear friends to me and siblings of a sort. I admit, it's been rather lonely watching you all leave, but it has also been exciting to watch you all pick your own paths. The lot of you are trailblazers, and I wish you nothing but the best of luck, wherever you go.

To Brian McCarthy, Eric Rountree, and Jillian Dempsey. Looking back on the last decade, I can think of only a few moments that truly defined my trajectory. Befriending you three and being a part of the Dempsey team was one of them. Thank you all for your friendship, your support, your well wishes, and your pK_a values.

To Yash Samantaray, Benjamin Groff, and Hannah Nedzbala. I am so proud of you three and of your growth as scientists. Not only has it been my pleasure to watch you grow, but also my privilege to be (at least partly) the mentor of stunning intellectuals like yourselves. Coming to graduate school, I did not realize how much being a mentor would impact my own development as a leader and as a scientist. I wanted to thank you three for giving me that opportunity. I have the highest hopes for your pursuits and wish you all good luck.

To my Family and to Katie Fisher. You all are unfaltering pillars in my life. While I could spend several pages describing all that you do and all that you mean to me, it would still pale next to the love and gratitude that I feel. Just know that I love you all very much and that I look forward to our future adventures.

1 Chapter 1 – Developing Scaling Relationships for Molecular Electrocatalysis through Studies of Fe-Porphyrin-Catalyzed O_2 Reduction

Adapted from Martin, D. J.; Wise, C. F.; Pegis, M. P.; Mayer, J. M. "Developing Scaling Relationships for Molecular Electrocatalysis through Studies of Fe-Porphyrin Catalyzed O_2 Reduction." *Acc. Chem. Res.* **2020**, DOI: 10.1021/acs.accounts.0c00044. DJM and CFW contributed equally to the writing and editing. DJM prepared and adapted figures. MLP and JMM helped with writing and editing. The authors thank all the co-workers, colleagues, and collaborators who contributed to the research discussed in this report.

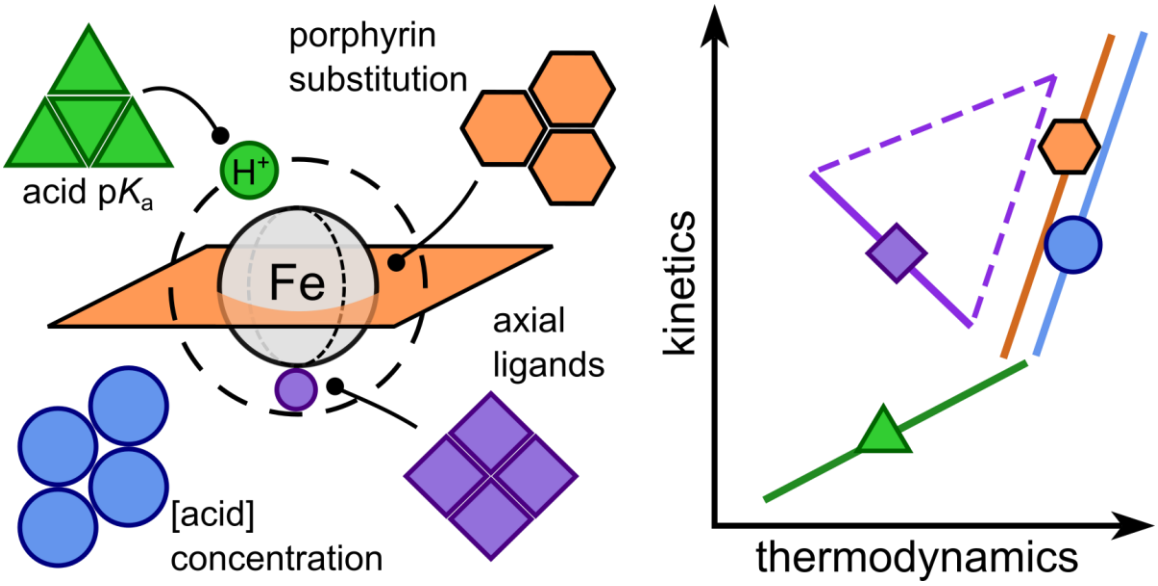

1.1 Conspectus

The oxygen reduction reaction (ORR) is a multi-proton/multi-electron transformation in which dioxygen (O_2) is reduced to water or hydrogen peroxide and serves as the cathode reaction in most fuel cells. The ORR ($O_2 + 4e^- + 4H^+ \rightarrow 2H_2O$) involves up to nine substrates and thus requires navigating a complicated reaction landscape, typically with several high-energy intermediates. Many catalysts can perform this reaction, though few operate with fast rates and at low overpotentials (close to the thermodynamic potential). Attempts to optimize these parameters, both in homogeneous and heterogeneous electrocatalytic systems, have focused on modifying catalyst design and understanding thermodynamic/kinetic relationships between catalytic intermediates. One such method for analyzing and predicting catalyst reactivity and efficiency has been the development of "molecular scaling relationships."

Here, we share our experience deriving and utilizing molecular scaling relationships for soluble, iron porphyrin-catalyzed O_2 reduction in organic solvents. These relationships correlate

turnover frequencies (TOF_{max}) and effective overpotentials (η_{eff}), properties uniquely defined for homogeneous catalysts. Following a general introduction of scaling relationships for both homogeneous and heterogeneous electrocatalysis, we describe the components of such scaling relationships: *i*) the overall thermochemistry of the reaction and *ii*) the rate and rate law of the catalyzed reaction. We then show how connecting these thermodynamic and kinetic parameters reveals *multiple* molecular scaling relationships for iron porphyrin-catalyzed O_2 reduction. For example, the log(TOF_{max}) responds steeply to changes in η_{eff} that result from different catalyst reduction potentials (18.5 decades in TOF_{max}/V in η_{eff}), but much less dramatically to changes in η_{eff} that arise from varying the pK_a of the acid buffer (5.1 decades in TOF_{max}/V in η_{eff}). Thus, a single scaling relationship is not always sufficient for describing molecular electrocatalysis. This is particularly evident when the catalyst identity and reaction conditions are coupled. Using these multiple scaling relationships, we demonstrate that the metrics of turnover frequency and effective overpotential can be predictably tuned to achieve faster rates at lowered overpotentials.

This chapter uses a collection of related stories describing our research on soluble iron porphyrin-catalyzed ORR to show how molecular scaling relationships can be derived and used for any electrocatalytic reaction. Such scaling relationships are powerful tools and connect the thermochemistry, mechanism, and rate law for a catalytic system. We hope that this collection shows the utility and simplicity of the molecular scaling approach for understanding catalysis, for enabling direct comparisons between catalyst systems, and for optimizing catalytic processes.

1.2 Introduction

The reduction of dioxygen (O_2) to water (H_2O) is a critical chemical transformation for many biological and artificial energy systems, such as cellular respiration and fuel cell technologies.[1-3] For energy applications, the four-electron/four-proton ($4e^-/4H^+$) reduction of O_2 to H_2O (eq 1.1) is preferred over the less exergonic $2e^-/2H^+$ reduction of O_2 to hydrogen peroxide (H_2O_2).

$$O_2 + 4e^- + 4H^+ \rightarrow 2H_2O \qquad \text{(eq 1.1)}$$

Performing the $4e^-/4H^+$ oxygen reduction reaction (ORR) at high rates and close to its thermodynamic potential (e.g. at low *overpotentials*) is a major challenge.[1,4-6] The best systems use

platinum-group-metal catalysts, but improved replacements with earth-abundant materials are required for next-generation energy technologies.[4] Many of the fundamental aspects of this challenge are more amenable to study with homogeneous molecular ORR electrocatalysts, though soluble catalysts are less likely to be the technological solution.[7-8] Research on molecular electrocatalysts provides new strategies for efficient catalysis of the ORR and other proton/electron energy-conversion reactions.

This chapter describes how our studies of soluble iron porphyrin ORR catalysts (Fe(por)) in organic solvents led us to develop "molecular scaling relationships." These relationships reveal how the primary metrics of catalysis (turnover frequency and overpotential) depend on the components of the catalytic system. Using ORR electrocatalysis by iron porphyrins as a case study, we develop the thermodynamic and kinetic parameters relevant to molecular electrocatalysis and then derive the corresponding molecular scaling relationships. We demonstrate how catalysis depends not on only on catalyst identity but also on the buffer and the medium. These quantitative relationships provide a powerful new way to understand, compare, and improve multi-proton/multi-electron electrocatalytic systems. We hope that this Account will stimulate our readers to use this approach for their catalytic applications.

1.3 Metrics for Homogeneous Molecular Electrocatalysis

Molecular electrocatalysis involves soluble catalysts, often in non-aqueous media, that are driven by the exchange of electrons with an electrode. The primary metrics that describe a catalytic system—defined as both the electrocatalyst and its surrounding medium—are rates, overpotentials, selectivity, and robustness. Emphasized here are the parameters of maximum turnover frequency (TOF_{max}), or moles product per mole catalyst (in the reaction diffusion layer) per second, and effective overpotential (η_{eff}, see below).[9-10] With this emphasis, the "best" catalyst is the one that attains the highest TOF_{max} at the lowest η_{eff}.

Cyclic voltammetry is the technique most often used to evaluate molecular electrocatalysis, where TOF_{max} is obtained by analyzing the response of the electrocatalyst in the presence and absence of substrate (blue and black curves in **Figure 1.1**).[11] In an ideal system, the catalytic current reaches a maximum at potentials beyond $E_{cat/2}$[11-12] and is limited by chemical steps in the

solution.[13-14] For non-ideal voltammograms, foot of the wave analysis (FOWA) is often used to extract TOF_{max} from the "foot" of the catalytic wave.[11,13] The η_{eff} is defined as the difference between $E_{cat/2}$ and the thermodynamic potential of the reaction of interest under catalytic conditions (E_{rxn}; eq 1.2).[9-10] In Fe(por)-catalyzed ORR, $E_{cat/2}$ is equivalent to the iron(III)/iron(II) reduction potential, $E_{1/2}(Fe^{III}/Fe^{II})$, and E_{rxn} is the ORR equilibrium potential under the reaction conditions, $E_{O2/H2O}$ (eq 1.3).[10-12,15]

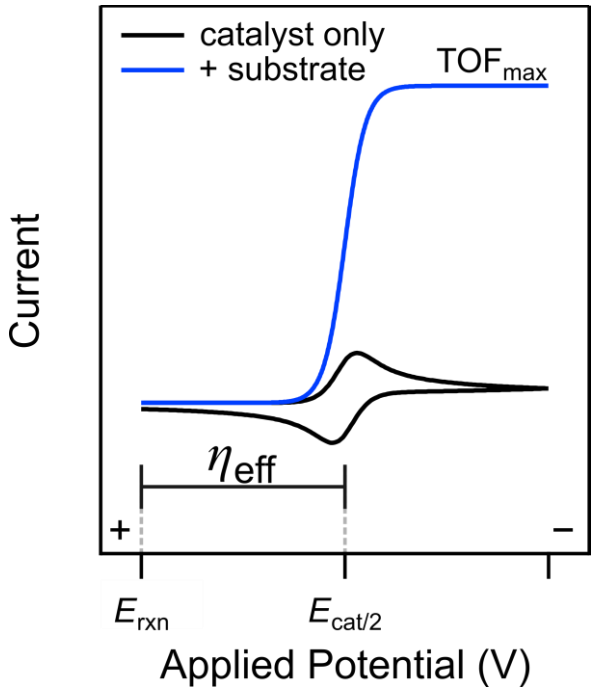

Figure 1.1. Simulated voltammograms of an electrocatalytic (*EC'*) reaction driven by a molecular catalyst in the presence (blue) and absence (black) of substrate. E_{rxn} is the equilibrium potential of the catalyzed reaction, and $E_{rxn} - E_{cat/2}$ is the reaction overpotential (η_{eff}). Adapted with permission from ref [7]. Copyright 2018 American Chemical Society.

$$\eta_{eff} = E_{rxn} - E_{cat/2} \quad \text{(eq 1.2)}$$

$$\eta_{eff} = E_{O_2/H_2O} - E_{1/2}(Fe^{III}/Fe^{II}) \quad \text{(eq 1.3)}$$

1.4 Standard and Equilibrium Potentials

The thermodynamic potential of a catalyzed reaction is needed to determine the η_{eff}.[9-10] Until recently, however, the standard potentials were not known for ORR or many other multi-proton/multi-electron reactions in organic solvents. Building on Roberts and Bullock's seminal work,[16] Roberts, Appel, and our laboratory developed a method to estimate such potentials from the aqueous standard potential and the nonaqueous standard hydrogen potential ($E^o_{H+/H2}$; collected

from open-circuit potential measurements in the organic solvent of interest containing an acid/base buffer of known pK_a) using a thermochemical cycle (**Scheme 1.1**).[17] This approach has been used to determine the standard potentials for reductions of O_2, CO_2, and N_2 to various products in acetonitrile (MeCN) and dimethylformamide (DMF).[17-18]

$$E_{O_2/H_2O} = E^{\circ}_{O_2/H_2O} - \frac{2.303RT}{4F}\log\left(\frac{[H_2O]^2[A^-]^4}{P_{O_2}[HA]^4}\right) - (0.0592\text{V})\text{p}K_a \qquad \text{(eq 1.4)}$$

The *equilibrium* potential under catalytic conditions (E_{rxn}) almost always differs from the standard potential because standard-state conditions (e.g. $[H_2O]$ = 1M) are almost never used. The equilibrium potential is given by the Nernst equation (eq 1.4 for the ORR), which includes the concentrations or pressures of all species involved and the acid pK_a. To determine E_{rxn}, we strongly recommend that catalytic solutions be buffered with 1:1 acid (HA) and conjugate base (A^-).[12,19-20] If only HA is present initially in a catalytic reduction, then the $[A^-]$ at the electrode is not known, and $E_{O2/H2O}$ is undefined. Additionally, homoconjugation of acids and their conjugate bases in organic media ($AH\cdots A^-$) can strongly affect the $[HA]/[A^-]$ ratio unless their concentrations are equal.[12,19-20]

The methods described in this section allow for straightforward determination of the thermodynamic efficiencies of molecular catalysis for many proton-coupled electron transfer (PCET) reactions. We encourage authors to take advantage of these approaches so that they may report η_{eff} in addition to TOF_{max} in their studies.

Scheme 1.1. Thermochemical cycle to estimate $E^{o}_{O2/H2O}$ in nonaqueous solvents from $E^{o}_{H+/H2}$. Adapted from [17]

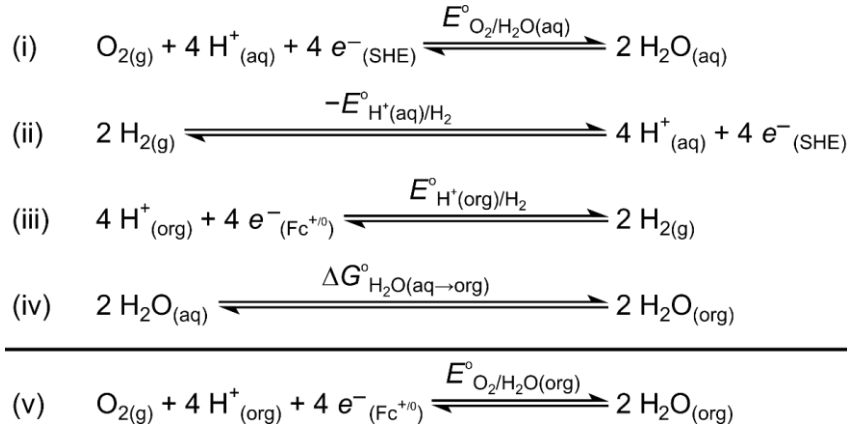

1.5 Scaling Relationships 1: Identifying Correlations

Using the above approaches, we determined kinetic (TOF_{max}) and thermodynamic (η_{eff}) values for many Fe(por) ORR catalysts under different conditions. Analysis of these data showed linear correlations between $\log(TOF_{max})$ and η_{eff} (eq 1.5, **Figure 1.2A**).[10] Such correlations between kinetic and thermodynamic parameters have often been used to derive structure/activity relationships for molecular electrocatalysts.[10,21-23] Correlations using TOF_{max} values are not quite linear free energy relationships (LFERs), because TOF_{max} values depend on reaction conditions. However, changes in $\log(TOF_{max})$ are linear with changes in $\Delta G^{\ddagger}$ as long as the reaction conditions do not change (eq 1.7). Most importantly, normal LFERs correlate a rate parameter with the free energy *for that particular step*. Thus, TOF_{max} values should not in general correlate with the *overall* reaction energetics η_{eff}, which cover many steps. In fact, there are multiple $\log(TOF_{max})/\eta_{eff}$ correlations, as described below.

$$\log(\mathrm{TOF}_{\max}) = m(\eta_{\mathrm{eff}}) + \mathrm{C} \qquad \text{(eq 1.5)}$$

$$k = (\kappa k_b T / h)\exp(-\Delta G^{\ddagger} / RT) \qquad \text{(eq 1.6)}$$

$$\Delta\log(\mathrm{TOF}_{\max}) = -\Delta(\Delta G^{\ddagger} / RT) \qquad \text{(eq 1.7)}$$

Plotting $\log(TOF_{max})$ vs. η_{eff} is the simplest way to compare the efficiencies of a set of molecular electrocatalytic systems (**Figure 1.2**), where each $(\log(TOF_{max}), \eta_{eff})$ point describes a catalytic system. The closer these points are to the top-left corner of the plot, the better the system (faster rates, lower overpotentials).[21,24-25] For instance, the points at the top right of **Figure 1.2A** represent spectacularly rapid ORR catalysts (TOF_{max} values $>10^6$ s^{-1}, the fastest known), yet the high rates come at a cost of high overpotentials (η_{eff} >1.2 V).[10] Similar tradeoffs in $\log(TOF_{max})/\eta_{eff}$ are observed for other electrocatalysts and reactions. For example, the scaling relationships in **Figure 1.2A** for eleven different Fe(por) ORR catalysts resemble those in **Figure 1.2B** for hydrogen evolution electrocatalysis by nickel phosphine-amine complexes.[26] The different slopes of the lines in **Figure 1.2B** indicate that the catalytic TOF_{max} varies in different ways depending on how η_{eff} is changed (see Sections 1.7-1.8).

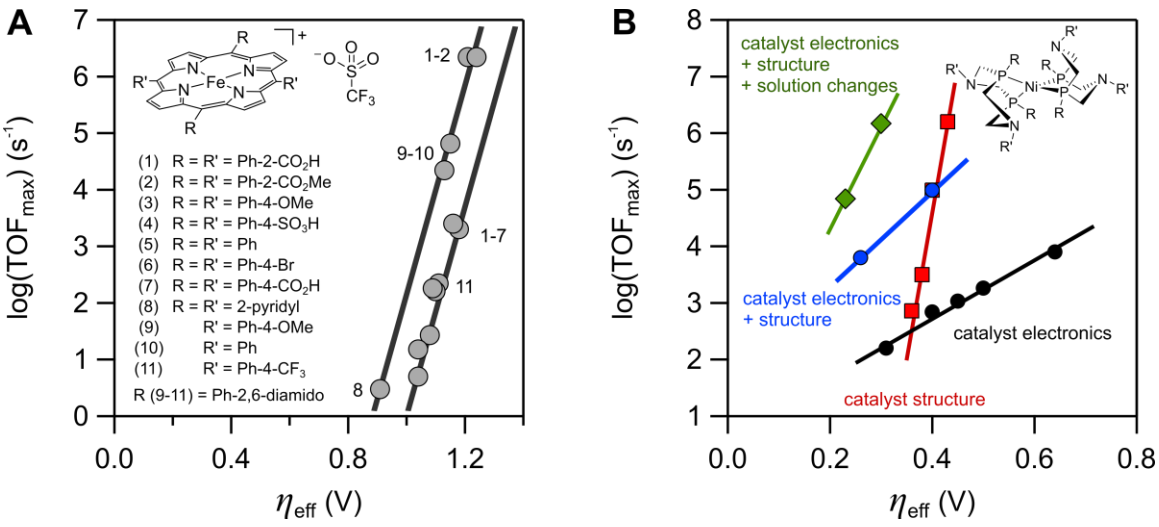

Figure 1.2. Plots of log(TOF$_{max}$) *vs.* η_{eff} for the ORR catalyzed by various Fe(por) complexes and for catalytic hydrogen evolution by a series of structurally similar nickel phosphine-amine complexes. (**A**) Fe(por) complexes studied using DMF-H$^+$ in MeCN and DMF (some catalysts [inset] were studied in both solvents, see[10]). (Adapted with permission from ref [10]. Copyright 2016 American Chemical Society.) (**B**) Nickel phosphine-amine complexes, where the lines describe scaling relationships between TOF$_{max}$ and η_{eff}. (Adapted with permission from ref [26]. Copyright 2018 American Chemical Society.)

The scaling relationships common to heterogeneous electrocatalysis are also kinetic/thermodynamic relationships,[5-6] but they are otherwise quite different from the molecular examples above. Heterogeneous scaling relationships typically correlate current density at a given overpotential with a single relevant scaling 'descriptor' chosen by the researcher. Thermochemical descriptors such as the surface–H or surface–OH bond strengths are common, because they are both relevant to catalytic steps and relatively easy to compute.[5-6] The heterogeneous analysis assumes that the free energies of the important intermediates all scale with the descriptor (the "*scaling"* relationship). Plots of rate vs. the descriptor frequently show a "volcano" shape, where the peak position can provide valuable predictions for a particular mechanism (see [27] regarding criticisms of this approach).[5,28-29]

In contrast, the next section shows that molecular electrocatalysts often have more complex mechanisms, in which electrons and protons are often added in separate steps. The subsequent Sections (1.7-1.9) then bring together these tools and results to understand ORR catalysis by soluble iron-porphyrins, and to thereby develop the more complex molecular scaling relationships that correlate TOF$_{max}$ and η_{eff}.

1.6 The Mechanism of O_2 Reduction by Iron Porphyrins in Nonaqueous Solvents

Deriving $\log(TOF_{max})/\eta_{eff}$ relationships for molecular electrocatalysts relies on knowing the catalytic rate law. This section describes our parallel electrochemical and homogeneous studies of O_2 reduction catalyzed by iron tetraphenylporphyrin, Fe(TPP), as a case study.[30] In acidified, anaerobic DMF, voltammograms of Fe(TPP) showed a reversible Fe^{III}/Fe^{II} redox couple.[30-31] Upon saturating the solution with O_2, a large, irreversible current appeared, centered over $E_{1/2}(Fe^{III}/Fe^{II})$ (**Figure 1.3A**). The shape of the voltammogram suggested an *EC'* mechanism, where rapid, reversible ET was followed by irreversible chemical step(s).[11] From such voltammograms, TOF_{max} values were calculated using foot-of-the-wave analysis (FOWA).[13,32] The variation of TOF_{max} with reaction conditions showed that the reaction was first-order in [Fe(TPP)], $[O_2]$, and [acid] and yielded the third-order rate constant, k_{cat} (eq 1.8-1.9).[30-31]

$$\frac{d[O_2]}{dt} = k_{cat}[HA][O_2][Fe(TPP)] \qquad \text{(eq 1.8)}$$

$$TOF_{max} = k_{cat}[HA][O_2] \qquad \text{(eq 1.9)}$$

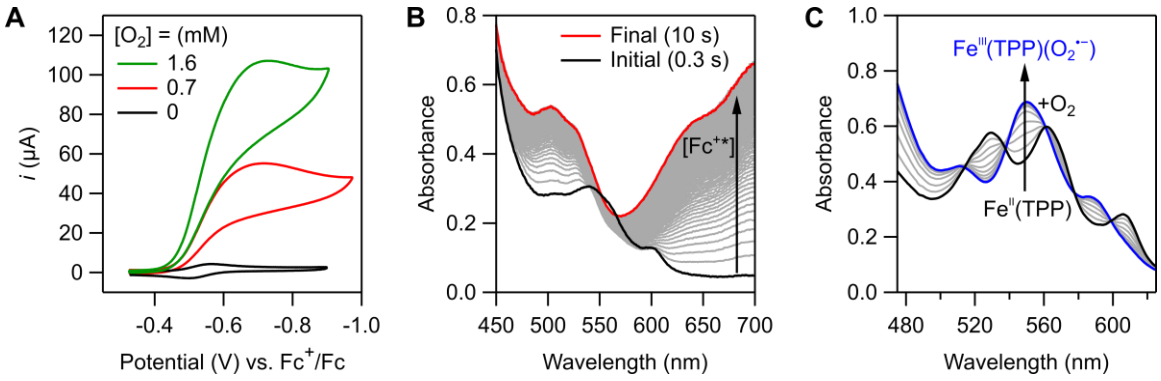

Figure 1.3. Representative voltammograms, stopped-flow, and optical spectra used to study O_2 reduction using Fe(TPP). (**A**) Voltammograms of 0.3 mM $[Fe^{III}(TPP)]OTf$ in the presence of 1 M *p*TsOH and varying $[O_2]$. (**B**) Stopped-flow optical spectra for the reaction of O_2 (0.33 mM), *p*TsOH (50 mM), and Fc* (3 mM) catalyzed by $[Fe^{III}(TPP)]OTf$ (30 μM), showing the formation of Fc^{*+} (arrow). (**C**) Optical spectra of a titration of O_2-saturated DMF into a solution of 50 μM $Fe^{II}(TPP)$ and 0.1 M $[n\text{-}Bu_4N][PF_6]$ at 213 K. Figures adapted with permission from ref [30]. Copyright 2019 American Chemical Society.

The rate law indicated an ORR mechanism of initial electron transfer (ET) to form $Fe^{II}(TPP)$, pre-equilibrium O_2-binding to form the iron-superoxo complex, $Fe^{III}(TPP)(O_2^{\bullet-})$, and rate-limiting protonation of $Fe^{III}(TPP)(O_2^{\bullet-})$ (**Figure 1.4**).[30] To probe the underlying thermochemistry of these intermediates, we examined both equilibrium and catalytic ORR reactions using

decamethylferrocene (Fc*) as the terminal reductant and *p*-toluene sulfonic acid (*p*TsOH) as the acid.

The thermodynamics of the two pre-equilibrium steps—ET and O_2 binding—were measured directly using variable temperature UV-vis spectroscopy. For example, addition of O_2 to Fe^{II}(TPP) showed reversible formation of Fe^{III}(TPP)($O_2^{\bullet-}$) (**Figure 1.3C**). Van ´t Hoff analyses of the derived equilibrium constants for ET (K_{ET}) and O_2 binding (K_{O2}) yielded the $\Delta H°$ and $\Delta S°$ for both steps.[30]

The catalytic reaction was monitored by variable-temperature optical stopped-flow, combining a solution of [Fe^{III}(TPP)]OTf, O_2, and *p*TsOH with a solution of Fc* (**Figure 1.3B**). Globally fitting the kinetic data using COPASI[33] gave thermochemical parameters for the ET and O_2 pre-equilibria that agreed with the values obtained from the van ´t Hoff analyses, providing strong evidence for the proposed mechanism. The derived rate constants showed a significant activation barrier for proton transfer (PT). Computations revealed that much of this barrier stemmed from the requisite formation of a pre-association complex involving an acid molecule, DMF solvent, and Fe^{III}(TPP)($O_2^{\bullet-}$). Under conditions where Fe^{II}(TPP) is the predominant catalyst resting state, $k_{cat} = K_{O2}k_{PT}$; thus, changes to either (or both) of these terms will impact TOF_{max}.[30]

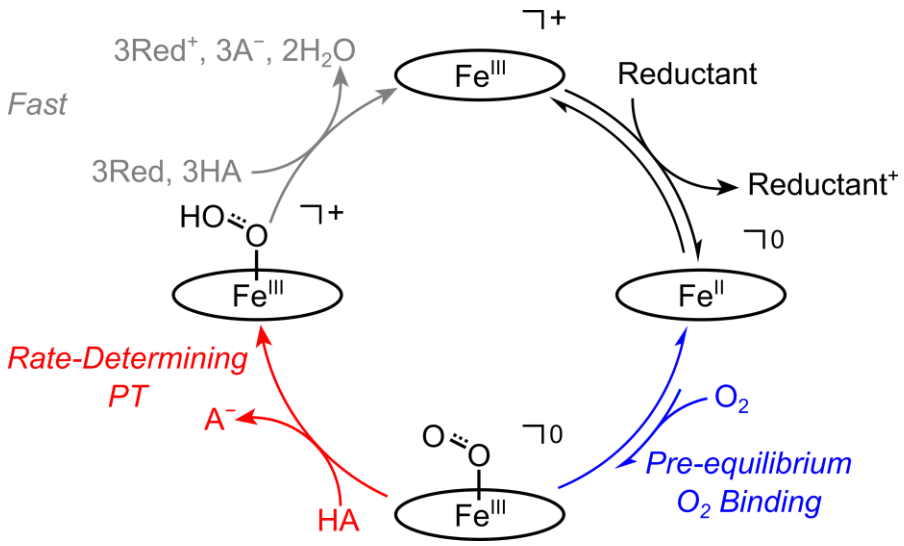

Figure 1.4. General mechanism for O_2 reduction catalyzed by Fe(por) in DMF or MeCN, with the porphyrin abbreviated as an oval. "Reductant" can be either a chemical reductant or an electrode. Adapted with permission from ref [30]. Copyright 2019 American Chemical Society.

1.7 Scaling Relationships 2: Effects of Catalyst $E_{1/2}$ and Buffer pK_a on Fe(por)-Catalyzed O_2 Reduction

The mechanistic conclusions provided a more quantitative understanding of the relationship between log(TOF_{max}) and η_{eff}. The variation in TOF_{max} is due to changes in $\Delta G^{\ddagger}$, which is (under most conditions) the sum of the free energy for pre-equilibrium O_2 binding ($\Delta G°_{O2}$) and the barrier for protonation ($\Delta G^{\ddagger}_{PT}$) of Fe^{III}(por)($O_2^{\bullet-}$) by exogenous acid (eq 1.10, **Figure 1.5**).[30] $\Delta G°_{O2}$ depends on the catalyst, and $\Delta G^{\ddagger}_{PT}$ is well approximated via the Brønsted law, as a fraction (α) of the PT driving force, $\Delta G°_{PT}$. $\Delta G°_{PT}$ is, in turn, given by the difference in pK_a between the acid and Fe^{III}(TPP)($O_2^{\bullet-}$) (eq 1.11). Values of $\Delta G°_{O2}$ and $\Delta G°_{PT}$ are therefore influenced by intrinsic properties of the catalyst system, namely the catalyst $E_{1/2}$ and buffer pK_a. Changes in the overpotential are described by (eq 1.3) above, $\eta_{eff} = E_{O2/H2O} - E_{1/2}(Fe^{III}/Fe^{II})$.

$$\Delta G^{\ddagger} = \Delta G^{\circ}_{O_2} + \Delta G^{\ddagger}_{PT} \qquad \text{(eq 1.10)}$$

$$\Delta G^{\ddagger}_{PT} = \alpha \Delta G^{\circ}_{PT} = \alpha 2.303\left[\mathrm{p}K_a(\mathrm{HA}) - \mathrm{p}K_a\left\{ \mathrm{Fe^{III}(por)}(\mathrm{O_2^{\bullet-}}) \right\} \right] \qquad \text{(eq 1.11)}$$

1.7.1 Effect of catalyst $E_{1/2}$

The empirical scaling line in **Figure 1.5A** corresponds to systems in which only $E_{1/2}$ was varied. Changes in $E_{1/2}$ do not shift the ORR equilibrium potential; thus, $\Delta\eta_{eff} = -\Delta E_{1/2}$. In terms of TOF_{max}, changes in $E_{1/2}$ affect both $\Delta G°_{O2}$ (K_{O2}) and the pK_a of the superoxide complex (eq 1.12).

A quantitative understanding of the effects of $E_{1/2}$ on TOF for Fe(por)-catalyzed ORR required computational determination of pK_{O2} and pK_a([Fe(por)($O_2H^{\bullet}$)]$^+$) values by our collaborators Dr. Neeraj Kumar and Dr. Simone Raugei. These values both correlated linearly with the experimental $E_{1/2}$: ΔpK_{O2} = 11($\Delta E_{1/2}$) and ΔpK_a([Fe(por)($O_2H^{\bullet}$)]$^+$) = −28($\Delta E_{1/2}$).[10] Inserting these values and the Brønsted α measured for Fe(por)-catalyzed ORR (0.3) into eq 1.12 gives eq 1.13, which predicts a log(TOF_{max})/η_{eff} slope of 19 decades (dec) in TOF_{max} per V in $\Delta\eta_{eff}$.[10,15]

$$\Delta \log(\mathrm{TOF_{max}}) = -\Delta \mathrm{p}K_{\mathrm{O_2}} + \alpha \Delta \mathrm{p}K_a\left(\left[\mathrm{Fe(por)(O_2H^{\bullet})} \right]^+ \right) \qquad \text{(eq 1.12)}$$

$$\Delta \log(\mathrm{TOF_{max}}) = -(11 + 28\alpha)\Delta E_{1/2} = (-19\ \mathrm{dec/V})\Delta E_{1/2} = (19\ \mathrm{dec/V})\Delta \eta_{\mathrm{eff}} \qquad \text{(eq 1.13)}$$

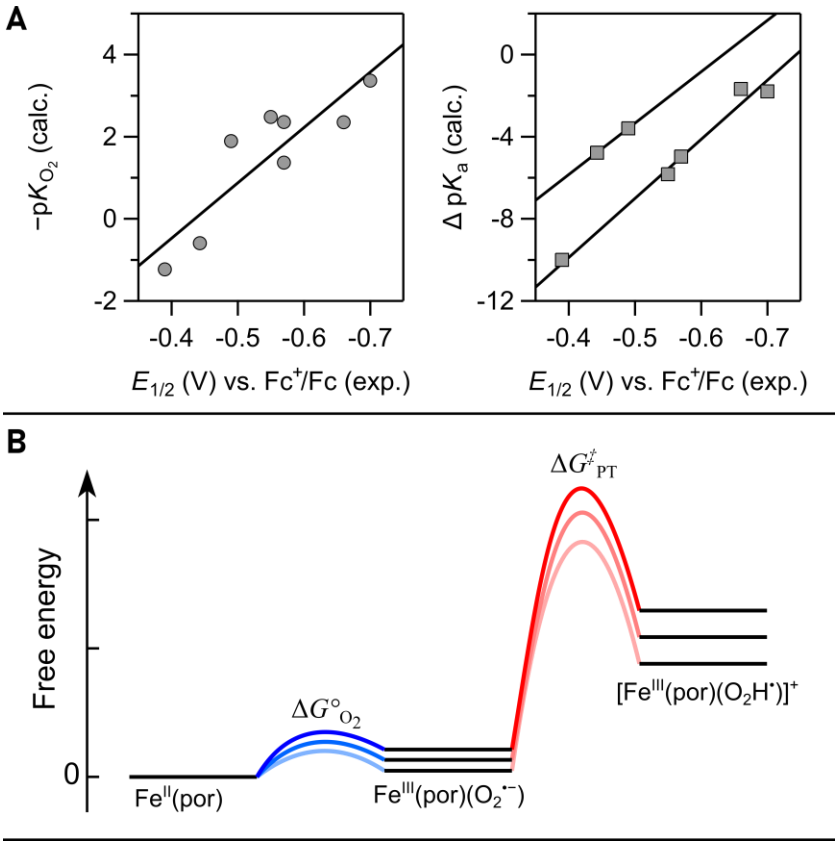

Figure 1.5. Thermodynamic relationships between (i) pK_{O2} and (ii) ΔpK_a[Fe^{III}(por)(O$_2$H$^\bullet$)]$^+$ − pK_a[DMF-H] with catalyst $E_{1/2}$ with representative free energy profiles. (**A**) Computed values for O_2 binding (pK_{O2}, left) and pK_a[Fe^{III}(por)(O$_2$H$^\bullet$)]$^+$ − pK_a[DMF-H]$^+$ (right) with $E_{1/2}$(Fe^{III}/Fe^{II}) for some of the Fe(por) in Fig. 2A (ref [10]). (**B**) Chemical steps to the rate-determining step and their free energy profile for three different Fe(por) catalysts, equivalent to eq 1.10. Adapted with permission from ref [10]. Copyright 2016 American Chemical Society.

This analysis shows how the electronic structure of the catalyst modulates the barrier for catalysis. Catalysts with more negative $E_{1/2}$ values yield faster TOF_{max} values because O_2 binding is more favorable (larger K_{O2}) and the iron superoxide intermediate is more basic (higher pK_a). The combination of experimental and computational results enabled us to quantitatively interpret the slopes of these intrinsic scaling relationships for a series of catalysts with similar electronic structures.

1.7.2 Effect of buffer pK_a

A similar scaling relationship can be derived for a set of catalytic systems in which a single Fe(por) catalyst is evaluated using buffers with different pK_a values.[15] Changing the buffer identity shifts the ORR equilibrium potential because higher proton activity makes O_2 reduction more favorable. From the Nernst equation (eq 1.14, above), each unit decrease in pK_a causes an

increase in E_{ORR} by 0.0592 V ($\Delta\eta_{eff}$ = –(0.0592 V)ΔpK_a). For the TOF_{max}, a change in the buffer acidity usually only affects the rate of the PT step via the Brønsted law (eq 1.14; exceptions are described below). This leads to a new scaling relationship (eq 1.15) with a predicted scaling slope *m* of 5.1 dec/V ($\alpha = 0.3$, as above). **Figure 1.6** shows this as the purple line, with experimental results (purple points).[15]

$$\Delta \log(\mathrm{TOF}_{max}) = -\alpha\left[\Delta pK_a(\mathrm{HA})\right] \quad \text{(eq 1.14)}$$

$$\alpha\left[\Delta pK_a(\mathrm{HA})\right] = m\left(0.0592\left[\Delta pK_a(\mathrm{HA})\right]\right)$$
$$\therefore\ m = (\alpha / 0.0592) = (5.1\ \mathrm{dec/V}) \quad \text{(eq 1.15)}$$

1.7.3 Discussion of $E_{1/2}$ and pK_a scaling relationships

Equations 1.13 and 1.15 show that changes in the two key intrinsic properties of the catalytic system, $E_{1/2}$ and buffer pK_a, have very different effects on the scaling slopes. The $\log(TOF_{max})/\eta_{eff}$ relationship is 3.6 times shallower when pK_a is changed rather than $E_{1/2}$. As a result, η_{eff} can be improved with less penalty to TOF_{max} by changing the buffer instead of catalyst identity. For example, replacing $[DMF\text{-}H]^+$ with trifluoroacetic acid (ΔpK_a = 6.0 in DMF) gave a 10^4 increase in TOF_{max} relative to the predicted value for changing η_{eff} by the same amount via $E_{1/2}$ (**Figure 1.6**).[15] The shallow dependence on pK_a arises because proton transfer is the rate-limiting step, and thus the proton transfer barrier ($\Delta G^{\ddagger}_{PT}$) changes by only a fraction ($\alpha = 0.3$) of the $\Delta G°_{PT}$. In contrast, pre-equilibrium steps will usually be more sensitive to η_{eff}. For example, Wang and Stahl discovered that cobalt-catalyzed O_2 reduction to H_2O_2 showed a shallow $\log(TOF_{max})/\eta_{eff}$ correlation as the catalyst was varied, 6 dec/V versus the 18.5 dec/V we found for Fe(por).[22] The origin of this difference was traced to differences in initial O_2 binding. The Fe(por) catalysts have unfavorable K_{O2} pre-equilibria that are strongly dependent on $E_{1/2}$. In contrast, O_2-binding to the cobalt catalysts is strongly favored regardless of $E_{1/2}$. These examples show that there are many possible $\log(TOF_{max})/\eta_{eff}$ scaling relationships, depending on the mechanism of catalysis and the property of the catalytic system being varied.

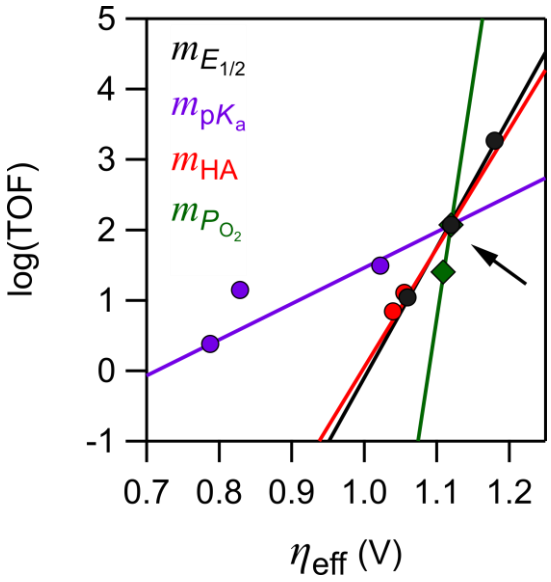

Figure 1.6. Various scaling relations for Fe(por) ORR catalysis predicted (lines) and measured (points) upon changing the acid concentration (red), partial pressure of O_2 (green), acid pK_a (purple), and catalyst $E_{1/2}$ (black; additional data points shown in **Figure 1.2A**). The intersection point (arrow) is Fe(TPP)OTf with 100 mM H-DMF$^+$ under 1 atm O_2. Adapted with permission from ref [15]. Copyright 2017 American Chemical Society.

1.8 Scaling Relationships 3: Effects of Concentrations

Molecular scaling relationships can also be derived for the effects of experimental or operational conditions on the catalyst system. The simplest operational choice is the concentrations of the reagents, which includes P_{O2}, [HA], [A^-], and [H_2O] for the ORR. Varying each of these parameters influences the log(TOF$_{max}$)/η_{eff} slopes in unique, predictable ways.[15]

For changes in concentrations, the slope m of a scaling relationship (eq 1.5) can be precisely derived from the kinetic and thermodynamic equations (eq 1.9 and eq 1.4, repeated here for ease of presentation).

$$\log(\mathrm{TOF}_{max}) = m(\eta_{eff}) + \mathrm{C} \qquad \text{(eq 1.5)}$$

$$\mathrm{TOF}_{max} = k_{cat}[\mathrm{HA}][\mathrm{O_2}] \qquad \text{(eq 1.9)}$$

$$E_{\mathrm{O_2/H_2O}} = E^{\circ}_{\mathrm{O_2/H_2O}} - \frac{2.303RT}{4F}\log\left(\frac{[\mathrm{H_2O}]^2[\mathrm{A^-}]^4}{P_{\mathrm{O_2}}[\mathrm{HA}]^4}\right) - (0.0592\mathrm{V})\mathrm{p}K_a \qquad \text{(eq 1.4)}$$

Since catalysis is first order in [HA] and P_{O2} (proportional to [O_2]), a 10-fold increase in either results in a 10-fold increase in TOF. Changing the [A^-] or [H_2O], however, does not influence the TOF, since neither appears in the rate law. Tenfold increases in these concentrations all shift η_{eff} in different ways: +59 mV for [HA], –59 mV for [A^-], –30 mV for [H_2O], and +15 mV for P_{O2}.

Experiments confirm these predictions, as shown by the red and green points (experiments) and lines (theory) in **Figure 1.6**.[15] The log(TOF_{max})/η_{eff} slopes for [HA] and P_{O2} differ by a factor of four because [HA] and P_{O2} contribute equally to the kinetics (eq 1.9) but have different stoichiometries in the ORR, four HA per O_2, which set the exponents in the Nernst equation (eq 1.4).

The ability to predict the relationship between log(TOF_{max}) and η_{eff} means that a wide parameter space can be predictably accessed simply by changing the solution conditions for a single catalyst. This conclusion is valuable because most catalysis research involves some searching of parameter space for the best catalytic results (including studies from the authors and those critical of this section[24,34]). Another important use of this log(TOF_{max})/η_{eff} concentration analysis is to enable quantitative comparisons of catalytic systems that were studied under different conditions.

1.9 Scaling Relationships 4: Summative Effects

We recently discovered a log(TOF_{max})/η_{eff} scaling relationship with a *negative* slope, using the polycationic iron αβαβ-trimethylanilinium porphyrin [Fe(*o*-TMA)] and various carboxylic acid buffers (**Figure 1.7**).[35] The simultaneous improvement in both TOF_{max} and η_{eff} was unlike all of the scaling relationships above, which had *positive* slopes and involved tradeoffs between TOF_{max} and η_{eff}. However, despite seemingly haven "broken" from the scaling relationships, we demonstrated that this unprecedented result could be predicted by combining the known pK_a and $E_{1/2}$ relationships developed for our Fe(por) systems.

When studied under conditions identical to those of other Fe(por) ORR catalysts (buffered [DMF-H^+]), Fe(*o*-TMA) fell close to one of the original $E_{1/2}$ scaling relationships.[10,35] Thus, the highly cationic ligand did not improve or even affect catalysis, in contrast to what was reported for CO_2 electroreduction.[25,36] The inverse scaling for Fe(*o*-TMA) with buffered carboxylic acids only occurred because the buffer affected both pK_a and $E_{1/2}$. Buffers with weaker acids (higher pK_a) gave much more negative $E_{1/2}$ values with a roughly linear dependence (**Figure 1.7B**). The $E_{1/2}$ shifts were due to axial ligand binding of the anionic carboxylates,[35,37] an electrostatic effect seen only with anionic ligands and only to the pentacationic catalyst.[15] Because the buffer identity affected both pK_a and $E_{1/2}$, neither individual scaling relationship predicted the composite changes

in the catalytic system. However, by considering changes made to *both* the pK_a and $E_{1/2}$ components, the individual data points and inverse log(TOF$_{max}$)/η_{eff} correlation could be predicted *quantitatively*.[35]

$$\vec{v}_{pK_a} = \left\langle \Delta\eta_{eff}, \Delta\log(TOF_{max}) \right\rangle = \left\langle -0.059(\Delta pK_a), -\alpha(\Delta pK_a) \right\rangle \quad \text{(eq 1.16)}$$

$$\vec{v}_{E_{1/2}} = \left\langle \Delta\eta_{eff}, \Delta\log(TOF_{max}) \right\rangle = \left\langle -\Delta E_{1/2}, -18.5(\Delta E_{1/2}) \right\rangle \quad \text{(eq 1.17)}$$

$$\vec{v}_{sum} = \vec{v}_{pK_a} + \vec{v}_{E_{1/2}} \quad \text{(eq 1.18)}$$

Using the scaling relations specifically derived for Fe(por)-catalyzed ORR, the *experimental* changes in pK_a and $E_{1/2}$ in this system were mathematically represented as vectors in the log(TOF$_{max}$)/η_{eff} space (eq 1.16-1.17). For instance, the vector in eq 1.16 describes how changes in pK_a (ΔpK_a) affect both η_{eff} and log(TOF$_{max}$) according to the pK_a relationship described in Section 1.7. An analogous vector exists for changes in $E_{1/2}$ (eq 1.17). The sum of these two vectors (eq 1.18) predicts net changes in η_{eff} and log(TOF$_{max}$) using only experimental values for ΔpK_a and $\Delta E_{1/2}$.

For example, replacing $CF_3C(O)OH$ with $CH_3C(O)OH$ gave ΔpK_a = 10.9 and $\Delta E_{1/2}$ = −0.302. The sum of these changes predicted (eq 1.16-1.18) both the directionality and distance in the observed data: the black + purple vectors sum to the blue vector in **Figure 1.7**. This result is a first-of-a-kind application of molecular scaling relationships, where a tandem, two-scaling relationship approach can be used to simultaneously improve both rates and overpotentials.[35]

We believe that similar vector analyses could be applied to any multi-step molecular electrocatalytic reaction where different properties of the catalyst system show different log(TOF$_{max}$)/η_{eff} relationships. This requirement is typically fulfilled because multi-step reactions often have pre-equilibrium and rate-limiting steps with different stoichiometries and free energies. Implementing different combinations of these scaling relationships should allow optimization—in some cases via inverse scaling—to achieve faster rates at lower overpotentials.

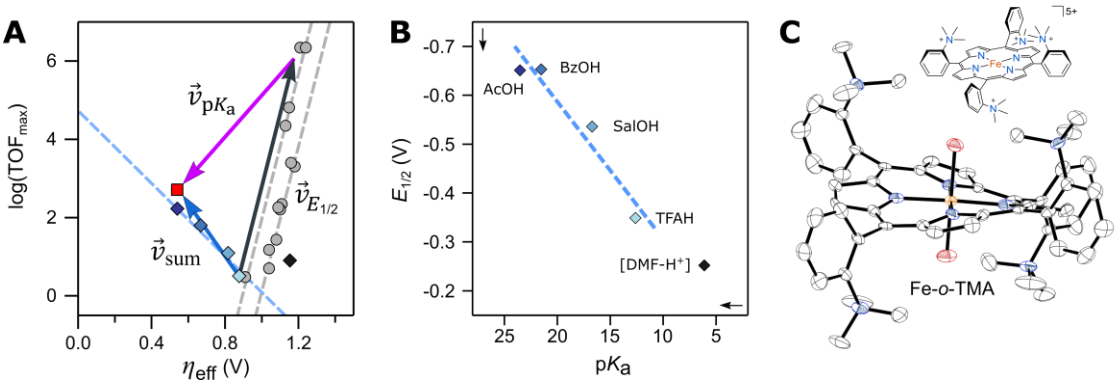

Figure 1.7. Catalytic system efficiencies, pK_a vs. $E_{1/2}$ relationship, and structure of Fe(*o*-TMA). (**A**) Plot of log(TOF$_{max}$) vs. η_{eff} for catalytic systems of Fe(*o*-TMA) and varying buffers (blue diamonds match buffers in (**B**)). Superimposed vectors show predicted changes from ΔpK_a (purple), $\Delta E_{1/2}$ (black) and summative effects (blue). The predicted/observed values for acetic acid buffer are the red square/dark-blue diamond. Prior Fe(por) data and $\Delta E_{1/2}$ scaling relationships included for reference (grey). (**B**) Plot of $E_{1/2}$ vs. acid pK_a at 0.1 M buffer. (**C**) Drawing of Fe(*o*-TMA) and solid-state x-ray crystal structure of [Fe(*o*-TMA)•2H$_2$O]OTf$_5$ (H atoms and triflates omitted, thermal ellipsoids at 50% probability). Figures adapted with permission from ref [35]. Copyright 2020 American Association for the Advancement of Science.

1.10 Coupling Intrinsic and Operational Parameters of a Catalytic System

The previous sections show how the efficiency of a *catalytic system* can be improved by changing the catalyst and solution conditions. In many of these examples, the "intrinsic" properties of the system (*e.g.*, $E_{1/2}$, pK_a, and catalyst identity) are independent of the "operational" conditions like substrate concentrations.[15,34] However, the intrinsic and operational parameters cannot always be separated. In the Fe(*o*-TMA) system above, the nature and concentration of the buffer affect $E_{1/2}$ via carboxylate binding to the catalyst. The change in catalyst speciation with respect to the solution composition is what enables inverse scaling.[35]

Another example occurs when a catalyst's ligand contains protonatable functionalities such that changes to acid concentration (an operational parameter) can influence the intrinsic properties of the catalyst. For instance, our studies of the ORR catalyzed by iron tetra-*o*-pyridylporphyrin showed a very unusual inverse-order dependence on [DMF-H$^+$].[10] The decrease in TOF$_{max}$ occurred in tandem with an 88 mV shift in $E_{1/2}$ per decade increase in [DMF-H$^+$], which was attributed to protonation equilibria among the many proteomers (**Figure 1.8**). The increase in $E_{1/2}$ caused decreases in both K_{O2} and the basicity of the superoxide adduct. Because variation in acid concentration, an operational parameter, changes the intrinsic *catalyst identity*, the two parameters are inherently connected and must be considered together when analyzing log(TOF$_{max}$)/η_{eff} relationships.

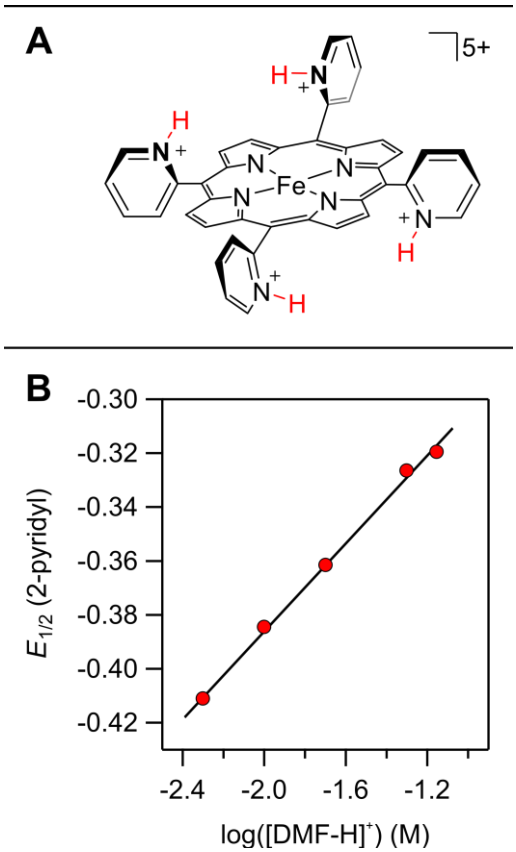

Figure 1.8. Iron *o*-pyridylporphyrin, shown as the tetra-protonated complex, and its $E_{1/2}$ as a function of [HA]. Adapted with permission from ref [10]. Copyright 2016 American Chemical Society.

Many other electrocatalytic systems likely exhibit similar complex relationships between intrinsic and operational parameters. It is therefore more valuable to consider globally how all solution components affect catalyst behavior. The alternative approach emphasizing only standard state conditions can miss these cooperative effects. In addition, measurements and extrapolations to standard states are challenging, and are in practice almost never done (even by those who advocate for such an approach[24-25]). We emphasize that the linkage between various parameters of a catalytic system is not a complication but rather *an opportunity*. Cooperativity between the catalyst active site and surrounding medium is an exciting, underexplored approach to improving catalysis.

1.11 Conclusions and Prospects

This Account surveys our examination of oxygen reduction reaction (ORR) catalysis by soluble iron porphyrins (Fe(por)) in organic solvents, which builds from a fundamental

understanding of the reaction thermodynamics, kinetics, and mechanism. We developed procedures to determine nonaqueous standard potentials for the ORR and other PCET half reactions, and we examined the rate law and mechanism of Fe(por)-catalyzed ORR using both electrochemical and homogeneous techniques. Key reaction intermediates were identified and their thermochemistry measured. Examining our large dataset of turnover frequencies and thermochemical overpotentials (η_{eff}) revealed a number of empirical linear correlations, $\log(TOF_{max}) = m(\eta_{eff}) + C$, when one component of the catalytic system is changed.

Such "molecular scaling relationships" have been found in several reactions, including H_2 evolution and O_2 reduction to water or hydrogen peroxide[10,14,22,27,35,38] and could be further developed for any multi-proton/multi-electron catalysis. Deriving relationships between $\log(TOF_{max})$ and η_{eff} requires knowing the rate law for catalysis and the thermodynamics of the reaction of interest. For operational parameters like substrate concentration, the reaction order in substrate and the stoichiometry of that substrate in the overall reaction dictate the slope of the scaling line. Molecular scaling relationships based on intrinsic properties like catalyst $E_{1/2}$ and buffer pK_a require additional experimental or computational inputs.

These connections between kinetics and thermodynamics require linear free energy relationships (LFERs). LFERs, while approximate, have been shown experimentally and computationally to hold for many reaction steps and are key to both molecular scaling relationships and heterogeneous analogs. They assume (*i*) that the free energies of intermediates scale with each other, here the linear scaling of both pK_{O2} and pK_a([Fe(por)($O_2H^{\bullet}$)]$^+$) with $E_{1/2}$, and (*ii*) that $\Delta G^{\ddagger}$ for each step correlates with the $\Delta G°$ for that step, here in the Brønsted catalysis 'law' relating k_{PT} to $\Delta G^{\ddagger}_{PT}$.

Electrocatalysis by soluble molecules is often found to follow mechanisms in which PT and ET occur in *separate* steps of the catalytic cycle. Therefore, changing one component of a catalytic system affects the different steps of the cycle in different ways, and a single scaling parameter cannot provide a complete description. The TOF_{max} for Fe(por)-catalyzed ORR responds very differently when the η_{eff} is varied via the buffer pK_a, which usually affects only the rate-limiting PT step, rather than by changing the catalyst $E_{1/2}$ which affects that step *and* the pre-equilibrium ET

and O_2-binding steps. In contrast, the mechanisms typically used for heterogeneous PCET scaling relationships involve e^-/H^+ addition together, so that the energetics of each step usually correlate with the overall energetics of the multiproton/multielectron reactions, allowing the use of a single scaling parameter such as a surface-H bond strength. For molecular electrocatalysis, using η_{eff} is advantageous as the thermochemical parameter because it considers contributions from multiple system components, and because it is a critical parameter to be optimized.

Molecular scaling relationships are powerful tools for understanding and improving molecular electrocatalytic processes. They predict behavior across a wide range of parameter space, thus enabling comparisons of catalytic systems examined under different conditions. The molecular scaling relationships developed here reveal underlying thermochemical insights about a catalytic system under any conditions, even when standard states are challenging to define. These molecular scaling relationships often can *predict* reactivity under a variety of conditions and with different catalysts. Most notably, these scaling relationships *quantitatively* explain the dramatic improvement in ORR electrocatalysis when using a highly cationic iron porphyrin with buffers containing carboxylic acid buffers. This improvement results from cooperativity between the nominal catalyst and the other components of the catalytic system, emphasizing that both intrinsic and operational parameters must be included in analyses of electrocatalytic processes.

We hope that this chapter will encourage other researchers in the field to use this approach for their systems. Once the thermochemistry and rate law have been established, molecular scaling relationships can be readily derived and used for understanding and improving catalytic performance.

1.12 References

1. Solomon, E. I.; Stahl, S. S., Introduction: Oxygen Reduction and Activation in Catalysis. *Chem. Rev.* **2018,** *118* (5), 2299-2301.
2. Wikström, M.; Krab, K.; Sharma, V., Oxygen Activation and Energy Conservation by Cytochrome c Oxidase. *Chem. Rev.* **2018,** *118* (5), 2469-2490.
3. Mano, N.; de Poulpiquet, A., O_2 Reduction in Enzymatic Biofuel Cells. *Chem. Rev.* **2018,** *118* (5), 2392-2468.
4. Gewirth, A. A.; Varnell, J. A.; DiAscro, A. M., Nonprecious Metal Catalysts for Oxygen Reduction in Heterogeneous Aqueous Systems. *Chem. Rev.* **2018,** *118* (5), 2313-2339.
5. Kulkarni, A.; Siahrostami, S.; Patel, A.; Nørskov, J. K., Understanding Catalytic Activity Trends in the Oxygen Reduction Reaction. *Chem. Rev.* **2018,** *118* (5), 2302-2312.
6. Montemore, M. M.; van Spronsen, M. A.; Madix, R. J.; Friend, C. M., O_2 Activation by Metal Surfaces: Implications for Bonding and Reactivity on Heterogeneous Catalysts. *Chem. Rev.* **2018,** *118* (5), 2816-2862.
7. Pegis, M. L.; Wise, C. F.; Martin, D. J.; Mayer, J. M., Oxygen Reduction by Homogeneous Molecular Catalysts and Electrocatalysts. *Chem. Rev.* **2018,** *118* (5), 2340-2391.
8. Ren, S.; Joulié, D.; Salvatore, D.; Torbensen, K.; Wang, M.; Robert, M.; Berlinguette, C. P., Molecular electrocatalysts can mediate fast, selective CO_2 reduction in a flow cell. *Science* **2019,** *365* (6451), 367-369.
9. Passard, G.; Ullman, A. M.; Brodsky, C. N.; Nocera, D. G., Oxygen Reduction Catalysis at a Dicobalt Center: The Relationship of Faradaic Efficiency to Overpotential. *J. Am. Chem. Soc.* **2016,** *138* (9), 2925-2928.
10. Pegis, M. L.; McKeown, B. A.; Kumar, N.; Lang, K.; Wasylenko, D. J.; Zhang, X. P.; Raugei, S.; Mayer, J. M., Homogenous Electrocatalytic Oxygen Reduction Rates Correlate with Reaction Overpotential in Acidic Organic Solutions. *ACS Cent. Sci.* **2016,** *2* (11), 850-856.
11. Rountree, E. S.; McCarthy, B. D.; Eisenhart, T. T.; Dempsey, J. L., Evaluation of Homogeneous Electrocatalysts by Cyclic Voltammetry. *Inorg. Chem.* **2014,** *53* (19), 9983-10002.
12. Appel, A. M.; Helm, M. L., Determining the Overpotential for a Molecular Electrocatalyst. *ACS Catal.* **2014,** *4* (2), 630-633.
13. Costentin, C.; Drouet, S.; Robert, M.; Savéant, J.-M., Turnover Numbers, Turnover Frequencies, and Overpotential in Molecular Catalysis of Electrochemical Reactions. Cyclic Voltammetry and Preparative-Scale Electrolysis. *J. Am. Chem. Soc.* **2012,** *134* (27), 11235-11242.
14. Costentin, C.; Passard, G.; Savéant, J.-M., Benchmarking of Homogeneous Electrocatalysts: Overpotential, Turnover Frequency, Limiting Turnover Number. *J. Am. Chem. Soc.* **2015,** *137* (16), 5461-5467.
15. Pegis, M. L.; Wise, C. F.; Koronkiewicz, B.; Mayer, J. M., Identifying and Breaking Scaling Relations in Molecular Catalysis of Electrochemical Reactions. *J. Am. Chem. Soc.* **2017,** *139* (32), 11000-11003.
16. Roberts, J. A. S.; Bullock, R. M., Direct Determination of Equilibrium Potentials for Hydrogen Oxidation/Production by Open Circuit Potential Measurements in Acetonitrile. *Inorg. Chem.* **2013,** *52* (7), 3823-3835.
17. Pegis, M. L.; Roberts, J. A. S.; Wasylenko, D. J.; Mader, E. A.; Appel, A. M.; Mayer, J. M., Standard Reduction Potentials for Oxygen and Carbon Dioxide Couples in Acetonitrile and *N*,*N*′-Dimethylformamide. *Inorg. Chem.* **2015,** *54* (24), 11883-11888.
18. Lindley, B. M.; Appel, A. M.; Krogh-Jespersen, K.; Mayer, J. M.; Miller, A. J. M., Evaluating the Thermodynamics of Electrocatalytic N_2 Reduction in Acetonitrile. *ACS Energy Lett.* **2016,** *1* (4), 698-704.
19. Hooe, S. L.; Rheingold, A. L.; Machan, C. W., Electrocatalytic Reduction of Dioxygen to Hydrogen Peroxide by a Molecular Manganese Complex with a Bipyridine-Containing Schiff Base Ligand. *J. Am. Chem. Soc.* **2018,** *140* (9), 3232-3241.
20. Fourmond, V.; Jacques, P.-A.; Fontecave, M.; Artero, V., H_2 Evolution and Molecular Electrocatalysts: Determination of Overpotentials and Effect of Homoconjugation. *Inorg. Chem.* **2010,** *49* (22), 10338-10347.

21. Nichols, E. M.; Derrick, J. S.; Nistanaki, S. K.; Smith, P. T.; Chang, C. J., Positional effects of second-sphere amide pendants on electrochemical CO_2 reduction catalyzed by iron porphyrins. *Chem. Sci.* **2018,** *9* (11), 2952-2960.
22. Wang, Y.-H.; Pegis, M. L.; Mayer, J. M.; Stahl, S. S., Molecular Cobalt Catalysts for O_2 Reduction: Low-Overpotential Production of H_2O_2 and Comparison with Iron-Based Catalysts. *J. Am. Chem. Soc.* **2017,** *139* (46), 16458-16461.
23. Kilgore, U. J.; Stewart, M. P.; Helm, M. L.; Dougherty, W. G.; Kassel, W. S.; DuBois, M. R.; DuBois, D. L.; Bullock, R. M., Studies of a Series of $[Ni(P^{R2}N^{Ph2})_2(CH_3CN)]^{2+}$ Complexes as Electrocatalysts for H_2 Production: Substituent Variation at the Phosphorus Atom of the P_2N_2. *Inorg. Chem.* **2011,** *50* (21), 10908-10918.
24. Costentin, C.; Drouet, S.; Robert, M.; Savéant, J.-M., A local proton source enhances CO_2 electroreduction to CO by a molecular Fe catalyst. *Science* **2012,** *338*, 90-94.
25. Azcarate, I.; Costentin, C.; Robert, M.; Savéant, J. M., Through-Space Charge Interaction Substituent Effects in Molecular Catalysis Leading to the Design of the Most Efficient Catalyst of CO_2-to-CO Electrochemical Conversion. *J. Am. Chem. Soc.* **2016,** *138* (51), 16639-16644.
26. Klug, C. M.; Cardenas, A. J. P.; Bullock, R. M.; O'Hagan, M.; Wiedner, E. S., Reversing the Tradeoff between Rate and Overpotential in Molecular Electrocatalysts for H_2 Production. *ACS Catal.* **2018,** *8* (4), 3286-3296.
27. Quaino, P.; Juarez, F.; Santos, E.; Schmickler, W., Volcano plots in hydrogen electrocatalysis – uses and abuses. *Journal of Nanotechnology* **2014,** *5*, 846-854.
28. Greeley, J.; Jaramillo, T. F.; Bonde, J.; Chorkendorff, I.; Nørskov, J. K., Computational high-throughput screening of electrocatalytic materials for hydrogen evolution. *Nat. Mater.* **2006,** *5* (11), 909-913.
29. Trasatti, S., Work function, electronegativity, and electrochemical behaviour of metals. *J. Electroanal. Chem.* **1972,** *39* (1), 163-184.
30. Pegis, M. L.; Martin, D. J.; Wise, C. F.; Brezny, A. C.; Johnson, S. I.; Johnson, L. E.; Kumar, N.; Raugei, S.; Mayer, J. M., Mechanism of Catalytic O_2 Reduction by Iron Tetraphenylporphyrin. *J. Am. Chem. Soc.* **2019,** *141*, 8315-8326.
31. Wasylenko, D. J.; Rodríguez, C.; Pegis, M. L.; Mayer, J. M., Direct Comparison of Electrochemical and Spectrochemical Kinetics for Catalytic Oxygen Reduction. *J. Am. Chem. Soc.* **2014,** *136* (36), 12544-12547.
32. Costentin, C.; Savéant, J.-M., Multielectron, Multistep Molecular Catalysis of Electrochemical Reactions: Benchmarking of Homogeneous Catalysts. *ChemElectroChem* **2014,** *1* (7), 1226-1236.
33. Hoops, S.; Sahle, S.; Gauges, R.; Lee, C.; Pahle, J.; Simus, N.; Singhal, M.; Xu, L.; Mendes, P.; Kummer, U., COPASI--a COmplex PAthway SImulator. *Bioinformatics* **2006,** *22* (24), 3067-3074.
34. Costentin, C.; Savéant, J.-M., Homogeneous Molecular Catalysis of Electrochemical Reactions: Manipulating Intrinsic and Operational Factors for Catalyst Improvement. *J. Am. Chem. Soc.* **2018,** *140* (48), 16669-16675.
35. Martin, D. J.; Mercado, B. Q.; Mayer, J. M., Combining scaling relationships overcomes rate versus overpotential trade-offs in O_2 molecular electrocatalysis. *Sci. Adv.* **2020,** *6* (11), eaaz3318.
36. Nichols, A. W.; Machan, C. W., Secondary-Sphere Effects in Molecular Electrocatalytic CO_2 Reduction. *Front. Chem.* **2019,** *7*, 397.
37. Lexa, D.; Rentien, P.; Savéant, J. M.; Xu, F., Methods for Investigating the Mechanistic and Kinetic Role of Ligand Exchange Reactions in Coordination Electrochemistry. *J. Electroanal. Chem.* **1985,** *191* (2), 253-279.
38. Wang, Y.-H.; Schneider, P. E.; Goldsmith, Z. K.; Mondal, B.; Hammes-Schiffer, S.; Stahl, S. S., Brønsted Acid Scaling Relationships Enable Control Over Product Selectivity from O_2 Reduction with a Mononuclear Cobalt Porphyrin Catalyst. *ACS Cent. Sci.* **2019,** *5* (6), 1024-1034.

2 Chapter 2 – Mechanism of Catalytic O_2 Reduction by Iron Tetraphenylporphyrin

Adapted from Pegis, M. P.; Martin, D. J.; Wise, C. F.; Brezny, A. C.; Johnson, S. I.; Johnson, L. E.; Kumar, N.; Raugéi, S; Mayer, J. M. "Mechanism of Catalytic O_2 Reduction by Iron Tetraphenylporphyrin." *J. Am. Chem. Soc.* **2019**, *141*, 8315-8326. MLP, DJM and CFW contributed equally to the writing and editing. MLP performed and analyzed the electrochemical data. DJM measured and analyzed the electron transfer and oxygen binding equilibria. CFW collected and analyzed the optical stopped-flow kinetics data. ACB performed kinetic modeling on the stopped-flow data. SIJ, LEJ, NK, and SR performed the computations. SIJ was the lead computationalist.

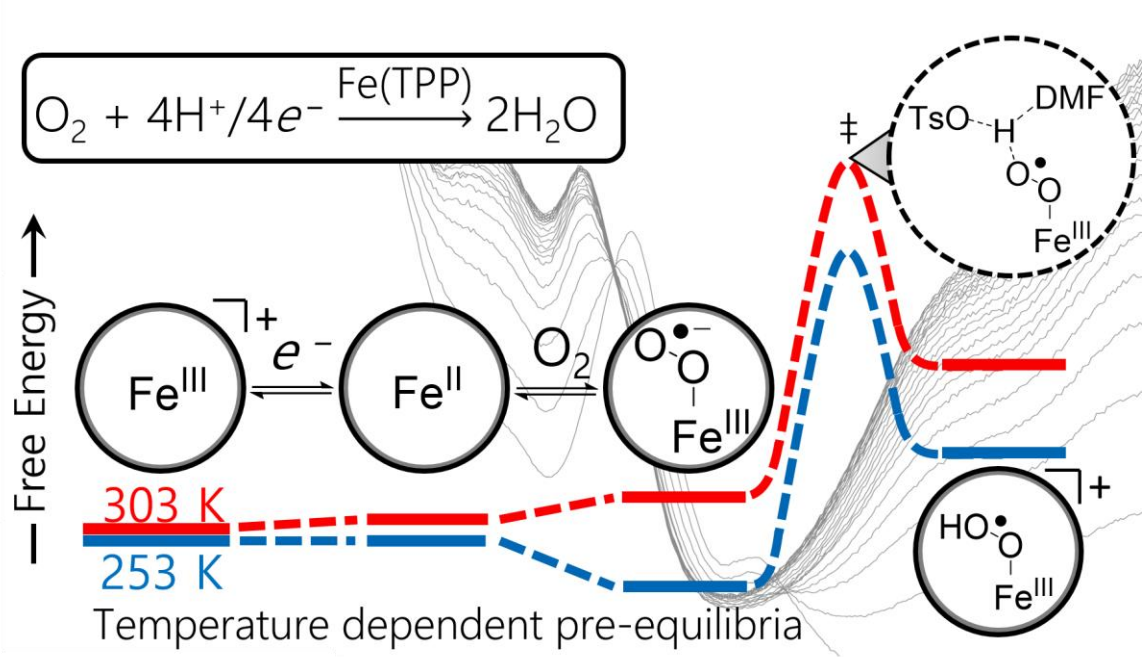

2.1 Introduction

Many diverse biological and energy processes involve the catalytic reduction of dioxygen (O_2).[1-5] In nature, cytochrome *c* oxidase reduces O_2 to drive ATP synthesis in cellular respiration,[6] and cytochromes P450 couple the reduction of O_2 to the oxidations of endogenous and xenobiotic substances in numerous synthetic and metabolic processes.[7-9] In energy conversion technologies such as fuel cells, the oxidation of a fuel (dihydrogen, methanol, etc.) is coupled to the oxygen reduction reaction (ORR, eq 2.1), producing usable electrochemical work for portable and stationary applications.[10] For such approaches to be practical, the ORR must be performed at fast rates and with high selectivity and energy efficiency over thousands of hours of operation. Achieving this goal will have vast implications for the global energy economy.

$$O_2 + 4e^- + 4H^+ \rightarrow 2H_2O \quad \text{(eq 2.1)}$$

Given the kinetic complexity of the ORR, widespread commercialization of fuel cell technologies requires identification of inexpensive and efficient electrocatalysts capable of delivering $4H^+$ and $4e^-$ to O_2 and cleaving the O=O bond. Numerous research efforts have focused on developing new catalytic systems and improving previously known ORR electrocatalysts.[3-4,11-12] Given their biological relevance as active sites, iron porphyrins have been widely studied as ORR catalysts under electrocatalytic conditions.[13-14] Notably, graphite-embedded iron porphyrinic-like materials have been shown to exhibit ORR activity rivaling that of platinum metal in acidic media; however, the exact nature of their active sites remains a continued discussion.[15-17]

Further improvement of ORR cathodic materials will require an understanding of the catalyst identity and turnover-limiting step(s) in the catalytic cycle. Such a detailed understanding is difficult to achieve for heterogeneous electrode surfaces, where the nature and catalytic activities of specific sites and intermediates are difficult to determine. Studying molecular ORR electrocatalysts that have been physi- or chemisorbed onto electrode surfaces can circumvent some of these complications, especially with the use of *in-situ* spectroscopic characterization.[18-23]

Reaction mechanisms are more easily analyzed in systems with homogeneous molecular catalysts, as these catalysts can be prepared in pure form and are readily examined using standard spectroscopic and kinetic methods for solution species. Optical spectroscopies have been extensively used to study iron porphyrins in the biomimetic context of dioxygen binding[24-26] and the oxidation of organic molecules.[27-28] However, surprisingly few studies have investigated the *catalytic* reduction of O_2 by iron porphyrins using soluble reductants.[11]

Nearly 30 years ago, two reports by Fukuzumi described the first mechanistic investigations of O_2 reduction by iron tetraphenylporphyrin (abbreviated herein as Fe(TPP) if the oxidation state and axial ligand(s) are not specified). These studies were performed in acetonitrile (MeCN) using substituted ferrocenes (Fc) as the source of electrons and perchloric acid ($HClO_4$) as the source of protons.[29-30] Under these conditions, the rate-determining step was proposed to be outer-sphere electron transfer from the reductant to $[Fe^{III}(TPP)]ClO_4$, based upon the first-order dependence on [Fc] and the zero-order dependences on $[O_2]$ and $[HClO_4]$. In this example, the

strongly acidic medium with relatively weak reductants resulted in no detectable intermediates within the catalytic cycle.

More recently, kinetic studies examined O_2 reduction catalyzed by Fe^{III}(TPP)Cl and other porphyrin derivatives in acidic acetonitrile and *N*,*N*-dimethylformamide solutions containing decamethylferrocene (Fc*) as a soluble reductant.[31-32] With excess of this stronger reductant, the rate law for catalysis via Fe^{III}(TPP)Cl was zero-order in reductant because electron transfer from Fc* to Fe^{III}(TPP)Cl was initially rapid and favorable. Under these conditions, the rate of ORR catalysis was first order in O_2, acid, and catalyst.[31] The same rate law and rate constant were obtained under electrocatalytic conditions. Subsequent studies found this rate law to be general for electrocatalytic O_2 reduction using substituted iron porphyrins[32] and in the presence of proton donors of varying acidity (pK_a).[33] The rate law implicates a mechanism of initial reduction of Fe^{III} to Fe^{II}, pre-equilibrium O_2 binding to Fe^{II}, and rate-limiting proton transfer from the acid to the Fe^{III}-superoxo intermediate (**Scheme 2.1**). However, efforts to decrease the proton transfer barrier by appending proton relays to the iron porphyrins did not result in rate enhancements.[32] To obtain direct support for the proposed mechanism and to better understand the factors affecting catalytic rates, a more thorough mechanistic analysis was needed.

Scheme 2.1. Proposed mechanism for oxygen reduction catalyzed by Fe(TPP), with TPP abbreviated as an oval. Red = Fc* or electrode.

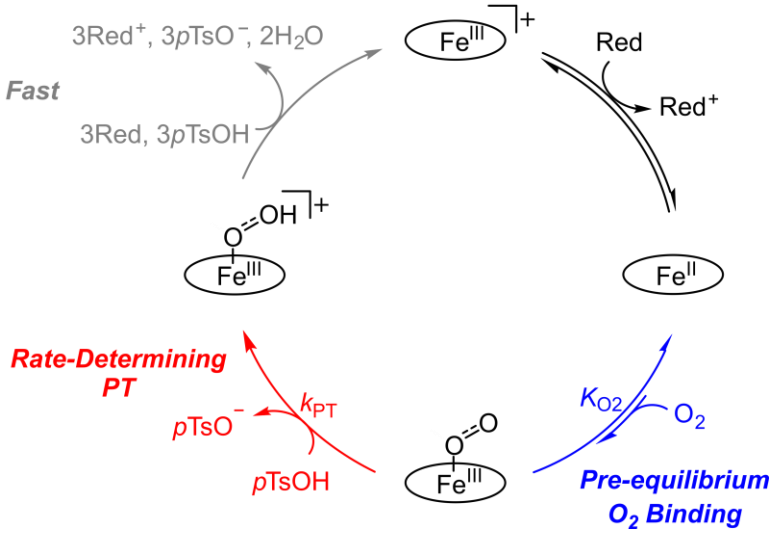

Herein, we report a much more complete and nuanced analysis of the $4H^+/4e^-$ reduction of O_2 to H_2O catalyzed by iron tetraphenylporphyrin, prepared as the triflate salt ([Fe^{III}(TPP)]OTf). The ferrous and ferric-superoxide porphyrin species are identified and observed as catalytic intermediates for the first time, and their temperature-dependent speciation is reported. This includes measurements of the equilibrium constants for electron transfer from Fc* to [Fe^{III}(TPP)]OTf and for O_2 binding to Fe^{II}(TPP). These shifting equilibria and speciation play a critical and previously unappreciated role in the kinetics of catalysis, as the catalyst resting state varies among three different species during the course of the reaction. The temperature-dependence of these equilibria combined with measurements of catalytic rates and catalyst speciation by optical stopped-flow and electrochemical methods provide an unusually rich dataset. Modelling these results gives a detailed view of the catalytic mechanism under different conditions. The model gives the activation parameters for protonation of the ferric-superoxo intermediate, the rate-determining step in the catalytic cycle. These results are used in conjunction with computational modeling to analyze the underlying factors limiting proton transfer to the ferric-superoxide intermediate. Such a detailed mechanistic understanding provides critical insight into iron porphyrin-catalyzed oxygen reduction and should enable further improvement of catalytic systems.

$$O_2 + 4\,p\mathrm{TsOH} + 4\mathrm{Fc}^* \xrightarrow{[\mathrm{Fe(TPP)}]\mathrm{OTf}} 2H_2O + 4\,p\mathrm{TsO}^- + 4\mathrm{Fc}^{*+} \qquad \text{(eq 2.2)}$$

2.2 Experimental

2.2.1 Materials

Iron tetraphenylporphyrin chloride, Fe^{III}(TPP)Cl, was synthesized by the metalation of *meso*-tetraphenylporphyrin with iron(II) chloride in refluxing DMF as previously reported[32] (see Appendix A, **Figure A1**−**Figure A2**). [Fe^{III}(TPP)]OTf was generated *in situ* from Fe(TPP)Cl and TlOTf in acidified DMF (Appendix A, **Figure A3**−**Figure A4**). Fe^{II}(TPP) was prepared from the well-known reduction of Fe^{III}(TPP)Cl by Zn/Hg amalgam and was recrystallized from toluene/THF mixtures.[34-35] This compound was also prepared using modified literature procedures (Appendix A, **Figure A7**−**Figure A8**). All solvents and electrolytes were purchased at high purity and purified as needed, as further described in Section A.1.2.

2.2.2 *Optical equilibrium and kinetics measurements*

Equilibrium measurements were performed by optical spectroscopy using a temperature-controlled Unisoku Unispeks cryostat. Equilibrium constants for electron transfer were made by fitting the UV-vis spectra of DMF solutions containing 0.1 M [*n*-Bu_4N][PF_6] and equimolar (100 μM) amounts of [Fe^{III}(TPP)]OTf, Fe^{II}(TPP), Fc*, and Fc*$^+$ between 213 K and 293 K. Likewise, equilibrium constants for O_2 binding were made by fitting the UV-vis spectra of O_2-saturated DMF solutions initially containing 0.1 M [*n*-Bu_4N][PF_6] and 60 μM Fe^{II}(TPP) between 213 K and 238 K. Both sets of equilibria data were analyzed using van 't Hoff plots to yield enthalpic and entropic parameters. See Sections A.2−A.3 for complete details.

Stopped-flow kinetics measurements were performed by mixing N_2-saturated DMF solutions of Fc* in one syringe with air-saturated DMF solutions containing [Fe^{III}(TPP)]OTf and *p*TsOH in a second syringe. The reaction progress was monitored by following the appearance of Fc*$^+$ over time. Experiments were performed at various [*p*TsOH], [catalyst], and temperature (253 – 303 K). Changes in catalyst speciation over time were determined by fitting optical spectra to linear combinations of three catalyst species: [Fe^{III}(TPP)]OTf, Fe^{II}(TPP), and Fe^{III}(TPP)($O_2^{\bullet-}$). The concentration time courses were modeled to obtain thermodynamic and kinetic parameters. See Sections A.5−A.6 for complete details.

2.2.3 *Kinetic modeling*

The time course data from the stopped-flow catalytic experiments were fit to a multi-step kinetic model in the program COPASI.[36] The thermodynamic parameters (ΔH^o and ΔS^o) for electron transfer and O_2 binding, as well as the activation parameters ($\Delta H^\ddagger$ and $\Delta S^\ddagger$) for proton transfer, were optimized in order to minimize the sum of squared deviations between the experimental concentrations and fitted time course concentrations. See Section A.6 for complete details.

2.2.4 *Computational modeling*

The present density functional theory (DFT) calculations build on previously reported work.[32] Stationary points were optimized using the PBE exchange and correlation functional.[37] The Stuttgart/Dresden basis set with relativistic effective core potential (SDD) was used for the Fe center, and the 6-31G** basis set[38-39] was used for all atoms except sulfur. Diffuse functions and

additional polarization functions (6-31++G(2df,2pd)) were used on sulfur in order to capture the sulfur–oxygen bonding correctly. Justification for this can be found in Section A.8. Single point solvation energies in DMF were modeled using the SMD continuum solvent.[40] Harmonic vibrational frequencies, calculated at the same level of theory, were used to estimate zero-point energy (ZPE) and the thermal contributions free energies. Free energies are referred to the standard state concentration of 1 M for the solute and 12.9 M for the solvent DMF at T = 298 K. See Section A.8 for complete details.

2.3 Results

2.3.1 Electron transfer equilibrium

The proposed mechanism involves initial reduction of [Fe^{III}(TPP)]OTf to Fe^{II}(TPP) by decamethylferrocene (Fc*). Qualitatively, addition of excess Fc* to [Fe^{III}(TPP)]OTf results in the predominant formation of Fe^{II}(TPP) (**Figure A9**−**Figure A10**). Adding Fc^{*+} to this solution reoxidizes some Fe^{II}(TPP) and confirms the equilibrium nature of this ET process (eq 2.3; **Figure A11**). Equilibrium constants in DMF were measured by preparing solutions containing the four species and 0.1 M [n-Bu_4N][PF_6], to make the conditions similar to those used in the electrocatalytic and optical measurements. After correcting for dilution, analysis of the optical spectra gave the ratio of [Fe^{III}(TPP)]OTf to Fe^{II}(TPP) (see Appendix A).

$$\mathrm{Fc^{*}} + \mathrm{Fe^{III}(TPP)^{+}} \rightleftharpoons \mathrm{Fc^{*+}} + \mathrm{Fe^{II}(TPP)} \qquad \text{(eq 2.3)}$$

$$K_{\mathrm{ET}} = \frac{[\mathrm{Fc^{*+}}][\mathrm{Fe^{II}(TPP)}]}{[\mathrm{Fc^{*}}][[\mathrm{Fe^{III}(TPP)}]^{+}]} \qquad \text{(eq 2.4)}$$

Following eq 2.4 and knowing the concentrations of all four species, K_{ET} was determined at 293 K to be 0.16 ± 0.03. This K_{ET} could also be determined from electrochemical measurements: $E_{1/2}$ (Fe^{III}(TPP)$^+$/Fe^{II}(TPP)) = –0.538 V vs. Fc^+/Fc (*vide infra*) and $E_{1/2}$(Fc^{*+}/Fc*) = –0.484 V vs. Fc^+/Fc in DMF[31] containing 0.1 M [n-Bu_4N][PF_6]. The 0.054 V difference in reduction potentials gives K_{ET} = 0.12 (Section A.2.2), very close to the K_{ET} = 0.16 from optical measurements. The optical measurements were repeated at temperatures between 213 and 293 K to investigate the temperature dependence of K_{ET} (**Figure 2.1A**). The resulting van ‘t Hoff plot yielded the enthalpy

and entropy for the electron transfer from Fc* to [Fe^{III}(TPP)]OTf: $\Delta H°_{ET}$ = 2.8 ± 0.1 kcal mol^{-1} and $\Delta S°_{ET}$ = 6 ± 2 cal mol^{-1} K^{-1} (**Figure 2.1B**).

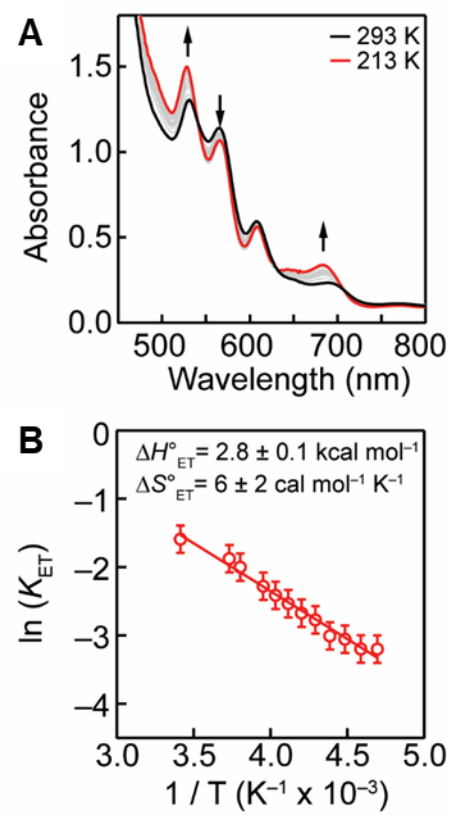

Figure 2.1. UV-vis spectra and van ′t Hoff plot for ET reactions between the oxidized and reduced forms of Fc* and Fe(TPP). (**A**) Spectra of a DMF solution containing 100 μM [Fe^{III}(TPP)]OTf, Fe^{II}(TPP), Fc*, and Fc*$^{+}$ and 0.1 M [*n*-Bu$_4$N][PF$_6$] in the Q-band region at temperatures between 293 K and 213 K. (**B**) van ′t Hoff analysis of ln(K_{ET}) derived from the data in (**A**).

2.3.2 Oxygen binding equilibrium

To test the hypothesis that O_2 binding follows the initial reduction of [Fe^{III}(TPP)]OTf, a genuine Fe^{II}(TPP) sample was prepared and exposed to O_2 at low temperatures in DMF. The addition of 1 atm O_2 to DMF solutions of Fe^{II}(TPP) at 213 K resulted in the quantitative conversion of Fe^{II}(TPP) to a new species with Q-band absorbance features at 542 and 580 nm, characteristic of a ferric tetra-arylporphyrin superoxide complex, Fe^{III}(TPP)($O_2^{\bullet-}$).[41-42] The chemically-generated Fe^{III}(TPP)($O_2^{\bullet-}$) complex was relatively stable (~30 minutes) at 213 K but decomposed quickly at temperatures above 238 K to the well-known μ-oxo dimer, [Fe^{III}(TPP)]$_2$O.[42]

The stoichiometry of O_2 binding was measured by titrating a DMF solution of Fe^{II}(TPP) at 213 K with a room temperature DMF solution containing 1 atm O_2 (3.1 mM [O_2]).[43] With

substoichiometric concentrations of O_2, the Q-bands of Fe^{II}(TPP) incrementally shifted to those of Fe^{III}(TPP)($O_2^{\bullet-}$) (**Figure 2.2A**). At 213 K, slightly more than one equivalent of O_2 was necessary to reach the end point of the titration, after which no additional changes occurred in the spectra (**Figure A13** and **Figure A15**).

The reversibility of O_2 binding to Fe^{II}(TPP) was investigated by sparging a solution of the generated Fe^{III}(TPP)($O_2^{\bullet-}$) adduct with argon at 213 K. A spectrum collected after 5 minutes of sparging closely matched the initial anaerobic spectrum of Fe^{II}(TPP) with some residual contributions from remaining Fe^{III}(TPP)($O_2^{\bullet-}$) (**Figure A16**). That Fe^{II}(TPP) could be formed from Fe^{III}(TPP)($O_2^{\bullet-}$) proved O_2 binding reversibility and enabled us to measure equilibrium constants (eq 2.5).

$$K_{O_2}(M^{-1}) = \frac{[Fe^{III}(TPP)(O_2^{\bullet-})]}{[O_2][Fe^{II}(TPP)]} \qquad \text{(eq 2.5)}$$

The equilibrium constants for O_2 binding to Fe^{II}(TPP) (K_{O_2}, eq 2.5) were measured at various temperatures. With excess O_2, a solution of Fe^{III}(TPP)($O_2^{\bullet-}$) was prepared at 213 K and incrementally warmed to 238 K. Upon warming, the initial spectrum gradually changed to contain Q-bands of both Fe^{III}(TPP)($O_2^{\bullet-}$) and Fe^{II}(TPP) (**Figure A17**). The UV-vis spectrum at each temperature was fit to a linear combination of independently measured Fe^{III}(TPP)($O_2^{\bullet-}$) and Fe^{II}(TPP) spectra (Section A.3.3). The concentrations of Fe^{II}(TPP), Fe^{III}(TPP)($O_2^{\bullet-}$), and of dissolved O_2 were then used to calculate K_{O_2} at each temperature (eq 2.5). At 213 K, the free energy of formation for Fe^{III}(TPP)($O_2^{\bullet-}$) is exergonic, $\Delta G°_{O2}$ = -3.68 kcal mol^{-1}. The slope and intercept of the resulting van 't Hoff plot (**Figure 2.2B**) yielded the enthalpy and entropy for the binding of O_2 to form Fe^{III}(TPP)($O_2^{\bullet-}$): $\Delta H°_{O2}$ = –10.5 ± 0.7 kcal mol^{-1} and $\Delta S°_{O2}$ = –32 ± 3 cal mol^{-1} K^{-1}. By extrapolating the van 't Hoff plot to 298 K, the equilibrium constant for O_2 binding at room temperature was determined to be ca. 5 M^{-1}. A T-test gave a 95% confidence interval for this extrapolated value at 298 K to be between 0.21 M^{-1} and 110 M^{-1} (see Appendix A for details).[44]

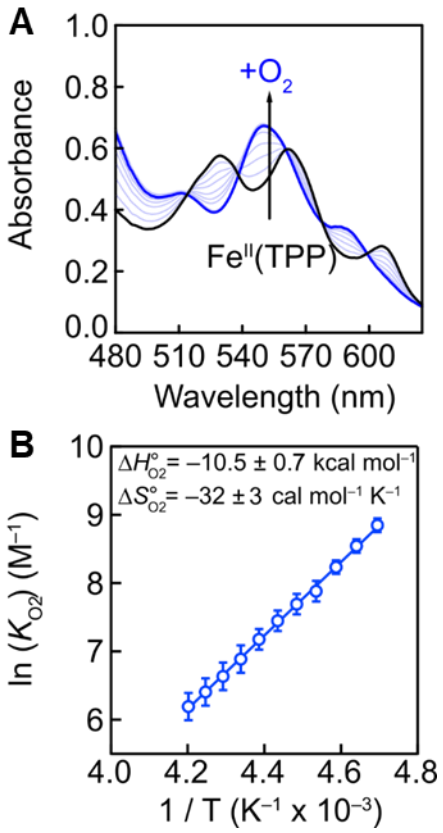

Figure 2.2. UV-vis spectra and van ′t Hoff plot for O_2 binding to Fe^{II}(TPP). (**A**) Optical spectra (corrected for dilution) of a titration at 213 K of a DMF solution containing 50 μM Fe^{II}(TPP) and 0.1 M [*n*-Bu_4N][PF_6] with DMF containing dissolved O_2. (**B**) van 't Hoff analysis of O_2 binding to Fe^{II}(TPP) (K_{O_2} in M^{-1}).

2.3.3 Electrochemical kinetics of catalytic O_2 reduction

Our previous studies have shown that the rate of ORR catalyzed by iron tetra-arylporphyrins exhibits first-order dependences on the concentrations of catalyst, O_2, and acid.[32] In order to verify that the same rate law applies to the system studied here, we investigated the kinetics of ORR catalyzed by [Fe^{III}(TPP)]OTf using cyclic voltammetry.

In anaerobic DMF solutions containing [Fe^{III}(TPP)]OTf and 0.1 M [*n*-Bu_4N][PF_6], a chemically reversible, diffusion-controlled reduction was observed at –0.538 ± 0.005 V vs. Fc^+/Fc (**Figure 2.3A** (black trace), **Figure A20**). This wave is diagnostic of the reduction of [Fe^{III}(TPP)]$^+$ to Fe^{II}(TPP), as previously reported by Savéant[45] and later by our group.[32-33] Addition of *p*TsOH did not affect $E_{1/2}$ (Fe^{III}(TPP)$^+$/Fe^{II}(TPP)) (**Figure A21**), in contrast to what has been observed for Fe(TPP) in the presence of chloride salts.[31] These results are consistent the preferred binding of DMF solvent over triflate, in both Fe(III) and Fe(II) redox states, as previously observed.[32,45] For

simplicity, we exclude explicit solvent molecules from the abbreviated formulas and continue to abbreviate these redox states as [Fe^{III}(TPP)]OTf and Fe^{II}(TPP).

When DMF solutions containing [Fe^{III}(TPP)]OTf, *p*TsOH, and [*n*-Bu_4N][PF_6] were sparged with 1 atm air (0.7 mM O_2 in DMF),[43] the voltammograms displayed significant current enhancements (>10x) centered above $E_{1/2}(Fe^{III}/Fe^{II})$ (**Figure 2.3A**, red trace). The magnitude of this irreversible current was linear with the square root of the scan rate, which suggests that the catalytic current arises from an electrogenerated, homogeneous catalyst.[31] Rotating ring-disk electrochemistry (RRDE) was used to quantify the amount of H_2O_2 produced during turnover. The RRDE measurements demonstrated that catalysis is selective for the $4H^+/4e^-$ reduction of O_2 to water and produces ~1.5% H_2O_2 (n_{cat} = 3.9) under these conditions (**Figure A50**−**Figure A51**).

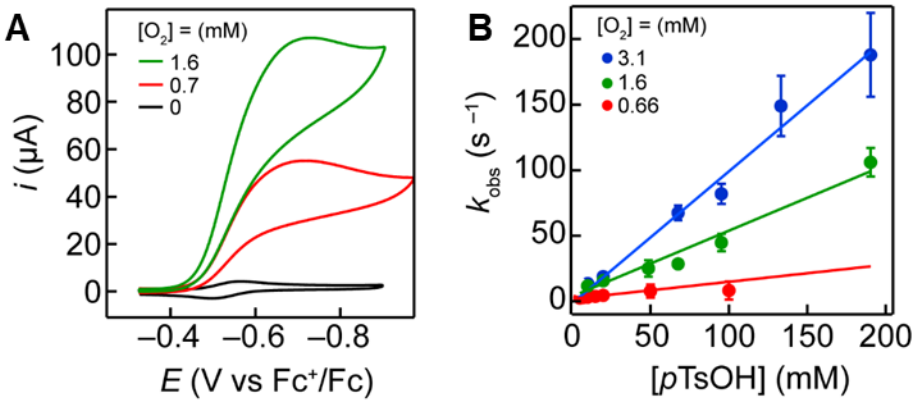

Figure 2.3. Electrochemical data and kinetic plots for O_2 reduction by Fe(TPP) using *p*TsOH. (**A**) Electrochemical response of 0.3 mM [Fe^{III}(TPP)]OTf in the presence of 1 M *p*TsOH and 1.6 mM O_2 (green), 0.7 mM O_2 (red, air sparged), and 0 mM O_2 (black, N_2 sparge) at 298 K. (**B**) Dependence of k_{obs} from FOWA on [*p*TsOH] at different O_2 concentrations. All CVs were taken in the presence of 0.1 M [*n*-Bu_4N][PF_6] electrolyte.

The pseudo-first order rate constant k_{obs} for ORR was quantified using foot-of-the-wave analysis (FOWA, equation 2.7),[46] where n_{cat} = 3.9 (determined by RRDE, see above). FOWA allows the determination of catalytic rate constants under conditions where the concentrations of the substrates in the reaction-diffusion layer (O_2 and pTsOH in this case) are essentially identical to the bulk solution concentrations.[46] The linearity of the foot-of-the-wave plots (**Figure A22**) indicated that the reaction was first order in catalyst. Additionally, k_{obs} was linearly dependent on both [O_2] and [*p*TsOH] (**Figure 2.3**), indicating the third-order rate law in equations 2.6 and 2.8. The quotient of k_{obs} and the reactant concentrations then afforded the third order rate constant k_{cat}. Considering

the upper and lower bounds for σ in eq 2.7 (see Appendix A), k_{cat} ranged from (3.2-6.4) × 10^5 M^{-2} s^{-1}.

$$rate = n_{cat} k_{obs} [\mathrm{Fe(TPP)}] \quad \text{(eq 2.6)}$$

$$\frac{i_c}{i_p} = \frac{2.24 n_{cat}^{\ \sigma} \sqrt{\frac{RT}{Fv} k_{obs}}}{1 + \exp\left[\frac{F}{RT}\left(E - E_{1/2}\right)\right]} \quad \text{(eq 2.7)}$$

$$k_{obs} = k_{cat} [\mathrm{O_2}][p\mathrm{TsOH}] \quad \text{(eq 2.8)}$$

2.3.4 Optical kinetics

The kinetics of Fe(TPP)-catalyzed ORR were also studied by optical spectroscopy, over a range of temperatures. These experiments were performed in DMF using *p*TsOH as the proton source and Fc* as the soluble reductant. During optical measurements, all solutions also contained 0.1 M [*n*-Bu_4N][PF_6] to mirror the electrochemical conditions. In a typical experiment, a solution of air-saturated DMF (0.7 mM O_2) containing [Fe^{III}(TPP)]OTf (60 μM) and *p*TsOH (50 mM) was rapidly mixed in a stopped-flow instrument with an equal volume of an anaerobic DMF solution of Fc* (6 mM, higher concentrations were limited by solubility), with all concentrations being halved upon mixing (see Appendix A). After mixing, optical spectra showed the growth of a broad absorbance feature between 600-700 nm, diagnostic of decamethylferrocenium (Fc^{*+}) formation, along with various changes in the porphyrin Q-band region (**Figure 2.4A** and **Figure A24**, discussed further below). Control experiments performed under identical conditions but in the absence of [Fe^{III}(TPP)]OTf catalyst formed a much smaller amount of Fc^{*+} over the same time course (~10%) (**Figure 2.4B**). The small amount of Fc* auto-oxidation likely results from unfavorable pre-equilibrium electron transfer with O_2 followed by irreversible chemical reactions of $O_2^{\bullet -}$.[47] When *p*TsOD was substituted for *p*TsOH, the rate of Fc^{*+} formation did not change (KIE ≈ 1, see **Figure A25**).

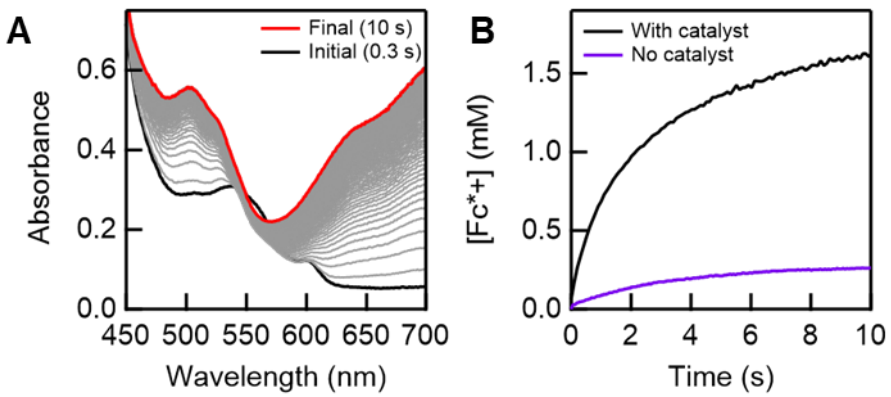

Figure 2.4. Representative stopped-flow UV-vis optical spectra and kinetic profile for O_2 reduction using Fc* and *p*TsOH catalyzed by Fe(TPP). (**A**) Spectral changes measured for the reaction of O_2 (0.33 mM) with *p*TsOH (50 mM) and Fc* (3 mM), catalyzed by [Fe^{III}(TPP)]OTf (30 μM) over a 30 second reaction at 298 K. (**B**) Rate of Fc^{*+} formation over the course of the first 10 s of reaction (**A**) (black trace), compared to the same reaction conducted in the absence of added [Fe^{III}(TPP)]OTf catalyst (purple trace). Concentrations of Fc^{*+} were calculated at 700 nm after removal of the absorbance contributions from [Fe^{III}(TPP)]OTf (see Appendix A, Section A.5.3).

The kinetics of the Fe(TPP)-catalyzed ORR were examined by stopped-flow methods at temperatures between 253 and 303 K. In these experiments, the air-saturated syringe was prepared at room temperature so that the initial concentration of dissolved O_2 remained constant for all catalytic runs. Notably, as shown in **Figure 2.5**, the spectrum collected 1 s after mixing was temperature dependent. At 253 K, absorbance features at 542 and 580 nm were immediately present (**Figure 2.5A**). These features match those of the independently prepared ferric superoxide, Fe^{III}(TPP)($O_2^{\bullet-}$), described above. However, at temperatures above 273 K, the initial spectrum resembled a mixture of Fe^{II}(TPP) and Fe^{III}(TPP)($O_2^{\bullet-}$) (**Figure 2.5B**). At all temperatures, the initial traces decayed with the formation of [Fe^{III}(TPP)]OTf and Fc^{*+}.

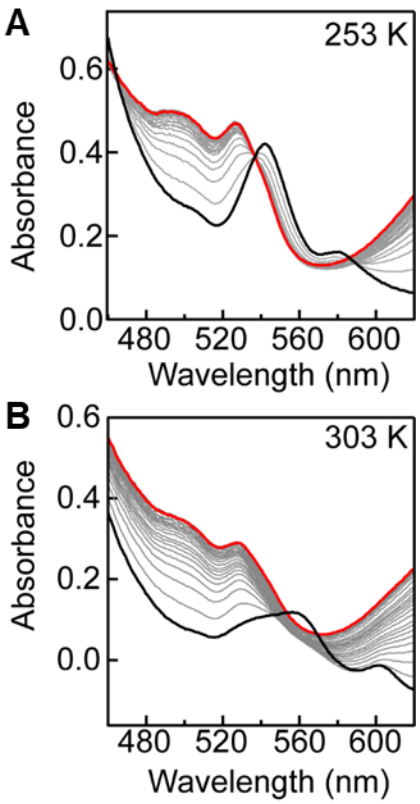

Figure 2.5. Stopped-flow optical spectra at 253 K and 303 K for O_2 reduction using Fc* and *p*TsOH catalyzed by Fe(TPP). (**A**) Spectral changes after stopped-flow mixing of [Fe^{III}(TPP)]OTf (30 μM), *p*TsOH (35 mM), Fc* (3 mM), and O_2 (0.33 mM) at 253 K. Black trace = initial spectra after mixing (1 s) Red trace = final spectra after mixing (50 s). (**B**) Same conditions as (**A**), at 303 K. Black trace = initial spectra after mixing (1 s) Red trace = final spectra after mixing (20 s).

The temperature dependence of the initial stopped-flow kinetic traces reflects the temperature-dependent equilibrium constant for O_2 binding. The initial spectra showed exclusively Fe^{III}(TPP)($O_2^{\bullet-}$) at low temperatures and a mixture of Fe^{II}(TPP) and Fe^{III}(TPP)($O_2^{\bullet-}$) at higher temperatures, consistent with the independent O_2 binding measurements described above. While the electron transfer equilibrium also shows a temperature dependence, ΔG_{ET} only changes by ~ 0.3 kcal mol^{-1} across this temperature range. Thus, the observed spectral differences are dominated by the difference in O_2-binding favorability between the two temperatures. Additionally, the observation of Fe^{II}(TPP) or Fe^{III}(TPP)($O_2^{\bullet-}$) as the initial catalyst resting state also supports the proposed mechanism in which the rate of ORR is limited by protonation of Fe^{III}(TPP)($O_2^{\bullet-}$) rather than initial electron transfer or O_2 binding (**Scheme 2.1**).

Over the course of the stopped-flow kinetics runs, the speciation of the iron catalyst changed, with [Fe^{III}(TPP)]OTf becoming the predominant species at the end of the reaction (when limiting O_2 is completely consumed). The changes in catalyst speciation reflect the positions of the time- and temperature-dependent equilibria between [Fe^{III}(TPP)]OTf, Fe^{II}(TPP), and Fe^{III}(TPP)($O_2^{\bullet-}$) during catalytic turnover, as discussed in more detail in the next section. In the absence of a constant catalyst resting state, the rate law for Fc*$^+$ formation needs to be defined with respect to total amount of catalyst in solution, $[Fe(TPP)]_{total}$. The resulting rate law (eq 2.9) includes the two pre-equilibria (K_{ET} and K_{O_2}) and the turnover-limiting protonation step, k_{PT}. The complexity of this rate law arises from the uphill electron transfer equilibrium between Fc* and [Fe^{III}(TPP)]OTf (K_{ET} < 1). As such, even with a large excess of Fc* (e.g. >40:1 ratio of [Fc*]:[O_2]), the growth of the oxidized product Fc*$^+$ shifts the initial electron transfer reaction away from the formation of catalytically active Fe^{II}(TPP), as demonstrated independently in Section 2.3.1 above. The complexity of this rate law and the inability to find experimental conditions under which it simplifies have precluded simple fitting and the determination of a simple reaction order in [Fc*] (Appendix A).

$$\frac{d[\mathrm{Fc}^{*+}]}{dt} = \frac{n_{cat} K_{ET} K_{O_2} k_{PT} [\mathrm{Fe(TPP)}]_{total} [\mathrm{O_2}][\mathrm{Fc}^*][p\mathrm{TsOH}]}{K_{ET}[\mathrm{Fc}^*](1 + K_{O_2}[\mathrm{O_2}]) + [\mathrm{Fc}^{*+}]} \qquad \text{(eq 2.9)}$$

Longer time-scale catalytic experiments were conducted by combining a large excess of Fc* (10 mM) and *p*TsOH (260 mM) relative to [Fe^{III}(TPP)]OTf (1 μM) and stirring the solution in ambient air. Over 15 minutes, significantly larger amounts of Fc*$^+$ were produced than an identical experiment conducted in the absence of [Fe^{III}(TPP)]OTf. Iodometric titrations of the resulting solution were used to quantify the amount of H_2O_2 produced during the catalyzed reaction and revealed that ~15% H_2O_2 (n_{cat} = 3.7 e^-/O_2, **Figure A51**) was formed under such conditions, in good agreement with the selectivity values obtained electrochemically (n_{cat} ≈ 3.9 e^-/O_2).[31] These results demonstrate that the catalyst remains active for ORR for at least 15 minutes and permit a rough estimation of the catalyst turnover number over 15 minutes, TON = 2000 moles O_2 consumed per mole catalyst, **Figure A26**.

2.3.5 Kinetic modeling

The constantly evolving catalyst speciation during ORR by Fe(TPP), observed by stopped-flow measurements, required us to use a complete kinetic model to fit the data. As described in this section, the model revealed the thermodynamic parameters for the ET and O_2-binding pre-equilibria and the kinetic parameters for the turnover-limiting step.

Fitting the optical data to a kinetic model first required the concentration of each catalyst species at every time point to be determined. These concentrations were obtained using Beer's Law and a system of linear equations that considered absorbance contributions from [Fe^{III}(TPP)]OTf, Fe^{II}(TPP), Fe^{III}(TPP)($O_2^{\bullet-}$), and Fc^{*+}. Absorbance contributions from Fc* were negligible in the wavelength region of interest and could be ignored (see Appendix A, Section A.5.3).

Global modeling of all the room temperature stopped-flow kinetic runs was performed with the software COPASI[36] using the kinetic model in **Scheme 2.2** and the corresponding rate law (eq 2.9 above). The only parameters input into the model were the fast rate constants (10^7 M^{-1} s^{-1}) for (1) electron transfer from Fc* to Fe^{III}(TPP)$^+$ and (2) O_2-binding to Fe^{II}(TPP). This was done to ensure that these steps were fast pre-equilibria, as observed experimentally (see above). Step 4 was included to account for mass balance in the reaction and was set to a fast enough rate to be kinetically invisible.

Scheme 2.2. Kinetic model and parameters used for global fitting of the stopped-flow kinetic data, to and obtain $\Delta H°_{ET}$, $\Delta S°_{ET}$, $\Delta H°_{O2}$, $\Delta S°_{O2}$, $\Delta H‡_{PT}$, and $\Delta S‡_{PT}$.

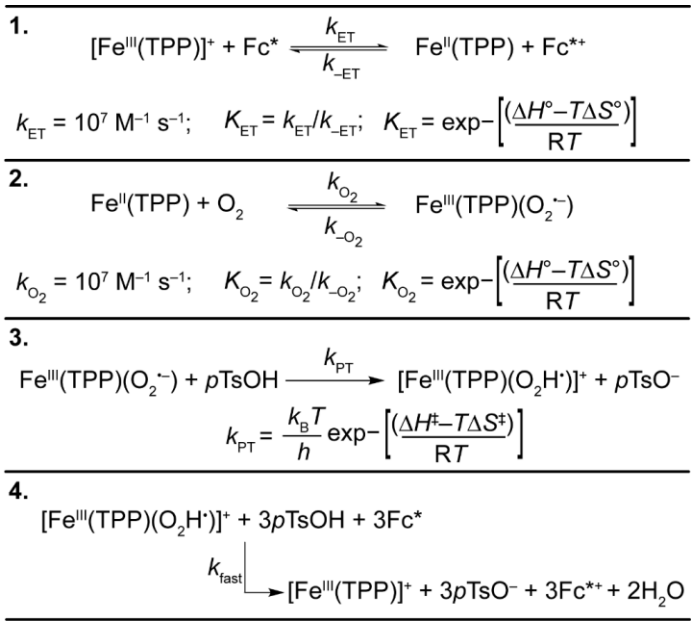

Table 2.1. Results of COPASI global fitting of stopped flow optical kinetic results and comparison with experimental values.[a]

Reaction	Parameter [b]	Model	Experimental [c]
Fc* + $Fe^{III}(TPP)^+$ ⇌ Fc*+ + $Fe^{II}(TPP)$	K_{ET}(298 K)	0.055(7)	0.18(3)
	$\Delta H°_{ET}$	2.9(1)	2.8(1)
	$\Delta S°_{ET}$	4.1(4)	6(2)
$Fe^{II}(TPP)$ + O_2 ⇌ $Fe^{III}(TPP)(O2^{\bullet-})$	K_{O2} (250 K, M^{-1})[d]	(2.7 - 6.4) × 10^4	(0.205 - 11.5) × 10^2 [e]
	$\Delta H°_{O2}$	−9.5(1)	−10.5(7)[e]
	$\Delta S°_{O2}$	−16.9(4)	−32 (3)[e]
$Fe^{III}(TPP)(O_2^{\bullet-})$ + *p*TsOH ⟶ $Fe^{III}(TPP)(O_2H^{\bullet})^+$ + *p*TsO^-	k_{PT} (298 K)	1.5(3) × 10^3 M^{-1} s^{-1}	2.0(9)[f] × 10^5 M^{-1} s^{-1}
	$\Delta H‡_{PT}$	12.0(1)	–
	$\Delta S‡_{PT}$	-3.1(2)	–
$Fe^{II}(TPP)$ + O_2 + *p*TsOH ⟶ $Fe^{III}(TPP)(O_2H^{\bullet})^+$ + *p*TsO^- [g]	k_{cat} (298 K, M^{-2} s^{-1}) = $K_{O2}k_{PT}$	(2-20) × 10^5 [h]	(3.2–6.4) × 10^5 [i]

[a] Optimized values from COPASI analysis of data at 253-303 K, 50-100 mM *p*TsOH, 30–50 µM Fe(TPP). COPASI values and experimental equilibrium parameters are given with the uncertainty in parentheses representing one standard deviation. [b] $\Delta H°$ and $\Delta H‡$ values in kcal mol^{-1}; $\Delta S°$ and $\Delta S‡$ values in cal K^{-1} mol^{-1}. [c] Direct experimental measurements of equilibrium parameters from optical spectra and van 't Hoff analyses (Sections I and II). [d] Values extrapolated from thermodynamic parameters from kinetic data (Model) or lower-temperature equilibrium measurements (Experimental). [e] The 95% confidence limits from a T-test are for K_{O_2} at 298 K: 0.21 to 110 M^{-1}; for $\Delta H°_{O2}$: -9.6 to -11.8 kcal mol^{-1}; and for ΔS_{O2}: -28 to -38 cal K^{-1} mol^{-1}, Appendix A Section A.3.4). [f] Calculated as $k_{cat(echem)}/K_{O_2(experimental)}$, where K_{O_2} was defined as the mean value, 5 M^{-1}. [g] Chemical steps involved in defining the catalytic rate constant, k_{cat}, determined electrochemically. [h] Calculated as K_{O_2}(model) × k_{PT} (model). [i] Calculated from foot-of-the-wave analysis, *vide infra.*

The model used in **Scheme 2.2** attempted to optimize both the simulated rate of decamethylferrocenium formation (*d*[Fc*+]/*d*t) and the catalyst speciation to the experimental data by varying the thermodynamic parameters for electron transfer ($\Delta H°_{ET}$ *and* $\Delta S°_{ET}$, step 1), the

thermodynamic parameters for O_2 binding (($\Delta H°_{O2}$ *and* $\Delta S°_{O2}$, step 2) and the activation parameters for proton transfer ($\Delta H^{‡}_{PT}$ *and* $\Delta S^{‡}_{PT}$, step 3). The six parameters were optimized to fit all stopped flow data simultaneously—including experiments between 253 and 303 K with varied concentrations of substrate (50–100 mM *p*TsOH) and catalyst (30–50 μM $[Fe(TPP)]_{total}$). The experiments have some uncertainty in the catalyst speciation with time due to the overlapping absorbance features, low concentrations of the different Fe(TPP) species, and the uncertainties in the experimental ε values (in part due to high air sensitivity at low concentrations and instability of the materials). Therefore, we sought a model that fit the general trends in catalyst speciation rather than the exact concentration profiles (**Figure 2.6).** The fits are good for the [Fc*$^+$] time courses and agree with the general trends of catalyst speciation. Notably, the model fits well to changes in initial [Fe^{II}(TPP)] and [Fe^{III}(TPP)($O_2^{\bullet-}$)] concentrations across a variety of temperatures and is representative of the temperature-dependent O_2 binding equilibrium. Across the whole temperature range, the model also correctly predicts that [Fe^{III}(TPP)]OTf is the predominant catalyst species at the end of the reaction, even when excess Fc* is used.

The accuracy of the model is evidenced by the remarkable agreement with experimental data for both the thermodynamic and kinetic parameters (**Table 2.1**). The modeled values for $\Delta H°_{ET}$, $\Delta H°_{O2}$ and $\Delta S°_{ET}$ very closely match the directly determined experimental values from Sections 2.3.1 and 2.3.2 above. The modeled value for $\Delta S°_{O2}$ is somewhat less negative than the experimental value, which is similar to typical entropies for O_2 binding in polar organic solvents.[48] The inconsistencies between modeled and experimental $\Delta S°_{O2}$ could be due to an unrecognized catalyst complex in the spectral fitting. Although we cannot rule out such a contribution, we believe the higher than expected modeled $\Delta S°_{O2}$ may instead be related to the lower than expected $\Delta S^{‡}_{PT}$, which would usually be a positive value for a bimolecular reaction. Thus, the $\Delta G^{‡}_{PT}$ of 11 kcal mol^{-1} at 298 K derived from the modeled may be an underestimation. At room temperature, the model predicts ln(k_{PT}) to be between 7.1-7.5 and ln(K_{O_2}) to be between 5.3-7.5. Under electrochemical conditions, where k_{cat} is the product of K_{O_2} and k_{PT}, the model predicts k_{cat} to be between 2-20 $\times$ 10^5 M^{-2} s^{-1}, which is within error of the experimental k_{cat} value of (3.2–6.4) $\times$ 10^5 M^{-2} s^{-1}. This agreement in rate constants at 298 K could also be suggestive of a balancing of errors in the modeled $\Delta S°_{O2}$

and $\Delta S^{\ddagger}_{PT}$. Although ΔS°_{O2} and $\Delta S^{\ddagger}_{PT}$ are not significantly correlated according to the COPASI statistical analysis, there is evidence that these parameters are not all known completely independently from one another. We can achieve similarly strong fits of the data with different parameter values when they are tightly constrained to the experimental results (see Appendix A, Section A.6).

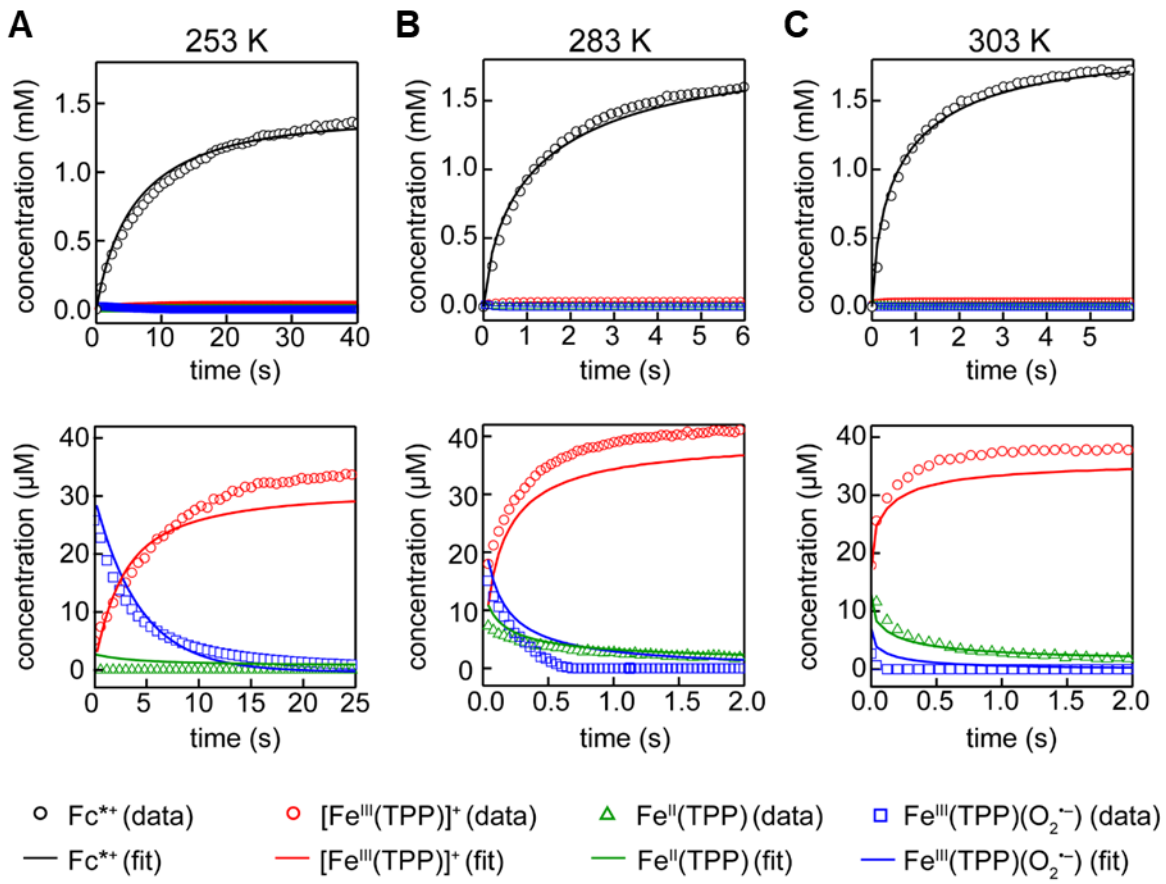

Figure 2.6. Data (points) and fits (lines) for three stopped-flow ORR time courses (0.3 μM Fe(TPP), 50 mM *p*TsOH, 0.33 mM O_2, 3 mM Fc*, varied temperatures: (**A**) 253 K, (**B**) 283 K, (**C**) 303 K. For each temperature column, the top figure shows the Fc^{*+} concentrations with an expansion for the Fe(TPP) speciation below.

2.3.6 Computational analysis of the barrier for protonation of $Fe^{III}(TPP)(O_2^{\bullet-})$

For the ORR by Fe(TPP) in DMF with [DMF-H]OTf as the acid, prior DFT and experimental studies identified protonation of $Fe^{III}(TPP)(O_2^{\bullet-})$ as the rate-limiting step.[11,32] This section extends that computational analysis to evaluate the thermochemistry and kinetics of protonation of $Fe^{III}(TPP)(O_2^{\bullet-})$ by *p*TsOH, the acid used in this work.

The thermochemistry and kinetics of $Fe^{III}(TPP)(O_2^{\bullet-})$ protonation are dictated by interactions between the proton source, solvent, and the superoxide adduct.[32] As such, DFT analysis was performed to quantify the energetics of interactions between explicit *p*TsOH, *p*TsO^-, and DMF molecules in DMF solvent. Calculations show that the free energy of the *p*TsOH•••DMF pair is stabilized by 1.6 kcal mol^{-1} relative to its constituent parts (separate *p*TsOH and DMF molecules). Formation of the [*p*TsOH•••*p*TsO]$^-$ homoconjugate is even more stable, favored by 5.9 kcal mol^{-1} relative to separate *p*TsOH and *p*TsO^- molecules; however, the experimental conditions ([DMF] >>> [*p*TsO^-]) favor the *p*TsOH•••DMF heteroconjugate. Therefore, the thermochemistry and kinetics of proton transfer to $Fe^{III}(TPP)(O_2^{\bullet-})$ were investigated using *p*TsOH•••DMF as the proton donor.

The computed free energy profiles for protonation of $Fe^{III}(TPP)(O_2^{\bullet-})$ (**1**) by *p*TsOH•••DMF are shown in **Figure 2.7A**, wherein all energetics are referenced to **1**. The free energy profile for protonation by *p*TsOH•••DMF first features the formation of a pre-association complex, **2**, in which the acid approaches $Fe^{III}(TPP)(O_2^{\bullet-})$ (**1**). Formation of **2** involves solvent reorganization and the establishment of a three-center site and has an overall energetic penalty of 8.5 kcal mol^{-1}. This energetic cost results from unfavorable entropic ($-T\Delta S$ = 10.7 kcal mol^{-1} at 298 K) and solvation terms (7.8 kcal mol^{-1}) that are only partially balanced by being electronically favorable (–9.9 kcal mol^{-1}). Proton transfer then yields the perhydroxyl (**3**) species, which was calculated to be 9.8 kcal mol^{-1} uphill from **1**. This result indicates that the proton transfer is unfavorable and is consistent with the experimental data.

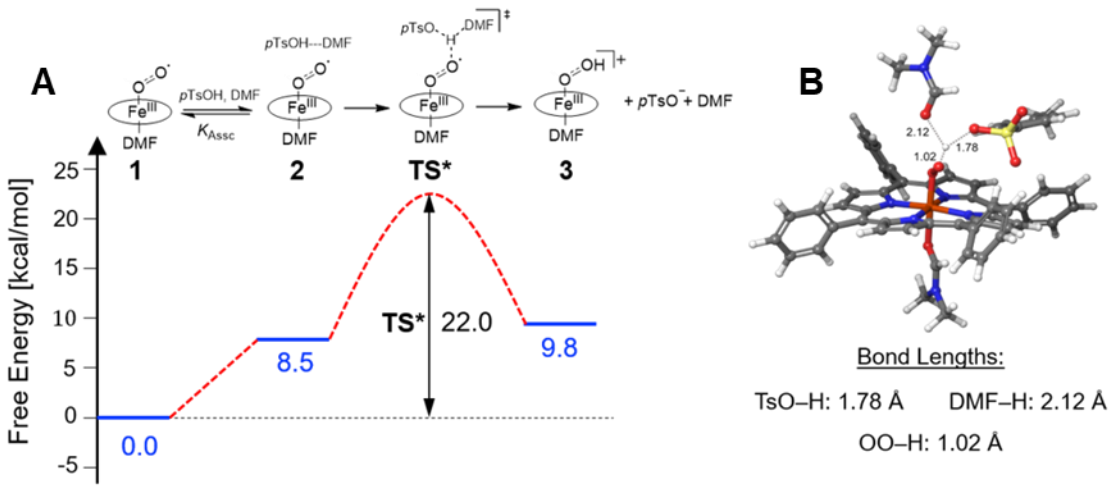

Figure 2.7. Computed free energy profile and optimized structure for rate-determining protonation of $Fe^{III}(TPP)(O_2^{\bullet-})$ by *p*TsOH in DMF. (**A**) Computed free energy profile for association (K_{assc}) and protonation of $Fe^{III}(TPP)(O_2^{\bullet-})$ by the *p*TsOH•••DMF heteroconjugate pair. (**B**) Optimized structure for the proton transfer transition state (k_{PT}) and the corresponding O-H bond lengths for the proton transfer donor (*p*TsOH), solvent (DMF), and acceptor $Fe^{III}(TPP)(O_2^{\bullet-})$. All distances in Ångstroms.

To further understand the kinetics of proton transfer, the barrier for protonation from the heteroconjugated pair *p*TsOH•••DMF was sought. As shown in **Figure 2.7**, the transition state (**TS***) involves proton transfer from the pre-association complex (**2**) and has an overall barrier of 22.0 kcal mol^{-1} relative to $Fe^{III}(TPP)(O_2^{\bullet-})$. This calculated barrier is an upper bound, as it does not compensate for the errors in computing sulfonate group energetics. Taking into account these errors as discussed in Appendix A, the estimated lower bound of this barrier is about 17.0 kcal mol^{-1}. The energetic contributions for the energy change between **2** and **TS*** show that the transition state energy is enthalpically driven. Additionally, at the transition state, the proton is closer to the acceptor $Fe^{III}(TPP)(O_2^{\bullet-})$ than the donor *p*TsOH•••DMF, as evidenced by the O-H bond lengths in the optimized structure (**Figure 2.7B**). The kinetic isotope effect for this transition state was calculated using *p*TsOD•••DMF as the proton donor, affording a KIE of 0.94 (see Section A.8).

2.4 Discussion

2.4.1 The mechanism of ORR catalysis by Fe(TPP)

The results of the spectroscopic, electrochemical, and computational experiments described above support the mechanism illustrated in **Scheme 2.1**. In this mechanism, Fc* or an electrode rapidly reduce $[Fe^{III}(TPP)]OTf$ to the ferrous porphyrin, $Fe^{II}(TPP)$. $Fe^{II}(TPP)$ then binds O_2 reversibly (K_{O_2}) to form the ferric superoxide, $Fe^{III}(TPP)(O_2^{\bullet-})$. The rate-determining step is

protonation of $Fe^{III}(TPP)(O_2^{\bullet-})$ (k_{PT}) to form the perhydroxyl-iron(III) complex, $[Fe^{III}(TPP)(O_2H^{\bullet})]^+$. The perhydroxyl complex is rapidly reduced and protonated under the catalytic conditions to produce two equivalents of H_2O and restart the catalytic cycle. The evidence in support of this mechanism is discussed below.

Reduction of $[Fe^{III}(TPP)]OTf$ to $Fe^{II}(TPP)$, the first step in the proposed catalytic cycle, was found to be a fast pre-equilibrium between $[Fe^{III}(TPP)]OTf$ and the reductant in both electrochemical and spectroscopic measurements. The cyclic voltammograms during electrocatalytic O_2 reduction fit well to a mechanism in which rapid pre-equilibrium electron transfer from the electrode ($[Fe^{III}(TPP)]^+ + e^- \rightleftharpoons Fe^{II}(TPP)$) is followed by a rate limiting catalytic step, k_{obs} (an EC′ mechanism). With Fc* as a chemical reductant, this pre-equilibrium is thermodynamically uphill at standard state ($\Delta G°_{ET}$ = +1.01(8) kcal mol^{-1}). Spectroscopic studies of the reduction of $[Fe^{III}(TPP)]OTf$ by Fc* at different temperatures have yielded the $\Delta H°_{ET}$ and $\Delta S°_{ET}$ for this equilibrium (Results Section 2.3.1). Those values are consistent with the electrochemically measured difference in reduction potentials between $[Fe(TPP)]^{+/0}$ and $Fc^{*+/0}$ at ambient temperatures. In the room temperature stopped-flow kinetics, the initial spectra show almost complete reduction of $[Fe^{III}(TPP)]OTf$ only because the starting concentration of Fc^{*+} is very small ~0 mM and the [Fc*]/Fc^{*+} ratio is very large. As catalysis progresses, however, the ratio of Fc* to Fc^{*+} decreases, quickly shifting this equilibrium so that $[Fe^{III}(TPP)]^+$ is the resting state of the catalyst for much, if not most, of the reaction (**Figure 2.6** and **Figure A34**−**Figure A49**).

Spectroscopic experiments have also quantified the rapid pre-equilibrium O_2 binding to $Fe^{II}(TPP)$, which is proposed to follow initial electron transfer. The distinct optical spectrum of the superoxide complex $Fe^{III}(TPP)(O_2^{\bullet-})$ enabled measurements of the equilibrium constants for binding (K_{O_2}) at low temperatures in the absence of reductant and acid. Low temperatures are required to avoid the decomposition of $Fe^{III}(TPP)(O_2^{\bullet-})$ to the well-known μ-oxo dimer.[42] The measured $\Delta H°_{O2}$ and $\Delta S°_{O2}$ could then be used to predict values of K_{O_2} at the higher temperatures of catalysis. The μ-oxo dimer is not formed under the catalytic conditions because of the presence of strong acid, as indicated reaction of independently prepared μ-oxo dimer with *p*TsOH (see Appendix, Section A.5.4) and by prior reports.[49-50] Consistent with these equilibrium measurements,

$Fe^{III}(TPP)(O_2^{\bullet-})$ is observed as the predominant initial catalyst resting state in catalytic stopped-flow experiments at low temperatures (e.g. 253 K). Under such conditions, $[Fe^{III}(TPP)]OTf$ is completely converted to $Fe^{III}(TPP)(O_2^{\bullet-})$ within 0.1 s (**Figure A29**). As the reaction proceeds, both $[O_2]$ and the ratio of Fc*:Fc*$^+$ decrease, leading to a change in resting state from reduced porphyrin intermediates to $[Fe^{III}(TPP)]^+$ (**Figure 2.6** and **Figure A34**−**Figure A49**).

The kinetics of the *electro*catalysis are not complicated by the shifts in the pre-equilibrium reduction or O_2-binding steps observed in the stopped flow data. The catalytic voltammograms are fit using FOWA, which yields rate constants for reactions catalyzed by the reduced $Fe^{II}(TPP)$ catalyst resting state. Additionally, because the current is analyzed at the 'foot' of the wave, the concentration of substrates in the reaction-diffusion layer is the same as the bulk solution (true pseudo-first order conditions). For these reasons, the electrocatalytic kinetics yield a simple third order rate law, as previously reported,[31] obtained by removing the K_{ET}, [Fc*], and [Fc*$^+$] terms from the complex rate law required for the stopped-flow data (eq 2.9). Despite the complex rate law using Fc* as a chemical reductant, the similarities between the k_{cat} values obtained electrochemically and chemically confirm that electron transfer kinetics are not involved in the rate limiting steps and remain a fast pre-equilibrium step under all conditions. Furthermore, the first order dependence on O_2, *p*TsOH and [Fe(TPP)] exclude bimolecular pathways that involve peroxo (Fe-O_2-Fe) or μ-oxo (Fe-O-Fe) dimeric intermediates, pathways that are observed in the absence of strong acids.[51-54]

Catalytic turnover requires the addition of four protons and three more electrons to $Fe^{III}(TPP)(O_2^{\bullet-})$, ultimately forming water and $[Fe^{III}(TPP)]OTf$. Several initial steps could be imagined for this transformation, but only those which have an acid dependence were considered since the rate of the ORR is first order in [*p*TsOH]. Within that constraint, the two possible pathways for the reaction of the superoxide complex involve *i.*) proton transfer (PT) from *p*TsOH to form perhydroxyl or *ii.*) concerted proton-coupled electron transfer (CPET) with *p*TsOH and a reductant to give a hydroperoxo complex. While option *ii.* should be thermodynamically advantageous, it is formally a termolecular CPET reaction and thus is kinetically challenging in the absence of a favorable pre-association with the proton donor.[55-56] As DFT calculations show that pre-association

of *p*TsOH with $Fe^{III}(TPP)(O_2^{\bullet-})$ is uphill by 8.5 kcal mol^{-1} (**Figure 2.7**), pathway *ii.* is unlikely, and rate-limiting proton transfer from *p*TsOH to $Fe^{III}(TPP)(O_2^{\bullet-})$ is the more plausible mechanism. Previous studies of ORR by Fe(TPP) under different conditions – using $HClO_4$ as the acid and in the presence of excess chloride – found a zero order dependence of turnover frequency on the concentration of Fc*.[31] In the model used successfully here (**Scheme 2.2**), the concentration of the electron donor appears only in the first pre-equilibrium. The rate determining step cannot be CPET because that would require a molecule of reductant.

The strongest support for the proposed mechanism is the close agreement between the equilibrium parameters determined by COPASI-fits to the stopped flow data and the directly measured equilibrium values of $\Delta H°_{ET}/\Delta S°_{ET}$ and $\Delta H°_{O2}/\Delta S°_{O2}$. In addition, the idealized third-order rate constant predicted by the COPASI-fit, (2-20) $\times$ 10^5 M^{-2} s^{-1}, is in excellent agreement with the value determined by electrocatalysis, k_{cat} = (3.2 – 6.4) $\times$ 10^5 M^{-2} s^{-1}.

The computational conclusions qualitatively agree with experimental results and show that proton transfer is the turnover-limiting step. The barrier extracted from the COPASI fits, $\Delta G^{‡}_{PT} \cong 11$ kcal mol^{-1}, is significant but smaller than the computed barrier. As noted above, the modeled $\Delta G^{‡}_{PT}$ may be low due to an underestimation of the $\Delta S^{‡}_{PT}$, which would bring the experimental and computed values into closer agreement. We note that the complexity of the COPASI kinetic modeling and the challenges of computing sulfonate groups make close agreement between experiment and theory unlikely. Still, good agreement between theory and experiment was obtained for the change in barrier heights upon changing the acid from *p*TsOH to $[DMF\text{-}H]^+$. The same value for this Brønsted $\alpha = \Delta\Delta G^{‡}_{PT}/\Delta\Delta G°_{PT} = 0.3$ was obtained from both experiment and theory.[32-33]

In this system, both the computational and experimental results highlight the challenges of proton delivery to the iron-dioxygen adduct. Even when using a relatively strong proton donor like *p*TsOH (pK_a = 2.3 in DMF), protonation of $Fe^{III}(TPP)(O_2^{\bullet-})$ is computed to be uphill by >5 kcal mol^{-1}. This shows the poor basicity of $Fe^{III}(TPP)(O_2^{\bullet-})$, which has an estimated pK_a of –1.7 in DMF.[32]

Beyond the endergonic nature of the proton transfer step, the computations and experiments implicate a significant *kinetic* barrier for protonation of $Fe^{III}(TPP)(O_2^{\bullet-})$. The computational results shown in **Figure 2.7** allow k_{PT} to be expressed as the product of

preassociation (K_{assc}, **Figure 2.7A**) and a unimolecular proton transfer step. The computed pre-association free energy of +8.6 kcal mol^{-1} is due to the unfavorable entropy (–TΔS = 10.7 kcal mol^{-1}) and partial desolvation penalty for *p*TsOH•••DMF (7.8 kcal mol^{-1}) are only partially offset by the hydrogen bonding between the superoxide moiety and *p*TsOH (ΔE = –9.9 kcal mol^{-1}). Overall, this unfavorable interaction contributed almost 50% to the overall reaction barrier height from $Fe^{III}(TPP)(O_2^{\bullet-})$ determined computationally. These results are consistent with the first order dependence of k_{obs} on the [*p*TsOH] determined electrochemically (**Figure 2.3B**), which further suggest that pre-association of the proton donor to $Fe^{III}(TPP)(O_2^{\bullet-})$ is unfavorable.

From the preassociated adduct, the transition state is achieved from a decrease in the O-H-O dihedral angle in the *p*TsOH•••DMF adduct, yielding a species where the proton is shared between the *p*TsO$^-$, DMF, and $Fe^{III}(TPP)(O_2^{\bullet-})$ oxygen atoms (**Figure 2.7B**). These results are consistent with a previous computational study that examined [DMF-H]$^+$ as the proton source.[32] The calculated barrier for proton transfer to $Fe^{III}(TPP)(O_2^{\bullet-})$ is smaller with the stronger acid [DMF-H]$^+$, as expected. Still, even with the stronger, cationic acid, pre-association is again unfavorable by >6 kcal mol^{-1}. As with *p*TsOH•••DMF, there is a significant desolvation penalty for the [DMF-H]$^+$•••DMF proton donor that is not offset by hydrogen bonding to the $Fe^{III}(TPP)(O_2^{\bullet-})$ intermediate.

A surprising feature of this ORR mechanism is that the slow, turnover-limiting step is proton transfer from one oxygen atom to another. The proton donor is para-toluenesulfonic acid, *p*TsOH, and the oxygen acceptor is the superoxide complex, $Fe^{III}(TPP)(O_2^{\bullet-})$. Proton transfers between oxygen atoms are typically fast, although that is not always the case.[57-60] Physical organic studies of proton transfer reactions have discussed pre-association, non-synchronicity, and other factors to explain slow PT rate constants, particularly for carbon acids.[57,59,61-62] Taken together, these results suggest that barriers to proton transfer can be an important component of ORR catalysis in DMF and perhaps other polar organic solvents. Given that pre-association dynamics have been shown to play a major role in the catalytic rates of the reduction of H^+ to H_2 by nickel phosphine-amine complexes,[32,63] our results suggest that pre-association for proton transfer to $Fe^{III}(TPP)(O_2^{\bullet-})$ may be more facile in media where the proton donor preferentially interacts with the $Fe^{III}(TPP)(O_2^{\bullet-})$ adduct over the solvent. These conditions may be realized by working with

strong proton donors in solvents with dielectric constants lower than DMF or MeCN (e.g. THF, CH_2Cl_2). More broadly, using the medium to target preassociation dynamics could be a general approach for improving PCET reactions that are limited by proton transfer steps, particularly for reactions with containing nonpolar adducts, such as the ORR.

2.5 Conclusion

[Fe^{III}(TPP)]OTf is a rapid catalyst and electrocatalyst for the oxygen reduction reaction (ORR). This Chapter describes a detailed mechanistic study of the catalytic chemical reduction of O_2 with decamethylferrocene (Fc*) and *p*-toluenesulfonic acid (*p*TsOH) in DMF, forming Fc^{*+}, *p*TsO^- and (predominantly) water. The various results indicate a mechanism initiated by pre-equilibrium electron transfer to form Fe^{II}(TPP), followed by O_2 binding to form the superoxide complex Fe^{III}(TPP)($O_2^{\bullet-}$) in a second pre-equilibrium step. Both these equilibria were studied independently as a function of temperature, and their equilibrium constants and enthalpies and entropies are reported. Stopped-flow optical monitoring of the reaction kinetics showed that the resting state of the iron catalyst varies substantially during the reactions and with temperature and reaction conditions. The complexity of the kinetics required global analysis of a large set of kinetic runs under different conditions using the COPASI software. This analysis gave an independent measure of the thermodynamic parameters for the pre-equilibria. The agreement between these kinetic-fit values and the directly measured equilibrium parameters provides very strong evidence for the proposed mechanism. In addition, parallel electrochemical kinetics showed complementary kinetic behavior and rate constants, further supporting the proposed mechanism.

The turnover-limiting step in catalysis is the protonation of Fe^{III}(TPP)($O_2^{\bullet-}$). Computational studies of this step showed that there is substantial energetic cost to assemble the pre-association complex of the acid and Fe^{III}(TPP)($O_2^{\bullet-}$) and that there is a substantial barrier to proton transfer within this complex. This work is a rare example of a mechanistic investigation of the ORR that directly observes and quantifies the pre-equilibria and rate-determining steps of three catalytic intermediates. The ability to correlate thermodynamic, chemical kinetic, electrochemical kinetic, and computational data provide an unusual level of detail about a multistep proton-coupled electron transfer catalytic process. In particular, the results highlight the importance of improving proton

transfer dynamics during catalytic transformations involving nonpolar small molecule adducts in organic solvents.

2.6 References and Notes

1. Sono, M.; Roach, M. P.; Coulter, E. D.; Dawson, J. H., Heme-Containing Oxygenases. *Chem. Rev.* **1996,** *96* (7), 2841-2888.
2. Lewis, E. A.; Tolman, W. B., Reactivity of Dioxygen−Copper Systems. *Chem. Rev.* **2004,** *104* (2), 1047-1076.
3. Shao, M.; Chang, Q.; Dodelet, J.-P.; Chenitz, R., Recent Advances in Electrocatalysts for Oxygen Reduction Reaction. *Chem. Rev.* **2016,** *116* (6), 3594-3657.
4. Dai, L.; Xue, Y.; Qu, L.; Choi, H.-J.; Baek, J.-B., Metal-Free Catalysts for Oxygen Reduction Reaction. *Chem. Rev.* **2015,** *115* (11), 4823-4892.
5. Huang, X.; Groves, J. T., Oxygen Activation and Radical Transformations in Heme Proteins and Metalloporphyrins. *Chem. Rev.* **2018,** *118* (5), 2491-2553.
6. Yoshikawa, S.; Shimada, A., Reaction Mechanism of Cytochrome c Oxidase. *Chem. Rev.* **2015,** *115* (4), 1936-1989.
7. Denisov, I. G.; Makris, T. M.; Sligar, S. G.; Schlichting, I., Structure and Chemistry of Cytochrome P450. *Chem. Rev.* **2005,** *105* (6), 2253-2278.
8. Meunier, B.; de Visser, S. P.; Shaik, S., Mechanism of Oxidation Reactions Catalyzed by Cytochrome P450 Enzymes. *Chem. Rev.* **2004,** *104* (9), 3947-3980.
9. Huang, X.; Groves, J. T., Beyond ferryl-mediated hydroxylation: 40 years of the rebound mechanism and C–H activation. *J. Biol. Inorg. Chem.* **2017,** *22* (2-3), 185-207.
10. Winter, M.; Brodd, R. J., What Are Batteries, Fuel Cells, and Supercapacitors? *Chem. Rev.* **2004,** *104* (10), 4245-4270.
11. Pegis, M. L.; Wise, C. F.; Martin, D. J.; Mayer, J. M., Oxygen Reduction by Homogeneous Molecular Catalysts and Electrocatalysts. *Chem. Rev.* **2018,** *118* (5), 2340-2391.
12. Gewirth, A. A.; Varnell, J. A.; DiAscro, A. M., Nonprecious Metal Catalysts for Oxygen Reduction in Heterogeneous Aqueous Systems. *Chem. Rev.* **2018,** *118* (5), 2313-2339.
13. Collman, J. P.; Boulatov, R.; Sunderland, C. J.; Fu, L., Functional Analogues of Cytochrome c Oxidase, Myoglobin, and Hemoglobin. *Chem. Rev.* **2004,** *104* (2), 561-588.
14. Zhang, W.; Lai, W.; Cao, R., Energy-Related Small Molecule Activation Reactions: Oxygen Reduction and Hydrogen and Oxygen Evolution Reactions Catalyzed by Porphyrin- and Corrole-Based Systems. *Chem. Rev.* **2017,** *117* (4), 3717-3797.
15. Lefèvre, M.; Proietti, E.; Jaouen, F.; Dodelet, J.-P., Iron-Based Catalysts with Improved Oxygen Reduction Activity in Polymer Electrolyte Fuel Cells. *Science* **2009,** *324* (5923), 71-74.
16. Wu, G.; More, K. L.; Johnston, C. M.; Zelenay, P., High-Performance Electrocatalysts for Oxygen Reduction Derived from Polyaniline, Iron, and Cobalt. *Science* **2011,** *332* (6028), 443-447.
17. Zitolo, A.; Goellner, V.; Armel, V.; Sougrati, M.-T.; Mineva, T.; Stievano, L.; Fonda, E.; Jaouen, F., Identification of catalytic sites for oxygen reduction in iron- and nitrogen-doped graphene materials. *Nat. Mater.* **2015,** *14* (9), 937-942.
18. Chang, C. J.; Loh, Z.-H.; Shi, C.; Anson, F. C.; Nocera, D. G., Targeted Proton Delivery in the Catalyzed Reduction of Oxygen to Water by Bimetallic Pacman Porphyrins. *J. Am. Chem. Soc.* **2004,** *126* (32), 10013-10020.
19. Collman, J. P.; Denisevich, P.; Konai, Y.; Marrocco, M.; Koval, C.; Anson, F. C., Electrode catalysis of the four-electron reduction of oxygen to water by dicobalt face-to-face porphyrins. *J. Am. Chem. Soc.* **1980,** *102* (19), 6027-6036.
20. Rigsby, M. L.; Wasylenko, D. J.; Pegis, M. L.; Mayer, J. M., Medium Effects Are as Important as Catalyst Design for Selectivity in Electrocatalytic Oxygen Reduction by Iron–Porphyrin Complexes. *J. Am. Chem. Soc.* **2015,** *137* (13), 4296-4299.
21. McGuire Jr, R.; Dogutan, D. K.; Teets, T. S.; Suntivich, J.; Shao-Horn, Y.; Nocera, D. G., Oxygen reduction reactivity of cobalt(II) hangman porphyrins. *Chem. Sci.* **2010,** *1* (3), 411-411.
22. Bhunia, S.; Rana, A.; Roy, P.; Martin, D. J.; Pegis, M. L.; Roy, B.; Dey, A., Rational Design of Mononuclear Iron Porphyrins for Facile and Selective $4e^-/4H^+$ O_2 Reduction: Activation of O–O Bond by 2nd Sphere Hydrogen Bonding. *J. Am. Chem. Soc.* **2018,** *140* (30), 9444-9457.

23. Chatterjee, S.; Sengupta, K.; Mondal, B.; Dey, S.; Dey, A., Factors Determining the Rate and Selectivity of $4e^-/4H^+$ Electrocatalytic Reduction of Dioxygen by Iron Porphyrin Complexes. *Acc. Chem. Res.* **2017,** *50* (7), 1744-1753.
24. Collman, J. P.; Brauman, J. I.; Iverson, B. L.; Sessler, J. L.; Morris, R. M.; Gibson, Q. H., Dioxygen and carbonyl binding to iron(II) porphyrins: a comparison of the "picket fence" and "pocket" porphyrins. *J. Am. Chem. Soc.* **1983,** *105* (10), 3052-3064.
25. Niederhoffer, E. C.; Timmons, J. H.; Martell, A. E., Thermodynamics of oxygen binding in natural and synthetic dioxygen complexes. *Chem. Rev.* **1984,** *84* (2), 137-203.
26. Collman, J. P., Synthetic models for the oxygen-binding hemoproteins. *Acc. Chem. Res.* **1977,** *10* (7), 265-272.
27. Groves, J. T.; Watanabe, Y., Reactive iron porphyrin derivatives related to the catalytic cycles of cytochrome P-450 and peroxidase. Studies of the mechanism of oxygen activation. *J. Am. Chem. Soc.* **1988,** *110* (25), 8443-8452.
28. McLain, J. L.; Lee, J.; Groves, J. T., Biomimetic Oxygenations Related to Cytochrome P450: Metal-Oxo and Metal-Peroxo Intermediates. Imperial College Press: 2000; pp 91-169.
29. Fukuzumi, S.; Mochizuki, S.; Tanaka, T., Efficient Reduction of Dioxygen with Ferrocene Derivatives, Catalyzed by Metalloporphyrins in the Presence of Perchloric Acid. *Inorg. Chem.* **1989,** *28* (Copyright (C) 2011 American Chemical Society (ACS). All Rights Reserved.), 2459-2465.
30. Fukuzumi, S.; Mochizuki, S.; Tanaka, T., Metalloporphyrin-Catalyzed Reduction of Dioxygen by Ferrocene Derivatives. *Chem. Lett.* **1989,** *18* (1), 27-30.
31. Wasylenko, D. J.; Rodríguez, C.; Pegis, M. L.; Mayer, J. M., Direct Comparison of Electrochemical and Spectrochemical Kinetics for Catalytic Oxygen Reduction. *J. Am. Chem. Soc.* **2014,** *136* (36), 12544-12547.
32. Pegis, M. L.; McKeown, B. A.; Kumar, N.; Lang, K.; Wasylenko, D. J.; Zhang, X. P.; Raugei, S.; Mayer, J. M., Homogenous Electrocatalytic Oxygen Reduction Rates Correlate with Reaction Overpotential in Acidic Organic Solutions. *ACS Cent. Sci.* **2016,** *2* (11), 850-856.
33. Pegis, M. L.; Wise, C. F.; Koronkiewicz, B.; Mayer, J. M., Identifying and Breaking Scaling Relations in Molecular Catalysis of Electrochemical Reactions. *J. Am. Chem. Soc.* **2017,** *139* (32), 11000-11003.
34. Safo, M. K.; Nesset, M. J. M.; Walker, F. A.; Debrunner, P. G.; Scheidt, W. R., Models of the Cytochromes. Axial Ligand Orientation and Complex Stability in Iron(II) Porphyrinates: The Case of the Noninteracting d_π Orbitals. *J. Am. Chem. Soc.* **1997,** *119* (40), 9438-9448.
35. Walker, F. A.; Simonis, U., Iron Porphyrin Chemistry. John Wiley & Sons, Ltd: Chichester, UK, 2006.
36. Hoops, S.; Sahle, S.; Gauges, R.; Lee, C.; Pahle, J.; Simus, N.; Singhal, M.; Xu, L.; Mendes, P.; Kummer, U., COPASI–a COmplex PAthway SImulator. *Bioinformatics* **2006,** *22* (24), 3067-3074.
37. Perdew, J. P.; Burke, K.; Ernzerhof, M., Generalized Gradient Approximation Made Simple. *Phys. Rev. Lett.* **1996,** *77* (18), 3865-3868.
38. Francl, M. M.; Pietro, W. J.; Hehre, W. J.; Binkley, J. S.; Gordon, M. S.; DeFrees, D. J.; Pople, J. A., Self-consistent molecular orbital methods. XXIII. A polarization-type basis set for second-row elements. *J. Chem. Phys.* **1982,** *77* (7), 3654-3665.
39. Hehre, W. J.; Ditchfield, R.; Pople, J. A., Self—Consistent Molecular Orbital Methods. XII. Further Extensions of Gaussian—Type Basis Sets for Use in Molecular Orbital Studies of Organic Molecules. *J. Chem. Phys.* **1972,** *56* (5), 2257-2261.
40. Marenich, A. V.; Cramer, C. J.; Truhlar, D. G., Universal Solvation Model Based on Solute Electron Density and on a Continuum Model of the Solvent Defined by the Bulk Dielectric Constant and Atomic Surface Tensions. *J. Phys. Chem. B* **2009,** *113* (18), 6378-6396.
41. Anderson, D. L.; Weschler, C. J.; Basolo, F., Reversible reaction of simple ferrous porphyrins with molecular oxygen at low temperatures. *J. Am. Chem. Soc.* **1974,** *96* (17), 5599-5600.
42. McCandlish, E.; Miksztal, A. R.; Nappa, M.; Sprenger, A. Q.; Valentine, J. S.; Stong, J. D.; Spiro, T. G., Reactions of superoxide with iron porphyrins in aprotic solvents. A high spin ferric porphyrin peroxo complex. *J. Am. Chem. Soc.* **1980,** *102* (12), 4268-4271.

43. James, H. J.; Broman, R. F., Modified winkler determination of oxygen in dimethylformamide: oxygen solubility as a function of partial pressure. *Anal. Chim. Acta* **1969,** *48* (2), 411-417.
44. Devore, J. L., *Probability and Statistics for Engineering and the Sciences*. 2nd ed.; Brooks/Cole Publishing Company: Monterey, 1987.
45. Lexa, D.; Rentien, P.; Savéant, J. M.; Xu, F., Methods for Investigating the Mechanistic and Kinetic Role of Ligand Exchange Reactions in Coordination Electrochemistry. *J. Electroanal. Chem.* **1985,** *191* (2), 253-279.
46. Costentin, C.; Drouet, S.; Robert, M.; Savéant, J.-M., Turnover Numbers, Turnover Frequencies, and Overpotential in Molecular Catalysis of Electrochemical Reactions. Cyclic Voltammetry and Preparative-Scale Electrolysis. *J. Am. Chem. Soc.* **2012,** *134* (27), 11235-11242.
47. Electron transfer from Fc* to O_2 in DMF has $E°$ = −0.69 V ($\Delta G°$ = +16 kcal mol^{-1}), and superoxide is likely reactive with both *p*TsOH and the ferrocene derivatives. (a) $E°(O_2^{0/\bullet -})$ in DMF: (a) Sawyer, D. T.; Chiericato, G.; Angelis, C. T.; Nanni, E. J.; Tsuchiya, T. Effects of Media and Electrode Materials on the Electrochemical Reduction of Dioxygen. Anal. Chem. 1982, 54, 1720−1724. (b) Astruc, D. Electron Transfer and Radical Processes in Transition-Metal Chemistry; VCH Publishers, Inc.: New York 1995; p10010.
48. Ghiladi, R. A.; Kretzer, R. M.; Guzei, I.; Rheingold, A. L.; Neuhold, Y.-M.; Hatwell, K. R.; Zuberbühler, A. D.; Karlin, K. D., $(F_8TPP)Fe^{II}/O_2$ Reactivity Studies {F_8TPP = Tetrakis(2,6-difluorophenyl)porphyrinate(2−)}: Spectroscopic (UV−Visible and NMR) and Kinetic Study of Solvent-Dependent (Fe/O_2 = 1:1 or 2:1) Reversible O_2-Reduction and Ferryl Formation. *Inorg. Chem.* **2001,** *40* (23), 5754-5767.
49. Evans, D. R.; Reed, C. A., Reversal of H_2O and OH^- Ligand Field Strength on the Magnetochemical Series Relative to the Spectrochemical Series. Novel 1-equiv Water Chemistry of Iron(III) Tetraphenylporphyrin Complexes. *J. Am. Chem. Soc.* **2000,** *122* (19), 4660-4667.
50. Ostfeld, D.; Colfax, J. A., Splitting of hematin dimers in nonaqueous solution. *Inorg. Chem.* **1978,** *17* (7), 1796-1799.
51. Hammond, G. S.; Wu, C.-H. S., Oxidation of Iron(II) Chloride in Nonaqueous Solvents. 1968; pp 186-207.
52. Chin, D.-H.; La Mar, G. N.; Balch, A. L., Mechanism of autoxidation of iron(II) porphyrins. Detection of a peroxo-bridged iron(III) porphyrin dimer and the mechanism of its thermal decomposition to the oxo-bridged iron(III) porphyrin dimer. *J. Am. Chem. Soc.* **1980,** *102* (13), 4344-4350.
53. Kao, O. H. W.; Wang, J. H., Kinetic Study of the Oxidation of Ferrohemochrome by Molecular Oxygen. *Biochemistry* **1965,** *4* (2), 342-347.
54. Cohen, I. A.; Caughey, W. S., Substituted deuteroporphyrins. IV. Kinetics and mechanism of reactions of iron(II) porphyrins with oxygen. *Biochemistry* **1968,** *7* (2), 636-641.
55. Miller, D. C.; Tarantino, K. T.; Knowles, R. R., Proton-Coupled Electron Transfer in Organic Synthesis: Fundamentals, Applications, and Opportunities. *Top. Curr. Chem.* **2016,** *374* (3), 30-30.
56. Morris, W. D.; Mayer, J. M., Separating Proton and Electron Transfer Effects in Three-Component Concerted Proton-Coupled Electron Transfer Reactions. *J. Am. Chem. Soc.* **2017,** *139* (30), 10312-10319.
57. Kresge, A. J., What makes proton transfer fast. *Acc. Chem. Res.* **1975,** *8* (10), 354-360.
58. Robinson, B. H., Hydrogen-Bonding and Proton-Transfer Reactions in Aprotic Solvents. Springer: Boston, 1975; pp 121-152.
59. Crooks, J. E., Fast and slow proton-transfer reactions in solution. Springer: Boston, 1975; pp 153-178.
60. Guthrie, J. P., Intrinsic Barriers for Proton Transfer Reactions Involving Electronegative Atoms, and the Water Mediated Proton Switch: An Analysis in Terms of Marcus Theory. *J. Am. Chem. Soc.* **1996,** *118* (51), 12886-12890.
61. Bernasconi, C. F., The principle of nonperfect synchronization: recent developments. 2010; Vol. 44, pp 223-324.

62. Bernasconi, C. F., The principle of nonperfect synchronization: more than a qualitative concept? *Acc. Chem. Res.* **1992,** *25* (1), 9-16.
63. O'Hagan, M.; Ho, M.-H.; Yang, J. Y.; Appel, A. M.; DuBois, M. R.; Raugei, S.; Shaw, W. J.; DuBois, D. L.; Bullock, R. M., Proton Delivery and Removal in $[Ni(P^{R2}N^{R2})_2]^{2+}$ Hydrogen Production and Oxidation Catalysts. *J. Am. Chem. Soc.* **2012,** *134* (47), 19409-19424.

3 Chapter 3 – Combining Scaling Relationships Overcomes Rate versus Overpotential Trade-offs in O_2 Molecular Electrocatalysis

Adapted from Martin, D. J.; Mercado, B. Q.; Mayer, J. M. "Combining scaling relationships overcomes rate versus overpotential trade-offs in O_2 molecular electrocatalysis." *Sci. Adv.* **2020**, *6*, eaaz3318. DJM and JMM conceived the project, constructed the scientific arguments, and wrote the paper. BQM performed x-ray crystallography and solved the structures. DJM performed all other experiments and analyzed and interpreted the data. The authors thank Dr. Michael L. Pegis for very helpful discussions and Dr. Fabian Menges of the Yale Chemical and Biophysical Instrumentation Center for collecting the HRMS data.

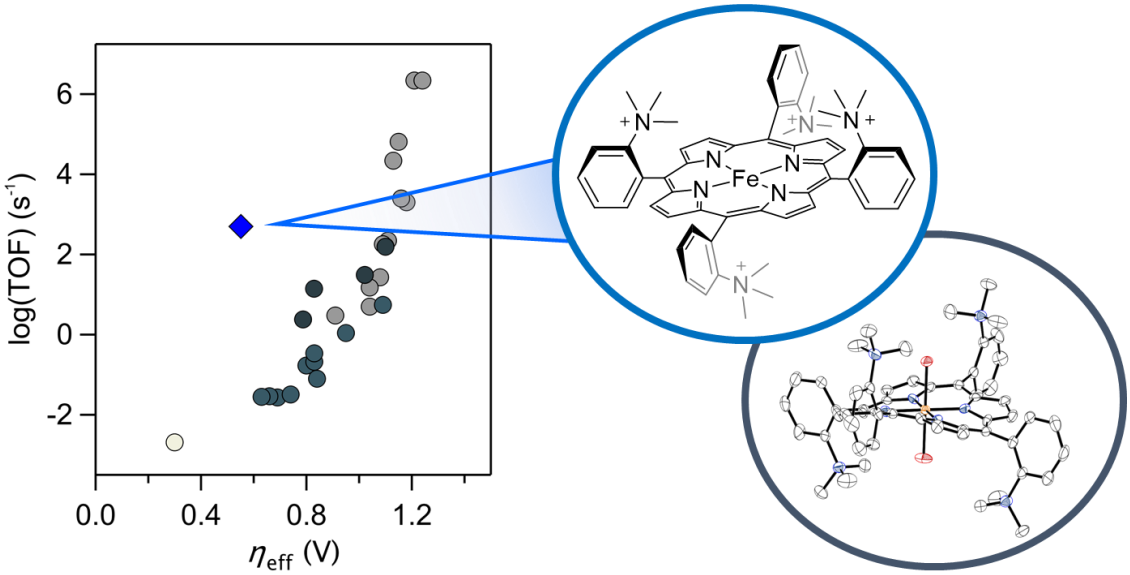

3.1 Introduction

Improving the rates and efficiencies of electrocatalytic reactions is critical to the development of chemical-to-electrical energy conversion technologies. The oxygen reduction reaction (ORR)—the combination of dioxygen (O_2), protons, and electrons to give water—is an important example common to fuel cells.[1-2] Because current ORR technologies use platinum catalysts, current research seeks replacements sourced from earth-abundant materials.[3] One approach for developing catalytic systems with high rates (turnover frequencies, TOFs) and high efficiencies (low overpotentials, η) has been the development of scaling relationships. The properties of heterogeneous electrocatalysts can often be understood and even predicted using a single scaling descriptor, typically the energy of substrate binding to the catalyst surface.[4] In contrast, soluble molecular electrocatalysts, which can be studied in more atomistic and mechanistic detail, follow multiple kinetic/thermodynamic scaling relationships.[5] These describe

how the maximum TOFs (log(TOF_{max})) scale with the various terms contributing to the effective overpotential (η_{eff}; see Appendix B).[5-8] To date, the reported log(TOF_{max})/η_{eff} relationships always describe a trade-off: faster catalysis is only achieved at lower efficiencies (higher η_{eff}).

We report here an *inverse* scaling relationship, one that allows for *faster rates at higher efficiencies*, using a polycationic iron-porphyrin catalyst with buffered weak acids in acetonitrile (MeCN) (**Figure 3.1**). With acetic acid/acetate buffer (AcOH/AcO^-), this system achieves a TOF_{max} of 170 s^{-1} at 0.54 V η_{eff}, which is ~10^4 faster than any previously reported molecular ORR catalyst at this η_{eff}.[2,9] As described below, this unprecedented result is *predictable* by combining two kinetic/thermodynamic scaling relationships. The coupling of the two scaling relationships is a result of the electrostatic ligand design of **1** enables cooperativity between the catalyst and buffer.

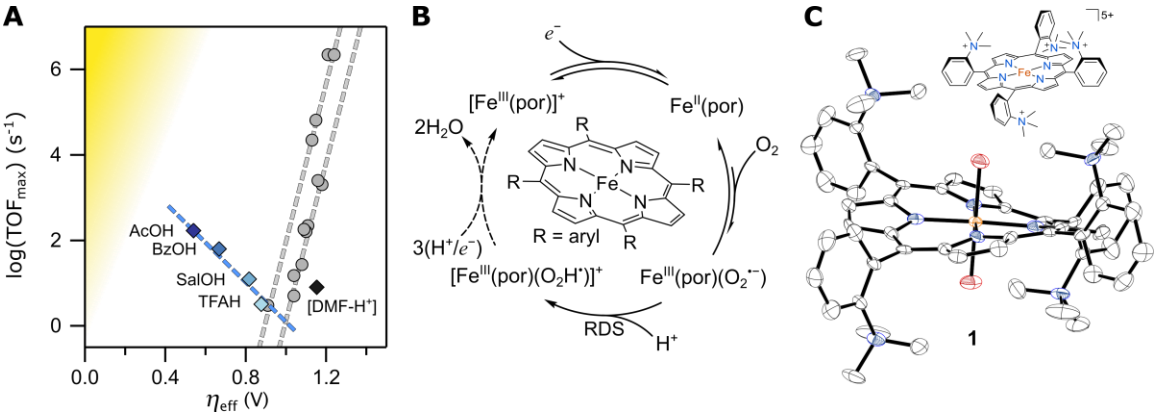

Figure 3.1. Catalytic system efficiencies, reaction mechanism, and structure of catalyst **1**. (**A**) Plot of log(TOF_{max})/η_{eff} values and fits (dashed lines) for **1** (diamonds; data and conditions in **Table 3.1**) and for previously reported iron-porphyrin (Fe(por)) catalysts (circles; 0.1 M [DMF-H^+] in DMF or MeCN, see ref [5]). The uncertainties are smaller than the data points. The yellow shading indicates an aspirational region. (**B**) Fe(por) catalyzed O_2 reduction mechanism, as described in the text.[10] (**C**) Drawings of **1** and of the cation in the solid-state x-ray crystal structure, [**1**•2H_2O]OTf_5 (Fe-orange, N-blue, C-white; O-red; H atoms omitted for clarity; thermal ellipsoids at 50% probability).

3.2 Results

Iron *tetra*(*o*-*N*,*N*,*N*-trimethylanilinium)porphyrin (**1**) was prepared as reported.[11] The di-aquo, penta-triflate salt of the αβαβ-isomer was identified as a component of the reaction product by single-crystal X-ray diffraction (**Figure 3.1C**; see Appendix B, Section B.9). [In Chapter 5 of this thesis, it was revealed that the product of this reaction yielded a mixture of catalyst atropiosmers, rather than just the αβαβ isomer, as was originally assumed.] Cyclic voltammograms (CVs) of **1** in MeCN containing 0.1 M tetra-*n*-butylammonium tetrafluoroborate electrolyte ([*n*-Bu_4N][BF_4])

showed three reversible redox features ($Fe^{III/II}$, $Fe^{II/I}$ and $Fe^{I/0}$; see Appendix B, Section B.2.1).[11] Solutions containing **1**, O_2, and buffered acid (1:1 [HA]/[A^-]) showed a large, irreversible current at the Fe^{III}/Fe^{II} reduction potential, indicative of catalysis.[5,7,10] All CV experiments were buffered (1:1 acid-to-conjugate base) in order to define the ORR equilibrium potential and η_{eff}, which was calculated using eq 3.1 (see Appendix B, Section B.6).[5,7,10]

Measurements of the H_2O/H_2O_2 selectivity were performed using rotating ring disk electrochemistry (RRDE). In all cases, electrocatalysis was found to give < 20% H_2O_2 (see Appendix B, Section B.7). This high selectivity for H_2O is similar to other iron porphyrin catalysts under comparable conditions.[5,7,10] With AcOH/AcO^- buffer, catalysis occurs at potentials below the equilibrium potential for O_2 to H_2O_2 and thus requires thermodynamic selectivity for H_2O (see ref [9]).

TOF_{max} were determined from the catalytic CVs by foot-of-the-wave analysis (FOWA), eq 3.2 (**Table 3.1**; see Appendix B, Section B.5).[5,10,12] This widely used approach normalizes the catalytic currents (i_c) to the non-catalytic peak current of the $Fe^{III/II}$ couple (i_p) at potentials (E) near the onset of the catalytic wave, where complications such as substrate depletion are minimized. Given the high selectivity for H_2O, n_{cat} was taken to be 4 (electrons per O_2 reduced), and the conservative σ = 1 value was used (see Appendix B, Section B.5). Measuring TOF_{max} values under different conditions showed that the catalytic rate law was first order in [**1**], P_{O2}, and [HA], similar to other Fe(por) catalysts.[5,7,10] [HA] is the concentration of free acid after considering homoconjugation (see Appendix B, Section B.4). These results implicate a catalytic mechanism of *i*) initial reduction of $[Fe^{III}(por)]^+$ to $Fe^{II}(por)$, *ii*) pre-equilibrium O_2-binding to form the superoxide complex, $Fe^{III}(por)(O_2^{\bullet -})$, and *iii*) rate-limiting proton transfer to form $[Fe^{III}(por)(O_2H^{\bullet})]^+$ (**Figure 3.1B**). Experimental and computational studies of this mechanism reported in ref [5,10] (Chapter 2).

$$\eta_{\text{eff}} = E^{\text{o}}_{\text{ORR}} - E_{1/2} - \frac{2.303\text{RT}}{n_{cat}\text{F}}\log\left(\frac{\left[\text{H}_2\text{O}\right]^2\left[\text{A}^-\right]^4}{P_{\text{O}_2}\left[\text{HA}\right]^4}\right) - (0.0592\text{V})\text{p}K_a \qquad \text{(eq 3.1)}$$

$$\frac{i_{\text{c}}}{i_{\text{p}}} = \frac{2.24 n_{cat}^{\sigma}\sqrt{\frac{\text{RT}}{\text{F}\nu}\text{TOF}_{\text{max}}}}{1+\exp\left[\frac{\text{F}}{\text{RT}}(E - E_{1/2})\right]} \qquad \text{(eq 3.2)}$$

ORR catalysis was studied in MeCN using **1** and a series of buffers. Using *N*,*N*-dimethylformamidium triflate ([DMF-H$^+$]OTf, pK_a = 6.1), TOF_{max} = 8.5 s^{-1} and η_{eff} = 1.16 V (**Table 3.1**). Within the log(TOF_{max})/η_{eff} space, this (η_{eff}, log(TOF_{max})) data point roughly fits the scaling relationships previously reported for Fe(por) electrocatalysts under similar conditions (black diamond, **Figure 3.1A**).[5] In contrast, using acetic acid (AcOH, pK_a = 23.5) gave dramatically improved catalysis: a faster TOF_{max} (170 s^{-1}) at less than half the η_{eff} (0.54 V). This result contradicts previously-derived log(TOF_{max})/η_{eff} relationships, which always predict that a lower overpotential will give a slower rate, as seen for iron tetra-arylporphyrins (see Appendix B, Section B.8).[7] Catalysis with **1** and trifluoroacetic acid (TFAH), salicylic acid (SalOH), or benzoic acid (BzOH) similarly show improvements in *both* TOF_{max} and η_{eff} vs. the [DMF-H$^+$] point (blue diamonds, **Figure 3.1**; **Table 3.1**). Together, the carboxylic acid (η_{eff}, log(TOF_{max})) points define an unexpected *inverse* log(TOF_{max})/η_{eff} relationship (dashed blue line, **Figure 3.1A**), a previously unachieved goal in molecular electrocatalysis.[5,13-14] The following sections describe a model that explains this inverse relationship as the sum of two known kinetic/thermodynamic scaling relationships.[7]

Table 3.1. Properties of catalytic systems with **1** and different buffers.[*]

Buffer[†]	pK_a[‡]	$E_{1/2}$ (V)[§]	η_{eff} (V)[¶]	TOF_{max} (s^{-1})[#]	log(TOF_{max})
None	-	−0.295	-	-	-
[DMF-H$^+$]/DMF	6.1	−0.25[‡]	1.16	8.5	0.91
TFAH/TFA$^-$	12.6	−0.349	0.88	3.2	0.51
[Lut-H$^+$]/Lut	14.1	−0.23[‡]	0.68	0.07	−1.17
SalOH/SalO$^-$	16.7	−0.536	0.82	12	1.08
BzOH/BzO$^-$	21.5	−0.653	0.67	63	1.80
AcOH/AcO$^-$	23.5	−0.651	0.54	170	2.23

[*] Experimental conditions: 0.1 mM **1**, 0.1 M buffer (1:1 HA/A or HB$^+$/B), 0.1 M [*n*-Bu_4N][BF_4] in MeCN (~15 mM H_2O), 1 atm O_2. [†] [DMF-H$^+$] = *N*,*N*-dimethylformamidium triflate; TFAH = trifluoroacetic acid; [Lut-H$^+$] = lutidinium tetrafluoroborate; SalOH = salicylic acid; BzOH = benzoic acid; AcOH = acetic acid. [‡] See Appendix B. [§] $E_{1/2}$($Fe^{III/II}$) reduction potential (vs. ferrocene/ferrocenium, under Ar, with 100 mM buffer). [¶] From eq 3.2; ±0.02 V. [#] From FOWA.

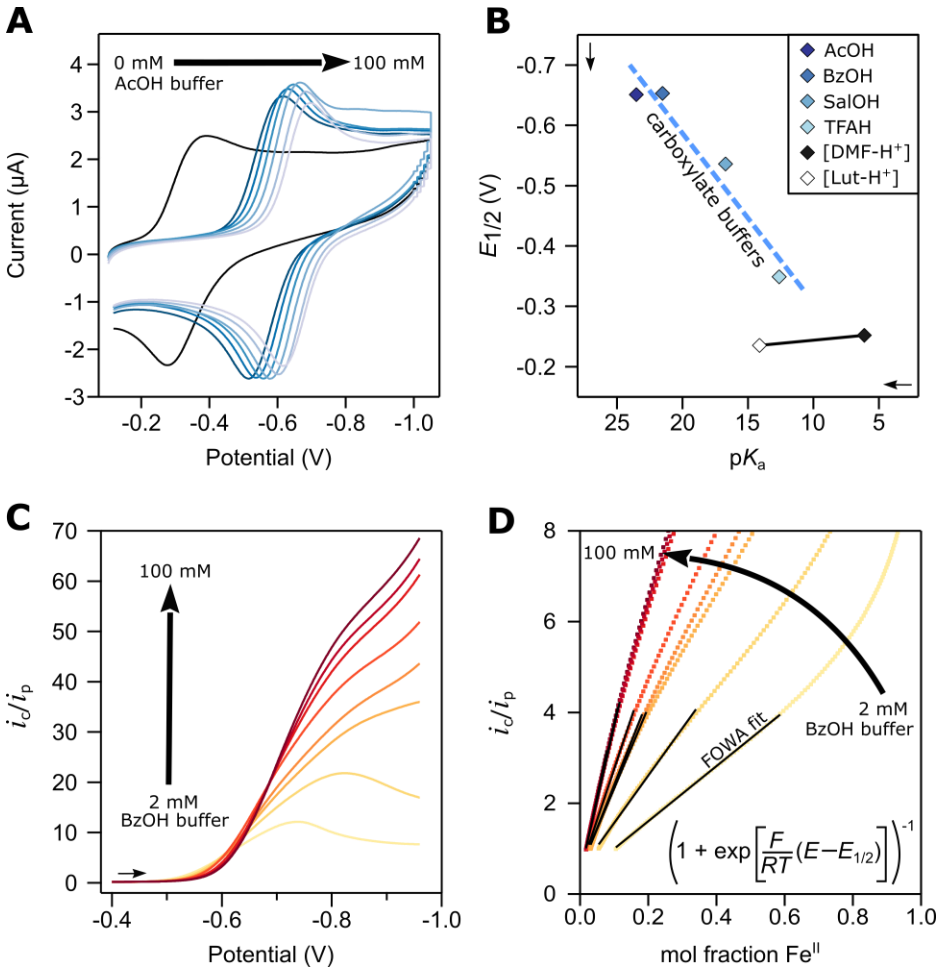

Figure 3.2. Electrochemical studies of **1** under non-catalytic and catalytic conditions. (**A**) CVs of **1** showing the shift of $E_{1/2}$ with increasing concentrations of 1:1 AcOH/AcO$^-$ buffer. (**B**) Plot of $E_{1/2}$ vs. the acid pK_a at 0.1 M buffer. (**C**) Linear sweep voltammograms under catalytic conditions with different BzOH buffer concentrations. (**D**) FOWA for voltammograms in **C**, with fits between i_c/i_p = 1–4.

3.3 Discussion

Catalyst **1** is unique among the Fe(por) series because changing the buffer significantly affects *two* properties of the catalytic system: the acid pK_a and also the catalyst $E_{1/2}$, due to carboxylate binding (see Appendix B, Section B.2.1.8). Since both pK_a and $E_{1/2}$ each modulate the TOF_{max} and η_{eff} in different ways (see Chapter 1, Appendix B, Section B.8 and ref [5,7] for further discussion), a single scaling relationship is not adequate for predicting the composite changes in $\log(TOF_{max})/\eta_{eff}$. Instead, the scaling relationships—which only establish directionality within the $\log(TOF_{max})/\eta_{eff}$ space—must be recast as vectors. Vectors have directionality *and length*, and are

additive. An alternative—but equally accurate—description of this approach is that it is a multivariable fit of independent scaling relationships.

The Nernst equation for this ORR reaction (eq 3.1) shows that a one-unit increase in acid pK_a decreases η_{eff} by 0.059 V: $\Delta\eta_{eff}$ = –(0.059 V)ΔpK_a.[15-16] In iron-porphyrin ORR catalysis, protonation is the rate-determining step and the TOF_{max} varies with pK_a according to the Brønsted equation: $\Delta\log(TOF_{max}) = -\alpha(\Delta pK_a)$, where $\alpha \approx 0.3$ (see Appendix B, Section B.8 for further discussion).[5,7,10] For the range of carboxylate buffers used here, TFAH/TFA^- to AcOH/AcO^-, the change in pK_a is 10.9 units. Therefore, with $\alpha = 0.3$ and holding all other properties constant, the changes in η_{eff} and log(TOF_{max}) associated with the 10.9-unit pK_a shift can be described as the vector $\vec{v}_{pK_a}$ in the (η_{eff}, log(TOF_{max})) space (eq 3.3, dec = decade in TOF_{max}; **Figure 3.3**).

$$\vec{v}_{pK_a} = \langle \Delta\eta_{eff}, \Delta\log(TOF_{max}) \rangle = \langle -0.059(\Delta pK_a), -\alpha(\Delta pK_a) \rangle = \langle -0.64\ \text{V}, -3.3\ \text{dec} \rangle \quad \text{(eq 3.3)}$$

In addition to acid pK_a, the buffer identity also affects the $E_{1/2}$. When buffered carboxylic acids are titrated into solutions of **1**, the catalyst $E_{1/2}$ shifts negatively, by as much as 350 mV (**Figure 3.2A**). This shift results from the conjugate base of the buffer (e.g. acetate) binding more strongly to the Fe^{III} vs. the Fe^{II} form of **1**. Such behavior was documented and explained many years ago for chloride binding to iron tetraphenylporphyrin.[17] At 0.1 M carboxylate buffer, the $E_{1/2}$ values vary linearly with acid pK_a (−28 ± 1 mV/pK_a, **Figure 3.2B**). In contrast, buffers with cationic acids and neutral conjugate bases ([DMF-H^+]/DMF and [Lut-H^+]/Lut) give only small shifts in $E_{1/2}$ (< 50 mV, **Figure 3.2B**). This unique distinction is due to the highly cationic nature of **1**, which enhances binding of anionic conjugate bases but not neutral ones (see Appendix B, Section B.2.1.8). Further supporting the importance of the cationic ligand, no significant change in catalyst $E_{1/2}$ was reported when iron tetraphenylporphyrin—an analogue without the cationic trimethylanilinium groups—was combined with similar buffers under similar conditions.[7]

Changes in $E_{1/2}$ also affect η_{eff}: $\Delta\eta_{eff} = -\Delta E_{1/2}$ (eq 3.2).[5,7,18] For the Fe(por) series, log(TOF_{max}) has empirically been shown to change according to $\log(TOF_{max}) = -18.5$ decade/$E_{1/2}$(V) (see Appendix B, Section B.8 for further discussion).[7] Conceptually, this is because catalysts with more negative $E_{1/2}$ values (and thus higher η_{eff} values) bind O_2 more strongly and

form more basic superoxide complexes, both of which lead to higher TOF_{max}.[5] As above, a vector $\vec{v}_{E_{1/2}}$ can be used to represent the log(TOF_{max})/$E_{1/2}$ scaling relation and the 0.302 V change in $E_{1/2}$ upon replacing TFAH/TFA^- with AcOH/AcO^- (eq 3.4, **Figure 3.3**).

$$\vec{v}_{E_{1/2}} = \langle \Delta\eta_{\text{eff}}, \Delta\log(\text{TOF}_{\text{max}}) \rangle = \langle -\Delta E_{1/2}, -18.5(\Delta E_{1/2}) \rangle = \langle 0.30\ \text{V}, 5.6\ \text{dec} \rangle \qquad \text{(eq 3.4)}$$

Because the buffer affects both the acid pK_a and catalyst $E_{1/2}$, both $\vec{v}_{pK_a}$ and $\vec{v}_{E_{1/2}}$ are needed to describe the changes in η_{eff} and log(TOF_{max}). The effects of these changes are *additive,* described by the vector sum: $\vec{v}_{\text{sum}} = \vec{v}_{pK_a} + \vec{v}_{E_{1/2}}$ (eq 3.5, **Figure 3.3**). While neither $\vec{v}_{pK_a}$ nor $\vec{v}_{E_{1/2}}$ alone fit the observed changes in log(TOF_{max})/η_{eff}, $\vec{v}_{\text{sum}}$ *predicts* both the directionality and distance from the experimental TFAH coordinate to the AcOH coordinate—within a factor of 3 in TOF_{max}.

$$\vec{v}_{\text{sum}} = \vec{v}_{pK_a} + \vec{v}_{E_{1/2}} = \langle -0.34\ \text{V}, 2.3\ \text{dec} \rangle \qquad \text{(eq 3.5)}$$

Qualitatively, using a less acidic buffer improves the overall catalysis because of two factors. The change in $E_{1/2}$ causes a large gain in TOF_{max} at relatively little cost to η_{eff} (a steep scaling slope). In contrast, the concomitant changes in pK_a decrease η_{eff} substantially with only small losses in TOF_{max} (a shallow slope). When combined, the different slopes—and thus the different coefficients of the multivariable fit—result in faster TOF_{max} at lower η_{eff}.

While $\vec{v}_{\text{sum}}$ is required to analyze the carboxylate buffer data, only $\vec{v}_{pK_a}$ is needed to predict the change in log(TOF_{max})/η_{eff} for the cationic buffers (e.g. [DMF-H^+]/DMF and [Lut-H^+]/Lut) (**Figure 3.3B**). This is because the change in cationic buffers affects primarily the pK_a, with little effect on the $E_{1/2}$. The lack of change in $E_{1/2}$ highlights the key role of the cationic macrocycle, which enhances anion binding but not binding of a neutral ligand. Unlike CO_2 electroreduction by catalyst **1**,[11] the remarkable log(TOF_{max})/η_{eff} data reported here are not just a feature of the catalyst but rather the combination of catalyst and buffer.

The additive or "tandem" scaling relationship approach developed here is surprisingly accurate given that the contributing scaling relationships were obtained for a somewhat different set of catalysts, iron-porphyrins with different meso-aryl substituents. Yet these scaling relationship

quantitatively hold for the different axial ligands in the **1** + *buffer* systems examined here. Paradoxically, the tandem approach circumvents the limitations implied by prior molecular scaling relationships—that there is always a tradeoff between TOF_{max} and η_{eff}—because of the robustness and generality of the same 'limiting' relationships.

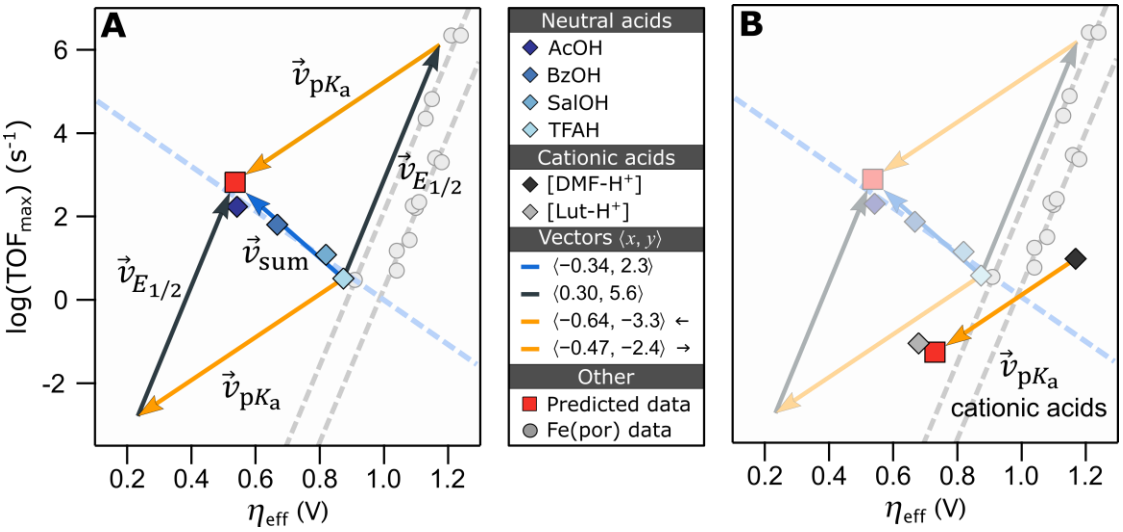

Figure 3.3. Vector analysis to predict the inverse scaling relationship for 1. Predicted coordinates using the vectors are shown as red squares. (**A**) Plot of log(TOF_{max}) vs. η_{eff} for catalytic systems of **1** and varying carboxylic acid buffers (data points match those in **Figure 3.1**). Superimposed vectors (gold, black, blue) show predicted changes caused pK_a, $E_{1/2}$, and summative effects, respectively. (**B**) Buffers with cationic acids follow only the pK_a vector (gold). Prior Fe(por) data and $E_{1/2}$ scaling relationships are included for reference (grey).[7] Uncertainties are smaller than the data points.

3.4 Conclusions

Here, we show that kinetic/thermodynamic scaling relationships for molecular electrocatalysts can be additive and that this tandem scaling approach is a powerful and predictive way to improve multistep electrocatalytic processes. Specifically, summing multiple known scaling relationships predicted an unprecedented, inverse log(TOF)/η_{eff} relationship that allowed for simultaneous improvement in both catalysis rates and efficiencies. This approach has yielded the best reported combination of TOF and η_{eff} for a soluble ORR catalyst.

The ability to combine scaling relationships should be applicable beyond this case study. Optimization by this method, and perhaps even inverse scaling, requires only is that the catalytic reaction have at least two properties that affect the TOF_{max} and η_{eff} in different ways (different slopes). Most molecular electrocatalysis meets this two-descriptor requirement because their mechanisms have pre-equilibrium and rate-limiting steps with different stoichiometries and/or

different relationships between the k, K_{eq} and the $\Delta G°$ for each step. ORR catalysis by **1** is a special case of the two-descriptor requirement because a single change to the system—changing the buffer—affects both the catalyst $E_{1/2}$ and the acid pK_a, each of which independently affects the pre-equilibrium and rate-determining steps. Ongoing work in our lab is extending this tandem scaling approach to simultaneous but independent changes in $E_{1/2}$ and pK_a, by changing both the catalyst and the buffer. A similar approach may also be applicable to heterogeneous electrocatalysis, since there is increasing recognition that those mechanisms may also have pre-equilibria and kinetic steps with different properties.[19] Therefore, this method of combining scaling relationships may have ramifications for the development of both homogeneous and heterogeneous electrocatalysis of energy-important processes.

3.5 Materials and Methods

3.5.1 Instrumentation

High resolution mass spectrometry was performed using a Waters Xevo G2-XS QTof mass spectrometer. UV-vis optical spectra were recorded on an Agilent 8452 diode-array spectrometer and were collected using a 1 cm pathlength cuvette. Infrared spectrum was recorded on a Bruker Alpha FTIR spectrophotometer equipped with an ATR attachment. The electrochemical set-up is described below. Information about the x-ray diffractometer is described below.

3.5.2 Materials

2-nitrobenzaldehyde (Sigma-Aldrich, >95%), tin(II) chloride dihydrate (Sigma-Aldrich, >99%), aqueous hydrochloric acid (Macron, 36-38% wt), iron (II) bromide (Sigma-Aldrich, >98%), 2,6-lutidine (Sigma-Aldrich, *ReagentPlus*® >98%), formaldehyde (Sigma-Aldrich, 37% w/t, containing 10-15% methanol as stabilizer), sodium cyanoborohydride (Acros, >98%), methyltrifluoromethylsulfonate (MeOTf, Sigma-Aldrich, >98%), trifluoromethylsulfonic acid (Acros, 99%), neutral aluminum oxide (Sigma-Aldrich, >99%), silica (Sigma-Aldrich, >99%), sodium chloride (Sigma-Aldrich, >99%), sodium bicarbonate (Sigma-Aldrich, >99%), ammonium hydroxide solution (Sigma-Aldrich, 25% wt), acetic acid (AcOH, Sigma-Aldrich, >99.9%), benzoic acid (BzOH, Sigma-Aldrich, >99.5%), salicylic acid (SalOH, Sigma-Aldrich, >99%), trifluoroacetic acid (TFA, Sigma-Aldrich, *ReagentPlus*®, >99%), tetra-*n*-butylammonium acetate (Sigma-Aldrich, 97%),

tetra-*n*-butylammonium benzoate (Sigma-Aldrich, >99%), tetra-*n*-butylammonium salicylate (TCI, 98%), and sodium trifluoroacetate (Sigma-Aldrich, 98%) were all used as received. All of the solid chemicals were stored in a N_2 glovebox when not in use.

Tetrahydrofuran, *N*,*N*-dimethylformamide (DMF), acetonitrile (MeCN), and diethyl ether were all degassed with argon and dried using a Pure Process Technology solvent system prior to use. Tetra-*n*-butylammonium tetrafluoroborate (Acros, >98%) was stored in a desiccator containing Drierite (calcium sulfate). Bis(cyclopentadienyl)iron(II) (ferrocene or Fc, Sigma-Aldrich, 95%) was recrystallized 2x from hexanes before being dried in a N_2 glovebox. Pyrrole (Acros, 99%) was freshly distilled immediately before each use. A Pur-A-Lyzer™ Mega Dialysis Kit (Sigma-Aldrich, 1 kDa MWCO) was soaked in Milli-Q water for 1h prior to dialysis of **1**. Dioxygen (Airgas, Ultra High Purity) and argon (Airgas, Ultra High Purity) were used as received. *N*,*N*-dimethylformamidium triflate ([DMF-H]OTf) and 2,6-lutidinium triflate ([Lut-H]OTf) were synthesized using previously reported methods.[20-21]

3.5.3 Synthesis of iron(III) tetra(o-N,N,N-trimethylanilinium)porphyrin

The synthesis of the known iron(III) α,β,α,β-5,10,15,20-tetra(ortho-*N*,*N*,*N*-trimethylanilinium)-porphyrin penta(trifluoromethanesulfonate), **1**, was slightly adapted from literature preparation.[11] The α,β,α,β-5,10,15,20-tetra(ortho-aminophenyl)porphyrin atropoisomer was isolated chromatographically using the conditions described in ref [11]. Later in the synthesis, during the final methylation reaction of iron(III) α,β,α,β-5,10,15,20-tetra(ortho-*N*,*N*-dimethylaminophenyl)porphyrin chloride (Chart S1, product **4**, from reference [11]) to the fully quaternized product, 300 equiv. MeOTf were used in place of the reported 100 equiv. Full quaternization was supported by the high-resolution mass spectrum (which did not reveal any partially quaternized products) and by cyclic voltammetry (see Appendix B, Section B.2.1). The product, which was collected in identical yields to the initial report, was purified by dialysis against Milli-Q water (10 mL sample inside dialyzing bag, 250 mL of surrounding water replaced every 90 minutes for a total of 12 hours). The product was then recrystallized via slow vapor diffusion of diethyl ether into MeCN containing the iron porphyrin. This recrystallization method yielded crystals suitable for x-ray diffraction (see Appendix B, Section B.9). HRMS (ESI/Q-TOF) *m*/*z*:

($[M]^{5+}$ + 4OTf^-) calcd for $C_{56}H_{60}FeN_8(CF_3SO_3)_4$ 1496.2373; found 1496.2493. ($[M]^{5+}$ + 3OTf^-) calcd for $C_{56}H_{60}FeN_8(CF_3SO_3)_3$ 673.6426; found 673.6395. UV-vis and IR spectra also agree with what was previously reported (Appendix B, Section B.1).[11]

3.5.4 Electrochemical methods

Cyclic voltammetry (CV) was performed on a CH Instruments model 650D potentiostat. Rotating ring disk electrochemistry (RRDE) was conducted using a BASi Epsilon potentiostat and a Pine Instruments rotator (see Appendix B for further details). CVs used a 3 mm glassy carbon working electrode, a platinum wire counter electrode, and a Ag wire pseudoreference. The Ag wire pseudoreference was prepared using the method reported by Dempsey et al.,[22] where a silver wire was sanded and fit snuggly into a capillary containing MeCN and 0.1 M [*n*-Bu_4N][BF_4]. The solution inside the capillary was separated from bulk solutions using a Vycor tip that had been mechanically sealed to the capillary using heat shrink tubing. The capillary was stored in a solution containing 0.1 M [*n*-Bu_4N][BF_4] in-between experiments. For analysis, each voltammogram was internally referenced to ferrocene. The glassy carbon working electrodes were polished after every voltammogram by vigorously polishing on a Buehler felt pad to a mirror-like finish using an alumina slurry (wetted 0.05 μm alumina powder). After polishing, the electrode was rinsed with water and MeCN. Internal resistance (iR) compensation was performed prior to each voltammogram using the CH Instruments integrated software. Typical resistance values were < 60 Ω. Considering the typical amount of current passed during catalysis (~200 μA), the iR compensation shifted the potential response <10 mV for most experiments.

All the buffered electrochemical experiments were performed with a 1-to-1 buffer of acid and conjugate base. Throughout, we identify the initial buffer concentrations rather than expressly list the acid and conjugate base concentrations. For example, a “10 mM AcOH buffer” means that the solution was prepared to initially contain 10 mM AcOH and 10 mM AcO^-. These values do not necessarily reflect the concentrations of non-homoconjugated acid and base (see Appendix B).

Electrocatalytic, aerobic measurements were performed after sparging the buffered solution and headspace with O_2. The sparging was done with pure O_2 at 1 atm unless otherwise noted. To minimize solvent evaporation and accompanying temperature changes, the O_2 was first

sparged through a secondary bubbler containing pure MeCN. Between each catalytic voltammogram, the working electrode was vigorously polished (see above). To ensure reproducibility, each catalytic voltammogram was also performed in duplicate and the rates were averaged (see Appendix B).

Unless otherwise specified, every voltammogram reported was collected at 0.1 V/s in a MeCN solution containing 0.1 mM **1** and 0.1 M [*n*-Bu_4N][BF_4].

3.5.5 Single crystal X-ray diffraction

Crystals of [Fe(*o*-TMA)]OTf_5•$2H_2O$ (identification code 007b-17062) were grown by slow vapor diffusion of diethyl ether into MeCN on the benchtop. Two water molecules were identified as axial ligands in the solid-state structure. Low-temperature diffraction data (ω-scans) were collected on a Rigaku MicroMax-007HF diffractometer coupled to a Saturn994+ CCD detector with Cu Kα (λ = 1.54178 Å) for the structure of [Fe(*o*-TMA)]OTf_5•$2H_2O$. The diffraction images were processed and scaled using Rigaku Oxford Diffraction software. The structure was solved with SHELXT and was refined against F^2 on all data by full-matrix least squares with SHELXL.[23] The data was refined as an inversion twin. The fractional volume contributions of the second twin component refined to a value of 0.432(18). All non-hydrogen atoms were refined anisotropically. Hydrogen atoms were included in the model at geometrically calculated positions and refined using a riding model. The isotropic displacement parameters of all hydrogen atoms were fixed to 1.2 times the U value of the atoms to which they are linked (1.5 times for methyl groups). The Fe-O distance was measured to be 2.101(8) Å, which suggested the assignment as water.

The asymmetric unit of the crystallographic model contains 0.25 of the formula unit $C_{56}H_{64}FeN_8O_2$•$5(CF_3O_3S)$. The iron resides on the crystallographic $\bar{4}$ rotation axis at (0, ½, ¼). The asymmetric unit also contains a quarter of the porphyrin and 1.25 triflates. One triflate site is on a general position (x,y,z) and the other site is near the crystallographic $\bar{4}$ rotation axis (½,½,½).

The triflate on the general position is disordered over two sites. The thermal ellipsoids for the triflate atoms were restrained to behave as rigid bodies. The site occupancies were fixed at 0.50, and all chemically equivalent 1,2 and 1,3 distances were restrained to be similar. The other triflate was disordered with respect to the $\bar{4}$ rotation axis. This modelled triflate was placed as a

constrained, rigid group based on the difference map (see Appendix B, Section B.9). The special position constraints were suppressed and the model occupancy was fixed at 0.25. The program SQUEEZE[24] was used to compensate for the contribution of disordered solvents contained in voids within the crystal lattice from the diffraction intensities. This procedure was applied to the data file and the submitted model is based on the solvent removed data. Based on the total electron density found in the voids (181 e/Å^3), it is possible that some combination of crystallization solvents is present in the unit cell. See "_platon_squeeze_details" in the .cif for more information.

The full details of the X-ray structure determination (CIF) can be found in the Cambridge Crystallographic Data Center, number 1947226 ([Fe(*o*-TMA)]OTf_5•$2H_2O$). These data can be obtained free of charge from the CCDC via www.ccdc.cam.ac.uk/data_request/cif.

3.6 References and Notes

1. Solomon, E. I.; Stahl, S. S., Introduction: Oxygen Reduction and Activation in Catalysis. *Chem. Rev.* **2018,** *118* (5), 2299-2301.
2. Pegis, M. L.; Wise, C. F.; Martin, D. J.; Mayer, J. M., Oxygen Reduction by Homogeneous Molecular Catalysts and Electrocatalysts. *Chem. Rev.* **2018,** *118* (5), 2340-2391.
3. Gewirth, A. A.; Varnell, J. A.; DiAscro, A. M., Nonprecious Metal Catalysts for Oxygen Reduction in Heterogeneous Aqueous Systems. *Chem. Rev.* **2018,** *118* (5), 2313-2339.
4. Kulkarni, A.; Siahrostami, S.; Patel, A.; Nørskov, J. K., Understanding Catalytic Activity Trends in the Oxygen Reduction Reaction. *Chem. Rev.* **2018,** *118* (5), 2302-2312.
5. Pegis, M. L.; McKeown, B. A.; Kumar, N.; Lang, K.; Wasylenko, D. J.; Zhang, X. P.; Raugei, S.; Mayer, J. M., Homogenous Electrocatalytic Oxygen Reduction Rates Correlate with Reaction Overpotential in Acidic Organic Solutions. *ACS Cent. Sci.* **2016,** *2* (11), 850-856.
6. Klug, C. M.; Cardenas, A. J. P.; Bullock, R. M.; O'Hagan, M.; Wiedner, E. S., Reversing the Tradeoff between Rate and Overpotential in Molecular Electrocatalysts for H_2 Production. *ACS Catal.* **2018,** *8* (4), 3286-3296.
7. Pegis, M. L.; Wise, C. F.; Koronkiewicz, B.; Mayer, J. M., Identifying and Breaking Scaling Relations in Molecular Catalysis of Electrochemical Reactions. *J. Am. Chem. Soc.* **2017,** *139* (32), 11000-11003.
8. Wang, Y.-H.; Pegis, M. L.; Mayer, J. M.; Stahl, S. S., Molecular Cobalt Catalysts for O_2 Reduction: Low-Overpotential Production of H_2O_2 and Comparison with Iron-Based Catalysts. *J. Am. Chem. Soc.* **2017,** *139* (46), 16458-16461.
9. Wang, Y.-H.; Schneider, P. E.; Goldsmith, Z. K.; Mondal, B.; Hammes-Schiffer, S.; Stahl, S. S., Brønsted Acid Scaling Relationships Enable Control Over Product Selectivity from O_2 Reduction with a Mononuclear Cobalt Porphyrin Catalyst. *ACS Cent. Sci.* **2019,** *5* (6), 1024-1034.
10. Pegis, M. L.; Martin, D. J.; Wise, C. F.; Brezny, A. C.; Johnson, S. I.; Johnson, L. E.; Kumar, N.; Raugei, S.; Mayer, J. M., Mechanism of Catalytic O_2 Reduction by Iron Tetraphenylporphyrin. *J. Am. Chem. Soc.* **2019,** *141*, 8315-8326.
11. Azcarate, I.; Costentin, C.; Robert, M.; Savéant, J. M., Through-Space Charge Interaction Substituent Effects in Molecular Catalysis Leading to the Design of the Most Efficient Catalyst of CO_2-to-CO Electrochemical Conversion. *J. Am. Chem. Soc.* **2016,** *138* (51), 16639-16644.
12. Costentin, C.; Passard, G.; Savéant, J.-M., Benchmarking of Homogeneous Electrocatalysts: Overpotential, Turnover Frequency, Limiting Turnover Number. *J. Am. Chem. Soc.* **2015,** *137* (16), 5461-5467.
13. Artero, V.; Saveant, J.-M., Toward the rational benchmarking of homogeneous H_2-evolving catalysts. *Energy Environ. Sci.* **2014,** *7* (11), 3808-3814.
14. Liu, H.; Wei, L.; Liu, F.; Pei, Z.; Shi, J.; Wang, Z.-J.; He, D.; Chen, Y., Homogeneous, Heterogeneous, and Biological Catalysts for Electrochemical N_2 Reduction toward NH_3 under Ambient Conditions. *ACS Catal.* **2019,** *9* (6), 5245-5267.
15. Appel, A. M.; Helm, M. L., Determining the Overpotential for a Molecular Electrocatalyst. *ACS Catal.* **2014,** *4* (2), 630-633.
16. Passard, G.; Dogutan, D. K.; Qiu, M.; Costentin, C.; Nocera, D. G., Oxygen Reduction Reaction Promoted by Manganese Porphyrins. *ACS Catal.* **2018,** *8* (9), 8671-8679.
17. Lexa, D.; Rentien, P.; Savéant, J. M.; Xu, F., Methods for Investigating the Mechanistic and Kinetic Role of Ligand Exchange Reactions in Coordination Electrochemistry. *J. Electroanal. Chem.* **1985,** *191* (2), 253-279.
18. Passard, G.; Ullman, A. M.; Brodsky, C. N.; Nocera, D. G., Oxygen Reduction Catalysis at a Dicobalt Center: The Relationship of Faradaic Efficiency to Overpotential. *J. Am. Chem. Soc.* **2016,** *138* (9), 2925-2928.
19. Chen, L. D.; Bajdich, M.; Martirez, J. M. P.; Krauter, C. M.; Gauthier, J. A.; Carter, E. A.; Luntz, A. C.; Chan, K.; Nørskov, J. K., Understanding the Apparent Fractional Charge of Protons in the Aqueous Electrochemical Double Layer. *Nat. Commun.* **2018,** *9* (1), 3202-3202.

20. McCarthy, B. D.; Dempsey, J. L., Decoding Proton-Coupled Electron Transfer with Potential–pK_a Diagrams. *Inorg. Chem.* **2017,** *56* (3), 1225-1231.
21. Favier, I.; Duñach, E., New protic salts of aprotic polar solvents. *Tetrahedron Lett.* **2004,** *45* (17), 3393-3395.
22. Elgrishi, N.; Rountree, K. J.; McCarthy, B. D.; Rountree, E. S.; Eisenhart, T. T.; Dempsey, J. L., A Practical Beginner's Guide to Cyclic Voltammetry. *J. Chem. Educ.* **2018,** *95* (2), 197-206.
23. Sheldrick, G. M., A short history of SHELX. *Acta Crystallogr. Sect. A: Found. Crystallogr.* **2008,** *64* (1), 112-122.
24. Spek, A. L., PLATON SQUEEZE: a tool for the calculation of the disordered solvent contribution to the calculated structure factors. *Acta Crystallogr. Sect. C: Cryst. Struct. Commun.* **2015,** *71* (1), 9-18.

4 Chapter 4 – Intramolecular Electrostatic Effects on O_2, CO_2, and Acetate Binding to a Cationic Iron Porphyrin

Adapted from Martin, D. J.; Johnson, S. I.; Mercado, B. Q.; Simoné, R.; Mayer, J. M. "Intramolecular, Electrostatic Stabilization Effects on Small Molecule Binding to a Cationic Iron Porphyrin." *Inorg. Chem*. **2020**. DOI: 10.1021/acs.inorgchem.0c02703. DJM and JMM conceived the projected, constructed the scientific arguments, and wrote the paper. SIJ and SR performed and interpreted the calculations and assisted with writing. BQM performed x-ray crystallography and solved the structures. The authors thank Dr. Neeraj Kumar, who initiated calculations of [Fe^{III}(TPP)($O_2^{\bullet-}$)] some years ago.

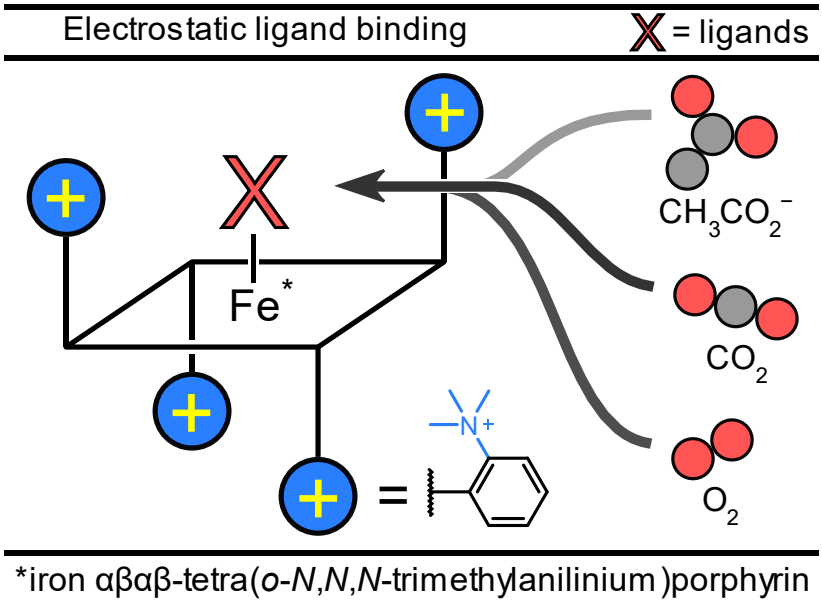

4.1 Introduction

Using molecularly-positioned charges and applied electric fields as "smart reagents" to improve rates and direct selectivities is an burgeoning area of reaction chemistry and catalysis (**Figure 4.1**).[1-4] Electrostatic properties have been used to modulate Diels-Alder chemistry,[2,5] direct regioselectivity,[6] activate C–H bonds,[7] facilitate epoxide rearrangements,[8] and substantially improve electrocatalysis rates and overpotentials.[9-10] The importance of internal electric fields is also well documented in enzymatic catalysis.[11-12] Charges and their resulting fields can be applied externally to an electrode or by placing charge(s) within a molecule or catalyst (**Figure 4.1A,B**). Electrostatic effects are particularly significant for chemical steps that involve charged species or have significant charge redistribution and are often complex and multi-faceted. The alignment of the reactants and transition state with respect to the electric field,[1-2,11] and the proximity of charge to an active site[1-3,13-14] have both been emphasized. However, there are many other important

factors such as the presence of a double-layer[4,15] and ion-pairing with counterions or electrolyte.[4,16-17] Developing electrostatic effects to modulate chemical reactivity and catalysis will depend on a fundamental understanding how electrostatics impact the thermodynamics of individual chemical reaction steps (**Figure 4.1C**).

Molecular reagents or catalysts with positioned charges are attractive for probing such electrostatic effects because they can be designed at the atomic level.[3,7,13,18-22] For instance, a catalyst can be modified to include a charge at specific distance and/or orientation to the active site (**Figure 4.1B**).[23-28] Such designs can affect thermochemical parameters like $E_{1/2}$ or the pK_a values of protonatable ligands[29-31] and are of particular value in molecular electrocatalysis, which by nature involves the movement of charges.[7,9-10,21,31-32] Despite this increasing interest in using electrostatics in molecular catalyst design, there are only limited data available that quantify electrostatic effects for individual steps in catalysis and little understanding of the factors that influence the magnitude of these effects.[29,33-34]

This Chapter examines electrostatic effects in the chemistry of the polycationic iron αβαβ-tetrakis(*ortho*-trimethylanilinium)porphyrin, Fe(*o*-TMA), a complex that has four positive $[N(CH_3)_3]^+$ groups on alternating sides of the porphyrin ligand. The analogous, unsubstituted complex is iron tetraphenylporphyrin (Fe(TPP)), which is used as a control molecule throughout (**Figure 4.1D**, both complexes shown as Fe^{II} forms). Fe(*o*-TMA) is a remarkable molecular electrocatalyst that can perform both CO_2 reduction[9] and O_2 reduction[10] with high rates and low overpotentials in polar, nonaqueous solvents.

The success of Fe(*o*-TMA) for CO_2 reduction, reported by Azcarate *et al.*, was hypothesized to be due to the stabilization of a key pre-equilibrium CO_2 adduct, $Fe^{I}(CO_2^{\bullet-})$, via electrostatic interactions between the $CO_2^{\bullet-}$ ligand and the nearby *o*-$[N(CH_3)_3]^+$ groups.[9,31,35] This hypothesis was based primarily on the slower rates for the *p*-$[N(CH_3)_3]^+$ and *p*-$[SO_3]^-$ analogs. Several following reports of enhanced CO_2 reduction using charged metalloporphyrins have simply referred to Azcarate's seminal work for their rationale.[34,36-38] To our knowledge, there are no published experimental or computational results to directly support the proposed electrostatic interaction or its role in the improved catalyst metrics.

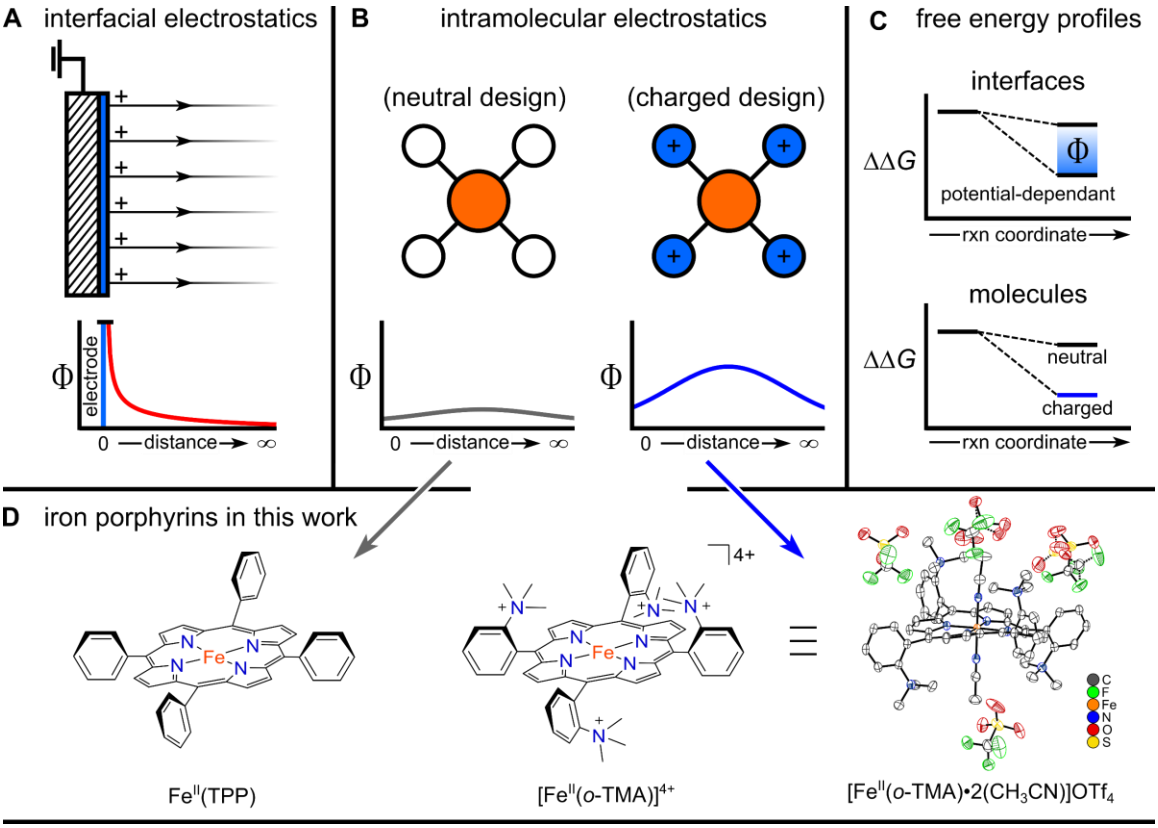

Figure 4.1. Conceptual drawings of electrostatic effects. **A**) Electrostatic field lines at a charged electrode, and the decay of electric potential (Φ) with distance from the electrode. **B**) Charged groups in a molecular system, with the related neutral complex, and the qualitative change in Φ moving across the molecule. **C**) Illustration of electrostatics in (**A**) and (**B**) making elementary reactions more favorable. **D**) Drawings of Fe^{II}(TPP) and $[Fe^{II}(o\text{-TMA})]^{4+}$ and the solid-state structure of $[Fe^{II}(o\text{-TMA})\bullet 2(CH_3CN)]OTf_4$ (H atoms omitted for clarity; thermal ellipsoids at 50% probability).

In our study of electrocatalytic O_2 reduction by Fe(*o*-TMA) (see Chapter 3), we proposed that the key electrostatic role was not substrate (O_2) binding but rather enhanced pre-equilibrium binding of acetate, the anionic conjugate base used in the buffer.[10] Carboxylate binding changed the catalyst $E_{1/2}$—a critical property known to control O_2 affinity and other elementary steps—and led to favorable changes in turnover frequency and overpotentials (Chapter 3).[10,39] This improvement in catalytic metrics could (after the discovery) be predicted from just the cyclic voltammetry data and known thermodynamic/kinetic relationships (Chapter 1).[10] As with the CO_2 examples, however, the quantitative effects of electrostatics on ligand binding were not known.

Reported here are experimental and computational studies of acetate, O_2, and CO_2 binding to Fe(*o*-TMA) and Fe(TPP). Equations 4.1-4.3 show these equilibria, with a generic iron porphyrin abbreviated as Fe(P); in some cases with an axial ligand (L). Ligand binding to iron porphyrins has

long been a canonical research topic,[40-41] especially for O_2 binding to ferrous (Fe^{II}) porphyrins (see Discussion below).[42-44] These prior studies therefore allow a clear view of the effects of the nearby *o*-$[N(CH_3)_3]^+$ groups on the unusual properties of Fe(*o*-TMA).

$$[Fe^{II}(P)]^{n+} + AcO^- \rightleftharpoons [Fe^{II}(P)(AcO)]^{(n-1)+} \quad \text{(eq 4.1)}$$

$$[Fe^{II}(P)(L)]^{n+} + O_2 \rightleftharpoons [Fe^{III}(P)(L)(O_2^{\bullet-})]^{n+} \quad \text{(eq 4.2)}$$

$$[Fe^{0}(P)]^{n+} + CO_2 \rightleftharpoons [Fe^{I}(P)(CO_2^{\bullet-})]^{n+} \quad \text{(eq 4.3)}$$

This Chapter shows that there are multiple ways that positioned charges can affect reactivity and catalysis. It presents some of the first thermodynamic data on electrostatic effects in molecular metal complexes and provides insights into the disparate magnitudes and origins of these effects.

For instance, acetate binding to the tetracationic $[Fe^{II}(o\text{-TMA})]^{4+}$ is 65 times more favorable than binding to the neutral Fe^{II}(TPP) complex in butyronitrile at low ionic strength, but this preference is reduced to only a factor of 2 in in the presence of 0.1 M $[^nBu_4N][PF_6]$. In contrast, at this 0.1 M ionic strength, the ferric form $[Fe^{III}(o\text{-TMA})]^{5+}$ binds acetate $10^{5.8}$ times more strongly than ferric $Fe^{III}(TPP)^+$, and $10^{14.7}$ more strongly than the ferrous $[Fe^{II}(o\text{-TMA})]^{4+}$. These are remarkable differences for having changed only a single unit of charge.

Binding of O_2 and CO_2 to the porphyrin complex are also affected. Surprisingly, $[Fe^{II}(o\text{-TMA})]^{4+}$ does not bind O_2, yet the acetate-bound analog binds O_2 readily and behaves much more similarly to other ferrous porphyrin complexes. This is an *indirect* effect of the four positive charges in $[Fe^{II}(o\text{-TMA})]^{4+}$, acting through a shift in the Fe^{III}/Fe^{II} reduction potential. Differences between O_2 vs. CO_2 binding are highlighted by computational studies that show calculated free energy differences for rotamers of bound O_2 and CO_2 ligands. From natural population analysis, the unique interactions between the bound ligands and the charged functional groups were traced to differences in ligand polarizabilities, reminiscent of pioneering work by de Visser.[45] Together, these results show the many nuanced effects of the *o*-$[N(CH_3)_3]^+$ charged groups and underscore the complexities that must be considered when invoking “electrostatic effects” in catalysis and coordination chemistry.

4.2 Methods

Key methods are summarized below. See Appendix C for complete details.

Optical Measurements. Equilibrium measurements were performed using UV-vis spectroscopy and a temperature-controlled stopped-flow instrument (details of specific measurements described below). Measurements were made in both acetonitrile (MeCN) (to compare with computations) and *n*-butyronitrile (PrCN) (for increased solubility of Fe^{II}(TPP)). Equilibrium constants for acetate binding to the ferrous porphyrin complexes were determined by globally fitting the UV-vis spectra at various acetate concentrations to linear combinations of the genuine spectra of the bound and unbound ferrous porphyrin using a combination of Igor 8.03 and Microsoft Excel. Equilibrium constants for O_2 binding were measured using a similar fitting method, see below and Appendix C.

Electrochemical Measurements. Cyclic voltammograms were collected using a CH Instruments model 600D potentiostat using a three-electrode configuration in a N_2 glovebox. Glassy carbon (CH Instruments, 3 mm) was used as the working electrode, with platinum and silver wires being used as the auxiliary and reference electrodes, respectively. The glassy carbon working electrode was polished on a felt pad using 0.05 μm alumina slurry (CH Instruments, containing no agglomerating agents). The silver wire pseudoreference was sanded prior to use and was submerged in a capillary containing 0.1 M [^{n}Bu$_4$N][PF_6] solution in PrCN, which was separated from the bulk solution by a fitted Vycor tip, following literature procedure.[32] All CVs were internally referenced to ferrocene or decamethylferrocene and were corrected for uncompensated resistance prior to analysis (typically < 150 ohms).

Computations. Density functional theory (DFT) calculations build on our previous work and thus use similar methods.[46-47] Geometry optimizations of intermediates were calculated using the PBE exchange and correlation functional.[48] The Stuttgart/Dresden basis set with relativistic effective core potential (SDD) was used for the Fe center, and the 6-31G** basis set[49-50] was used for all atoms. Single point solvation energies in MeCN were modeled using the SMD continuum solvent.[51] Harmonic vibrational frequencies, calculated at the same level of theory, were used to estimate zero-point energy (ZPE) and the thermal contributions free energies. Free energies are

referred to the standard state concentration of 1 M for the solute and 19.1 M for the solvent MeCN at T = 298 K. Complexes involving bound oxygen have been calculated as open shell singlets.[52] For calculations involving binding and dissociation, basis set superposition error was approximated using the counterpoise correction. These have been incorporated in the free energies of binding. These calculations were completed in Gaussian 09.[53]

Comparisons between CO_2 and O_2 binding were optimized at the same level of theory but were augmented with large basis (6-311G**) single point calculations. For CO_2 binding, both the high and low spin states were investigated, in accordance to recent literature probing the electronic structure of these complexes.[54-55] These calculations were completed in Orca 4.0.0.2. Natural populations and orbital stabilization effects were calculated using the standalone NBO 6.0 software.[56] Reduction potentials were obtained with respect to a ferrocenium/ferrocene couple calculated with the same methods as described for the porphyrin.

4.3 Results

Iron(III) αβαβ-tetra(*o*-*N*,*N*,*N*-trimethylanilinium)porphyrin penta-triflate ([Fe(*o*-TMA)]OTf_5) was synthesized by the sequential methylation and metalation of αβαβ-tetra(*o*-aminophenyl)porphine, using a modified literature procedure (see Appendix C.2).[9] The tetracationic, ferrous salt, [Fe^{II}(*o*-TMA)]OTf_4, was prepared using solid Zn(Hg) amalgam and was characterized by single-crystal X-ray diffraction (as the bis-acetonitrile complex, **Figure 4.1D** and **Figure C26**) and ^{1}H NMR.[40,57] The ^{1}H NMR spectrum of the crystals confirmed the bulk purity of [Fe^{II}(*o*-TMA)]$^{4+}$ as the αβαβ atropisomer seen in the solid-state structure, with the *ortho*-[$N(CH_3)_3$]$^+$ groups on alternating sides of the porphyrin ring (approximate D_{2d} point group). The spectrum in CD_3CN (**Figure C2**) shows a sharp signal due to free CH_3CN indicating exchange of the iron-bound ligands in the crystal with the solvent. The average distance from the nitrogen atoms at the center of the *o*-[$N(CH_3)_3$]$^+$ groups to the iron atom is 5.76 ± 0.07 Å in the solid-state structure.

4.3.1 Acetate binding constants

Acetate binding to [Fe^{II}(*o*-TMA)]$^{4+}$ was measured optically by titration of tetra(*n*-butyl)ammonium acetate (AcO^-) into air-free solutions of [Fe^{II}(*o*-TMA)]$^{4+}$ in butyronitrile (PrCN). The spectra red-shifted with sharp isosbestic points upon addition of AcO^- (**Figure 4.2A**). The Job plot

(**Figure 4.2B**)[58-59] displayed a maximum at 0.5 mole fraction, indicating a 1:1 stoichiometry of acetate-to-porphyrin in the product, $[Fe^{II}(o\text{-TMA})(AcO)]^{3+}$. The titration data were globally fit to a linear combination of the $[Fe^{II}(o\text{-TMA})]^{4+}$ and $[Fe^{II}(o\text{-TMA})(AcO)]^{3+}$ spectra, and the ratio of the derived concentrations gave the equilibrium constant for acetate binding (K_{AcO}) (**Figure 4.2C**, eq 4.4, **Table 4.1**; see Appendix C for details). The same method was also used to measure acetate binding to Fe^{II}(TPP), which also forms a 1:1 complex with acetate and fits well to eq 4.4 (**Figure C7**-**Figure C8**).[60] Adding acetate to $[Fe^{III}(o\text{-TMA})]^{5+}$ stoichiometrically formed $[Fe^{III}(o\text{-TMA})(AcO)]^{4+}$, indicating a very large binding constant (**Figure C9**).

$$K_{AcO}(M^{-1}) = \frac{\left[[Fe^{II}(P)(AcO)]^{n-1}\right]}{\left[[Fe^{II}(P)]^{n}\right]\left[AcO^{-}\right]} \qquad \text{(eq 4.4)}$$

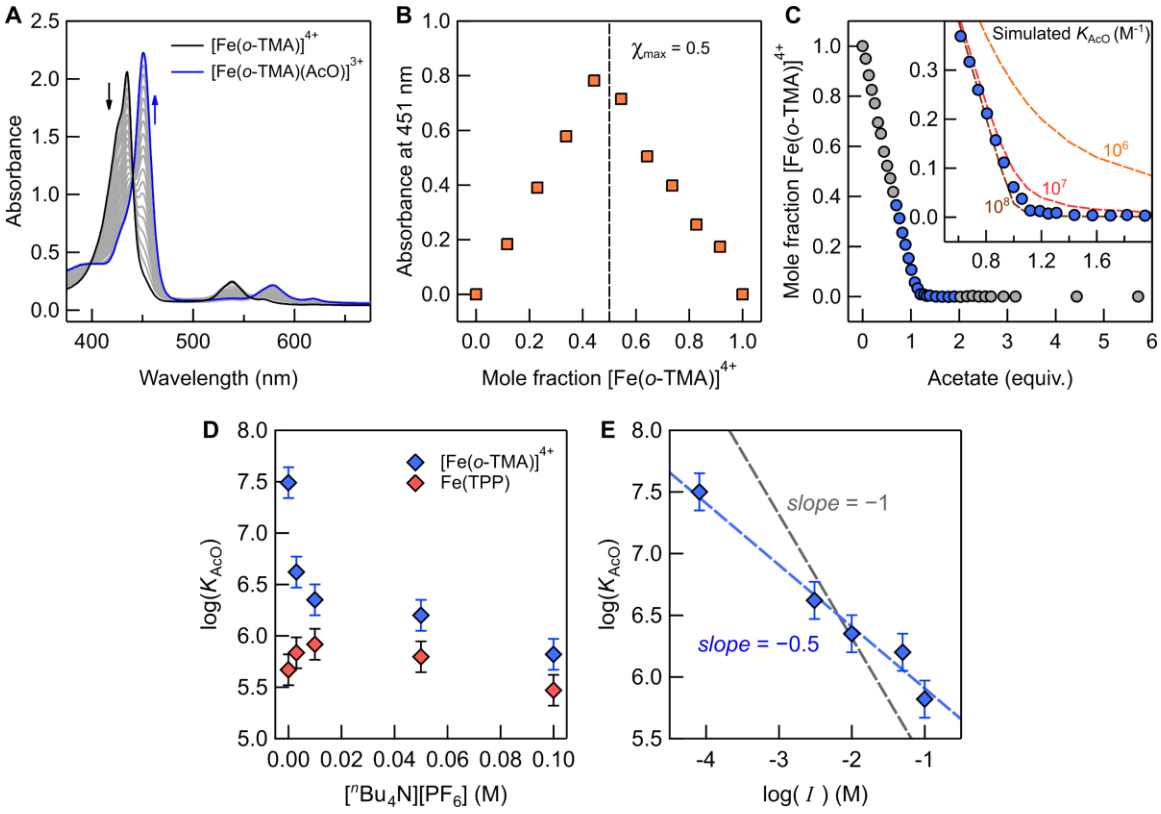

Figure 4.2. UV-visible data for acetate binding to $[Fe^{II}(o\text{-TMA})]^{4+}$ and Fe^{II}(TPP). **A**) UV-vis spectra of 8 μM $[Fe^{II}(o\text{-TMA})]^{4+}$ with titrations of $[^{n}Bu_4N][AcO]$. **B**) Job plot for AcO^- binding to $[Fe^{II}(o\text{-TMA})]^{4+}$ (see SI). **C**) Mole fraction $[Fe^{II}(o\text{-TMA})]^{4+}$ with increasing $[AcO^-]$, from fitting the optical spectra in (**A**); inset shows curvature of data near 1 equiv AcO^- and simulated curves for K_{AcO} values, as noted. (**D**) K_{AcO} values for $[Fe^{II}(o\text{-TMA})]^{4+}$ and Fe^{II}(TPP) at concentrations of $[^{n}Bu_4N][PF_6]$ from 0 to 0.1 M. (**E**) The binding constants from (**D**) in blue plotted versus log(*I*) with inverse half-order (blue line) and first-order (grey line) dependence fits for reference. All data collected in PrCN.

In PrCN, K_{AcO} for acetate binding to [Fe(*o*-TMA)]$^{4+}$ is large, $\log(K_{AcO}/M^{-1}) = 7.5 \pm 0.3$. Under identical conditions, K_{AcO} for acetate binding to Fe^{II}(TPP) is 65 times smaller (**Table 4.1**). The acetate binding constant to [Fe^{II}(*o*-TMA)]$^{4+}$ in MeCN is smaller than in PrCN but is still large, $\log(K_{AcO}/M^{-1}) = 6.3 \pm 0.3$ (**Table C1**). The larger value in PrCN is likely due to the lower static dielectric constant of that solvent: PrCN, 20.3; MeCN, 38.0.[61] Fe^{II}(TPP) is not soluble in MeCN, so its K_{AcO} could not be obtained in this solvent.

The free energies for acetate binding to [Fe^{II}(*o*-TMA)]$^{4+}$ and Fe^{II}(TPP) were also computed using density functional theory (DFT, **Table 4.1**). These calculations used a polarized continuum model for the MeCN solvent, without explicit counterions.[46-47] As found experimentally, acetate binding to [Fe^{II}(*o*-TMA)]$^{4+}$ is more favorable than to Fe^{II}(TPP), though the computational model gives a larger difference: $\Delta\Delta G_{comp}$ = 6.5 kcal mol^{-1}, $\Delta\Delta G_{exp}$ = 2.5 kcal mol^{-1}. It is unfavorable to bind a second AcO$^-$ to either complex, and significantly more unfavorable for Fe(TPP).

To probe the effects of ionic strength (*I*) and to match the electrochemical conditions used below, K_{AcO} values were also measured in solutions containing [^{n}Bu$_4$N][PF$_6$], up to 0.1 M. For Fe^{II}(TPP), the measured K_{AcO} did not change substantially with increasing electrolyte, less than a factor of 2. In contrast, adding electrolyte decreased K_{AcO} for [Fe^{II}(*o*-TMA)]$^{4+}$ by nearly two orders of magnitude (**Figure 4.2D**). When plotted as $\log(K_{AcO}/M^{-1})$ versus $\log(I)$, the data are linear with a slope of −0.51 ± 0.04 (**Figure 4.2E**). In MeCN, the analogous slope is −0.46 ± 0.07 (**Table C1**). The implications of this half-order dependence are discussed below.

Table 4.1. Experimental equilibrium constants and calculated free energies for acetate binding to [Fe^{II}(*o*-TMA)]$^{4+}$ and Fe^{II}(TPP).[a]

	Reaction	Experimental		Computed [b]
		log(K_{AcO}) (M^{-1})	$\Delta G°$ (kcal mol^{-1})	$\Delta\Delta G°$ (kcal mol^{-1})
1	[Fe^{II}(*o*-TMA)]$^{4+}$ + AcO^- ⇌ [Fe^{II}(*o*-TMA)(AcO)]$^{3+}$	7.5 ± 0.3 (6.3 ± 0.3)	−10.2 ± 0.4 (−8.6 ± 0.4)	−6.5
	with 0.1 M [^{n}Bu$_4$N][PF_6]	5.8 ± 0.3 (4.9 ± 0.3)	−7.9 ± 0.4 (−6.7 ± 0.4)	
2	[Fe^{II}(*o*-TMA)(AcO)]$^{3+}$ + AcO^- ⇌ [Fe^{II}(*o*-TMA)$(AcO)_2$]$^{2+}$			3.3
3	Fe^{II}(TPP) + AcO^- ⇌ [Fe^{II}(TPP)(AcO)]$^-$	5.7 ± 0.3	−7.7 ± 0.2	[0.0][b]
	with 0.1 M [^{n}Bu$_4$N][PF_6]	5.5 ± 0.3	−7.5 ± 0.2	
4	[Fe^{II}(TPP)(AcO)]$^-$ + AcO^- ⇌ [Fe^{II}(TPP)$(AcO)_2$]$^{2+}$			14.2
5	[Fe^{III}(*o*-TMA)]$^{5+}$ + AcO^- ⇌ [Fe^{III}(*o*-TMA)(AcO)]$^{4+}$			
	with 0.1 M [^{n}Bu$_4$N][PF_6][c]	20.5 ± 0.4	−27.9 ± 0.5	
6	[Fe^{III}(TPP)]$^+$ + AcO^- ⇌ Fe^{II}(TPP)(AcO)			
	with 0.1 M [^{n}Bu$_4$N][PF_6][c]	14.8 ± 0.4	−20.1 ± 0.5	

[a] Measured in PrCN with or without electrolyte, 0.1 M [^{n}Bu$_4$N][PF_6]. Values reported in parentheses measured in MeCN. [b] $\Delta\Delta G°$ values calculated using a continuum model for the MeCN solvent (see Appendix C) and reported relative to line 3. [c] Determined from equilibrium and electrochemical data (**Scheme 4.1**, eq 4.5).

4.3.2 Acetate effects on the Fe(III/II) reduction potential

Adding acetate to solutions of Fe(*o*-TMA) also causes a change in the electrochemical $E_{1/2}$ for the Fe^{III}/Fe^{II} redox couple.[10] In PrCN containing 0.1 M [^{n}Bu$_4$N][PF_6] and 0.1 mM [Fe^{II}(*o*-TMA)]$^{4+}$, the $E_{1/2}$ = 0.061 V vs. Fc^+/Fc. With 20 equiv. acetate, enough to form >99% [Fe^{II}(*o*-TMA)(AcO]$^{3+}$ (**Table C1**), the $E_{1/2}$ shifts to −0.807 V vs. Fc^+/Fc (**Figure 4.3**, **Table C2**). The dramatic change in $E_{1/2}$ upon acetate binding, –0.868 V, is directly related to the difference in Fe^{III} and Fe^{II} acetate binding constants, as required by Hess' Law (**Scheme 4.1**, given algebraically in eq 4.5).[62] Thus, the shift in $E_{1/2}$ implies that acetate binding is far stronger to the ferric complex than to the ferrous form, *by* $10^{14.7}$. The derived value for log(K_{AcO}) to [Fe^{III}(*o*-TMA)]$^{5+}$ in PrCN containing 0.1 M [^{n}Bu$_4$N][PF_6] is enormous, 20.5 ± 0.4 (**Table 4.1**).

Scheme 4.1. Square scheme for acetate binding to the Fe^{III} and Fe^{II} forms of Fe(*o*-TMA).

$$\begin{array}{ccc} [Fe^{III}(o\text{-TMA})]^{5+} + AcO^- & \overset{K_{AcO}(Fe^{III})}{\rightleftharpoons} & [Fe^{III}(o\text{-TMA})(AcO)]^{4+} \\ \Downarrow E_{1/2} & & \Downarrow E_{1/2}(AcO) \\ [Fe^{II}(o\text{-TMA})]^{4+} + AcO^- & \overset{K_{AcO}(Fe^{II})}{\rightleftharpoons} & [Fe^{II}(o\text{-TMA})(AcO)]^{3+} \end{array}$$

$$E_{1/2} - E_{1/2}(\mathrm{AcO}) = (0.059\ \mathrm{mV})\left\{\log(K_{\mathrm{AcO}}(\mathrm{Fe^{III}})) - \log(K_{\mathrm{AcO}}(\mathrm{Fe^{II}}))\right\} \qquad \text{(eq 4.5)}$$

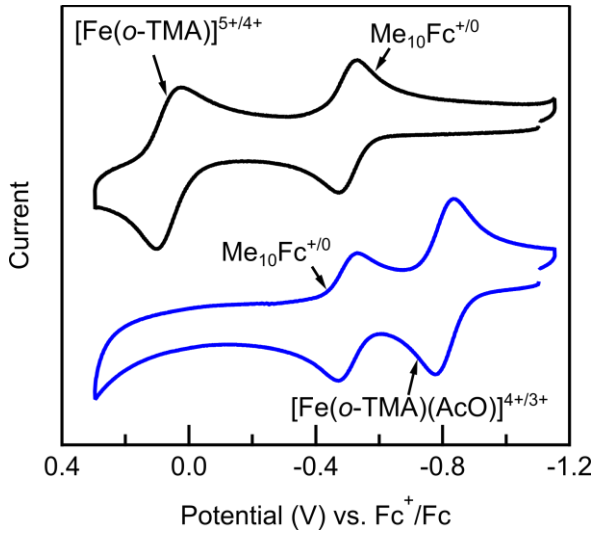

Figure 4.3. Cyclic voltammograms of 0.1 mM $[Fe^{II}(o\text{-TMA})]^{4+}$ before (black) and after (blue) adding 20 equivalents (2 mM) $[^{n}Bu_4N][AcO]$ (0.1 V s^{-1} in PrCN with 0.1 M $[^{n}Bu_4N][PF_6]$). The reversible feature at −0.499 V is due to decamethylferrocene (**Figure C15**).

Adding acetate also shifted the $E_{1/2}(Fe^{III}/Fe^{II})$ of Fe^{II}(TPP) more negative, $\Delta E_{1/2}$ = 0.552 V (**Figure C16**, **Table 4.2**). This yields $\log(K_{AcO}) = 14.8 \pm 0.4$ for acetate binding to $[Fe^{III}(TPP)]^{+}$ under electrochemical conditions (**Table 4.1**). Thus, K_{AcO} values for two ferric complexes, $[Fe^{III}(o\text{-TMA})]^{5+}$ and $[Fe^{III}(TPP)]^{+}$, differ by $10^{5.7}$. This factor of almost a million is a dramatic contrast with the factor-of-two difference in K_{AcO} values for the ferrous porphyrins in similar 0.1 M $[^{n}Bu_4N][PF_6]$ solutions. This contrast is discussed below.

To better understand these effects, $E_{1/2}$ values and Mulliken charges on the iron center were calculated by DFT for various acetate and solvent-bound adducts of $[Fe^{III/II}(o\text{-TMA})(L)_n]^{m+/(m-1)+}$, assuming the same ligands for the Fe^{III} and Fe^{II} complexes. The computations, as above and below, used a polarized continuum model for the MeCN solvent. The calculations show a trend of increasingly negative $E_{1/2}$ values with the addition of acetate ligands, consistent with the experimental electrochemistry (**Table 4.2**). While the $E_{1/2}$(calc.) values do not precisely match $E_{1/2}$(exp.), the calculations do capture the magnitude of $\Delta E_{1/2}$ due to acetate binding, with an $\Delta E_{1/2}$(calc.) between Fe(*o*-TMA)$(MeCN)_2$ and Fe(*o*-TMA)(AcO) complexes of 0.86 V, vs. $\Delta E_{1/2}$(exp.) = 0.87 V (**Table 4.2**, lines 1, 5). The Mulliken charge of the iron center is remarkably invariant across this series of complexes and does not trend with the computed $E_{1/2}$ values or with the overall charge on the molecules.

Table 4.2. Calculated reduction potentials and Fe^{II} Mulliken charges for $[Fe^{II}(o\text{-TMA})]^{4+}$ with various axial ligands.[a]

	complex [b]	$E_{1/2}$ (calc.) [c]	$q_{Fe(II)}$	overall charge [a]
1	$[Fe(o\text{-TMA})(MeCN)_2]^{4+}$	0.333	0.427	4
2	$[Fe(o\text{-TMA})(MeCN)]^{4+}$	0.237	0.559	4
3	$[Fe(o\text{-TMA})]^{4+}$	0.152	0.578	4
4	$[Fe(o\text{-TMA})(MeCN)(AcO)]^{3+}$	−0.454	0.491	3
5	$[Fe(o\text{-TMA})(AcO)]^{3+}$	−0.532	0.552	3
6	$[Fe(o\text{-TMA})(AcO)_2]^{2+}$	−1.086	0.420	2

[a] Using a polarized continuum model for the MeCN solvent. [b] Charge indicated for Fe^{II} complex. [c] Computed values of $E_{1/2}(Fe^{III}/Fe^{II}$ $Fe^{III}/Fe^{II})$, obtained with respect to a Fc^+/Fc potential that was calculated using the same methods.

4.3.3 O_2 binding constants

Initial experiments to probe O_2 binding used solutions of $[Fe^{II}(o\text{-TMA})]^{4+}$ and $[Fe^{II}(o\text{-TMA})(AcO)]^{3+}$, which were prepared in the glovebox and cooled to −80 °C. The acetate complex was generated *in situ* using 10 equiv. acetate (>99% complexation). For $[Fe^{II}(o\text{-TMA})]^{4+}$, gently bubbling O_2 through the solution did not change the optical spectra, indicating that no reaction had occurred (**Figure 4.4A**). The spectra only changed after warming the aerobic solution to 20 °C, though this reaction was slow (>24 h). This is very unusual behavior for a coordinatively unsaturated ferrous porphyrin complex (see below).

For the acetate complex, in contrast, there was an immediate change in the UV-vis spectrum upon O_2 addition. At −80 °C, the product spectrum of the aerobic solution was the same using both O_2 (1 atm) and dry air (0.21 atm) and contained no absorbance features unique to $[Fe^{II}(o\text{-TMA})(AcO)]^{3+}$ (for instance, no shoulder at its λ_{max} = 579 nm; **Figure 4.4B**). Sparging the cold solution with Ar regenerated the anaerobic $[Fe(o\text{-TMA})(AcO)]^{3+}$ spectrum within 2-3 minutes, showing reversibility (**Figure C21**). Such reversibility has been reported for several examples of O_2-binding to ferrous porphyrins and indicates the reversible formation of ferric-superoxo complexes (eq 4.2 above). For all these reasons, we assign the product optical spectrum to the acetate-bound superoxide complex, $[Fe^{III}(o\text{-TMA})(AcO)(O_2^{\bullet-})]^{4+}$ (eq 4.6).[46,63-64]

$$[Fe^{II}(o\text{-TMA})(AcO)]^{3+} + O_2 \rightleftharpoons [Fe^{III}(o\text{-TMA})(AcO)(O_2^{\bullet-})]^{3+} \qquad \text{(eq 4.6)}$$

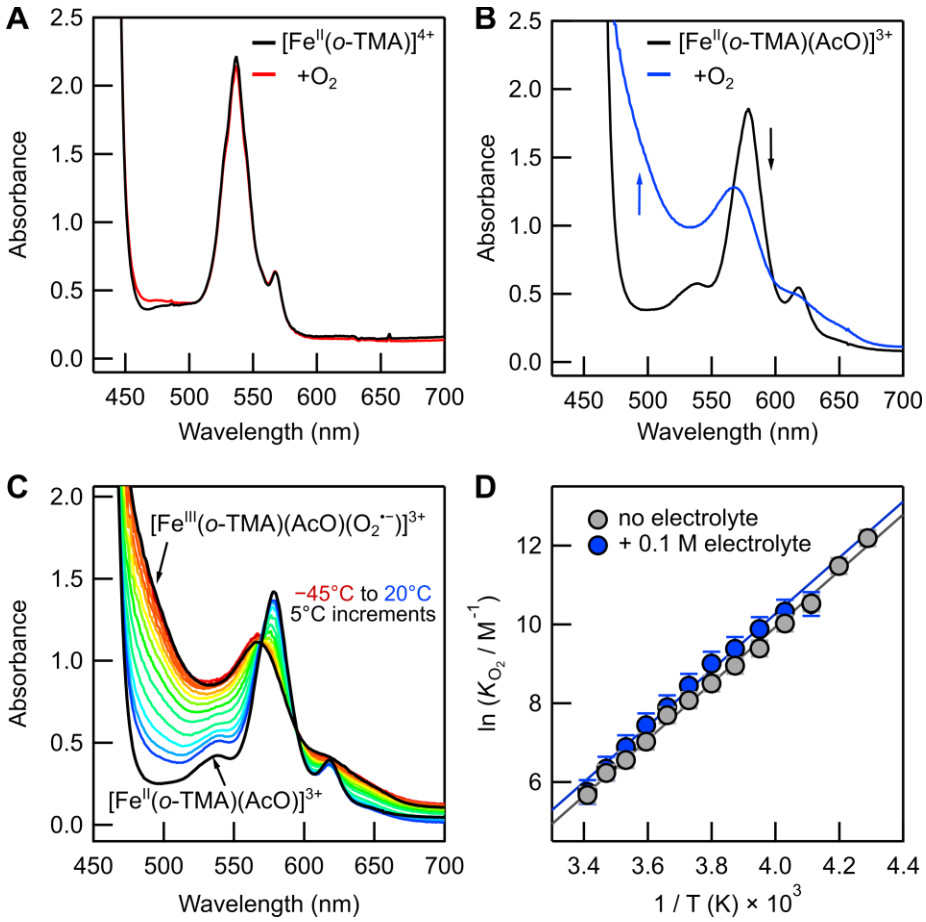

Figure 4.4. Dioxygen binding to Fe^{II}(*o*-TMA) complexes. (**A**) UV-vis spectra of 85 μM $[Fe^{II}(o\text{-TMA})]^{4+}$ at −80 °C under 1 atm Ar (black) and 1 atm O_2 (red). (**B**) Identical experiment using $[Fe^{II}(o\text{-TMA})(AcO)]^{3+}$, prepared *in situ* with 10 equiv $[^nBu_4N][AcO]$. (**C**) UV-vis spectra (colored lines) for O_2-binding measurements at temperatures between −45 °C and 20 °C (5 °C increments). Black lines are reference spectra for O_2-bound and unbound complexes (at −80 °C and 20 °C, respectively) as noted. (**D**) van ′t Hoff plots for O_2 binding to $[Fe^{II}(o\text{-TMA})(AcO)]^{3+}$ with and without 0.1 M $[^nBu_4N][PF_6]$. All data in PrCN.

Equilibrium constants for O_2 binding (K_{O2}) were measured in both PrCN and MeCN between –45 °C and 20 °C using a stopped-flow mixing instrument.[64] In a typical measurement, two gas-tight syringes were prepared: one containing 0.1 mM $[Fe^{II}(o\text{-TMA})]^{4+}$, and the other containing 1.0 mM $[^nBu_4N][AcO]$ and 1.1 mM $[O_2]$ (see Appendix C, **Table C3**). If $[^nBu_4N][PF_6]$ was used, it was added *only* to the syringe containing $[Fe^{II}(o\text{-TMA})]^{4+}$ to avoid changes in O_2 solubility due to ionic strength.[65] Upon mixing (all concentrations halved), the spectra evolved quickly as equilibrium was established (**Figure C22**-**Figure C23**). The unchanging, final spectra were fit to a linear combination of the genuine $[Fe^{II}(o\text{-TMA})(AcO)]^{3+}$ and $[Fe^{III}(o\text{-TMA})(AcO)(O_2^{\bullet-})]^{3+}$ spectra, yielding K_{O2} (M^{-1}) (eq 4.7, **Figure 4.4C**; see Appendix C). Plotting $\ln(K_{O2}/M^{-1})$ vs. 1/T (van ′t Hoff plots, **Figure 4.4D**) gave the $\Delta H°$ and $\Delta S°$ for O_2 binding (**Table 4.3**).

$$K_{O_2}(\mathrm{M}^{-1}) = \frac{\left[[\mathrm{Fe^{III}}(o\text{-TMA})(\mathrm{AcO})(\mathrm{O_2}^{\bullet-})]^{3+}\right]}{\left[[\mathrm{Fe^{II}}(o\text{-TMA})(\mathrm{AcO})]^{3+}\right]\left[\mathrm{O_2}\right]} \qquad \text{(eq 4.7)}$$

The O_2 binding constants measured with and without electrolyte are the same at every temperature—within the uncertainty of the measurements—in both PrCN and MeCN (**Figure 4.4D** and **Table C4**). These results directly contrast the acetate-binding experiments described above, for which supporting electrolyte changed K_{AcO} by $10^{1.7}$.

Table 4.3. van ′t Hoff parameters for O_2 binding to $[Fe^{II}(o\text{-TMA})(AcO)]^{3+}$ [a]

Additive	solvent	$\Delta H°$ (kcal mol^{-1})	$\Delta S°$ (cal mol^{-1} K^{-1})
none	PrCN	−14.2 ± 0.3	−37.0 ± 1.0
+ 0.1 M [^{n}Bu$_4$N][PF$_6$]	PrCN	−14.1 ± 0.4	−36.2 ± 1.6
None	MeCN	−14.0 ± 0.2	−35.2 ± 0.7
+ 0.1 M [^{n}Bu$_4$N][PF$_6$]	MeCN	−14.1 ± 0.4	−35.9 ± 1.6

[a] Standard state defined at 20 °C and 1 M O_2.

4.3.4 Computational study of O_2 and CO_2 rotamer orientations

We hypothesized that significant electrostatic stabilization interactions between non-cylindrical ligands bound to the iron and the $[N(CH_3)_3]^+$ groups would affect the rotameric preference of the bound ligand. κ^1-O_2, CO_2 and acetate ligands all have oxygen atoms that lie off the Fe–L axis. Because Fe(*o*-TMA) was prepared as the αβαβ atropisomer, there are only two limiting rotamers. The off-axis oxygen can be oriented either towards (∥) or away from (⊥) a $[N(CH_3)_3]^+$ group. The κ^1-acetate ligand in the optimized DFT structure of $[Fe^{II}(o\text{-TMA})(AcO)]^{3+}$ is in the ∥ orientation, supporting this hypothesis and indicating an electrostatic interaction between the acetate distal oxygen and a $[N(CH_3)_3]^+$ group. To probe this effect for the $O_2^{\bullet-}$ and $CO_2^{\bullet-}$ ligands, DFT computations were done of their ∥ and ⊥ rotamers (see Appendix C for details).

Calculations examined the superoxide-acetate complex, $[Fe^{III}(o\text{-TMA})(AcO)(O_2^{\bullet-})]^{3+}$ because it is a key intermediate in ORR catalysis.[10,66] With the acetate ligand fixed in the ∥ orientation (**Figure 4.5A**) and the O_2 rotamers constrained to either the ∥ or ⊥ orientations, $\Delta\Delta G°$ = 1.1 kcal mol^{-1} (**Figure 4.5A**,**B**), with a slight preference for O_2 to be oriented *away* from the $[N(CH_3)_3]^+$ groups (⊥). For the CO_2 adduct $[Fe^{I}(o\text{-TMA})(CO_2^{\bullet-})]^{2+}$, the corresponding key intermediate in CO_2 reduction (**Figure 4.5C**, **D**), the difference is more substantial: $\Delta\Delta G°$ = –5.5

kcal mol^{-1}, favoring the ∥ orientation with the oxygens close to two $[N(CH_3)_3]^+$ groups. This result is not a direct comparison because O_2 binds to the acetate-ligated Fe^{II} complex while CO_2 only binds the formal Fe^0 oxidation state of soluble iron porphyrins, which have no axial ligands (eq 4.3).[35,40] Still, these results clearly indicate that the $[N(CH_3)_3]^+$ groups do not substantially stabilize the $O_2^{\bullet-}$ ligand but contribute significantly to $CO_2^{\bullet-}$ binding.

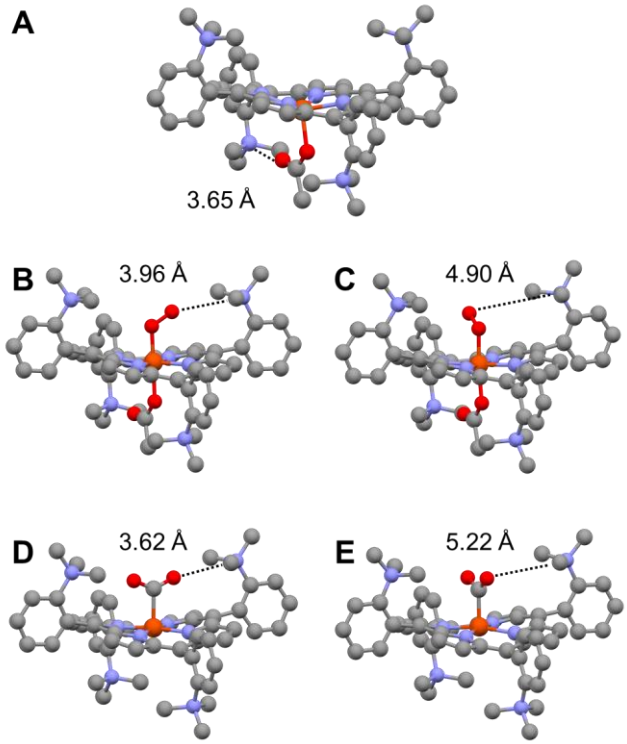

Figure 4.5. DFT-optimized structures bound axial ligand rotamers. (**A**) $[Fe^{III}(o\text{-TMA})(AcO)]^{3+}$ and rotational isomers (∥ and ⊥) for $O_2^{\bullet-}$ and $CO_2^{\bullet-}$ adducts. **B**,**C**: ∥ and ⊥ rotamers of $[Fe^{III}(o\text{-TMA})(AcO)(O_2^{\bullet-})]^{3+}$. **D**,**E**: ∥ and ⊥ rotamers of $[Fe^{I}(o\text{-TMA})(CO_2^{\bullet-})]^{2+}$. Key bond lengths are identified between the distal O-atom(s) of the bound ligand and the N-atom of the nearest *o*-$[N(CH_3)_3]^+$ group.

Natural population analysis based on the DFT electron densities showed that the origin of the contrasting rotamer stabilities is the difference in charge distribution on the formal radical-anion ligands. The natural charges on the Fe, C and O atoms—for the $Fe^{III}(O_2^{\bullet-})$ and $Fe^{I}(CO_2^{\bullet-})$ complexes of both *o*-TMA and TPP ligands—are given in **Table 4.4**. Below, we refer only to the antiferromagnetically coupled-singlet $Fe^{III}(O_2^{\bullet-})$ states and to the singlet models of the $Fe^{I}(CO_2^{\bullet-})$ complexes, which are the typical states invoked in the literature (quintet states are also common for $CO_2^{\bullet-}$ adducts, though these are higher in energy in our calculations; see Appendix C).[54-55,67-68]

To simplify the analysis and remove possible *trans* effects, the $Fe^{III}(O_2^{\bullet-})$ calculations for Fe(*o*-TMA) reported in **Table 4.4** were done in the absence of acetate.

The natural population analysis shows that each of the O-atoms of the $CO_2^{\bullet-}$ adducts has about five times more negative charge than the distal oxygen (O_d) of the $O_2^{\bullet-}$ complexes (**Table 4.4**). This trend is independent of the porphyrin ligand and the spin state and is consistent with higher-level calculations.[69-71] Thus, there is cumulatively 10× more anionic character on the outermost O-atoms of the $Fe^{I}(CO_2^{\bullet-})$ complexes than on the single, O_d-atom of the $Fe^{III}(O_2^{\bullet-})$ complexes. The overall charge on the ligands was more similar, with $q[C + O_a + O_b]$ for the CO_2 (–0.4 to –0.7) less than twice as negative than the charge on the O_2, ($q[O_d + O_p] \cong -0.36$. These results are consistent with simple Lewis-dot descriptions: in $Fe^{III}(O_2^{\bullet-})$, the negative charge on the $O_2^{\bullet-}$ ligand is localized on the proximal O-atom bound to Fe^{III}, while the $Fe^{I}(CO_2^{\bullet-})$ complexes are formally metallacarboxylates, with the negative charge of the $CO_2^{\bullet-}$ ligand localized on the O-atoms.

The $[N(CH_3)_3]^+$ groups also appear to have an effect on the $CO_2^{\bullet-}$ ligand itself. While the singlet and quintet calculations give different values (**Table S7**), both sets of calculations show more negative charge on the $CO_2^{\bullet-}$ ligand for $[Fe^{I}(o\text{-TMA})(CO_2^{\bullet-})]^{2+}$ than for $[Fe^{I}(TPP)(CO_2^{\bullet-})]^{2-}$. This difference is presumably due to the stabilization of negative charge on the $CO_2^{\bullet-}$ ligand by the $[N(CH_3)_3]^+$ groups (**Table 4.4**). In contrast, the charge on the O_2 ligands in $[Fe^{III}(o\text{-TMA})(AcO)(O_2^{\bullet-})]^{3+}$ and $[Fe^{III}(TPP)(O_2^{\bullet-})]$ are surprisingly similar despite a four-unit difference in overall charge.

In sum, both the rotamer energetics and natural population analysis indicate that bound $O_2^{\bullet-}$ is almost unaffected by the $[N(CH_3)_3]^+$ groups but that $CO_2^{\bullet-}$ is significantly stabilized, as proposed in ref 9. This contrast originates from the difference in anionic charge on the O-atoms closest to the $[N(CH_3)_3]^+$ groups. For $O_2^{\bullet-}$, there is little anionic charge on the distal O-atom and thus poor interaction with the charged groups. For the $CO_2^{\bullet-}$ ligands, however, there is nearly 10× more anionic charge on the O-atoms, leading to a preferential ligand orientation towards the $[N(CH_3)_3]^+$ groups.

Table 4.4. Atom charges (q) from natural population analysis for CO_2 and O_2 bound adducts of Fe(*o*-TMA) and Fe(TPP).

CO_2 radical anion complex[a,b,c] 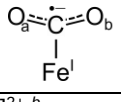	q(Fe)	q(C)	q(O_a)[c]	q[O_a + O_b]	q[C + O_a + O_b]
1 [Fe^{I}(*o*-TMA)($CO_2^{\bullet-}$)]$^{2+}$ [b]	1.514	0.620	−0.661	−1.322	–0.702
2 [Fe^{I}(TPP)($CO_2^{\bullet-}$)]$^{2-}$	1.514	0.417	−0.528	−1.056	–0.639
3 Δq (line 1 – line 2) [d]	0.000	0.203	−0.133	−0.266	−0.064
O_2 radical anion complex[d,e] 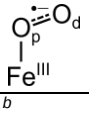	q(Fe)	q(O_p)[f]	q(O_d)[f]	Δq[O_d]	q[O_d + O_p]
7 [Fe^{III}(*o*-TMA)($O_2^{\bullet-}$)]$^{4+}$ [b]	1.718	−0.254	−0.107		–0.361
8 [Fe^{III}(TPP)($O_2^{\bullet-}$)]	1.706	−0.262	−0.093		–0.355
9 Δq (line 7 – line 8) [c]	0.012	0.008	−0.014	−0.014	−0.006

[a] Values for the || rotamer in the singlet state. [b] Values for higher spin states (SI Section VIII). [c] O_a and O_b are symmetry equivalent. [d] Δq is the difference in the charges between similar atoms in complexes with different porphyrin ligands, Δq = q(TMA) – q(TPP). [e] For the || rotamer antiferromagnetic singlet. [f] O_p = proximal oxygen; O_d = distal oxygen.

4.4 Discussion

This Chapter highlights the electrostatic effects on ligand binding that result from derivatizing an iron porphyrin with four *ortho*-substituted trimethylanilinium cations. The discussion below is divided into two parts. The first part discusses O_2 and CO_2 binding, ligands that are initially neutral. The second part discusses acetate binding, which involves cation-anion interactions and raises the importance of ionic strength, supporting electrolyte and solvent identity.

4.4.1 Oxygen binding to [Fe(o-TMA)]$^{4+}$: comparisons with other porphyrin complexes and with CO_2 binding

The binding of O_2 to synthetic iron-porphyrin complexes and heme enzymes has been widely studied because of its importance to most aerobic organisms. The studies in this work probe the direct and indirect effects of the cationic groups in [Fe^{II}(*o*-TMA)]$^{4+}$ on O_2 binding. To contextualize these data, **Table 4.5** gives thermodynamic parameters for O_2 binding to iron(II) porphyrin complexes and a few hemes. Such data are available only for a small fraction of known iron porphyrins because their reactions with O_2 often rapidly lead to μ-oxo dimers and decomposition.[46,63-64] The values measured here use a standard state of 1 M O_2 dissolved in the solvent to avoid variations in the solubility of O_2 with temperature, solvent, and ionic strength. Values in parentheses in **Table 4.5** refer to 1 atm O_2 standard state, as was common in prior reports.

Table 4.5. Summary of thermodynamic parameters for O_2 binding to iron(II) porphyrins and hemes.[a]

Compound [b]	motif	solvent	$E_{1/2}$ (V vs. Fc)	$\Delta G°$ [c] (kcal mol^{-1})	$\Delta H°$ (kcal mol^{-1})	$\Delta S°$ (cal mol^{-1} K^{-1})	ref
$[Fe^{II}(o\text{-TMA})]^{4+}$	Cationic	PrCN	0.061		no binding observed		d
$[Fe^{II}(o\text{-TMA})]^{4+}$	Cationic	MeCN			no binding observed		
$[Fe^{II}(o\text{-TMA})(AcO)]^{3+}$	Cationic	PrCN		−3.4 ± 0.6	−14.2 ± 0.3	−37.0 ± 1.0	d
+ 0.1 M $[^nBu_4N][PF_6]$	Cationic	PrCN	−0.807	−3.5 ± 0.9	−14.1 ± 0.4	−36.2 ± 1.6	d
	Cationic	MeCN		−3.7 ± 0.4	−14.0 ± 0.2	−35.2 ± 0.7	d
+ 0.1 M $[^nBu_4N][PF_6]$	Cationic	MeCN		−3.6 ± 0.9	−14.1 ± 0.4	−35.9 ± 1.6	d
Fe^{II}(TPP)		DMF	−0.530	−1.4 ± 1.5	−10.5 ± 0.7	−31 ± 3	40
$Fe^{II}(F_8TPP)$		EtCN	−0.530[e]	−2.2 ± 2.8	−9.6 ± 1.2	−25.1 ± 5.5	g
		THF	−0.425[f]	−1.4 ± 0.2	−9.0 ± 0.1	−26.0 ± 0.5	g
hemoglobin		H_2O pH 7.4			(−13.6 to −15.5)	(−27.7 to −31.7)	63
myoglobin		H_2O pH 7.4-8.8			(−15.3 to −21.0)	(−38.0 to −56.2)	g
Chelated protoheme		H_2O pH 7.3		(−3.7 ± 0.9)	(−14.0 ± 0.9)	(−35)	g
$Fe^{II}(Piv_3(5ClmP)P)$	H-bond	Toluene		(−4.6 ± 1.7)	(−16.3 ± 0.8)	(−40 ± 3)	g
$Fe^{II}(Piv_3(4ClmP)P)$	H-bond	Toluene		(−4.4 ± 1.1)	(−16.7 ± 0.5)	(−42.1 ± 2.0)	g
$Fe^{II}(T_{piv}PP)(Me_2Im)$	H-bond	Toluene		(−2.0 ± 1.1)	(−14.3 ± 0.5)	(−42 ± 2)	g
Fe^{II}(durene-4/4)Me_2Im)	Capped	Toluene		(0.2)	(−13.1)	(−45.5)	g
Fe^{II}(durene-4/4)(DcIm)	Capped	Toluene		(−0.8)	(−15.3)	(−49.5)	g
$Fe^{II}(C_2\text{-cap})$(1-MeIm)	Capped	Toluene		(−2.3)	(−10.5)	(−27.9)	g
$Fe^{II}(C_2\text{-cap})(Me_2Im)$	Capped	Toluene		(0.8)	(−9.7)	(−35.9)	g

[a] Standard state defined at 20 °C and 1 M O_2; values in parentheses refer to 1 atm O_2 standard state. [b] See Appendix C.7.5 for abbreviations. [c] Determined from the $\Delta H°$ and $\Delta S°$ values. [d] This work. [e] Converted from reported value, 0.100 V vs. SCE in benzonitrile, data and conversion from ref. [72]. [f] Converted from reported value, 0.025 V vs. SCE in DMF, from ref. [73]. Conversion from ref. [74]. [g] From ref. [64].

A striking result of this study is that $[Fe^{II}(o\text{-TMA})]^{4+}$ does not bind O_2, unlike most coordinatively unsaturated iron(II) porphyrins. Even the irreversible decay of $[Fe^{II}(o\text{-TMA})]^{4+}$ to oxidized materials is slow at 20 °C, suggesting a significantly unfavorable O_2 binding step. Yet upon adding one acetate ligand, $[Fe^{II}(o\text{-TMA})(AcO)]^{3+}$ binds O_2 strongly. The difference in reactivity between these two complexes can be rationalized thermochemically by separating the free energy of O_2 binding ($\Delta G°_{O2}$) into the free energy for electron transfer from Fe^{II} to O_2 to form Fe^{III} and $O_2^{\bullet-}$ ($\Delta G°_{ET}$) plus the $\Delta G°_{O2^{\bullet-}}$–free energy for $O_2^{\bullet-}$ binding to the corresponding ferric porphyrin (**Scheme 4.2**, following Stanbury[75]). From this perspective, the lack of O_2 binding is likely due to the unusually positive Fe^{III}/Fe^{II} reduction potential of $[Fe^{II}(o\text{-TMA})]^{4+}$, $E_{1/2}$ = 0.061 V vs. Fc^+/Fc. In contrast, the $E_{1/2}$ for the acetate form $[Fe^{II}(o\text{-TMA})(AcO)]^{3+}$ is remarkably more negative, −0.807 V.

Scheme 4.2. Thermochemical cycle relating the free energy of dioxygen binding ($\Delta G°_{O2}$) to the free energies of electron transfer ($\Delta G°_{ET}$) and superoxide binding ($\Delta G°_{O2•-}$).

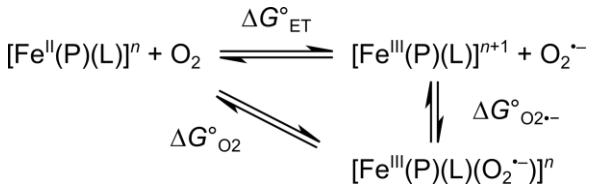

Assigning the dramatic difference in O_2 binding between $[Fe^{II}(o\text{-TMA})]^{4+}$ and $[Fe^{II}(o\text{-TMA})(AcO)]^{3+}$ reactivity towards O_2 to the difference in reduction potentials is consistent with prior literature, as $\Delta G°_{O2}$ is often proportional to $E_{1/2}$ for metalloporphyrin and other complexes.[47,76-77] Basolo reported such correlations in 1974 using cobalt complexes.[76] For iron porphyrin complexes in DMF, computations have also showed a relationship between pK_{O2} and $E_{1/2}$ of 11 decades per V.[47] Assuming this correlation for Fe(*o*-TMA), the predicted $\Delta\Delta G°_{O2}$ for $[Fe^{II}(o\text{-TMA})]^{4+}$ versus $[Fe^{II}(o\text{-TMA})(AcO)]^{3+}$ {$\Delta E_{1/2}$ = −0.868 V} is ~+13 kcal mol^{-1}. Thus, the $\Delta G°_{O2}$ for O_2 binding to $[Fe^{II}(o\text{-TMA})]^{4+}$ is thermodynamically inaccessible and consistent with the observed *lack* of reactivity.

If the unfavorable free energy of electron transfer from $[Fe^{II}(o\text{-TMA})]^{4+}$ to O_2 were simply due to an overall electrostatic attraction between the 4+ cation and the 1– electron leaving the Fe^{II} center, then a similar electrostatic effect should equally enhance the binding of corresponding $O_2^{\bullet-}$ to the Fe^{III} complex. In other words, the Coulombic attraction of $[Fe^{III}(o\text{-TMA})]^{5+}$ for e^- and for $O_2^{\bullet-}$ should be similar, to a first approximation. Yet the *lack* of reactivity shows that the binding of superoxide, $\Delta G°_{O2•-}$, is not enhanced sufficiently by the $[N(CH_3)_3]^+$ groups to balance the high reduction potential. In sum, $[Fe^{II}(o\text{-TMA})]^{4+}$ does not bind O_2 because the cationic groups have a larger effect on the ET component of O_2 binding than the superoxide-binding component.

Table 4.5 compares the enthalpy and entropy for O_2 binding to $[Fe^{II}(o\text{-TMA})(AcO)]^{3+}$ with values for other iron porphyrins, including values reported at 1 M O_2 and those reported vs. 1 atm O_2 (in parentheses). The enthalpies can be compared because the enthalpy of solvation of O_2 is not large; however, the entropies are not as easily compared at different standard states in different solvents.

In general, the enthalpic parameters for O_2 binding to $[Fe^{II}(o\text{-TMA})(AcO)]^{3+}$ are close to values reported for sterically-hindered “picket-fence” and “capped” porphyrins.[42,78-80] This was

initially surprising because all of these metalloporphyrins are *neutral* complexes. The ligand motifs in these various complexes—cations, hydrogen-bond donors, axial ligands, or protected faces—have remarkably little effect on O_2 binding. The largest difference—other than the absence of binding by $[Fe^{II}(o\text{-TMA})]^{4+}$—is the weaker enthalpic binding for the electron-deficient $Fe^{II}(F_8TPP)$ metalloporphyrin.[64] Fe^{II}(TPP) also has a weak enthalpic parameter, but it is also the most sterically accessible complex in **Table 4.5** and may involve competitive binding of DMF solvent.[46]

The computational comparison of the O_2- and CO_2-derived ligands provides insight into the factors that contribute to an electrostatic effect on neutral ligand binding. The *ortho*-$[N(CH_3)_3]^+$ groups have stronger charge-charge interactions with the formal $CO_2^{\bullet-}$ ligand because there is nearly 10× more negative charge on the O-atoms of $CO_2^{\bullet-}$ than on the distal O-atom of $O_2^{\bullet-}$. Not only is the excess charge on $O_2^{\bullet-}$ localized on the proximal oxygen, but there is also less negative charge on the $O_2^{\bullet-}$ ligand overall because O_2 binds Fe^{II} while CO_2 binds the Fe^0 analog.

Overall, the O_2 binding data provide no evidence for significant electrostatic effects on O_2 binding by $[Fe^{II}(o\text{-TMA})(AcO)]^{3+}$. This conclusion is strongly supported by the lack of an electrolyte dependence and by the computational result that the $O_2^{\bullet-}$ ligand does not strongly interact with the $[N(CH_3)_3]^+$ cations, based on the rotamer preference. Even though there is little *direct* stabilization of the $O_2^{\bullet-}$ ligand by the nearby charged groups, we emphasize that the cationic charges have a large, *indirect* effect on O_2 binding. The addition of the *ortho*-$[N(CH_3)_3]^+$ groups to Fe(TPP) completely removes its ability to bind O_2 due to the rise in the reduction potential. However, the charged groups also facilitate the binding of an acetate ligand, which causes a shift the reduction potential to more negative values and an increase in O_2 binding.

4.4.2 Acetate binding to Fe(o-TMA): inductive, electrostatic, and ionic strength effects

4.4.2.1 Through-bond inductive effects

The *ortho*-$[N(CH_3)_3]^+$ groups on Fe(*o*-TMA) are highly electron-withdrawing. The significance of these inductive effects can be interpreted quantitatively using the $E_{1/2}(Fe^{III}/Fe^{II})$ values of $[Fe^{II}(o\text{-TMA})]^{4+}$ and Fe^{II}(TPP). For *para*-substituted iron porphyrin complexes, Kadish *et al.* showed that the $E_{1/2}(Fe^{III}/Fe^{II})$ in PrCN varied with the Hammett σ_p parameter, with a slope of 0.051 V vs. $4\sigma_p$ (using $4\times\sigma_p$ because of the four aryl groups).[81] For this analysis, we approximated

the inductive effect of the *ortho*-$[N(CH_3)_3]^+$ using the *para*-$[N(CH_3)_3]^+$ Hammett parameter, σ_p = 0.82.[82] Using $4\sigma_p$ = 3.28, the Kadish correlation predicts that $E_{1/2}(Fe^{III}/Fe^{II})$ for Fe(*o*-TMA) will be 0.17 V more positive than for Fe(TPP). However, the experimentally observed difference in $E_{1/2}$ is 0.32 V [Fe(*o*-TMA), 0.061 V; Fe(TPP), −0.259 V]. These data would suggest that roughly half of the difference in $E_{1/2}(Fe^{III}/Fe^{II})$, 0.17 V out of 0.32 V, is due to inductive effects.

In contrast, the $E_{1/2}(Fe^{III}/Fe^{II})$ values of the *acetate-bound complexes*, Fe(*o*-TMA)(AcO) and Fe(TPP)(AcO), are essentially identical: −0.807 and −0.809 V, respectively. Using the same arguments as above, the similarity of these reduction potentials would imply that there is *no inductive contribution* from the $[N(CH_3)_3]^+$ groups. It is possible that ion pairing between the excess acetate ions and the $[N(CH_3)_3]^+$ groups could reduce the inductive effect, but it seems unlikely that such effects would *completely* negate the electron-withdrawing nature of the functional groups. The DFT calculations also illustrate the multi-faceted nature of these effects since acetate binding shifts the $E_{1/2}$ tremendously but the Mulliken charge at the iron center is almost unchanged. Such phenomena indicate that—for the acetate-bound complex—any through-space effects of the charged groups on the $E_{1/2}$ value are screened by acetate binding and decrease in overall charge. These data show the challenges in identifying specific cause-and-effect relationships that result from electrostatic effects, in this case inductive vs. through-space influences. This challenge is amplified in more complex systems, such as ORR and CO_2RR catalysis, that undergo dynamic changes in multiple reaction steps, including ligand binding and charge rearrangements.

4.4.2.2 Through-space electrostatic effects

While the optimized geometry of $[Fe(o\text{-TMA})(AcO)]^{3+}$ does indicate favorable interactions between the κ^1-acetate ligand and the $[N(CH_3)_3]^+$ groups, the strongest marker of electrostatic interactions in acetate binding is the experimental relationship between K_{AcO} and ionic strength (I) for the Fe^{II} complexes. Whereas K_{AcO} values are relatively unperturbed for Fe^{II}(TPP) at varying [I], the binding constants to $[Fe^{II}(o\text{-TMA})]^{4+}$ decrease precipitously with addition of $[^nBu_4N][PF_6]$. The difference in acetate binding constants to $[Fe^{II}(o\text{-TMA})]^{4+}$ vs. Fe^{II}(TPP) in the absence of electrolyte is a factor of 65 in K_{AcO}. At 3 mM $[^nBu_4N][PF_6]$, the difference is within a factor of 5; at 0.1 M electrolyte, only a factor of 2 (**Figure 4.2D**). If the increased K_{AcO} values for $[Fe(o\text{-TMA})]^{4+}$ were

primarily due to through-bond, inductive effects, one would expect only a modest influence of ionic strength, if any. We note that while the factor of 65 difference in binding constants to $[Fe^{II}(o\text{-TMA})]^{4+}$ vs. $[Fe^{II}(TPP)]$ in the absence of electrolyte is significant, it seems small given that the complexes are different by *four positive charges positioned close to the binding site*.

The change in $E_{1/2}$ due to acetate binding ($\Delta E_{1/2}$) reveals a much more striking difference in K_{AcO} for the ferric porphyrins, $[Fe^{III}(o\text{-TMA})]^{5+}$ and $[Fe^{III}(TPP)]^{+}$. In PrCN containing 0.1 M $[^{n}Bu_4N][PF_6]$, the $E_{1/2}(Fe^{III}/Fe^{II})$ for $[Fe^{II}(o\text{-TMA})]^{4+}$ decreases by 0.868 V upon binding one acetate, and the $E_{1/2}(Fe^{III}/Fe^{II})$ of $Fe^{II}(TPP)$ decreases by 0.553 V. Using **Scheme 4.2**, the acetate binding constants to the ferric porphyrins were determined from these $\Delta E_{1/2}$ values and the K_{AcO} values for binding to the ferrous porphyrins at 0.1 M $[^{n}Bu_4N][PF_6]$ (**Table 4.1**). The K_{AcO} values for the ferric porphyrins are enormous: $10^{20.5}$ M^{-1} for $[Fe^{III}(o\text{-TMA})]^{5+}$ and $10^{14.8}$ M^{-1} for $[Fe^{III}(TPP)]^{+}$. The difference between the two ferric complexes is also large, $10^{5.7}$. These values were measured in solutions containing 0.1 M electrolyte, where the *ferrous* binding constants are much smaller and more similar, $10^{5.8}$ M^{-1} and $10^{5.5}$ M^{-1}, respectively.

The difference between $[Fe^{III}(o\text{-TMA})]^{5+}$ and $[Fe^{II}(o\text{-TMA})]^{4+}$ is only one unit of charge, so the difference of $10^{14.7}$ between their acetate binding constants (ΔK[Fe(*o*-TMA)]) is remarkable. The origins of this difference are likely multi-faceted. One contribution is likely from changes in the frontier orbitals, which can be estimated from the corresponding difference in K_{AcO} for $[Fe(TPP)]^{+}$ vs. $Fe^{II}(TPP)$: $\log(\Delta K[Fe(TPP)]) = 9.3$. This still leaves a large difference in acetate binding constants: $\log(\Delta K[Fe(o\text{-TMA})]) - \log(\Delta K[Fe(TPP)]) = 5.5$. Since inductive effects are not be expected to depend strongly on the iron redox state, this remaining difference indicates a sizable contribution from electrostatics.

These data, like those in part 4.4.2.1 just above, indicate the complexities of unravelling electrostatic effects. In 0.1 M electrolyte, the addition of four positive charges to convert neutral $[Fe^{II}(TPP)]$ to $[Fe^{II}(o\text{-TMA})]^{4+}$ causes a shift in the acetate binding constants by only a factor of 2. Yet for the ferric complexes under these conditions, acetate binding to $[Fe^{III}(o\text{-TMA})]^{5+}$ is 630,000 times stronger than binding to $[Fe^{III}(TPP)]^{+}$.

4.4.2.3 The role of ionic strength

The solution ionic strength (I) plays a crucial role in modulating the electrostatic effects for acetate binding in this system, as has been noted in other studies.[83-84] For instance, K_{AcO} for $[Fe^{II}(o\text{-TMA})]^{4+}$ drops by about two orders of magnitude when [I] is increased from 80 μM to 100 mM. At higher ionic strengths, the $[N(CH_3)_3]^+$ groups (A^+) have more anions from the electrolyte (B^-) in their vicinity, perhaps in the form of ion pairs $[A^+]\bullet[B^-]$. Nearby anions may reduce the electrostatic potential and the electric field of the charged groups, and thus decrease the affinity for an anionic acetate ligand.

Such sensitivity to ionic strength is a caution to researchers in this area. Electrochemical studies are usually done at high [I], while measurements of ligand binding constants, pK_a values, rate constants, etc. do not typically add electrolyte. Data measured under such different conditions should be used together only with great caution. For instance, it would not be appropriate to use a $\Delta G°_{ET}$ at high [I] with a $\Delta G°_{O2}$ at low [I] in a thermochemical cycle such as **Scheme 4.2**.

Quantitative analysis of the acetate binding constants shows that K_{AcO} decreases with an inverse half-order dependence on [I] in both PrCN and MeCN solvents (**Figure 4.2E**). This electrolyte screening behavior is analogous to that of an electrochemical double layer.[85] In an electrolyte solution, the electrostatic potential decays with distance from an ion or polarized surface with a characteristic Debye length (κ^{-1}). In first-order models, κ^{-1} is given by eq 4.8, where ε is the dielectric constant of the solvent, ε_0 the permittivity of the vacuum, I is the ionic strength and R, T and F are the gas constant, temperature and Faraday's constant, respectively.[85] For 1:1 electrolytes such as used here, I is equal to the electrolyte concentration. Thus, both the acetate binding constants to $[Fe^{II}(o\text{-TMA})]^{4+}$ and the Debye length have the same inverse square root dependence on the concentration of ions. This dependence is proposed to be a clear demonstration of an electrostatic effect. More studies are needed to determine the generality of this $I^{-1/2}$ dependence for molecular electrostatic effects.

$$\kappa^{-1} = \sqrt{\frac{\varepsilon\varepsilon_0 RT}{2\times 10^3 F^2 I}} \qquad \text{(eq 4.8)}$$

In PrCN (ε = 20.3)[61] containing 0.1 M [^{n}Bu$_4$N][PF$_6$], the Debye length is ~5 Å. Under identical conditions in MeCN (ε = 38.0),[61] $\kappa^{-1} \cong 7$ Å. These characteristic lengths are similar to the distance between the [N(CH$_3$)$_3$]$^+$ groups and the iron center in [Fe^{II}(*o*-TMA)]$^{4+}$, ~5.7 Å, and to the van der Waals diameter of the PF_6^- anion in the electrolyte, ~5 Å.[86] These distances provide some intuition as to why electrostatic effects on acetate binding are attenuated with the addition of [^{n}Bu$_4$N][PF$_6$]. In PrCN containing no electrolyte and 8 μM [Fe^{II}(*o*-TMA)](OTf)$_4$, the ionic strength is only 80 μM. Under these conditions the Debye length is ~175 Å, 35 times larger than solutions containing 0.1 M electrolyte. It is also tempting to speculate that the much higher electrostatic effects for the ferric complex, [Fe^{III}(*o*-TMA)]$^{5+}$, reflect the granularity of these ions. It is perhaps more difficult for enough large electrolyte anions (PF_6^-) to localize near the porphyrin and counterbalance the higher, pentacationic charge.

4.5 Conclusions

The introduction of charged groups into the second coordination sphere is increasingly being used to enhance molecular electrocatalysis. “Electrostatic stabilization effects” are frequently invoked, however it is often unclear how the added charges affect the individual steps in the complex reaction landscape. The results here show that ligand binding can be enhanced by spatially positioned *ortho*-trimethylanilinium groups in the second-coordination sphere of an iron porphyrin complex (Fe(*o*-TMA)), but only for anionic ligands (acetate) or for ligands develop substantial negative charge near the cationic groups (CO_2 becoming a metallacarboxylate). O_2 binding is not enhanced even though this ligand formally becomes superoxide and computationally develops an overall –0.35*e* charge. The difference in stabilization for O_2 versus CO_2 stems from a difference in the amount and location of the anionic charges, and the polarizability of the corresponding radical anion ligands: $CO_2^{\bullet-}$ has ten times as much negative charge on the distal oxygens as $O_2^{\bullet-}$. While there are no *direct* electrostatic effects that stabilize O_2 binding, there is a dramatic *indirect effect*: the cationic charges promote acetate binding, which drastically lowers $E_{1/2}$(Fe^{III}/Fe^{II}) and thereby enhances O_2 binding.

Acetate binding to the ferrous Fe(*o*-TMA)$^{4+}$ is directly enhanced by electrostatic interactions with the cationic porphyrin ligand, with its K_{AcO} being 65 times larger than that of the

neutral Fe^{II}(TPP) under low ionic strength conditions. However, this difference decreases to only a factor of 2 with addition of 0.1 M [$^{n}Bu_4N$][PF_6]. *We propose that the inverse half-order dependence of the binding constant on ionic strength is a clear marker for an electrostatic effect; we look forward to future tests of this initial hypothesis.* For the ferric complexes, [Fe^{III}(*o*-TMA)]$^{5+}$ binds acetate almost a million times more strongly than [Fe^{III}(TPP)]$^{+}$ at high ionic strength.

These results are among the first in the literature to identify and quantify how intramolecular electrostatic interactions affect ligand binding and small molecule activation. Together, the results here show that adding charged groups can have several effects. Many factors determine the magnitude of these effects, including the charge of the incoming ligand, the polarizability of the substrate, the ionic strength in solution, and the dielectric of the solvent. Thus, simple generalizations about how charged groups affect binding should be avoided. All these effects are important and must be considered in the pursuit of improved catalyst design and in the field of electrostatically-modulated chemistry.

4.6 References and Notes

1. Shaik, S.; Mandal, D.; Ramanan, R., Oriented electric fields as future smart reagents in chemistry. *Nat. Chem.* **2016,** *8* (12), 1091-1098.
2. Xiang, L.; Tao, N. J., Organic chemistry: Reactions triggered electrically. *Nature* **2016,** *531* (7592), 38-39.
3. Yoo, C.; Dodge, H. M.; Miller, A. J. M., Cation-controlled catalysis with crown ether-containing transition metal complexes. *ChemComm* **2019,** *55* (35), 5047-5059.
4. Ciampi, S.; Darwish, N.; Aitken, H. M.; Díez-Pérez, I.; Coote, M. L., Harnessing electrostatic catalysis in single molecule, electrochemical and chemical systems: a rapidly growing experimental tool box. *Chem. Soc. Rev.* **2018,** *47* (14), 5146-5164.
5. Aragonès, A. C.; Haworth, N. L.; Darwish, N.; Ciampi, S.; Bloomfield, N. J.; Wallace, G. G.; Diez-Perez, I.; Coote, M. L., Electrostatic catalysis of a Diels-Alder reaction. *Nature* **2016,** *531* (7592), 88-91.
6. Lau, V. M.; Gorin, C. F.; Kanan, M. W., Electrostatic control of regioselectivity via ion pairing in a Au(I)-catalyzed rearrangement. *Chem. Sci.* **2014,** *5* (12), 4975-4979.
7. Chantarojsiri, T.; Ziller, J. W.; Yang, J. Y., Incorporation of redox-inactive cations promotes iron catalyzed aerobic C–H oxidation at mild potentials. *Chem. Sci.* **2018,** *9* (9), 2567-2574.
8. Gorin, C. F.; Beh, E. S.; Kanan, M. W., An Electric Field–Induced Change in the Selectivity of a Metal Oxide–Catalyzed Epoxide Rearrangement. *J. Am. Chem. Soc.* **2012,** *134* (1), 186-189.
9. Azcarate, I.; Costentin, C.; Robert, M.; Savéant, J. M., Through-Space Charge Interaction Substituent Effects in Molecular Catalysis Leading to the Design of the Most Efficient Catalyst of CO_2-to-CO Electrochemical Conversion. *J. Am. Chem. Soc.* **2016,** *138* (51), 16639-16644.
10. Martin, D. J.; Mercado, B. Q.; Mayer, J. M., Combining scaling relationships overcomes rate versus overpotential trade-offs in O_2 molecular electrocatalysis. *Sci. Adv.* **2020,** *6* (11), eaaz3318.
11. Fried, S. D.; Boxer, S. G., Electric Fields and Enzyme Catalysis. *Annu. Rev. Biochem* **2017,** *86* (1), 387-415.
12. Warshel, A.; Sharma, P. K.; Kato, M.; Xiang, Y.; Liu, H.; Olsson, M. H., Electrostatic basis for enzyme catalysis. *Chem. Rev.* **2006,** *106* (8), 3210-35.
13. Miller, A. J. M., Controlling ligand binding for tunable and switchable catalysis: cation-modulated hemilability in pincer-crown ether ligands. *Dalton Trans.* **2017,** *46* (36), 11987-12000.
14. Gryn'ova, G.; Coote, M. L., Origin and scope of long-range stabilizing interactions and associated SOMO-HOMO conversion in distonic radical anions. *J. Am. Chem. Soc.* **2013,** *135* (41), 15392-403.
15. Newman, J.; Thomas-Alyea, K. E., The Electric Potential. In *Electrochemical Systems*, John Wiley & Sons, Inc: Hoboken, New Jersey, 2004.
16. Noble, B. B.; Norcott, P. L.; Hammill, C. L.; Ciampi, S.; Coote, M. L., Mechanism of Oxidative Alkoxyamine Cleavage: The Surprising Role of the Solvent and Supporting Electrolyte. *J. Phys. Chem. C* **2019,** *123* (16), 10300-10305.
17. Klinska, M.; Smith, L. M.; Gryn'ova, G.; Banwell, M. G.; Coote, M. L., Experimental demonstration of pH-dependent electrostatic catalysis of radical reactions. *Chem. Sci.* **2015,** *6* (10), 5623-5627.
18. Kang, K.; Fuller, J., 3rd; Reath, A. H.; Ziller, J. W.; Alexandrova, A. N.; Yang, J. Y., Installation of internal electric fields by non-redox active cations in transition metal complexes. *Chem. Sci.* **2019,** *10* (43), 10135-10142.
19. Reath, A. H.; Ziller, J. W.; Tsay, C.; Ryan, A. J.; Yang, J. Y., Redox Potential and Electronic Structure Effects of Proximal Nonredox Active Cations in Cobalt Schiff Base Complexes. *Inorg. Chem.* **2017,** *56* (6), 3713-3718.
20. Smith, J. B.; Camp, A. M.; Farquhar, A. H.; Kerr, S. H.; Chen, C.-H.; Miller, A. J. M., Organometallic Elaboration as a Strategy for Tuning the Supramolecular Characteristics of Aza-Crown Ethers. *Organometallics* **2019,** *38* (22), 4392-4398.

21. Chantarojsiri, T.; Reath, A. H.; Yang, J. Y., Cationic Charges Leading to an Inverse Free-Energy Relationship for N-N Bond Formation by Mn(VI) Nitrides. *Angew. Chem. Int. Ed. Engl.* **2018,** *57* (43), 14037-14042.
22. La, T.; Richards, R.; Miskelly, G. M., Synthesis and Characterization of the Cationic Porphyrin Meso-Tetrakis(2,3,5,6-Tetrafluoro-*N*,*N*,*N*-Trimethyl-4-Aniliniumyl)Porphyrin. *Inorg. Chem.* **1994,** *33* (14), 3159-3163.
23. Tsui, E. Y.; Agapie, T., Reduction potentials of heterometallic manganese-oxido cubane complexes modulated by redox-inactive metals. *Proc. Natl. Acad. Sci. U.S.A.* **2013,** *110* (25), 10084-8.
24. Tsui, E. Y.; Tran, R.; Yano, J.; Agapie, T., Redox-inactive metals modulate the reduction potential in heterometallic manganese-oxido clusters. *Nat. Chem.* **2013,** *5* (4), 293-9.
25. Lin, P. H.; Takase, M. K.; Agapie, T., Investigations of the effect of the non-manganese metal in heterometallic-oxido cluster models of the oxygen evolving complex of photosystem II: lanthanides as substitutes for calcium. *Inorg. Chem.* **2015,** *54* (1), 59-64.
26. Herbert, D. E.; Lionetti, D.; Rittle, J.; Agapie, T., Heterometallic triiron-oxo/hydroxo clusters: effect of redox-inactive metals. *J. Am. Chem. Soc.* **2013,** *135* (51), 19075-8.
27. Cammarota, R. C.; Lu, C. C., Tuning Nickel with Lewis Acidic Group 13 Metalloligands for Catalytic Olefin Hydrogenation. *J. Am. Chem. Soc.* **2015,** *137* (39), 12486-9.
28. Ramirez, B. L.; Lu, C. C., Rare-Earth Supported Nickel Catalysts for Alkyne Semihydrogenation: Chemo- and Regioselectivity Impacted by the Lewis Acidity and Size of the Support. *J. Am. Chem. Soc.* **2020,** *142* (11), 5396-5407.
29. Franke, A.; Scheitler, A.; Kenkel, I.; Lippert, R.; Zahl, A.; Balbinot, D.; Jux, N.; Ivanovic-Burmazovic, I., Positive Charge on Porphyrin Ligand and Nature of Metal Center Define Basic Physicochemical Properties of Cationic Manganese and Iron Porphyrins in Aqueous Solution. *Inorg. Chem.* **2019,** *58* (15), 9618-9630.
30. Dhar, D.; Yee, G. M.; Tolman, W. B., Effects of Charged Ligand Substituents on the Properties of the Formally Copper(III)-Hydroxide ([CuOH](2+)) Unit. *Inorg. Chem.* **2018,** *57* (16), 9794-9806.
31. Nichols, A. W.; Machan, C. W., Secondary-Sphere Effects in Molecular Electrocatalytic CO_2 Reduction. *Front. Chem.* **2019,** *7*, 397.
32. Elgrishi, N.; Rountree, K. J.; McCarthy, B. D.; Rountree, E. S.; Eisenhart, T. T.; Dempsey, J. L., A Practical Beginner's Guide to Cyclic Voltammetry. *J. Chem. Educ.* **2018,** *95* (2), 197-206.
33. Zhang, R.; Warren, J. J., Controlling the Oxygen Reduction Selectivity of Asymmetric Cobalt Porphyrins by Using Local Electrostatic Interactions. *J. Am. Chem. Soc.* **2020,** *142* (31), 13426-13434.
34. Margarit, C. G.; Asimow, N. G.; Gonzalez, M. I.; Nocera, D. G., Double Hangman Iron Porphyrin and the Effect of Electrostatic Nonbonding Interactions on Carbon Dioxide Reduction. *J. Phys. Chem. Lett.* **2020,** *11* (5), 1890-1895.
35. Costentin, C.; Robert, M.; Savéant, J. M., Current Issues in Molecular Catalysis Illustrated by Iron Porphyrins as Catalysts of the CO_2-to-CO Electrochemical Conversion. *Acc. Chem. Res.* **2015,** *48* (12), 2996-3006.
36. Rao, H.; Schmidt, L. C.; Bonin, J.; Robert, M., Visible-light-driven methane formation from CO_2 with a molecular iron catalyst. *Nature* **2017,** *548* (7665), 74-77.
37. Sung, S.; Kumar, D.; Gil-Sepulcre, M.; Nippe, M., Electrocatalytic CO_2 Reduction by Imidazolium-Functionalized Molecular Catalysts. *J. Am. Chem. Soc.* **2017,** *139* (40), 13993-13996.
38. Zhu, M.; Yang, D.-T.; Ye, R.; Zeng, J.; Corbin, N.; Manthiram, K., Inductive and electrostatic effects on cobalt porphyrins for heterogeneous electrocatalytic carbon dioxide reduction. *Catal. Sci. Technol.* **2019,** *9* (4), 974-980.
39. Martin, D. J.; Wise, C. F.; Pegis, M. L.; Mayer, J. M., Developing Scaling Relationships for Molecular Electrocatalysis through Studies of Fe-Porphyrin-Catalyzed O_2 Reduction. *Acc. Chem. Res.* **2020,** *53* (5), 1056-1065.
40. Walker, F. A.; Simonis, U., Iron Porphyrin Chemistry. John Wiley & Sons, Ltd: Chichester, UK, 2006.
41. Kadish, K. M.; Smith, K. M.; Guilard, R. *The Porphyrin Handbook*.

42. Collman, J. P.; Brauman, J. I.; Iverson, B. L.; Sessler, J. L.; Morris, R. M.; Gibson, Q. H., Dioxygen and carbonyl binding to iron(II) porphyrins: a comparison of the "picket fence" and "pocket" porphyrins. *J. Am. Chem. Soc.* **1983,** *105* (10), 3052-3064.
43. Niederhoffer, E. C.; Timmons, J. H.; Martell, A. E., Thermodynamics of oxygen binding in natural and synthetic dioxygen complexes. *Chem. Rev.* **1984,** *84* (2), 137-203.
44. Collman, J. P.; Brauman, J. I.; Suslick, K. S., Oxygen binding to iron porphyrins. *J. Am. Chem. Soc.* **1975,** *97* (24), 7185-7186.
45. de Visser, S. P., On the relationship between internal energy and both the polarizability volume and the diamagnetic susceptibility. *PCCP* **1999,** *1* (5), 749-753.
46. Pegis, M. L.; Martin, D. J.; Wise, C. F.; Brezny, A. C.; Johnson, S. I.; Johnson, L. E.; Kumar, N.; Raugei, S.; Mayer, J. M., Mechanism of Catalytic O_2 Reduction by Iron Tetraphenylporphyrin. *J. Am. Chem. Soc.* **2019,** *141*, 8315-8326.
47. Pegis, M. L.; McKeown, B. A.; Kumar, N.; Lang, K.; Wasylenko, D. J.; Zhang, X. P.; Raugei, S.; Mayer, J. M., Homogenous Electrocatalytic Oxygen Reduction Rates Correlate with Reaction Overpotential in Acidic Organic Solutions. *ACS Cent. Sci.* **2016,** *2* (11), 850-856.
48. Perdew, J. P.; Burke, K.; Ernzerhof, M., Generalized Gradient Approximation Made Simple. *Phys. Rev. Lett.* **1996,** *77* (18), 3865-3868.
49. Francl, M. M.; Pietro, W. J.; Hehre, W. J.; Binkley, J. S.; Gordon, M. S.; DeFrees, D. J.; Pople, J. A., Self-consistent molecular orbital methods. XXIII. A polarization-type basis set for second-row elements. *J. Chem. Phys.* **1982,** *77* (7), 3654-3665.
50. Hehre, W. J.; Ditchfield, R.; Pople, J. A., Self—Consistent Molecular Orbital Methods. XII. Further Extensions of Gaussian—Type Basis Sets for Use in Molecular Orbital Studies of Organic Molecules. *J. Chem. Phys.* **1972,** *56* (5), 2257-2261.
51. Marenich, A. V.; Cramer, C. J.; Truhlar, D. G., Universal Solvation Model Based on Solute Electron Density and on a Continuum Model of the Solvent Defined by the Bulk Dielectric Constant and Atomic Surface Tensions. *J. Phys. Chem. B* **2009,** *113* (18), 6378-6396.
52. Huang, X.; Groves, J. T., Oxygen Activation and Radical Transformations in Heme Proteins and Metalloporphyrins. *Chem. Rev.* **2018,** *118* (5), 2491-2553.
53. Frisch, M. J.; Trucks, G. W.; Schlegel, H. B.; Scuseria, G. E.; Robb, M. A.; Cheeseman, J. R.; Scalmani, G.; Barone, V.; Mennucci, B.; Petersson, G. A.; Nakatsuji, H.; Caricato, M.; Li, X.; Hratchian, H. P.; Izmaylov, A. F.; Bloino, J.; Zheng, G.; Sonnenberg, J. L.; Hada, M.; Ehara, M.; Toyota, K.; Fukuda, R.; Hasegawa, J.; Ishida, M.; Nakajima, T.; Honda, Y.; Kitao, O.; Nakai, H.; Vreven, T.; Montgomery, J. A.; Peralta, J. E.; Ogliaro, F.; Bearpark, M.; Heyd, J. J.; Brothers, E.; Kudin, K. N.; Staroverov, V. N.; Kobayashi, R.; Normand, J.; Raghavachari, K.; Rendell, A.; Burant, J. C.; Iyengar, S. S.; Tomasi, J.; Cossi, M.; Rega, N.; Millam, J. M.; Klene, M.; Knox, J. E.; Cross, J. B.; Bakken, V.; Adamo, C.; Jaramillo, J.; Gomperts, R.; Stratmann, R. E.; Yazyev, O.; Austin, A. J.; Cammi, R.; Pomelli, C.; Ochterski, J. W.; Martin, R. L.; Morokuma, K.; Zakrzewski, V. G.; Voth, G. A.; Salvador, P.; Dannenberg, J. J.; Dapprich, S.; Daniels, A. D.; Farkas; Foresman, J. B.; Ortiz, J. V.; Cioslowski, J.; Fox, D. J. *Gaussian 09*, Wallingford, CT, 2009.
54. Sen, P.; Mondal, B.; Saha, D.; Rana, A.; Dey, A., Role of 2(nd) sphere H-bonding residues in tuning the kinetics of CO2 reduction to CO by iron porphyrin complexes. *Dalton Trans.* **2019,** *48* (18), 5965-5977.
55. Davethu, P. A.; de Visser, S. P., CO_2 Reduction on an Iron-Porphyrin Center: A Computational Study. *J. Phys. Chem. A* **2019,** *123* (30), 6527-6535.
56. Glendening, E. D.; Landis, C. R.; Weinhold, F., NBO 6.0 : Natural bond orbital analysis program. *J. Comput. Chem.* **2013,** *34* (16), 1429-1437.
57. Safo, M. K.; Nesset, M. J. M.; Walker, F. A.; Debrunner, P. G.; Scheidt, W. R., Models of the Cytochromes. Axial Ligand Orientation and Complex Stability in Iron(II) Porphyrinates: The Case of the Noninteracting d_π Orbitals. *J. Am. Chem. Soc.* **1997,** *119* (40), 9438-9448.
58. Renny, J. S.; Tomasevich, L. L.; Tallmadge, E. H.; Collum, D. B., Method of Continuous Variations: Applications of Job Plots to the Study of Molecular Associations in Organometallic Chemistry. *Angew. Chem. Int. Ed.* **2013,** *52* (46), 11998-12013.
59. Gil, V. M. S.; Oliveira, N. C., On the use of the method of continuous variations. *J. Chem. Educ.* **1990,** *67* (6), 473-478.

60. Kadish, K. M.; Rhodes, R. K., Thin-layer spectroelectrochemical evidence of anion binding to (tetraphenylporphinato)iron(II) in nonaqueous media. *Inorg. Chem.* **1983,** *22* (7), 1090-1094.
61. Conway, B. E., The Electrolyte Factor in Supercapacitor Design and Performance: Conductivity, Ion Pairing and Solvation BT - Electrochemical Supercapacitors: Scientific Fundamentals and Technological Applications. Conway, B. E., Ed. Springer US: Boston, MA, 1999; pp 335-375.
62. Geiger, D. K.; Paviak, E. J.; Kass, L. T., The determination of axial ligand binding constants for iron porphyrins by cyclic voltammetry. *J. Chem. Educ.* **1991,** *68* (4), 337.
63. Collman, J. P.; Gagne, R. R.; Reed, C.; Halbert, T. R.; Lang, G.; Robinson, W. T., Picket fence porphyrins. Synthetic models for oxygen binding hemoproteins. *J. Am. Chem. Soc.* **1975,** *97* (6), 1427-1439.
64. Ghiladi, R. A.; Kretzer, R. M.; Guzei, I.; Rheingold, A. L.; Neuhold, Y.-M.; Hatwell, K. R.; Zuberbühler, A. D.; Karlin, K. D., (F_8TPP)Fe^{II}/O_2 Reactivity Studies {F_8TPP = Tetrakis(2,6-difluorophenyl)porphyrinate(2−)}: Spectroscopic (UV−Visible and NMR) and Kinetic Study of Solvent-Dependent (Fe/O_2 = 1:1 or 2:1) Reversible O_2-Reduction and Ferryl Formation. *Inorg. Chem.* **2001,** *40* (23), 5754-5767.
65. Sawyer, D. T.; Chiericato, G.; Angelis, C. T.; Nanni, E. J.; Tsuchiya, T., Effects of media and electrode materials on the electrochemical reduction of dioxygen. *Anal. Chem.* **1982,** *54* (11), 1720-1724.
66. Martin, D. J.; Wise, C. F.; Pegis, M. L.; Mayer, J. M., Developing Molecular Scaling Relationships for Molecular Electrocatalysis through Studies of Fe Porphyrin-Catalyzed O_2 Reduction. *Acc. Chem. Res.* **2020**.
67. Kim, H.; Rogler, P. J.; Sharma, S. K.; Schaefer, A. W.; Solomon, E. I.; Karlin, K. D., Heme-Fe^{III} Superoxide, Peroxide and Hydroperoxide Thermodynamic Relationships: Fe^{III}-$O_2^{\bullet-}$ Complex H-Atom Abstraction Reactivity. *J. Am. Chem. Soc.* **2020,** *142* (6), 3104-3116.
68. Huang, X.; Groves, J. T., Oxygen Activation and Radical Transformations in Heme Proteins and Metalloporphyrins. *Chem. Rev.* **2018,** *118* (5), 2491-2553.
69. Yamamoto, S.; Kashiwagi, H., CASSCF calculation on dioxygen heme complex with extended basis set. *Chem. Phys. Lett.* **1993,** *205* (2-3), 306-312.
70. Yamamoto, S.; Kashiwagi, H., CASSCF study on the Fe-O_2 bond in a dioxygen heme complex. *Chem. Phys. Lett.* **1989,** *161* (1), 85-89.
71. Kirchner, R. F.; Loew, G. H., Semiempirical calculations of model oxyheme: variation of calculated electromagnetic properties with electronic configuration and oxygen geometry. *J. Am. Chem. Soc.* **1977,** *99* (14), 4639-4647.
72. Moore, K. T.; Fletcher, J. T.; Therien, M. J., Syntheses, NMR and EPR spectroscopy, electrochemical properties, and structural studies of [5,10,15,20-tetrakis (perfluoroalkyl)porphinato]iron(II) and -iron(III) complexes. *J. Am. Chem. Soc.* **1999,** *121* (22), 5196-5209.
73. Oliveira, R.; Zouari, W.; Herrero, C.; Banse, F.; Schollhorn, B.; Fave, C.; Anxolabehere-Mallart, E., Characterization and Subsequent Reactivity of an Fe-Peroxo Porphyrin Generated by Electrochemical Reductive Activation of O2. *Inorg. Chem.* **2016,** *55* (23), 12204-12210.
74. Connelly, N. G.; Geiger, W. E., Chemical Redox Agents for Organometallic Chemistry. *Chem. Rev.* **1996,** *96* (2), 877-910.
75. Stanbury, D. M. In *Mechanistic Aspects of Inorganic Reactions. ACS Symposium Series 198*, 1982; pp 443-447.
76. Carter, M. J.; Rillema, D. P.; Basolo, F., Oxygen carrier and redox properties of some neutral cobalt chelates. Axial and in-plane ligand effects. *J. Am. Chem. Soc.* **1974,** *96* (2), 392-400.
77. Walker, F. A.; Beroiz, D.; Kadish, K. M., Electronic effects in transition metal porphyrins. 2. The sensitivity of redox and ligand addition reactions in para-substituted tetraphenylporphyrin complexes of cobalt (II). *J. Am. Chem. Soc.* **1976,** *98* (12), 3484-9.
78. David, S.; James, B. R.; Dolphin, D.; Traylor, T. G.; Lopez, M. A., Dioxygen and carbon monoxide binding to apolar cyclophane hemes: durene-capped hemes. *J. Am. Chem. Soc.* **1994,** *116* (1), 6-14.

79. Hashimoto, T.; Baldwin, J. E.; Basolo, F.; Dyer, R. L.; Crossley, M. J., Ligand, oxygen, and carbon monoxide affinities of iron(II) modified "capped" porphyrins. *J. Am. Chem. Soc.* **1982,** *104* (8), 2101-2109.
80. Rose, E. J.; Venkatasubramanian, P. N.; Swartz, J. C.; Jones, R. D.; Basolo, F.; Hoffman, B. M., Carbon monoxide binding kinetics in "capped" porphyrin compounds. *Proc. Natl. Acad. Sci. U.S.A.* **1982,** *79* (18), 5742-5745.
81. Kadish, K. M.; Morrison, M. M.; Constant, L. A.; Dickens, L.; Davis, D. G., A study of solvent and substituent effects on the redox potentials and electron-transfer rate constants of substituted iron meso-tetraphenylporphyrins. *J. Am. Chem. Soc.* **1976,** *98* (26), 8387-90.
82. Hansch, C.; Leo, A.; Taft, R. W., A Survey of Hammett Substituent Constants and Resonance and Field Parameters. *Chem. Rev.* **1991,** *91* (2), 165-195.
83. Smith, A. M.; Lee, A. A.; Perkin, S., The Electrostatic Screening Length in Concentrated Electrolytes Increases with Concentration. *J. Phys. Chem. Lett.* **2016,** *7* (12), 2157-2163.
84. Brown, M. A.; Goel, A.; Abbas, Z., Effect of Electrolyte Concentration on the Stern Layer Thickness at a Charged Interface. *Angew. Chem. Int. Ed.* **2016,** *55* (11), 3790-3794.
85. Bard, A. J.; Faulkner, L. R., *Electrochemical Methods: Fundamentals and Applications, Second Edition*. 2nd ed.; John Wiley & Sons, Inc.: New York, 2000; p 548-548.
86. Ue, M.; Murakami, A.; Nakamura, S., A Convenient Method to Estimate Ion Size for Electrolyte Materials Design. *J. Electrochem. Soc.* **2002,** *149* (10), A1385.

5 Chapter 5 – All Four Atropisomers of the Polycationic Iron(III) and Iron(II) Tetra(*o*-*N*,*N*,*N*-trimethylanilinium)porphyrin

Adapted from Martin, D. J.; Mercado, B. Q.; Mayer, J. M. *Unsubmitted work*. DJM and JMM conceived the project, constructed the scientific arguments, and wrote the paper. BQM performed x-ray crystallography and solved the structures.

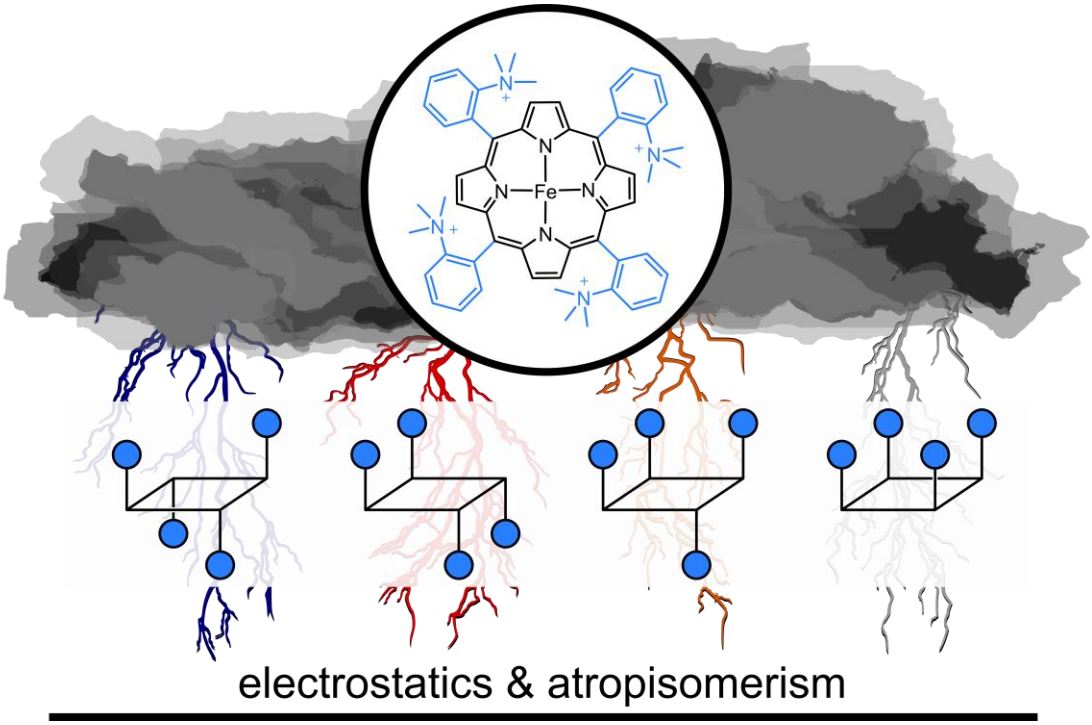

5.1 Introduction

Electrostatic and electric field effects are increasingly recognized as key to the success of many challenging, multi-step reactions, especially those that involve charged intermediates or significant charge redistribution.[1-3] Such complex reactions are common in molecular electrocatalysis, which often involves single electron or proton transfer steps and the formation of charged species.[4-7] Stabilizing these intermediates and decreasing the kinetic barriers is required to improve reaction rates and efficiencies. Recently, these goals have prompted the design of molecular (electro)catalysts that contain spatially positioned charged groups that can stabilize charged intermediates via electrostatic interactions.[6,8-14]

One such design is the tetra-cationic tetra(*o*-*N*,*N*,*N*-trimethylanilinium)porphyrin ligand (*o*-TMA), which has four positive charges positioned around the porphyrin ring. Iron complexes of this ligand are among the leading molecular electrocatalysts for both CO_2 and O_2 reduction in terms of

in reaction rates and efficiencies.[10,12] The success of this catalyst is owed in part to the stabilization of pre-equilibria that involve anionic ligands or ligands that become sufficiently anionic upon binding,[15] effects not often emphasized in studies that used highly charged ligands.

Traditionally, charged groups have been added to macrocyclic ligand designs to improve solubility, especially solubility in aqueous solutions.[16-17] Pyridinium, carboxylate, and sulfonate-derivatized macrocycles are the most common examples of these designs, where solubility is controlled, at least in part, by the pH of the solution. Alkylated pyridinium and ammonium functional groups offer a more permanent form of charge installation and have been used in porphyrin designs to facilitate aqueous O_2/CO binding and superoxide dismutase studies.[18-22] There are a few examples of highly charged ligand designs (8+/8−) affecting basic physicochemical properties of metalloporphyrins, but these studies have only probed charge-symmetric systems in aqueous solvents.[23-27] There are no systems, insofar as we can find, that report on macrocycles bearing asymmetric charge distributions in nonaqueous solvents.

For this reason, the (*o*-TMA) ligand and corresponding metal complexes are highly unusual. By nature of the mono-ortho substitution pattern on the aryl rings and the restricted rotational freedom at the porphyrin meso-carbons, there are four atropisomers available to the (*o*-TMA) ligand—αβαβ, ααββ, αααβ, and αααα—and thus four unique electrostatic environments (**Scheme 5.1**). Savéant *et al*. reported the first preparation of Fe(*o*-TMA) for CO_2 reduction and claimed the successful synthesis of the αβαβ atropisomer, in which the cationic functional groups alternate on either side of the porphyrin ring.[10] The characterization data, however, was limited only to infrared spectroscopy, UV-vis absorbance, elemental analysis, and mass spectrometry – techniques that cannot necessarily distinguish between the atropisomers. Crystallographic data from our group showed that the αβαβ isomer was indeed a component of the product synthesized via the reported method (see Chapter 3),[12] however, bulk purity was never established.

Here, we report improved synthesis and separation procedures for isolating all four atropisomers of Fe(*o*-TMA) in both the ferric (Fe^{III}) and ferrous (Fe^{II}) forms. Each of the atropisomers was fully characterized using ^{1}H NMR, high-resolution mass spectroscopy, and cyclic voltammetry. Seven of the eight molecules were characterized by single-crystal X-ray diffraction.

The ways in which intra- and intermolecular electrostatics affect (and do not affect) the molecular and solid-state properties are identified and discussed. In addition to these characterization data, we show that the previous synthetic route reported by Savéant led to unwanted rotamerization of the aryl groups and scrambling of the isomers, resulting in a mixture of atropisomeric catalysts under the conditions of the reported electrocatalysts.

Scheme 5.1. The four different atropisomers available to $[Fe^{III}(o\text{-TMA})](OTf)_5$. Stick figures are used to represent orientation of the $o\text{-}[N(CH_3)_3]^+$ groups.

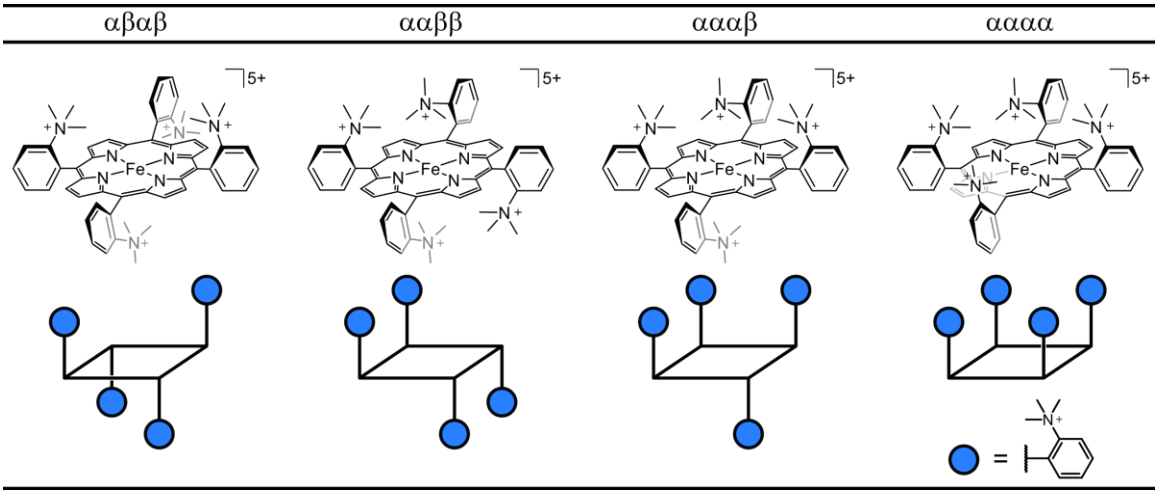

5.2 Results

5.2.1 Synthesis

The $[Fe^{III}(o\text{-TMA})](OTf)_5$ atropisomers can be obtained in six steps using commercially available reagents and without heating later-stage intermediates (**Scheme 5.2**). Following literature,[10] the target products first require the atropisomers of tetra(*o*-aminophenyl)porphyrin, H_2(*o*-AMP) (**Figure D5-Figure D8**). These were obtained from the acid-catalyzed condensation of *o*-nitrobenzaldehyde and pyrrole, followed by reduction of the corresponding tetra(*o*-nitrophenyl)porphyrin with stannous chloride/hydrochloric acid and repeated chromatography.[28] Several chromatography conditions and eluents have been reported for isolating the various atropisomers of H_2(*o*-AMP).[10,28-32] After trying several of these conditions, we found that the most consistent method of obtaining atropisomerically pure samples (>95%) required a minimum of three separate columns with various eluent mixtures (conditions reported in the Experimental, below). The atropisomeric purity of the target $[Fe^{III}(o\text{-TMA})](OTf)_5$ salts was dictated by this early-stage

chromatography, so it was imperative that the atropisomers of tetra(*o*-aminophenyl)porphyrin were carefully separated and were not heated as to avoid re-isomerization.[28]

Scheme 5.2. Synthesis route used to prepare the $[Fe^{III}(o\text{-TMA})](OTf)_5$ atropisomers.

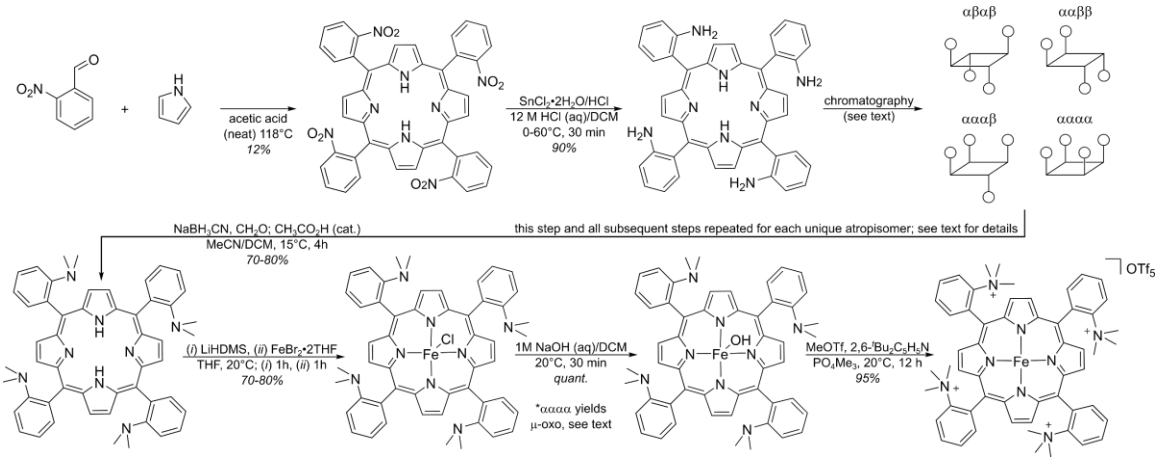

The individual H_2(*o*-AMP) atropisomers were then methylated by reductive amination using formaldehyde and sodium cyanoborohydride to yield the respective tetra(*o*-*N*,*N*-dimethylaminophenyl)porphyrins, H_2(*o*-DMA). The ^{1}H NMR spectra for these molecules were diagnostic but typically contained minor components (<5%) that could not be separated by chromatography (see Appendix D, **Figure D10**-**Figure D13**).

The corresponding iron(III) chloride tetra(*o*-*N*,*N*-dimethylaminophenyl)porphyrins, $Fe^{III}Cl$(*o*-DMA), were prepared in 60-80% yields at 20 °C via transmetallation of the corresponding dilithium porphyrin complexes.[33] The forest green dithilium materials *i*) were generated *in-situ* by reacting the H_2(*o*-DMA) isomers with two equivalents LiHDMS in THF and *ii*) were reacted with ferrous bromide ($FeBr_2$•2THF). Iron insertion proceeds more readily with the lithiated porphyrins than with the free base analogues, likely a result of forming LiCl or LiBr, which are poorly soluble in THF. The ^{1}H NMR spectra of the product metalloporphyrins were broad due to the paramagnetism. Chloride binding introduced additional asymmetry, which was identified in the diagnostic pyrrole region of the spectra (75-85 ppm; see SI).

The $Fe^{III}Cl$(*o*-DMA) compounds were then converted to the respective hydroxo complexes, $Fe^{III}OH$(*o*-DMA), by dissolving them in DCM and stirring with 1M NaOH (aq) for 30 min.[34] This ligand substitution more consistently yielded the desired penta-triflate salts in the final methylation

step. The hydroxo form of the $\alpha\alpha\alpha\alpha$ atropisomer rapidly hydrolyzed to form the corresponding μ-oxo dimer (by ^{1}H NMR and MS), which was the isolated product after chromatography. The other isomers did not form μ-oxo dimers, presumably due to steric bulk on both sides of the porphyrin ring.

Finally, the $Fe^{III}OH$(*o*-DMA) complexes (and μ-oxo dimer of the $\alpha\alpha\alpha\alpha$) were quaternized to the target $[Fe^{III}$(*o*-TMA)$](OTf)_5$ molecules using excess methyl triflate in trimethylphosphate containing a few drops of 2,6-di-*tert*-butylpyridine. Adding the sterically bulky base was key to the success of the reaction, as it sequestered disadvantageous triflic acid present in the commercial methyl triflate.[18] After stirring (12h at 20 °C), excess methyl triflate was quenched with methanol, and the products were precipitated by adding the reaction mixture dropwise into stirring Et_2O. Quenching the methyl triflate with methanol generated triflic acid, which protonated the hydroxo ligands and hydrolyzed the μ-oxo dimer of the $\alpha\alpha\alpha\alpha$ isomer (see SI). Both these reactions resulted in the convenient, and near-quantitative formation of the penta-triflate salts, as determined by the nearly doubled mass of the product (due to its higher molecular weight; **Figure D20**-**Figure D23**). The crude solids were slowly recrystallized from MeCN/Et_2O mixtures in a glovebox, and the crystalline samples of the $[Fe^{III}$(*o*-TMA)$](OTf)_5$ isomers were characterized by ^{1}H NMR, single-crystal X-ray crystallography, and cyclic voltammetry (see below and Appendix D).

The corresponding iron(II) atropisomers were prepared by stirring the iron(III) salts over Zn(Hg) amalgam in the glovebox.[15,35-37] Within an hour, the reactions were complete, and the solutions had lightened in color from maroon to cherry red. After filtering and rinsing the amalgams, the iron(II) porphyrin-containing solutions were recrystallized by vapor diffusion and the products were isolated as blocky purple crystals. These crystalline solids were also characterized by ^{1}H NMR (**Figure D29**-**Figure D32**) and single-crystal X-ray crystallography (see below and Appendix D).

Together, the synthesis described in this work offers a major improvement over the original report (ref [10]) because it introduces several steps to circumvent heating and extended reaction-times, avoiding rotamerization. We note that this route also introduces a potentially useful tool for preparing $\alpha\alpha\alpha\alpha$ iron porphyrin atropisomers. Unlike all other atropisomers, only the $\alpha\alpha\alpha\alpha$ can form u-oxo dimers, which can be separated from on basic alumina before being cleaved with acid.

5.2.2 *^{1}H NMR spectra of the Fe(III) and Fe(II) porphyrin salts*

The ferric (Fe^{III}) pentatriflate atropisomers each had unique, paramagnetic ^{1}H NMR spectra, with signals corresponding to the β-pyrrolic, aromatic, and trimethylanilinium protons (**Figure 5.1A** and **Figure D20**-**Figure D23**). The β-pyrrolic protons were assigned by integration (8*H*) and were typically the most downfield signals (ranging from 13−50 ppm). These signals appeared as broad singlets for the αβαβ and αααα atropisomers and as a set of two overlapping singlets for the ααββ isomer, in which there are two different sets of pyrroles. The β-pyrrolic signal for the αααβ atropisomer was broad and asymmetric. The aromatic protons were less downfield (ranging from 7−14 ppm) and were generally sharper. The spectra of the αβαβ, ααββ, and αααα atropisomers each contained four unique aromatic peaks (4*H* per peak), while the spectrum of the αααβ atropisomer contained a more complicated set of peaks (16*H* total). The 36 protons that corresponded to the trimethylanilinium groups were the most upfield signals in the spectra (1−5 ppm). These protons appeared as broad singlets for each of the αβαβ, ααββ, and αααα atropisomers, respectively, and as three broad singlets (1:1:2 ratio) in the αααβ spectrum.

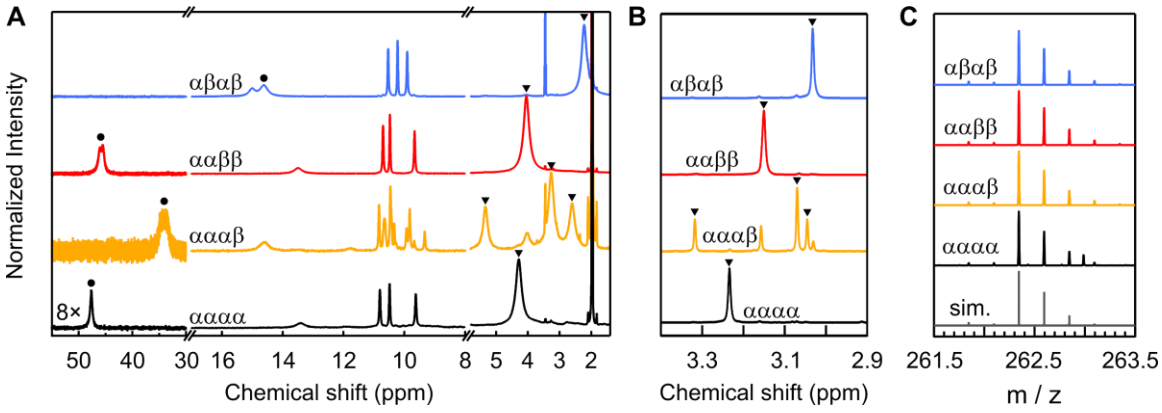

Figure 5.1. Partial ^{1}H NMR and mass spectra for the Fe(*o*-TMA) atropisomers. (**A**) Partial ^{1}H NMR spectra in CD_3CN of the αβαβ, ααββ, αααβ, and αααα atropisomers for $[Fe^{III}(o\text{-TMA})](OTf)_5$ (see SI for full spectra). The downfield regions are enhanced by 8× for clarity. The β-pyrrolic and trimethylanilinium protons are identified with black circles and triangles, respectively. (**B**) Partial ^{1}H NMR spectra of the ferrous compounds, showing the region containing the o-$[N(CH_3)_3]^+$ protons. The αααβ spectra contain ca. 10% impurity due to the ααββ atropisomer, as shown by the peak at ca. 4.0 ppm in (**A**) and 3.18 ppm in (**B**). (**C**) High resolution mass spectra and simulated spectrum of the $[Fe(o\text{-TMA})(OTf)]^{4+}$ cation ($C_{57}H_{60}N_8FeO_3SF_3$) in the samples from (**A**). Full spectra available in Appendix D.

The ferrous (Fe^{II}) atropisomers had ^{1}H NMR spectra in CD_3CN that were diamagnetic with no evidence of remaining paramagnetic impurities, showing complete reduction (**Figure D29**-

Figure D32). Like the ferric complexes, the ^{1}H NMR spectra contained signals that corresponded to the β-pyrrolic (8*H*), aromatic (16*H*), and trimethylanilinium (36*H*) protons, which were assigned by relative integrations (**Figure 5.1B**).

The ^{1}H NMR spectra of the product porphyrins show their atropisomeric purity. For the $\alpha\beta\alpha\beta$, $\alpha\alpha\beta\beta$, and $\alpha\alpha\alpha\alpha$ porphyrins, the synthesis method described in this Chapter allowed for preparation with >95% isomeric purity. The $\alpha\alpha\alpha\beta$ complex was isolated with >90% purity, with the $\alpha\alpha\beta\beta$ atropisomer accounting for nearly all the remaining signal in the ^{1}H NMR. As expected, the mass spectra are indistinguishable and cannot be used to identify any individual isomer (**Figure 5.1C**).

5.2.3 Thermal atropisomer rotamerization

The rates of tetra-arylporphyrin rotamerization have been documented for several ortho-substituted porphyrins, including the H_2(*o*-AMP) isomers used in this work.[30,32,38-40] Generally, rotamerization rates increase with temperature and decrease when sterically bulky groups are added at the *ortho*-position of the aryl rings.[38,40]

Here, the relative rates of isomerization for the $\alpha\beta\alpha\beta$ atropisomers of H_2(*o*-AMP), H_2(*o*-DMA), and [Fe^{III}(*o*-TMA)](OTf)$_5$ were measured using a ^{1}H NMR time course (**Figure D34**-**Figure D36**). A solution of each molecule was prepared in deutero-solvent, loaded into a J-young tube, and heated to 80 °C using a pre-heated oil bath for 48h with regular spectra being collected. A portion of the aromatic region of the spectra was fit using MestReNova to yield the percent $\alpha\beta\alpha\beta$ isomer remaining at each time point, which are plotted below (**Figure 5.2**).

As shown in **Figure 5.2**, both the $\alpha\beta\alpha\beta$ H_2(*o*-AMP) and H_2(*o*-DMA) porphyrins rotamerize with similar time profiles and approach the theoretical limit (12.5%) expected for the statistical mixture of isomers.[28] At 80 °C, the half-life of both reactions is <0.5h and complete isomerization was reached within 6h. While rapid isomerization of H_2(*o*-AMP) was expected at 80 °C, it was surprising that the more sterically encumbered H_2(*o*-DMA) isomerized just as quickly. In contrast, there was no evidence of isomerization for the $\alpha\beta\alpha\beta$ atropisomer of [Fe^{III}(*o*-TMA)](OTf)$_5$ under these conditions, even with additional heating to 100 °C for 48h (**Figure D36**). The more sterically

encumbered αααα [Fe^{III}(*o*-TMA)](OTf)$_5$ atropisomer was also stable at these higher temperatures (**Figure D37**).

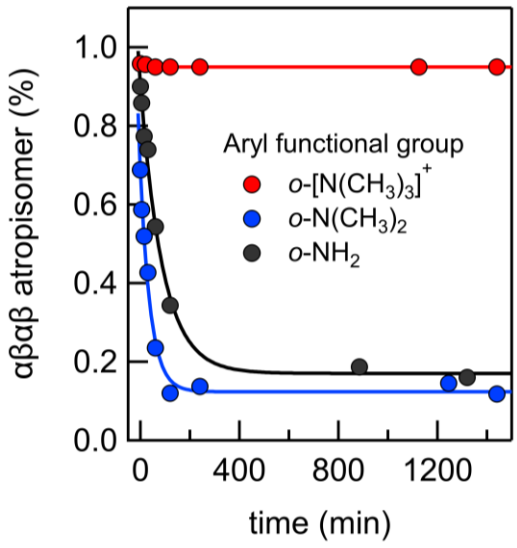

Figure 5.2. Isomerization profiles for the rotamerization of [Fe^{III}(*o*-TMA)](OTf)$_5$, H$_2$(*o*-DMA), and H$_2$(*o*-AMP) at 80 °C. Solvent was CD$_3$CN for [Fe^{III}(*o*-TMA)](OTf)$_5$ and CDCl$_3$ for H$_2$(*o*-AMP), and H$_2$(*o*-DMA) porphyrins. ^{1}H NMR spectra available in Appendix D.

The difference in isomerization rates for the *o*-N(CH$_3$)$_2$ and *o*-[N(CH$_3$)$_3$]$^+$ substituted molecules was surprising and led us to question the atropisomeric fidelity of the original synthesis reported by Savéant *et al.*, which required extended heating of αβαβ Fe^{III}Cl(*o*-DMA) during the final methylation step (24h at 100 °C in DMF).[10] To probe whether atropisomeric purity could be preserved under these harsh conditions, these synthetic procedures were repeated using an isolated sample of the αβαβ Fe^{III}Cl(*o*-DMA) precursor. After workup, the ^{1}H NMR of the product was compared to the genuine spectra of the atropisomers isolated in this work. Rather than the singular αβαβ atropisomer, as was reported, the product was a mixture of isomers (**Figure 5.3**). The αβαβ and αααβ isomers made up approximately equal fractions (40% and 38%, respectively), followed by the ααββ (17%), and αααα (5%) atropisomers (**Figure D27**-**Figure D28**). These data show that original synthesis does not yield a single isomer, as was assumed, but rather a mixture of all four atropisomers. The ramifications of this are discussed below.

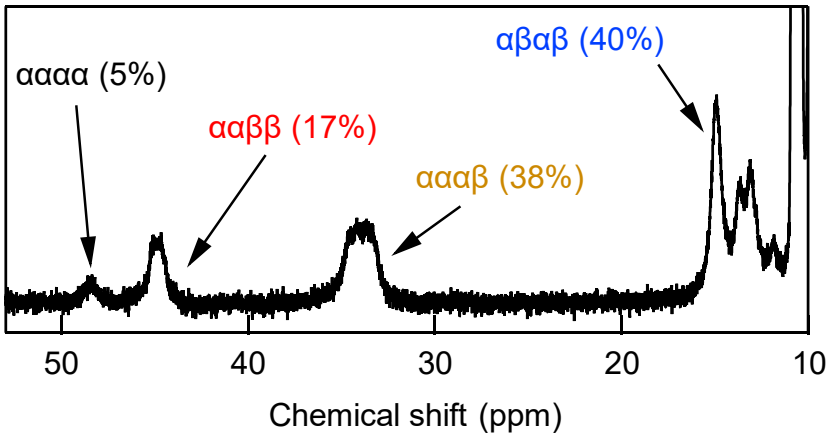

Figure 5.3. Partial ^{1}H NMR spectrum of the Fe(*o*-TMA) product obtained using the synthesis conditions reported by Savéant *et al*.[10] The isomers are identified using the respective pyrrolic peaks (8*H*) which were integrated using MestReNova. Spectra recorded in CD_3CN at 400 MHz. Full spectra available in Appendix D.

5.2.4 Single-crystal X-ray characterization

Crystals suitable for single-crystal X-ray diffraction were obtained for both the ferric and ferrous forms of the αβαβ, ααββ, and αααα atropisomers and for the ferrous-only form of the αααβ isomer by vapor diffusion of Et_2O into MeCN (**Figure 5.4**). The ferrous αβαβ structure has already been reported and is repeated here for reference.[15] A bis-aquo complex of the ferric αβαβ porphyrin was reported in reference 12, but the triflate-bound structure reported here is new. Five triflate anions were identified in each of the ferric porphyrin crystal structures and four were identified in each of the ferrous structures. Many of the triflate anions were disordered and had to be modeled, as described in the Appendix D. The crystals formed for the ferric αααβ atropisomer were too disordered for single-crystal studies.

All seven structures have ligands bound to the iron center. For the three ferric structures, a single triflate was bound to the metal. The α and β faces of the αβαβ and ααββ structures are symmetry equivalent, thus there is no site-selectivity for the bound triflate. The αααα atropisomer, however, has inequivalent sides with different steric and electrostatic environments. In the solid-state structure, a triflate ligand was bound to the more crowded, more cationic α face, and a water molecule was bound to the β face (**Figure 5.4**). The triflate being bound to the α face is the opposite of what one might expect based on sterics. The α face of the αααα atropisomer is by-far the most

congested site across the series of structures in this work and is intuitively the least likely site for a large anion to bind. The structures of the ferrous αβαβ, ααββ, and αααβ complexes each had two acetonitrile ligands bound to the iron. The αααα isomer did not have any acetonitrile ligands; rather, a triflate ligand was bound to the metal, again on the α-face.

The packing of anions and cations in the αβαβ, ααββ, and αααβ structures showed repeating units of metalloporphyrin with triflate molecules localized near the trimethylanilinium groups. In contrast, both the ferric and ferrous forms of the αααα atropisomer packed as a bilayer structure (αβ|βα|αβ|βα) with a densely packed layer of triflates appearing between the α-faces (**Figure 5.5**). In the ferric structure, the β faces are parallel and separated by 5.17 Å, longer than typical porphyrin π-π interaction distances.[41] The ferrous structure has non-parallel β faces and no evidence of π-π interactions.

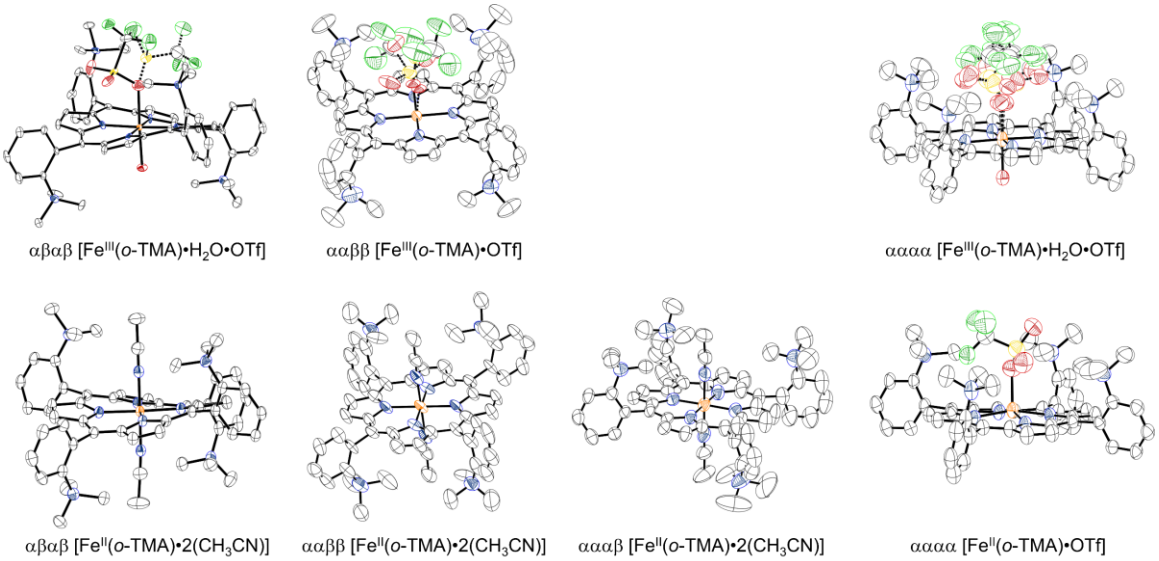

Figure 5.4. Single-crystal x-ray structures of the αβαβ, ααββ, and αααα atropisomers in both the ferric and ferrous forms and the αααβ isomer in the ferrous form only. In the ferric structures on the top, the multiple disordered orientations of the single bound triflate ligand are shown. Fe, orange; N, blue; C, white; H atoms and nonbound triflates omitted for clarity; thermal ellipsoids shown at 50% probability. The αβαβ [Fe^{II}(*o*-TMA)•2(CH$_3$CN)] structure is reported in ref. 15 and below in Appendix C.

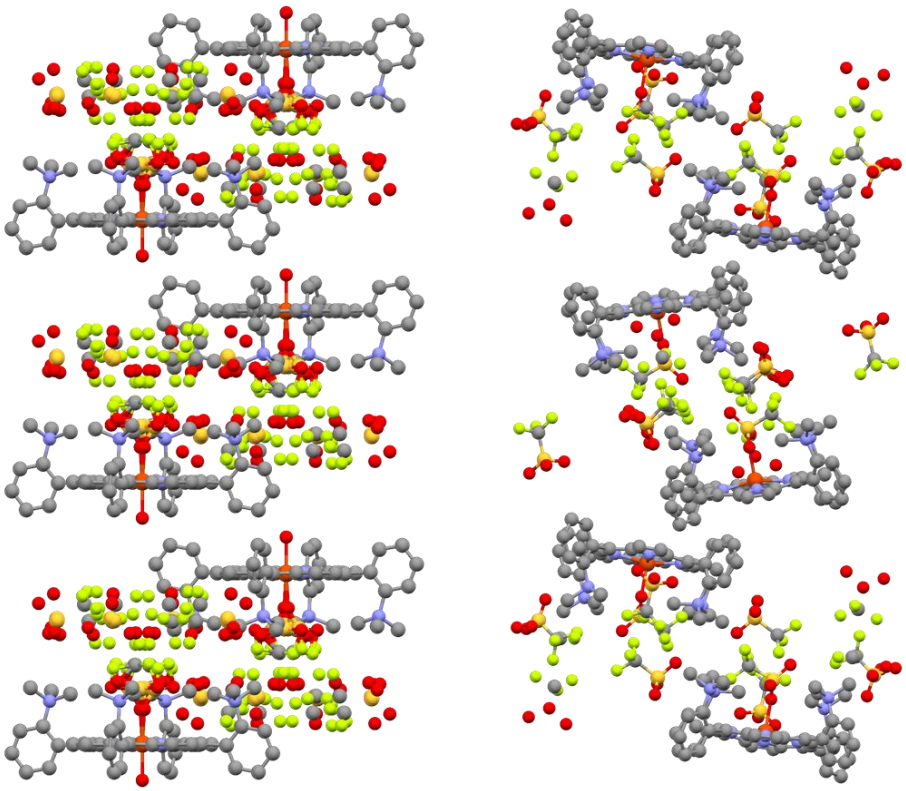

Figure 5.5. Packing structures of the αααα isomer of Fe(*o*-TMA).(**Left**) Packing structure of the ferric αααα [Fe^{III}(*o*-TMA)•H_2O•OTf](OTf)$_4$ complex. (**Right**) Packing structure of the ferrous αααα [Fe^{II}(*o*-TMA)•OTf](OTf)$_3$ complex. The layered structure has the α-faces (with the anilinium groups) oriented towards one another in a repeating βα|αβ pattern, with the triflates concentrated between the α faces. All the atoms of the different orientations of the disordered triflates are shown. Color coding: C, grey; N, blue; O, red; S, orange; F, light green; Fe, dark orange; H atoms omitted for clarity.

5.2.5 Electrochemistry

Cyclic voltammograms (CVs) of the four atropisomers were measured in acetonitrile (MeCN) containing 0.1 M tetrabutylammonium hexafluorophosphate [*n*-Bu_4N][PF_6]. The voltammograms were internally referenced to decamethylferrocene, which was independently referenced to ferrocene (Fc) using a separate solution (to avoid overlaps between $E_{1/2}(Fc^{+/0})$ and metalloporphyrin redox features). Each of the atropisomers showed three reversible reductions, which were assigned to the corresponding Fe^{III}/Fe^{II}, "Fe^{II}/Fe^{I}", and "Fe^{I}/Fe^{0}" redox couples, as is typical for iron porphyrins in nonaqueous solvent (**Table 5.1**, **Figure 5.6**).[36,42] The iron(I) and iron(0) complexes are in quotations to indicate that these complexes may involve a significant amount of ligand-centered reduction, as was shown both experimentally and by computation;[43-44] however, characterization of these low-valent species was not pursued in this work.

As a result of the four cationic, electron withdrawing *o*-$[N(CH_3)_3]^+$ groups, each of the respective redox couples have $E_{1/2}$ values that are several hundred millivolts more positive than those typical for iron porphyrin complexes in polar organic solvents (acetonitrile, *n*-butyronitrile, *N*,*N*-dimethylformamide, among others).[42,45-46] Despite similar inductive effects, the various $E_{1/2}$ values are also more than 0.1-0.2 V more positive than the corresponding values for Fe(*p*-TMA), a control molecule bearing *para*-$[N(CH_3)_3]^+$ groups (**Table 5.1**). Yet, while the magnitudes of the positive shifts are unusual, the Fe(*o*-TMA) $E_{1/2}$ values were quite similar between the four atropisomers. The range of $E_{1/2}(Fe^{III}/Fe^{II})$ and $E_{1/2}(Fe^{II}/Fe^{I})$ values was only ~10 mV across the series. The range was ~40 mV for the $E_{1/2}(Fe^{I}/Fe^{0})$ values, however, this larger deviation was due only to the positively shifted $E_{1/2}(Fe^{I}/Fe^{0})$ of the αβαβ atropisomer. In *N*,*N*-dimethylformamide (DMF) containing 0.1 M electrolyte, the same conditions reported by Savéant *et al*. in reference 10, the $E_{1/2}(Fe^{I}/Fe^{0})$ values span only 22 mV and three of the four isomers have $E_{1/2}(Fe^{I}/Fe^{0})$ values are within the error of the measurement (**Table 5.1**).

Table 5.1. Reduction potentials for the four atropisomers of $[Fe^{III}(o\text{-TMA})]^{5+}$ and for $[Fe^{III}(p\text{-TMA})]^{5+}$ [a]

Structural Isomer	Atropisomer	Solvent	$E_{1/2}(Fe^{III}/Fe^{II})$	$E_{1/2}(Fe^{II}/Fe^{I})$	$E_{1/2}(Fe^{I}/Fe^{0})$
Fe(*o*-TMA)	αβαβ	MeCN	0.142	−1.194	−1.594
	ααββ	MeCN	0.143	−1.201	−1.640
	αααβ	MeCN	0.130	−1.200	−1.632
	αααα	MeCN	0.135	−1.187	−1.635
	Average	MeCN	0.14 ± 0.01	−1.20 ± 0.01	−1.63 ± 0.02
	αβαβ	DMF	−0.351	−1.166	−1.683
	ααββ	DMF	−0.337	−1.198	−1.705
	αααβ	DMF	−0.341	−1.194	−1.698
	αααα	DMF	−0.329	−1.195	−1.695
	Average	DMF	−0.34 ± 0.01	−1.19 ± 0.01	−1.70 ± 0.01
$[Fe(p\text{-TMA})]^{5+}$		MeCN	−0.089	−1.316	ca −1.8 [b]
		DMF	−0.55 [c]	−1.40 [c]	−1.92 [c]

[a] In MeCN or DMF containing 0.1 M $[n\text{-Bu}_4N][PF_6]$. Potentials (± 0.005 V) referenced vs. Fc^+/Fc. [b] This redox feature was broad and poorly reversible. Reported value equal to the midpoint potential from the maximum and minimum current responses. [c] Reported values in DMF for $[Fe(p\text{-TMA})](Cl)_5$.[47]

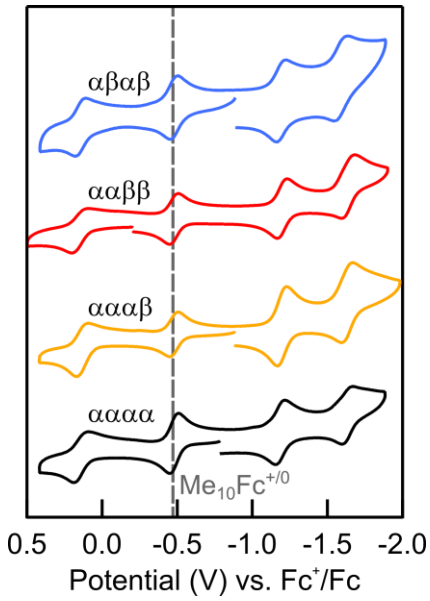

Figure 5.6. Cyclic voltammograms for the four atropisomers of $[Fe^{III}(o\text{-TMA})](OTf)_5$ in MeCN containing 0.1 M $[n\text{-Bu}_4N][PF_6]$. All voltammograms collected at 0.1 V s^{-1} and referenced to Fc^+/Fc.

5.3 Discussion

5.3.1 The effects of oriented charge on the properties of Fe(o-TMA)

The spectroscopic, electrochemical, and structural data for the four Fe(*o*-TMA) atropisomers provide unusual insights into the role of *orientation* regarding electrostatic effects on molecular properties. In contrast to most studies of electrostatics in small molecule and inorganic chemistries, this work yields information on the effects of positioned charges without changing the number or position of covalent bonds.

By nature of the *o*-TMA ligand design, there are four potential atropisomers available to the single iron porphyrin complex, each of which has a unique symmetry and electrostatic environment. The αβαβ (D_{2d}) isomer has the highest point group symmetry of the series, followed by the ααββ (C_{2h}), αααα (C_{4v}), and αααβ (C_s) atropisomers. As shown above and discussed below, these unique atropisomers could not be differentiated by cyclic voltammetry and were only distinguishable by ^{1}H NMR spectroscopy and single-crystal X-ray characterization data.

The electrochemistry of the four atropisomers was almost completely unaffected by the orientation of the *o*-$[N(CH_3)_3]^+$ groups in both MeCN and DMF, respectively. This was a surprising result, especially considering the structural differences and local charge density immediately

adjacent to the metal center. It is important to emphasize that these results do not imply the charged groups are unimportant, only that the relative orientations with respect to the metal center do not significantly affect the electrochemistry.

The *lack* of variation between the atropisomer $E_{1/2}$ values indicates that overall reduction energetics are essentially indistinguishable. From a physics perspective, these data show that the energy required to bring a negative point charge (e.g. the e^-) from infinity to a polycationic, quasi-spherical species is largely unaffected by the precise orientation of the charges within the cation. Rather, the overall energetics chiefly concern the addition of an monoanion to a compact polycation. These data also indicate that the accompanying double layers that surround the respective atropisomers (e.g. $[OTf]^-$ or $[PF_6]^-$ anions) are not so different as to affect the energetics of charge-charge annihilation upon reduction.

The most important function of the *o*-$[N(CH_3)_3]^+$ groups on the electrochemistry is that they increase the $E_{1/2}$ values of the three redox couples beyond what is expected of inductive effects. The $E_{1/2}$ values of the control molecule, Fe(*p*-TMA), which contains the same cationic functional groups but at the *para*-position, are more negative than those of Fe(*o*-TMA). In MeCN, these differences are significant: −0.23 V ($\Delta E_{1/2}[Fe^{III}/Fe^{II}]$), −0.12 V ($\Delta E_{1/2}[Fe^{II}/Fe^{I}]$), and −0.17 V ($\Delta E_{1/2}[Fe^{I}/Fe^{0}]$) in MeCN. Similar trends were also observed in DMF: −0.21 V ($\Delta E_{1/2}[Fe^{III}/Fe^{II}]$), −0.21 V ($\Delta E_{1/2}[Fe^{II}/Fe^{I}]$), and −0.22 V ($\Delta E_{1/2}[Fe^{I}/Fe^{0}]$), respectively.[15,42]

The consistent ca. 0.1-0.2 eV difference in reduction potentials for the *ortho*-and *para*-substituted complexes shows that the cationic *o*-$[N(CH_3)_3]^+$ groups improve the reduction energetics beyond inductive-only effects. Given that *i*) both the *ortho*- and *para*-substituted porphyrins have the same overall charge and *ii*) the difference in redox potentials for the four atropisomers of Fe(*o*-TMA) is ~0.02 V, the difference in energetics must largely be due to the difference in charge density for the two complexes. For instance—treating the Fe(*o*-TMA)/Fe(*p*-TMA) isomers as approximate spheres—the *ortho*-substituted atropisomers are small and compact, with cations that are localized near the metal center. In contrast, the Fe(*p*-TMA) analog, while bearing the same overall charge, has charges that are more spread out. Approximating the metal ion as the center of the each sphere and the $[N(CH_3)_3]^+$ groups as the surface, the radius is

smaller for Fe(*o*-TMA) than for Fe(*p*-TMA). The difference in radii results in an increased charge density for the Fe(*o*-TMA) atropisomers, and thus the higher reduction potential (i.e. the distance between e^- and the sphere center is smallest, and thus most favorable). This is an important result for catalyst design, because it shows that both the magnitude and overall *distribution* of charge on the molecule is important, not necessarily the charge orientation.

The crystallographic data not only distinguish the isomers, but also indicate that electrostatic interactions control both the primary coordination environment and packing structure of the solids. The ferric and ferrous structures of the $\alpha\alpha\alpha\alpha$ atropisomer are the most indicative of these effects, which show a bound triflate ligand to the more crowded α face—irrespective of the metal oxidation state—and a layered packing structure. These data contrast the structures obtained for the three remaining isomers, which have triflate ligands bound only to the ferric structures and do not pack in layers.

The difference in primary coordination environments for the ferric and ferrous structures is evidence to the strength of local, *intramolecular* electrostatic interactions between the bound triflate ligand and the *o*-$[N(CH_3)_3]^+$ groups. For the $\alpha\beta\alpha\beta$, $\alpha\alpha\beta\beta$, and $\alpha\alpha\alpha\beta$ atropisomers, only the ferric structures have a bound triflate ligand. The ferrous structures, which have a smaller overall charge and softer metal ion,[48] have two bound acetonitrile ligands. In contrast, both the ferric and ferrous forms of the $\alpha\alpha\alpha\alpha$ atropisomer have a bound triflate. Even more striking is that—in both structures—the triflate is bound to the sterically crowded α-face of the $\alpha\alpha\alpha\alpha$ atropisomer. Not only do these data indicate that local, short range interactions exist between the triflate ligand and the tetra-cationic α-face of the $\alpha\alpha\alpha\alpha$ atropisomer, but also that the electrostatic attraction overcomes the intrinsic preference of the ferrous ion. Even the $\alpha\alpha\alpha\beta$, with three $[N(CH_3)_3]^+$ groups on the same side, does not sufficiently stabilize triflate in order to overcome the Fe^{II} preference for acetonitrile ligands.

Local electrostatic interactions also impact the packing structure of the solids. In both the ferric and ferrous forms of the $\alpha\beta\alpha\beta$, $\alpha\alpha\beta\beta$ and $\alpha\alpha\alpha\beta$ atropisomers, the polycationic iron porphyrin—$[Fe^{III}$(*o*-TMA)•$(OTf)]^{4+}$ or $[Fe^{II}$(*o*-TMA)•$(CH_3CN)_2]^{4+}$—is surrounded by four triflate anions that are evenly distributed around each 4+ cation. The 3D lattice of alternating ions is

reminiscent of crystal packing for common ionic solids. In contrast, the ferric and ferrous αααα solids pack in dense, 2D layers of cations and anions. This unique packing emphasizes the strength of the local electrostatic interactions that exist between the alternating layers of Fe(*o*-TMA) α-faces and triflate anions, which persists despite the change in overall charge of the cation: $[Fe^{III}(o\text{-TMA})\bullet(OTf)]^{4+}$ vs. $[Fe^{II}(o\text{-TMA})\bullet(OTf)]^{3+}$.

5.3.2 Genuine catalyst identity in prior electrocatalytic CO_2 and O_2 reduction studies

The αβαβ atropisomer of Fe(*o*-TMA) was first designed and reported as a CO_2 reduction electrocatalyst.[10] To date, it remains one of the leading molecular CO_2RR catalysts in both rates and overpotentials and has gained significant attention in the literature (223 references as of 11/18/2020). Yet, as shown above, duplicating the reported conditions used to prepare this catalyst results in a mixture of Fe(*o*-TMA) atropisomers and not just the target αβαβ product.

The unwanted rotamerization is caused by extended heating during the final methylation step, which involves heating the FeCl(*o*-DMA) precursor at 100 °C for 24h. Given that *i*) the target αβαβ isomer made up 40% of the isolated product and not the 12.5% expected from a statistical mixture and *ii*) αβαβ $[Fe^{III}(o\text{-TMA})](OTf)_5$ does not isomerize at 100 °C, the rotamerization of the FeCl(*o*-DMA) precursor must occur with rates that are commensurate with the methylation reaction under the reported conditions. Rotamerization can only be avoided using milder conditions, such as those described in this work.

It is unsurprising that this error was not detected. In reference 10, the final metalloporphyrin was characterized by IR, UV-vis, mass spectroscopy, and elemental analysis. Although these techniques are informative, none of them can be used to determine the atropisomeric purity of $[Fe^{III}(o\text{-TMA})](OTf)_5$. As shown in this work, the $E_{1/2}$ values are also sufficiently similar in both MeCN and DMF, respectively, such that the authors would not have detected any obvious evidence of isomerization by voltammetry. Our group is also guilty of this oversight in reference 12, and we have only recently taken to using milder synthetic conditions to avoid isomerization (Chapter 4).[15]

This result is directly relevant to (electro)catalysis reported by both our group (see Chapter 3) and the Savéant group and indicate that both reference 10 and 12 report (electro)catalysis using a mixture of atropisomers rather than with a single, isolated species. In our work, reference 12, the

only values required for analysis were the change in buffer pK_a and accompanying changes in catalyst $E_{1/2}(Fe^{III}/Fe^{II})$. Both these values were experimental and could be obtained *in-situ*; thus, atropisomeric purity of the catalyst was not required. In the Savéant work, the authors hypothesize that the enhanced catalysis is "most likely [due to] the stabilization of the initial Fe(0)−CO_2 adduct by the interaction of the negative charge borne by the oxygens of CO_2 in this adduct with the nearby positive charges borne by the trimethylanilinium substituents." Computational results from our group support this argument;[15] however, it is now clear that the experimental voltammetry data reflect a composite set of electrocatalysts. This could perhaps account for the somewhat unusual shape of the voltammograms under argon in Figure 4 of reference 10, but further studies are required.

5.4 Conclusions

The addition of well-positioned charged groups to molecular, inorganic complexes is an increasingly popular topic and has garnered significant attention in the molecular electrocatalysis literature. Here we report the synthesis and characterization of all four atropisomers of iron(III) tetra(*o*-*N*,*N*,*N*-trimethylanilinium)porphyrin pentatriflate and the corresponding reduced, iron(II) tetratriflate salts. Each of these complexes contains four spatially resolved, cationic functional groups that are unique arranged around a redox-active iron. Both the single-crystal X-ray structures and ^{1}H NMR spectra show the nature and high purity of the separate atropisomers that are available from this new synthesis. The previously reported synthesis is shown to form a mixture of atropisomers, because rotamerization occurred upon heating in one of the steps after the atropisomer separation. Material from the prior synthesis, incorrectly assumed to be the single $\alpha\beta\alpha\beta$ isomer, was used in an earlier study of CO_2 reduction electrocatalysis[10] and in our earlier paper on O_2 reduction.[12] Since the CO_2 reduction study is currently the leading molecular CO_2-to-CO catalyst in combined turnover frequency and overpotential and has been highly cited, the actual multiple-isomer nature of the catalyst present in those solutions is of some significance.

The impact of unique charge positioning around the iron center was probed by examining the properties of these atropisomers. The single-crystal X-ray structures suggest that triflate binding to the iron center is enhanced by electrostatics much more strongly in the $\alpha\alpha\alpha\alpha$ isomer, where the

charges all lie on the same side of the molecule. The ferric and ferrous $\alpha\alpha\alpha\alpha$ structures also have layered packing arrangements in the solid state, different from the more typical 3D packing seen in the other structures. In contrast, the electrochemistry of the atropisomers was almost unaffected by the orientation of the charged groups, with their reduction potentials being all within ~20 mV. The *ortho*-positioned cationic groups are clearly important, shifting the metalloporphyrin redox couples more positive than the same groups in the *para* position. These studies show the varied effects of positioned charges in a metal complex, and they provide guidelines for future catalyst designs.

5.5 Experimental Methods

5.5.1 Synthesis

An atropisomeric mixture of 5,10,15,20-tetra(*o*-aminophenyl)porphyrin was prepared from the sequential *i*) condensation of pyrrole and 2-nitrobenzaldehyde and *ii*) reduction of the resulting 5,10,15,20-tetra(*o*-nitrophenyl)porphyrin, following literature methods.[28] Each of the four atropisomers was isolated by repeated chromatography on silica (see below and Appendix D) with ^{1}H NMR that matched reported spectra (**Figure D5**-**Figure D8**).[28]

5.5.1.1 5,10,15,20-tetra(o-aminophenyl)porphyrin

($\alpha\beta\alpha\beta$). ^{1}H NMR (CD_3Cl, ppm): 8.91 (s, 8H), 7.87 (d, 4H), 7.60 (t, 4H), 7.16 (t, 4H), 7.11 (d, 4H), 3.50 (s, 8H), and −2.67 (s, 2H). HRMS (ESI/Q-TOF): *m*/*z* $[M + H]^+$ calcd for $[C_{44}H_{35}N_8]^+$, 675.298; found 675.30.

($\alpha\alpha\beta\beta$). ^{1}H NMR (CD_3Cl, ppm): 8.90 (s, 8H), 7.84 (d, 4H), 7.60 (t, 4H), 7.16 (t, 4H), 7.11 (d, 4H), 3.55 (s, 8H), and −2.68 (s, 2H). HRMS (ESI/Q-TOF): *m*/*z* $[M + H]^+$ calcd for $[C_{44}H_{35}N_8]^+$, 675.298; found 675.30.

($\alpha\alpha\alpha\beta$). ^{1}H NMR (CD_3Cl, ppm): 8.90 (s, 8H), 7.85 (m, 4H), 7.60 (t, 4H), 7.17 (m, 4H), 7.11 (m, 4H), 3.54 (br. s, 8H), and −2.68 (s, 2H). HRMS (ESI/Q-TOF): *m*/*z* $[M + H]^+$ calcd for $[C_{44}H_{35}N_8]^+$, 675.298; found 675.30.

($\alpha\alpha\alpha\alpha$). ^{1}H NMR (CD_3Cl, ppm): 8.92 (s, 8H), 7.89 (d, 4H), 7.62 (t, 4H), 7.21 (m, 4H), 7.13 (d, 4H), 3.54 (s, 8H), and −2.66 (s, 2H). HRMS (ESI/Q-TOF): *m*/*z* $[M + H]^+$ calcd for $[C_{44}H_{35}N_8]^+$, 675.298; found 675.30.

The atropisomers were methylated by reductive amination using formaldehyde and sodium cyanoborohydride (4h at 15 °C) and purified by chromatography on silica (see Appendix D, **Figure D10**-**Figure D13**). The ^{1}H NMR for the αβαβ isomer matched literature.[10]

5.5.1.2 5,10,15,20-tetra(o-N,N-dimethylaminophenyl)porphyrin

(αβαβ). ^{1}H NMR (CD_3Cl, ppm): 8.75 (s, 8H), 8.00 (d, 4H), 7.69 (t, 4H), 7.41 (d, 4H), 7.30 (t, 4H), 2.23 (s, 24H), and −2.30 (s, 2H). HRMS (ESI/Q-TOF): *m*/*z* $[M + H]^+$ calcd for $[C_{52}H_{51}N_8]^+$, 787.424; found 787.43.

(ααββ). ^{1}H NMR (CD_3Cl, ppm): 8.76 (s, 4H), 8.76 (s, 4H), 7.90 (d, 4H), 7.68 (t, 4H), 7.40 (d, 4H), 7.29 (t, 4H), 2.25 (s, 24H), and −2.32 (s, 2H). HRMS (ESI/Q-TOF): *m*/*z* $[M + H]^+$ calcd for $[C_{52}H_{51}N_8]^+$, 787.424; found 787.43.

(αααβ). ^{1}H NMR (CD_3Cl, ppm): 8.76 (s, 4H), 8.75 (s, 4H), 7.90 (m, 4H), 7.68 (m, 4H), 7.41 (m, 4H), 7.28 (m, 4H), 2.30 (s, 12H), 2.27 (s, 6H), 2.23 (s, 6H), and −2.30 (s, 2H). HRMS (ESI/Q-TOF): *m*/*z* $[M + H]^+$ calcd for $[C_{52}H_{51}N_8]^+$, 787.424; found 787.42.

(αααα). ^{1}H NMR (CD_3Cl, ppm): 8.75 (s, 8H), 7.86 (d, 4H), 7.70 (t, 4H), 7.46 (d, 4H), 7.28 (t, 4H), 2.37 (s, 24H), and −2.25 (s, 2H). HRMS (ESI/Q-TOF): *m*/*z* $[M + H]^+$ calcd for $[C_{52}H_{51}N_8]^+$, 787.424; found 787.43.

The iron (III) chloride tetra(*o*-*N*,*N*-dimethylaminophenyl)porphyrins were prepared by transmetallation of the corresponding di-lithium porphyrin salts—generated in situ—with $FeBr_2(THF)_2$.[33] The ^{1}H NMR spectra are far more complicated for these iron (III) chloride metalloporphyrins due to slow chloride exchange, but are qualitatively unique and are reported in Appendix D (**Figure D15-Figure D18**).

The iron (III) tetra(*o*-*N*,*N*,*N*-trimethylanilinium)porphyrin pentatriflate salts were prepared using methyl triflate in trimethylphosphate following a modified literature procedure (**Figure D20-Figure D23**; see Appendix D and discussion above).[15,18] After recrystallization by vapor diffusion of Et_2O into MeCN solutions containing the porphyrins, lustrous purple crystals were collected for all four products. The crystals of the αβαβ, ααββ, and αααα atropisomers were suitable for single-crystal X-ray diffraction.

5.5.1.3 Iron (III) tetra(o-N,N,N-trimethylanilinium)porphyrin pentatriflate

($\alpha\beta\alpha\beta$). ^{1}H NMR (CD_3CN, ppm): 15.0 (4H, Ar-*H*), 14.6 (8H, pyrr-*H*), 10.53 (4H, Ar-*H*), 10.22 (4H, Ar-*H*), 9.90 (4H, Ar-*H*), and 2.22 (36H, −(C*H*$_3$)$_{12}$). HRMS (ESI/Q-TOF): *m*/*z* [M – 4(OTf)]$^{4+}$ calcd for [$C_{57}H_{60}N_8FeO_3SF_3$]$^{4+}$, 262.345; found 262.34.

($\alpha\alpha\beta\beta$). ^{1}H NMR (CD_3CN, ppm): 46.0 (4H, pyrr-*H*), 45.6 (4H, pyrr-*H*), 13.49 (4H, Ar-*H*), 10.70 (4H, Ar-*H*), 10.47 (4H, Ar-*H*), 9.66 (4H, Ar-*H*), and 4.03 (36H, −(C*H*$_3$)$_{12}$). HRMS (ESI/Q-TOF): *m*/*z* [M – 4(OTf)]$^{4+}$ calcd for [$C_{57}H_{60}N_8FeO_3SF_3$]$^{4+}$, 262.345; found 262.34.

($\alpha\alpha\alpha\beta$). ^{1}H NMR (CD_3CN, ppm): 34.0 (8H, pyrr-*H*), 14.57-9.32 (16H, Ar-*H*), 5.33 (9H, −(C*H*$_3$)$_3$), 3.26 (18H, −(C*H*$_3$)$_6$), and 2.60 (9H, −(C*H*$_3$)$_3$). HRMS (ESI/Q-TOF): *m*/*z* [M – 4(OTf)]$^{4+}$ calcd for [$C_{57}H_{60}N_8FeO_3SF_3$]$^{4+}$, 262.345; found 262.34.

($\alpha\alpha\alpha\alpha$). ^{1}H NMR (CD_3CN, ppm): 47.6 (8H, pyrr-*H*), 13.36 (4H, Ar-*H*), 10.80 (4H, Ar-*H*), 10.48 (4H, Ar-*H*), 9.62 (4H, Ar-*H*), and 4.29 (36H, −(C*H*$_3$)$_{12}$). HRMS (ESI/Q-TOF): *m*/*z* [M – 4(OTf)]$^{4+}$ calcd for [$C_{57}H_{60}N_8FeO_3SF_3$]$^{4+}$, 262.345; found 262.34.

The reduced, iron (II) tetra(*o*-*N*,*N*,*N*-trimethylanilinium)porphyrin tetratriflate complexes were prepared by stirring the ferric porphyrin salts with solid Zn(Hg) amalgam in the glovebox, following a reported procedure. The porphyrin products were then precipitated by vapor diffusion of Et_2O into the collected MeCN solutions (**Figure D29-Figure D32**). As before, purple crystals were collected, all of which were suitable for single-crystal X-ray diffraction. The ^{1}H NMR for the $\alpha\beta\alpha\beta$ atropisomer matched the reported spectrum.[15]

5.5.1.4 Iron (II) tetra(o-N,N,N-trimethylanilinium)porphyrin tetratriflate

($\alpha\beta\alpha\beta$). ^{1}H NMR (CD_3CN, ppm): 8.56 (s, 8H, pyrr-*H*), 8.54 (d, 4H, Ar-*H*), 8.24 (d, 4H, Ar-*H*), 8.09 (t, 4H, Ar-*H*), 7.99 (t, 4H, Ar-*H*), and 3.05 (s, 36H, −(C*H*$_3$)$_{12}$).

($\alpha\alpha\beta\beta$). ^{1}H NMR (CD_3CN, ppm): 8.86 (s, 4H, pyrr-*H*), 8.83 (s, 4H, Ar-*H*), 8.30 (d, 4H, Ar-*H*), 8.28 (d, 4H, Ar-*H*), 8.08 (t, 4H, Ar-*H*), 7.87 (t, 4H, Ar-*H*), 3.15 (s, 36H, −(C*H*$_3$)$_{12}$).

($\alpha\alpha\alpha\beta$). ^{1}H NMR (CD_3CN, ppm): 8.87 (m, 8H, pyrr-*H*), 8.51 (d, 1H, Ar-*H*), 8.44 (d, 2H, Ar-*H*), 8.36 (d, 1H, Ar-*H*), 8.26 (d, 4H, Ar-*H*), 8.07 (m, 4H, Ar-*H*), 7.96 (t, 1H, Ar-*H*), 7.93 (t, 2H, Ar-*H*), 7.77 (t, 1H, Ar-*H*), 3.32 (s, 9H, −(C*H*$_3$)$_3$), 3.07 (s, 18H, −(C*H*$_3$)$_6$), 3.04 (s, 9H, −(C*H*$_3$)$_3$).

(αααα). ^{1}H NMR (CD_3CN, ppm): 10.80 (br. s, 8H, pyrr-*H*), 8.30 (d, 4H, Ar-*H*), 8.22 (d, 4H, Ar-*H*), 8.06 (t, 4H, Ar-*H*), 7.82 (4H, Ar-*H*), 3.22 (s, 36H, −(CH_3)$_{12}$).

5.5.2 *Column conditions for isolating the atropisomers of 5,10,15,20-tetra(o-aminophenyl)porphyrin*

αβαβ: Column 1 was an 8" x 3" column of silica, slurry loaded with DCM. The αβαβ and ααββ atropisomers were separated from the ααβ and αααα isomers by flash chromatography using 80:20 DCM/Et_2O eluent (R_f = 0.8 and 0.7). The ratio of αβαβ to ααββ in the collected fractions was approximately 1:2, consistent with the statistical mixture of isomers. Column 2 was an 8" x 2" column of silica, slurry loaded with DCM. Using a 90:10 DCM/Et_2O eluent, the bulk of the αβαβ atropisomer was separated from the ααββ (R_f = 0.7 and 0.5). The ratio of αβαβ to ααββ in the collected fractions was atropisomerically enriched, though often still impure (9:1). The dimensions and eluent mixture for Column 3 was the same as Column 2. Only the first few fractions were collected and carefully monitored by TLC for contamination by the ααββ atropisomer. After combining fractions and removing the solvent, the αβαβ atropisomer was obtained with high purity.

ααββ: Columns 1, 2 and 3 were the same as described above for the isolation of the αβαβ atropoisomer. Fractions of ααββ were collected and carefully monitored by TLC for trace ααβ and αβαβ contamination in the 2nd and 3rd columns, respectively (R_f = 0.7, 0.5, and 0.2, respectively). It is worth noting that the solubility of this porphyrin in DCM is lowest of the atropisomers, and so care should be taken to avoid overloading the columns. In general, the ααββ isomer was the easiest atropisomer to purity.

ααβ: The dimension of Column 1 is the same as described above. After eluting the αβαβ and ααββ atropisomers using 80:20 DCM/Et_2O, the ααβ could be obtained by eluting with 50:50 DCM/Et_2O (R_f = 0.8). Columns 2 and 3 were the same dimensions as described above and used the same two-stage eluant mixtures (80:20 followed by 50:50 DCM/Et_2O). Care should be taken to avoid contamination by the ααββ atropisomer.

αααα: The dimension of Column 1 is the same as described above. After eluting the column with 50:50 DCM/Et_2O, the αααα aminophenylporphyrin was eluted using 50:50 acetone/Et_2O (R_f = 0.9). Columns 2 and 3 were the same dimensions as those used above, but

were loaded with 50:50 DCM/Et_2O and eluted with the same mixture until the eluent was clear. The $\alpha\alpha\alpha\alpha$ porphyrin was obtained in high atropisomeric purity by final elution with 50:50 acetone/Et_2O. Of note, the $\alpha\alpha\alpha\alpha$ isomer could be conveniently enriched prior to Column 1 by refluxing the statistical mixture of atropisomers in the presence of silica.[49]

5.6 References

1. Fried, S. D.; Boxer, S. G., Electric Fields and Enzyme Catalysis. *Annu. Rev. Biochem* **2017,** *86* (1), 387-415.
2. Warshel, A.; Sharma, P. K.; Kato, M.; Xiang, Y.; Liu, H.; Olsson, M. H., Electrostatic basis for enzyme catalysis. *Chem. Rev.* **2006,** *106* (8), 3210-35.
3. Shaik, S.; Mandal, D.; Ramanan, R., Oriented electric fields as future smart reagents in chemistry. *Nat. Chem.* **2016,** *8* (12), 1091-1098.
4. Elgrishi, N.; Rountree, K. J.; McCarthy, B. D.; Rountree, E. S.; Eisenhart, T. T.; Dempsey, J. L., A Practical Beginner's Guide to Cyclic Voltammetry. *J. Chem. Educ.* **2018,** *95* (2), 197-206.
5. Rountree, E. S.; McCarthy, B. D.; Eisenhart, T. T.; Dempsey, J. L., Evaluation of Homogeneous Electrocatalysts by Cyclic Voltammetry. *Inorg. Chem.* **2014,** *53* (19), 9983-10002.
6. Costentin, C.; Robert, M.; Savéant, J. M., Current Issues in Molecular Catalysis Illustrated by Iron Porphyrins as Catalysts of the CO_2-to-CO Electrochemical Conversion. *Acc. Chem. Res.* **2015,** *48* (12), 2996-3006.
7. Costentin, C.; Savéant, J.-M., Multielectron, Multistep Molecular Catalysis of Electrochemical Reactions: Benchmarking of Homogeneous Catalysts. *ChemElectroChem* **2014,** *1* (7), 1226-1236.
8. Chantarojsiri, T.; Reath, A. H.; Yang, J. Y., Cationic Charges Leading to an Inverse Free-Energy Relationship for N-N Bond Formation by Mn(VI) Nitrides. *Angew. Chem. Int. Ed. Engl.* **2018,** *57* (43), 14037-14042.
9. Nichols, A. W.; Machan, C. W., Secondary-Sphere Effects in Molecular Electrocatalytic CO_2 Reduction. *Front. Chem.* **2019,** *7*, 397.
10. Azcarate, I.; Costentin, C.; Robert, M.; Savéant, J. M., Through-Space Charge Interaction Substituent Effects in Molecular Catalysis Leading to the Design of the Most Efficient Catalyst of CO_2-to-CO Electrochemical Conversion. *J. Am. Chem. Soc.* **2016,** *138* (51), 16639-16644.
11. Zhang, R.; Warren, J. J., Controlling the Oxygen Reduction Selectivity of Asymmetric Cobalt Porphyrins by Using Local Electrostatic Interactions. *J. Am. Chem. Soc.* **2020,** *142* (31), 13426-13434.
12. Martin, D. J.; Mercado, B. Q.; Mayer, J. M., Combining scaling relationships overcomes rate versus overpotential trade-offs in O_2 molecular electrocatalysis. *Sci. Adv.* **2020,** *6* (11), eaaz3318.
13. Margarit, C. G.; Asimow, N. G.; Gonzalez, M. I.; Nocera, D. G., Double Hangman Iron Porphyrin and the Effect of Electrostatic Nonbonding Interactions on Carbon Dioxide Reduction. *J. Phys. Chem. Lett.* **2020,** *11* (5), 1890-1895.
14. Sampson, M. D.; Kubiak, C. P., Manganese Electrocatalysts with Bulky Bipyridine Ligands: Utilizing Lewis Acids To Promote Carbon Dioxide Reduction at Low Overpotentials. *J. Am. Chem. Soc.* **2016,** *138* (4), 1386-93.
15. Martin, D. J.; Johnson, S. I.; Mercado, B. Q.; Raugei, S.; Mayer, J. M., Intramolecular Electrostatic Effects on O_2, CO_2, and Acetate Binding to a Cationic Iron Porphyrin. *Inorg. Chem.* **2020,** *59* (23), 17402-17414.
16. Kalyanasundaram, K.; Neumannspallart, M., Photophysical and Redox Properties of Water-Soluble Porphyrins in Aqueous-Media. *J. Phys. Chem.* **1982,** *86* (26), 5163-5169.
17. Kano, K.; Minamizono, H.; Kitae, T.; Negi, S., Self-Aggregation of Cationic Porphyrins in Water. Can π−π Stacking Interaction Overcome Electrostatic Repulsive Force? *J. Phys. Chem. A* **1997,** *101* (34), 6118-6124.
18. La, T.; Richards, R.; Miskelly, G. M., Synthesis and Characterization of the Cationic Porphyrin Meso-Tetrakis(2,3,5,6-Tetrafluoro-*N*,*N*,*N*-Trimethyl-4-Aniliniumyl)Porphyrin. *Inorg. Chem.* **1994,** *33* (14), 3159-3163.
19. Miskelly, G. M.; Webley, W. S.; Clark, C. R.; Buckingham, D. A., Acidity and dimerization of three water-soluble iron(III) porphyrin cations: (meso-α,β,α,β-tetrakis(o-(N-methylnicotinamido)phenyl)porphyrinato)iron(III), (meso-α,α,α,α-tetrakis(o-(N-

methylnicotinamido)phenyl)porphyrinato)iron(III), and (meso-tetrakis(1-methylpyridinium-4-yl)porphyrinato)iron(III). *Inorg. Chem.* **1988,** *27* (21), 3773-3781.
20. Tovmasyan, A.; Weitner, T.; Sheng, H.; Lu, M.; Rajic, Z.; Warner, D. S.; Spasojevic, I.; Reboucas, J. S.; Benov, L.; Batinic-Haberle, I., Differential coordination demands in Fe versus Mn water-soluble cationic metalloporphyrins translate into remarkably different aqueous redox chemistry and biology. *Inorg. Chem.* **2013,** *52* (10), 5677-91.
21. Batinić-Haberle, I.; Spasojević, I.; Hambright, P.; Benov, L.; Crumbliss, A. L.; Fridovich, I., Relationship among Redox Potentials, Proton Dissociation Constants of Pyrrolic Nitrogens, and in Vivo and in Vitro Superoxide Dismutating Activities of Manganese(III) and Iron(III) Water-Soluble Porphyrins. *Inorg. Chem.* **1999,** *38* (18), 4011-4022.
22. Weitner, T.; Budimir, A.; Kos, I.; Batinic-Haberle, I.; Birus, M., Acid-base and electrochemical properties of manganese meso(ortho- and meta-*N*-ethylpyridyl)porphyrins: potentiometric, spectrophotometric and spectroelectrochemical study of protolytic and redox equilibria. *Dalton Trans.* **2010,** *39* (48), 11568-76.
23. Franke, A.; Scheitler, A.; Kenkel, I.; Lippert, R.; Zahl, A.; Balbinot, D.; Jux, N.; Ivanovic-Burmazovic, I., Positive Charge on Porphyrin Ligand and Nature of Metal Center Define Basic Physicochemical Properties of Cationic Manganese and Iron Porphyrins in Aqueous Solution. *Inorg. Chem.* **2019,** *58* (15), 9618-9630.
24. Brausam, A.; Eigler, S.; Jux, N.; van Eldik, R., Mechanistic investigations of the reaction of an iron(III) octa-anionic porphyrin complex with hydrogen peroxide and the catalyzed oxidation of diammonium-2,2'-azinobis(3-ethylbenzothiazoline-6-sulfonate). *Inorg. Chem.* **2009,** *48* (16), 7667-78.
25. Jee, J. E.; Eigler, S.; Hampel, F.; Jux, N.; Wolak, M.; Zahl, A.; Stochel, G.; van Eldik, R., Kinetic and mechanistic studies on the reaction of nitric oxide with a water-soluble octa-anionic iron(III) porphyrin complex. *Inorg. Chem.* **2005,** *44* (22), 7717-31.
26. Jee, J. E.; Wolak, M.; Balbinot, D.; Jux, N.; Zahl, A.; van Eldik, R., A comparative mechanistic study of the reversible binding of NO to a water-soluble octa-cationic Fe(III) porphyrin complex. *Inorg. Chem.* **2006,** *45* (3), 1326-37.
27. Jee, J. E.; Eigler, S.; Jux, N.; Zahl, A.; van Eldik, R., Influence of an extremely negatively charged porphyrin on the reversible binding kinetics of NO to Fe(III) and the subsequent reductive nitrosylation. *Inorg. Chem.* **2007,** *46* (8), 3336-52.
28. Collman, J. P.; Gagne, R. R.; Reed, C. A.; Halbert, T. R.; Lang, G.; Robinson, W. T., "Picket fence porphyrins." Synthetic models for oxygen binding hemoproteins. *J. Am. Chem. Soc.* **1975,** *97* (6), 1427-39.
29. Nishino, N.; Kobata, K.; Mihara, H.; Fujimoto, T., Efficient Preparation of αβαβ-Atropisomer ofmeso-Tetra(o-aminophenyl)porphyrin. *Chem. Lett.* **1992,** *21* (10), 1991-1994.
30. Rose, E.; Cardonpilotaz, A.; Quelquejeu, M.; Bernard, N.; Kossanyi, A.; Desmazieres, B., Efficient Preparation of the α,α,β,β-Atropoisomer of meso-Tetrakis(o-aminophenyl)porphyrin. *J. Org. Chem.* **1995,** *60* (12), 3919-3920.
31. Rose, E.; Cardon-Pilotaz, A.; Quelquejeu, M.; Bernard, N.; Kossanyi, A.; Desmazieres, B., Efficient Preparation of the α,α,β,β-Atropoisomer of meso-Tetrakis(o-aminophenyl)porphyrin. *The Journal of Organic Chemistry* **1995,** *60* (12), 3919-3920.
32. Rose, E.; Quelquejeu, M.; Pochet, C.; Julien, N.; Kossanyi, A.; Hamon, L., Large-scale preparation of α,β,α,β atropisomer of meso-Tetrakis(o-aminophenyl)porphyrin. *J. Org. Chem.* **1993,** *58* (19), 5030-5031.
33. Arnold, J.; Dawson, D. Y.; Hoffman, C. G., Synthesis and Characterization of Lithium, Sodium, and Potassium Porphyrin Complexes - X-Ray Crystal-Structures of $Li_2(C_6H_{12}O_2)_2$TMPP, $Na_2(THF)_4$OEP, and K_2(pyridine)$_4$OEP. *J. Am. Chem. Soc.* **1993,** *115* (7), 2707-2713.
34. Boersma, A. D.; Goff, H. M., Multinuclear magnetic resonance spectroscopy of spin-admixed S = 5/2, 3/2 iron(III) porphyrins. *Inorg. Chem.* **1982,** *21* (2), 581-586.
35. Safo, M. K.; Nesset, M. J. M.; Walker, F. A.; Debrunner, P. G.; Scheidt, W. R., Models of the Cytochromes. Axial Ligand Orientation and Complex Stability in Iron(II) Porphyrinates: The Case of the Noninteracting d_π Orbitals. *J. Am. Chem. Soc.* **1997,** *119* (40), 9438-9448.
36. Walker, F. A.; Simonis, U., Iron Porphyrin Chemistry. John Wiley & Sons, Ltd: Chichester, UK, 2006.

37. Pegis, M. L.; Martin, D. J.; Wise, C. F.; Brezny, A. C.; Johnson, S. I.; Johnson, L. E.; Kumar, N.; Raugei, S.; Mayer, J. M., Mechanism of Catalytic O_2 Reduction by Iron Tetraphenylporphyrin. *J. Am. Chem. Soc.* **2019,** *141*, 8315-8326.
38. Tomé, A. C.; Silva, A. M. S.; Alkorta, I.; Elguero, J., Atropisomerism and conformational aspects of meso-tetraarylporphyrins and related compounds. *J. Porphyrins Phthalocyanines* **2012,** *15* (01), 1-28.
39. Zimmer, B.; Bulach, V.; Drexler, C.; Erhardt, S.; Hosseini, M. W.; De Cian, A., Design, synthesis, structural analysis and atropoisomerisation studies of polynucleating ligands based on porphyrins bearing catechol units. *New J. Chem.* **2002,** *26* (1), 43-57.
40. Crossley, M. J.; Field, L. D.; Forster, A. J.; Harding, M. M.; Sternhell, S., Steric Effects on Atropisomerism in Tetraarylporphyrins. *J. Am. Chem. Soc.* **1987,** *109* (2), 341-348.
41. Nozawa, R.; Tanaka, H.; Cha, W. Y.; Hong, Y.; Hisaki, I.; Shimizu, S.; Shin, J. Y.; Kowalczyk, T.; Irle, S.; Kim, D.; Shinokubo, H., Stacked antiaromatic porphyrins. *Nat. Commun.* **2016,** *7*, 13620.
42. Kadish, K. M.; Morrison, M. M.; Constant, L. A.; Dickens, L.; Davis, D. G., A study of solvent and substituent effects on the redox potentials and electron-transfer rate constants of substituted iron meso-tetraphenylporphyrins. *J. Am. Chem. Soc.* **1976,** *98* (26), 8387-90.
43. Romelt, C.; Song, J.; Tarrago, M.; Rees, J. A.; van Gastel, M.; Weyhermuller, T.; DeBeer, S.; Bill, E.; Neese, F.; Ye, S., Electronic Structure of a Formal Iron(0) Porphyrin Complex Relevant to CO_2 Reduction. *Inorg. Chem.* **2017,** *56* (8), 4746-4751.
44. Romelt, C.; Ye, S.; Bill, E.; Weyhermuller, T.; van Gastel, M.; Neese, F., Electronic Structure and Spin Multiplicity of Iron Tetraphenylporphyrins in Their Reduced States as Determined by a Combination of Resonance Raman Spectroscopy and Quantum Chemistry. *Inorg. Chem.* **2018,** *57* (4), 2141-2148.
45. Pegis, M. L.; McKeown, B. A.; Kumar, N.; Lang, K.; Wasylenko, D. J.; Zhang, X. P.; Raugei, S.; Mayer, J. M., Homogenous Electrocatalytic Oxygen Reduction Rates Correlate with Reaction Overpotential in Acidic Organic Solutions. *ACS Cent. Sci.* **2016,** *2* (11), 850-856.
46. Nichols, E. M.; Derrick, J. S.; Nistanaki, S. K.; Smith, P. T.; Chang, C. J., Positional effects of second-sphere amide pendants on electrochemical CO_2 reduction catalyzed by iron porphyrins. *Chem. Sci.* **2018,** *9* (11), 2952-2960.
47. Bonin, J.; Maurin, A.; Robert, M., Molecular catalysis of the electrochemical and photochemical reduction of CO_2 with Fe and Co metal based complexes. Recent advances. *Coord. Chem. Rev.* **2017,** *334*, 184-198.
48. Parr, R. G.; Pearson, R. G., Absolute Hardness - Companion Parameter to Absolute Electronegativity. *J. Am. Chem. Soc.* **1983,** *105* (26), 7512-7516.
49. Lindsey, J., Increased Yield of a Desired Isomer by Equilibria Displacement on Binding to Silica-Gel, Applied to Meso-Tetrakis(*o*-aminophenyl)Porphyrin. *J. Org. Chem.* **1980,** *45* (25), 5215-5215.

6 Spatial Electrostatic Effects on O_2 and CO_2 Reduction by a Cationic Iron Porphyrin

Adapted from Martin, D. J. and Mayer, J. M. "Spatial Electrostatic Effects on O_2 and CO_2 Reduction by a Cationic Iron Porphyrin." *Unsubmitted work*. DJM conceived the project and executed the experiments. DJM and JMM constructed the scientific arguments and wrote the paper.

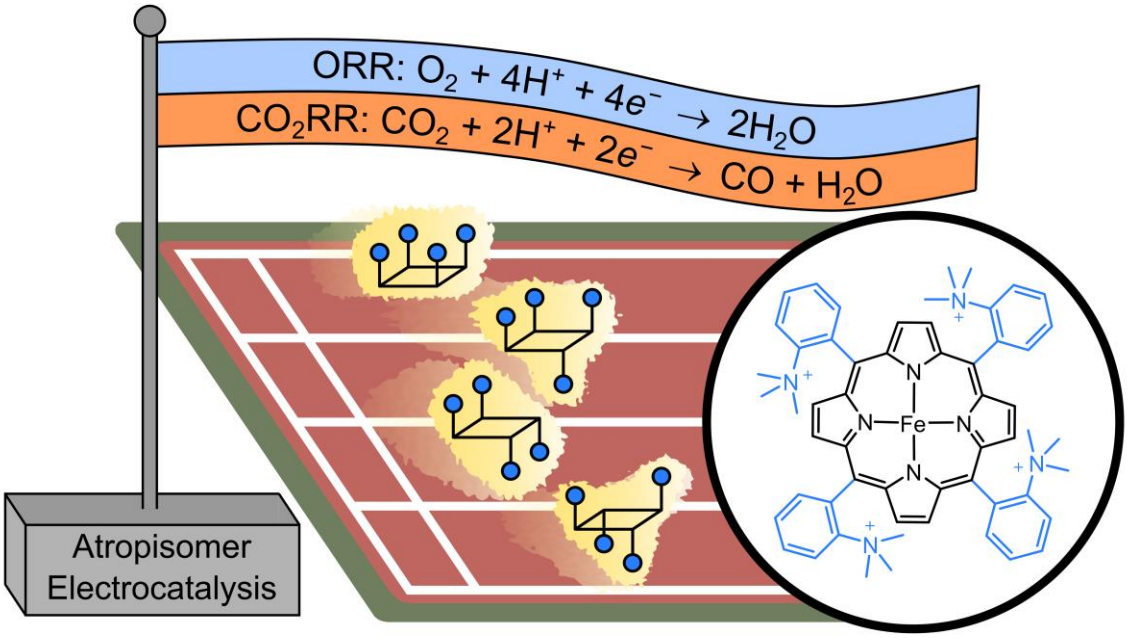

6.1 Introduction

Electrostatic effects and electric fields are known to enable challenging reactions in biology, chemistry and catalysis.[1-3] They are especially effective at facilitating reactions that involve charge redistribution or high-energy charged intermediates or transition states. Such reaction steps are common in molecular electrocatalysis, wherein multi-electron, multi-proton processes are often required for important chemical-to-electrical energy conversion reactions. To explore and utilize electrostatic effects, there has recently been a burgeoning interest in adding charged motifs to molecular (electro)catalysts.[4-12] The advantage of molecular catalysts in this context is that they can be designed with atomic precision and well-defined active sites.

Perhaps the leading example of the value of adding charges to a catalyst is the polycationic iron porphyrin, Fe(*o*-TMA), with four *ortho*-trimethylanilinium (*o*-$[N(CH_3)_3]^+$) groups on the porphyrin ligand. Under optimized conditions, this single catalyst has been used to catalyze O_2 reduction and CO_2 reduction (ORR and CO_2RR) electrochemically with fast rates and at low overpotentials.[13-15]

The success of Fe(*o*-TMA) towards both reactions has been ascribed, at least in part, to electrostatic interactions between the cationic groups on the porphyrin and ligands that bind to the metal center during turnover. In CO_2 reduction, the primary electrostatic interaction is hypothesized to be the stabilization of a high-energy $Fe^{I}(CO_2^{\bullet-})$ adduct using the well-positioned *o*-$[N(CH_3)_3]^+$ groups on the porphyrin ligand.[13,15] In O_2 reduction, electrostatic effects increase the binding affinity of Fe(*o*-TMA) towards acetate, the anionic conjugate base used to buffer the solution.[14-15] Acetate binding causes a subsequent change in the catalyst $E_{1/2}(Fe^{III}/Fe^{II})$, a property that controls O_2 binding and the rates of catalysis,[16-17] and thus ultimately defines the catalyst effectiveness.

Studies from the Savéant group and from our group have established Fe(*o*-TMA) among the leading soluble, molecular electrocatalysts for the CO_2RR and ORR, respectively. However, as was shown in Chapter 5, neither of these studies reported catalysis using genuine samples of the αβαβ atropisomer, as had been assumed. Rather—because a late-stage step in the reported synthesis involved heating and caused rotamerization of the αβαβ isomer—the reported catalysis in ref. 13 and 14 used a mixture of all four atropisomers (**Scheme 6.1**). Thus, it is not known which isomer(s) contribute most significantly to the catalytic prowess reported in the literature, or whether the positioning of the cationic groups has a significant effect on catalysis.

Scheme 6.1. Drawings of the four atropisomers of the $[Fe(o\text{-TMA})]^{5+}$ cation.

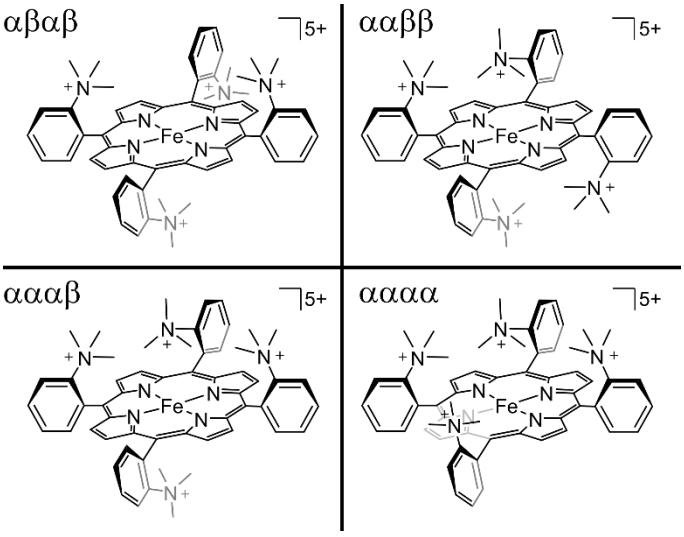

Here, we report electrocatalysis of the ORR and CO_2RR using the four individual atropisomers of Fe(*o*-TMA) and identify the similarities/differences that exist between the isomers.

Both kinetic and thermodynamic data suggest that the oriented, electrostatic groups in the Fe(*o*-TMA) ligand design play a complex role, beyond the stabilization of a single charged intermediate. From these comparisons, the most important electrostatic factors were identified and detailed for catalysis of both reactions. The results and conclusions of this work have important implications for the design of molecular (electro)catalysts with atomically positioned charged groups.

6.2 Results and Discussion

The four atropisomers of iron(III) tetra(*N*,*N*,*N*-trimethylanilinium)porphyrin pentatriflate and the ferrous (Fe^{II}) tetratriflate salts were prepared as previously reported in Chapter 5.[15,18] The isomers were stable as solids at room temperature and were stored in the glovebox. All the cyclic voltammograms (CVs) reported below are referenced versus ferrocene (Fc^{+}/Fc). Electrochemical studies were done in acetonitrile (MeCN) or *N*,*N*-dimethylformamide (DMF), as noted, and were collected using solutions that contained 0.1 M tetra-*n*-butylammonium hexafluorophosphate ([*n*-Bu_4N][PF_6]). The working electrode was glassy carbon, with a platinum auxiliary electrode and a silver wire pseudoreference. The unique solution conditions for specific experiments are given below and in Appendix E.

The electrochemistry of the four atropisomers was first reported in reference 18 (Chapter 5, above). In MeCN and DMF, all four isomers of Fe(*o*-TMA) have reversible iron(III/II), iron(II/I), and iron(I/0) redox features under argon. The values of $E_{1/2}(Fe^{III}/Fe^{II})$, $E_{1/2}(Fe^{II}/Fe^{I})$, and $E_{1/2}(Fe^{I}/Fe^{0})$ vary between the two solvents, but all are positive of typical values reported for neutral iron tetra-aryporphyrins. The identity of the atropisomer does not significantly affect the reduction potentials, which indicates that the orientation of the charged groups largely does not affect the reduction thermodynamics. The *ortho*-substitution pattern is important, however, and results in $E_{1/2}$ values that are 0.1-0.2 V more positive than the corresponding *para*-$[N(CH_3)_3]^+$ substituted complex, Fe(*p*-TMA), in each respective solvent.[18] As reported below, the voltammetry data under catalytic conditions is more varied for the set of Fe(*o*-TMA) atropisomers.

6.2.1 O_2 reduction

6.2.1.1 ORR electrocatalysis

Here, we measured the electrochemistry for all four atropisomers using the solution conditions reported in ref 14 to yield the most optimal catalysis (MeCN containing 0.1 M H_2O, [*n*-Bu_4N][PF_6], and buffered AcOH). A single stock solution was prepared and divided into four separate containers, to each of which was added one of the Fe(*o*-TMA) isomers. This method ensured that the isomers were compared under *identical* solution conditions and that the equilibrium potential for O_2 reduction was constant across the series (see Appendix E). Cyclic voltammograms were collected for each of these solutions under both argon and O_2 (1 atm) (**Figure E1-Figure E2**).

Under buffered conditions, all four isomers have reversible iron(III/II) redox features under argon, with $E_{1/2}(Fe^{III}/Fe^{II})$ values between −0.595 V ($\alpha\alpha\alpha\alpha$) and −0.644 V ($\alpha\beta\alpha\beta$). Under O_2, a large, irreversible current appeared near the corresponding $E_{1/2}(Fe^{III}/Fe^{II})$ values, indicating turnover (**Figure 6.1A**). Rinse tests indicated that this current was the result of a homogeneous catalytic process (**Figure E3**).[19-20] Following prior methods,[14] foot-of-the-wave analysis (FOWA) was used to determine the TOF_{max} values from "foot" of these voltammograms, a region where unwanted side-phenomena such as substrate depletion are minimized (**Figure 6.1B**; see Appendix E for details and fits).[21-22] **Table 6.1** summarizes the $E_{1/2}(Fe^{III}/Fe^{II})$, η_{eff}, and TOF_{max} values for the isomers under identical conditions.

Table 6.1. Catalyst system properties for O_2 reduction by Fe(*o*-TMA) atropisomers.

Atropisomer	$E_{1/2}(Fe^{III}/Fe^{II})$ [a]		$\Delta E_{1/2}$ (V)	η_{eff} (V)	TOF_{max} (s^{-1})	$\log(TOF_{max}/s^{-1})$
	+ 0.1 M AcOH buffer					
$\alpha\beta\alpha\beta$	0.142	−0.644	0.786	0.491	58	1.76
$\alpha\alpha\beta\beta$	0.143	−0.626	0.769	0.474	7.0	0.84
$\alpha\alpha\alpha\beta$	0.130	−0.611	0.741	0.458	6.3	0.80
$\alpha\alpha\alpha\alpha$	0.135	−0.595	0.730	0.442	0.9	−0.04

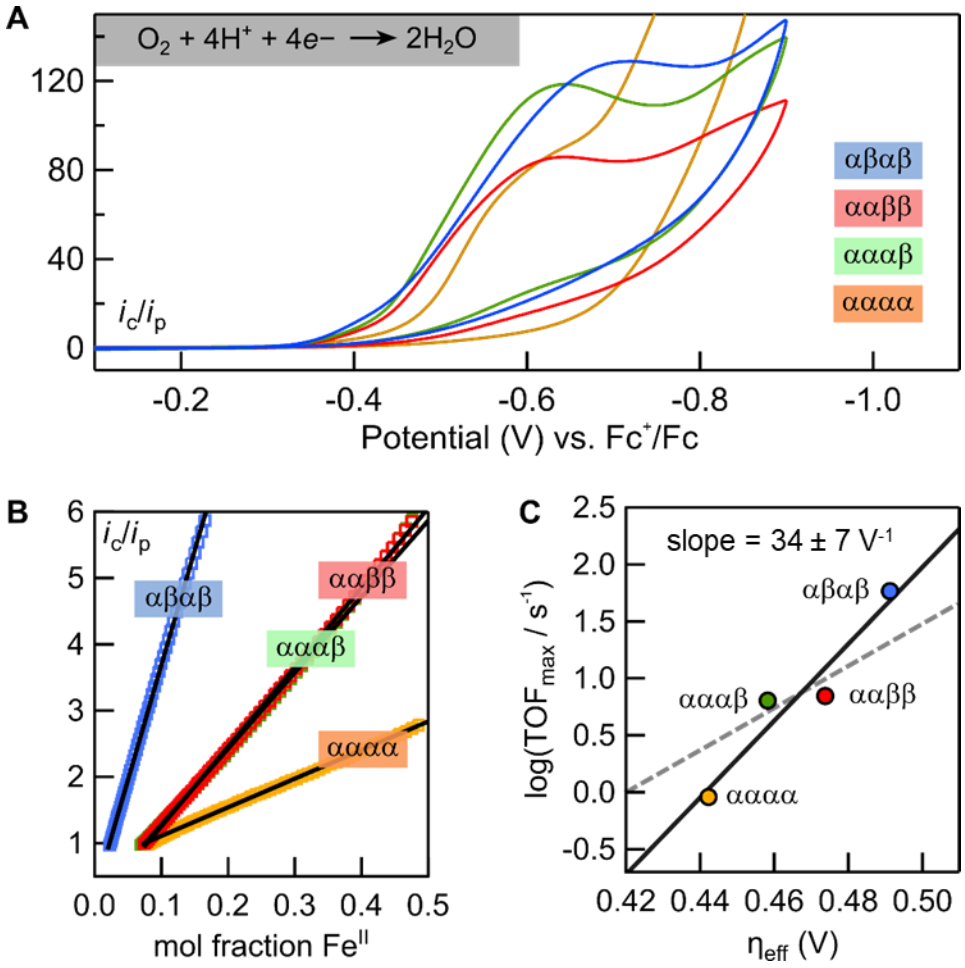

Figure 6.1. Electrochemical O_2 reduction by Fe(*o*-TMA) atropisomers. (**A**) Cyclic voltammograms for O_2 reduction by the Fe(*o*-TMA) isomers. (**B**) FOWA plots, showing fits to the linear region (see SI). (**C**) Plot of log(TOF_{max}) versus η_{eff} for the data shown in (**A,B**); solid line is linear fit, dashed line shows fit using a slope of 18.5 dec. V^{-1}, for reference (slope from ref. 17). All data collected using O_2-saturated (1 atm) solutions of MeCN containing 0.1 M acetic acid buffer, H_2O, and [*n*-Bu_4N][PF_6].

The four isomers of Fe(*o*-TMA) are all competent O_2 reduction electrocatalysts under these conditions, with TOF_{max} that range from 1−50 s^{-1} and η_{eff} from 0.44−0.49 V. The αβαβ isomer is the fastest of the series and the αααα isomer is the slowest, with the ααββ and αααβ isomers having TOF_{max} that are in between. As shown in **Figure 6.1C**, there is a linear relationship between log(TOF_{max}) and $E_{1/2}(Fe^{III}/Fe^{II})$—and thus η_{eff}—with a slope of 34 ± 7 dec. V^{-1}.

Linear relationships between log(TOF_{max}) and η_{eff} are powerful tools for understanding and interpreting complex, multi-proton, multi-electron processes. Such “scaling relationships” have been thoroughly studied for O_2 reduction by soluble iron porphyrin complexes because the mechanism is well known in nonaqueous solvents. As shown in Chapter 2 for iron

tetraphenylporphyrin and in Chapter 3 for the atropisomeric mixture of Fe(*o*-TMA) catalysts, catalysis involves *i*) initial reduction of the ferric porphyrin ($[Fe^{III}(P)]^+$) to the ferrous form ($Fe^{II}(P)$), *ii*) rapid O_2-binding to form the corresponding ferric superoxide complex ($Fe^{III}(P)(O_2^{\bullet -})$) and *iii*) rate-limiting proton transfer by exogenous acid to form $[Fe^{III}(P)(O_2H^{\bullet})]^+$. An additional $3e^-/3H^+$ are added in rapid follow-up steps to complete turnover (see references 14 and 23 for complete details).

For O_2 reduction by substituted iron tetra-arylporphyrin catalysts, a relationship between $\log(TOF_{max})$ and $E_{1/2}$ has already been reported with a slope of 18.5 decades per volt.[17] While the slope of this relationship is empirical, it can be quantitatively derived from the dependence of O_2 binding and the barrier for proton transfer on the catalyst $E_{1/2}(Fe^{III}/Fe^{II})$. Catalysts with more negative $E_{1/2}(Fe^{III}/Fe^{II})$ values are more nucleophilic, which results in stronger O_2 binding and a more basic iron superoxide intermediate.

What is striking about the $\log(TOF_{max})$ vs. $E_{1/2}$ relationship for the Fe(*o*-TMA) atropisomers is that it is almost 2× *steeper* than the previously reported slope for differently substituted catalysts. Given that the rate law is unchanged (see Chapter 3 and ref. [14]), the steeper slope implicates a more sensitive relationship between $E_{1/2}$, the free energy of O_2-binding ($\Delta G_{O2} \propto pK_{O2}$), and the distal O-atom basicity of the corresponding ferric superoxide complexes ($pK_a[O_d]$). Dioxygen binding was not measured in this work, but previous computational data on the rotamers of bound O_2 (see Chapter 4) suggests that there is little-to-no stabilization effect of bound superoxide by the charged *o*-$[N(CH_3)_3]^+$ groups, at least for the $\alpha\beta\alpha\beta$ isomer. While differences in dioxygen binding to the different atropisomers cannot be ruled out, the barrier for proton transfer—which involves the formation of an *anionic* acetate molecule next to the polycationic porphyrin—is more likely to be affected by small changes in electron distribution on the iron superoxide complex. A detailed study on these effects is left to future members of the Mayer group.

Simply identifying the *existence* of a linear relationship between $\log(TOF_{max})$ and $E_{1/2}(Fe^{III}/Fe^{II})$ is valuable, because it indicates that catalytic efficacy of the Fe(*o*-TMA) atropisomers is—at least in part—due to differences in the atropisomer $E_{1/2}(Fe^{III}/Fe^{II})$ values. The steepness of the $\log(TOF_{max})/E_{1/2}$ slope is also important, though the nature of the corresponding $pK_{O2}/E_{1/2}$ and $pK_a[O_d]/E_{1/2}$ relationships are currently unknown.

6.2.1.2 Acetate binding

In MeCN containing only supporting electrolyte, the Fe(*o*-TMA) atropisomers have $E_{1/2}(Fe^{III}/Fe^{II})$ values that range between 0.130 and 0.143 V vs. Fc^+/Fc. In solutions containing 0.1 M buffered AcOH, acetate binding causes the $E_{1/2}(Fe^{III}/Fe^{II})$ values to shift to more negative potentials, between −0.595 and −0.644 V vs. Fc^+/Fc (**Table 6.1**).

The shift in $E_{1/2}(Fe^{III}/Fe^{II})$ that accompanies acetate binding ($\Delta E_{1/2}$) reflects the difference in acetate binding constants to the iron(III) and iron(II) oxidation states—$K_{AcO}(Fe^{III})$ and $K_{AcO}(Fe^{II})$—for each of the respective atropisomers.[15] This is a result of Hess' Law, which relates the binding constants and $E_{1/2}(Fe^{III}/Fe^{II})$ values by their respective difference in free energies (**eq 6.1** and Chapter 4.3.2). The large, negative shift in $E_{1/2}(Fe^{III}/Fe^{II})$ indicates that $K_{AcO}(Fe^{III}) >> K_{AcO}(Fe^{II})$ for all four isomers, by 12 or 13 orders of magnitude. It is important to emphasize that this analysis gives the *ratio* of the $K_{AcO}(Fe^{III})$ and $K_{AcO}(Fe^{II})$ for each isomer, but it cannot be used to obtain either binding constant directly.

$$E_{1/2} - E_{1/2}(\mathrm{AcO}) = (0.059\ \mathrm{mV})\left\{\log(K_{\mathrm{AcO}}(\mathrm{Fe^{III}})) - \log(K_{\mathrm{AcO}}(\mathrm{Fe^{II}}))\right\} \qquad \text{(eq 6.1)}$$

The changes in $E_{1/2}$ upon acetate binding ($\Delta E_{1/2}$) are significantly different for the four atropisomers, over a range of 71 mV (Table 1). Thus the ratio of $K_{AcO}(Fe^{III})$ and $K_{AcO}(Fe^{II})$ varies between the atropisomers, by a factor of 16. This is the primary origin of the unique $E_{1/2}(Fe^{III}/Fe^{II})$ values under electrocatalytic conditions. The reason that the $\alpha\beta\alpha\beta$ isomer has the most negative $E_{1/2}(Fe^{III}/Fe^{II})$ is because the difference between $K_{AcO}(Fe^{III})$ and $K_{AcO}(Fe^{II})$ is largest for this atropisomer. Likewise, the $\alpha\alpha\alpha\alpha$ isomer has the most positive $E_{1/2}(Fe^{III}/Fe^{II})$ because the difference in binding constants to Fe^{III} and Fe^{II} is smallest (i.e. they are most similar).

To better understand these differences, acetate binding was measured to both the ferric and ferrous forms of the Fe(*o*-TMA) atropisomers. The ferrous binding constants $K_{AcO}(Fe^{II})$ were measured by UV-visible spectroscopy. The addition of *n*-tetrabutylammonium acetate, [*n*-Bu_4N][AcO], to solutions of the $[Fe^{II}(o\text{-TMA})]^{4+}$ isomers results in a color change and the formation of a new, green species (**Figure E6-Figure E9**). The product of this reaction has already been reported for the $\alpha\beta\alpha\beta$ isomer as the 1:1 acetate-to-iron complex, $[Fe^{II}(o\text{-TMA})(AcO)]^{3+}$.[15] The optical spectra for the acetate-bound and acetate-free complexes were not affected by the identity of the

atropisomer, respectively, and so the acetate-to-iron stoichiometry was also assumed to be 1:1 for the other isomers (**Figure E10**-**Figure E11**).

$$K_{\mathrm{AcO}}(\mathrm{M}^{-1}) = \frac{\left[[\mathrm{Fe^{II}(P)(AcO)}]^{n-1}\right]}{\left[[\mathrm{Fe^{II}(P)}]^{n}\right]\left[\mathrm{AcO^-}\right]} \qquad \text{(eq 6.2)}$$

Equilibrium constants for acetate binding to each $[Fe^{II}(o\text{-TMA})]^{4+}$ atropisomer (**eq 6.2**) were measured by variable temperature UV-vis. For each isomer, a solution containing ~35 μM $[Fe^{II}(o\text{-TMA})]^{4+}$, 0.1 mM [*n*-$Bu_4N$][AcO], and 0.1 M [*n*-$Bu_4N$][$PF_6$] was equilibrated at various temperature between −40 °C and 40 °C with regular spectra being collected (**Figure E12**-**Figure E15**). The UV-vis spectra were fit to linear combinations of the genuine $[Fe^{II}(o\text{-TMA})]^{4+}$ and $[Fe^{II}(o\text{-TMA})(AcO)]^{3+}$ spectra, following the fitting methods reported in reference 18. The 0.1 M supporting electrolyte was added to match electrochemical conditions and to minimize differences in ionic strength between samples. A van ′t Hoff analysis was used to probe the enthalpy and entropy components of acetate binding to the ferrous complexes (**Figure 6.2**). The ferric binding constants ($K_{AcO}(Fe^{III})$) were determined using **eq 6.1** with the experimental $K_{AcO}(Fe^{II})$ and $\Delta E_{1/2}$ values (**Table 6.1**). The pertinent binding constants, free energies, enthalpies, and entropies are summarized in **Table 6.2**. All other binding constants are reported in Appendix E (**Table E1**).

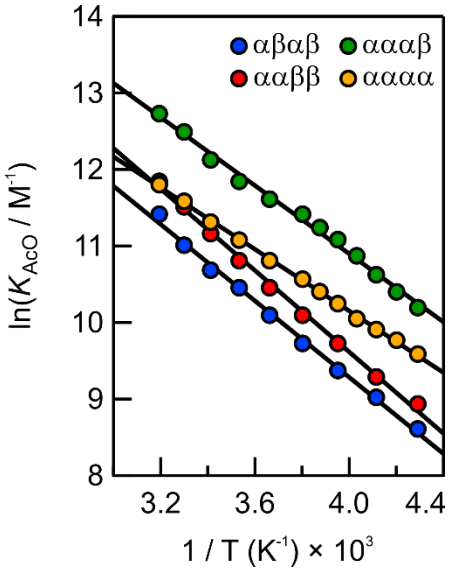

Figure 6.2. van ′t Hoff plots for acetate binding to the $[Fe^{II}(o\text{-TMA})]^{4+}$ isomers in MeCN containing 0.1 M [*n*-Bu_4N][PF_6]. Thermochemical parameters summarized in **Table 6.2**.

Table 6.2. Thermochemical parameters for acetate binding to Fe(*o*-TMA) atropisomers [a]

Reaction	$\Delta H°$ (kcal mol^{-1})	$\Delta S°$ (cal mol^{-1} K^{-1})	ΔG (kcal mol^{-1}) [b]	log(K_{AcO}/M^{-1})
$[Fe^{II}(o\text{-TMA})]^{4+} + AcO^- \rightleftharpoons [Fe^{II}(o\text{-TMA})(AcO)]^{3+}$				
αβαβ	5.0 ± 0.1	38 ± 2	−6.3 ± 0.3 [c]	4.7 ± 0.2
ααββ	5.3 ± 0.1	40 ± 2	−6.5 ± 0.3	4.8 ± 0.2
αααβ	4.4 ± 0.1	39 ± 2	−7.1 ± 0.3	5.3 ± 0.2
αααα	4.0 ± 0.1	36 ± 2	−6.6 ± 0.3	4.9 ± 0.2
$[Fe^{III}(o\text{-TMA})]^{5+} + AcO^- \rightleftharpoons [Fe^{III}(o\text{-TMA})(AcO)]^{4+}$			ΔG (kcal mol^{-1}) [c]	log(K_{AcO}/M^{-1})
αβαβ	−	−	−24.3 ± 0.3	18.0 ± 0.2
ααββ	−	−	−24.1 ± 0.3	17.8 ± 0.2
αααβ	−	−	−24.1 ± 0.3	17.9 ± 0.2
αααα	−	−	−23.3 ± 0.3	17.3 ± 0.2

[a] MeCN solutions containing 0.1 M [*n*-Bu_4N][PF_6]. [b] At 20 °C, the temperature at which the electrochemistry was performed, calculated using $\Delta H°$ and $\Delta S°$. [c] The value reported in reference 18 is −6.5 kcal mol^{-1}, which was determined using a single temperature measurement. The two values are within error of one another. [d] Estimated using eq 1 and ΔG values for acetate binding to $[Fe^{II}(o\text{-TMA})]^{4+}$ at 20 °C.

The free energies for acetate binding to $[Fe^{II}(o\text{-TMA}]^{4+}$ are large at 20 °C, with $\Delta G(Fe^{II})$ = −6.3 to −7.1 kcal mol^{-1}. The corresponding energies for acetate binding to $[Fe^{III}(o\text{-TMA})]^{5+}$ are even larger, $\Delta G(Fe^{III})$ = −24.3 to −23.3 kcal mol^{-1}. A similar result was previously reported for the αβαβ isomer of Fe(*o*-TMA) in *n*-butyronitrile, where the increased binding constants to the ferric porphyrin were thought to result from an increase in overall charge on the pentacationic $[Fe^{III}(o\text{-TMA})]^{5+}$ complex.[15]

There is no clear relationship between the free energies of acetate binding and the orientations of the charges in the different atropisomers, in either the ferrous or ferric forms. The $\Delta G(Fe^{II})$ values trend slightly more negative with increasing charge density on a given face, but the $\Delta G(Fe^{III})$ values do not. The αααα isomer breaks both these trends. For instance, acetate binding to the ferrous αααα isomer is less favorable than binding to the αααβ form, despite the increased charge density on the α-face. Likewise, acetate binding is weakest to the ferric αααα isomer, moreso than to any of the other atropisomers. While the origin of these deviations are unknown, it is possible that the highly-charged α-face may be competitively binding OTf^- or PF_6^- anions. This hypothesis is consistent with crystallographic data reported in reference 18 (Chapter 5, above), which showed a triflate ligand bound to the αααα atropisomer in both ferric and ferrous solids. While the other ferric atropisomer structures showed a bound triflate, only the αααα had a bound

anion in the ferrous form. In both the Fe^{III} and Fe^{II} oxidation states, the triflate ligand was bound to the more crowded, more cationic α-face. Assuming a similar interaction exists in the solution state, the enhanced interaction with supporting anions may decrease the favorability of acetate binding measured in this work.

In all cases, the van ′t Hoff parameters reveal that the free energies of acetate binding to the ferrous forms are dominated by large, positive entropy terms (average $\Delta S°(Fe^{II}) = 38 \pm 2$), while the enthalpies of binding are unfavorable. The large and positive entropy terms were initially surprising, especially given that the forward equilibrium is bimolecular. However, these data are consistent with the decrease in the *i*) number of charged species and *ii*) overall charge of the metalloporphyrin complex upon ligand binding, both of which necessitate solvent/electrolyte reorganization.

These thermochemical data indicate that the *orientation* of the *o*-$[N(CH_3)_3]^+$ groups does not affect $\Delta S°(Fe^{II})$ and only subtly affects $\Delta H°(Fe^{II})$ for acetate binding. Rather, the *net* change in charge upon ligand binding is far more important than the through-space position of the charges. This is an important result because these thermochemical parameters control the favorability of acetate binding, the $E_{1/2}(Fe^{III}/Fe^{II})$ values, and ultimately the rate and overpotential of the electrocatalysis.

6.2.1.3 ORR summary

All four atropisomers of Fe(*o*-TMA) are highly competent, molecular catalysts for O_2 reduction in MeCN containing buffered acetic acid. The most important factor controlling both TOF_{max} and η_{eff} is the catalyst $E_{1/2}(Fe^{III}/Fe^{II})$ under electrocatalytic conditions. The slope of the $\log(TOF_{max})/E_{1/2}$ relationship for the Fe(*o*-TMA) atropisomers is nearly 2× steeper than the $E_{1/2}$ relationship previously reported for a series of substituted iron tetra-arylporphyrin catalysts. The steeper slope indicates a more sensitive relationship between the catalyst $E_{1/2}(Fe^{III}/Fe^{II})$, the dioxygen binding constant, and the basicity of the corresponding superoxide intermediates. From electrochemical data and optical van ‘t Hoff plots, the $E_{1/2}(Fe^{III}/Fe^{II})$ values under catalytic conditions were shown to depend on the *difference* in acetate binding thermodynamics to the ferric and ferrous forms of Fe(*o*-TMA) and *not* the acetate binding constant to the active, ferrous form of

the catalyst. For instance, acetate binding is least favorable to the ferrous αβαβ isomer, yet the same isomer has the most negative $E_{1/2}(Fe^{III}/Fe^{II})$ and fastest TOF_{max}. Though there are some small enthalpic differences between the isomers, the acetate binding constants are similar in both the ferric and ferrous forms, respectively. A large, positive entropy term dominates the free energy of acetate binding, which originates from the overall change in charge that accompanies ligand binding. Given that acetate binding is relatively independent of *o*-$[N(CH_3)_3]^+$ orientation, the strong log(TOF)/$E_{1/2}$ dependence suggests that the highly charged porphyrin ligand amplifies the effect of minute differences in metal center nucleophilicity that result from acetate binding.

6.2.2 CO_2 reduction

6.2.2.1 Catalytic rates for the different atropisomers

Fe(*o*-TMA), as a mixture of the four atropisomers, is among the leading molecular catalysts for CO_2 electroreduction.[13,18] With the four isolated isomers in hand, we set out to determine their relative activity and the effects of the positioned cations. As an added benefit, the results provide an indirect test of the hypothesis by Savéant et al. that the success of this catalyst is due, at least in part, to the stabilization of a high energy $Fe^I(CO_2^{\bullet-})$ intermediate by the well-positioned *o*-$[N(CH_3)_3]^+$ groups in the αβαβ atropisomer. Computational studies support stabilization of the $CO_2^{\bullet-}$ ligand when its partially anionic oxygens are near the cations of the αβαβ isomer;[15] however, there is no direct experimental or computational evidence connecting this proposed stabilization with improved catalysis.

A single, bulk solution was first prepared to match the electrochemical conditions reported in ref. 13 (DMF containing 0.1 M [*n*-Bu_4N][PF_6], 0.1 M H_2O, and 3.0 M PhOH; perhaps better described as electrolyte and water in a mixed solvent of 0.76 mole fraction DMF and 0.24 mole fraction phenol). This single solution was divided into four containers before dissolving each of the respective atropisomers. CVs were collected for each of the four solutions under both argon and 1 atm CO_2 (**Figure E17-Figure E18)**.

Under Ar, the formal iron(I/0) redox couple is almost unaffected by the atropisomer identity, with an average $E_{1/2}(Fe^I/Fe^0)$ = −1.695 ± 0.006 V (**Table 6.3**; called the "formal" Fe^I/Fe^0 couple because the possible redox non-innocence of the porphyrin ligand makes the assignment of low

iron oxidation states complicated). Under 1 atm of CO_2, a large, irreversible current appeared in place of the reversible iron(I/0) couple for each solution. The irreversible, cathodic current is indicative of catalysis and is consistent with data previously reported by the Savéant group.[13] A loss of reversibility in the iron(II/I) redox feature and formation of a new anodic peak at more negative potentials indicates that CO is a significant product formed during turnover (**Figure 6.3**).[24-25]

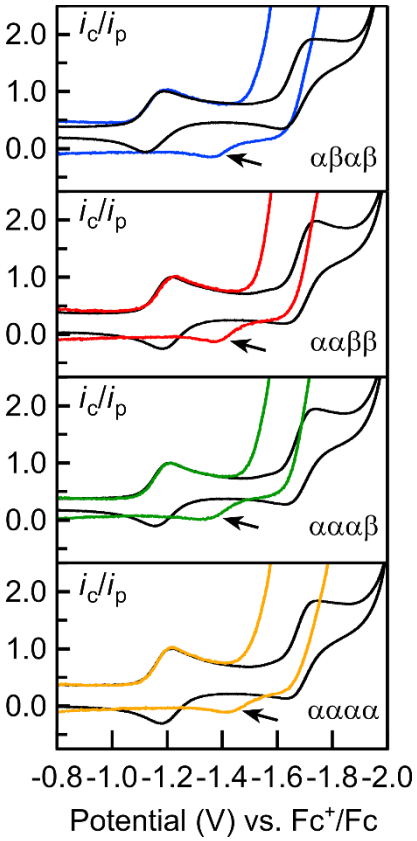

Figure 6.3. Cyclic voltammograms of Fe(*o*-TMA) atropisomers under 1.0 atm Ar (black traces) and CO_2 (colored traces), showing region containing Fe^{II}/Fe^{I} and Fe^{I}/Fe^{0} redox features. The arrow in each panel implicates the formation of carbon monoxide as the product, which reacts with Fe^{II} generated during the anodic sweep.[24-25] All data were collected at 0.1 V s^{-1} in DMF containing 3.0 M PhOH, 0.1 M H_2O, and 0.1 M [*n*-Bu_4N][PF_6]. Data shown are normalized to the non-catalytic peak current of the Fe^{II}/Fe^{I} redox couple, which is constant under both Ar and CO_2.

Following the methodology reported by Savéant et al, the TOF_{max} values for CO_2-to-CO reduction were derived from currents obtained at fast scan rates.[13,24-26] At low scan rates (0.1 V s^{-1}), the current-potential responses were peak-like, indicating the presence of confounding factors such as substrate depletion, product inhibition, or other phenomena. Raising the scan rate decreased the significance of these unwanted side processes and lead to more canonical S-shaped

voltammograms. At fast scan rates (>100 V s^{-1}), the plateau currents saturated and ultimately reached scan rate-independent values (i_{pl}). Under these limiting conditions, **eq 6.3** can be used to derive TOF_{max} using only n (the $\#e^-$ required during turnover; n = 2 for $CO_2 + 2H^+ + 2e^- \rightarrow CO + H_2O$), v (0.1 V s^{-1}), and the constants R, T, and F.[13]

$$\frac{i_{pl}}{i_p} = 2.24\sqrt{\frac{n\mathrm{TOF}_{max}RT}{vF}} \qquad \text{(eq 6.3)}$$

All four atropisomers reach large, current-limiting plateaus at fast scan rates (**Figure 6.4**). While the normalized plateau currents (i_{pl}/i_p) are different by inspection, the corresponding log(TOF_{max}) values are quite similar. The log(TOF_{max}) values range from 4.9 ± 0.2 for the αβαβ atropisomer to 5.5 ± 0.2 for the αααα, near the estimated upper-limit [log(TOF_{max}) < 6] previously reported in reference 13, and are summarized in **Table 6.3**.

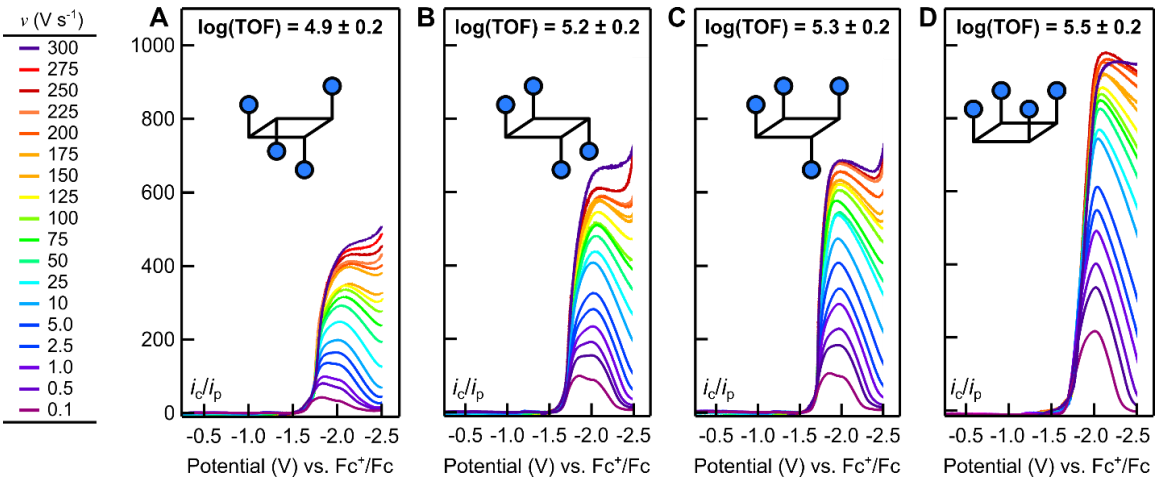

Figure 6.4. Linear sweep voltammograms for CO_2 reduction at various scan rates, showing an approach to the canonical S-shaped current-potential response for the (**A**) αβαβ, (**B**) ααββ, (**C**) αααβ, and (**D**) αααα isomers of Fe(*o*-TMA). Data was corrected for internal resistance and capacitive currents before being normalized to i_p (collected at 0.1 V s^{-1}). See Appendix E for raw data and complete details.

Table 6.3. Catalyst system properties for CO_2 reduction by Fe(*o*-TMA) atropisomers.[a]

Atropisomer	$E_{1/2}(Fe^{II/I})^a$	$E_{1/2}(Fe^{I/0})^b$	$E°_{Q'/B}$ (V)	η_{eff} (V)[c]	TOF_{max} (s^{-1})	log(TOF_{max}/s^{-1})
αβαβ	−1.157	−1.691	−1.82	0.39	7.9×10^4	4.9 ± 0.2
ααββ	−1.199	−1.705	−1.82	0.39	1.7×10^5	5.2 ± 0.2
αααβ	−1.183	−1.693	−1.80	0.37	2.0×10^5	5.3 ± 0.2
αααα	−1.196	−1.694	−1.90	0.48	3.5×10^5	5.5 ± 0.2

[a] In DMF solutions containing 3.0 M PhOH, 0.1 M H_2O, 0.1 M [*n*-Bu_4N][PF_6] and 1 atm CO_2. [b] Same conditions as a except without CO_2. [c] Values assumed constant equilibrium potential for CO_2/CO reduction (E_{CO2RR} = −1.43 V vs. Fc^+/Fc), see text and reference 13.

These results are impactful for two reasons. First, all four isomers are exceptional catalysts for CO_2 reduction and achieve some of the fastest rates in the homogeneous electrochemistry literature. Second, and perhaps more striking, the maximum difference in rates for the four electrostatic isomers is only a factor of 5. The similarity in rates is surprising and shows that the orientation of the *o*-$[N(CH_3)_3]^+$ groups does *not* substantially affect the reaction kinetics. Rather, *only the existence of the charged groups in the porphyrin design is important*. This is in spite of the fact that the $\alpha\alpha\alpha\alpha$ isomer should generate a significant electric field along its C_4 axis, while the D_{2d} $\alpha\beta\alpha\beta$ isomer has higher symmetry and no net dipole moment.

These results do not support any large kinetic benefit of local charge positioning during catalysis. In particular, the $\alpha\alpha\beta\beta$ isomer being a factor of two faster than the $\alpha\beta\alpha\beta$ does not support the suggestion that a $CO_2^{\bullet-}$ ligand is *specifically* stabilized by cations on opposite sides of the porphyrin. This conclusion does not preclude the possibility that the *o*-$[N(CH_3)_3]^+$ groups improve the thermodynamics of the resting state or an unfavorable transition state (e.g. CO_2 binding),[13,15] only that such changes have little effect on the overall kinetic profile or are balanced by unfavorable changes, such as the barrier for reaction from the stabilized intermediate. Such behavior is often rationalized using the Sabatier Principle, for which the reaction profile of a complex, multi-step sequence often involves balancing favorable and unfavorable thermodynamic changes to maximize reaction rates and minimize thermodynamic sinks.[27-28]

The TOF_{max} values and linear sweep voltammograms collected at fast scan rates are comparable to those reported by Savéant et al.[13] For the atropisomers reported in this work, the determined TOF_{max} values are between $10^{4.9}$ s^{-1} and $10^{5.5}$ s^{-1}. These values are not as fast as the 10^6 s^{-1} upper-limit estimate reported by Savéant et al; however, the reported rates are remarkably close. The similarity of the atropisomer TOF_{max} values makes it challenging to determine the ratio of atropisomers in the reported Savéant data. While the exact composition of the catalyst in reference [13] is unknown, the unusual broadness in the reported voltammograms under argon and the fast linear sweep voltammograms indicate that some composite mixture of catalysts is likely present. As shown in our recent work, ^{1}H NMR spectroscopy is necessary for determining the exact nature of the reported catalyst.[18]

6.2.2.2 *Mechanistic insights*

The mechanism of CO_2 reduction by Fe(*o*-TMA) is complex. At low phenol concentrations, 10-200 mM PhOH in DMF with 1 atm CO_2, the catalytic wave for the αβαβ isomer is observed *only at ~0.3 V more negative potentials than* $E_{1/2}(Fe^{I}/Fe^{0})$ (**Figure 6.5A**, **Figure E27-Figure E29**). Under these conditions, the potential and reversibility of the iron(I/0) couple were almost completely unaffected. The loss of reversibility about the iron(II/I) couple indicates that turnover sill results in CO, and background proton reduction occurs at even more negative potentials (**Figure E19**).

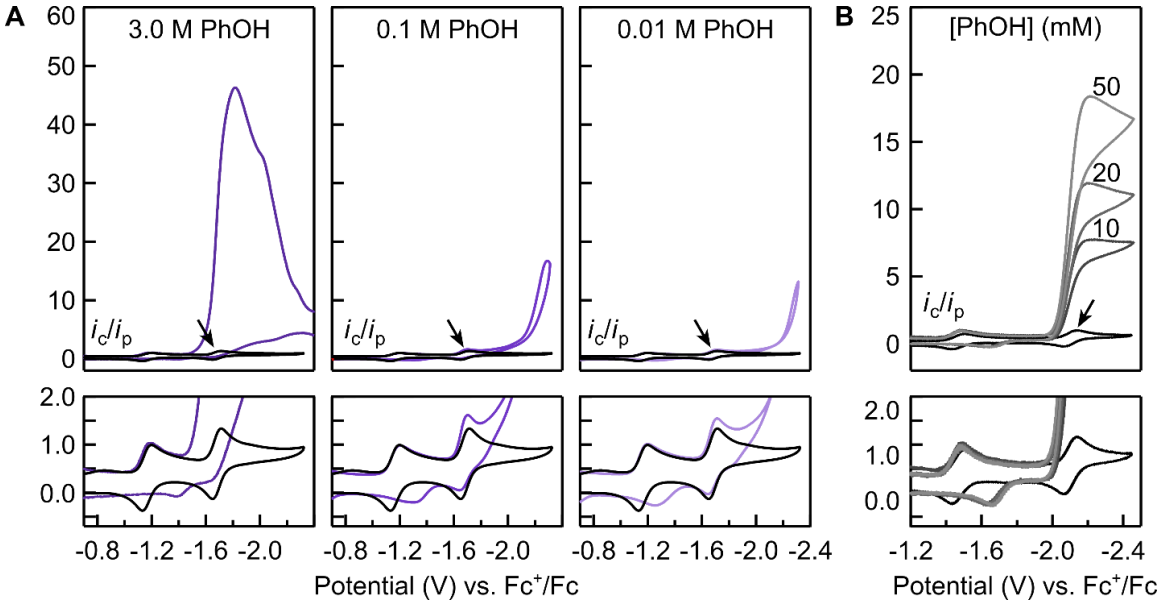

Figure 6.5. Cyclic voltammograms of CO_2 reduction at three different phenol concentrations by (**A**) αβαβ Fe(*o*-TMA) and (**B**) Fe(TPP). The top panels show the irreversible, catalytic currents with arrows that indicate the Fe^{I}/Fe^{0} redox couple; the bottom panels have an expanded current scale to show the catalyst couples and the base of the catalytic wave. All currents were normalized to i_p values of the Fe^{II}/Fe^{I} couple. All data collected at 0.1 V s^{-1} in DMF containing 0.1 M [*n*-Bu_4N][PF_6], 0.1 M [H_2O], and 1.0 atm CO_2.

With increasing [PhOH], the reversibility of the iron(I/0) couple decreased, the irreversible current rose steeply, and the onset of catalysis moved to substantially more positive potentials. Above 1.0 M PhOH, the catalytic wave ultimately obscured $E_{1/2}(Fe^{I}/Fe^{0})$, **Figure 6.5A**. The same behavior was observed for the ααββ, αααβ, and αααα isomers. This behavior is unusual and contrasts the more common current-potential responses observed using iron tetraphenylporphyrin, Fe(TPP) and other neutral iron porphyrin catalysts (**Figure 6.5B**).[24-26] The typical behavior is characterized by the onset of catalysis at the potential of a catalyst redox couple, in this case at the

$E_{1/2}$ for Fe^{I}/Fe^{0}. In addition, the potential of the catalytic wave in a prototypical CV response does not move significantly as substrate concentrations are added.

Taken together, the CV behavior for the Fe(*o*-TMA) atropisomers rules out the typical *E*C′ mechanism common to iron porphyrins that catalyze CO_2 reduction, where *E* is the Fe^{I}/Fe^{0} reduction and C′ is a composite set of pre-equilibria and turnover limiting steps.[24] Rather, it is more consistent with an E_1CE_2C' reaction (where $E_1 > E_2$), **Scheme 6.2**. In this mechanism, E_1 is an initial reduction event, C is some chemical step (e.g. a pre-equilibrium or series of pre-equilibria), E_2 is the reduction of the product formed in-situ following C, and C′ is the turnover limiting step (or series of steps). A version of this mechanism has been previously reported for CO_2 reduction by iron *o*,*o*-dihydroxyphenylporphyrin, for which E_1 corresponded to $E_{1/2}(Fe^{I}/Fe^{0})$, C represented pre-equilibrium CO_2 binding and protonation by PhOH, and E_2 was proposed to be coupled to C′ in a single, concerted electron transfer, proton transfer, and C-O bond breaking event.[24,29]

Scheme 6.2. Generalized electrochemical mechanism and effective overpotential definitions for an *E*C′ and E_1CE_2C' reaction, where $E_1 > E_2$.

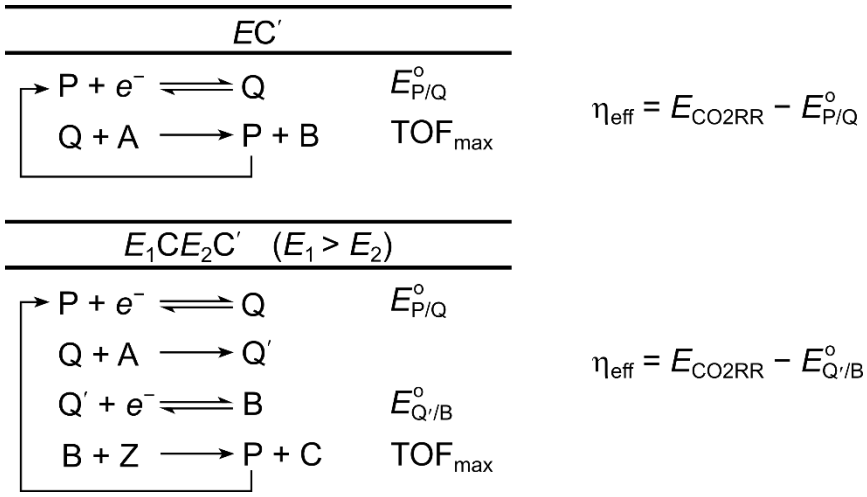

Identifying an E_1CE_2C' response has key mechanistic implications. Perhaps most significant is that catalysis does not occur at the Fe^{I}/Fe^{0} couple (P/Q, in **Scheme 6.2**). Rather, turnover only occurs after reducing a complex that is generated in-situ from the product of Fe^{0} and some solution species (Q′/B, in **Scheme 6.2**). The data do not give much insight into the chemical natures of the active catalysts Q′ and B, but some general conclusions can be made. In the absence

of PhOH, the Fe^{I}/Fe^{0} couple does not change under 1 atm CO_2. Thus, CO_2 binding to Fe^{0}—if occurring—is reversible and unfavorable at 20 °C. The change in catalytic onset potential with increasing concentrations of phenol suggests that E_2 (Q′/B) is either *i*) coupled to the rate-determining chemical step, which must involve PhOH, or *ii*) dependent on the concentration of PhOH/[PhO^-] in the reaction diffusion layer, as would be the case for [PhO^-] binding to either species Q′ or B. The former option is unlikely, given that the shift in the catalytic onset potential is >0.5 V from 0.1 to 3.0 M PhOH (**Figure 6.5A**) [for a reaction with a first order dependence on PhOH, a 30× increase in substrate would result in a shift of only ~0.09 V]. The latter option cannot be ruled out with the given data. The need for very large concentrations of phenol and the high propensity of Fe(*o*-TMA) to bind anionic ligands leads us to speculate that the reduced, active catalyst Q′/B might bind trace phenoxide under these highly non-standard conditions. Similar parallelisms occur for O_2 reduction catalyzed by Fe(*o*-TMA) in acetate buffer, for which only the acetate-bound form of the Fe^{II} catalyst is active. Regardless of specific mechanistic pathway, the clear dependence of E_2 on [PhOH] makes estimating the effective overpotential troublesome, discussed below.

6.2.2.3 Implications about the overpotential for CO_2 reduction

For molecular electrocatalytic processes, the effective overpotential is usually defined as the difference between the equilibrium potential for the catalytic process under the reaction conditions (E_{CO2RR}) and the half-wave potential of the catalytic wave ($E_{cat/2}$). For standard *EC′* electrocatalytic processes, such as in **Figure 6.5B**, the $E_{cat/2}$ occurs at the catalyst reduction potential ($E_{1/2}$), in this case the $E_{1/2}(Fe^{I}/Fe^{0})$. For an E_1CE_2C' reaction, however, $E_{cat/2}$ occurs at the E_2 potential, $\eta_{eff} = E_{CO2RR} - E_2$, or more specifically the standard potential of $E°_{Q'/B}$ (**Scheme 6.2**).[30] We confirmed that $E_{cat/2}$ occurs at $E°_{Q'/B}$ following the methodology of Costentin and Savéant,[30] simulating the plateau-shaped voltammograms at 3.0 M PhOH and using the TOF_{max} values in **Table 6.3**. For these simulations, the potential at which half the plateau current is obtained ($E_{pl/2}$) is equal to $E°_{Q'/B}$ and thus E_2 (see Appendix E, including **Figure E26**). The four atropisomers have $E°_{Q'/B}$ values that are very close to each other, within the error of the estimation (average $E°_{Q'/B}$ = 1.84 ± 0.04 V, **Table 6.3**). The value of E_{CO2RR} has been estimated under these conditions as −1.43

V vs. Fc^+/Fc.[13] This estimated value uses the unusual standard state of 1 M CO_2 and using pK_a values and the Henry's law constant for CO_2 in DMF for these highly non-standard conditions of 0.24 mol fraction PhOH, 0.76 mol fraction DMF, and 0.1 M ionic strength.

The values for η_{eff} were estimated for the set of atropisomers and are reported in **Table 6.3**. The range in these estimates is small, with the $\alpha\beta\alpha\beta$, $\alpha\alpha\beta\beta$ and $\alpha\alpha\alpha\beta$ having $\eta_{eff} \approx 0.39$, 0.39 and 0.37 V, and the $\alpha\alpha\alpha\alpha$ being higher, ≈ 0.48 V. More accurate values could not be obtained from the voltammetry due to the method of fitting (see Appendix E). The similarity in η_{eff} values was expected because the atropisomers have nearly the same $E°_{Q'/B}$ (i.e. E_2) values and were studied under the same conditions. The average η_{eff} for CO_2 reduction by the Fe(*o*-TMA) isomers is $\eta_{eff} \approx$ 0.41 V, at least 0.19 V larger than the value reported by Savéant et al.[13] Even with this correction, the TOF_{max} and overpotential metrics for Fe(*o*-TMA) are still among the best molecular catalysts for CO_2 reduction, similar to the metrics reported by these researchers for the iron *o*,*o*-dihydroxyphenylporphyrin electrocatalyst.[31]

6.2.2.4 CO_2 reduction conclusions

Three important conclusions are evident from these CO_2 studies:

i. The four atropisomers of Fe(*o*-TMA) are all competent molecular catalysts for CO_2 electroreduction and are largely indistinguishable. The largest difference in TOF_{max} is only a factor of 5, and the estimated overpotentials are all within 0.1 V. Thus, *the orientations of the four, cationic o-$[N(CH_3)_3]^+$ groups do not affect the effectiveness of the catalysts towards CO_2 reduction*. This argues against a specific cation geometry for stabilizing a particular intermediate. The cationic charges are certainly important, as these catalysts have exceptional metrics for the CO_2RR under these peculiar conditions (24 mol% phenol in the solution). The impact of the *o*-$[N(CH_3)_3]^+$ groups seems to come from the total charge on the catalyst, not from the distribution of charges.

ii. The voltammograms of CO_2 reduction by Fe(*o*-TMA) do not support an *EC′* mechanism; rather, they are more consistent with an E_1CE_2C' mechanism. The voltammograms are perhaps more evident in the current work using the individual

atropisomers rather than the prior studies with a mixture. The E_1CE_2C' mechanism means that the $[Fe^0(o\text{-TMA})]^{2+}$ species is not involved in the rate-determining step. Rather, turnover is defined by a follow-up reduction and chemical steps. The potential of this further-reduced species is strongly dependent on the concentration of PhOH in solution, suggesting some relevant pre-equilibrium between the active catalyst and PhOH/[PhO^-] in solution.

iii. The conclusion of an E_1CE_2C' mechanism also implies a revision of the estimated overpotentials. This is an important topic not addressed in the original literature and affects the reported η_{eff} values. From simulations and sigmoidal S-shaped current-potential responses collected at fast scan rates, we conservatively estimate $\eta_{eff} \approx 0.41$ V under these conditions, which is >0.19 V larger than the overpotentials originally reported.[13]

6.3 Overall Conclusions from ORR and CO_2RR studies

The polycationic Fe(*o*-TMA) system is an exceptional electrocatalyst for the reduction of both O_2 and CO_2, as previously shown using mixtures of the four atropisomeric forms. Using isolated samples of each atropisomer, the studies here show that each is an excellent catalyst. Their catalytic properties vary only modestly with the positioning of the positive charges, from two-on-each-side of the porphyrin ring ($\alpha\beta\alpha\beta$ and $\alpha\alpha\beta\beta$) to one that bears all four charges on the same side ($\alpha\alpha\alpha\alpha$). The ORR catalysis shows the larger variation, with the $\alpha\beta\alpha\beta$ isomer being 64 times faster than the $\alpha\alpha\alpha\alpha$ isomer. For CO_2RR under the conditions reported by Savéant (3M PhOH), the difference between the isomers is less than a factor of 5. These results show that the primary catalytic benefits of the *o*-TMA^{4+} ligand come from its overall charge, and the oriented positioning of those charges is much less important.

The variation in the ORR turnover frequencies closely parallel the $E_{1/2}$ and overpotential values of the atropisomers under catalytic conditions. The $\alpha\beta\alpha\beta$ isomer is the fastest and has an overpotential that is 49 mV larger than the slowest, $\alpha\alpha\alpha\alpha$ isomer. This is qualitatively in-line with prior studies of the ORR that showed correlations between TOF_{max} and η_{eff}.[17,20] For CO_2RR, the

catalytic system with the highest η_{eff} is again the fastest, though this pattern is not monotonic (perhaps because of the small ranges of TOF_{max} and η_{eff}). In CO_2RR, which utilizes much more reduced iron centers, the rate order between the atropisomers is mostly reversed, with the $\alpha\alpha\alpha\alpha$ isomer being the fastest.

The variations in TOF_{max} and η_{eff} in the ORR catalysis results from the different catalyst $E_{1/2}(Fe^{III}/Fe^{II})$ values under catalytic conditions. The $E_{1/2}(Fe^{III}/Fe^{II})$ values of the isomers are different because of relative differences in acetate binding to the ferric and ferrous forms of Fe(*o*-TMA), with larger $K_{AcO}(Fe^{III})$: $K_{AcO}(Fe^{II})$ ratios resulting in more negative $E_{1/2}(Fe^{III}/Fe^{II})$ values. These directly measured binding constants are very different between the ferric and ferrous complexes, but the differences between the atropoisomers are smaller, within a factor of 4 in both series. Thus, again, the positioning of the cationic charges plays a more minor role than the overall charge of the porphyrin ligand.

The CO_2RR cyclic voltammograms for the individual atropisomers shows that the catalysis is more complicated than the *EC′* mechanism previously suggested. Rather, an E_1CE_2C' mechanism is more consistent with the data. The data show the $[Fe^0(o\text{-TMA})]^{2+}$ species, previously thought to be the species that binds CO_2, does not define catalytic turnover. Instead, catalysis requries more negative potentials than is needed to generate that species. The mechanistic re-evaluation also indicates a higher overpotential for the CO_2-to-CO catalysis than was previously reported.

In sum, the excellent catalysis by Fe(*o*-TMA) complexes is due to the high cationic charge from the four trimethylanilium groups that are close to the iron center. However, the relative positions of the cationic charges about the porphyrin ring have a modest or small effect. The charges seem to affect catalysis mostly indirectly, by enhancing ligand binding to change the nature of the catalytic species.

6.4 References

1. Fried, S. D.; Boxer, S. G., Electric Fields and Enzyme Catalysis. *Annu. Rev. Biochem* **2017,** *86* (1), 387-415.
2. Shaik, S.; Mandal, D.; Ramanan, R., Oriented electric fields as future smart reagents in chemistry. *Nat. Chem.* **2016,** *8* (12), 1091-1098.
3. Xiang, L.; Tao, N. J., Organic chemistry: Reactions triggered electrically. *Nature* **2016,** *531* (7592), 38-39.
4. Cammarota, R. C.; Lu, C. C., Tuning Nickel with Lewis Acidic Group 13 Metalloligands for Catalytic Olefin Hydrogenation. *J. Am. Chem. Soc.* **2015,** *137* (39), 12486-9.
5. Chantarojsiri, T.; Reath, A. H.; Yang, J. Y., Cationic Charges Leading to an Inverse Free-Energy Relationship for N-N Bond Formation by Mn(VI) Nitrides. *Angew. Chem. Int. Ed. Engl.* **2018,** *57* (43), 14037-14042.
6. Chantarojsiri, T.; Ziller, J. W.; Yang, J. Y., Incorporation of redox-inactive cations promotes iron catalyzed aerobic C–H oxidation at mild potentials. *Chem. Sci.* **2018,** *9* (9), 2567-2574.
7. Ciampi, S.; Darwish, N.; Aitken, H. M.; Díez-Pérez, I.; Coote, M. L., Harnessing electrostatic catalysis in single molecule, electrochemical and chemical systems: a rapidly growing experimental tool box. *Chem. Soc. Rev.* **2018,** *47* (14), 5146-5164.
8. Kang, K.; Fuller, J., 3rd; Reath, A. H.; Ziller, J. W.; Alexandrova, A. N.; Yang, J. Y., Installation of internal electric fields by non-redox active cations in transition metal complexes. *Chem. Sci.* **2019,** *10* (43), 10135-10142.
9. Margarit, C. G.; Asimow, N. G.; Gonzalez, M. I.; Nocera, D. G., Double Hangman Iron Porphyrin and the Effect of Electrostatic Nonbonding Interactions on Carbon Dioxide Reduction. *J. Phys. Chem. Lett.* **2020,** *11* (5), 1890-1895.
10. Rao, H.; Schmidt, L. C.; Bonin, J.; Robert, M., Visible-light-driven methane formation from CO_2 with a molecular iron catalyst. *Nature* **2017,** *548* (7665), 74-77.
11. Tsui, E. Y.; Tran, R.; Yano, J.; Agapie, T., Redox-inactive metals modulate the reduction potential in heterometallic manganese-oxido clusters. *Nat. Chem.* **2013,** *5* (4), 293-9.
12. Ramirez, B. L.; Lu, C. C., Rare-Earth Supported Nickel Catalysts for Alkyne Semihydrogenation: Chemo- and Regioselectivity Impacted by the Lewis Acidity and Size of the Support. *J. Am. Chem. Soc.* **2020,** *142* (11), 5396-5407.
13. Azcarate, I.; Costentin, C.; Robert, M.; Savéant, J. M., Through-Space Charge Interaction Substituent Effects in Molecular Catalysis Leading to the Design of the Most Efficient Catalyst of CO_2-to-CO Electrochemical Conversion. *J. Am. Chem. Soc.* **2016,** *138* (51), 16639-16644.
14. Martin, D. J.; Mercado, B. Q.; Mayer, J. M., Combining scaling relationships overcomes rate versus overpotential trade-offs in O_2 molecular electrocatalysis. *Sci. Adv.* **2020,** *6* (11), eaaz3318.
15. Martin, D. J.; Johnson, S. I.; Mercado, B. Q.; Raugei, S.; Mayer, J. M., Intramolecular Electrostatic Effects on O_2, CO_2, and Acetate Binding to a Cationic Iron Porphyrin. *Inorg. Chem.* **2020,** *59* (23), 17402-17414.
16. Martin, D. J.; Wise, C. F.; Pegis, M. L.; Mayer, J. M., Developing Scaling Relationships for Molecular Electrocatalysis through Studies of Fe-Porphyrin-Catalyzed O_2 Reduction. *Acc. Chem. Res.* **2020,** *53* (5), 1056-1065.
17. Pegis, M. L.; McKeown, B. A.; Kumar, N.; Lang, K.; Wasylenko, D. J.; Zhang, X. P.; Raugei, S.; Mayer, J. M., Homogenous Electrocatalytic Oxygen Reduction Rates Correlate with Reaction Overpotential in Acidic Organic Solutions. *ACS Cent. Sci.* **2016,** *2* (11), 850-856.
18. Martin, D. J.; Mercado, B. Q.; Mayer, J. M., All Four Atropisomers of Iron(III) and Iron(II) Tetra(*o*-*N*,*N*,*N*-trimethylanilinium)porphyrin. In preparation.
19. Elgrishi, N.; Rountree, K. J.; McCarthy, B. D.; Rountree, E. S.; Eisenhart, T. T.; Dempsey, J. L., A Practical Beginner's Guide to Cyclic Voltammetry. *J. Chem. Educ.* **2018,** *95* (2), 197-206.
20. Pegis, M. L.; Wise, C. F.; Koronkiewicz, B.; Mayer, J. M., Identifying and Breaking Scaling Relations in Molecular Catalysis of Electrochemical Reactions. *J. Am. Chem. Soc.* **2017,** *139* (32), 11000-11003.

21. Costentin, C.; Drouet, S.; Robert, M.; Savéant, J.-M., Turnover Numbers, Turnover Frequencies, and Overpotential in Molecular Catalysis of Electrochemical Reactions. Cyclic Voltammetry and Preparative-Scale Electrolysis. *J. Am. Chem. Soc.* **2012,** *134* (27), 11235-11242.
22. Rountree, E. S.; McCarthy, B. D.; Eisenhart, T. T.; Dempsey, J. L., Evaluation of Homogeneous Electrocatalysts by Cyclic Voltammetry. *Inorg. Chem.* **2014,** *53* (19), 9983-10002.
23. Pegis, M. L.; Martin, D. J.; Wise, C. F.; Brezny, A. C.; Johnson, S. I.; Johnson, L. E.; Kumar, N.; Raugei, S.; Mayer, J. M., Mechanism of Catalytic O_2 Reduction by Iron Tetraphenylporphyrin. *J. Am. Chem. Soc.* **2019,** *141*, 8315-8326.
24. Costentin, C.; Robert, M.; Savéant, J. M., Current Issues in Molecular Catalysis Illustrated by Iron Porphyrins as Catalysts of the CO_2-to-CO Electrochemical Conversion. *Acc. Chem. Res.* **2015,** *48* (12), 2996-3006.
25. Saveant, J. M., Molecular catalysis of electrochemical reactions. Mechanistic aspects. *Chem. Rev.* **2008,** *108* (7), 2348-78.
26. Azcarate, I.; Costentin, C.; Robert, M.; Savéant, J.-M., Dissection of Electronic Substituent Effects in Multielectron–Multistep Molecular Catalysis. Electrochemical CO2-to-CO Conversion Catalyzed by Iron Porphyrins. *J. Phys. Chem. C* **2016,** *120* (51), 28951-28960.
27. Stegelmann, C.; Andreasen, A.; Campbell, C. T., Degree of rate control: how much the energies of intermediates and transition states control rates. *J. Am. Chem. Soc.* **2009,** *131* (23), 8077-82.
28. Kozuch, S.; Shaik, S., Kinetic-quantum chemical model for catalytic cycles: the Haber-Bosch process and the effect of reagent concentration. *J. Phys. Chem. A* **2008,** *112* (26), 6032-41.
29. Costentin, C.; Passard, G.; Robert, M.; Saveant, J. M., Pendant acid-base groups in molecular catalysts: H-bond promoters or proton relays? Mechanisms of the conversion of CO_2 to CO by electrogenerated iron(0)porphyrins bearing prepositioned phenol functionalities. *J. Am. Chem. Soc.* **2014,** *136* (33), 11821-9.
30. Costentin, C.; Savéant, J.-M., Multielectron, Multistep Molecular Catalysis of Electrochemical Reactions: Benchmarking of Homogeneous Catalysts. *ChemElectroChem* **2014,** *1* (7), 1226-1236.
31. Costentin, C.; Drouet, S.; Robert, M.; Savéant, J.-M., A local proton source enhances CO_2 electroreduction to CO by a molecular Fe catalyst. *Science* **2012,** *338*, 90-94.

7 Chapter 7 – Synthesis and Prior Misidentification of 4-*tert*-butyl-2,6-dinitrobenzaldehyde

Adapted from Martin, D. J.; Mercado, B. Q.; Mayer, J. M. "Synthesis and Prior Misidentification of 4-*tert*-butyl-2,6-dinitrobenzadelhyde." *J. Org. Chem*. **2019**, *84*, 12172-12176. DJM and JMM conceived the projected, constructed the scientific arguments, and wrote the paper. BQM performed x-ray crystallography and solved the structures.

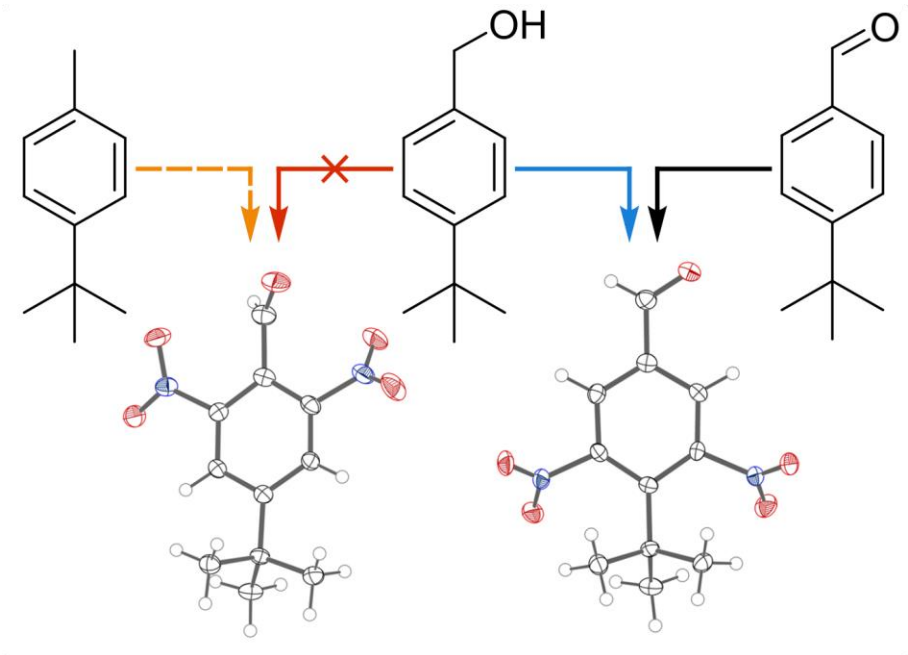

7.1 Results and Discussion

Substituted 2,6-dinitrobenzaldehydes are useful reagents for the preparation of dyes, pigments and macrocycles such as porphyrins and corroles.[1-6] In particular, 2,6-dinitrobenzaldehydes are used in the synthesis of tetrakis-5,10,15,20-(2′,6′-dinitrophenyl)porphyrins, precursor molecules for bis-picket fence porphyrin derivatives.[4] The acid-catalyzed condensation of 2,6-dinitrobenzaldehyde or related derivatives with pyrrole produces substituted 2′,6′-dinitrophenylporphyrins, but typically only in low yields, ranging from 0.5% to 9%. The highest yields are for the tetrakis-5,10,15,20-(4′-*tert*-butyl-2′,6′-dinitrophenyl)porphyrin, a common derivative.[3] In order to make reasonable amounts of this porphyrin target (>100 mg), its synthesis requires sizable amounts of 4-*tert*-butyl-2,6-dinitrobenzaldehyde, the starting benzaldehyde precursor.

Scheme 7.1. Preparations of 4-*tert*-butyl-2,6-dinitrobenzaldehyde and 4-*tert*-butyl-3,5-dinitrobenzaldehyde, showing incorrect prior report (red), corrected reaction product (blue), previously available route (black), and new—chromium and column-free—procedures (gold).

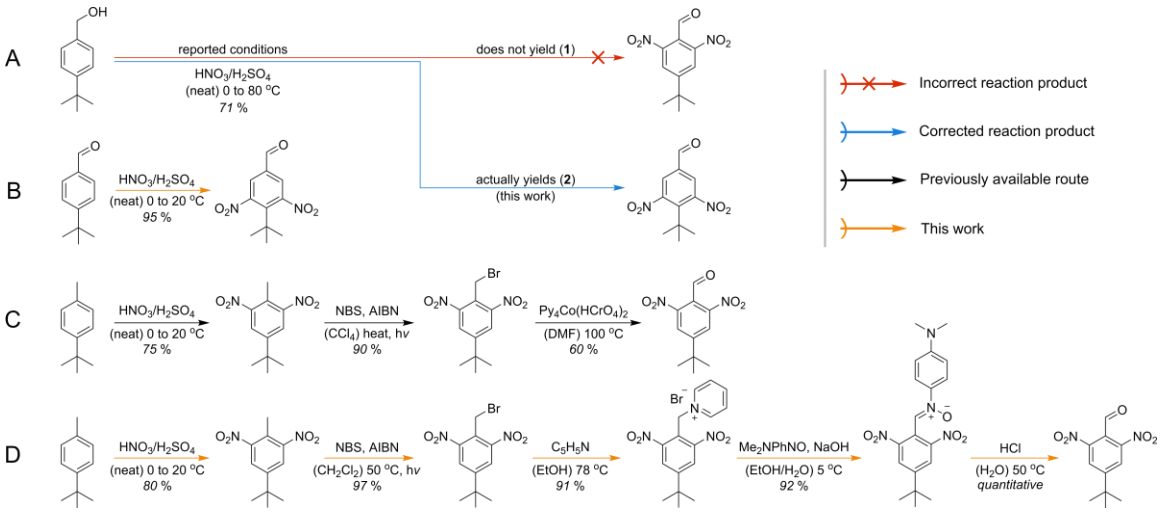

Method A: reported synthesis in reference 6; actually yields **2** (this work). Method B: high yield synthesis of **2**, this work. Method C: previously reported synthesis of (**1**) requiring chromium reagents and chromatography purification, reference 3. Method D: high yield, high throughput synthesis of (**1**), this work.

The synthesis of 4-*tert*-butyl-2,6-dinitrobenzaldehyde (**1**) has been reported using two different routes, Methods A and C in Scheme 1.[3,6] Method A reported what seemed to be the most direct synthesis, a one-pot nitration and oxidation of 4-*tert*-butylbenzylalcohol.[6] This synthesis was stated to be “noteworthy since it occurs with concomitant chemoselective oxidation of the benzylic alcohol to the corresponding aldehyde and represents the by far most practical route to this common porphyrin precursor”.[6] Following this preparation, we obtained a product in similar yields, which had ^{1}H NMR and ^{13}C NMR spectra identical to the reported spectra (**Figure F1**-**Figure F2**). Slow evaporation of this product from ethyl acetate yielded crystals suitable for single-crystal x-ray diffraction. The single-crystal data revealed that the product of this reaction was not **1** but was instead the isomeric *3,5-dinitro* compound, 4-*tert*-butyl-3,5-dinitrobenzaldehyde (**2**) (**Figure 7.1**, Right; **Scheme 7.1**, Method A). Presumably the hot HNO_3/H_2SO_4 oxidation of the benzyl alcohol proceeds by initial formation of 4-*tert*-butylbenzaldehyde, which directs nitration to positions *meta* to the aldehyde. Consistent with this possible intermediate formation, we report the synthesis of the 3,5-dinitro isomer, product **2**, in much higher yields (>95%) from the nitration of 4-*tert*-butylbenzaldehyde (**Scheme 7.1**, Method B; procedure in the Experimental Section). After a literature search of articles citing reference 6, we believe that this incorrect assignment may have

led to a synthesis and misidentification of what is actually tetrakis-5,10,15,20-(4′-*tert*-butyl-3′,5′-dinitrophenyl)porphyrin.[7]

An earlier paper by Rose *et al*. reported a three-step preparation of the target 2,6-dinitro isomer (**1**) from 4-*tert*-butyltoluene (Scheme 1, Method C).[3] Following this procedure, including chromatography and recrystallization, we obtained a product with ^{1}H NMR and ^{13}C NMR spectra (**Figure F3**-**Figure F4**) that were identical to those reported in reference 3. Crystals were obtained from ethyl acetate/ethanol mixtures and single-crystal x-ray diffraction showed that the product of this reaction was correctly assigned as 4-*tert*-butyl-2,6-dinitrobenzaldehyde (**1**) (**Figure 7.1**, Left). The ^{1}H NMR and ^{13}C NMR spectra for **1** and **2** are quite distinct, as are the solid-state structures.

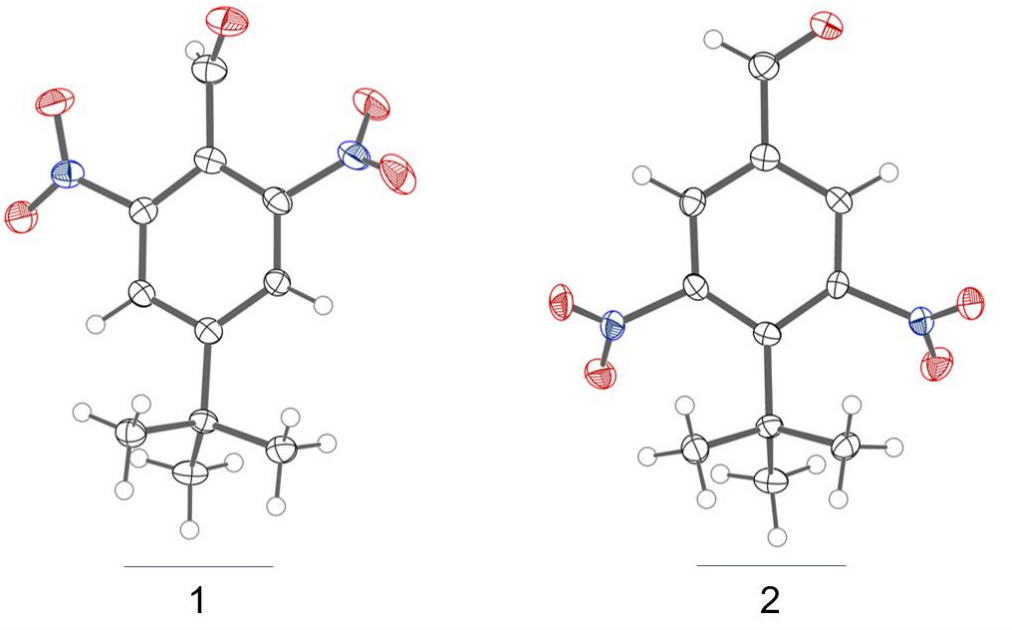

Figure 7.1. Thermal ellipsoid plots (50% probability level) of X-ray structures for 4-*tert*-butyl-2,6-dinitrobenzaldehyde and 4-*tert*-butyl-3,5-dinitrobenzaldehyde. The unit cell of **1** contained two chemically identical, crystallographically distinct molecules of **1** (Z′ = 2); only one molecule is shown for clarity.

It is unfortunate that the apparently scalable Method A does not produce the desired compound **1**. While Method C is suitable for the synthesis of **1** in small quantities, it does not scale well to larger amounts. After three steps, the overall yield of **1** is only 41% from 4-*tert*-butytoluene, and the synthesis requires stoichiometric amounts of chromium reagents and multiple chromatography columns. We are pleased to report an improved route to **1**, starting from

inexpensive 4-*tert*-butyltoluene, that can be done on much larger scales and without the need for chromatography or chromium reagents.

Our synthesis of **1** (Method D, **Scheme 7.1**) was adapted from the reported syntheses of other ortho-substituted aldehydes, including 2,6-dinitrobenzaldehyde.[8-9] First, 4-*tert*-butyl-2,6-dinitrotoluene was prepared by nitration of 4-*tert*-butyltoluene. The synthesis of this compound has been reported in several articles[3,6,10-11] and we have found no reports of hazards such as being explosive or forming explosive species. Bromination using *N*-bromosuccinimide yielded 4-*tert*-butyl-2,6-dinitrobenzylbromide. Heating 4-*tert*-butyl-2,6-dinitrobenzylbromide with pyridine in ethanol resulted in the precipitation of 4-*tert*-butyl-2,6-dinitro-benzylpyridinium bromide as a white, crystalline solid. Base-catalyzed condensation of the pyridinium salt with *N*,*N*-dimethyl-4-nitrosoaniline generated the *N*-(4-dimethylaminophenyl)-α-(4-*tert*-butyl-2,6-dinitrophenyl)nitrone, which precipitated as an orange solid from cold ethanol/water. Acid-catalyzed hydrolysis of the nitrone precipitated **1** as a yellow solid from acidic water. The ^{1}H NMR and ^{13}C NMR for all the intermediates are reported in Appendix F (**Figure F5**-**Figure F12**). While this synthesis has more steps, it gives **1** in 65% overall yield (starting from one mole of the parent toluene) and requires only recrystallization and solubility differences for purification (Method D, **Scheme 7.1**). An alternative synthesis via direct oxidation of the benzyl bromide intermediate using DMSO/Et_3N was briefly explored. While this gave the target product in fewer steps than the method detailed here, it was not pursued because it required chromatography to separate the unreacted benzyl bromide and was therefore less attractive at large scale.

In sum, we report here that a published method[6] yields 4-*tert*-butyl-3,5-dinitrobenzaldehyde (**2**) rather than the claimed 2,6-dinitro isomer, 4-*tert*-butyl-2,6-dinitrobenzaldehyde (**1**). Since the 2,6−isomer is a valuable synthetic intermediate, we have developed an improved synthesis without the need for chromatography or chromium reagents. This synthesis has been scaled to yield more than 150 grams of **1** with an overall yield of 65%. We also report a convenient synthesis of **2**. The ^{1}H NMR and ^{13}C NMR spectra and the x-ray crystal structures of both isomers are reported.

7.2 Experimental Materials

7.2.1 Instrumentation

^{1}H NMR spectra were recorded on an Agilent 500 MHz spectrometer and were referenced to proteo solvent impurities. High resolution mass spectrometry was performed using a Waters Xevo G2-XS QTof mass spectrometer. Gas-chromatography mass spectroscopy was performed using an Agilent 6890N/5973 mass spectrometer. Elemental analyses were performed by Robertson Microlit Laboratories, Ledgewood, NJ.

7.2.2 Materials

Potassium nitrate (Sigma,-Aldrich, *ReagentPlus*®, >99%), sulfuric acid (J.T. Baker, 98%), 4-*tert*-butylbenzylalcohol (Sigma-Aldrich, 95%), 4-*tert*-butylbenzaldehyde (Sigma-Aldrich, 97%), 4-*tert*-butyltoluene (Sigma-Aldrich, 95%), *N*-bromosuccinimide (Sigma-Aldrich, *ReagentPlus*®, 99%), 2,2'-azobis(2-methylpropionitrile (Sigma-Aldrich, 98%), pyridine (Sigma-Aldrich, 99.8%), *N*,*N*-dimethyl-4-nitrosoaniline (Sigma-Aldrich, 97%), aqueous hydrochloric acid (Macron, 36-38% wt), sodium chloride (Sigma-Aldrich, >99%), sodium bicarbonate (Sigma-Aldrich, >99%), sodium hydroxide (Macon, 95%), chloroform (Sigma-Aldrich, 99.8%), ethyl acetate (Sigma-Aldrich, 99.8%), absolute ethanol (Decon Labs, 200 proof), diethyl-ether (Sigma-Aldrich, 99%), and acetone (Sigma Aldrich, 99.8%) were all used as received. Dichloromethane was degassed with argon and dried using a Pure Process Technology solvent system prior to use.

7.2.3 Single crystal X-ray diffraction methods

Low-temperature diffraction data (ω-scans) were collected on a Rigaku SCX Mini diffractometer coupled to a Rigaku Mercury275R CCD with Mo Kα radiation (λ = 0.71073 Å). The diffraction images were processed and scaled using Rigaku Oxford Diffraction software (CrysAlisPro; Rigaku OD: The Woodlands, TX, 2015). The structures were solved with SHELXT and were refined against F^2 on all data by full-matrix least squares with SHELXL.[12] All non-hydrogen atoms were refined anisotropically. Hydrogen atoms were included in both models at geometrically calculated positions and refined using a riding model. The isotropic displacement parameters of all hydrogen atoms were fixed to 1.2 times the U value of the atoms to which they are linked (1.5 times for methyl groups). For **2**, the dataset was refined as a 2-component twin. The fractional volume contribution of the minor twin component was freely refined to a converged value

of 0.3850(19). For **1**, the dataset yielded a unit cell containing two chemically identical, crystallographically distinct molecules.

The full numbering scheme of compounds **1** and **2** can be found in the full details of the X-ray structure determinations (CIFs). CCDC number 1923128 (**1**) and 1923129 (**2**) contain the supplementary crystallographic data for this paper. These data can be obtained free of charge from The Cambridge Crystallographic Data Center via www.ccdc.cam.ac.uk/data_request/cif.

7.2.4 Mixed acid preparation for nitration reactions

Fuming nitric acid (FNA) is a corrosive strong acid and a strong oxidant; concentrated sulfuric acid is a corrosive strong acid; and the mixture of the two is considered a stronger acid and oxidant. All of these materials are highly hazardous and should be handled with substantial caution with emphasis on appropriate specialized personal protective equipment (PPE). Our laboratory's standard operating procedure (SOP) for FNA and the mixed acid are available online. Fuming nitric acid (FNA, +98%) was freshly prepared immediately before use via distillation of HNO_3 at 80 °C from a mixture of potassium nitrate and concentrated sulfuric acid, prepared as described in the SOP. FNA (1 part by volume, for instance 50 mL) was cooled to 5 °C in an ice bath before slowly adding concentrated sulfuric acid (1.4 parts by volume, for instance 70 mL). Upon addition, the mixed acid warms to 15 °C. The mixed acid solution was then cooled back to 5 °C before being used immediately for nitration reactions.

*7.2.5 Improved synthesis of 4-tert-butyl-3,5-dinitrobenzaldehyde (**2**)*

Approximately 120 mL of the mixed H_2SO_4/HNO_3 acid (see preparation above) was prepared in a 500 mL round bottom flask with a large stirbar and was cooled to 5 °C with an ice bath [**Caution:** hazardous! See above]. Above the round bottom was suspended a dropping funnel filled with 4-*tert*-butylbenzaldehyde (25 mL, 0.149 mmol). The benzaldehyde was added dropwise to the stirring solution and the flow rate was adjusted such that the reaction temperature did not rise above 15 °C. After complete addition, the solution was yellow/orange and the reaction flask was allowed to warm to room temperature before being gently heated to 40 °C for 1-2h. During this time, some off-white precipitate formed. The reaction was then quenched by *carefully* pouring the entire reaction into a large amount of crushed ice (ca. 500 mL). The precipitated product was filtered

off and washed with excess water. The dilute, acidic filtrate was neutralized and added to the aqueous waste. After air drying, the crude yellow solid (crude yield by weight: 36g, 97%) was dissolved in chloroform and filtered through Celite to remove any over-oxidized 4-*tert*-butyl-2,6-dinitrobenzoic acid (the white solid formed during synthesis). The filtrate was collected and removed with a rotary evaporator to dryness. The collected solid was then recrystallized from boiling ethyl acetate to yield pale yellow crystals (**Figure F18**). After filtration and air drying, the isolated yield was 29 g (80% yield). ^{1}H NMR ($CDCl_3$, 500 MHz): δ (ppm) = 9.99 (s, 1H, C*H*O), 7.99 (s, 2H, Ar-*H*), 1.49 (s, 9H, C(C*H*$_3$)$_3$). ^{13}C NMR ($CDCl_3$, 500 MHz): δ (ppm) = 187.0, 153.7, 141.1, 135.3, 126.6, 38.2, 30.0. Anal. Calcd for $C_{11}H_{12}N_2O_5$: C, 52.38; H, 4.80; N, 11.11. Found: C, 52.13; H, 4.65; N, 10.95. MS (EI) *m*/*z* = 252.1 ($[M]^+$), 237.1 ($[M]^+ - CH_3$).

7.2.6 4-tert-butyl-2,6-dinitrotoluene

This synthesis was adapted from the literature.[4] Approximately 240 mL of the mixed H_2SO_4/HNO_3 acid (see preparation above) was prepared in a 1L round bottom flask with a large stirbar and was cooled to 5 °C with an ice bath [**Caution:** hazardous! See above]. Above the round bottom was suspended a dropping funnel filled with 4-*tert*-butyltoluene (173 mL, 1.0 mol). The 4-*tert*-butyltoluene was added dropwise to the stirring solution over the course of three hours such that the temperature of the reaction stayed between 5-10 °C. The yellow product formed and floated to the reaction surface during the addition. After complete addition, the reaction flask was allowed to warm to room temperature and was stirred for another 12h. The reaction was quenched by *carefully* pouring the reaction mixture into 500 mL of crushed ice. After filtration, the collected yellow solid was washed with excess water. The dilute, acidic filtrate was neutralized and added to the aqueous waste. The damp solid was then recrystallized from boiling EtOH (approx. 750 mL). Upon cooling, large yellow crystals formed (**Figure F13**). The solution was cooled at 0 °C overnight before the crystals were filtered and washed with cold EtOH. After drying, the isolated yield was 190 g flaky crystalline solid (80% yield). ^{1}H NMR ($CDCl_3$, 500 MHz): δ (ppm) = 7.97 (s, 2H, Ar-*H*), 2.52 (s, 3H, C*H*$_3$), 1.37 (s, 9H, C(C*H*$_3$)$_3$). ^{13}C NMR ($CDCl_3$, 500 MHz): δ (ppm) = 152.2, 151.6, 124.7, 124.1, 35.3, 30.8, 14.5. Anal. Calcd for $C_{11}H_{14}N_2O_4$: C, 55.46; H, 5.92; N, 11.76. Found: C, 55.42; H, 5.78; N, 11.68. MS (EI): *m*/*z* = 238.1 ($[M]^+$), 223.1 ($[M]^+ - CH_3$).

7.2.7 4-tert-butyl-2,6-dinitrobenzylbromide

To a 3L three-necked round bottom flask was added a large stirbar, 4-*tert*-butyl-2,6-dinitrotoluene (190 g, 0.798 mol, 1 eq.), *N*-bromosuccinimide (170 g, 0.998 mol, 1.25 eq.), and AIBN (1.5 g, 0.009 mol, 0.01 eq). Two of the three ports were stoppered and 1.5 L of dry dichloromethane was added to the solids. The solution was sparged with N_2 for 20 minutes before a condenser was attached to the third port and the reaction was heated to a gentle reflux (45-50 °C). A white LED light (14 V dc, 0.7 A from Digi-Key) was clamped a few inches away from the flask and the reaction was loosely shrouded in aluminum foil. At the 12h, 48h, 74h, and 82h marks, additional NBS (20 g, 0.117 ml, 0.15 eq.) and AIBN (0.5 g, 0.0045 mol, 0.005 eq.) were added. The solid additions were made by funneling the NBS/AIBN through an opened port under gently flowing N_2 only after cooling the reaction to room temperature. After four days, the reaction was nearly complete (>98% conversion based on the ratio of product to starting material by ^{1}H NMR). The solvent was removed using a rotary evaporator to yield a damp solid. The solid was resuspended in chloroform and filtered to remove the bulk of the succinimide. The filtrate was separated with sat. Na_2CO_3 solution to remove residual succinimide before being dried with $MgSO_4$ and filtered. The solvent was removed and the product was recrystallized from hot diethyl ether to yield extremely large pale-yellow crystals (5-7 grams apiece, **Figure F14**). Isolated yield was 235.5 g large yellow crystals and 13.2 g non-crystalline powder with matching ^{1}H NMR spectra (97.7%). ^{1}H NMR ($CDCl_3$, 500 MHz): δ (ppm) = 8.04 (s, 2H, Ar-*H*), 4.84 (s, 2H, C*H*$_2$Br), 1.37 (s, 9H, C(C*H*$_3$)$_3$). ^{13}C NMR ($CDCl_3$, 500 MHz): δ (ppm) = 155.3, 150.1, 125.9, 123.6, 35.7, 30.7, 20.4. Anal. Calcd for $C_{11}H_{13}BrN_2O_4$: C, 41.7; H, 4.1; N, 8.8. Found: C, 41.69; H, 4.01; N, 8.71. MS (EI): *m*/*z* = 301.0 ($[M]^+$ – CH_3), 237.1 ($[M]^+$ – Br), parent ion not observed.

7.2.8 4-tert-butyl-2,6-dinitrobenzylpyridinium bromide

The crude 4-*tert*-butyl-2,6-dinitrobenzylbromide (246 g, 0.778 mol, 1eq.) was added to a 2 L beaker. The solid was dissolved in 1 L EtOH (200 proof) and was heated to 78°C with stirring. Pyridine (130 mL, 1.55 mol, 2 eq.) was added dropwise to the stirring solution, which darkened and eventually precipitated flocculent, white crystals (**Figure F15**). After complete addition, the solution was stirred for an additional hour at reflux before an additional hour of stirring at room temperature.

The crystals were filtered and washed with EtOH and acetone. After drying, the first crop of crystals weighed 258 g. The filtrate was pumped to a solid using a rotary evaporator and was repeatedly recrystallized from EtOH to yield an additional 25 g of off-white solid with ^{1}H NMR that matched the crystalline material (total solid collected: 283.0 g, 91.3% yield. ^{1}H NMR (d_6-DMSO, 500 MHz): δ (ppm) = 9.06 (d, *J* = 6.0 Hz, 2H, 2,6-py-*H*), 8.72 (t, *J* = 7.8 Hz, 1H, 4-py-*H*), 8.53 (s, 2H, Ar-*H*), 8.21 (t, *J* = 7.1 Hz, 2H, 3,5-py-*H*), 6.14 (s, 2H, Ar-C*H*$_2$-py), 1.41 (s, 9H, C(C*H*$_3$)$_3$). ^{13}C NMR (d_6-DMSO, 500 MHz): δ (ppm) = 157.9, 152.0, 146.7, 144.5, 128.5, 127.6, 116.5, 56.0, 36.2, 30.5. Anal. Calcd for $C_{16}H_{18}N_3O_4Br$: C, 48.50; H, 4.58; N, 10.60. Found: C, 48.31; H, 4.32; N, 10.38. HRMS (ESI/Q-TOF) *m*/*z*: [M – Br]$^+$ calcd for $C_{16}H_{18}N_3O_4^+$ 316.1297; found 316.1296.

7.2.9 N-(4-dimethylaminophenyl)-α-(4-tert-butyl-2,6-dinitrophenyl)nitrone

To a large Erlenmeyer flask was added approximately 1/3 of the dry 4-*tert*-butyl-2,6-dinitrobenzylpyridinium bromide (85.4 g, 0.215 mol, 1 eq.) and *N*,*N*-dimethyl-4-nitrosoaniline (40.0 g, 0.266 mol, 1.24 eq). The solids were suspended in 1.0 L of ethanol (200 proof) and the solution was cooled to 5 °C with an ice bath. An addition funnel was suspended above the reaction and was filled with 600 mL of 1 *N*-sodium hydroxide solution. With vigorous stirring, the NaOH solution was added dropwise such that the temperature was kept between 5-10 °C. After complete addition, the solution was stirred for another 2h before being diluted with 1 L ice water. The nitrone precipitated as an orange solid (**Figure F16**), which was filtered and washed with excess water. This procedure was repeated until nearly all of the benzylpyridinium bromide was used (279.3 g, 0.714 mol). All of the orange solids were collected and dried in a vacuum oven at 50^{o}C until reaching a constant mass (2-3 days). After drying, the yield was 257.7 g of orange powder (92.4% yield). ^{1}H NMR ($CDCl_3$, 500 MHz): δ (ppm) = 8.44 (s, 1H, Ar-C*H*=N), 8.30 (s, 2H, Ar-*H*), 7.67 (d, *J* = 9.1 Hz, 2H), 6.67 (d, *J* = 9.1 Hz, 2H), 3.04 (s, 6H, N(C*H*$_3$)$_2$), 1.42 (s, 9H, C(C*H*$_3$)$_3$). ^{13}C NMR ($CDCl_3$, 500 MHz): δ (ppm) = 155.3, 152.1, 149.6, 136.8, 126.1, 122.8, 122.5, 117.8, 111.4, 40.5, 35.9, 30.9. Anal. Calcd for $C_{19}H_{22}N_4O_5$: C, 59.06; H, 5.74; N, 14.50. Found: C, 58.92; H, 5.56; N, 14.34. HRMS (ESI/Q-TOF) *m*/*z*: [M + H$^+$] calcd for $C_{19}H_{23}N_4O_5^+$ 387.1668; found 387.1682.

*7.2.10 4-tert-butyl-2,6-dinitrobenzaldehyde (**1**)*

In a large beaker, nearly all of the *N*-(4-dimethylaminophenyl)-α-(4-*tert*-butyl-2,6-dinitrophenyl)nitrone (257.2 g) was suspended in 2L of water. Concentrated sulfuric acid was added slowly and the solution warmed to approximately 50 °C. The suspension was stirred for 30 minutes, during which the solution color lightened to a pale yellow-brown. The suspension was filtered and the collected solid was washed with excess water. After drying, 164 g of pale-yellow powder was collected (98% yield). The solid can be recrystallized from hot ethanol or from mixtures of ethanol/ethyl acetate to yield golden flake-like crystals (**Figure F18**). ^{1}H NMR ($CDCl_3$, 500 MHz): δ (ppm) = 10.57 (s, 1H, C*H*O), 8.45 (s, 2H, Ar-*H*), 1.45 (s, 9H, C(C*H*$_3$)$_3$). ^{13}C NMR ($CDCl_3$, 500 MHz): δ (ppm) = 186.2, 157.1 147.7, 129.0, 126.8, 36.1, 30.9. Anal. Calcd for $C_{11}H_{12}N_2O_5$: C, 52.38; H, 4.80; N, 11.11. Found: C, 52.13; H, 4.61; N, 10.94. MS (EI) *m*/*z* = 252.1 ([M]$^+$), 237.1 ([M]$^+$ – CH_3).

7.3 References

1. Rose, E.; Soleilhavoup, M.; Christ-Tommasino, L.; Moreau, G.; Collman, J. P.; Quelquejeu, M.; Straumanis, A., Bis-Faced Aminoporphyrin Templates for the Synthesis of Chiral Catalysts and Hemeprotein Analogues. *J. Org. Chem.* **1998,** *63* (6), 2042-2044.
2. Quintana, C. A.; Assink, R. A.; Shelnutt, J. A., Synthesis and spectroscopic characterization of bis-pocket porphyrins: tetrakis(2',6'-dinitrophenyl)porphyrin and catalytic activity of a manganese(III) chloride derivative in alkane oxidation. *Inorg. Chem.* **1989,** *28* (18), 3421-3425.
3. Rose, E.; Kossanyi, A.; Quelquejeu, M.; Soleilhavoup, M.; Duwavran, F.; Bernard, N.; Lecas, A., Synthesis of Biomimetic Heme Precursors: The "Double Picket Fence" 5,10,15,20-Tetrakis(2′,6′-dinitro-4′-tert-butylphenyl)porphyrin. *J. Am. Chem. Soc.* **1996,** *118* (6), 1567-1568.
4. Rose, E.; Lecas, A.; Quelquejeu, M.; Kossanyi, A.; Boitrel, B., Synthesis of biomimetic heme precursors. *Coord. Chem. Rev.* **1998,** *178-180*, 1407-1431.
5. Drain, C. M.; Corden, B. B., Synthesis and characterization of copper(II) 5,10,15,20-tetrakis(2,6-dipivalamidophenyl)porphyrinate: a bis-picket-fence porphyrin. *Inorg. Chem.* **1989,** *28* (24), 4374-4376.
6. Peters, M. V.; Stoll, R. S.; Goddard, R.; Buth, G.; Hecht, S., On the Illusive Nature of o-Formylazobenzenes: Exploiting the Nucleophilicity of the Azo Group for Cyclization to Indazole Derivatives. *J. Org. Chem.* **2006,** *71* (20), 7840-7845.
7. Goodrich, L. E.; Roy, S.; Alp, E. E.; Zhao, J.; Hu, M. Y.; Lehnert, N., Electronic Structure and Biologically Relevant Reactivity of Low-Spin {FeNO}^{8} Porphyrin Model Complexes: New Insight from a Bis-Picket Fence Porphyrin. *Inorg. Chem.* **2013,** *52* (13), 7766-7780.
8. Kalir, A., o-Nitrobenzaldehyde. *Org. Synth.* **1966,** *46*, 81-81.
9. Clarke, K., Some Aromatic Aldehydes. *J. Chem. Soc.* **1957,** (Aug), 3807-3808.
10. Brady, O. L.; Lahiri, J. K., 430. The nitration of alkyl benzenes. Part III. The orientation of dinitro-p-tert.-butyltoluene. *J. Chem. Soc.* **1934,** (0), 1954-1954.
11. Yamato, T.; Arimura, T.; Tashiro, M., Metacyclophanes and related compounds. Part 16. Preparation of 8-fluoro-t-butyl[2.2]metacyclophanes and their treatment with aluminium chloride–nitromethane in benzene. *J. Chem. Soc., Perkin Trans. 1* **1987,** (0), 1-7.
12. Sheldrick, G. M., A short history of SHELX. *Acta Crystallogr. Sect. A: Found. Crystallogr.* **2008,** *64* (1), 112-122.

It’s dangerous to go alone! Take this.

Appendix

List of Appendix Figures

List of Schemes

List of Tables

A Supporting Information for Chapter 2

Adapted from Pegis, M. P.; Martin, D. J.; Wise, C. F.; Brezny, A. C.; Johnson, S. I.; Johnson, L. E.; Kumar, N.; Raugéi, S; Mayer, J. M. "Mechanism of Catalytic O_2 Reduction by Iron Tetraphenylporphyrin." *J. Am. Chem. Soc.* **2019**, *141*, 8315-8326.

A.1 General

A.1.1 Instrumentation

^{1}H NMR spectra were recorded on Agilent 400 MHz or 500 MHz spectrometers and were referenced to proteo solvent impurities.[1] UV-vis optical spectra were recorded on Agilent 8452 diode-array spectrometers. These spectra used a 1 cm pathlength cuvette unless otherwise noted. For the sake of clarity (and analysis in Chapter 2), the reported UV-vis spectra only show the Q-band portion of the porphyrin absorbance features. Stopped-flow measurements were performed on TgK Scientific and Olis single-mixing instruments. Cyclic voltammetry was conducted on CH Instruments potentiostats (models 600D/650D) using a 3 mm glassy carbon working electrode, a platinum wire auxiliary electrode, and a Ag/AgCl pseudoreference electrode made using a CHI non-aqueous reference electrode kit. Prior to use, the silver wire was roughened with 600 grit sand paper and submerged in an aqueous 0.1 M HCl solution, where it was anodized (0-500 mV vs Ag/AgCl (aq)) with a linear sweep. The electrode was then immersed in a jacketed compartment (separated from solution with a glass frit) containing 0.1 M [*n*-Bu_4N][PF_6] in DMF and allowed to equilibrate for 24 hours prior to use. IR Compensation was performed for all experiments using CHI software to determine the resistance within the electrochemical window of interest ($E \approx E_{1/2}$). Resistance values typically measured < 20 Ohms. Given that the current passed rarely exceeded 100 μA, iR compensation shifted the potential response < 2 mV for most experiments, suggesting that the ohmic drop is negligible for analyses herein.

A.1.2 Materials

Chlorin-free *meso*-tetraphenylporphyrin (Frontier Scientific, >99%), iron(II) chloride (Sigma-Aldrich, >99%), *para*-toluenesulfonic acid monohydrate (Sigma-Aldrich, >99%), bis(pentamethylcyclopentadienyl)iron(II) (Fc*) (Sigma-Aldrich, 97%), lithium bis(trimethylsilyl)amide (Sigma-Aldrich, 97%), 2,6-lutidine (Sigma-Aldrich, ReagentPlus®, 98%), sodium chloride (Macron, 99%), aqueous hydrogen chloride (Macron, 38% w/t), magnesium sulfate

(Fisher), thallium trifluoromethanesulfonate (Sigma-Aldrich, 97%), Celite (Fisher), deuterated dichloromethane (99.9%, Cambridge Isotope Laboratories), and deuterated *N*,*N*-dimethylformamide (99.9% Cambridge Isotope Laboratories) were used as received. Decamethylferrocenium (Fc^{*+}) was prepared as the PF_6^- salt by oxidizing Fc* with $AgPF_6$ according to literature procedures.[2]

Prior to use, tetrabutylammonium hexafluorophosphate, [*n*-Bu_4N][PF_6], (Acros, 98%) was recrystallized twice from hot ethanol and dried under vacuum at 65 °C for 18 h. Ferrocene (Sigma-Aldrich, 98%) was recrystallized from hexanes. *N*,*N*-dimethylformamide (DMF, Sigma-Aldrich, 99.8% anhydrous) and diethyl ether (Sigma-Aldrich, 99.9%, inhibitor-free) were degassed with argon and dried using a Pure Process Technology solvent system. DMF was thoroughly sparged and/or sonicated prior to use to remove trace dimethylamine and/or carbon monoxide. Dioxygen (Airgas, Ultra High Purity) was used as received. Iron(II) bromide was gifted to us by the laboratory of Professor Patrick Holland as the bis-tetrahydrofuran adduct, which was prepared using a reported procedure.[3] The THF adduct was obtained by heating $FeBr_2$ in THF at 60 °C for 4 h; the white solid was collected on a medium frit and the volatile materials were removed under vacuum.

Anhydrous tosic acid (*p*TsOH) was prepared by drying tosic acid monohydrate (*p*TsOH•H_2O) in a vacuum oven at 80 °C until all of the water was removed, evidenced by the melting of the hydrated solid and verified via ^{1}H NMR spectroscopy. After drying, the liquid was immediately stored in a dry glove box, during which time it re-solidified to form a white solid. *p*TsOD•D_2O was prepared from anhydrous *p*TsOH by repeated dissolution in D_2O followed by drying in an identical manner until the ^{1}H NMR lacked the downfield OH protonic signal. Anhydrous *p*TsOD was prepared in the same manner as anhydrous *p*TsOH and was quickly removed and transferred into a glovebox, where it was further dissolved in MeOD and the solvent removed under vacuum. The MeOD washing step was to remove any residual H_2O introduced between the vacuum oven and glovebox. Full isotopic enrichment and complete removal of MeOD was confirmed using ^{1}H NMR.

A.1.3 Iron Porphyrin Metalations and Salt Metatheses

The syntheses of iron (III) tetraphenylporphyrin chloride (Fe^{III}(TPP)Cl), iron (III) tetraphenylporphyrin triflate ([Fe^{III}(TPP)]OTf), iron(III) tetraphenylporphyrin μ-oxo dimer ([Fe^{III}(TPP)]$_2$O), and iron(II) tetraphenylporphyrin (Fe^{II}(TPP)) have all been reported, using a variety of methods.[4-7] The ^{1}H NMR and UV-vis spectra of these compounds have also been reported in the cited papers. Below, we report our modified preparation of these compounds and the ^{1}H NMR/UV-vis spectra of our materials for the convenience of the reader. In all cases, our prepared molecules have ^{1}H NMR and UV-vis spectra that match literature reports.

A.1.3.1 Iron porphyrin metalations and salt metatheses

Metalation of *meso*-tetraphenylporphyrin to form Fe^{III}(TPP)Cl was accomplished using a previously reported procedure.[4] In a N_2-glovebox, excess iron(II) chloride (149 mg, 1.17 mmol) was added to a 20 mL DMF solution containing *meso*-tetraphenylporphyrin (101 mg, 0.164 mmol) and 2,6-lutidine (67 μL, 0.57 mmol). The mixture was refluxed at 165 °C for 18 hours under N_2. Upon cooling, the mixture was exposed to atmosphere (ca. 90 °C). The solution was evaporated to dryness using a rotary-evaporator and re-dissolved in dichloromethane before being washed sequentially with water (3×), 1 M HCl (1×), and brine (sat. NaCl). The organic layer was stirred with $MgSO_4$, filtered, and dried under vacuum. ^{1}H NMR (DMF-d_7, ppm): 82.05 (s, 8H), 13.11 (s, 4H), 12.09 (s, 4H), 7.59 (s, 4H), 6.80 (s, 4H), 5.81 (s, 4H). Q-band absorption spectrum in DMF [λ_{max}, nm (ε, M^{-1} cm^{-1})]: 508 ((7.7 ± 0.5) × 10^3), 573 ((1.9 ± 0.3) × 10^3), 692 ((1.7 ± 0.3) × 10^3).

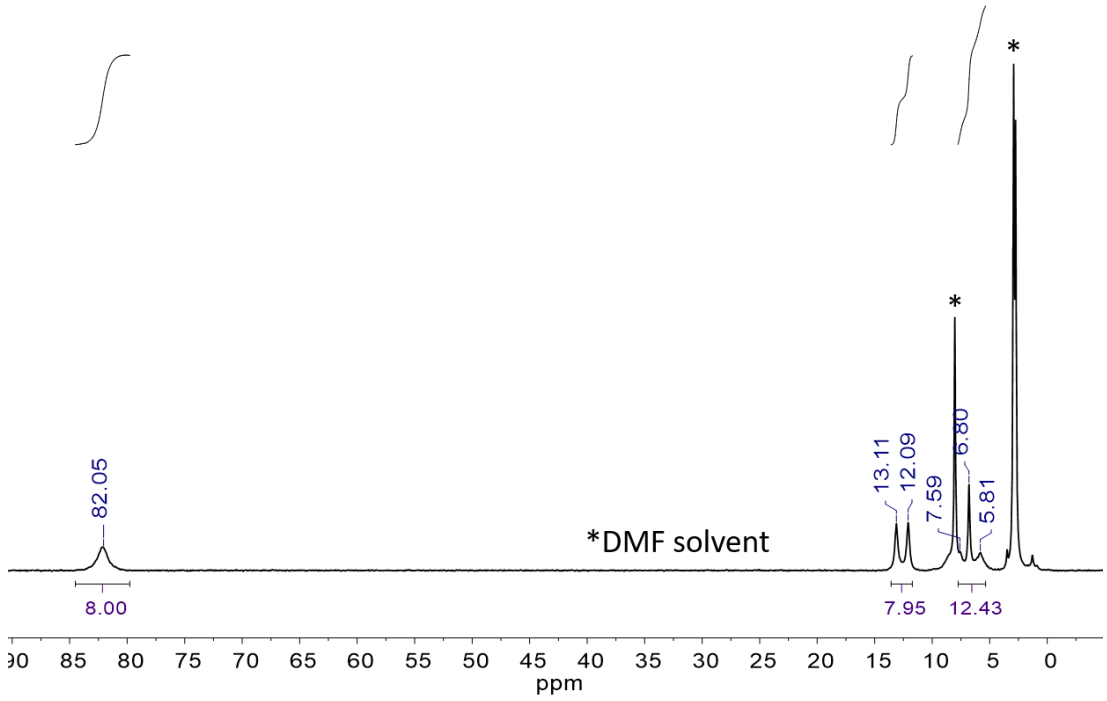

Figure A1. ^{1}H NMR spectrum of Fe^{III}(TPP)Cl in DMF-d_7.

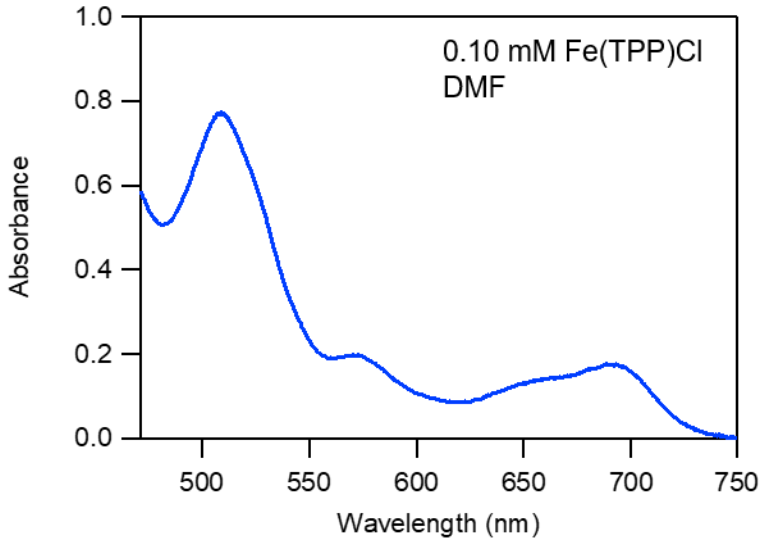

Figure A2. The optical absorbance spectrum of 0.10 mM Fe^{III}(TPP)Cl in DMF containing 0.1 M [*n*-Bu_4N][PF_6] in a 1 cm path-length cuvette.

A.1.3.2 Synthesis of [Fe^{III}(TPP)]OTf

Salt metathesis to prepare [Fe^{III}(TPP)]OTf was accomplished by stoichiometric addition of thallium triflate to a solution of Fe^{III}(TPP)Cl (78.5 mg, 0.111 mmol) dissolved in 5 mL of dichloromethane, as previously described.[4] Formation of a white precipitate (presumed to be TlCl) was evident immediately, and the solution was further stirred for 1 hour. Solvent was removed under vacuum, and the solids were re-dissolved in dichloromethane before being filtered through a Celite plug to remove the insoluble TlCl. ^{1}H NMR spectroscopy was used to confirm complete conversion to the triflate analogue by monitoring the chemical shift of the *β*-pyrrolic protons, which shift to higher fields upon chloride removal. For electrochemical experiments, halide abstraction was done *in situ* by adding a 10-fold excess of thallium triflate to a solution of Fe^{III}(TPP)Cl containing *p*TsOH. Acid must be present during halide abstraction in order to avoid formation of the μ-oxo dimer. ^{1}H NMR (DMF-d_7, ppm): 67.35 (s, 8H), 13.59 (s, 8H), 10.11 (s, 4H), 9.96 (s, 8H). Q-band absorption spectrum in DMF [λ_{max}, nm (ε, M^{-1} cm^{-1})]: 508 ((11.4 ± 0.7) × 10^3), 531 ((15.0 ± 0.7) × 10^3), 695 ((2.8 ± 0.5) × 10^3).

Caution! Safety Hazard: Thallium triflate is a toxic compound and must be handled with care. Halide abstraction with silver salts is possible; however, the use of thallium triflate simplified electrochemical experiments, as the $Tl^{+/0}$ potential is far more cathodic than the electrochemical window of interest.

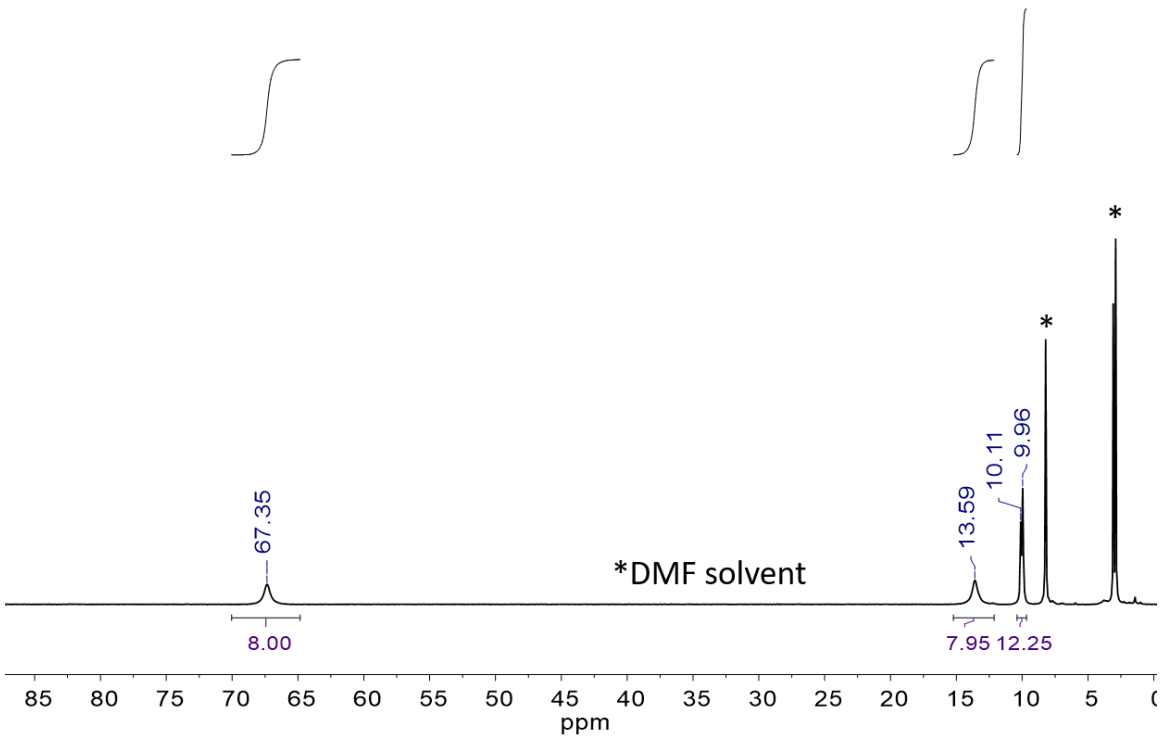

Figure A3. ^{1}H NMR spectrum of [Fe^{III}(TPP)]OTf in DMF-d$_7$. The diagnostic peak for Fe(TPP)Cl at 82 ppm is no longer present after complete metathesis.

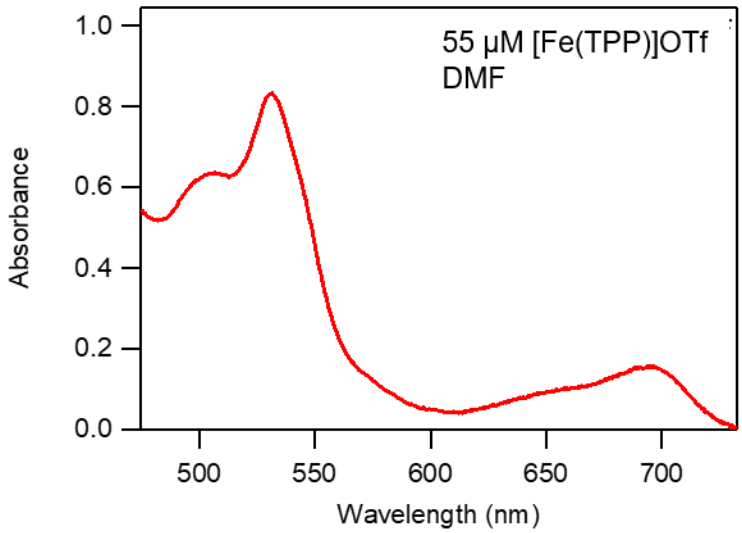

Figure A4. The optical absorbance spectrum of 70 µM [Fe^{III}(TPP)]OTf in DMF containing 0.1 M [*n*-Bu$_4$N][PF$_6$] taken in a 1 cm path-length cuvette.

A.1.3.3 Synthesis of $[Fe^{III}(TPP)]_2O$

The μ-oxo dimer of Fe^{III}(TPP) was prepared as reported.[5] A dichloromethane solution of Fe^{III}(TPP)Cl was shaken with 1 M NaOH in a separatory funnel, forming a green solution in the dichloromethane layer. The solution was then passed through a basic Al_2O_3 column before being dried and isolated as a dark purple solid. ^{1}H NMR (DMF-d_7, ppm): 50.67 (s, 16H), 8.96 (s, 16H), 8.29 (s, 16H), 8.19 (s, 8H). Q-band absorption spectrum in DMF [λ_{max}, nm (ε, M^{-1} cm^{-1})]: 569 ((8.9 ± 0.5) × 10^3), 609 ((4.5 ± 0.5) × 10^3).

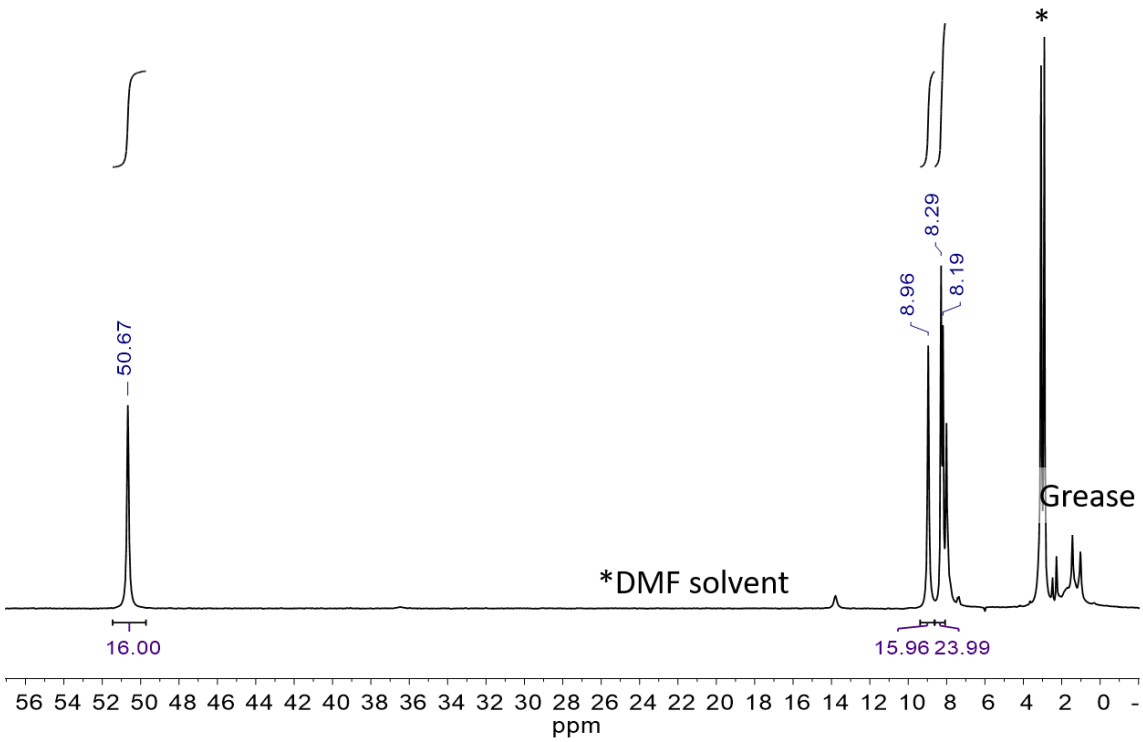

Figure A5. ^{1}H NMR spectrum of $[Fe^{III}(TPP)]_2O$ in DMF-d_7.

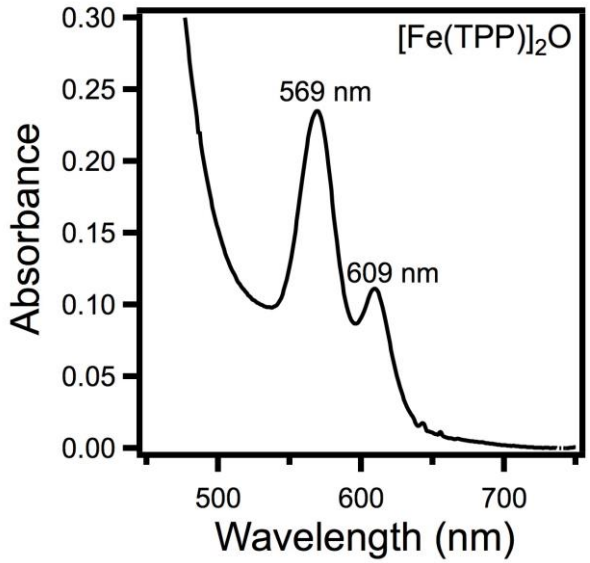

Figure A6. Optical spectrum of 26 μM $[Fe^{III}(TPP)]_2O$ in DMF containing 0.1 M [*n*-Bu_4N][PF_6] taken in a 1 cm path-length cuvette.

A.1.3.4 Synthesis of Fe^{II}(TPP)

The synthesis of Fe^{II}(TPP) was carried out in a glovebox under N_2. In a vial, lithium bis(trimethylsilyl)amide, (Li-HMDS), (24.2 mg, 0.145 mmol) was dissolved in 10 mL of tetrahydrofuran (THF). 5,10,15,20-*meso*-tetraphenylporphyrin (36.2 mg, 0.0589 mmol) and iron(II) bromide THF-adduct ($FeBr_2(THF)_2$), (26.1 mg, 0.0728 mmol) were added as solids, and the solution was stirred for 20 hours. The sample was dried, re-dissolved in toluene, and filtered through Celite to remove LiBr. Microcrystals were obtained by diffusion of pentane into a concentrated solution of Fe^{II}(TPP) in toluene. Fe^{II}(TPP) was also readily prepared in 2-10 mg scale quantities by reducing Fe^{III}(TPP)Cl over Zn(Hg) amalgam in toluene, as has been previously used to prepare other ferrous porphyrins.[6-7] ^{1}H NMR (CD_2Cl_2, ppm): 21.93 (s, 8H), 13.41 (t, 4H), 13.25 (d, 8H), 3.63 (s, 8H). Q-band absorption spectrum in DMF [λ_{max}, nm (ε, M^{-1} cm^{-1})]: 538 sh. ((7.8 ± 0.7) $\times$ 10^3), 563 ((10.4 ± 0.7) $\times$ 10^3), 606 ((5.1 ± 0.5) $\times$ 10^3). This spectrum is in agreement with the reported spectrum.[8]

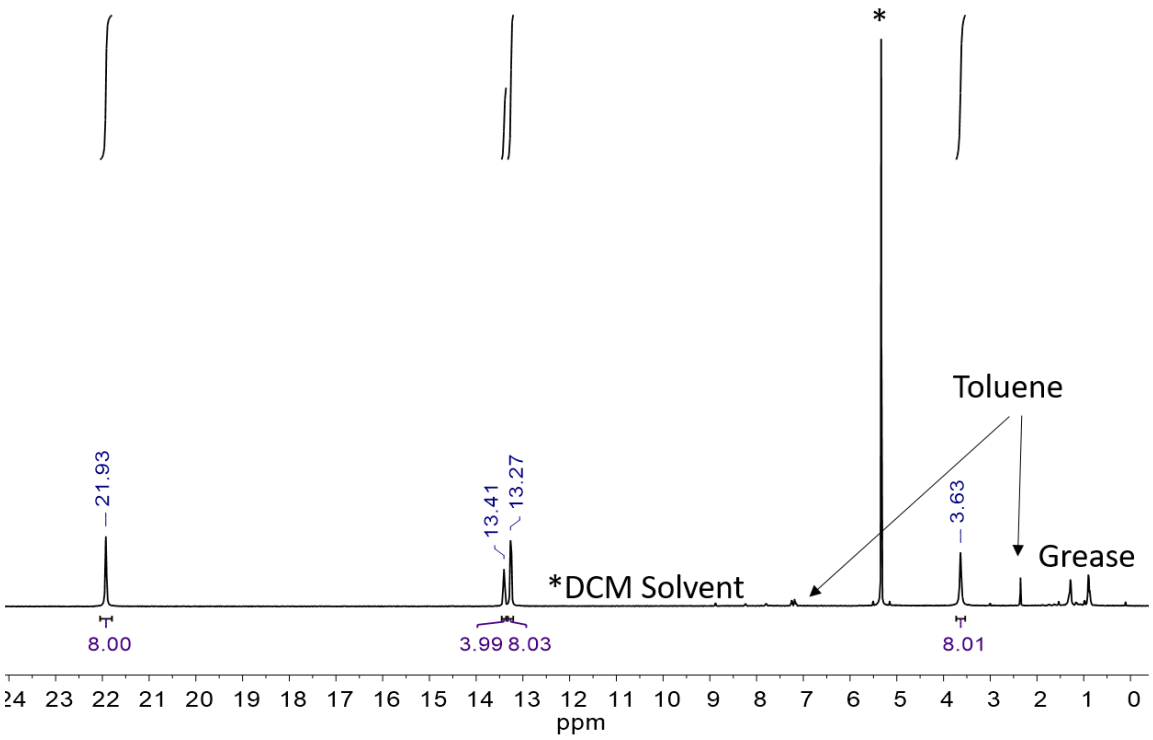

Figure A7. ^{1}H NMR spectrum of Fe^{II}(TPP) in CD_2Cl_2.

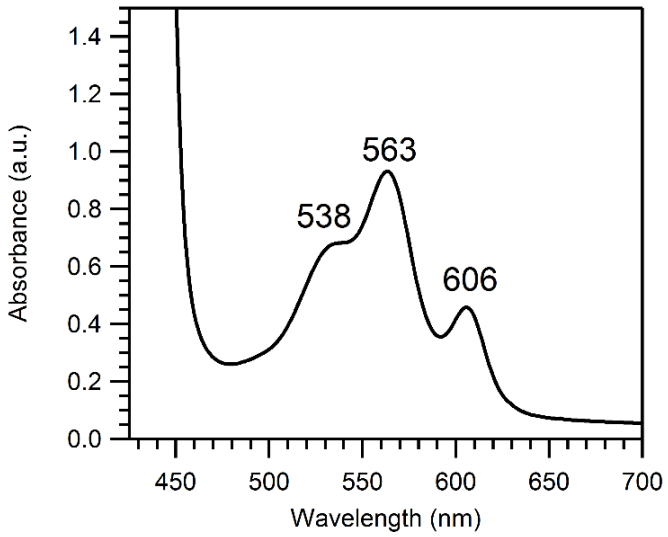

Figure A8. Optical spectrum of 0.1 mM Fe^{II}(TPP) Q-bands in DMF containing 0.1 M [*n*-Bu_4N][PF_6].

A.2 Electron Transfer Equilibrium

A.2.1 Optical UV-vis measurements of K_{ET}

In order to probe the equilibrium between [Fe^{III}(TPP)]OTf + Fc* and Fe^{II}(TPP) + Fc*$^{+}$, two UV-vis experiments were performed.

A.2.1.1 Titration of Fc to a [Fe^{III}(TPP)]OTf solution*

In one experiment, spectra were obtained for solutions in which [Fe^{III}(TPP)]OTf was titrated with Fc* (amounts in the **Figure A9** caption). These experiments were done in DMF with 0.1 M [*n*-Bu$_4$N][PF$_6$] to match the ionic strength of parallel electrochemical measurements. The optical spectra of the Q-bands show the conversion of [Fe^{III}(TPP)]OTf to Fe^{II}(TPP) (eq A.1, **Figure A9**) upon addition of Fc*. After correcting for dilution, single wavelength fittings were performed at 524, 563, and 685 nm to calculate the percent of Fe^{II}(TPP) after each Fc* addition (eq A.2, **Table A1**, **Figure A10**). The absorbance contributions from Fc* and Fc*$^{+}$ at these wavelengths were small and could be neglected. The average amount of Fe^{II}(TPP) approaches 74 ± 5% when 100-fold excess Fc* is added. From the ratio of [Fe^{III}(TPP)]OTf to Fe^{II}(TPP) and the known concentration of added Fc*, the average K_{ET} was estimated as 0.08 ± 0.03 (eq A.3). This value was similar to the equilibrium constant estimated electrochemically, K_{ET} = 0.12 ± 0.03.

$$\mathrm{Fc^{*}} + \mathrm{Fe^{III}(TPP)^{+}} \rightleftharpoons \mathrm{Fc^{*+}} + \mathrm{Fe^{II}(TPP)} \qquad \text{(eq A.1)}$$

$$\mathrm{A_x} = \varepsilon_{\mathrm{x,Fe(III)}} \times [\mathrm{Fe^{III}(TPP)]OTf} + \varepsilon_{\mathrm{x,Fe(II)}} \times [\mathrm{Fe^{II}(TPP)}] \qquad \text{(eq A.2)}$$

$$K_{\mathrm{ET}} = \frac{[\mathrm{Fc^{*+}}][\mathrm{Fe^{II}(TPP)}]}{[\mathrm{Fc^{*}}][[\mathrm{Fe^{III}(TPP)}]^{+}]} \qquad \text{(eq A.3)}$$

Table A1. Molar absorptivity values (M^{-1} cm^{-1}) for fitting used in eq A.2.

Compound	ε_{528}	ε_{564}	ε_{685}
[Fe^{III}(TPP)]OTf	$(11.9 \pm 0.7) \times 10^3$	$(3.1 \pm 0.1) \times 10^3$	$(3.1 \pm 0.5) \times 10^3$
Fe^{II}(TPP)	$(7.5 \pm 0.7) \times 10^3$	$(10.4 \pm 0.7) \times 10^3$	$(4.8 \pm 0.6) \times 10^1$

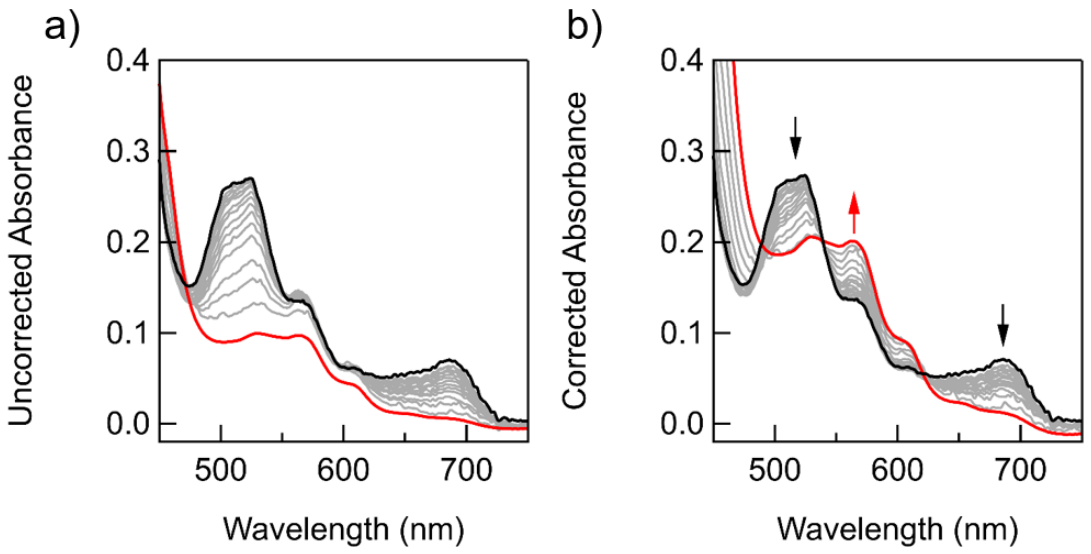

Figure A9. (**A**) Optical spectra in the Q-band region for a titration of a 3.0 mM solution of Fc* into a 30 μM solution [Fe^{III}(TPP)]OTf containing 0.1 M [*n*-Bu_4N][PF_6]. Equivalents of [Fc*] added (from black to red): 0, 0.2, 0.4, 0.6, 0.8, 1, 2, 3, 5, 7, 15, 25, 50, and 100 equivalents. Black trace: initial spectrum of 30 μM [Fe^{III}(TPP)]OTf in DMF. Red trace: final spectrum of Fe^{II}(TPP) after 100 equivalents of Fc* had been added to the [Fe^{III}(TPP)]OTf solution. (**B**) The same spectra after being corrected for dilution.

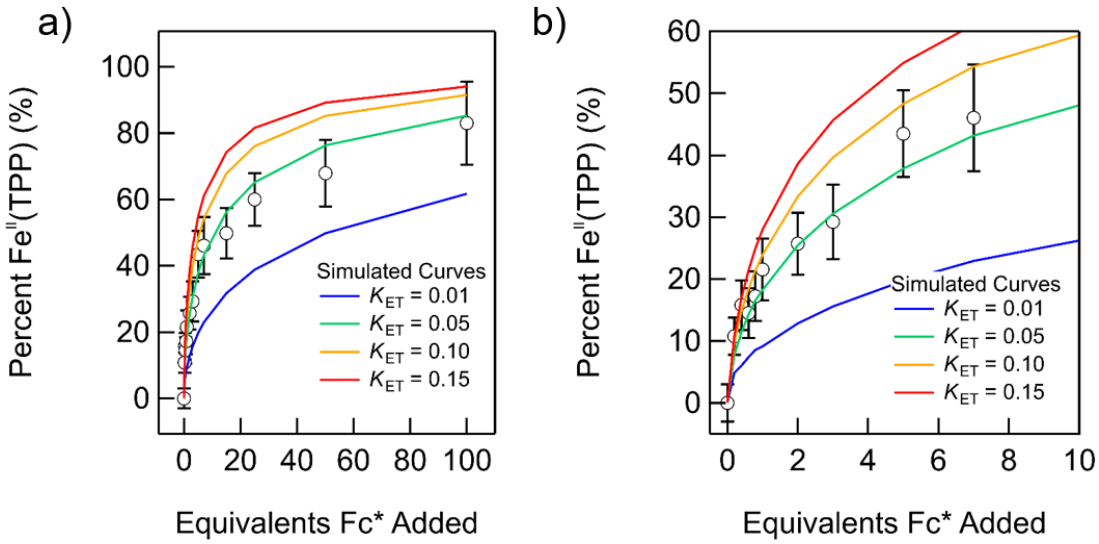

Figure A10. (**A**) Open circles: the percent Fe^{II}(TPP) upon titration of Fc* to [Fe^{III}(TPP)]OTf (amounts in **Figure A9** caption), averaged from single wavelength fittings at 524 nm, 563 nm, and 685 nm (see above for details). Simulated equilibrium curves are shown atop experimental data with K_{ET} values noted in the legend. (**B**) The same data, focused on the 0 – 10 equivalent Fc* portion of the titration.

A.2.1.2 Re-oxidation of Fe^{II}(TPP) via Fc^{*+} addition

To the final solution from **Figure A9** was added 50 equivalents Fc^{*+} (vs. initial [Fe^{III}(TPP)]OTf). After correcting the spectra for dilution and for absorbance contributions from excess Fc^{*+}, the Q-band spectra show the re-formation of [Fe^{III}(TPP)]OTf from the Fe^{II}(TPP) sample at the end of the Fc* titration experiment (**Figure A11**). That [Fe^{III}(TPP)]OTf could be reformed from the oxidation of Fe^{II}(TPP) via Fc^{*+} evidences electron transfer reversibility.

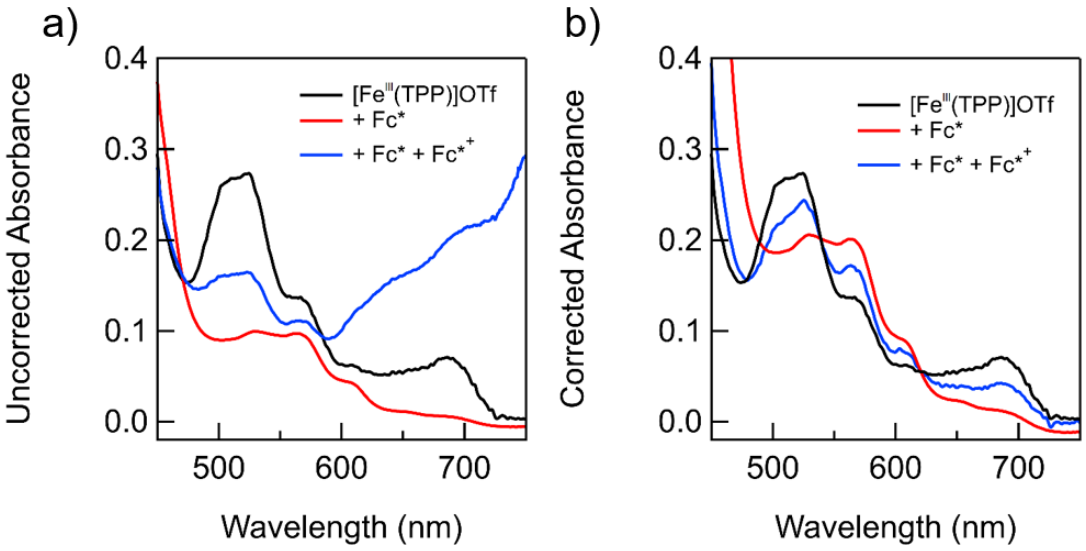

Figure A11. (**A**) Optical spectra in the Q-band region after the titration of a 3.0 mM solution of Fc* and a 3.0 mM solution of Fc^{*+} into a 30 μM solution [Fe^{III}(TPP)]OTf containing 0.1 M [*n*-Bu_4N][PF_6]. Black trace: initial spectrum of 30 μM [Fe^{III}(TPP)]OTf in DMF. Red trace: spectrum of Fe^{II}(TPP) after 100 equivalents of Fc* had been added to the [Fe^{III}(TPP)]OTf solution. Blue trace: spectrum of the same sample after addition of ~50 equivalents of Fc^{*+}. (**B**) The same spectra after being corrected for dilution and contributions from excess Fc^{*+} absorbance.

A.2.1.3 Electron transfer van 't Hoff analysis

A second UV-vis experiment was performed to measure K_{ET} at a variety of temperatures and to construct a van 't Hoff plot, as presented in the Chapter 2 (**Figure 2.1**). In this experiment, a Kontes cuvette was charged with DMF containing 0.1 M [*n*-Bu_4N][PF_6] and 100 μM of Fc^{*+}, Fc*, [Fe^{III}(TPP)]OTf, and Fe^{II}(TPP). The cuvette was placed in a cryostat set to 293 K and allowed to thermally equilibrate for five minutes before a UV-vis spectrum was collected. The sample was then cooled to 213 K before a second spectrum was collected. The solution was warmed incrementally (5 degrees at a time) with spectra being collected at each temperature (see **Figure 2.1** in Chapter 2).

As described above for the Fc* titration data, the variable temperature spectra were analyzed by fitting the absorbance contributions from $[Fe^{III}(TPP)]OTf$ and $Fe^{II}(TPP)$ using eq A.2. As before, the absorbance contributions from Fc* and Fc^{*+} were small and were ignored in the fitting. Single wavelength fits were performed at 524, 563, and 685 nm and averaged to determine the mol percentage of $[Fe^{III}(TPP)]OTf$ and $Fe^{II}(TPP)$ (the sum of the two concentrations being equal to 1.0) at each temperature (**Figure A12**). Using the ratio of $Fe^{III}(TPP)^{+}/Fe^{II}(TPP)$ and assuming mass balance reactions with Fc* and Fc^{*+} respectively, K_{ET} was determined at each temperature. The values of K_{ET} are reported in **Table A2**.

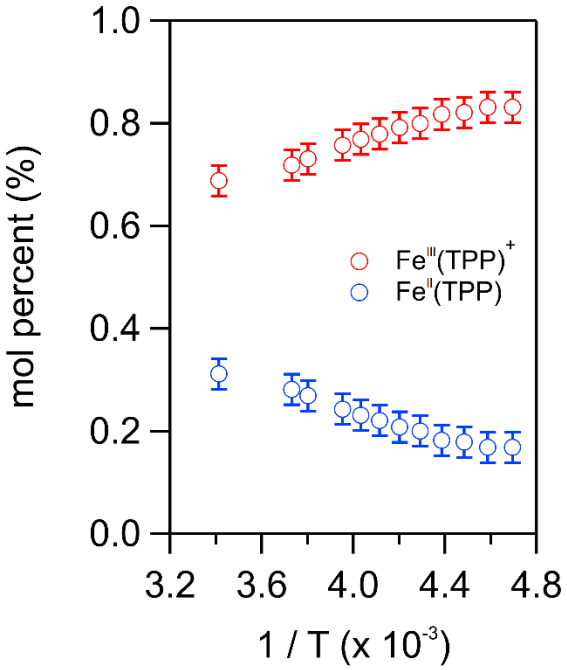

Figure A12. The mol percentage of $[Fe^{III}(TPP)]OTf$ and $Fe^{II}(TPP)$ at each temperature used to construct the van 't Hoff plot. These values were calculated by averaging three single wavelength fits at 524, 563, and 685 nm for the UV-vis experiment described in the text.

Table A2. K_{ET} values for electron transfer between Fc* + [Fe^{III}(TPP)]OTf and Fc*$^{+}$ + Fe^{II}(TPP). The data below was used to construct the van 't Hoff plot presented in Chapter 2.

Temperature (K)	ln(K_{ET})
213.0	-3.20 ± 0.20
218.0	-3.19 ± 0.20
223.0	-3.06 ± 0.20
228.0	-3.00 ± 0.20
233.0	-2.77 ± 0.20
238.0	-2.67 ± 0.20
243.0	-2.53 ± 0.20
248.0	-2.41 ± 0.20
253.0	-2.28 ± 0.20
263.0	-2.00 ± 0.20
268.0	-1.88 ± 0.20
293.0	-1.59 ± 0.20

A.2.2 Electrochemical measurement of K_{ET}

Finally, K_{ET} was estimated from the difference in the reduction potentials of decamethylferrocenium ($E_{1/2}$(Fc*$^{+}$/Fc*) = -0.484 V vs. Fc^{+}/Fc) and [Fe^{III}(TPP)]OTf ($E_{1/2}$([Fe^{III}(TPP)]OTf/Fe^{II}(TPP) = -0.538 V vs. Fc^{+}/Fc). The reduction potential of Fc*$^{+}$/Fc* has been reported elsewhere.[9] The reduction potential of [Fe^{III}(TPP)]OTf/Fe^{II}(TPP) was averaged from 30 experiments, each of which was conducted in DMF containing *p*TsOH and 0.1 M [*n*-Bu$_4$N][PF$_6$] and was internally referenced to Fc^{+}/Fc. (See electrochemistry section below for further experimental details.) The 54 mV difference in reduction potential corresponds to $\Delta G°_{ET}$ = 1.22 kcal mol^{-1} and K_{ET} = 0.122 at 293 K using the equations for Gibbs free energy, below. As noted above and in Chapter 2, this value for K_{ET} is in close agreement with optical UV-vis measurements of K_{ET}.

$$\Delta G° = -nFE°$$

$$\Delta G° = -nF\left(E_{1/2}\left([\mathrm{Fe^{III}(TPP)]OTf\ /\ Fe^{II}(TPP)}\right) - E_{1/2}(\mathrm{Fc^{*+}\ /Fc^{*}})\right)$$

$$= -(1)(96485)\left(-0.538-(-0.484)\right) = 5105\ \mathrm{J\ mol^{-1}}\ \text{or}\ 1.22\ \mathrm{kcal\ mol^{-1}}$$

$$\Delta G° = -RT\ln\left(K_{ET}\right)$$

$$K_{ET} = \exp(-\Delta G° / RT)$$

$$= \exp\left(-(5105)/(8.314\times 293)\right) = 0.122$$

K_{ET} was independently measured using a variety of methods, including:

1. Optically via titration of Fc* into a solution of [Fe^{III}(TPP)]OTf. The collected spectra were fit to yield rough estimates for K_{ET} at 293 K.
2. Using van 't Hoff analysis of a DMF solution containing electrolyte and equimolar Fc^{*+}, Fc*, [Fe^{III}(TPP)]OTf and Fe^{II}(TPP).
3. By taking the difference in the reported reduction potentials of $E_{1/2}(Fc^{*+}/Fc^{*})$ and $E_{1/2}([Fe^{III}(TPP)]^{+}/Fe^{II}(TPP))$, see Chapter 2.

The values for K_{ET} at 293 K are consistent across all of these independent measurements and are reported in **Table A3**.

Table A3. K_{ET} values obtained using optical measurements and electrochemical measurements.

Method	K_{ET} (293 K)
UV-vis titrations [a]	0.08 ± 0.03
van 't Hoff analysis [b]	0.16 ± 0.03
Electrochemical [c]	0.122 ± 0.01

[a] From titration of Fc* into [Fe^{III}(TPP)]OTf, see above discussion. [b] From the enthalpy and entropy values obtained using the van 't Hoff plot. [c] From the difference in $E_{1/2}(Fc^{*+}/Fc^{*})$ and $E_{1/2}(Fe^{III}(TPP)^{+}/Fe^{II}(TPP))$ reduction potentials, see Chapter 2.

A.3 O_2 Binding Equilibrium

The equilibrium constants for O_2 binding to Fe^{II}(TPP) in DMF containing 0.1 M [*n*-Bu_4N][PF_6] were determined by optical spectroscopy. Electrolyte was included in these measurements in order to match the conditions used for electrochemistry and stopped-flow kinetics. These measurements were made using a Unisoku Unispeks cryostat at temperatures between 213 K and 238 K to minimize the decomposition of Fe^{III}(TPP)($O_2^{\bullet-}$) into the μ-oxo dimer. At 213 K, Fe^{III}(TPP)($O_2^{\bullet-}$) decomposed slowly within an hour. Temperatures below 213 K were prohibited by the solvent freezing temperature (ca. 212 K, in the absence of electrolyte).

A.3.1 Titrations with Dissolved O_2

In a typical experiment, a DMF solution of 60-80 μM Fe^{II}(TPP) and 0.1 M [*n*-Bu_4N][PF_6] was loaded under N_2 into a 1 cm pathlength quartz cuvette (with a stirbar) and capped with an air-tight rubber septum. The sample was removed from the glovebox, placed in a spectrometer equipped with a cryostat, cooled to 213 K, and allowed to thermally equilibrate, while stirring, for 15 minutes. A separate DMF solution containing 0.1 M [*n*-Bu_4N][PF_6] was sparged with dry O_2 before being taken up in a syringe. Aliquots (5-20 μL) of the oxygenated solvent were titrated into the cold, stirring solution of Fe^{II}(TPP). UV-vis spectra were collected after every aliquot addition (**Figure A13**). Approximately 100 μL of the oxygenated solvent was required to reach 1 equivalent of [O_2] relative to [Fe^{II}(TPP)] (**Figure A14**).

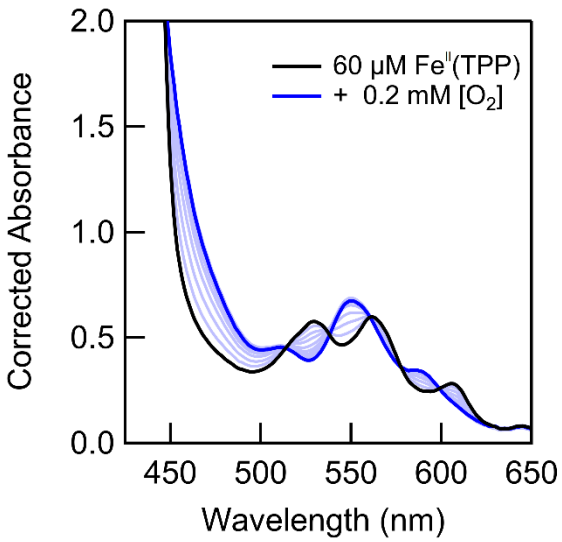

Figure A13. Optical spectra in the Q-band region for a titration that added solutions of O_2 in DMF into a 213 K sample of 60 μM Fe^{II}(TPP) in DMF containing 0.1 M [*n*-Bu_4N][PF_6]. Titrations were made such that [O_2] was between 0 to 3 equivalents vs. [Fe^{II}(TPP)]. Spectra are corrected for dilution.

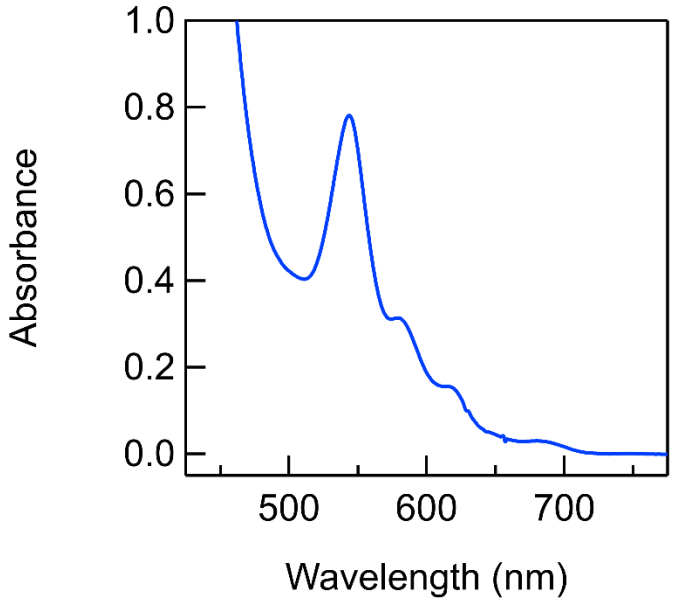

Figure A14. The Q-band section of the optical absorbance spectrum of 70 μM Fe^{III}(TPP)($O_2^{\bullet-}$) in DMF containing 0.1 M [*n*-Bu_4N][PF_6] at 213 K. λ_{max}, nm (ε, M^{-1} cm^{-1}): 544 ((1.2 ± 0.1) × 10^4), 570 sh ((4.7 ± 0.5) × 10^3).

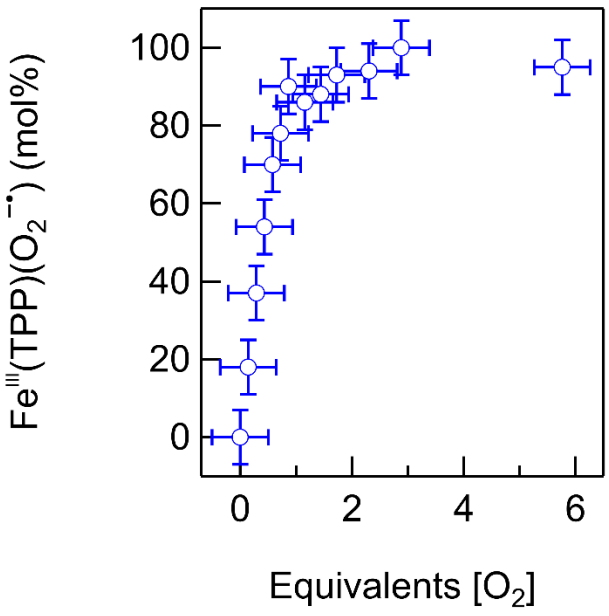

Figure A15. Mol percent $Fe^{III}(TPP)(O_2^{\bullet-})$ formed upon titrating 60 μM $Fe^{II}(TPP)$ with DMF containing dissolved O_2 at 213 K. The mol percentages were determined by fitting dilution-corrected UV-vis data to linear combinations of the $Fe^{II}(TPP)$ and $Fe^{III}(TPP)(O_2^{\bullet-})$ spectra.

A.3.2 Reversible O_2 Binding

The reversibility of O_2 binding was studied by first preparing a sample of $Fe^{II}(TPP)$ in DMF containing 0.1 M [*n*-Bu_4N][PF_6]. The sample was cooled to 213 K before a spectrum was collected. The sample of $Fe^{II}(TPP)$ was then gently bubbled with O_2 (1 atm) for five minutes before removing the needle and collecting another spectrum. The same solution at 213 K was then sparged with argon for five minutes before a final spectrum was collected. The final spectrum contains absorbance contributions from both $Fe^{II}(TPP)$ and $Fe^{III}(TPP)(O_2^{\bullet-})$, with more than 90% $Fe^{II}(TPP)$ (**Figure A16**). In a related study of O_2 binding to $Fe^{II}(F_8TPP)$ in toluene, the authors report difficulty in completely removing O_2 from solution. As reported, complete reversibility was only observed after both sparging with argon and pulling vacuum on the oxygenated sample.[10] In our experiment, it is possible that partial degradation to the μ-oxo dimer occurs; however, the region between 500 nm and 560 nm (where there is no significant absorbance from the dimer) fits well to a combination of $Fe^{II}(TPP)$ and $Fe^{III}(TPP)(O_2^{\bullet-})$ with good mass-balance.

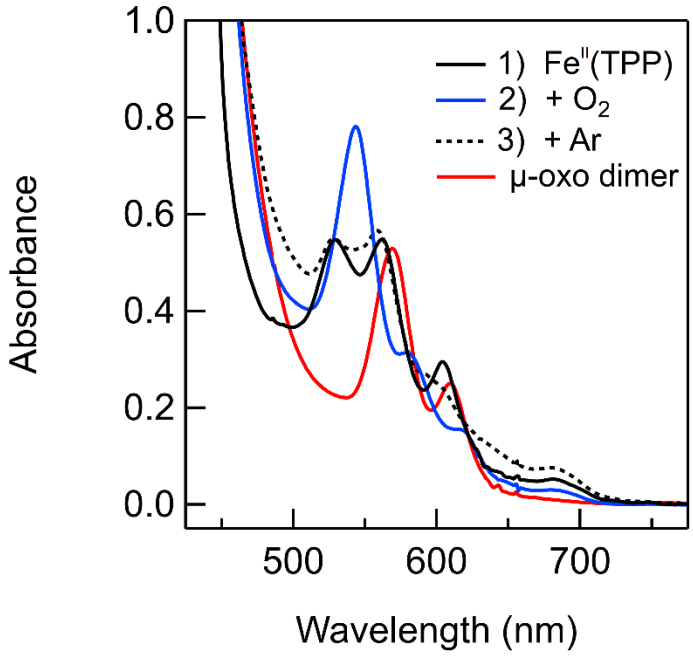

Figure A16. Black line (solid): Optical spectrum of $Fe^{II}(TPP)$ at 213 K. Blue line: Optical spectrum of $Fe^{III}(TPP)(O_2^{\bullet-})$, generated by bubbling $Fe^{II}(TPP)$ with O_2. Black line (dashed): Product spectrum after bubbling $Fe^{III}(TPP)(O_2^{\bullet-})$ with argon. All spectra collected at 213 K on the same sample, which was originally prepared as 70 μM $Fe^{II}(TPP)$ in DMF containing 0.1 M [*n*-Bu_4N][PF_6]. Red line: Reference spectrum of 70 μM $Fe^{III}(TPP)_2O$ under identical conditions.

A.3.3 Experimental and Fitting Methods for K_{O2}

Measuring the O_2-binding equilibrium – Method 1. To a quartz cuvette was added a stirbar and 2.0 mL of a solution of DMF containing 0.1 M [*n*-Bu_4N][PF_6]. The solution was sparged with 1 atm O_2 for five minutes before the cuvette was tightly capped with a rubber septum. The cuvette was cooled to 213 K with gentle stirring such that the gas-liquid interface was observed to be still. A separate solution of 0.1 mM $Fe^{II}(TPP)$ in DMF was prepared in a N_2 glovebox and was taken up in a syringe with some extra N_2 headspace. The tip of the syringe needle was stoppered by semi-puncturing a rubber septum before being removed from the glovebox. The syringe was removed from the glovebox, and the needle was driven through the rubber septum of the cuvette. The needle was flushed with the N_2 headspace taken up in the syringe before submerging the tip of the needle in the cold DMF. Approximately 150 μL of the room temperature $Fe^{II}(TPP)$ solution was very slowly added to the cold solution and was left to equilibrate for 5 minutes before taking an initial spectrum. The solution was then heated incrementally from 213 K to 238 K with spectra being collected every 2.5 degrees (**Figure A17A**). By this method, we know that [O_2] is 3.1 mM at the beginning of the

experiment and that the small cuvette headspace (~1 mL) contains 1 atm O_2. The gas-liquid interface was still during cooling, so it was assumed that the dissolution of additional O_2 was slow and negligible during the length of the experiment. Under these conditions and before addition of the anaerobic Fe^{II}(TPP solution, the [O_2] concentration at 213 K was approximately equal to 3.1 mM. After addition of the Fe^{II}(TPP) solution, [O_2] was corrected for dilution.

In order to estimate any potential effects of having underestimated the dissolved [O_2] concentration using Method 1, a second method for estimating K_{O_2} values was performed (detailed below). In this complementary experiment, a solution of Fe^{II}(TPP) was *first* cooled to 213 K *before* the solution was bubbled with O_2. As before, the generated Fe^{III}(TPP)($O_2^{\bullet-}$) was then warmed with spectra being collected at each temperature (**Figure A17B**). These spectra were fit to the same K_{O_2} expression (again assuming initial [O_2] = 3.1 mM). All of the K_{O_2} values were consistently larger than those measured using Method 1 (**Table A5**). This was unsurprising given that [O_2] using Method 2 is likely higher than 3.1 mM. The maximum deviation between Method 1 and Method 2 data was 0.5 ln(K_{O_2}) units, which suggests that [O_2] in cold DMF (between 213 K and 238 K) at 1 atm O_2 is roughly 70% larger than [O_2] under the same conditions at room temperature. If we assume the maximum error in [O_2], the calculated entropy term could – at most – be affected by 2 cal mol^{-1} K^{-1} due to changes in O_2 solubility. When this error is summed with the error of the van 't Hoff linear regression, $\Delta S = 32 \pm 4$ cal mol^{-1} K^{-1}.

Measuring the O_2-binding equilibrium – Method 2. In a N_2 glovebox, a solution of DMF containing 0.1 M [*n*-Bu_4N][PF_6] and 60 μM Fe^{II}(TPP) was prepared and loaded into a quartz cuvette with a stirbar. The cuvette was tightly capped with a rubber septum before being removed from the glovebox and cooled to 213 K in the spectrometer. While cooling, the solution was bubbled with argon. After reaching 213 K, an initial spectrum was collected of Fe^{II}(TPP). The argon line was then replaced with an O_2 stream, and the solution was gently bubbled for five minutes before a second spectrum was collected. The O_2 needle was removed from the cuvette, which was left under a still atmosphere of O_2 and the 213 K solution was then incrementally heated to 238 K with spectra being collected every 2.5 degrees (**Figure A17**). By this method, we know that [O_2] is greater than 3.1 mM for all temperatures. This is evident by comparing the spectra collected at 238 K for the

two methods (**Figure A17**), where the spectrum for Method 1 shows a higher percentage of Fe^{II}(TPP) than does the spectrum for Method 2.

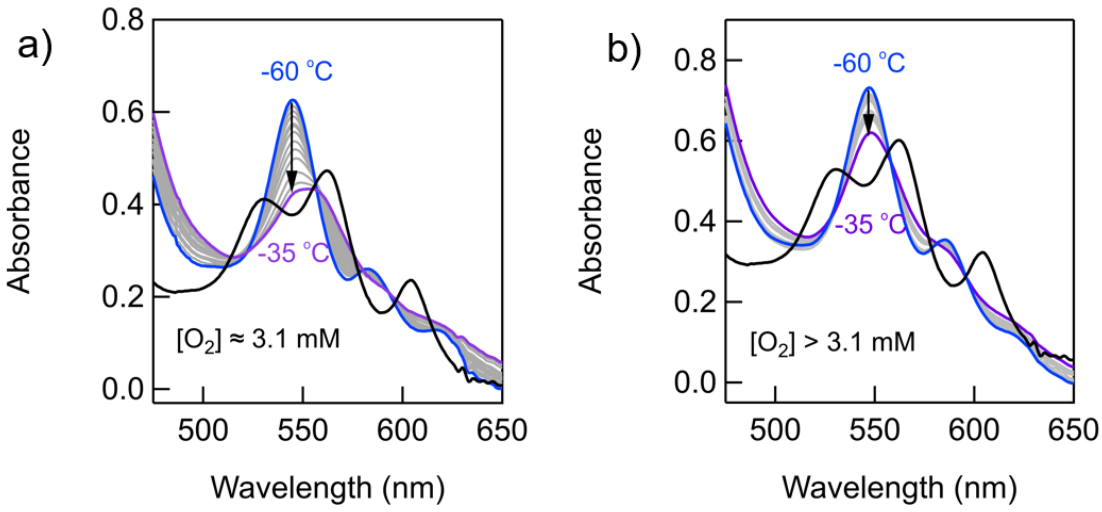

Figure A17. (**A**) Optical spectra of the equilibrium conversion between Fe^{II}(TPP) and Fe^{III}(TPP)($O_2^{\bullet-}$) at different temperatures using Method 1. The black trace is a reference spectrum of 50 μM Fe^{II}(TPP). Grey traces are intermediate temperatures between 213 K and 238 K in 2.5-degree increments. (**B**) Optical spectra of the equilibrium conversion between Fe^{II}(TPP) and Fe^{III}(TPP)($O_2^{\bullet-}$) at different temperatures using Method 2. Grey traces are intermediate temperatures between 213 K and 238 K in 2.5-degree increments. All spectra collected in DMF solutions containing 0.1 M [*n*-Bu_4N][PF_6].

Fitting methods and examples for K_{O_2} measurements. In order to measure K_{O_2} values, the ratio of Fe^{II}(TPP) and Fe^{III}(TPP)($O_2^{\bullet-}$) were determined from the temperature-dependent UV-vis spectra. In all cases, the total concentration of iron tetraphenylporphyrin is known. The presence of isosbestic points indicates mass-balance and allows us write eq A.4.

$$[\mathrm{Fe(TPP)}]_{\mathrm{total}} = [\mathrm{Fe^{II}(TPP)}] + [\mathrm{Fe^{III}(TPP)}(\mathrm{O_2^{\bullet-}})] \qquad \text{(eq A.4)}$$

In the case of Method 1 (see above), the total concentration of dissolved O_2 is also known and can be written using eq A.4, where $[O_2]_{\mathrm{total}}$ = 3.1 mM and $[O_2]_{\mathrm{free}}$ is the concentration of dissolved O_2 not bound as Fe^{III}(TPP)($O_2^{\bullet-}$).

$$[\mathrm{O_2}]_{\mathrm{total}} = [\mathrm{O_2}]_{\mathrm{free}} + [\mathrm{Fe^{III}(TPP)}(\mathrm{O_2^{\bullet-}})] \qquad \text{(eq A.5)}$$

Eq A.4 and A.5 can be combined with the equilibrium constant for O_2 binding (eq A.6) to yield a convenient expression that only requires knowing: $[O_2]_{total}$, $[Fe(TPP)]_{total}$ and the mol percent Fe^{III}(TPP)($O_2^{\bullet-}$) (expressed as x) at each temperature.

$$K_{O_2}(M^{-1}) = \frac{[Fe^{III}(TPP)(O_2^{\bullet-})]}{[O_2]_{free}[Fe^{II}(TPP)]}$$

$$K_{O_2}(M^{-1}) = \frac{x}{(1-x)([O_2]_{total} - x[Fe(TPP)]_{total})} \quad \text{(eq A.6)}$$

At each temperature the ratio of $Fe^{II}(TPP)$ to $Fe^{III}(TPP)(O_2^{\bullet-})$ was measured by simulating a combination of the two known spectra (using mass balance) and minimizing the difference. Below are examples in which the simulated and experimental data are compared (**Figure A18**). Between 213 K and 238 K, the fits are very good and are accurate within 3% of the actual mol percentages of $Fe^{II}(TPP)$ and $Fe^{III}(TPP)(O_2^{\bullet-})$. At warmer temperatures, the fits are poorer due to the formation of the μ-oxo dimer.

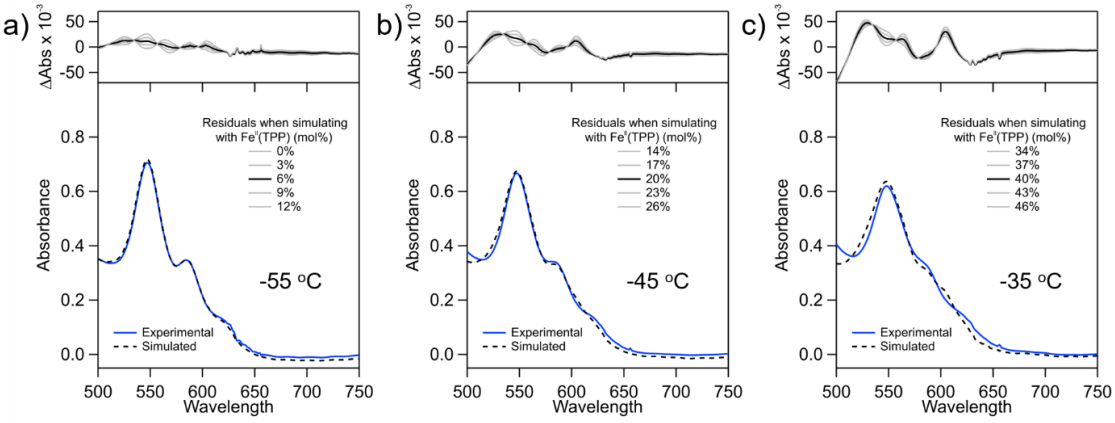

Figure A18. Experimental and simulated optical spectra for a solution of 60 μM $Fe^{II}(TPP)$ and 3.1 mM $[O_2]$ in DMF containing 0.1 M $[n\text{-}Bu_4N][PF_6]$. Simulating the data with varying amounts of $Fe^{II}(TPP)$ and subtracting the experimental spectrum yields residuals (ΔAbs) that can be minimized. The data shown are for solutions at (**A**) 218 K, (**B**) 228 K, and (**C**) 238 K.

In order to estimate the percent μ-oxo dimer formed during the warming experiments, a secondary fitting analysis was used to interpret the spectrum collected at the warmest temperature, 238 K. A system of linear equations based on Beer's Law was used to calculate the absorbance contributions from $Fe^{II}(TPP)$, $Fe^{III}(TPP)(O_2^{\bullet-})$, and $Fe^{III}(TPP)_2O$. Each of these species has a distinct spectroscopic signature, so the catalyst speciation could be calculated using the epsilons at 542, 564, and 572 nm, the λ_{max} values of $Fe^{II}(TPP)$, $Fe^{III}(TPP)(O_2^{\bullet-})$, and $Fe^{III}(TPP)_2O$, respectively.

$$A_{542} = \varepsilon_{542,Fe^{III}(TPP)(O_2^{\bullet-})}[Fe^{III}(TPP)(O_2^{\bullet-})] + \varepsilon_{542,Fe^{III}(TPP)_2O}[Fe^{III}(TPP)_2O] + \varepsilon_{542,Fe^{II}(TPP)}[Fe^{II}(TPP)] \quad \text{(eq A.7)}$$

$$A_{564} = \varepsilon_{564,Fe^{III}(TPP)(O_2^{\bullet-})}[Fe^{III}(TPP)(O_2^{\bullet-})] + \varepsilon_{564,Fe^{III}(TPP)_2O}[Fe^{III}(TPP)_2O] + \varepsilon_{564,Fe^{II}(TPP)}[Fe^{II}(TPP)] \quad \text{(eq A.8)}$$

$$A_{572} = \varepsilon_{572,Fe^{III}(TPP)(O_2^{\bullet-})}[Fe^{III}(TPP)(O_2^{\bullet-})] + \varepsilon_{572,Fe^{III}(TPP)_2O}[Fe^{III}(TPP)_2O] + \varepsilon_{572,Fe^{II}(TPP)}[Fe^{II}(TPP)] \quad \text{(eq A.9)}$$

Equations A.7-A.9 can be simplified as a product of matrices (eq A.10):

$$\begin{bmatrix} A_{542} \\ A_{564} \\ A_{572} \end{bmatrix} = \begin{bmatrix} \varepsilon_{542,Fe^{III}(TPP)(O_2^{\bullet-})} & \varepsilon_{542,Fe^{III}(TPP)_2O} & \varepsilon_{542,Fe^{II}(TPP)} \\ \varepsilon_{564,Fe^{III}(TPP)(O_2^{\bullet-})} & \varepsilon_{564,Fe^{III}(TPP)_2O} & \varepsilon_{564,Fe^{II}(TPP)} \\ \varepsilon_{572,Fe^{III}(TPP)(O_2^{\bullet-})} & \varepsilon_{572,Fe^{III}(TPP)_2O} & \varepsilon_{572,Fe^{II}(TPP)} \end{bmatrix} \begin{bmatrix} [Fe^{III}(TPP)(O_2^{\bullet-})] \\ [Fe^{III}(TPP)_2O] \\ [Fe^{II}(TPP)] \end{bmatrix} \quad \text{(eq A.10)}$$

The molar absorptivity values of $Fe^{III}(TPP)_2O$, $Fe^{II}(TPP)$, and $Fe^{III}(TPP)(O_2^{\bullet-})$ at the wavelengths of interest were determined by independent optical measurements and are reported in **Table A4**.

Table A4. Molar absorptivity values (M^{-1} cm^{-1}) for catalyst species used to fit the O_2 binding data at 238 K

Compound	ε_{542}	ε_{564}	ε_{572}
$Fe^{III}(TPP)(O_2^{\bullet-})$	$(1.2 \pm 0.1) \times 10^4$	$(6.4 \pm 0.6) \times 10^3$	$(5.2 \pm 0.4) \times 10^3$
$Fe^{II}(TPP)$	$(7.6 \pm 0.6) \times 10^3$	$(10.4 \pm 0.7) \times 10^3$	$(8.9 \pm 0.5) \times 10^3$
$Fe^{III}(TPP)_2O$	$(4.0 \pm 0.5) \times 10^3$	$(8.9 \pm 0.4) \times 10^3$	$(10.0 \pm 0.7) \times 10^3$

Using equations A.7−A.10 and the molar absorptivity values in **Table A4**, the concentrations of $Fe^{II}(TPP)$, $Fe^{III}(TPP)(O_2^{\bullet-})$ and $Fe^{III}(TPP)_2O$ were determined at 238 K. From the solved matrix, the mass-balance is within 5% of the actual cumulative [Fe(TPP)]. The percent contributions of the three species were: 60.7, 45,1, and 0.2% for $Fe^{II}(TPP)$, $Fe^{III}(TPP)(O_2^{\bullet-})$ and $Fe^{III}(TPP)_2O$, respectively. The contributions from $Fe^{II}(TPP)$ and $Fe^{III}(TPP)(O_2^{\bullet-})$ are within the original estimates reported in **Figure A18**. The percent contribution of $Fe^{III}(TPP)_2O$ is small and negligible for the analysis herein.

Table A5. K_{O2} (M^{-1}) values for O_2 binding to Fe^{II}(TPP). Only Method 1 data was used to construct the van 't Hoff plot.

Temperature (K)	ln(K_{O_2}) (M^{-1}) Method 1	ln(K_{O_2}) (M^{-1}) Method 2
213.0	8.85 ± 0.10	9.27 ± 0.10
215.5	8.54 ± 0.10	8.97 ± 0.10
218.0	8.23 ± 0.10	8.74 ± 0.10
220.5	7.88 ± 0.15	8.23 ± 0.15
223.0	7.69 ± 0.15	7.99 ± 0.15
225.5	7.45 ± 0.15	7.69 ± 0.15
228.0	7.18 ± 0.15	7.53 ± 0.15
230.5	6.89 ± 0.20	7.18 ± 0.20
233.0	6.64 ± 0.20	7.00 ± 0.20
235.5	6.41 ± 0.20	7.00 ± 0.20
238.0	6.19 ± 0.20	6.64 ± 0.20

As a reference, all $K_{O_2}(M^{-1})$ values from both Method 1 and Method 2 were also reproduced on the same van 't Hoff plot, below (**Figure A19**). All of the Method 2 values for K_{O_2} are consistently higher than those of Method 1. This is to be expected, because Method 2 is assumed to generate a more concentrated solution of [O_2] (directly sparging a cold DMF solution) than Method 1 (sparging at room temperature), which would lead to an overestimation of ln(K_{O2}) by up to 0.5 units.

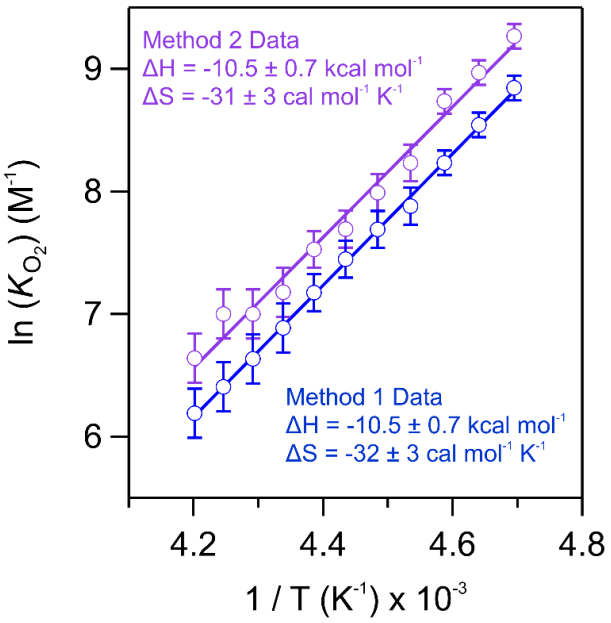

Figure A19. van 't Hoff plots for K_{O2} vs T^{-1} with equilibrium measurements using both Method 1 and Method 2.

A.3.4 Statistical Analysis of the O_2 Binding van 't Hoff plot

As detailed above, the experimental measurements of $K_{O_2}(M^{-1})$ were performed between 213 K and 238 K. In order to compare to the data modeled using COPASI, below, the van 't Hoff plot must be extrapolated to room temperature (298 K), more than 60 degrees warmer than the highest temperature accessed during the O_2-binding measurements. A T-test statistical analysis on the van 't Hoff plot was used to determine the 95% confidence intervals of ΔH_{O2}, ΔS_{O2}, and K_{O_2} at 298 K.

The O_2 binding van 't Hoff plot produced using Method 1 of K_{O_2} was fit to a linear regression of the form y = *m*x + b, where *m* = 5376 ± 63.1 and b = -16.421 ± 0.28 (average ± standard deviation). This experiment was performed twice, so the number of samples is two (*N* = 2).

The 95% confidence interval for *m* is between 4809 and 5942. The 95% confidence interval for *b* is between -18.93 and -13.91. These confidence intervals were converted into values for ΔH_{O2} and ΔS_{O2} using the van 't Hoff equation. The 95% confidence interval for ΔH_{O2} is between -9.55 and -11.80 kcal mol^{-1} when rounded to three significant figures. Likewise, the 95% confidence interval for ΔS_{O2} is between -37.6 and -27.6 cal mol^{-1} K^{-1} when rounded to three significant figures. Using the confidence intervals for ΔH_{O2} and ΔS_{O2} and accounting for error propagation, ΔG_{O2} (at 298 K) = -0.94 ± 1.85. The 95% confidence interval for K_{O_2} at 298 K is therefore between 0.211 M^{-1} and 111 M^{-1}. The data modeled using COPASI fits within this confidence interval (see **Table A7**, below).

A.4 Electrochemical Kinetic Data

The voltammetric response of the iron(III) tetraphenylporphyrin catalyst was analyzed in the absence of O_2 at various scan rates (10-1000 mV/s). Plots of peak current vs. the square root of scan rate ($v^{1/2}$) were linear, as expected for a diffusion-limited response (**Figure A20**).[11]

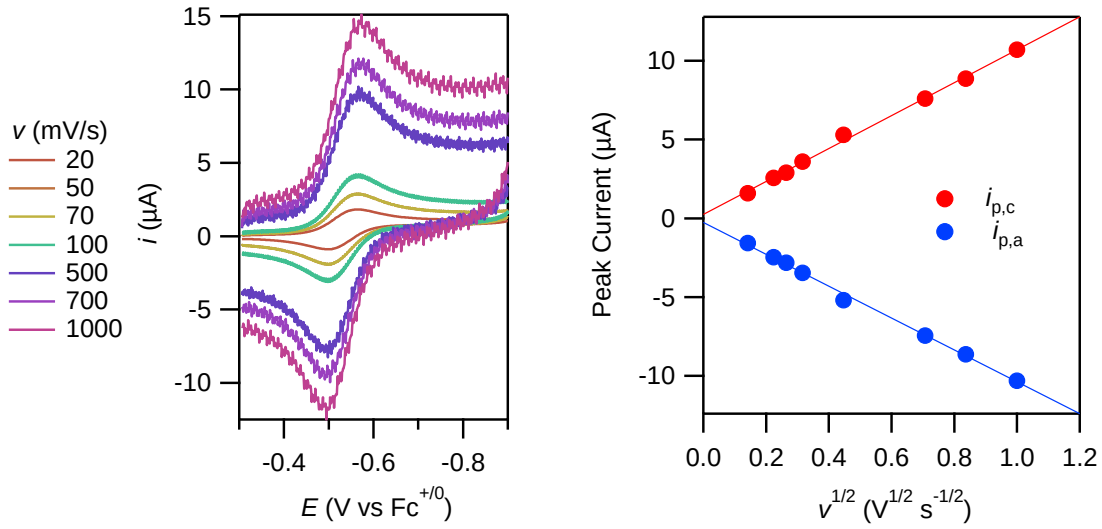

Figure A20. (**A**) Scan rate dependence of [Fe^{III}(TPP)]OTf in the presence of 10 mM *p*TsOH. (**B**) Plot of peak cathodic ($i_{p,c}$) and anodic ($i_{p,a}$) current from (a) as a function of the square root of the scan rate.

For kinetic measurements, 0.3 mM Fe^{III}(TPP)Cl was added to a solution of DMF containing 0.1 M [*n*-Bu_4N][PF_6], ~1 mg ferrocene, and 1-100 mM *p*TsOH (from a freshly prepared 2 M stock solution in DMF). A 10-fold excess of thallium triflate was added to the solution to form iron(III) tetraphenylporphyrin triflate, [Fe^{III}(TPP)]OTf, in-situ. Using triflate as the counteranion in this work simplified kinetic analysis. The $Fe^{III/II}$ redox potential of [Fe^{III}(TPP)]OTf did not shift as [*p*TsOH] was varied (**Figure A21**). The solution was analyzed under both N_2 and O_2. The catalytic scans were performed in triplicate, and overlay of the catalytic waves indicated good reproducibility. Between scans, the working electrode was vigorously polished on a Buehler felt pad to a mirror-like finish using 0.05 μm alumina. The electrode was then sequentially rinsed with water and DMF before immediate use. Contributions from adsorbed species have been excluded through use of a rinse-test as previously described.[4,9,12]

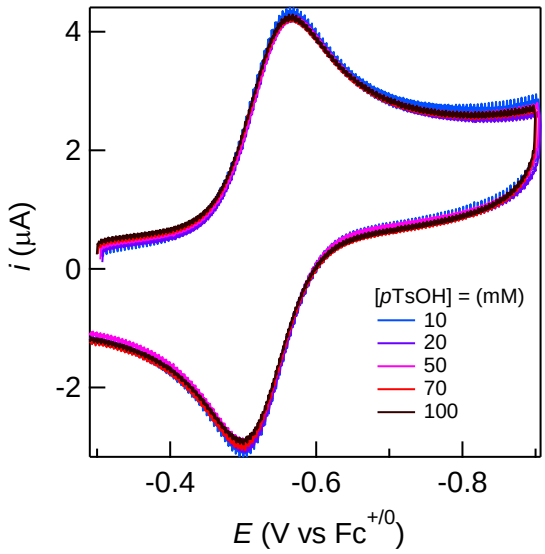

Figure A21. Cyclic voltammograms of [Fe(TPP)]OTf (0.3 mM) in the presence of various amounts of *p*TsOH, showing that $E_{1/2}(Fe^{III/II})$ does not shift with added acid.

For CVs taken under catalytic conditions (in the presence of O_2 and *p*TsOH), electrochemical kinetics were examined using foot-of-the-wave analysis (FOWA, eq S11, **Figure A22**), as previously reported.[9] To acquire the observed rate constant (k_{obs}, s^{-1}), the catalytic current normalized to the peak current acquired under 1 atm N_2 (i_c/i_p) was plotted as a function of the mole fraction of reduced catalyst (between 0 and 1) and fit linearly between catalytic onset[13] (i_c/i_p = 1) and deviation from linearity (defined as where R^2 < 0.980). Values of i_p and $E_{1/2}(Fe^{III/II})$ were determined from N_2-sparged solutions under identical conditions (e.g. same acid concentration, scan rate, etc.). The lack of an observed "concave up" FOWA plot eliminates the possibility of a mechanism involving a second order-dependence on [Fe(TPP)].[13]

$$\frac{i_c}{i_p} = \frac{2.24 n_{cat}^{\sigma} \sqrt{\frac{RT}{Fv} TOF_{max}}}{1 + \exp\left[\frac{F}{RT}(E - E_{1/2})\right]} \qquad \text{(eq A.11)}$$

Equation A.11 was originally derived for an *EC′* mechanism. It can be readily applied to higher order (n > 1) transformations if the chemical step (*C*) after the first electron transfer (*E*) is rate determining. In this case, the chemical step represents the aggregate product of the rate limiting proton transfer (k_{PT}) to $Fe^{III}(TPP)(O_2^{\bullet-})$, the product of a fast, O_2-binding pre-equilibrium

(K_{O2}). The subsequent chemical and electrochemical steps are fast, permitting the use of FOWA for this system.[9] The value of σ ranges between ½ and 1, depending on whether electron transfer is entirely homogeneous (in solution) or heterogeneous (at the electrode). Since k_{obs} varies as $n_{cat}{}^{\sigma}$ (eq A.6), the uncertainty in the value of σ between ½ and 1 gives an uncertainty in the derived k_{obs} of a factor of $n_{cat}{}^{1/2}$ (≈ 2).

As discussed in Chapter 2, the reaction was found to be first order in both [O_2] (**Figure A23**) and [*p*TsOH]. Using the relationship between k_{obs} and the electrochemical rate law (eq A.12−A.13), the third order rate constant (k_{cat}) was estimated as (0.32–0.64) × 10^6 M^{-2} s^{-1} (or ln(k_{cat}) = 13.0 ± 0.3). The range of these values represents the minimum and maximum values for σ = 1 and σ = 1/2, respectively. This rate constant agrees well with the rate constant estimated by fitting the stopped flow kinetics at room temperature k_{cat} = 1.1–6.5 x 10^6 M^{-2} s^{-1} (ln(k_{cat}) = 14.8 ± 0.9).

$$rate = n_{cat} k_{obs} [\mathrm{Fe(TPP)}] \qquad \text{(eq A.12)}$$

$$k_{obs} = k_{cat} [\mathrm{O_2}][p\mathrm{TsOH}] \qquad \text{(eq A.13)}$$

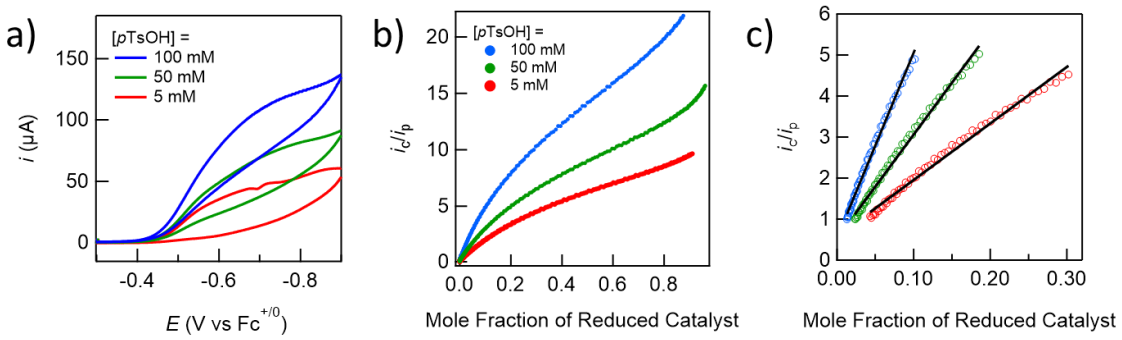

Figure A22. (**A**) Catalytic voltammograms for ORR catalyzed by [Fe(TPP)]OTf in DMF containing 5-100 mM *p*TsOH. (**B**) Foot-of-the-wave analysis for 5 mM data, highlighting the "foot" of the wave for fitting in red. (**C**) Foot-of-the wave data and linear fit.

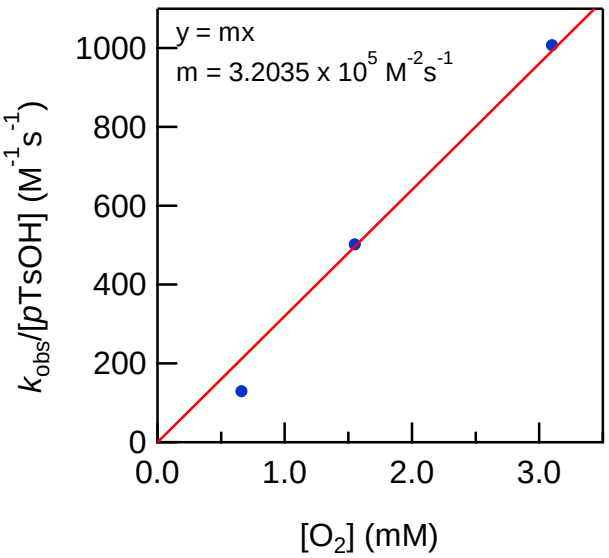

Figure A23. Dependence of k_{obs} from FOWA on [O_2] (σ taken as 1). The first order dependencies in acid (k_{obs}/[*p*TsOH]) were plotted as a function of the [O_2].

A.5 Optical Kinetic Data

A.5.1 Catalytic Oxygen Reduction Kinetics by Stopped-Flow

Stopped-flow kinetics data were acquired using a HI-TECH SCIENTIFIC CryoStopped-Flow System (SF-61DX2) equipped with a diode array detector or using an OLIS RSM-1000 stopped-flow. The Olis stopped-flow instrument was controlled by Kinetic Studio 2.20 software. The details of experimental setup and analysis have been previously reported.[9]

In a typical catalytic stopped-flow experiment, a solution of twice the desired concentration of [Fe^{III}(TPP)]OTf and *p*TsOH was prepared in a DMF solution containing 0.1 M [*n*-Bu_4N][PF_6]. The solution was sparged with air for 15 minutes and loaded into a gastight syringe. A separate gastight syringe was filled with a solution of twice the desired concentration of Fc* in N_2-saturated DMF containing 0.1 M [*n*-Bu_4N][PF_6]. Upon mixing the two solutions, optical spectra were obtained periodically from times as short as 1 ms to as long as 30 s. The progress of the catalytic reaction is most easily monitored by the increase in absorbance of Fc^{*+} at 700 nm.

Figure A24 presents representative spectra during catalytic stopped flow reactions at a variety of temperatures. These data were fit to yield [Concentration] vs. time plots for [Fe^{III}(TPP)]OTf, Fe^{II}(TPP), Fe^{III}(TPP)($O_2^{\bullet-}$) and Fc^{*+}, as discussed in Chapter 2 and below in section 5.3. Stopped-flow experiments were also performed using *p*TsOH and *p*TsOD under otherwise identical conditions to investigate a KIE for the reaction. Close overlay of the kinetics traces (**Figure A25**) indicates a KIE of around 1.

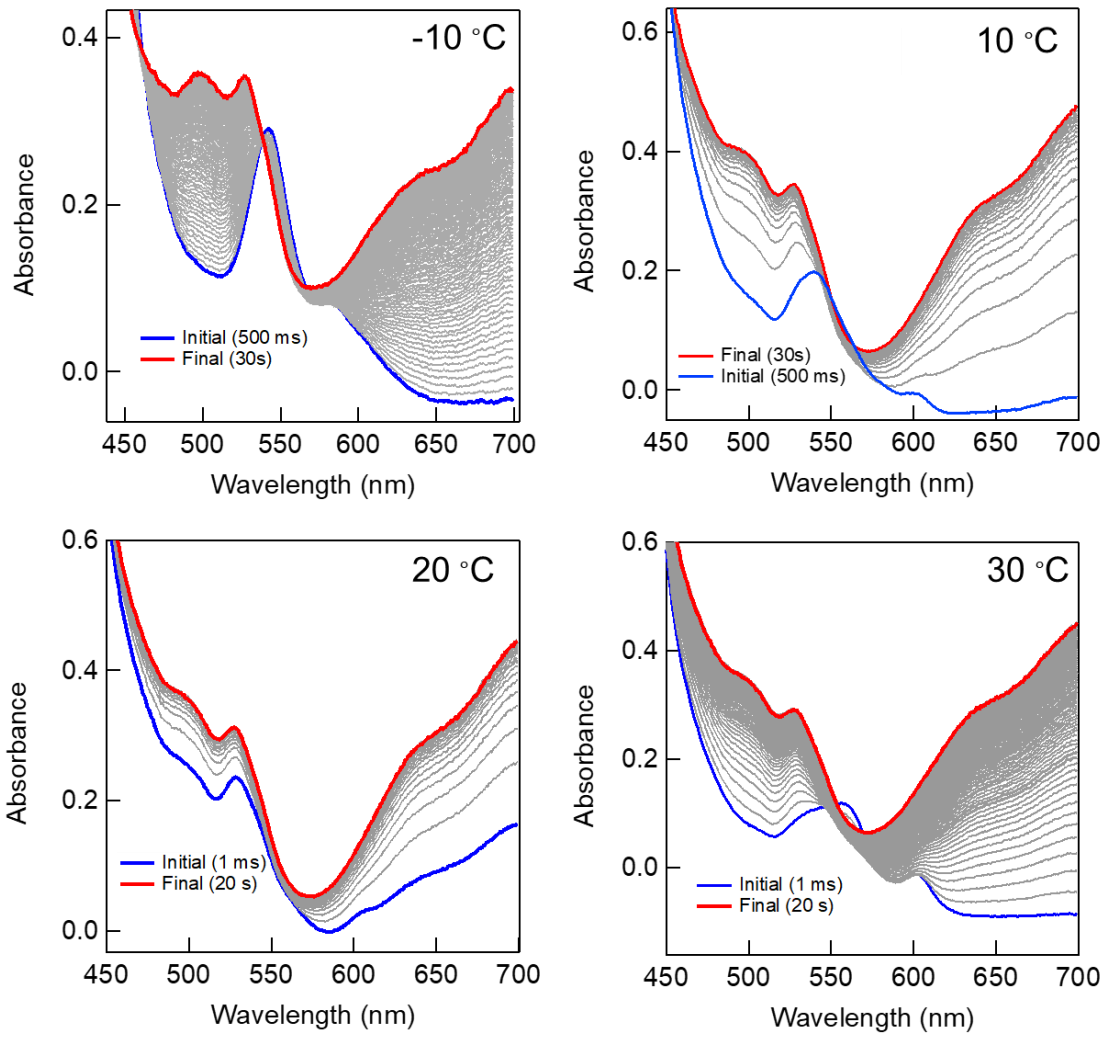

Figure A24. Reactions of [Fe^{III}(TPP)]OTf (30 μM) with O_2 (0.33 mM) in the presence of *p*TsOH (10 mM) and Fc* (3 mM) at various temperatures. Note the differences in the initial spectra at different temperatures. Reported concentrations are after mixing.

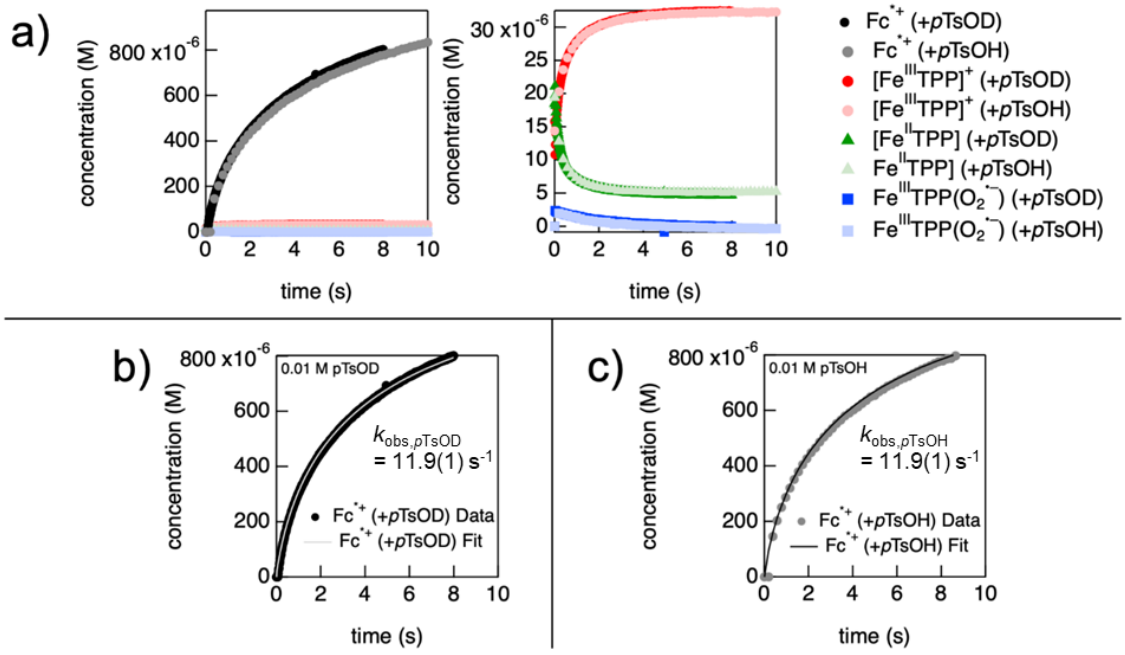

Figure A25. (**A**) Concentrations of all observable species (left) and expansion of catalyst species (right) versus time for the reaction between [Fe^{III}(TPP)]OTf (30 μM), O_2 (0.33 mM), and Fc* (3 mM) in the presence of 10 mM *p*TsOH and 10 mM H_2O (light points) or 10 mM *p*TsOD and 10 mM D_2O (dark points). (**B**) Experimental versus fit data of [Fc^{*+}] versus time with *p*TsOD revealing k_{obs} = 11.9(1) s^{-1}. (**C**) Experimental versus fit data of [Fc^{*+}] versus time with *p*TsOH revealing k_{obs} = 11.9(1) s^{-1}. These data suggest a kinetic isotope of 1.0 ± 0.2.

A.5.2 Longer Timescale ORR with Air

Longer time-scale experiments were conducted by combining 10 mM Fc* and 260 mM *p*TsOH with 1 μM [Fe^{III}(TPP)]OTf. The mixture was stirred vigorously under aerobic conditions (open cuvette on benchtop). The formation of Fc*$^{+}$ was identified by the growth of a broad feature around 700 nm. Within 15 minutes, the reaction was complete, as evidenced by the lack of additional Fc*$^{+}$ formation (**Figure A26**). In a control experiment, far less Fc*$^{+}$ was formed in the same amount of time under identical conditions but in the *absence* of [Fe^{III}(TPP)]OTf. At the end of the catalyzed reaction, only 8 mM Fc*$^{+}$ had been produced. That the reaction did not go to competition (expected 10 mM Fc*$^{+}$) is consistent with the electron transfer equilibrium data where electron transfer from Fc* to [Fe^{III}(TPP)]OTf becomes less favorable as the concentration of Fc*$^{+}$ increases during turnover.

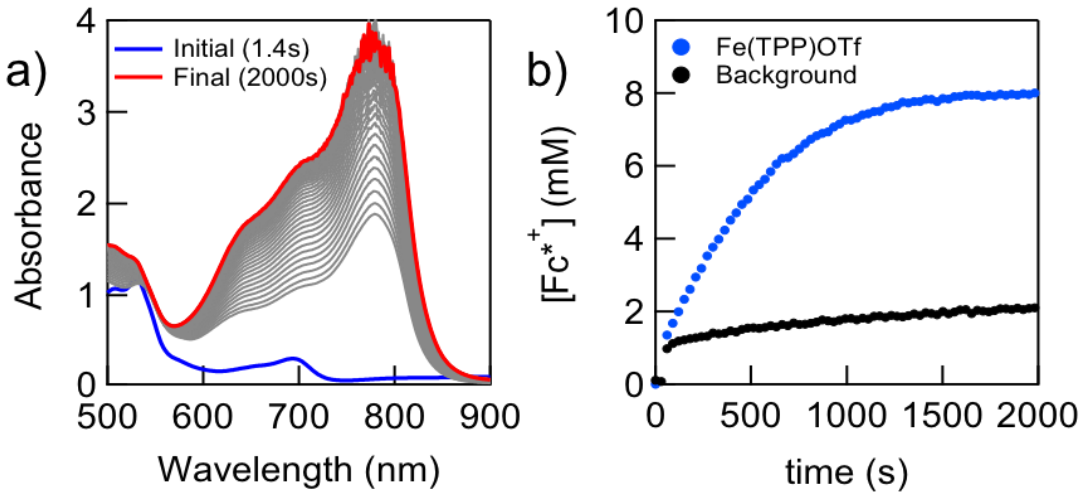

Figure A26. (**A**) Absorbance changes during the reaction of Fe^{III}(TPP)OTf (1 μM) with *p*TsOH (260 mM), Fc* (10 mM), and O_2 (1 atm air) over 2000 s at room temperature. (**B**) Formation of Fc^{*+} from a), monitoring absorbance at 700 nm. The black trace shows formation of Fc^{*+} under identical conditions to a) but without [Fe^{III}(TPP)]OTf.

A.5.3 Determining Catalyst Speciation and Fc⁺ Concentrations*

In order to fit the stopped-flow data using a kinetic model, the concentrations of catalyst and Fc^{*+} over the course of the reaction had to be determined. Depending on the experimental conditions and reaction progress, the catalyst exists as [Fe^{III}(TPP)]OTf, Fe^{III}(TPP)($O_2^{\bullet-}$), or Fe^{II}(TPP). Each of these species has a distinct spectroscopic signature (see **Figure A4**, **Figure A8**, and **Figure A14**), so the catalyst speciation at every time point could be calculated using a system of equations based on Beer's Law (eq A.14−A.17). The system of equations considered the absorbance at 528, 542, 564, and 700 nm, which are the λ_{max} values of [Fe^{III}(TPP)]OTf, Fe^{III}(TPP)($O_2^{\bullet-}$), Fe^{II}(TPP), and Fc^{*+}, respectively, in the wavelength region monitored by stopped-flow. Absorbance contributions from Fc* are negligible in this region and thus were ignored in the analysis.

$$A_{528,t} = \varepsilon_{528,Fe^{III}(TPP)(O_2^{\bullet-})}[Fe^{III}(TPP)(O_2^{\bullet-})]_t + \varepsilon_{528,Fe^{III}(TPP)}[Fe^{III}(TPP)]_t + \varepsilon_{528,Fe^{II}(TPP)}[Fe^{II}(TPP)]_t + \varepsilon_{528,Fc^{*+}}[Fc^{*+}]_t \quad \text{(eq A.14)}$$

$$A_{542,t} = \varepsilon_{542,Fe^{III}(TPP)(O_2^{\bullet-})}[Fe^{III}(TPP)(O_2^{\bullet-})]_t + \varepsilon_{542,Fe^{III}(TPP)}[Fe^{III}(TPP)]_t + \varepsilon_{542,Fe^{II}(TPP)}[Fe^{II}(TPP)]_t + \varepsilon_{542,Fc^{*+}}[Fc^{*+}]_t \quad \text{(eq A.15)}$$

$$A_{564,t} = \varepsilon_{564,Fe^{III}(TPP)(O_2^{\bullet-})}[Fe^{III}(TPP)(O_2^{\bullet-})]_t + \varepsilon_{564,Fe^{III}(TPP)}[Fe^{III}(TPP)]_t + \varepsilon_{564,Fe^{II}(TPP)}[Fe^{II}(TPP)]_t + \varepsilon_{564,Fc^{*+}}[Fc^{*+}]_t \quad \text{(eq A.16)}$$

$$A_{700,t} = \varepsilon_{700,Fe^{III}(TPP)(O_2^{\bullet-})}[Fe^{III}(TPP)(O_2^{\bullet-})]_t + \varepsilon_{700,Fe^{III}(TPP)}[Fe^{III}(TPP)]_t + \varepsilon_{700,Fe^{II}(TPP)}[Fe^{II}(TPP)]_t + \varepsilon_{700,Fc^{*+}}[Fc^{*+}]_t \quad \text{(eq A.17)}$$

Equations A.14-A.17 can be simplified as a product of matrices (eq A.18):

$$\begin{bmatrix} A_{528} \\ A_{542} \\ A_{564} \\ A_{700} \end{bmatrix}_t = \begin{bmatrix} \varepsilon_{528,Fe^{III}(TPP)(O_2^{\bullet-})} & \varepsilon_{528,Fe^{III}(TPP)} & \varepsilon_{528,Fe^{II}(TPP)} & \varepsilon_{528,Fc^{*+}} \\ \varepsilon_{542,Fe^{III}(TPP)(O_2^{\bullet-})} & \varepsilon_{542,Fe^{III}(TPP)} & \varepsilon_{542,Fe^{II}(TPP)} & \varepsilon_{542,Fc^{*+}} \\ \varepsilon_{564,Fe^{III}(TPP)(O_2^{\bullet-})} & \varepsilon_{564,Fe^{III}(TPP)} & \varepsilon_{564,Fe^{II}(TPP)} & \varepsilon_{564,Fc^{*+}} \\ \varepsilon_{700,Fe^{III}(TPP)(O_2^{\bullet-})} & \varepsilon_{700,Fe^{III}(TPP)} & \varepsilon_{700,Fe^{II}(TPP)} & \varepsilon_{700,Fc^{*+}} \end{bmatrix} \begin{bmatrix} [Fe^{III}(TPP)(O_2^{\bullet-})] \\ [Fe^{III}(TPP)] \\ [Fe^{II}(TPP)] \\ [Fc^{*+}] \end{bmatrix}_t \quad \text{(eq A.18)}$$

The molar absorptivity values of $Fe^{III}(TPP)$, $Fe^{II}(TPP)$, $Fe^{III}(TPP)(O_2^{\bullet-})$, and Fc^{*+} at the wavelengths of interest were determined by independent optical measurements and are reported in **Table A6**. Various experiments indicated that these values did not change significantly with temperature.

Table A6. Molar absorptivity values (M^{-1} cm^{-1}) for catalyst species and Fc^{*+}.

Compound	ε_{528}	ε_{542}	ε_{564}	ε_{700}
$[Fe^{III}(TPP)]OTf$	$(11.9 \pm 0.7) \times 10^3$	$(9.2 \pm 0.5) \times 10^3$	$(3.1 \pm 0.1) \times 10^3$	$(2.7 \pm 0.1) \times 10^3$
$Fe^{III}(TPP)(O_2^{\bullet-})$	$(7.1 \pm 0.8) \times 10^3$	$(1.2 \pm 0.1) \times 10^4$	$(6.4 \pm 0.6) \times 10^3$	$(2.4 \pm 0.2) \times 10^2$
$Fe^{II}(TPP)$	$(7.5 \pm 0.57 \times 10^3$	$(7.6 \pm 0.6) \times 10^3$	$(10.4 \pm 0.7) \times 10^3$	$(3.0 \pm 0.3) \times 10^2$
Fc^{*+}	65 ± 7	50 ± 5	40 ± 5	$(2.8 \pm 0.3) \times 10^2$

These molar absorptivity values were then used with absorbance vs time traces from the stopped-flow kinetics data to determine the concentrations of each catalyst species at every point during the reaction. Representative data near the low and high ends of the examined temperature range are shown in **Figure A27**. Concentration values that are negative or higher than the total catalyst concentration can be attributed to uncertainties in the molar absorptivities or baseline changes during the stopped-flow experiments. Nonetheless, reasonable mass balance was observed over the course of catalysis in all cases, suggesting the validity of the analysis.

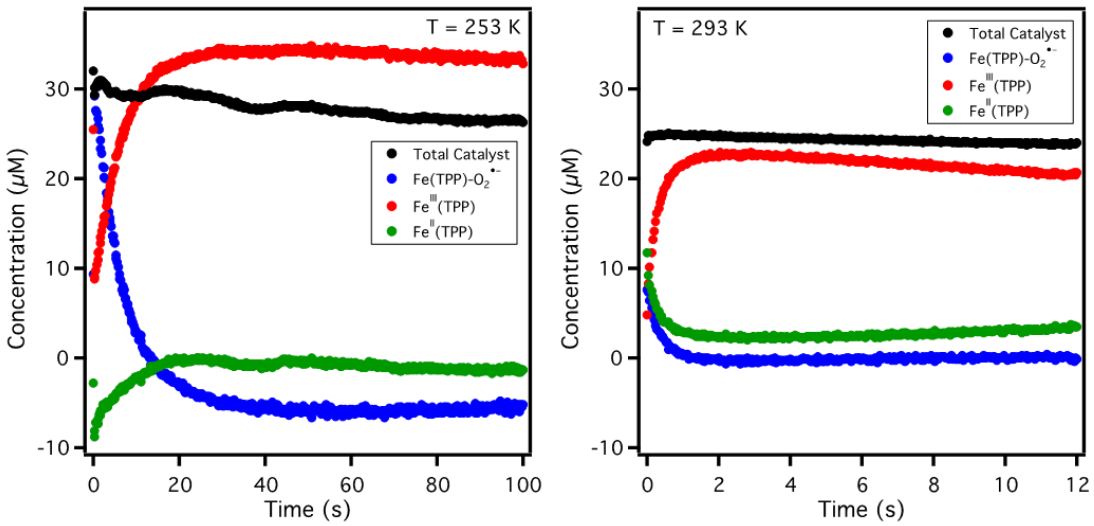

Figure A27. Catalyst speciation over time at 253 K (left) and 293 K (right), showing changes in the concentration of $Fe^{III}(TPP)(O_2^{\bullet-})$ (blue), $[Fe^{III}(TPP)]OTf$ (red), $Fe^{II}(TPP)$ (green), and total catalyst (black). At both temperatures, the reaction was run with 30 μM catalyst, 50 mM *p*TsOH, 0.33 mM O_2, and 3 mM Fc*.

The multi-Beer's Law analysis of stopped-flow data (eq A.18) also yielded the time course of the Fc^{*+} concentration. This is the best measure of the reaction progress, as discussed in Chapter 2. Plots of $[Fc^{*+}]$ vs time for data collected at two different temperatures are shown in **Figure A28**. The same approach was used to convert A700(t) to $[Fc^{*+}](t)$ for the catalytic data shown in **Figure 2.4B** in the Chapter 2.

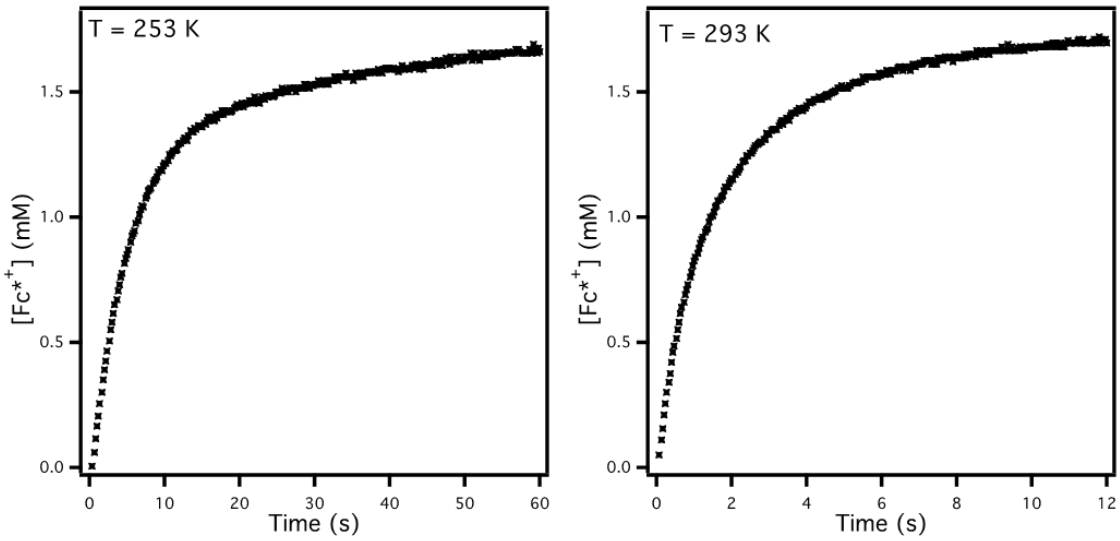

Figure A28. $[Fc^{*+}]$ over time for the reaction of 50 mM *p*TsOH, 0.33 mM O_2, and 3 mM Fc* in the presence of 30 μM Fe(TPP) at temperatures of 253 K (left) and 293 K (right).

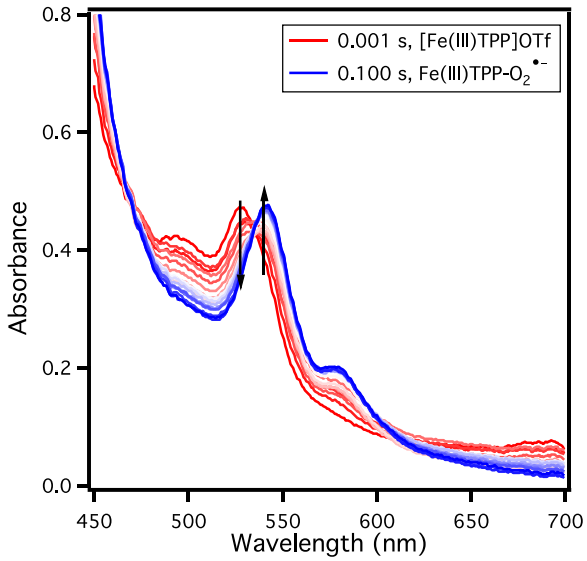

Figure A29. Spectra taken in the first 0.1 seconds of the reaction of [Fe^{III}(TPP)]OTf (30 μM) with O_2 (0.33 mM) and pTsOH (50 mM) in the presence of 3 mM Fc* at 253 K. Conversion from [Fe^{III}(TPP)]OTf (red) to [Fe^{III}(TPP)($O_2^{\bullet-}$)] (blue) is observed.

A.5.4 Decomposition of the [Fe^{III}(TPP)]$_2$O Dimer under Catalytic Conditions

As discussed above in Section A.3, the reaction of O_2 with Fe^{II}(TPP) in the absence of acid results in the formation of the μ-oxo dimer, [Fe^{III}(TPP)]$_2$O. Under catalytic conditions where acid is in excess, the μ-oxo dimer rapidly decomposes to regenerate the Fe^{III}(TPP)$^+$ monomer. This was independently shown in a UV-vis experiment where 100 equiv. *p*TsOH were added to a sample of 15 μM [Fe^{III}(TPP)]$_2$O in DMF containing 0.1 M [*n*-Bu_4N][PF_6]. Within the acid mixing time, the μ-oxo dimer decomposed to yield a spectrum identical to one prepared using a genuine sample of [Fe^{III}(TPP)]OTf and *p*TsOH (**Figure A30**).

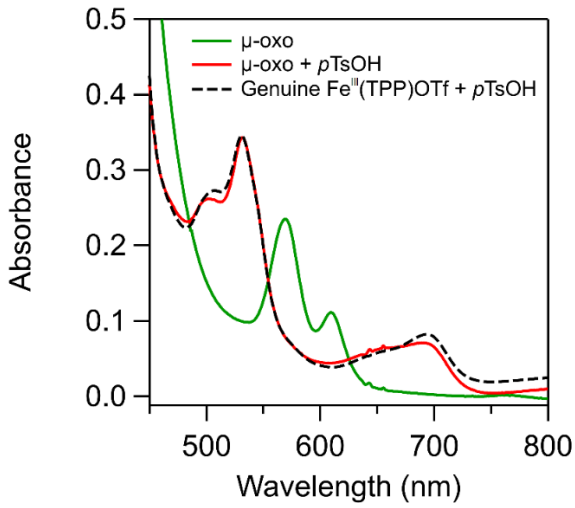

Figure A30. Spectra collected for a sample of the $Fe^{III}(TPP)_2O$ dimer before (green line) and after (red line) addition of excess *p*TsOH. After addition of acid, the product spectrum resembles a genuine sample of $Fe^{III}(TPP)OTf$ + *p*TsOH (dashed black line).

A.5.5 Influence of Fc and Fc*⁺ in the Mechanistic Model*

*A.5.5.1 Equilibrium of K_{ET} between Fe(TPP) and Fc**

The stopped-flow kinetic data are qualitatively consistent with independent measurements of K_{ET}. *At early times, before significant ORR has taken place,* the initial concentrations were [Fc*] = 100[$Fe^{III}(TPP)^+$], and [$Fe^{II}(TPP)$] = [Fc^{*+}] = 0.

Therefore, assuming a rapid equilibrium is established, we calculate that approximately 93% of the total iron porphyrin concentration is expected to be in a reduced form (assuming K_{ET} is 0.12, the equilibrium constant from the difference in reduction potential measurements). Thus, it is unsurprising that all of the initial kinetic traces look predominantly like reduced products (e.g. $Fe^{II}(TPP)$, $Fe^{III}(TPP)(O_2^{\bullet-})$, or combinations thereof).

$$K_{ET} = \frac{[Fc^{*+}][Fe^{II}(TPP)]}{[Fc^*][[Fe^{III}(TPP)]^+]} = 0.12 = \frac{(x\ \text{mM})(x\ \text{mM})}{(3.0\ \text{mM})(0.030\ \text{mM} - x\ \text{mM})} \therefore\ x = 0.028\ \text{mM}$$

Near the end of the stopped-flow experiments, [$Fe^{III}(TPP)$]OTf appears concomitant with Fc^{*+} formation, despite the excess of unreacted Fc* (approximately 1.8 mM). Reduction to $Fe^{II}(TPP)$ ceases to occur because the ratios of i) Fc* to $Fe^{III}(TPP)^+$ and ii) Fc* to Fc^{*+} have changed *significantly* from the initial conditions. Using K_{ET} and the conditions of the final time points, we calculate that only 17% of the total iron porphyrin should be $Fe^{II}(TPP)$.

$$K_{ET} = \frac{[Fc^{*+}][Fe^{II}(TPP)]}{[Fc^{*}][[Fe^{III}(TPP)]^{+}]} = 0.12 = \frac{(1.2\text{ mM})(x\text{ mM})}{(1.8\text{ mM})(0.030\text{ mM} - x\text{ mM})} \therefore\ x = 0.0046\text{ mM}$$

An independent UV-vis experiment was performed to obtain spectra of the three solutions described below, prepared in the absence of air and any added acid.

1. A DMF solution containing 30 μM [Fe^{III}(TPP)]OTf and 0.1 M [*n*-Bu_4N][PF_6].
2. A DMF solution containing 30 μM [Fe^{III}(TPP)]OTf, 3.0 mM Fc* and 0.1 M [*n*-Bu_4N][PF_6].
3. A DMF solution containing 30 μM [Fe^{III}(TPP)]OTf, 1.8 mM Fc*, 1.2 mM Fc^{*+}, and 0.1 M [*n*-Bu_4N][PF_6].

Solution 1 was a reference spectrum of $Fe^{III}(TPP)^{+}$. Solution 2 was prepared to mimic the initial electron transfer conditions of the stopped-flow experiments. Solution 3 was prepared to mimic the final electron transfer conditions of the stopped-flow experiments. The spectra of all three solutions are presented in **Figure A31**. The spectrum of solution 3 needed to be corrected for absorbance contributions from Fc* and Fc^{*+} (**Figure A31A**). The spectra of Solutions 1 and 2 are overlaid atop the corrected spectrum of Solution 3 in **Figure A31B**. The spectrum of Solution 2 closely matched the Q-band spectrum of an authentic sample of Fe^{II}(TPP) (**Figure A31B**, grey dashed line). The spectrum of Solution 3 shows a combination of [Fe^{III}(TPP)]OTf and Fe^{II}(TPP) Q-band features and was fit to a combination of the two individual spectra. Under these conditions 71 ± 5% of all Fe(TPP) in solution is [Fe^{III}(TPP)]OTf (average of three single wavelength fittings at 524 nm, 563 nm, and 685 nm). As discussed above, under these conditions and assuming K_{ET} = 0.12, the expected amount of [Fe^{III}(TPP)]OTf would be 85%. Both the experimental and expected percentages match the stopped-flow kinetics measurements, which show conversion from Fe^{II}(TPP) to [Fe^{III}(TPP)]OTf as the Fc*/Fc^{*+} ratio decreases over time.

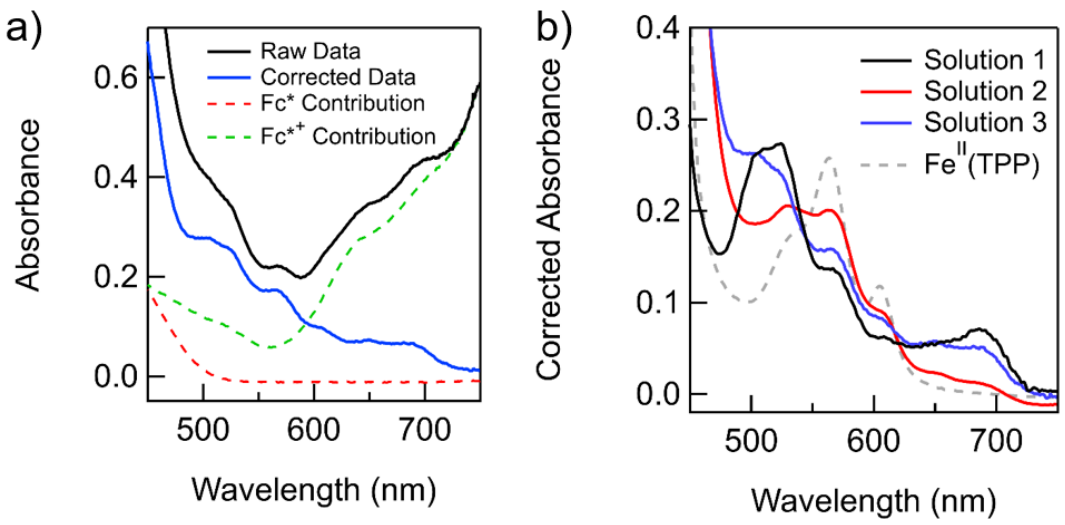

Figure A31. (**A**) Black: the raw optical spectrum of Solution 3, containing 30 μM [Fe^{III}(TPP)]OTf after addition of 1.8 mM Fc* and 1.2 mM Fc^{*+}. Dashed lines are the independent spectra of Fc^{*+} and Fc*, as noted in the legend. Blue: the corrected optical spectrum for the Fe(TPP) Q-band region after correcting for absorbance contributions from Fc* and Fc^{*+}. (**B**) Optical spectrum of 30 μM [Fe^{III}(TPP)]OTf in DMF containing 0.1 M [*n*-Bu_4N][PF_6]. Black: Solution 1 containing [Fe^{III}(TPP)]OTf in the absence of Fc* or Fc^{*+}. Red: Solution 2 containing the same sample after addition of 3.0 mM Fc*, corrected for absorbance contributions from Fc*. Blue: Solution 3 containing 30 μM [Fe^{III}(TPP)]OTf after addition of 1.8 mM Fc* and 1.2 mM Fc^{*+}, corrected for absorbance contributions from Fc* and Fc^{*+}.

A.5.5.2 Influence of [Fc] on the kinetics of ORR*

The rate law for the catalytic stopped-flow experiments (eq 2.9, see Chapter 2) suggests a complex reaction order in Fc*. To probe this directly, room temperature stopped-flow experiments were performed with the initial [Fc*] ranging from 2-5 mM. In these experiments, a solution of N_2-saturated DMF containing twice the desired [Fc*] was mixed with a solution of air-saturated DMF containing 60 μM [Fe(TPP)]OTf, 0.7 mM O_2, and 60 mM *p*TsOH. Both solutions contained 0.1 M [*n*-Bu_4N][PF_6].

Figure A32 below shows [Fc^{*+}] over time for two runs at each initial [Fc*]. For all runs, the [Fc^{*+}] was calculated using the multi-Beer's law analysis described above in Section A.5.3. These concentrations were then normalized to span from 0 to 1 to account for baseline issues that affected the absolute absorbance values. The lack of overlay between runs at different initial [Fc*] indicates that the reaction is not zero-order in reductant. While there appear to be slight increases in rate with higher initial [Fc*], the significant scatter in the data suggests that the dependence on reductant is also not first order.

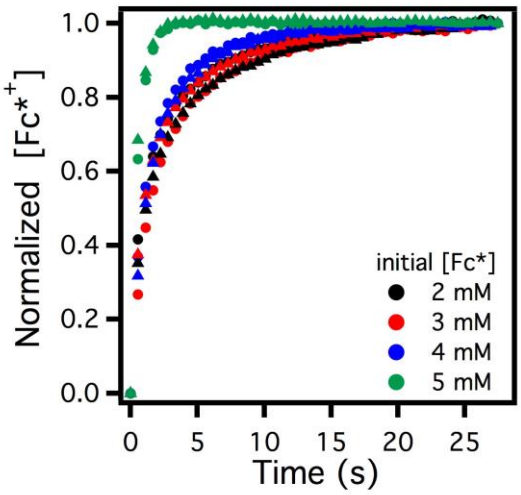

Figure A32. Variation of the [Fc*+] over time for reactions of [Fe^{III}(TPP)]OTf (30 μM) with O_2 (0.33 mM) and *p*TsOH (30 mM) in the presence of varying [Fc*] (2-5 mM) at 298 K. The circular and triangular data points represent two runs under the same conditions and illustrate the scatter in the data, which is particularly evident at lower [Fc*].

Furthermore, attempting to fit the plots of [Fc*+] vs time to a single exponential expression demonstrates that the reactions do not follow first order kinetics (**Figure A33**). Rather, the data show regions of fast and then slow Fc*+ growth, presumably reflecting the changing ΔG_{ET} during the course of the reaction.

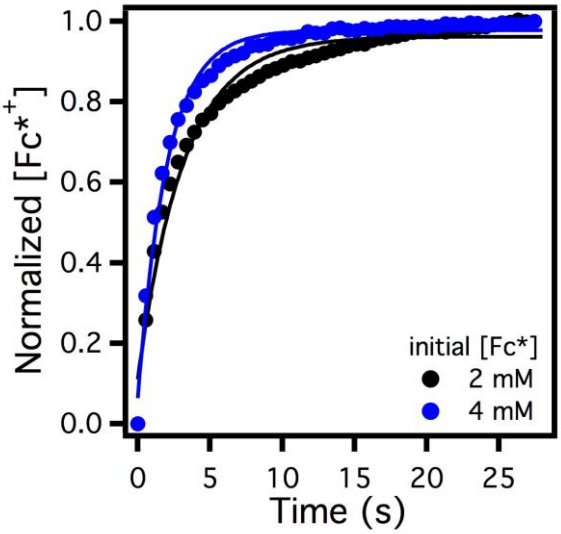

Figure A33. Single exponential fits of the variation in [Fc*+] over time for reactions of [Fe^{III}(TPP)]OTf (30 μM) with O_2 (0.33 mM) and *p*TsOH (30 mM) in the presence of 2 mM (black) or 5 mM (blue) Fc* at 298 K. Fits to single exponential growth are poor, indicating that the reactions do not follow simple first order kinetics.

A.6 Kinetic Modeling and Fits using COPASI

All of the stopped-flow time course data across a range of temperatures were globally fit using the kinetic modeling software COPASI.[14] The model used is given in **Figure A34** (**Scheme 2.2** in the Chapter 2). The input parameters for steps (i) and (ii), k_{ET} and k_{O2}, respectively, were chosen to make these steps fast on the timescale of the other processes occurring. The chosen values are arbitrary as long as they are large enough to ensure that these steps are fast pre-equilibria, as observed experimentally (see above). Increasing these values for the rate constants (to greater than 10^7 M^{-1} s^{-1}) had no effect on the kinetic modeling results. Step (iv) was included to account for mass balance in the reaction and was set to a fast enough rate to be kinetically invisible. The fit parameters were the thermodynamic entropies and enthalpies for steps (i) and (ii), and the activation parameters for the proton transfer step (iii). Due to the low concentration of total Fe(TPP) (<30 μM), uncertainties of molar absorptivities, and baseline changes during the stopped-flow experiments, the exact concentrations of catalyst species were not determined extremely accurately. The inaccuracy manifested as some concentration values determined to be extra negative values or higher than the total catalyst concentration.

Overall, the optimized COPASI model fits very well to the general catalyst speciation and catalytic reaction lifetimes. The plots below give kinetic time course data at a variety of temperatures and COPASI fits based on the parameters derived from the entire global kinetic dataset (**Figure A35**–**Figure A49**). These plots show that the model fits well, particularly to the formation of Fc*+.

Model

(i) $[Fe^{III}(TPP)]^+ + Fc^* \underset{k_{-ET}}{\overset{k_{ET}}{\rightleftharpoons}} Fe^{II}(TPP) + Fc^{*+}$

(ii) $Fe^{II}(TPP) + O_2 \underset{k_{-O2}}{\overset{k_{O2}}{\rightleftharpoons}} Fe^{III}(TPP)(O_2^{\bullet-})$

(iii) $Fe^{III}(TPP)(O_2^{\bullet-}) + p\text{TsOH} \xrightarrow{k_{PT}} [Fe^{III}(TPP)(O_2H^{\bullet})]^+ + p\text{TsO}^-$

(iv) $[Fe^{III}(TPP)(O_2H^{\bullet})]^+ + 3\ p\text{TsOH} + 3Fc^* \xrightarrow{k_{fast}} [Fe^{III}(TPP)]^+ + 2\ H_2O + 3\ p\text{TsO}^- + 3\ Fc^{*+}$

Parameters

$k_{ET} = 10^7$

$k_{-ET} = k_{ET}/K_{ET}$

$K_{ET} = e^{-\frac{(\Delta H_{ET} - T\Delta S_{ET})}{1.987\,T}}$

$k_{O2} = 10^7$

$k_{-O2} = k_{O2}/K_{O2}$

$K_{O_2} = e^{-\frac{(\Delta H_{O_2} - T\Delta S_{O_2})}{1.987\,T}}$

$k_{PT} = 2.0837 \times 10^{10}(T)e^{\frac{-(\Delta H^{\ddagger}_{PT} - T\Delta S^{\ddagger}_{PT})}{1.987\,T}}$

Figure A34. Kinetic model (left) and parameters (right) used to obtain rate and equilibrium constants and $\Delta H°_{ET}$, $\Delta S°_{ET}$, $\Delta H°_{O2}$, $\Delta S°_{O2}$, $\Delta H^{\ddagger}_{PT}$, and $\Delta S^{\ddagger}_{PT}$ from global fitting of all of the stopped-flow time course data from different reaction conditions.

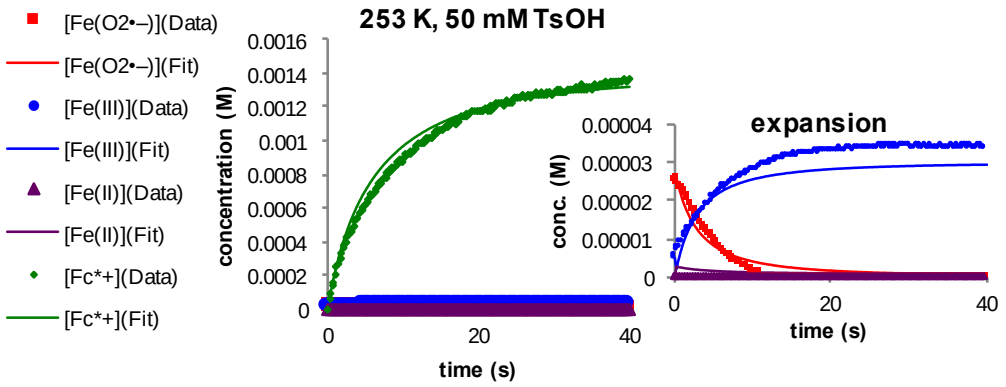

Figure A35. Data (points) and fits (lines) for kinetic model of stopped-flow time course experiments at 253 K. Initial conditions before mixing (all concentrations halved upon mixing): 60 μM [Fe^{III}(TPP)]OTf, 0.7 mM O_2, 6 mM Fc*, 100 mM *p*TsOH, 0.1 M [*n*-Bu_4N][PF_6] in DMF.

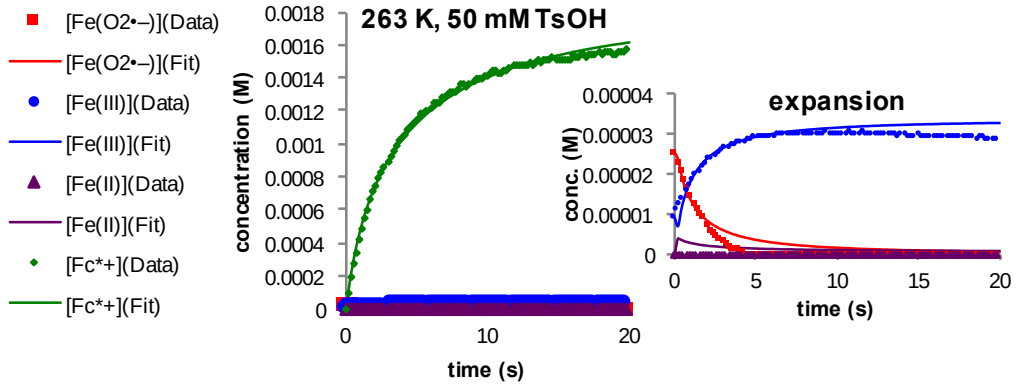

Figure A36. Data (points) and fits (lines) for kinetic model of stopped-flow time course experiments at 263 K. Initial conditions before mixing (all concentrations halved upon mixing): 60 μM [Fe^{III}(TPP)]OTf, 0.7 mM O_2, 6 mM Fc*, 100 mM *p*TsOH, 0.1 M [*n*-Bu_4N][PF_6] in DMF.

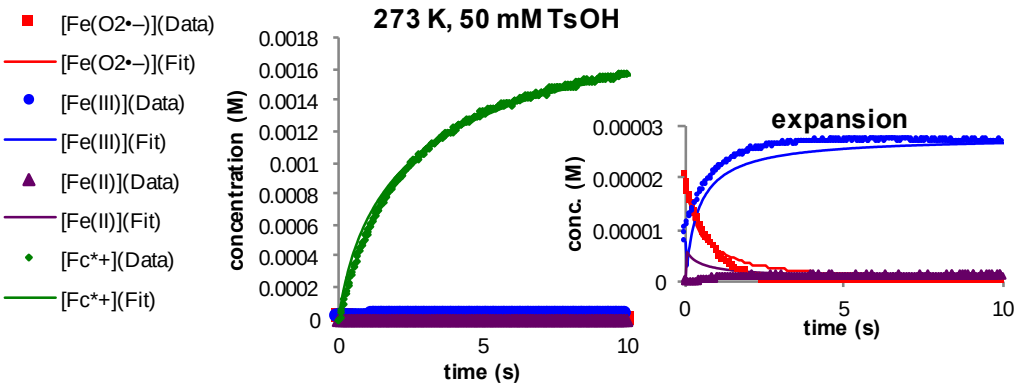

Figure A37. Data (points) and fits (lines) for kinetic model of stopped-flow time course experiments at 273 K. Initial conditions before mixing (all concentrations halved upon mixing): 60 μM [Fe^{III}(TPP)]OTf, 0.7 mM O_2, 6 mM Fc*, 100 mM *p*TsOH, 0.1 M [*n*-Bu_4N][PF_6] in DMF.

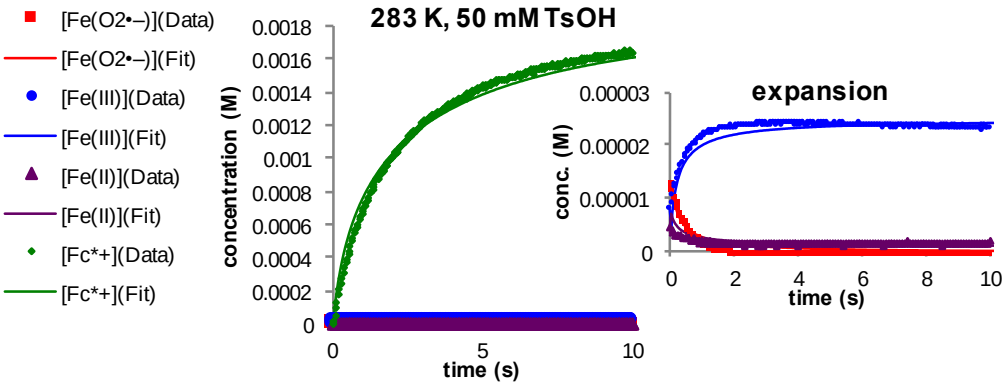

Figure A38. Data (points) and fits (lines) for kinetic model of stopped-flow time course experiments at 283 K. Initial conditions before mixing (all concentrations halved upon mixing): 60 μM [Fe^{III}(TPP)]OTf, 0.7 mM O_2, 6 mM Fc*, 100 mM *p*TsOH, 0.1 M [*n*-Bu_4N][PF_6] in DMF.

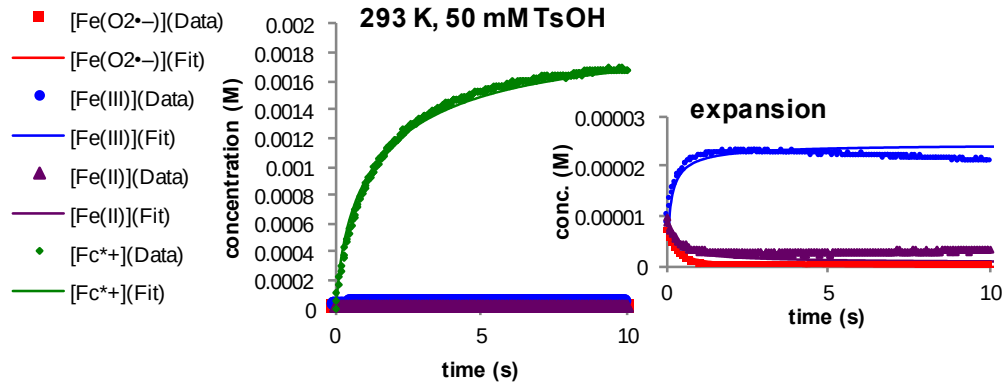

Figure A39. Data (points) and fits (lines) for kinetic model of stopped-flow time course experiments at 293 K. Initial conditions before mixing: 60 μM [Fe^{III}(TPP)]OTf, 0.7 mM O_2, 6 mM Fc*, 100 mM *p*TsOH, 0.1 M [*n*-Bu_4N][PF_6] in DMF.

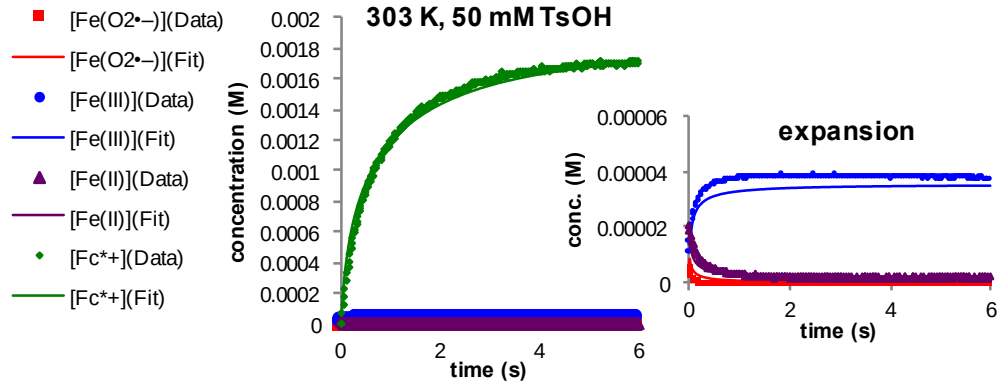

Figure A40. Data (points) and fits (lines) for kinetic model of stopped-flow time course experiments at 303 K. Initial conditions before mixing (all concentrations halved upon mixing): 60 μM [Fe^{III}(TPP)]OTf, 0.7 mM O_2, 6 mM Fc*, 100 mM *p*TsOH, 0.1 M [*n*-Bu_4N][PF_6] in DMF.

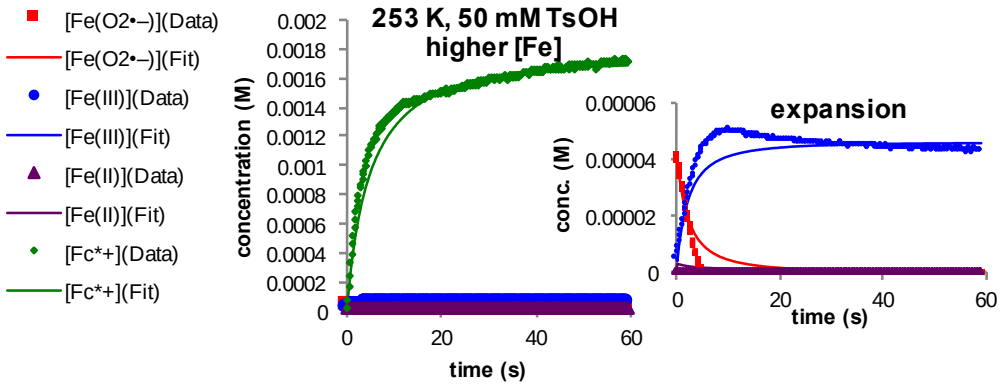

Figure A41. Data (points) and fits (lines) for kinetic model of stopped-flow time course experiments at 253 K. Initial conditions before mixing (all concentrations halved upon mixing): 100 μM [Fe^{III}(TPP)]OTf, 0.7 mM O_2, 6 mM Fc*, 100 mM *p*TsOH, 0.1 M [*n*-Bu_4N][PF_6] in DMF.

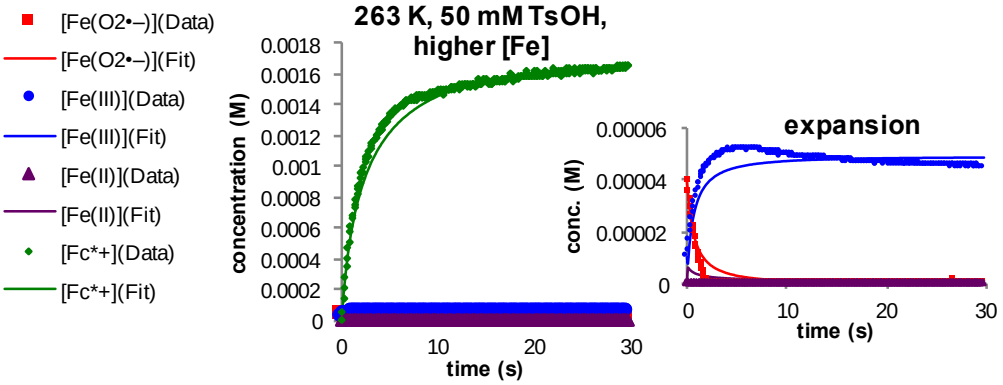

Figure A42. Data (points) and fits (lines) for kinetic model of stopped-flow time course experiments at 263 K. Initial conditions before mixing (all concentrations halved upon mixing): 100 μM [Fe^{III}(TPP)]OTf, 0.7 mM O_2, 6 mM Fc*, 100 mM *p*TsOH, 0.1 M [*n*-Bu_4N][PF_6] in DMF.

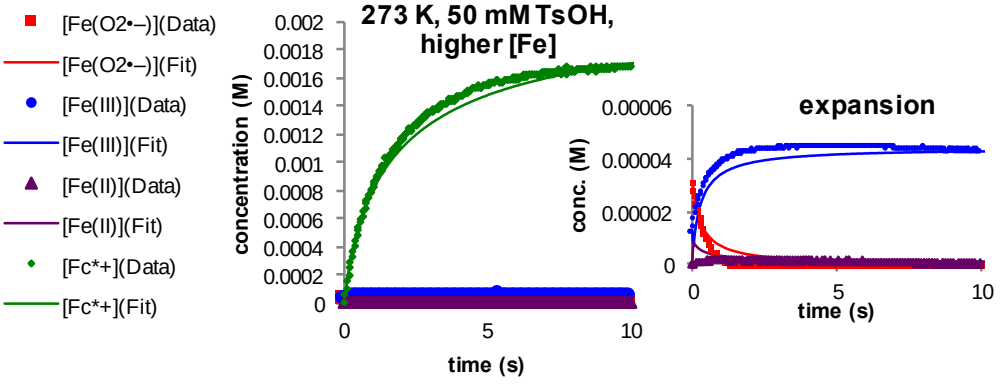

Figure A43. Data (points) and fits (lines) for kinetic model of stopped-flow time course experiments at 273 K. Initial conditions before mixing (all concentrations halved upon mixing): 100 μM [Fe^{III}(TPP)]OTf, 0.7 mM O_2, 6 mM Fc*, 100 mM *p*TsOH, 0.1 M [*n*-Bu_4N][PF_6] in DMF.

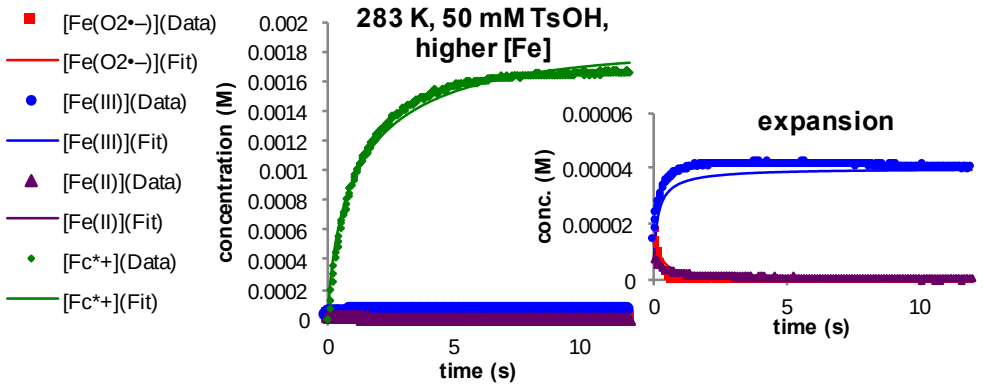

Figure A44. Data (points) and fits (lines) for kinetic model of stopped-flow time course experiments at 283 K. Initial conditions before mixing (all concentrations halved upon mixing): 100 μM [Fe^{III}(TPP)]OTf, 0.7 mM O_2, 6 mM Fc*, 100 mM *p*TsOH, 0.1 M [*n*-Bu_4N][PF_6] in DMF.

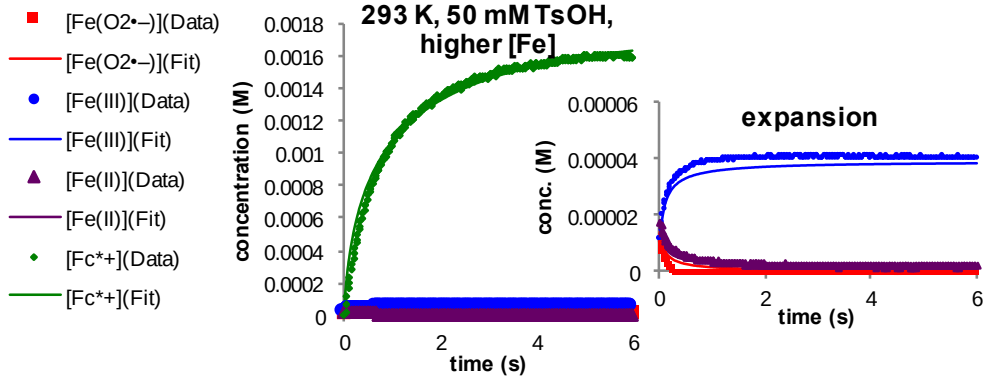

Figure A45. Data (points) and fits (lines) for kinetic model of stopped-flow time course experiments at 293 K. Initial conditions before mixing (all concentrations halved upon mixing): 100 μM [Fe^{III}(TPP)]OTf, 0.7 mM O_2, 6 mM Fc*, 100 mM *p*TsOH, 0.1 M [*n*-Bu_4N][PF_6] in DMF.

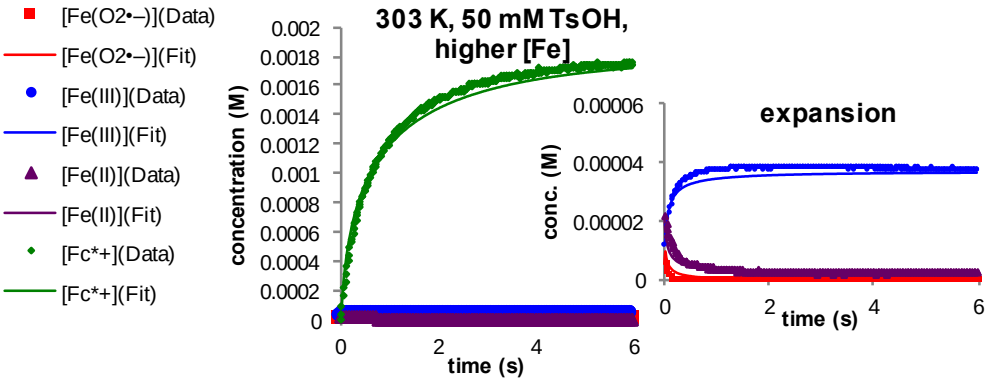

Figure A46. Data (points) and fits (lines) for kinetic model of stopped-flow time course experiments at 303 K. Initial conditions before mixing (all concentrations halved upon mixing): 100 μM [Fe^{III}(TPP)]OTf, 0.7 mM O_2, 6 mM Fc*, 100 mM *p*TsOH, 0.1 M [*n*-Bu_4N][PF_6] in DMF.

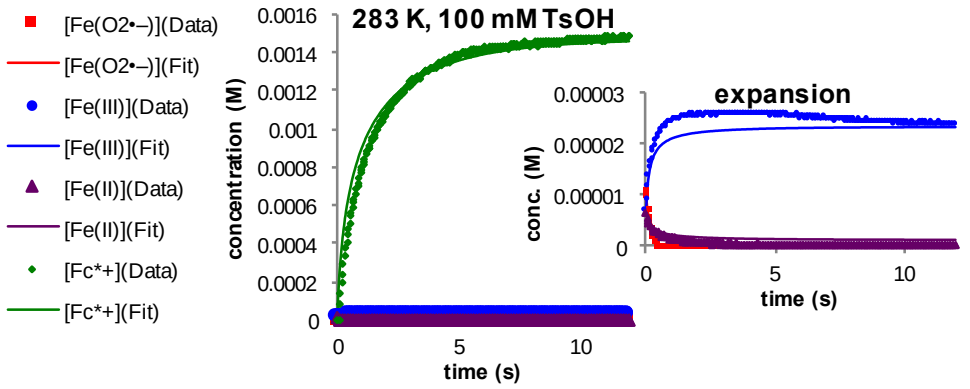

Figure A47. Data (points) and fits (lines) for kinetic model of stopped-flow time course experiments at 283 K. Initial concentrations before mixing (all concentrations halved upon mixing): 60 μM [Fe^{III}(TPP)]OTf, 0.7 mM O_2, 6 mM Fc*, 200 mM *p*TsOH, 0.1 M [*n*-Bu_4N][PF_6] in DMF.

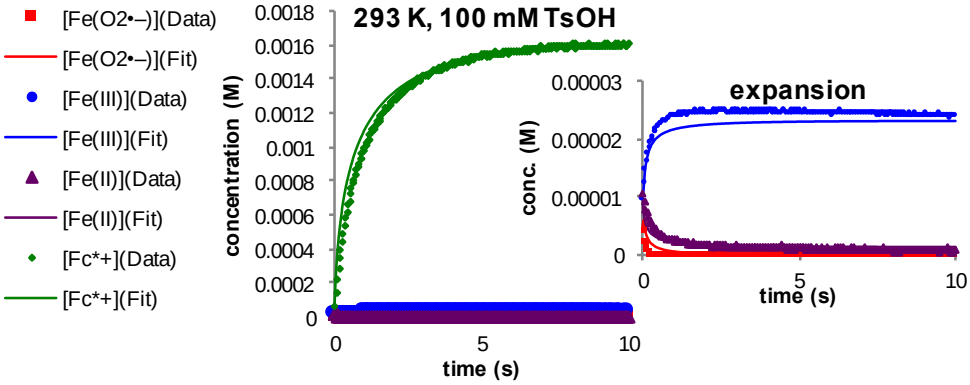

Figure A48. Data (points) and fits (lines) for kinetic model of stopped-flow time course experiments at 293 K. Initial concentrations before mixing (all concentrations halved upon mixing): 60 μM [Fe^{III}(TPP)]OTf, 0.7 mM O_2, 6 mM Fc*, 200 mM *p*TsOH, 0.1 M [*n*-Bu_4N][PF_6] in DMF.

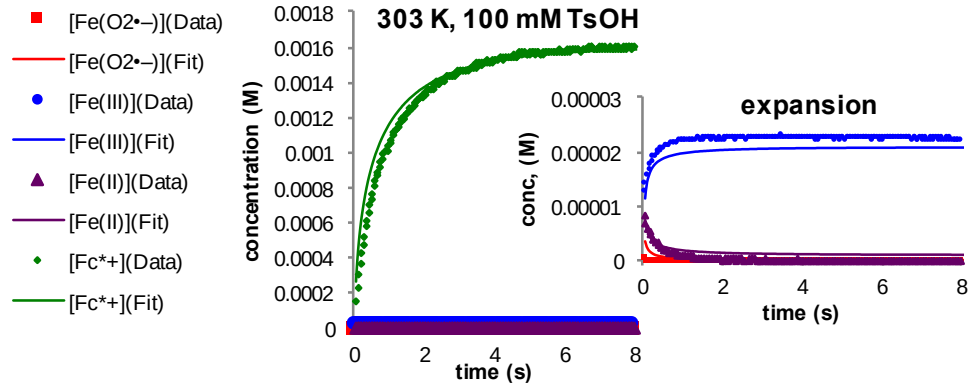

Figure A49. Data (points) and fits (lines) for kinetic model of stopped-flow time course experiments at 303 K. Initial concentrations before mixing (all concentrations halved upon mixing): 60 μM [Fe^{III}(TPP)]OTf, 0.7 mM O_2, 6 mM Fc*, 200 mM *p*TsOH, 0.1 M [*n*-Bu_4N][PF_6] in DMF.

When the six optimized parameters are constrained to be very close to experimental values, COPASI is able to find a local minimum that fits the spectrochemical data adequately (**Table A7**). The weighted sum of squared deviations (SSD) for the tightly constrained modeling results (2.54×10^{-7}) is not much larger than the SSD for the modeled values presented in the Chapter 2 (2.48×10^{-7}) (**Table 2.1**). This indicates that $\Delta H°_{O2}$, $\Delta S°_{O2}$, $\Delta H^{‡}_{PT}$, and $\Delta S^{‡}_{PT}$ are correlated with one another such that similar fits can be obtained with multiple combinations of these parameters. The COPASI statistical correlation matrix reveals parameters that are strongly dependent on one another, but surprisingly this analysis does not show strong correlations between K_{O2} and k_{PT}.

Table A7. Optimized values for a kinetic model with tightly constrained boundaries for all experimental parameters.

Parameter	Optimized Value	Constrained Boundaries
$\Delta H°_{ET}$	2.93(9) kcal mol^{-1}	2.5 to 3 kcal mol^{-1}
$\Delta S°_{ET}$	4.6(3) cal mol^{-1} K^{-1}	4 to 10 cal mol^{-1} K^{-1}
$\Delta H°_{O2}$	–11.68(1) kcal mol^{-1}	–12 to –10 kcal mol^{-1}
$\Delta S°_{O2}$	–26.4(4) cal mol^{-1} K^{-1}	–35 to –25 cal mol^{-1} K^{-1}
$\Delta H^{‡}_{PT}$	15.23(8) kcal mol^{-1}	10 to 20 kcal mol^{-1}
$\Delta S^{‡}_{PT}$	9.9(3) cal mol^{-1} K^{-1}	0 to 35 cal mol^{-1} K^{-1}

A.7 Quantification of H_2O_2

A.7.1 Rotating Ring Disc Voltammetry

Rotating Ring Disk Voltammetry (RRDV) was used to electrochemically quantify the selectivity of the ORR catalysis for H_2O vs H_2O_2. The RRDV experiments were conducted with a BASi Epsilon potentiostat and a Pine Instruments rotator using a 5 mm glassy carbon (GC) disk electrode (BASi Epsilon), Pt ring secondary working electrode, and Ag/AgCl reference electrode (prepared as described above). Solutions were analyzed in a custom-built reservoir made from a 20 mL shot glass with a plastic top. Prior to use, all electrochemical cells were thoroughly rinsed with DMF, water, and acetone before being dried in an oven. The GC disc and Pt ring working electrodes were polished on Buehler felt pads with 0.05 μm alumina. The two working electrodes were polished on separate pads to avoid contaminating the GC disc with Pt. The collection efficiency (CE, eq A.19) was calculated to be 23% using ferrocene in DMF (**Figure A50**). Electrochemical conditioning of the ring electrode was occasionally performed for maintenance, cycling the ring electrode between +1 and -1 V (vs Ag/AgCl) in 0.5 M H_2SO_4 until the current

response stabilized, followed by rinsing with DI H_2O. Experiments with Fe(TPP) were done in the absence of ferrocene, but it was added at the end of the experiment as an internal reference.

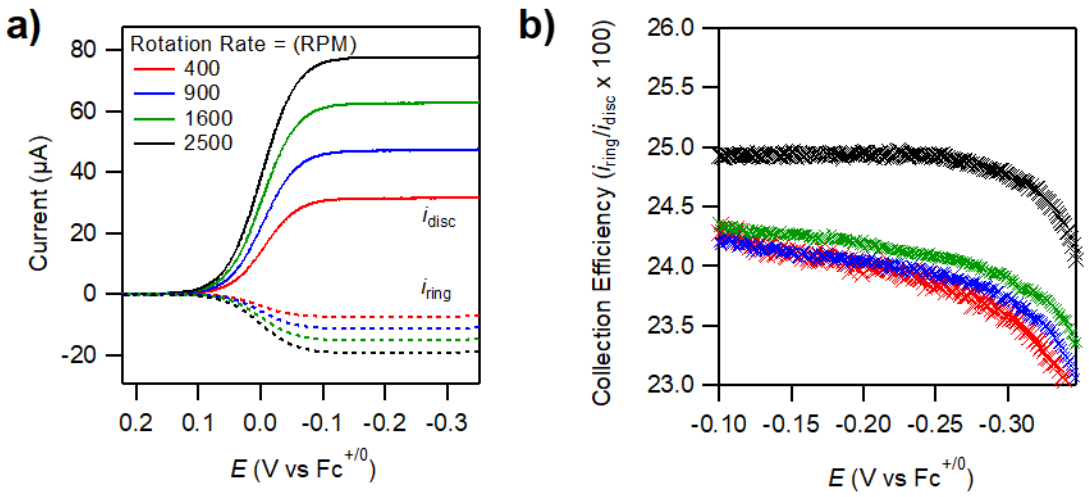

Figure A50 (**A**) Rotating ring disc electrochemistry data for ferrocene in the presence of 100 mM *p*TsOH. (**B**) Collection efficiency as a function of potential, the average value was used between -0.1 and -0.3 V vs $Fc^{+/0}$.[12]

In a typical RRDE experiment, a DMF solution containing 0.5 mM [Fe^{III}(TPP)]OTf and 0.1 M [Bu_4N][PF_6] was sparged with N_2 for 20 minutes. The disc was swept from -0.4 V to -0.9 V vs $Fc^{+/0}$ at 20 mV/s to reduce Fe^{III} to Fe^{II}, and the ring was held at a constant potential of 0.6 V vs $Fc^{+/0}$. More oxidizing ring potentials did not substantially change the ring currents. In the absence of O_2, [Fe^{III}(TPP)]OTf displayed Levich behavior, as is expected for mass-transport limited current.[11] Non-Levich behavior was observed in the presence of O_2, suggesting that the current is limited by the chemical steps of ORR. The percent of H_2O_2 produced was calculated using equation A.19 and expressed as an average of all rotation rates. Values of i_{disc} and i_{ring} were collected at three potentials negative of the catalyst $E_{1/2}$.[9,15]

$$\mathrm{H_2O_2(\%)} = \frac{100\left(\frac{2i_{ring}}{CE}\right)}{i_{disk} + \frac{i_{ring}}{CE}} \qquad \text{(eq A.19)}$$

While equation A.19 was originally derived for heterogeneous systems, it can be readily applied to homogeneous catalysts,[15-17] provided that the limiting ring and disc currents are both independent of rotation rate. Hydrogen peroxide quantification was verified through indirect iodometric titration methods using a previously reported procedure,[9] as described below.

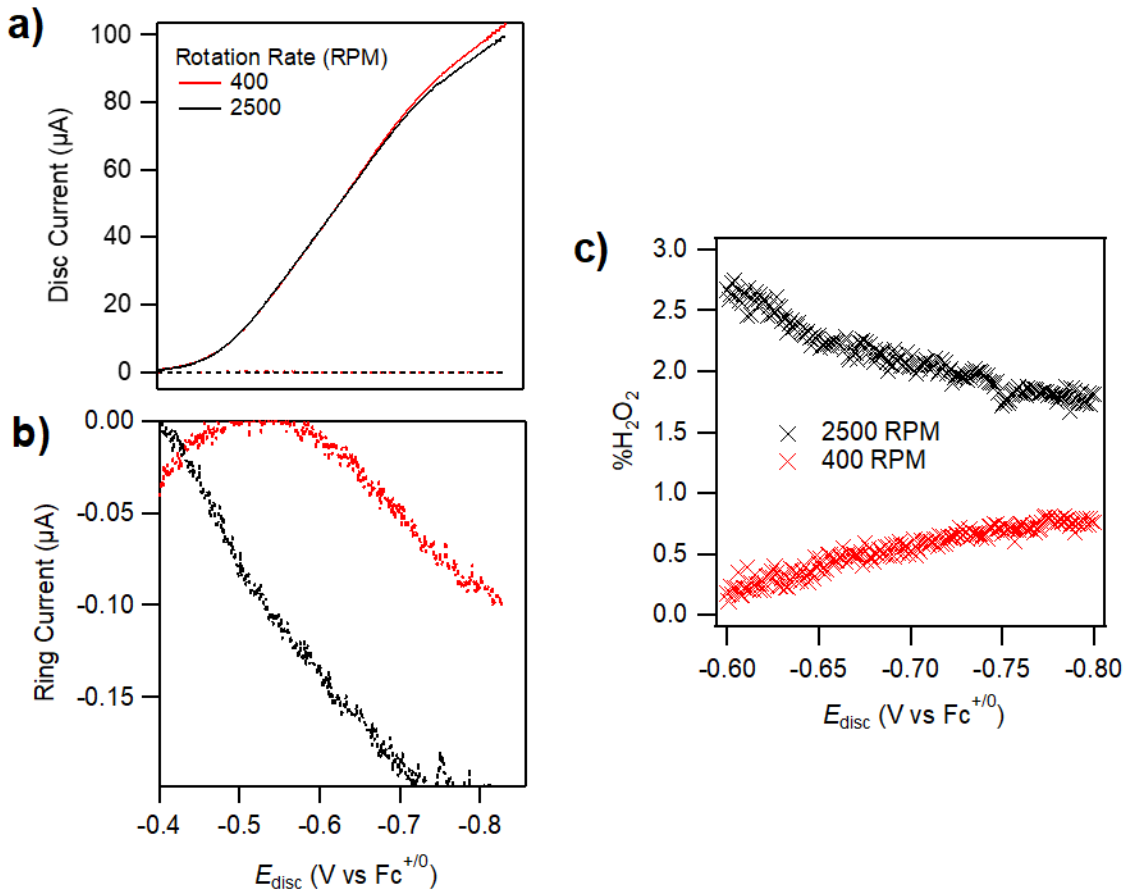

Figure A51 (**A**) Rotating disc voltammograms at 400 and 2500 RPM during [Fe^{III}(TPP)]OTf-catalyzed ORR in the presence of 100 mM *p*TsOH. The dotted lines are the ring current, enlarged in (**B**). (**B**) Ring current during (**A**), with the ring polarized at +0.6 V vs $Fc^{+/0}$. (**C**) $\%H_2O_2$ as a function of the disc potential and the rotation rate. The average value is 1.4 ± 0.6%.[12]

A.7.2 Iodometric Titrations

The amount of H_2O_2 produced during ORR was quantified by titrating a solution of the post-catalytic mixture (in DMF) into an iodide-containing aqueous solution.[9] H_2O_2 production was quantified by monitoring the growth of triiodide (I_3^-) at 352 nm according to the reaction in **Scheme A1**.

Scheme A1. Quantitation of H_2O_2 via its stoichiometric production of I_3^- from $3I^-$.

$$H_2O_2 + 2KI + 2H_2SO_4 \xrightarrow{\text{cat.}} 2H_2O + I_2 + 2KHSO_4$$

$$I_2 + I^- \xrightarrow{\text{cat.}} I_3^-$$

The aqueous iodide solution was prepared by combining 2 mL of 0.5 mM $(NH_4)_2Mo_7O_{24}$ catalyst in 0.5 N sulfuric acid, 41-45 mg of KI, and a small stir bar in a cuvette. The solution was

kept under 1 atm N_2 to minimize background oxidation of I^- from air. Subsequently, a blank spectrum was taken with UV-visible spectrometer (Agilent 8452), and an appropriate volume of solution containing H_2O_2 (obtained after reaction of [Fe^{III}(TPP)]OTf (1 μM), Fc* (10 mM) *p*TsOH (260 mM) and O_2 from ambient air) was added while keeping the cuvette under N_2 atmosphere. Kinetics mode was used to accurately account for absorbance changes due to the background oxidation of I^-. The background oxidation of I^- was subtracted from the baseline using the baseline fitting software in Igor Pro (**Figure A52**). A standard calibration curve at 352 nm was made using a solution of known %H_2O_2, and the resulting tri-iodide extinction coefficient was ε_{352} = 22,600 L mol^{-1} cm^{-1}. The %H_2O_2 during catalytic turnover was then quantified by the ratio of Fc* used to produce H_2O_2 (2 x moles H_2O_2)/moles Fc^{*+} produced after subtracting contributions from background auto-oxidation of Fc*. The amount of H_2O_2 produced in the catalytic solution revealed that the homogeneous catalysis shown in **Figure A26** produced ~15% H_2O_2 (n_{cat} = 3.7 e^-/O_2). The n_{cat} value measured using iodometric titrations is similar to the value measured by RRDE (n_{cat} = 3.9 e^-/O_2) and provides independent confirmation of the selectivity of the catalyzed reaction.

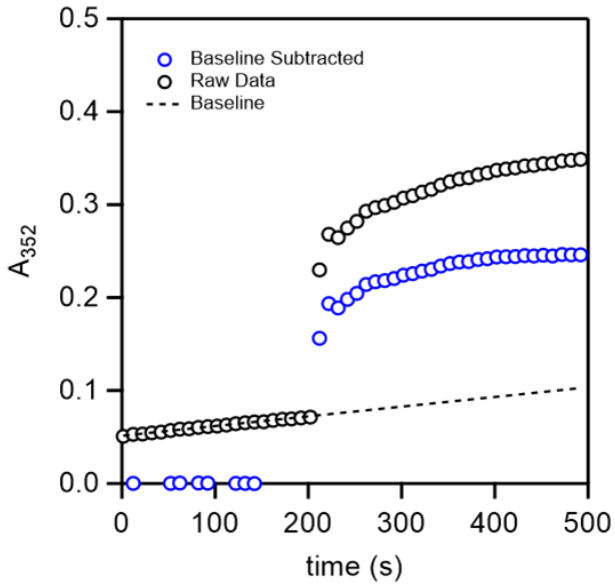

Figure A52 Iodometric titration of an H_2O_2-containing DMF solution from an ORR reaction into an aqueous solution containing KI and $(NH_4)_2Mo_7O_{24}$ catalyst. The addition of the H_2O_2-containing DMF solution occurred at 200 s.

A.8 Computational Data

A.8.1 Methods

The computational methods are reproduced here from Chapter 2 and further elaborated on below:

The present density functional theory (DFT) calculations build on our previous work.[4] Stationary points were optimized using the PBE exchange and correlation functional.[18] The Stuttgart/Dresden basis set with relativistic effective core potential (SDD) was used for the Fe center, and the 6-31G** basis set[19-20] was used for all atoms except sulfur. Diffuse functions and additional polarization functions (6-31++G(2df,2pd)) were used on sulfur in order to capture the sulfur–oxygen bonding correctly. This isolates the source of error as residing in the presence and participation of the sulfonate group (*vide infra*). Single point solvation energies in DMF were modeled using the SMD continuum solvent.[21] Harmonic vibrational frequencies, calculated at the same level of theory, were used to estimate zero-point energy (ZPE) and the thermal contributions free energies. Free energies are referred to the standard state concentration of 1 M for the solute and 12.9 M for the solvent DMF at T = 298 K.

Subsequent intrinsic reaction coordinate calculations were completed to further verify the identity of transition states. Kinetic isotope effects (KIE) were predicted by calculating both the hydrogenated and deuterated analogues of the relevant transition state at the same geometry. Non-classical effects in KIEs were approximated using Skodje and Truhlar's approximation for tunneling through an asymmetric parabolic barrier.[22]

Calculations to understand the effect of sulfonate groups were completed in Orca 4.0,[23] while all other calculations were completed in Gaussian 09.[24]

A.8.2 Characterizing Error in Sulfonate Group Calculations

Capturing bonding in sulfonate groups has been shown to be difficult using the standard double-ζ basis set,[25-27] but this has traditionally been overcome by using larger basis sets on sulfur atoms. As such, we too used a larger basis set on sulfur. Even with this modification, the pK_a of tosic acid (*p*TsOH) referenced to dimethylformamide (DMF) in DMF is calculated to be 5.9 units, which is higher than the experimental value of 2.3 units. To discern the source of error, the pK_a can

be alternatively referenced to methanesulfonic acid in an isodesmic reaction, which cancels out the error of SO-H bond breaking and forming. This gives a pK_a of tosic acid (referenced to methanesulfonic acid) of −0.9 units, which compares well to the experimental value of −0.75 units. Additionally, referencing in this manner isolates the source of error as residing in the presence and participation of the sulfonate group.

A.8.3 Structures of Calculated Complexes

The Cartesian coordinates of calculated complexes are found in the accompanying .XYZ file. This file can be viewed with a free program such as Mercury, which can be found at www.ccdc.cam.ac.uk.

A.8.4 Tabulated Energies of Calculated Complexes

Table A8. Gas phase and solution phase energies for calculated complexes are reported below in Hartrees.

Complex	G (Gas Phase) [Hartree]	G (Solution phase -DMF) [Hartree]
TsOH	-894.55546	-894.57354
DMF	-248.13806	-248.14873
TsOH + DMF	-1142.70324	-1142.72840
TsO^-	-894.04199	-894.13183
1	-2432.05223	-2432.10741
2	-3574.75411	-3574.80080
TS*	-3574.72260	-3574.82233
3	-2432.45336	-2432.53999

A.9 References

1. Fulmer, G. R.; Miller, A. J. M.; Sherden, N. H.; Gottlieb, H. E.; Nudelman, A.; Stoltz, B. M.; Bercaw, J. E.; Goldberg, K. I., NMR Chemical Shifts of Trace Impurities: Common Laboratory Solvents, Organics, and Gases in Deuterated Solvents Relevant to the Organometallic Chemist. *Organometallics* **2010,** *29* (9), 2176-2179.
2. Connelly, N. G.; Geiger, W. E., Chemical Redox Agents for Organometallic Chemistry. *Chem. Rev.* **1996,** *96* (2), 877-910.
3. Inorganic Syntheses. Wold, A.; Ruff, J. K., Eds. John Wiley & Sons, Inc.: Hoboken, 1973; pp 102-103.
4. Pegis, M. L.; McKeown, B. A.; Kumar, N.; Lang, K.; Wasylenko, D. J.; Zhang, X. P.; Raugei, S.; Mayer, J. M., Homogenous Electrocatalytic Oxygen Reduction Rates Correlate with Reaction Overpotential in Acidic Organic Solutions. *ACS Cent. Sci.* **2016,** *2* (11), 850-856.
5. Boersma, A. D.; Goff, H. M., Multinuclear magnetic resonance spectroscopy of spin-admixed S = 5/2, 3/2 iron(III) porphyrins. *Inorg. Chem.* **1982,** *21* (2), 581-586.
6. Safo, M. K.; Nesset, M. J. M.; Walker, F. A.; Debrunner, P. G.; Scheidt, W. R., Models of the Cytochromes. Axial Ligand Orientation and Complex Stability in Iron(II) Porphyrinates: The Case of the Noninteracting d_π Orbitals. *J. Am. Chem. Soc.* **1997,** *119* (40), 9438-9448.
7. Walker, F. A.; Simonis, U., Iron Porphyrin Chemistry. John Wiley & Sons, Ltd: Chichester, UK, 2006.
8. Lexa, D.; Momenteau, M.; Mispelter, J., Characterization of the reduction steps of Fe(III) porphyrins. *Biochim. Biophys. Acta* **1974,** *338* (1), 151-163.
9. Wasylenko, D. J.; Rodríguez, C.; Pegis, M. L.; Mayer, J. M., Direct Comparison of Electrochemical and Spectrochemical Kinetics for Catalytic Oxygen Reduction. *J. Am. Chem. Soc.* **2014,** *136* (36), 12544-12547.
10. Ghiladi, R. A.; Kretzer, R. M.; Guzei, I.; Rheingold, A. L.; Neuhold, Y.-M.; Hatwell, K. R.; Zuberbühler, A. D.; Karlin, K. D., $(F_8TPP)Fe^{II}/O_2$ Reactivity Studies {F_8TPP = Tetrakis(2,6-difluorophenyl)porphyrinate(2−)}: Spectroscopic (UV−Visible and NMR) and Kinetic Study of Solvent-Dependent (Fe/O_2 = 1:1 or 2:1) Reversible O_2-Reduction and Ferryl Formation. *Inorg. Chem.* **2001,** *40* (23), 5754-5767.
11. Bard, A. J.; Faulkner, L. R., *Electrochemical Methods: Fundamentals and Applications, 2nd Edition*. John Wiley & Sons, Ltd: 2000.
12. Pegis, M. L.; Wise, C. F.; Koronkiewicz, B.; Mayer, J. M., Identifying and Breaking Scaling Relations in Molecular Catalysis of Electrochemical Reactions. *J. Am. Chem. Soc.* **2017,** *139* (32), 11000-11003.
13. Costentin, C.; Drouet, S.; Robert, M.; Savéant, J.-M., Turnover Numbers, Turnover Frequencies, and Overpotential in Molecular Catalysis of Electrochemical Reactions. Cyclic Voltammetry and Preparative-Scale Electrolysis. *J. Am. Chem. Soc.* **2012,** *134* (27), 11235-11242.
14. Hoops, S.; Sahle, S.; Gauges, R.; Lee, C.; Pahle, J.; Simus, N.; Singhal, M.; Xu, L.; Mendes, P.; Kummer, U., COPASI–a COmplex PAthway SImulator. *Bioinformatics* **2006,** *22* (24), 3067-3074.
15. Carver, C. T.; Matson, B. D.; Mayer, J. M., Electrocatalytic Oxygen Reduction by Iron Tetra-arylporphyrins Bearing Pendant Proton Relays. *J. Am. Chem. Soc.* **2012,** *134* (12), 5444-5447.
16. Matson, B. D.; Carver, C. T.; Von Ruden, A.; Yang, J. Y.; Raugei, S.; Mayer, J. M., Distant protonated pyridine groups in water-soluble iron porphyrin electrocatalysts promote selective oxygen reduction to water. *Chem. Commun.* **2012,** *48* (90), 11100-11100.
17. Costentin, C.; Dridi, H.; Savéant, J.-M., Molecular Catalysis of O_2 Reduction by Iron Porphyrins in Water: Heterogeneous versus Homogeneous Pathways. *J. Am. Chem. Soc.* **2015,** *137* (42), 13535-13544.
18. Perdew, J. P.; Burke, K.; Ernzerhof, M., Generalized Gradient Approximation Made Simple. *Phys. Rev. Lett.* **1996,** *77* (18), 3865-3868.
19. Francl, M. M.; Pietro, W. J.; Hehre, W. J.; Binkley, J. S.; Gordon, M. S.; DeFrees, D. J.; Pople, J. A., Self-consistent molecular orbital methods. XXIII. A polarization-type basis set for second-row elements. *J. Chem. Phys.* **1982,** *77* (7), 3654-3665.

20. Hehre, W. J.; Ditchfield, R.; Pople, J. A., Self—Consistent Molecular Orbital Methods. XII. Further Extensions of Gaussian—Type Basis Sets for Use in Molecular Orbital Studies of Organic Molecules. *J. Chem. Phys.* **1972,** *56* (5), 2257-2261.
21. Marenich, A. V.; Cramer, C. J.; Truhlar, D. G., Universal Solvation Model Based on Solute Electron Density and on a Continuum Model of the Solvent Defined by the Bulk Dielectric Constant and Atomic Surface Tensions. *J. Phys. Chem. B* **2009,** *113* (18), 6378-6396.
22. Skodje, R. T.; Truhlar, D. G., Parabolic tunneling calculations. *J. Phys. Chem.* **1981,** *85* (6), 624-628.
23. Neese, F., Software update: the ORCA program system, version 4.0. *Wiley Interdicip. Rev. Comput. Mol. Sci.* **2018,** *8* (1), e1327.
24. Frisch, M. J.; Trucks, G. W.; Schlegel, H. B.; Scuseria, G. E.; Robb, M. A.; Cheeseman, J. R.; Scalmani, G.; Barone, V.; Mennucci, B.; Petersson, G. A.; Nakatsuji, H.; Caricato, M.; Li, X.; Hratchian; H, P.; Izmaylov, A. F.; Bloino, J.; Zheng, G.; Sonnenberg, J. L.; Hada, M.; Ehara, M.; Toyota, K.; Fukuda, R.; Hasegawa, J.; Ishida, M.; Nakajima, T.; Honda, Y.; Kitao, O.; Nakai, H.; Vreven, T.; Montgomery Jr, J. A.; Peralta, J. E.; Ogliaro, F.; Bearpark, M. J.; Heyd, J.; Brothers, E. N.; Kudin, K. N.; Staroverov, V. N.; Kobayashi, R.; Normand, J.; Raghavachari, K.; Rendell, A. P.; Burant, J. C.; Iyengar; S, S.; Tomasi, J.; Cossi, M.; Rega, N.; Millam, N. J.; Klene, M.; Knox, J. E.; Cross, J. B.; Bakken, V.; Adamo, C.; Jaramillo, J.; Gomperts, R.; Stratmann, R. E.; Yazyev, O.; Austin, A. J.; Cammi, R.; Pomelli; C; Ochterski, J. W.; Martin, R. L.; Morokuma, K.; Zakrzewski, V. G.; Voth, G. A.; Salvador, P.; Dannenberg, J. J.; Dapprich, S.; Daniels, A. D.; Farkas, Ö.; Foresman, J. B.; Ortiz, J. V.; Cioslowski, J.; Fox, D. J., Gaussian 09. Gaussian Inc.: Wallingford, 2009.
25. Wilson, A. K.; Dunning, T. H., The HSO−SOH Isomers Revisited: The Effect of Tight d Functions. *J. Phys. Chem. A* **2004,** *108* (15), 3129-3133.
26. Wilson, A. K.; Dunning, T. H., SO_2 revisited: Impact of tight d augmented correlation consistent basis sets on structure and energetics. *J. Chem. Phys.* **2003,** *119* (22), 11712-11714.
27. Denis, P. A., Basis Set Requirements for Sulfur Compounds in Density Functional Theory: a Comparison between Correlation-Consistent, Polarized-Consistent, and Pople-Type Basis Sets. *J. Chem. Theory Comput.* **2005,** *1* (5), 900-907.

B Supporting Information for Chapter 3

Adapted from Martin, D. J.; Mercado, B. Q.; Mayer, J. M. “Combining scaling relationships overcomes rate versus overpotential trade-offs in O_2 molecular electrocatalysis.” *Sci*. *Adv.* **2020**, *6*, eaaz3318.

B.1 Spectroscopic Characterization of 1

B.1.1 High Resolution Mass Spectra of 1

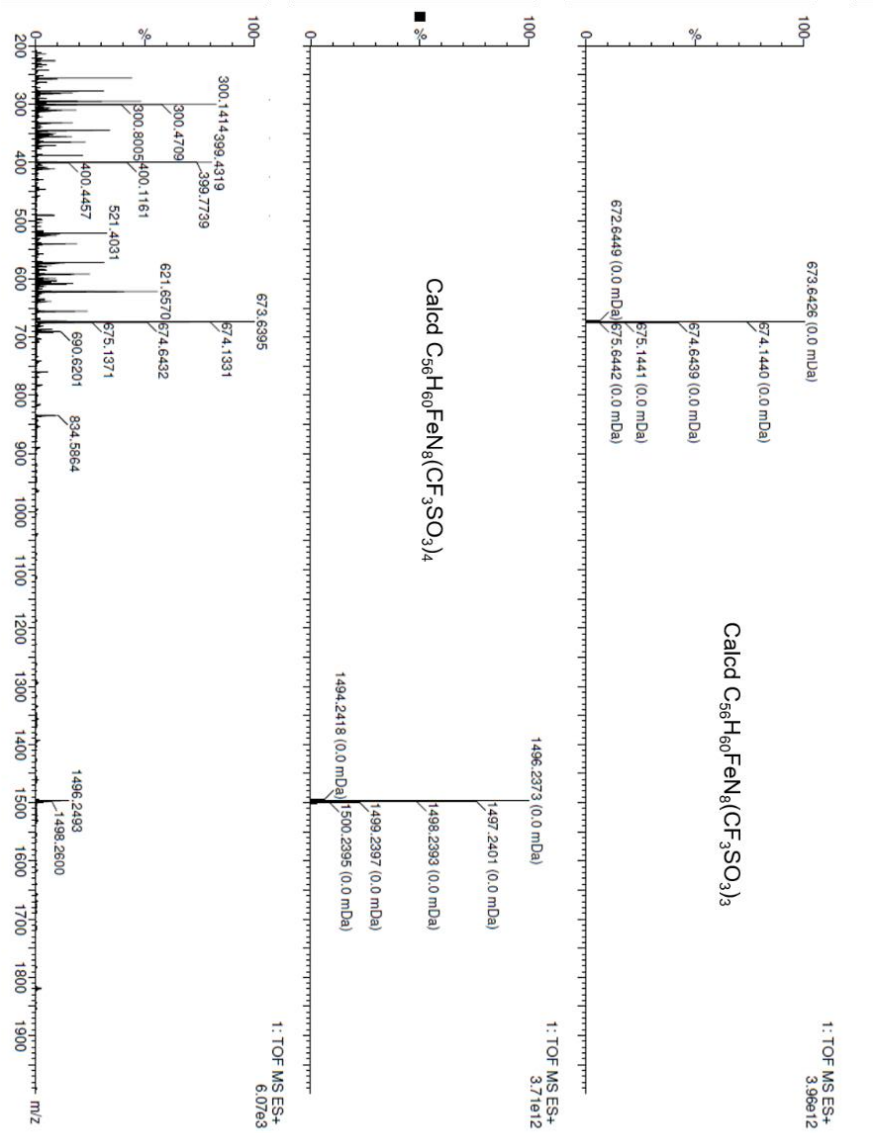

Figure B1. Full high-resolution ESI mass spectrum of **1** with identified peaks, as labeled.

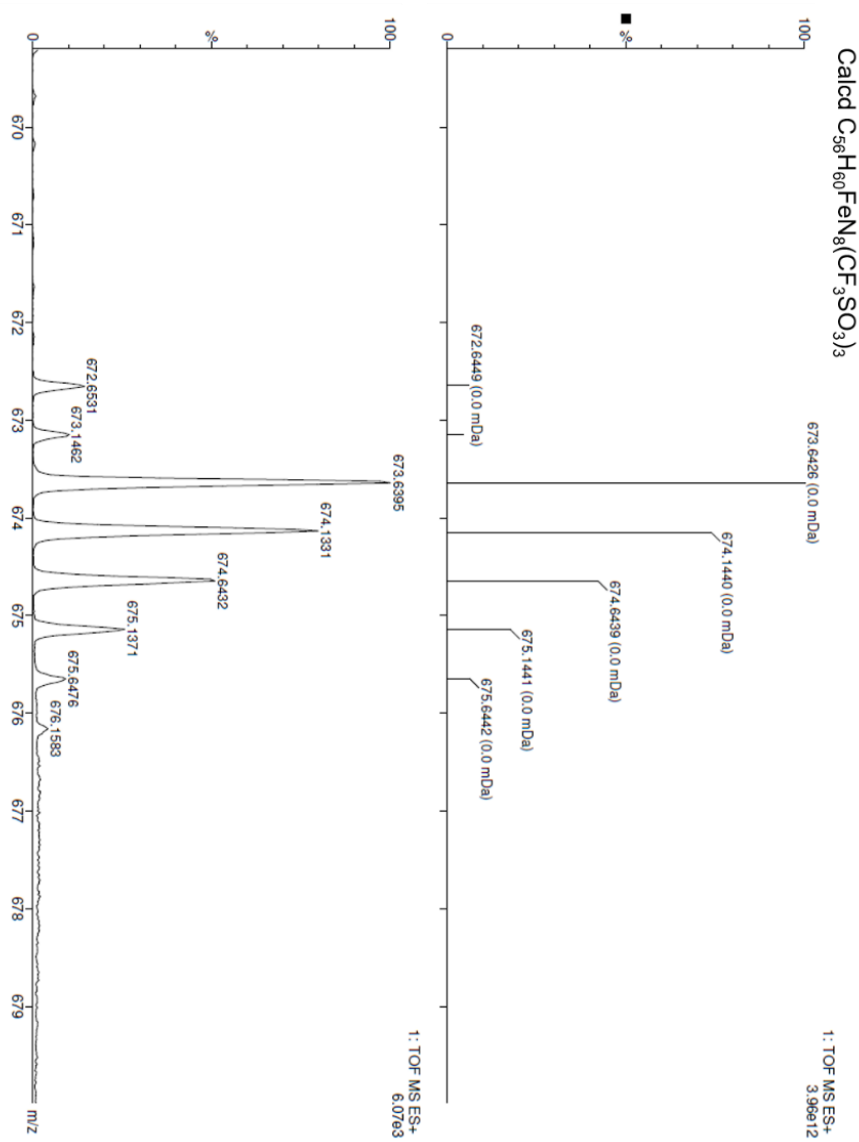

Figure B2. High-resolution ESI mass spectrum and isotopic fits for the [M^{5+} + 3OTf^-] ion.

B.1.2 UV-visible Spectrum of 1

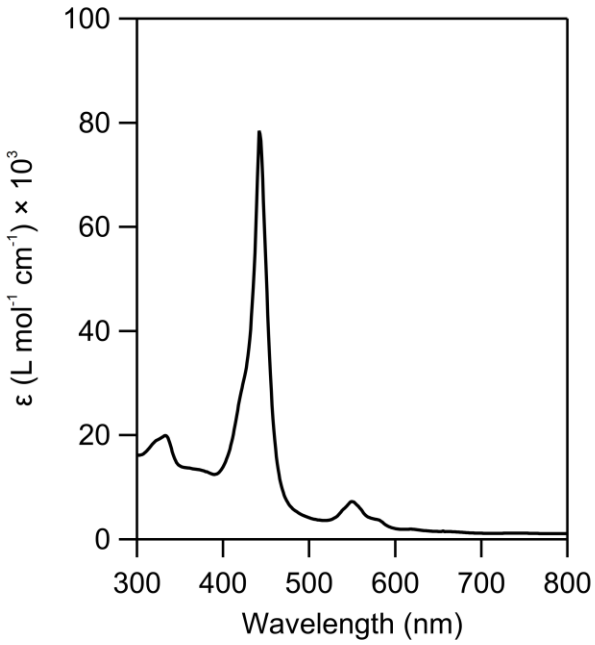

Figure B3. UV-vis spectrum of **1** in *N*,*N*-dimethylformamide. This matches the reported spectrum.[1]

B.1.3 IR Spectrum of 1

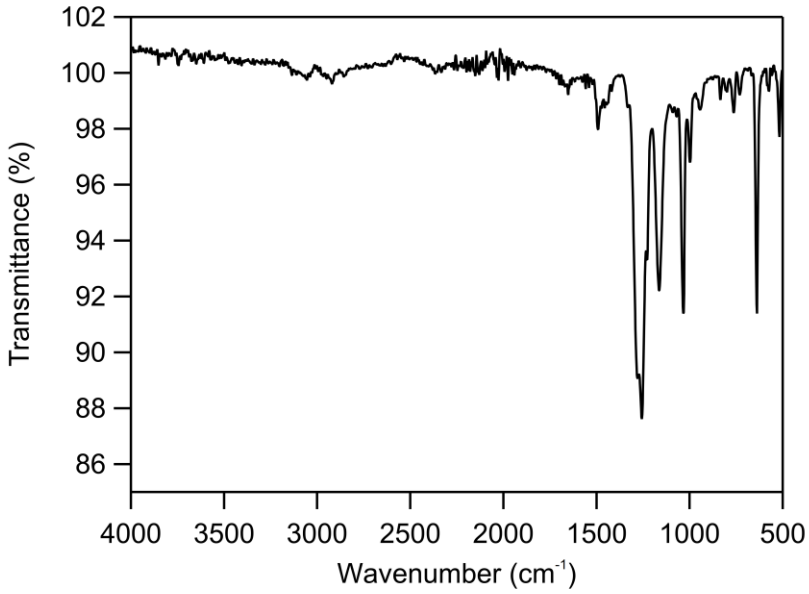

Figure B4. IR spectrum of **1**. The sample was dropcast from a MeCN solution containing **1** directly onto the ATR-IR crystal and letting the solvent evaporate. The collected spectrum matches the reported spectrum.[1]

B.2 Voltammetry of 1

B.2.1 Voltammetry under Non-Catalytic Conditions

The voltammetry of **1** was investigated under argon in MeCN containing 0.1 M [*n*-Bu_4N][BF_4]. This section has been divided into subsections that are identified by the buffer identity that was added to solution (or lack thereof). In general, **1** has three reversible couples in the absence of any added buffer ($E_{1/2}(Fe^{III}/Fe^{II})$, $E_{1/2}(Fe^{II}/Fe^{I})$, and $E_{1/2}$ (Fe^{I}/Fe^{0}), respectively). When a carboxylate buffer was added to solution, the Fe^{III}/Fe^{II} redox couple shifted negatively (see **Figure B8**, **Figure B10**, and **Figure B14**). The Fe^{II}/Fe^{I} redox couple also shifted negatively, though to a lesser extent; no change was observed for the Fe^{I}/Fe^{0} redox couple (**Figure B7**).

B.2.1.1 In the absence of buffer

The voltammetry of **1** under argon and in the absence of added buffer was investigated in MeCN containing 0.1 M [*n*-Bu_4N][BF_4]. In solutions containing only 0.1 [*n*-Bu_4N][BF_4] and **1**, three reversible couples were observed and correspond to $E_{1/2}(Fe^{III}/Fe^{II})$, $E_{1/2}(Fe^{II}/Fe^{I})$, and $E_{1/2}$ (Fe^{I}/Fe^{0}). The reduction potentials (averaged from eight independent experiments) were -0.295V, -1.265 V, and -1.673 V vs. Fc^{+}/Fc, respectively (**Figure B5**). The Fe^{III}/Fe^{II} redox couple was chemically reversible and diffusion controlled (**Figure B6**).

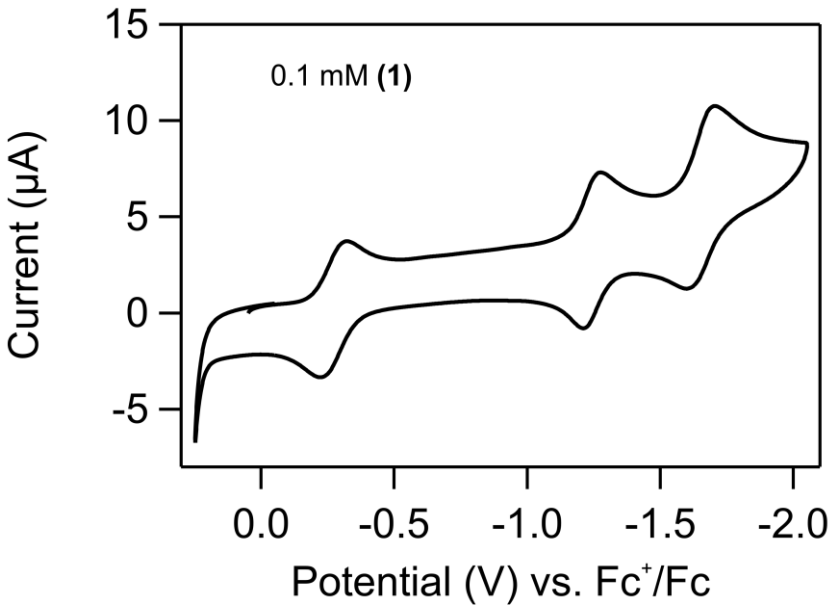

Figure B5. A cyclic voltammogram of an Ar-sparged solution of **1**.

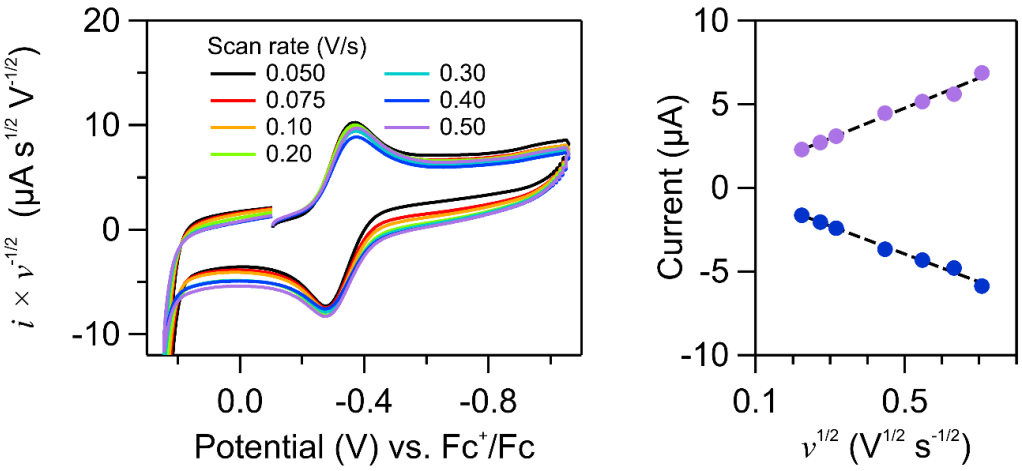

Figure B6. Scan rate investigation of the Fe^{III}/Fe^{II} redox couple of **1** in unbuffered solution. (**Left**) Voltammograms of **1** at varying scan rates, where the current has been divided by the square root of scan rate. (**Right**) The anodic and cathodic peak currents are linear with $v^{1/2}$, showing that the redox couple is diffusion controlled.

B.2.1.2 In the presence of AcOH/AcO⁻

To a MeCN solution containing 0.1 M [*n*-Bu_4N][BF_4] and 0.1 mM **1** was added a 1:1 buffer of acetic acid (AcOH) and tetra-*n*-butylammonium acetate (AcO^-). Under argon, the addition of buffer shifted $E_{1/2}(Fe^{III}/Fe^{II})$ and $E_{1/2}(Fe^{II}/Fe^{I})$ negatively; $E_{1/2}(Fe^{I}/Fe^{0})$ did not change (**Figure B7** and **Figure B8**). After addition of 100 mM AcOH buffer, the $E_{1/2}(Fe^{III}/Fe^{II})$ was -0.656 V vs. Fc^+/Fc (**Figure B8**). In solutions containing 100 mM AcOH buffer, the Fe^{III}/Fe^{II} couple was chemically reversible and diffusion controlled (**Figure B9**).

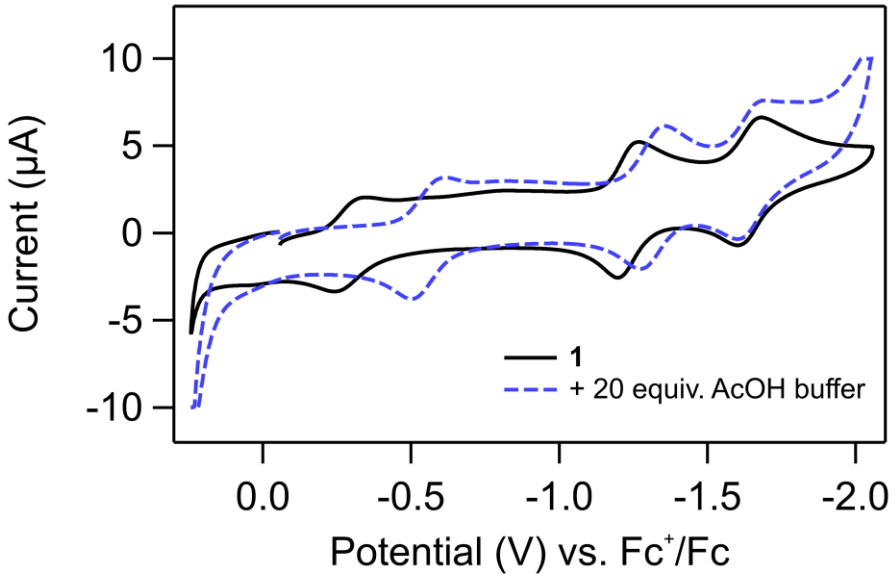

Figure B7. Voltammograms of an Ar-sparged solution of **1** before and after addition of buffered AcOH. $E_{1/2}(Fe^{III}/Fe^{II})$ and $E_{1/2}(Fe^{II}/Fe^{I})$ shift negatively upon addition of the carboxylate buffer.

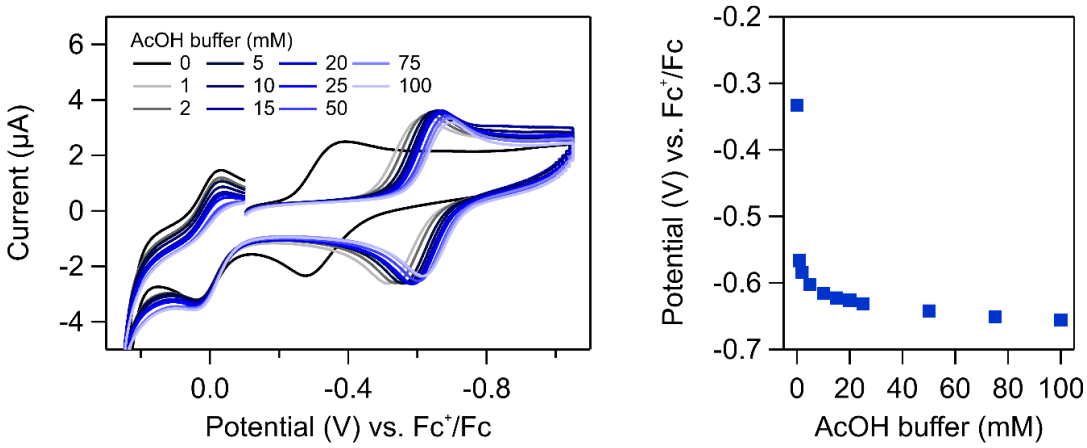

Figure B8. Investigation of the Fe^{III}/Fe^{II} redox couple of **1** with titrations of AcOH buffer. (**Left**) Cyclic voltammograms of an Ar-sparged solution of **1** with various concentrations of AcOH buffer (as noted). (**Right**) $E_{1/2}(Fe^{III}/Fe^{II})$ plotted against the concentration of added AcOH buffer.

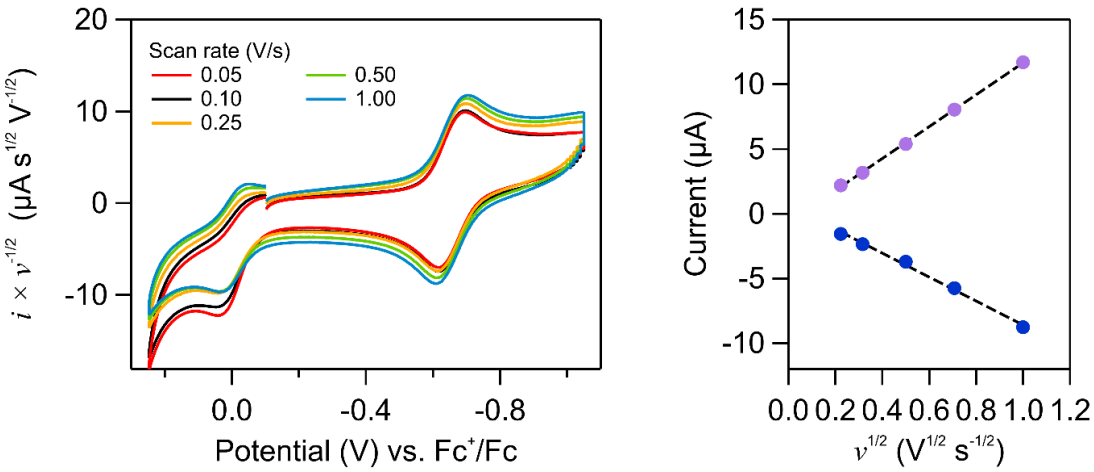

Figure B9. Scan rate investigation of the Fe^{III}/Fe^{II} redox couple of **1** in AcOH buffered solution. (**Left**) Voltammograms of an Ar-sparged solution of **1** containing 100 mM AcOH buffer at varying scan rates, where the current has been divided by the square root of the scan rate. (**Right**) The anodic and cathodic peak currents are linear with $v^{1/2}$, showing that the redox couple is diffusion controlled.

B.2.1.3 In the presence of BzOH/BzO⁻

To a MeCN solution containing 0.1 M [*n*-Bu$_4$N][BF$_4$] and 0.1 mM **1** was added a 1:1 buffer of benzoic acid (BzOH) and tetra-*n*-butylammonium benzoate (BzO$^-$). Under argon, the addition of buffer shifted the $E_{1/2}$(Fe^{III}/Fe^{II}) couple negatively (**Figure B10**). After addition of 100 mM BzOH buffer, the $E_{1/2}$(Fe^{III}/Fe^{II}) was -0.663 V vs. Fc$^+$/Fc. In solutions containing 100 mM BzOH buffer, the Fe^{III}/Fe^{II} couple was chemically reversible and diffusion controlled (**Figure B11**).

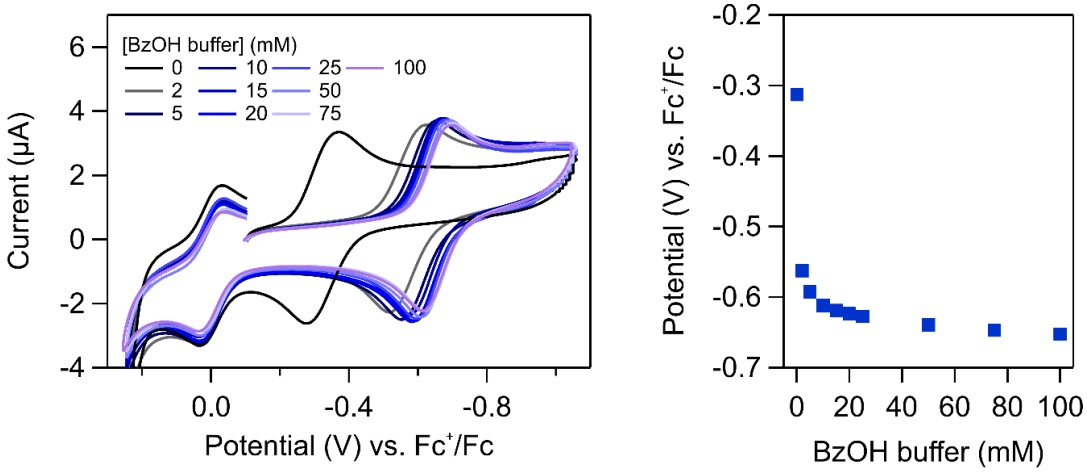

Figure B10. Investigation of the Fe^{III}/Fe^{II} redox couple of **1** with titrations of BzOH buffer. (**Left**) Cyclic voltammograms of an Ar-sparged solution of **1** with various concentrations of BzOH buffer (as noted). (**Right**) $E_{1/2}$(Fe^{III}/Fe^{II}) plotted against the concentration of added BzOH buffer.

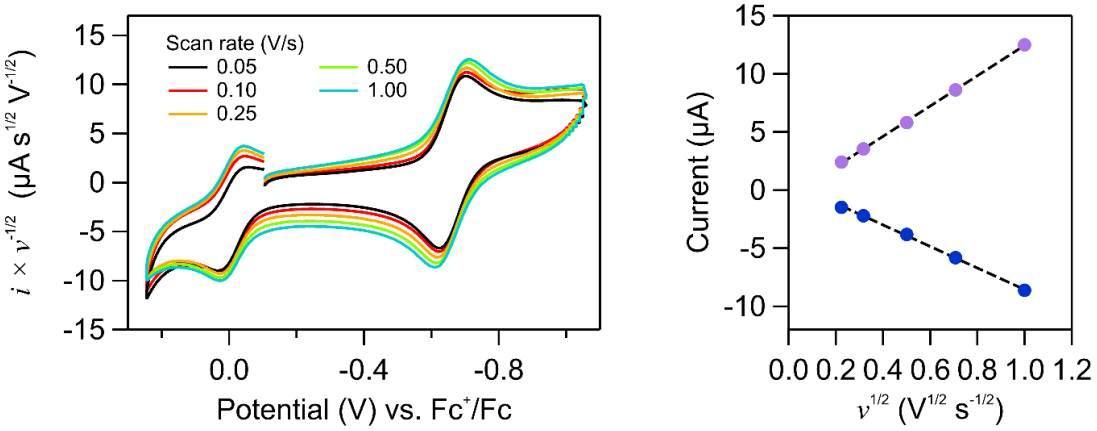

Figure B11. Scan rate investigation of the Fe^{III}/Fe^{II} redox couple of **1** in BzOH buffered solution. (**Left**) Voltammograms of an Ar-sparged solution of **1** containing 100 mM BzOH buffer at varying scan rates, where the current has been divided by the square root of the scan rate. (**Right**) The anodic and cathodic peak currents are linear with $v^{1/2}$, showing that the redox couple is diffusion controlled.

B.2.1.4 In the presence of SalOH/SalO⁻

To a MeCN solution containing 0.1 M [*n*-Bu$_4$N][BF$_4$] and 0.1 mM **1** was added a 1:1 buffer of salicylic acid (SalOH) and tetrabutylammonium salicylate (TFA$^-$). Under argon, the addition of buffer shifted the $E_{1/2}$(Fe^{III}/Fe^{II}) couple negatively (**Figure B12**). After addition of 100 mM SalOH buffer, the $E_{1/2}$(Fe^{III}/Fe^{II}) was -0.533 V vs. Fc$^+$/Fc. In solutions containing 100 mM SalOH buffer, the Fe^{III}/Fe^{II} couple was chemically reversible and diffusion controlled (**Figure B13**).

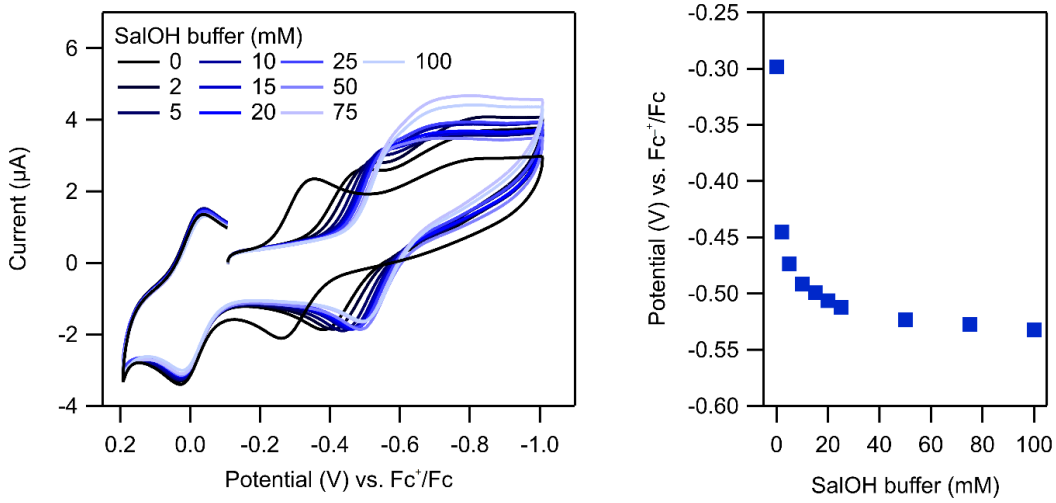

Figure B12. Investigation of the Fe^{III}/Fe^{II} redox couple of **1** with titrations of SalOH buffer. (**Left**) Cyclic voltammograms of an Ar-sparged solution of **1** with various concentrations of SalOH buffer (as noted). (**Right**) $E_{1/2}$(Fe^{III}/Fe^{II}) plotted against the concentration of added SalOH buffer.

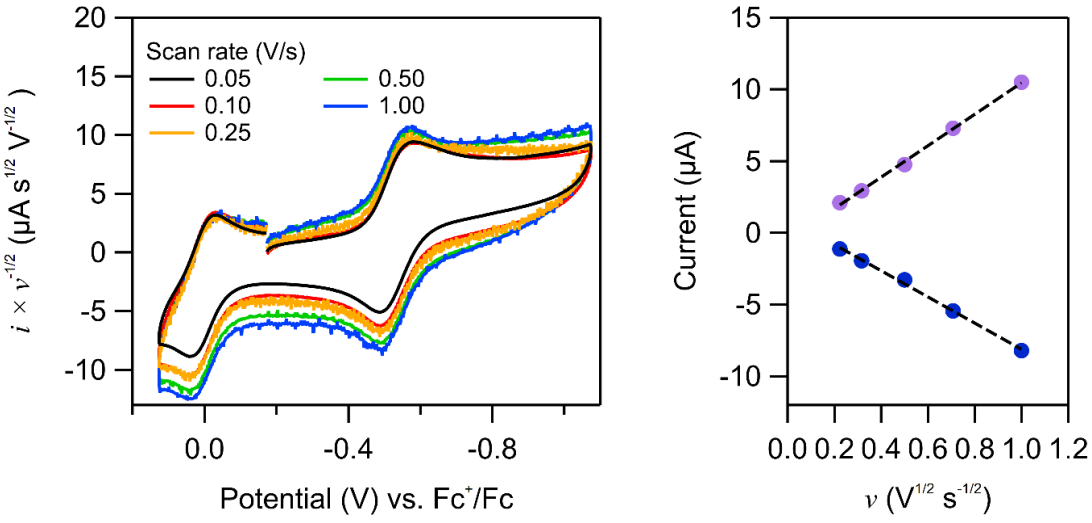

Figure B13. Scan rate investigation of the Fe^{III}/Fe^{II} redox couple of **1** in SalOH buffered solution. (**Left**) Voltammograms of an Ar-sparged solution of **1** containing 100 mM SalOH buffer at varying scan rates, where the current has been divided by the square root of the scan rate. (**Right**) The anodic and cathodic peak currents are linear with $v^{1/2}$, showing that the redox couple is diffusion controlled.

B.2.1.5 In the presence of TFAH/TFA⁻

To a MeCN solution containing 0.1 M [*n*-Bu$_4$N][BF$_4$] and 0.1 mM **1** was added a 1:1 buffer of trifluoroacetic acid (TFA) and sodium trifluoroacetate (TFA$^-$). Under argon, the addition of buffer shifted the $E_{1/2}$(Fe^{III}/Fe^{II}) couple negatively (**Figure B14**). After addition of 100 mM TFA buffer, the $E_{1/2}$(Fe^{III}/Fe^{II}) was -0.349 V vs. Fc$^+$/Fc. In solutions containing 100 mM TFA buffer, the Fe^{III}/Fe^{II} couple was chemically reversible and diffusion controlled (**Figure B15**).

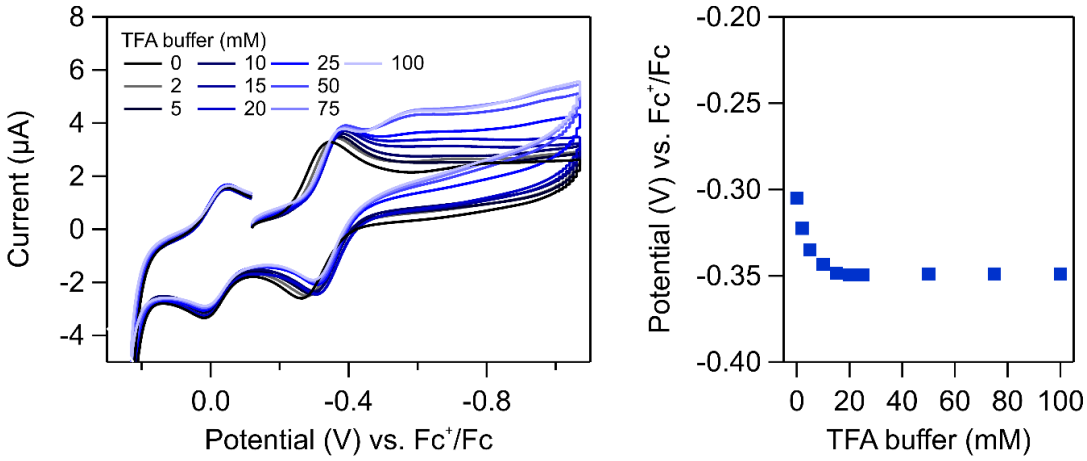

Figure B14. Investigation of the Fe^{III}/Fe^{II} redox couple of **1** with titrations of TFA buffer. (**Left**) Cyclic voltammograms of an Ar-sparged solution of **1** with various concentrations of TFA buffer (as noted). (**Right**) $E_{1/2}$(Fe^{III}/Fe^{II}) plotted against the concentration of added TFA buffer.

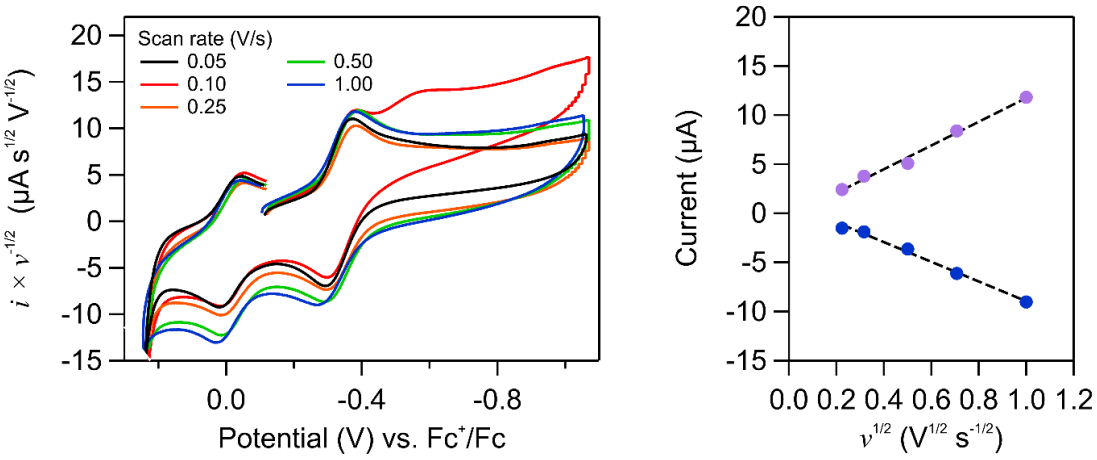

Figure B15. Scan rate investigation of the Fe^{III}/Fe^{II} redox couple of **1** in TFA buffered solution. (**Left**) Voltammograms of an Ar-sparged solution of **1** containing 100 mM TFA buffer at varying scan rates, where the current has been divided by the square root of the scan rate. (**Right**) The anodic and cathodic peak currents are linear with $v^{1/2}$, showing that the redox couple is diffusion controlled.

B.2.1.6 In the presence of [DMF-H]OTf/DMF

To a MeCN solution containing 0.1 M [*n*-Bu_4N][BF_4] and 0.1 mM **1** was added a 1:1 buffer of *N*,*N*-dimethylformamidium triflate ([DMF-H]OTf) and *N*,*N*-dimethylformamide (DMF). Under argon, the addition of large buffer concentrations (>20 mM) broadened the reversible couple (**Figure B16**). This broadening was attributed to the slow exchange of multiple axial ligands (e.g. MeCN and DMF), as has been reported for other iron porphyrins in coordinating solvents.[2] $E_{1/2}(Fe^{III}/Fe^{II})$ values could be directly measured when the concentration of [DMF-H]OTf buffer was less than 20 mM. For higher buffer concentrations, the change in the cathodic peak potential ($E_{p,c}$) was used as a stand-in for changes in $E_{1/2}$.

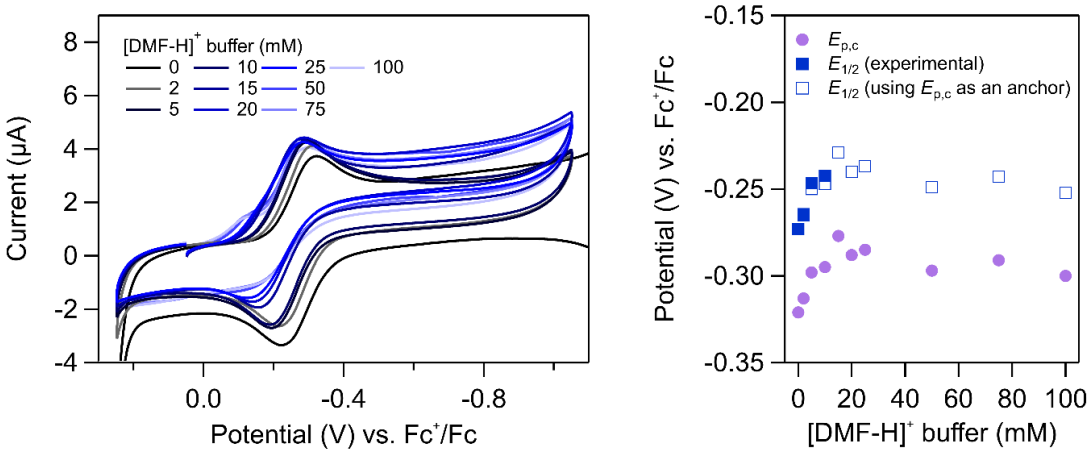

Figure B16. Investigation of In the presence of []the Fe^{III}/Fe^{II} redox couple of **1** with titrations of [DMF-H]OTf buffer. (**Left**) Cyclic voltammograms of an Ar-sparged solution of **1** with various concentrations of [DMF-H]OTf buffer (as noted). (**Right**) $E_{1/2}(Fe^{III}/Fe^{II})$ and $E_{p,c}$ plotted against the concentration of added [DMF-H]OTf buffer. The estimated values of $E_{1/2}$ using $E_{p,c}$ are shown using hollow blue squares.

B.2.1.7 In the presence of [Lut-H]BF_4/Lut

To a MeCN solution containing 0.1 M [*n*-Bu_4N][BF_4] and 0.1 mM **1** was added a 1:1 buffer of 2,6-lutidinium tetrafluoroborate ([Lut-H^+]) and 2,6-lutidine (Lut). Under argon, the addition of buffer shifted the $E_{1/2}(Fe^{III}/Fe^{II})$ couple positively (**Figure B17**). As was the case with [DMF-H]OTf/DMF buffer, the reversible couple broadened somewhat at high concentrations of buffer and a similar estimate for $E_{1/2}$ was made using $E_{p,c}$. After addition of 100 mM [Lut-H^+] buffer, the $E_{1/2}(Fe^{III}/Fe^{II})$ was -0.236 V vs. Fc^+/Fc.

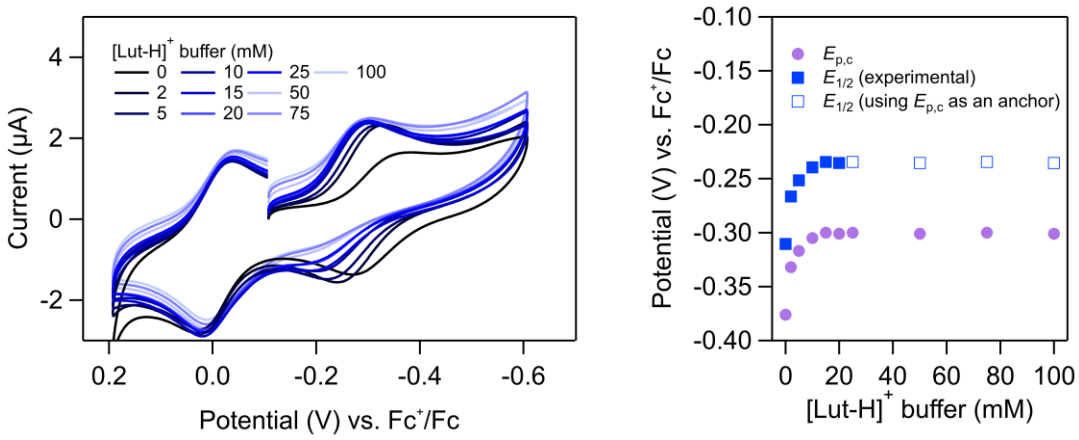

Figure B17. Investigation of the Fe^{III}/Fe^{II} redox couple of **1** with titrations of [Lut-H]BF_4 buffer. (**Left**) Cyclic voltammograms of an Ar-sparged solution of **1** with various concentrations of [Lut-H^+] buffer (as noted). (**Right**) $E_{1/2}(Fe^{III}/Fe^{II})$ and $E_{p,c}$ plotted against the concentration of added [Lut-H]BF_4 buffer. The estimated values of $E_{1/2}$ using $E_{p,c}$ are shown using hollow blue squares.

B.2.1.8 Summary of $E_{1/2}$ dependence on buffer identity and concentration

In the absence of any added buffer, **1** has a reversible, diffusion-controlled redox wave at -0.295 V vs. Fc^+/Fc (averaged from eight separate experiments). The addition of carboxylic acid buffers shifts $E_{1/2}$ negatively. The values of $E_{1/2}$ are sensitive to both the pK_a of the buffer and to the total buffer concentration in solution. For all of the carboxylic acid buffers the redox feature at 100 mM buffer is reversible and diffusion controlled. The addition of buffered $[Lut\text{-}H]BF_4$ or [DMF-H]OTf to **1** shifts the $E_{1/2}$ slightly positive. For a summary of $E_{1/2}(Fe^{III}/Fe^{II})$ values measured under the reported conditions, see **Figure B18** and **Table B1**.

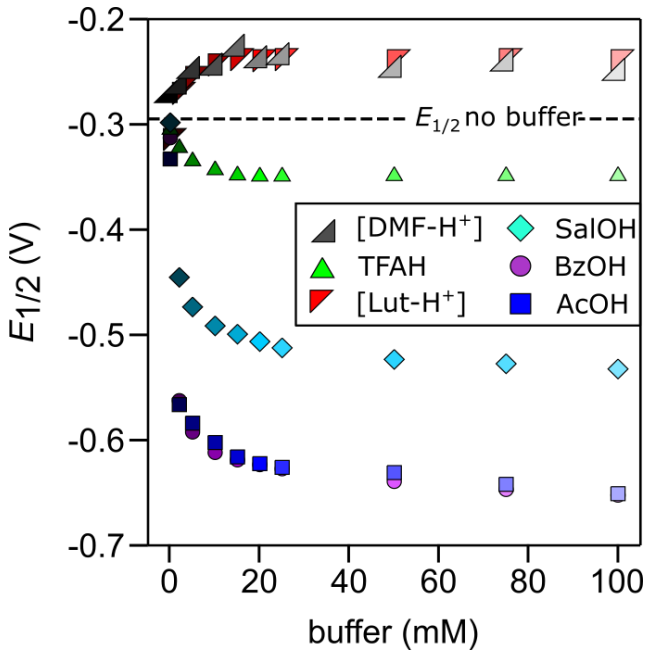

Figure B18. Changes in $E_{1/2}(Fe^{III}/Fe^{II})$ with varying buffers (and concentrations).

Table B1. Summary of $E_{1/2}(Fe^{III}/Fe^{II})$ (V) vs. Fc^+/Fc values measured under the conditions reported in Chapter 3; errors are ± 0.005 V.

[buffer] (mM)	$E_{1/2}$ (AcOH)	$E_{1/2}$ (BzOH)	$E_{1/2}$ (SalOH)	$E_{1/2}$ (TFA)	$E_{1/2}$ ([DMF-H$^+$])	$E_{1/2}$ ([Lut-H$^+$])
2	-0.567	-0.563	-0.446	-0.323	-0.265	-0.267
5	-0.584	-0.593	-0.474	-0.335	-0.250	-0.252
10	-0.603	-0.613	-0.492	-0.343	-0.247	-0.240
15	-0.616	-0.620	-0.500	-0.349	-0.229	-0.235
20	-0.623	-0.624	-0.507	-0.349	-0.240	-0.236
25	-0.626	-0.628	-0.513	-0.350	-0.237 [a]	-0.235 [a]
50	-0.631	-0.640	-0.524	-0.349	-0.249 [a]	-0.236 [a]
75	-0.642	-0.648	-0.528	-0.349	-0.243 [a]	-0.235 [a]
100	-0.651	-0.653	-0.536	-0.349	-0.252 [a]	-0.236 [a]

[a] From $E_{p,c}$; see B.2.1.6 and B.2.1.7.

B.2.2 Voltammetry under Catalytic Conditions

In the presence of oxygen and buffered acid, a large irreversible current is observed at the potential of the Fe^{III}/Fe^{II} redox couple. When buffered with AcOH, this current is more than 200 mV positive of glassy carbon catalyzed ORR under identical conditions and is ascribed to ORR catalysis via **1** (**Figure B19**). Electrochemical ORR was examined using multiple buffers at varying concentrations and at different partial pressures of O_2 (air vs. 1 atm O_2). The effect of added water was also studied. To ensure reproducibility, each catalytic voltammogram was performed in duplicate and the rates were averaged.

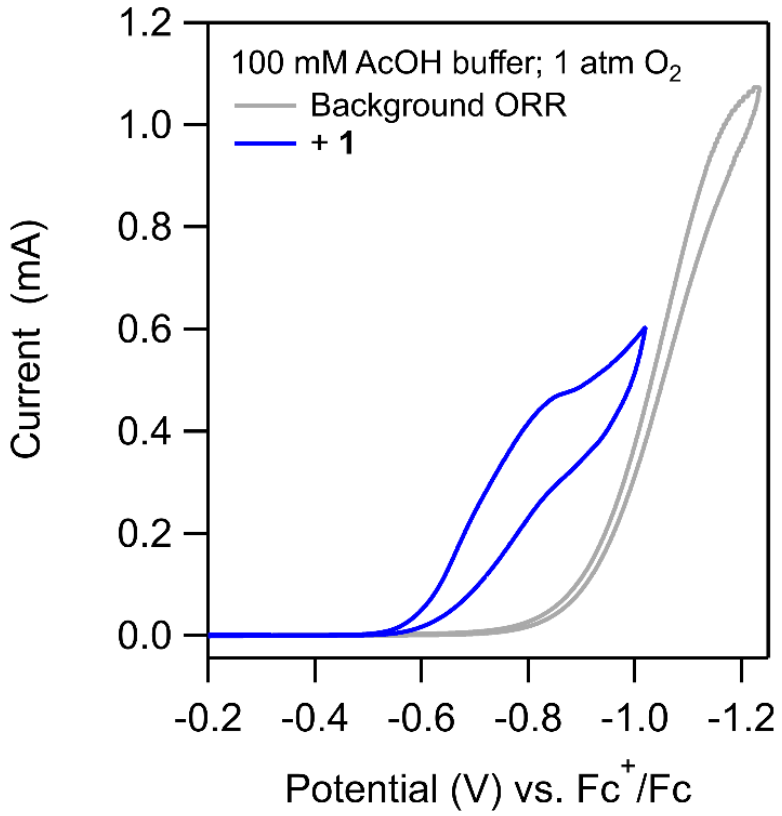

Figure B19. Cyclic voltammograms of an O_2-sparged MeCN solution containing 100 mM [AcOH] buffer before (black) and after (blue) adding 30 μM **1**. No significant background ORR is observed until -0.8 V vs. Fc^+/Fc.

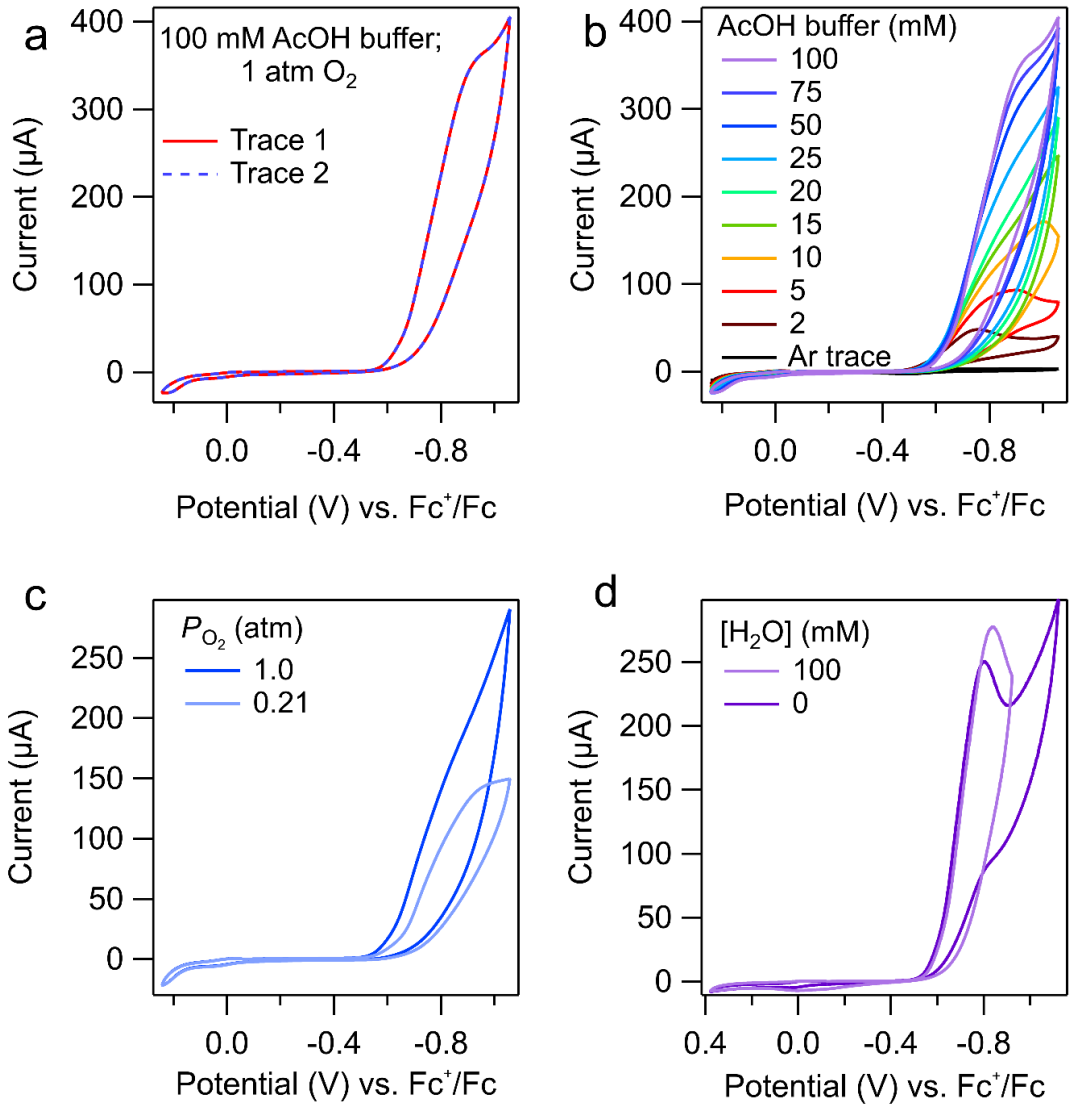

Figure B20. Voltammograms of **1** with AcOH buffer under various solution conditions. (**A**) Repeated voltammograms of O_2-sparged (1 atm) solution containing 0.1 mM **1** and 100 mM AcOH buffer, displaying scan-to-scan reproducibility. (**B**) Voltammograms of an O_2-sparged (1 atm) solution containing 0.1 mM **1** and varying amounts of AcOH buffer, as noted in legend. The Ar-sparged 100 mM AcOH buffered solution is included for reference (black trace). (**C**) Catalytic voltammograms of a solution containing 0.1 mM **1** and 20 mM AcOH buffer after being sparged with O_2 and air (as noted). (**D**) Voltammograms of an O_2-sparged (1 atm) solution containing 0.1 mM **1** and 100 mM AcOH buffer in the presence and absence of water.

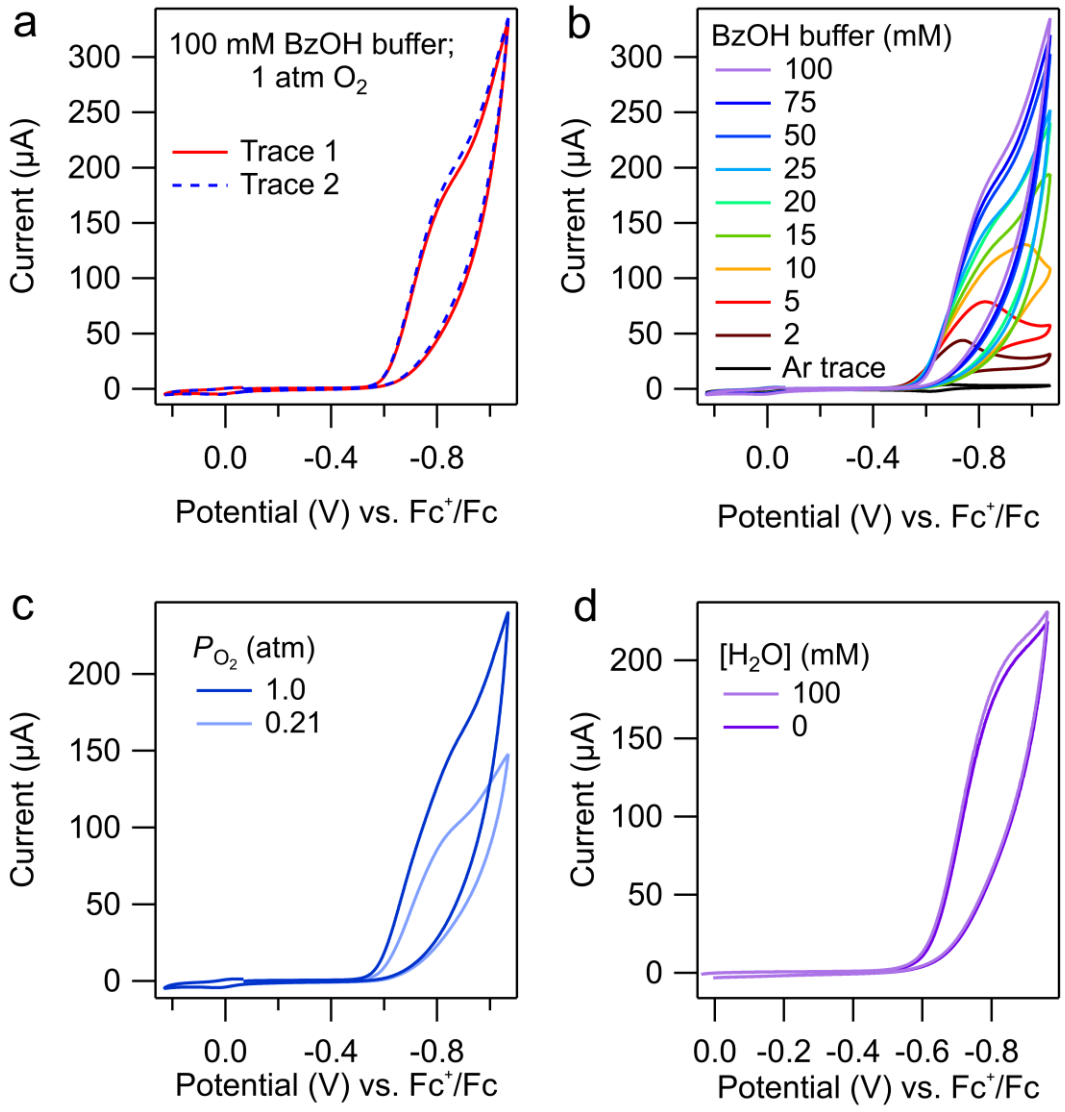

Figure B21. Voltammograms of **1** with BzOH buffer under various solution conditions. (**A**) Repeated voltammograms of O_2-sparged (1 atm) solution containing 0.1 mM **1** and 100 mM BzOH buffer, displaying scan-to-scan reproducibility. (**B**) Voltammograms of an O_2-sparged (1 atm) solution containing 0.1 mM **1** and varying amounts of BzOH buffer, as noted in legend. The Ar-sparged 100 mM BzOH buffered solution is included for reference (black trace). (**C**) Catalytic voltammograms of a solution containing 0.1 mM **1** and 20 mM BzOH buffer after being sparged with O_2 and air (as noted). (**D**) Voltammograms of an O_2-sparged (1 atm) solution containing 0.1 mM **1** and 100 mM BzOH buffer in the presence and absence of water.

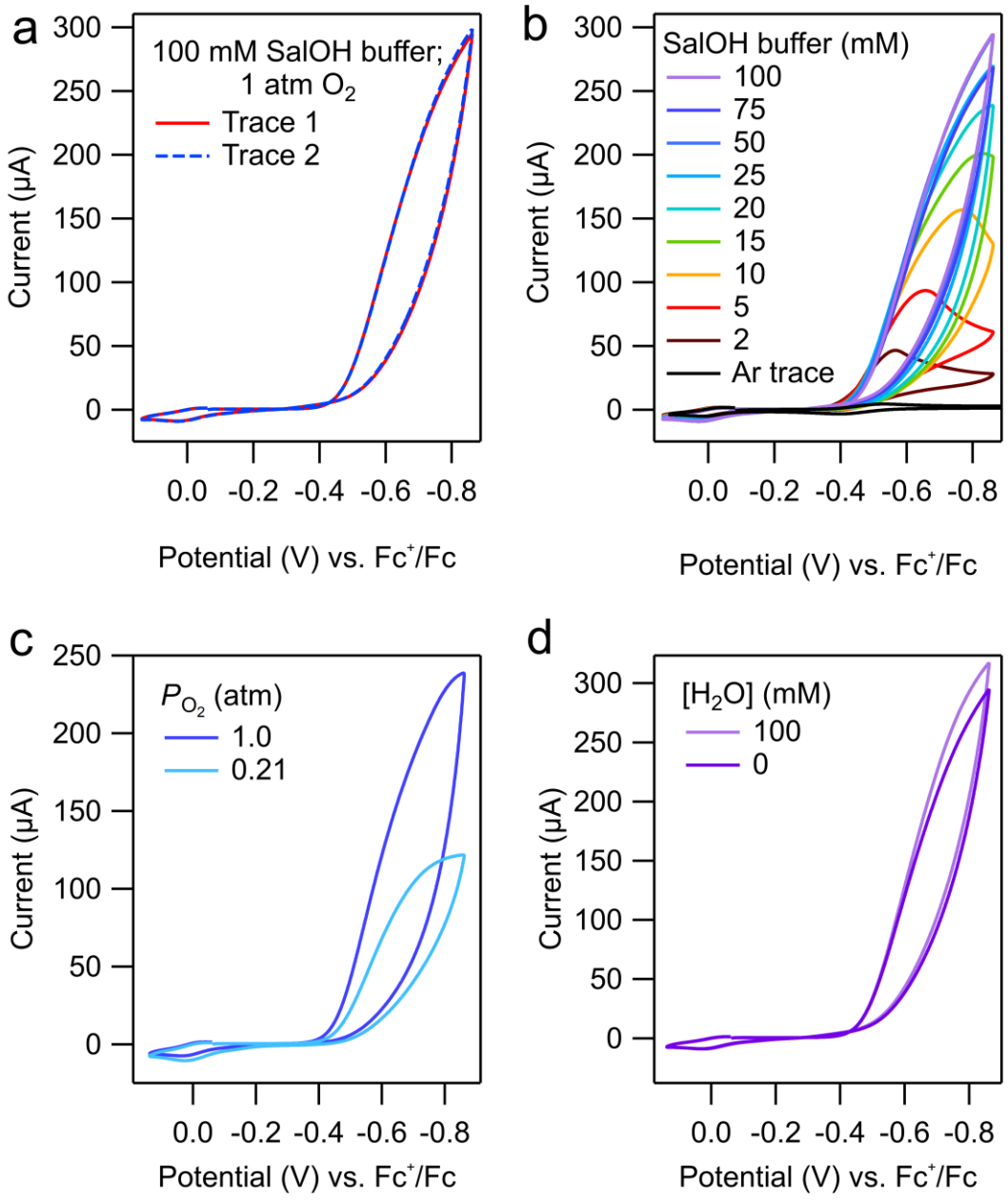

Figure B22. Voltammograms of **1** with SalOH buffer under various solution conditions. (**A**) Repeated voltammograms of O_2-sparged (1 atm) solution containing 0.1 mM **1** and 100 mM SalOH buffer, displaying scan-to-scan reproducibility. (**B**) Voltammograms of an O_2-sparged (1 atm) solution containing 0.1 mM **1** and varying amounts of SalOH buffer, as noted in legend. The Ar-sparged 100 mM SalOH buffered solution is included for reference (black trace). (**C**) Catalytic voltammograms of a solution containing 0.1 mM **1** and 20 mM SalOH buffer after being sparged with O_2 and air (as noted). (**D**) Voltammograms of an O_2-sparged (1 atm) solution containing 0.1 mM **1** and 100 mM SalOH buffer in the presence and absence of water.

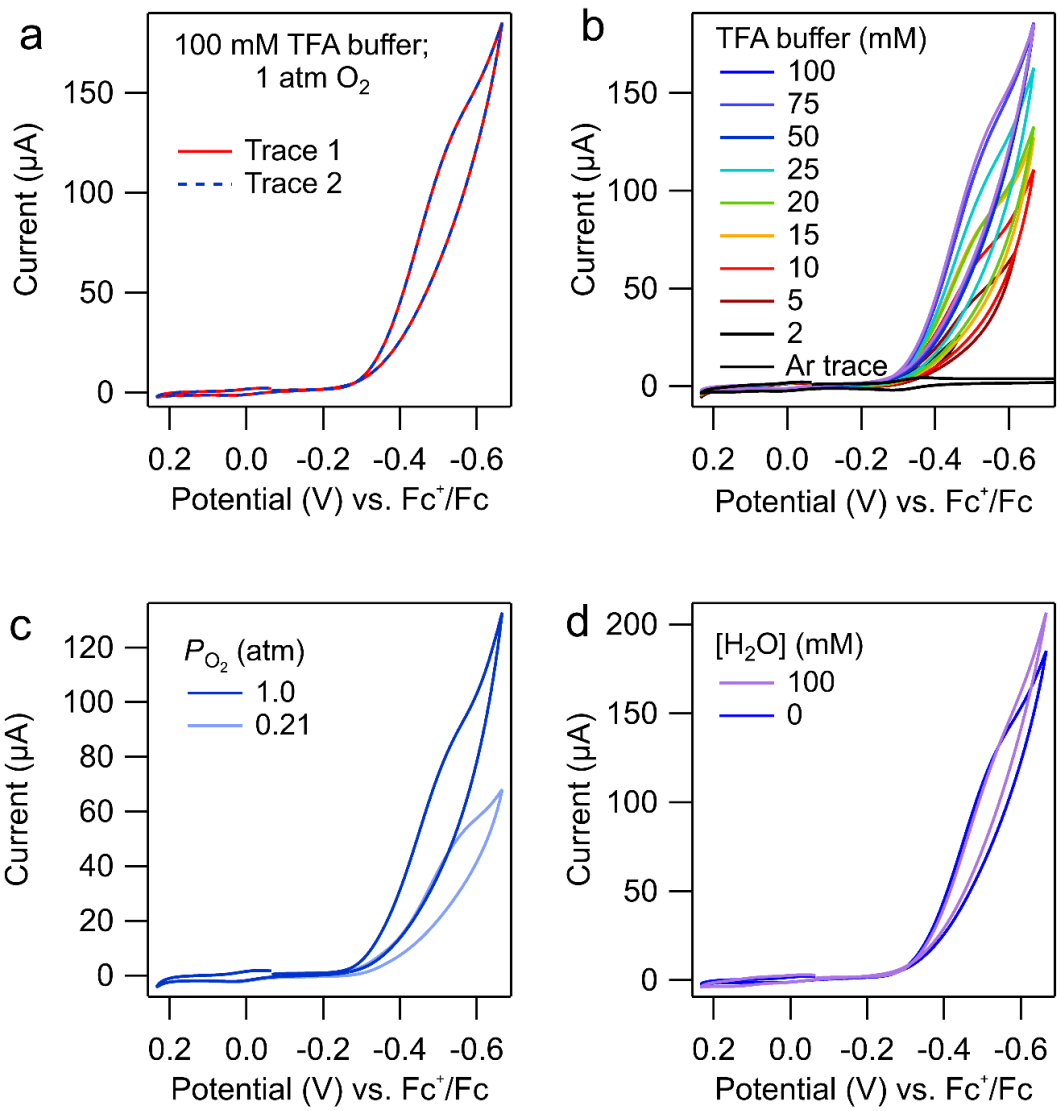

Figure B23. Voltammograms of **1** with TFA buffer under various solution conditions. (**A**) Repeated voltammograms of O_2-sparged (1 atm) solution containing 0.1 mM **1** and 100 mM TFA buffer, displaying scan-to-scan reproducibility. (**B**) Voltammograms of an O_2-sparged (1 atm) solution containing 0.1 mM **1** and varying amounts of TFA buffer, as noted in legend. The Ar-sparged 100 mM TFA buffered solution is included for reference (black trace). (**C**) Catalytic voltammograms of a solution containing 0.1 mM **1** and 20 mM TFA buffer after being sparged with O_2 and air (as noted). (**D**) Voltammograms of an O_2-sparged (1 atm) solution containing 0.1 mM **1** and 100 mM TFA buffer in the presence and absence of water.

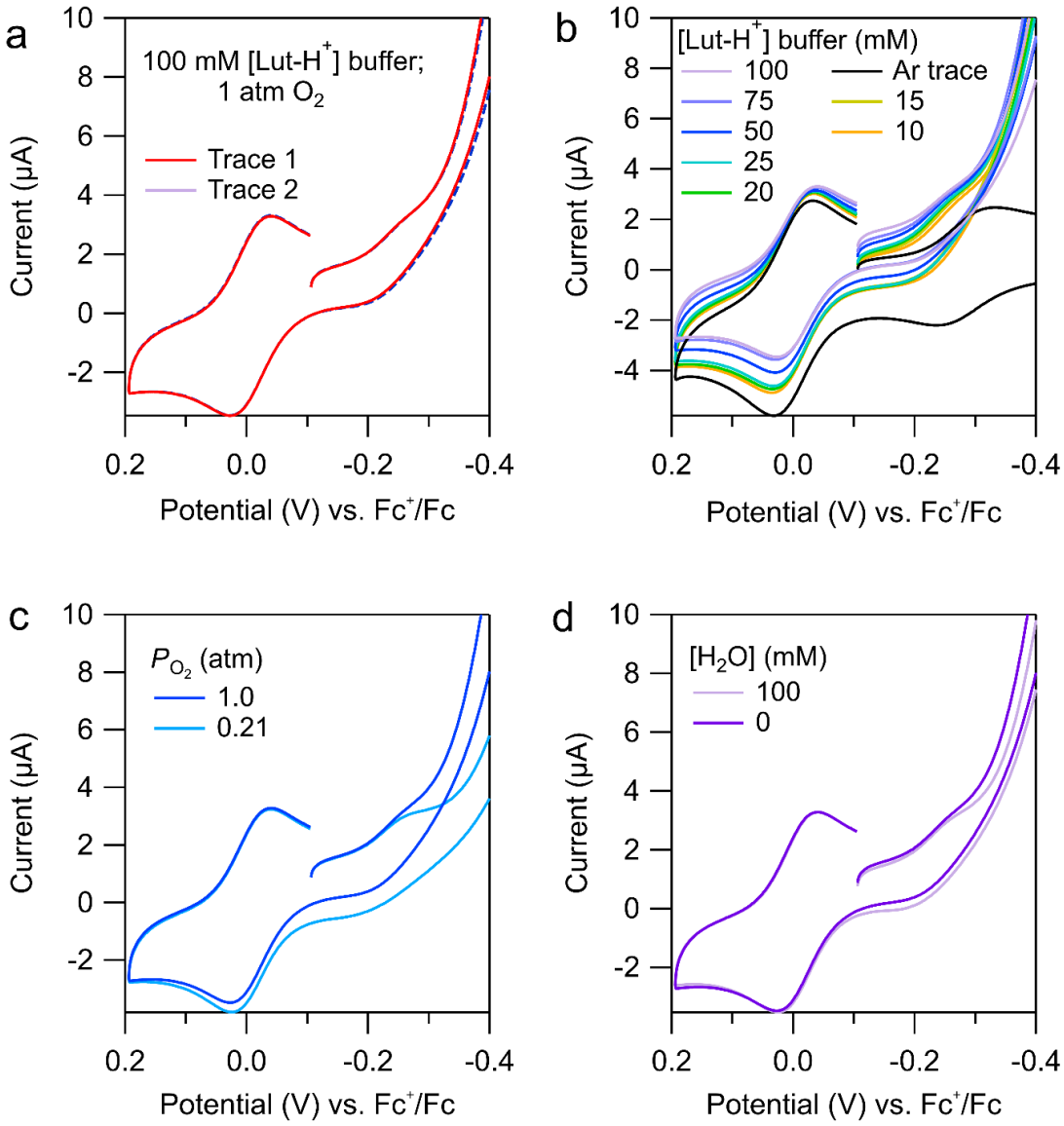

Figure B24. Voltammograms of **1** with [Lut-H$^+$] buffer under various solution conditions. (**A**) Repeated voltammograms of O_2-sparged (1 atm) solution containing 0.1 mM **1** and 100 mM [Lut-H$^+$] buffer, displaying scan-to-scan reproducibility. (**B**) Voltammograms of an O_2-sparged (1 atm) solution containing 0.1 mM **1** and varying amounts of [Lut-H$^+$] buffer, as noted in legend. The Ar-sparged 100 mM [Lut-H$^+$] buffered solution is included for reference (black trace). Only small amounts of current enhancement were observed at $E_{1/2}$, consistent with the very slow catalysis. Background ORR can be observed as the steeper current at potentials more negative than $E_{1/2}$. (**C**) Catalytic voltammograms of a solution containing 0.1 mM **1** and 20 mM [Lut-H$^+$] buffer after being sparged with O_2 and air (as noted). (**D**) Voltammograms of an O_2-sparged (1 atm) solution containing 0.1 mM **1** and 100 mM [Lut-H$^+$] buffer in the presence and absence of water.

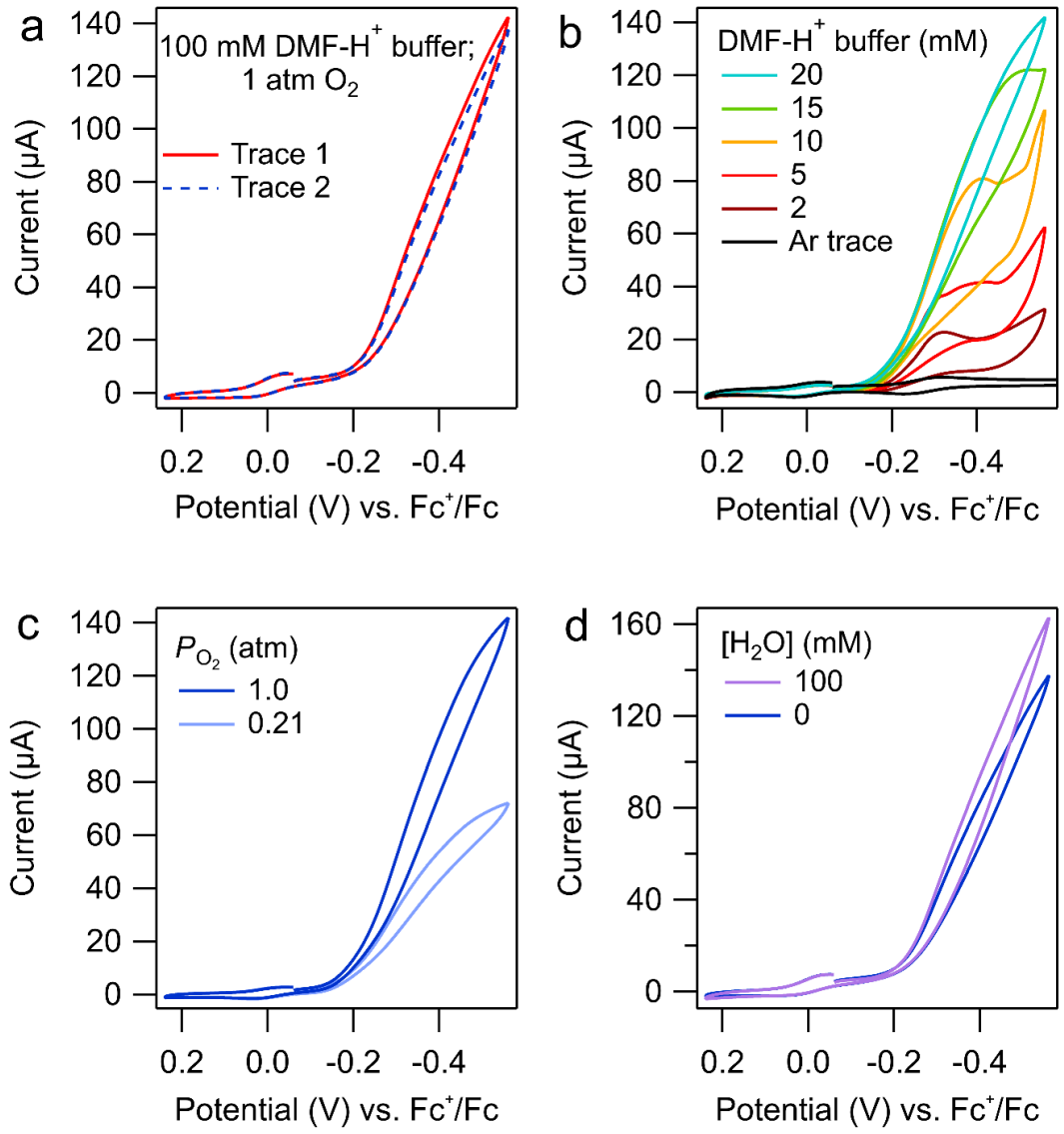

Figure B25. Voltammograms of **1** with [DMF-H]OTf buffer under various solution conditions. (**A**) Repeated voltammograms of O_2-sparged (1 atm) solution containing 0.1 mM **1** and 100 mM [DMF-H]OTf buffer, displaying scan-to-scan reproducibility. (**B**) Voltammograms of an O_2-sparged (1 atm) solution containing 0.1 mM **1** and varying amounts of [DMF-H]OTf buffer, as noted in legend. The Ar-sparged 20 mM [DMF-H]OTf buffered solution is included for reference (black trace). Unlike the [Lut-H^+] data, these catalytic currents were more substantial and indicated faster catalysis. (**C**) Catalytic voltammograms of a solution containing 0.1 mM **1** and 20 mM [DMF-H]OTf buffer after being sparged with O_2 and air (as noted). (**D**) Voltammograms of an O_2-sparged (1 atm) solution containing 0.1 mM **1** and 100 mM [DMF-H]OTf buffer in the presence and absence of water.

B.2.3 Rinse tests

Rinse tests were performed on the 100 mM buffered solutions to test for contributions from electrode-adsorbed catalyst.[3-4] In these experiments, the working electrode was dipped into the catalyst-containing solution before being rinsed with excess MeCN and placed into a fresh solution of MeCN containing 0.1 M [*n*-Bu_4N][BF_4] and 100 mM of the respective buffer (no added catalyst). The solution was sparged with O_2 and a voltammogram was collected. Only small amounts of current, relative to the homogeneous mixtures, were observed during the rinse tests (**Figure B26**).

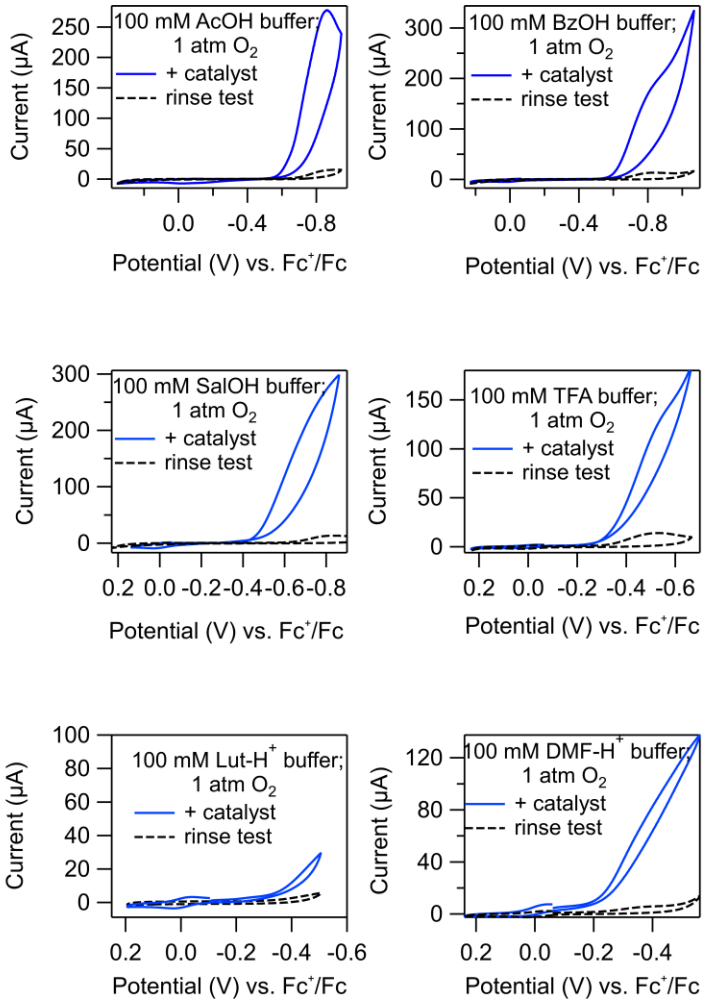

Figure B26. Rinse tests for all of the buffers used in Chapter 3. (Dark blue) catalytic voltammogram collected in an O_2-sparged MeCN solution containing 0.1 mM **1** and 100 mM buffer (as noted). (Light blue) A voltammogram collected in an O_2-sparged MeCN solution containing 100 mM of the same buffer (as noted) using the same electrode after dipping it into the catalyst-containing solution and rinsing it with excess MeCN. The peak current passed during the rinse tests were always less than < 10% of the peak current measured in the catalyst-containing solution.

B.3 UV-vis Spectroscopy of 1 + Varying Buffers

For the buffers used in Chapter 3, the addition of buffer changed the color of the catalyst-containing solutions used for electrochemical measurements. Immediately after the electrochemistry was performed, an aliquot of the buffered, catalyst-containing solution was diluted by approximately half with MeCN and a UV-vis spectrum was collected. The UV-vis spectra of all the buffered solutions were normalized to the strongest absorbing feature and are shown in **Figure B27**. As shown, the Q-band region—which is diagnostic for iron porphyrins[5]—reveals that each of the spectra have different λ_{max} values (**Table B2**). The varying λ_{max} values indicate that the catalyst identity is different in the presence of the varying buffers.

Table B2. Q-band region λ_{max} values for ~ 0.05 mM **1** in MeCN containing ~0.05 M [*n*-Bu_4N][BF_4] and ~0.05 M buffer.

Buffer	λ_{max} (nm)
-	575
$AcOH/AcO^-$	553, 621, 660
$BzOH/BzO^-$	555, 623, 661
$SalOH/SalO^-$	569, 631, 666
$TFAH/TFA^-$	576, 643, 669
$[DMF\text{-}H^+]$/DMF	587, 660, 693
$[Lut\text{-}H^+]$/Lut	579, 651 (sh)

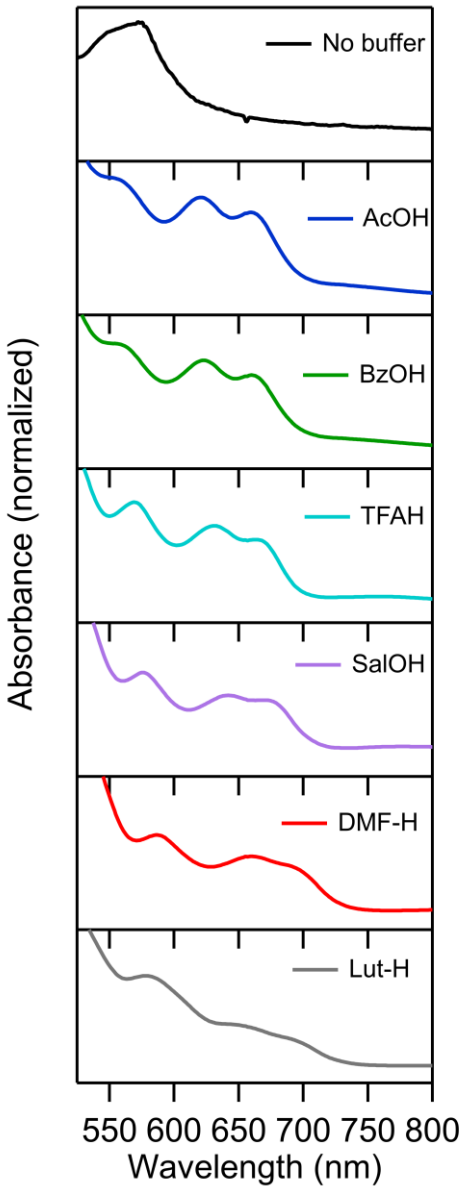

Figure B27. UV-vis spectra of MeCN solutions containing **1** (~ 0.05 mM), [*n*-Bu_4N][BF_4] (~0.05 M), and varying 1:1 buffers (~0.05 M, as identified). Samples were prepared by taking the solutions used for electrochemistry measurements and diluting with approximately the same volume of MeCN.

B.4 Homoconjugation

Solutions of acids and their conjugate bases (buffer solutions) in aprotic organic solvents often form hydrogen-bonded complexes, as in eq B.1 and eq B.2. This effect is termed homoconjugation; the hydrogen-bonded complex is called a homoconjugate, and the concentrations of the uncomplexed acid and base are denoted here by the subscript "free". The effects of homoconjugation on electrocatalytic measurements, such as on the overpotential and turnover frequency, have been previously discussed, especially for non-buffered solutions.[6-8] Chapter 3 used exclusively one-to-one buffer mixtures of acid and conjugate base to minimize these effects, as described in the three sections below.

B.4.1 Formation Constants

Homoconjugation formation constants (K_f) in MeCN have been tabulated **Table B3**,[7,9] and the values relevant to Chapter 3 are given in **Table B3**. In general, such K_f values are fairly large for neutral acids and anionic bases (eq B.1), and all of the carboxylic acid/carboxylate anion buffers used here have log(K_f) = 3.6 ± 0.3. The formation of homoconjugates are typically less extensive for cationic Bronsted acids (eq B.2).

$$[\mathrm{HA}]_{\mathrm{free}} + [\mathrm{A}^-]_{\mathrm{free}} \rightleftharpoons [\mathrm{AH}\cdots\mathrm{A}^-];\ K_{\mathrm{f}}\,(\mathrm{M}^{-1}) \qquad \text{(eq B.1)}$$

$$[\mathrm{HB}^+]_{\mathrm{free}} + [\mathrm{B}]_{\mathrm{free}} \rightleftharpoons [\mathrm{BH}^+\cdots\mathrm{B}];\ K_{\mathrm{f}}\,(\mathrm{M}^{-1}) \qquad \text{(eq B.2)}$$

$[\mathrm{HA}]_{\mathrm{free}}$ = concentration of non-homoconjugated, neutral acid

$[\mathrm{A}^-]_{\mathrm{free}}$ = concentration of non-homoconjugated, anionic conjugate base

$[\mathrm{HB}^+]_{\mathrm{free}}$ = concentration of non-homoconjugated, cationic acid

$[\mathrm{B}]_{\mathrm{free}}$ = concentration of non-homoconjugated, neutral conjugate base

$[\mathrm{AH}\cdots\mathrm{A}^-]$ and $[\mathrm{BH}^+\cdots\mathrm{B}]$ = concentrations of homoconjugates (1:1 adducts)

$K_{\mathrm{f}}\,(\mathrm{M}^{-1})$ = homoconjugation formation constants

Table B3. Homoconjugation formation constants for the buffers used in Chapter 3.

Buffer	log(K_f)[a]
[DMF-H$^+$]/DMF	1.7
TFAH/TFA$^-$	3.9
[LutH$^+$]/Lut	< 0.8 [b]
SalOH/SalO$^-$	3.3
BzOH/BzO$^-$	3.6
AcOH/AcO$^-$	3.9

[a] Homoconjugation formation constants.[7,9] [b] log(K_f) = 0.8 for pyridinium/pyridine and is estimated as a maximum value for lutidinium/lutidine.

B.4.2 The Effect of Homoconjugation on Effective Overpotential

The Nernst equation for the ORR includes the concentrations of the acid and its conjugate base. Therefore, the use of buffered solutions is required to accurately define the ORR equilibrium potential and thus the effective overpotential, η_{eff} (Eq. 3.1 in Chapter 3, reproduced below as eq B.3). In the 1:1 buffers used here, homoconjugation to form a 1:1 adduct (eq B.1) changes the absolute concentrations of HA and A$^-$ but does not change their ratio. Because the η_{eff} considers only the ratio of acid to conjugate base, the use of 1:1 buffer results in an η_{eff} expression that is unaffected by homoconjugation, eq B.4. This simplification is unique to 1:1 buffers and is the reason for the use of only 1:1 buffers in Chapter 3.

$$\eta_{\text{eff}} = E^{\text{o}}_{\text{ORR}} - E_{1/2} - \frac{2.303\text{RT}}{n_{\text{cat}}\text{F}}\log\left(\frac{\left[\text{H}_2\text{O}\right]^2\left[\text{A}^-\right]^4}{P_{\text{O}_2}\left[\text{HA}\right]^4}\right) - (0.0592\text{V})\text{p}K_a \qquad \text{(eq B.3)}$$

$$\eta_{\text{eff}} = E^{\text{o}}_{\text{ORR}} - E_{1/2} - \frac{2.303\text{RT}}{n_{\text{cat}}\text{F}}\log\left(\frac{\left[\text{H}_2\text{O}\right]^2}{P_{\text{O}_2}}\right) - (0.0592\text{V})\text{p}K_a;\ \text{when } [\text{HA}] = [\text{A}^-] \qquad \text{(eq B.4)}$$

η_{eff} = effective overpotential

$E^{\text{o}}_{\text{ORR}}$ = standard chemical potential of O_2 to H_2O

E_{ORR} = equilibrium potential of O_2 to H_2O under catalytic conditions

$E_{1/2}$ = catalyst $E_{1/2}(\text{Fe}^{\text{III}}/\text{Fe}^{\text{II}})$

n_{cat} = number of electrons in one catalytic turnover, assumed to be 4 for $\text{O}_2/\text{H}_2\text{O}$

pK_a = pK_a of the proton donor (HA), the strongest acid in solution. For all of the acids used, the linear plots of TOF_{max} vs. $[\text{HA}]_{\text{free}}$ implicate HA (or HB$^+$) as the proton donor and not the homoconjugate.

B.4.3 Effect of Homoconjugation on $[HA]_{free}$ and on TOF_{max}

As introduced above, homoconjugation affects the concentration of uncomplexed acid and conjugate base, which are indicated by subscripted "free" labels. Using reported formation constants (K_f, **Table B3**) and following eq B.5 and eq B.6 (for neutral and cationic acids, respectively), values of $[HA]_{free}$, $[A^-]_{free}$, $[HB^+]_{free}$, and $[B]_{free}$ were calculated for all of the buffer concentrations used in Chapter 3. These concentrations were used in **Figure B30** and are listed for convenience in **Table B4**.

$$K_f\,(\mathrm{M}^{-1}) = \frac{[\mathrm{AH}\cdots\mathrm{A}^-]}{[\mathrm{HA}]_{free}[\mathrm{A}^-]_{free}} \qquad \text{(eq B.5)}$$

$$K_f\,(\mathrm{M}^{-1}) = \frac{[\mathrm{BH}^+\cdots\mathrm{B}]}{[\mathrm{HB}^+]_{free}[\mathrm{B}]_{free}} \qquad \text{(eq B.6)}$$

Table B4. Calculated values for non-homoconjugated acid and conjugate base ($[HA]_{free}=[A^-]_{free}$ and $[HB^+]_{free}=[B]_{free}$) for varying buffer identities and concentrations.

[buffer] (mM)	**$[DMF\text{-}H^+]_{free}$ (mM)**	**$[TFAH_{free}]$ (mM)**	**$[LutH^+]_{free}$ (mM)**	**$[SalOH_{free}]$ (mM)**	**$[BzOH_{free}]$ (mM)**	**$[AcOH_{free}]$ (mM)**
0	0	0	0	0	0	0
2	1.84	0.443	1.98	0.782	0.595	0.443
5	4.16	0.734	4.85	1.35	1.00	0.734
10	7.36	1.06	9.44	2.00	1.47	1.06
15	10.1	1.32	13.8	2.50	1.82	1.32
20	12.4	1.53	18.0	2.93	2.12	1.53
25	14.6	1.72	22.0	3.30	2.38	1.72
50	23.3	2.45	40.0	4.76	3.42	2.45
75	30.2	3.01	55.6	5.89	4.22	3.01
100	36.1	3.49	70.0	6.83	4.89	3.49

For all of the carboxylic acids used in Chapter 3, $\log(K_f)$ is in the narrow range of 3.6 ± 0.3. Because the homoconjugation formation constants are similar, the calculated values of $[HA]_{free}$ and $[A^-]_{free}$ are similar for the different carboxylate buffers at each of the respective buffer concentrations, at least on the $\log(TOF_{max})$ scale in Figures 1 and 3. The K_f values for the cationic acids, however, are much smaller, $\log(K_f) < 2$. Therefore, the calculated values of $[HB^+]_{free}$ and $[B]_{free}$ are significantly different from $[HA]_{free}$ and $[A^-]_{free}$ at the same concentration of buffer.

Here, we report a rate law that is first order in $[HA]_{free}$ (or $[HB^+]_{free}$). Previously, we reported rate laws that were first order in the total concentration of HA or HB^+ rather than being first order in the concentration of uncomplexed acid. Those earlier studies used DMF as the solvent, where the homoconjugation formation constants are much smaller: e.g., $\log(K_f)$ for BzOH is only 1.2 in DMF

vs. 3.6 in MeCN. Under those conditions, there was little difference between “free” and “total” acid concentrations. Here, in MeCN—*and particularly for the weak acids*—homoconjugation is more significant and must be considered.

This interpretation is consistent with the plots of TOF_{max} vs. [substrate] in **Figure B30** in the Kinetics section below. Note that our definition of TOF_{max} values specifies the *total* concentration of acid and conjugate base (0.1 M for the values in Table 1 of Chapter 3), not the $[acid]_{free}$. At low concentrations of buffer, plots of TOF_{max} vs. [buffer] are approximately linear. At higher concentrations, where homoconjugation is more significant, these plots become concave down. In contrast, plots of TOFmax vs. $[HA]_{free}$ or $[HB^+]_{free}$ are linear across the entire titration, **Figure B30**. These data thus implicate $[HA]_{free}$ (or $[HB^+]_{free}$) as the proton donor, consistent with the conclusion that the proton donor is likely the strongest acid in solution.

Because the homoconjugation formation constants (and thus $[HA]_{free}$ concentrations) are similar between the carboxylic acids, the TOF_{max} values can be directly compared and interpreted using the vector analysis presented in Chapter 3. Likewise, the TOF_{max} values of [DMF-H^+] and [Lut-H^+] can be directly compared and interpreted. However, comparing the TOF_{max} values between the cationic buffer data and the neutral buffer data requires taking the different homoconjugation constants into account.

For example, at the same buffer concentration and pK_a, the proton activity of a solution containing cationic buffer is *higher* than the activity of a solution containing buffered carboxylic acid (e.g. at 0.1 M buffer, $[HA]_{free} << [HB^+]_{free}$). It is because of this difference that the TOF_{max} reported in **Table 3.1** of Chapter 3 for the carboxylic acids are not directly comparable to those of the cationic buffers. If we had chosen an alternative definition of TOF_{max} based on the free acid concentrations, the values would be significantly larger. For the catalysis reported here, to compare the cationic vs. neutral acid data for 0.1 M buffer at $[HA]_{free} \approx [HB^+]_{free}$ (instead of $[HA]_{total} = [HB^+]_{total}$), the carboxylic acid TOF_{max} values would have to be multiplied by about a factor of 10.

B.5 Kinetic Analysis

In an idealized catalytic reaction, in which substrate depletion (e.g. O_2) , catalyst depletion and side reactions negligible, a canonical S-shaped voltammogram is predicted.[10-12] Under such conditions and at potentials far negative (for reductive chemistry) of the catalyst $E_{1/2}$, the currents reach a plateau that reflects the rate of chemical steps away from the electrode. This limiting current and can be directly used to measure TOF_{max}. The catalytic voltammograms presented in Chapter 3 do not reach plateau currents due to background ORR on glassy carbon and instead have upwards tailing current at potentials more negative than the catalytic wave. To circumvent these background complications, Foot-of-the-wave analysis (FOWA) was used to measure TOF_{max} by extrapolating data from the early part of the catalytic wave, a region where substrate depletion and side phenomena are small.[13]

Here, we use the FOWA equation derived for an *EC'* mechanism (Chapter 3 eq 3.1 and eq B.7).[13] As shown elsewhere, the FOWA equation for an *EC'* mechanism is valid for reactions where the number of electrons per catalytic turnover (n_{cat}) is greater than 1, provided the electron transfer (E) and chemical steps (C) following initial electron transfer and rate-limiting chemical step are fast.[14] In this work, as in the prior studies, we assume that all electron transfer steps occur from the electrode and not from reduced homogeneous species ($\sigma = 1$), as this yields a lower-limit TOF_{max}.[15] Likewise, n_{cat} was taken to be 4.0, the maximum value for dioxygen reduction (see Section B.7), as this also is the most conservative estimate of the TOF_{max}.

$$\frac{i_c}{i_p} = \frac{2.24 n_{cat}^{\sigma} \sqrt{\frac{RT}{F\nu} TOF_{max}}}{1 + \exp\left[\frac{F}{RT}(E - E_{1/2})\right]} \quad \text{(eq B.7)}$$

$i_c =$ current measured under catalytic conditions

$i_p =$ non-catalytic current of the $1e^-$ Fe^{III}/Fe^{II} wave

$n_{cat} =$ number of electrons in one catalytic turnover, taken to be 4 (reduction of O_2 to 100% H_2O and no H_2O_2; see Section B.7)

$\sigma =$ stoichiometric factor, assumed to be 1 to give the most conservative estimate of TOF_{max}

$\nu =$ scan rate

$E_{1/2} = E_{1/2}(Fe^{III}/Fe^{II})$

$E =$ applied potential

FOWA was performed by plotting the i_c/i_p vs. the denominator of eq B.7 and by fitting the slope between i_c/i_p = 1 to 4 (or when the fit deviated from linearity, when $R^2 < 0.980$), **Figure B28** and **Figure B29**.[15] Each fit was performed using the $E_{1/2}$ measured under each respective set of conditions. Using eq B.7 and the slope of the fit region, TOF_{max} was estimated for each set of buffer concentrations and identities.

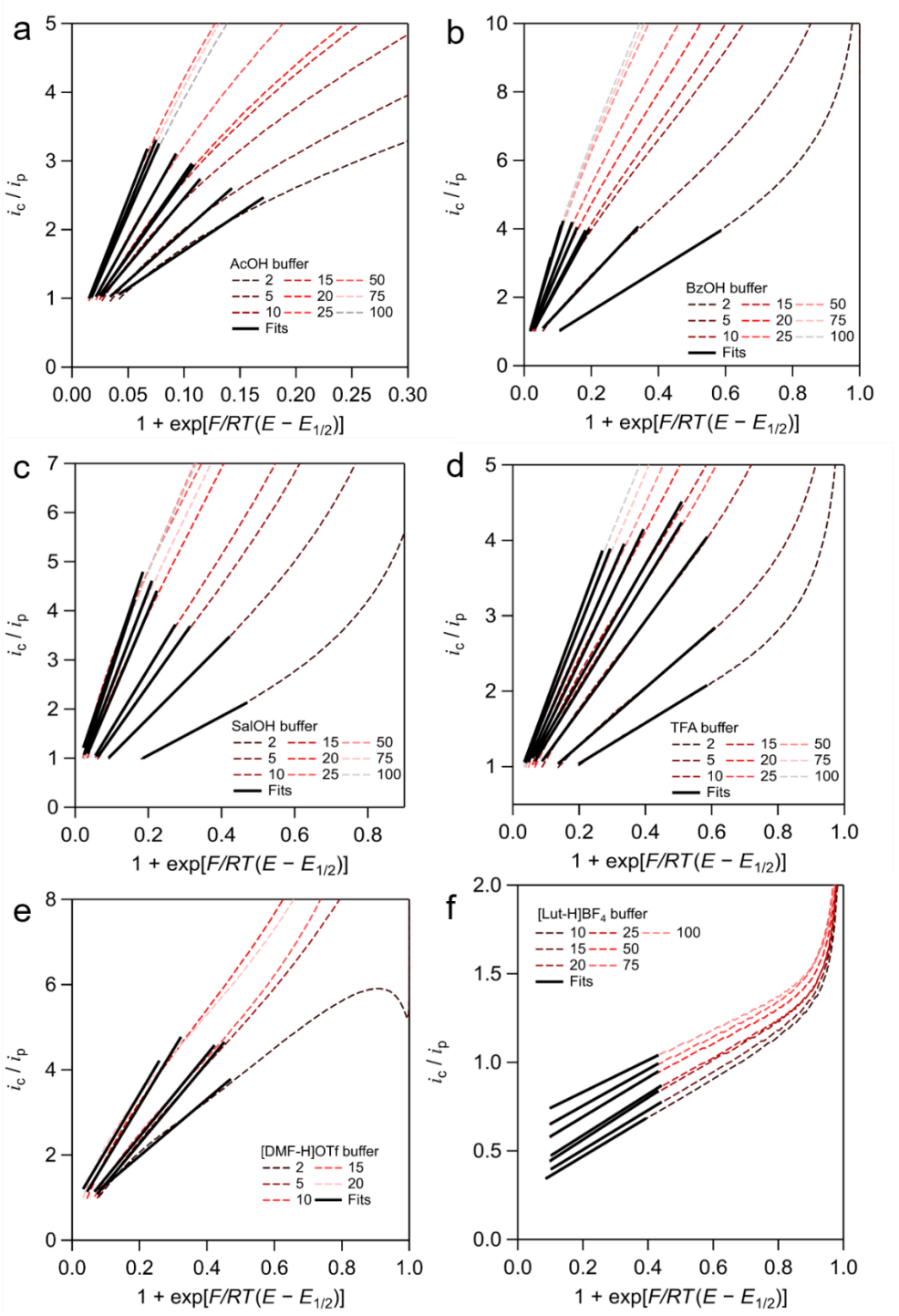

Figure B28. Foot-of-the-wave analysis for the buffer concentrations used in Chapter 3 (all at 1 atm O_2). Plots are of i_c/i_p (the catalytic current divided by the non-catalytic peak current) plotted against the denominator of eq B.7. Linear fits were made as described above. The buffer identities and concentrations are noted in the legends, where (**A**) is buffered AcOH, (**B**) is buffered BzOH, (**C**) is buffered SalOH, (**D**) is buffered TFAH, (**E**) is buffered [DMF-H]OTf and (**F**) is buffered [Lut-H]BF_4. The FOWA fits are poor for [Lut-H]BF_4 because catalysis is so slow. See **Figure B20**, **Figure B21**, **Figure B22**, **Figure B23**, **Figure B24**, and **Figure B25** for original voltammograms.

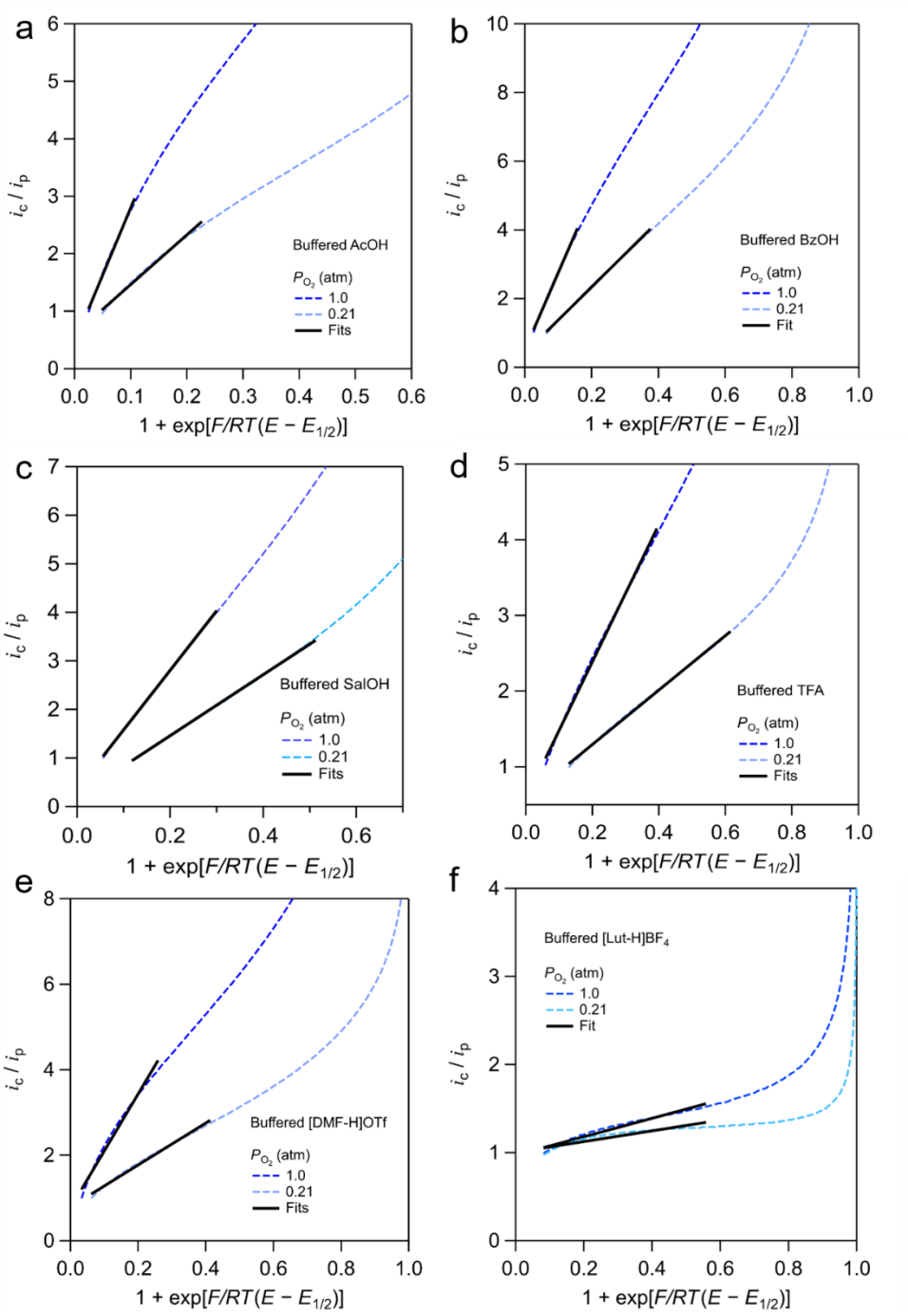

Figure B29. Foot-of-the-wave analysis for all the partial pressure O_2 measurements performed in Chapter 3 (all at 20 mM buffer). Plots are of i_c/i_p (the catalytic current divided by the non-catalytic peak current) plotted against the denominator of eq B.7. Linear fits were made as described above. The buffer identities and partial pressures are noted in the legends, where (**A**) is buffered AcOH, (**B**) is buffered BzOH, (**C**) is buffered SalOH, (**D**) is buffered TFAH, (**E**) is buffered [DMF-H]OTf, and (**F**) is buffered [Lut-H]BF_4. See **Figure B20**, **Figure B21**, **Figure B22**, **Figure B23**, **Figure B24**, and **Figure B25** for original voltammograms.

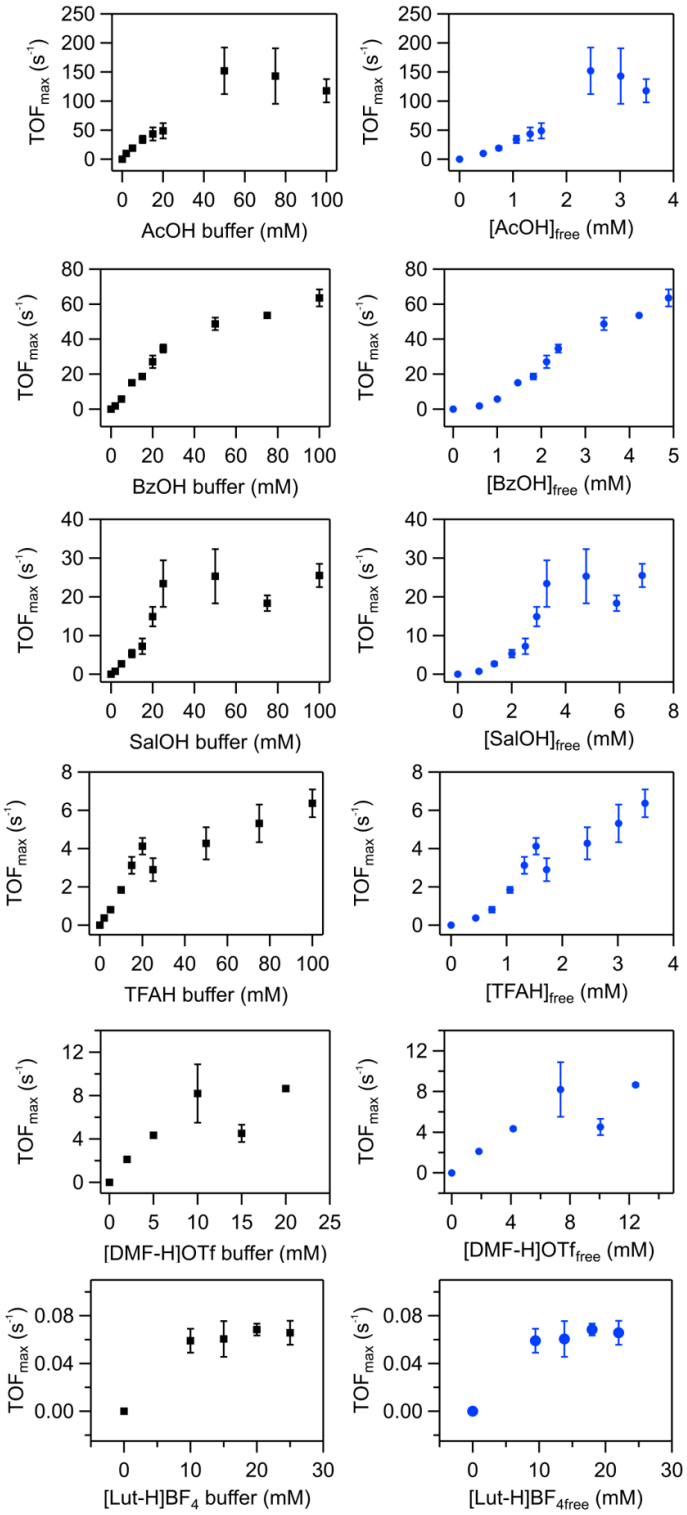

Figure B30. TOF$_{max}$ vs. [substrate] plots for the buffers used in Chapter 3. (Left column) Plots of TOF$_{max}$ vs. total buffer concentration. (Right column) Plots of TOF$_{max}$ vs. the concentration of free acid after considering homoconjugation. For all solutions, TOF$_{max}$ values were measured using FOWA (above), all at 1.0 atm O_2, and were averaged from duplicate voltammograms. Error bars represent one standard deviation from replicates.

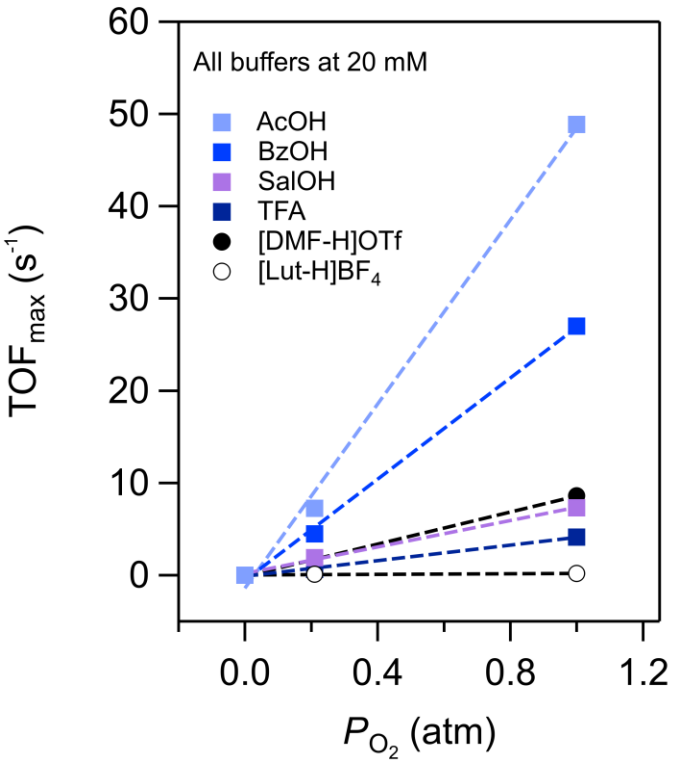

Figure B31. Plot of k_{obs} vs. partial pressure of O_2 for each of the buffers used in Chapter 3. The k_{obs} values were measured using FOWA (above), all at 20 mM buffer, and were averaged from duplicate voltammograms.

B.6 Effective Overpotential Determination

The effective overpotential for iron porphyrin catalyzed ORR is defined as the difference between the equilibrium potential of the four electron, four proton reduction of O_2 to $2H_2O$ under relevant catalytic conditions (E_{ORR}) and the catalyst $E_{1/2}$ (eq B.8).[15-16] The equilibrium potential of O_2 reduction under catalytic conditions is determined using the standard potential of O_2/H_2O in MeCN (E^0_{ORR}), reported elsewhere, and the Nernst law (eq B.9 and eq B.10).[15,17] All pK_a values previously reported in MeCN.[9,18-19]

$$\eta_{\text{eff}} = E_{\text{ORR}} - E_{1/2} \qquad \text{(eq B.8)}$$

$$\mathrm{O_{2(g)} + 4HA_{(org)} + 4}e^-_{(\mathrm{Fc^+/Fc})} \rightleftharpoons \mathrm{2H_2O_{(org)} + 4A^-_{(org)}};\ E^{\circ}_{\text{ORR}} \qquad \text{(eq B.9)}$$

$$\eta_{\text{eff}} = E^{\circ}_{\text{ORR}} - E_{1/2} - \frac{2.303\text{RT}}{n_{\text{cat}}\text{F}}\log\left(\frac{\left[\mathrm{H_2O}\right]^2\left[\mathrm{A^-}\right]^4}{P_{\mathrm{O_2}}\left[\mathrm{HA}\right]^4}\right) - (0.0592\text{V})\text{p}K_a \qquad \text{(eq B.10)}$$

$\eta_{\text{eff}} =$ effective overpotential

$E^{\circ}_{\text{ORR}} =$ standard chemical potential of O_2 to H_2O

$E_{\text{ORR}} =$ equilibrium potential of O_2 to H_2O under catalytic conditions

$E_{1/2} =$ catalyst $E_{1/2}(\mathrm{Fe^{III}/Fe^{II}})$

$n_{\text{cat}} =$ number of electrons in one catalytic turnover, assumed to be 4 for O_2/H_2O

pK_a = pK_a of the proton donor (HA), the strongest acid in solution. For all of the acids used, the linear plots of TOF_{max} vs. $[\text{HA}]_{\text{free}}$ implicate HA (or HB^+) as the proton donor and not the homoconjugate. The following pK_a values have been reported in MeCN: $\text{p}K_a(\text{AcOH}) = 23.5$; $\text{p}K_a(\text{BzOH}) = 21.5$; $\text{p}K_a(\text{SalOH}) = 16.7$; $\text{p}K_a([\text{Lut-H}]^+) = 14.1$; $\text{p}K_a(\text{TFAH}) = 12.6$; $\text{p}K_a([\text{DMF-H}]^+) = 6.1$

For the studies performed herein, we report the effective overpotential and turnover frequencies for **1** catalyzed ORR under conditions similar to those reported for the other iron porphyrin catalysts. All of the reported $\text{TOF}_{\text{max}}/\eta_{\text{eff}}$ values were measured from MeCN solutions containing 0.1 mM **1**, 1 atm O_2, 100 mM acid (HA) and 100 mM conjugate base (A^-). The 1-to-1 concentration of [HA]-to-[A^-] was used such that the ratio of the concentrations is minimally perturbed by homoconjugation, see discussion above.[6] The native water concentration in the solvent was 15 ± 10 mM, as measured by Karl Fischer titrations and reported elsewhere.[15] For the reported overpotentials, no additional water was added (which would affect the pK_a of the acids

used). The uncertainty in the water content affects the overpotential by as much as 20 mV, which is approximately the width of the data points used in **Figure 3.1**.

We note that, during catalysis, larger concentrations of water are generated during turnover and would result in even lower overpotentials. As such, the values we report are the upper-limits for η_{eff}. Regardless, the vector analysis presented in Chapter 3 requires only the shift in the effective overpotential and not the absolute values.

B.7 Selectivity for H_2O vs. H_2O_2

Selectivity for H_2O vs. H_2O_2 formation (n_{cat} = 4.0 vs. n_{cat} = 2.0, respectively) was measured by rotating ring disk electrochemistry (RRDE) using the methodology detailed elsewhere.[20-22] A glassy carbon disk (5 mm) and platinum ring were used as working electrodes and were polished separately to avoid potential platinum contamination. The reference and auxiliary electrodes were the same as those described in "Electrochemical methods" (see Chapter 3). Using ferrocene, the collection efficiency (CE) was determined to be 21% in MeCN (**Figure B32**) by averaging a set of measurements at 400, 900, 1600, and 2500 RPM.

For catalytic measurements, 10 mL acetonitrile solutions were prepared containing 0.1 M [*n*-Bu_4N][BF_4], 0.1 M buffer (1:1 acid to conjugate base), and 0.1 mM **1**. No ferrocene was added to the solutions until the end of each experiment. For each buffer, the solution was sparged with O_2 and the electrode was rotated at 900, 1600, and 2500 RPM. In order to reduce Fe^{III} to Fe^{II}, the disk electrode was swept from 0 to -1.0 V vs. Fc^+/Fc. In order to oxidize any generated H_2O_2, the ring electrode was held at +0.6 V vs. Fc^+/Fc. Following a method reported elsewhere[20] (and accompanying references therein), the general procedure was to estimate the percent H_2O_2 using eq B.11 and the ratio of the disk to ring currents (i_{disk} and i_{ring}, respectively) for each rotation rate **Figure B33**−**Figure B37**. Specific cases are discussed below and the average values for H_2O_2 formation are reported in (**Table B5**).

$$\mathrm{H_2O_2}(\%) = \frac{100\left(\frac{2i_{\mathrm{ring}}}{CE}\right)}{i_{\mathrm{disk}} + \frac{i_{\mathrm{ring}}}{CE}} \qquad \text{(eq B.11)}$$

$\mathrm{H_2O_2}(\%) =$ percent $\mathrm{H_2O_2}$ formed during turnover
$i_{\mathrm{ring}} =$ the ring current for any given potential
$i_{\mathrm{disk}} =$ the disk current for any given potential
$CE =$ collection efficiency ($CE = 0.21$ from control experiments using ferrocene)

- Using [DMF-H^+], TFAH, and SalOH buffers, the general procedures above worked well and the currents show that < 20% H_2O_2 is formed. These results are consistent with previous reports of other soluble iron porphyrin complexes under similar conditions.[15,21-22]
- Catalysis using buffered [Lut-H^+] was too slow to study by RRDE.
- With BzOH or AcOH buffers, measuring the percent H_2O_2 using was complicated by background oxidation of excess carboxylate at the potentials required to oxidize any generated H_2O_2, as shown by the large, potential-independent current at the ring (**Figure B36** and **Figure B37**). For these buffers the %H_2O_2 could be estimated by subtracting background current due to carboxylate oxidation and then fitting the residual data using the ratio of ring to disk currents. Very little indication of H_2O_2 was observed in the difference ring currents (**Figure B36** and **Figure B37**), and our rough estimates of < 5% make us confident in the <20% value reported in Chapter 3.

Table B5. Average percent H_2O_2 formed for **1**-catalyzed ORR in MeCN containing various buffers

buffer[a]	[DMF-H^+]	TFAH	[Lut-H^+]	SalOH	BzOH	AcOH
% H_2O_2	16.2 ± 1.8	12.0 ± 8.1	-[b]	16.3 ± 5.2	~2[c]	~0[c,d]

[a] All experiments in MeCN containing 0.1 M [*n*-Bu_4N][BF_4], 0.1 M buffer, and 1 atm O_2. [b] Too slow to measure. [c] Rough estimation after subtracting background carboxylate oxidation currents. [d] Ring currents after subtraction were slightly negative, within the estimated uncertainty of zero.

For the “best” catalytic system reported in Chapter 3, with AcOH buffer, the measured overpotentials occur below the equilibrium potential of O_2 to H_2O_2. Therefore, thermodynamic arguments require that *only* H_2O be formed, consistent with the estimates reported in **Table B5**. We refer the reader elsewhere[23] for a more detailed discussion and examples of such thermodynamic selectivity control, in the context of cobalt porphyrin-catalyzed ORR.

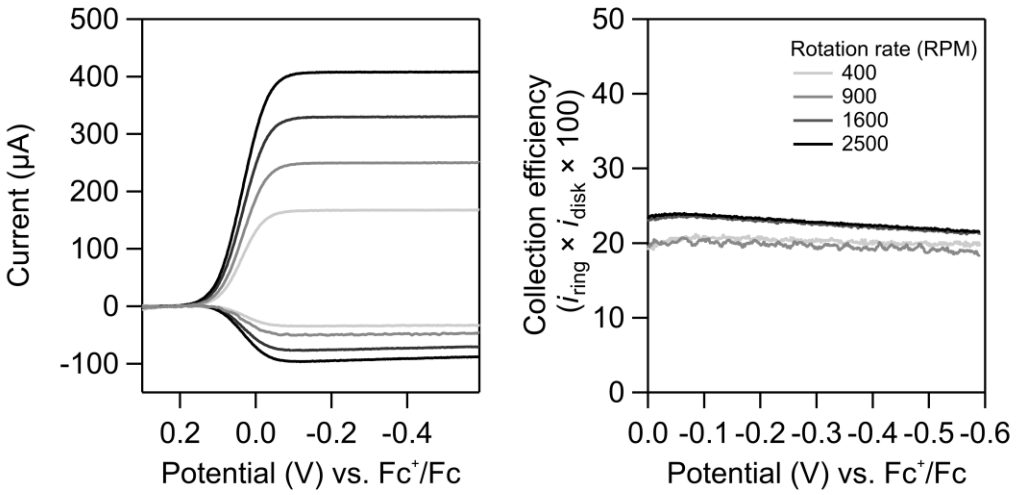

Figure B32. (**Left**) RRDE data for 1.0 mM ferrocene in MeCN at four different rotation rates. The disk was swept from 0.3 to -0.6 V vs. Fc^+/Fc while the ring was held at 0.3 V vs. Fc^+/Fc. (**Right**) Collection efficiencies measured at the same rotation rates.

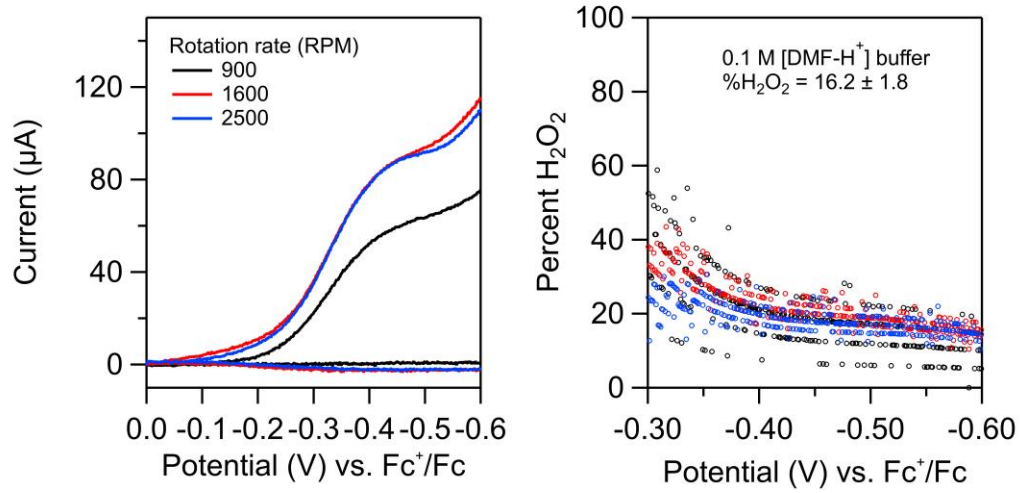

Figure B33. (**Left**) RRDE data for the ORR catalyzed by **1** in 0.1 M [DMF-H^+] buffer at three different rotation rates. (**Right**) Percent H_2O_2 measured as a function of disk potential at the same three rotation rates.

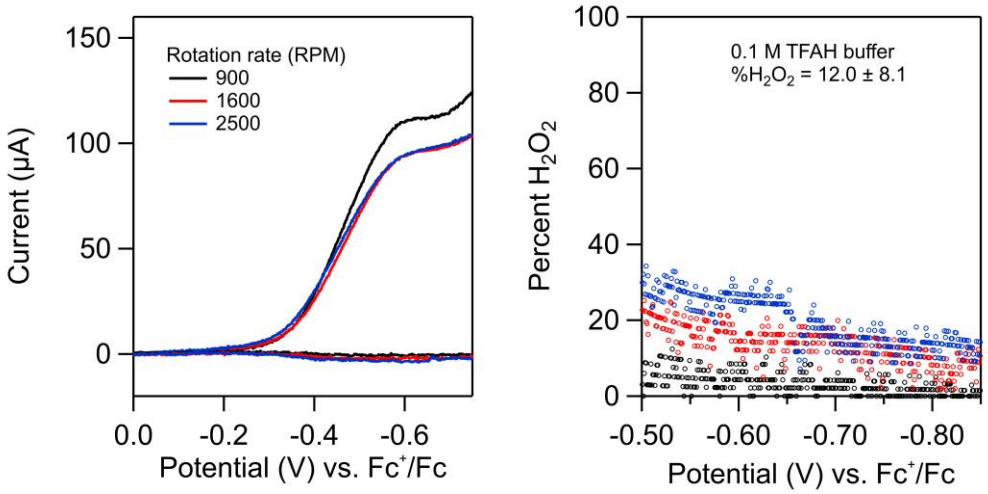

Figure B34. (**Left**) RRDE data for the ORR catalyzed by **1** in 0.1 M TFAH buffer at three different rotation rates. (**Right**) Percent H_2O_2 measured as a function of disk potential at the same three rotation rates.

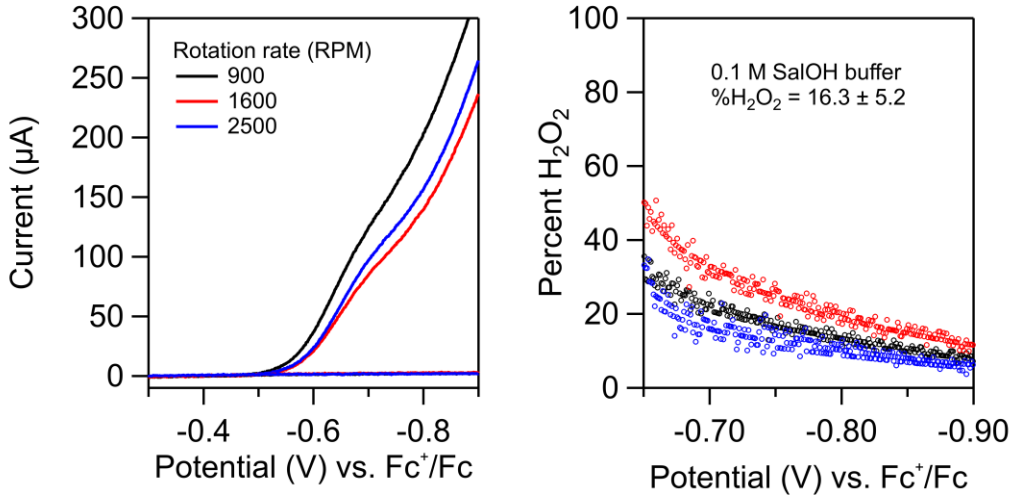

Figure B35. (**Left**) RRDE data for the ORR catalyzed by **1** in 0.1 M SalOH buffer at three different rotation rates. (**Right**) Percent H_2O_2 measured as a function of disk potential at the same three rotation rates.

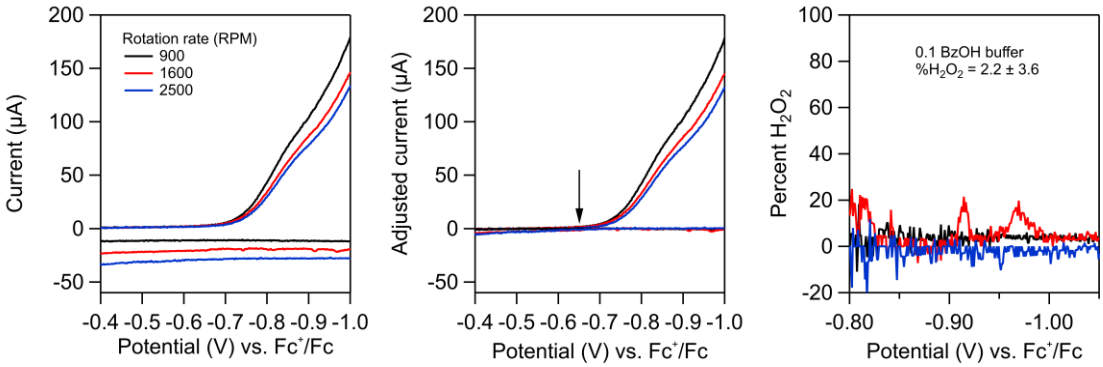

Figure B36. (**Left**) Raw RRDE data for the ORR catalyzed by **1** in 0.1 M BzOH buffer at three different rotation rates. (**Middle**) The same data after subtracting currents due to background benzoate oxidation at the ring. Arrow indicates potential at which the ring currents were brought to zero. (**Right**) Percent H_2O_2 measured as a function of disk potential at the same three rotation rates for the adjusted data.

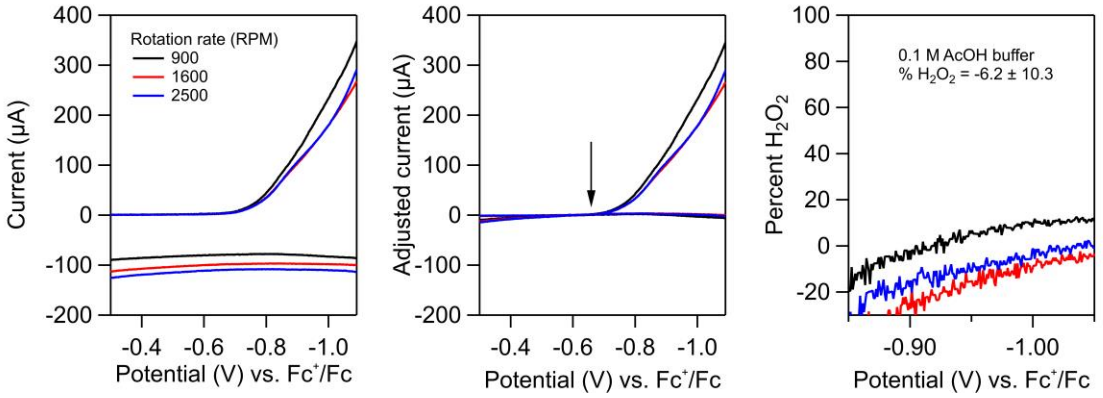

Figure B37. (**Left**) Raw RRDE data for the ORR catalyzed by **1** in 0.1 M AcOH buffer at three different rotation rates. (**Middle**) The same data after subtracting currents due to background acetate oxidation at the ring. Arrow indicates potential at which the ring currents were brought to zero. (**Right**) Percent H_2O_2 measured as a function of disk potential at the same three rotation rates for the adjusted data.

B.8 Conceptual Background for $E_{1/2}$ and pK_a Scaling Relationships

This section provides a more conceptual description of the $E_{1/2}$ and pK_a scaling relationships used in Chapter 3. Interested readers should be sure to refer to the original studies for more complete derivations and descriptions.[15,20]

In 2016, Pegis et al.[15] studied a series of substituted iron tetra-arylporphyrins in MeCN and DMF and found empirical correlations between the $E_{1/2}$ of the catalyst and the measured log(TOF_{max}). Catalysts with more negative $E_{1/2}$s had higher TOF_{max}s. A combination of Bells-Polanyi-Evans arguments and density functional theory computations were used to rationalize that the catalysts with more negative $E_{1/2}$s were more electron rich and therefore bound O_2 more strongly and formed more basic iron superoxide intermediates, resulting in faster turnover.

The definition of the overpotential or effective overpotential (η_{eff}) for a electrocatalytic system with a dissolved molecular catalyst has been discussed by several groups in a number of publications.[6,8,14,24-25] In general, the overpotential is the difference between the equilibrium potential of the reaction under the catalytic conditions and the applied potential. Typically for homogeneous, molecular electrocatalysts, the applied potential is taken as the $E_{1/2}$ of the catalyst because this is roughly the half-wave potential of the catalytic wave in a linear sweep voltammogram. For homogeneous electrocatalysis (unlike heterogeneous electrocatalysis), the half-wave potential is well defined because the TOF_{max} is limited by chemical steps in solution rather than by the applied potential at the electrode.[6] Using these definitions, changes in $E_{1/2}$ change η_{eff} by the same amount (see eq 3.1 of Chapter 3). Thus, the original log(TOF_{max})/$E_{1/2}$ relationship could be recast as log(TOF_{max})/η_{eff}, of the same slope (with opposite sign).

A 2017 paper derived formulae for the slopes of the log(TOF_{max})/η_{eff} correlations, as a function of the concentrations of reagents, the $E_{1/2}$s of the catalysts, and the pK_a of the buffer.[20] These are the correlations that are used in this work.

Equation 3.1 of Chapter 3 includes the equilibrium potential of the ORR under a given set of conditions, determined using the Nernst equation. Increasing the pK_a of the buffer decreases the equilibrium potential—and thus η_{eff}—by 0.0592 V per pK_a unit. The effect of pK_a on log(TOF_{max}) is derived from the Brønsted “Law,” which empirically relates proton transfer rate constants to driving

force: $\Delta\log(k_{PT}) = \alpha\Delta pK_a$. For Fe(por) catalyzed ORR, the Brønsted α has been reported to be approximately 0.3.[15] As a result, $\log(TOF_{max})$ decreases by 0.3 for every unit increase in the proton donor pK_a. The combined changes in log(TOF) and η_{eff} with pK_a yield the pK_a scaling relationship.

B.9 Single Crystal X-ray Structure

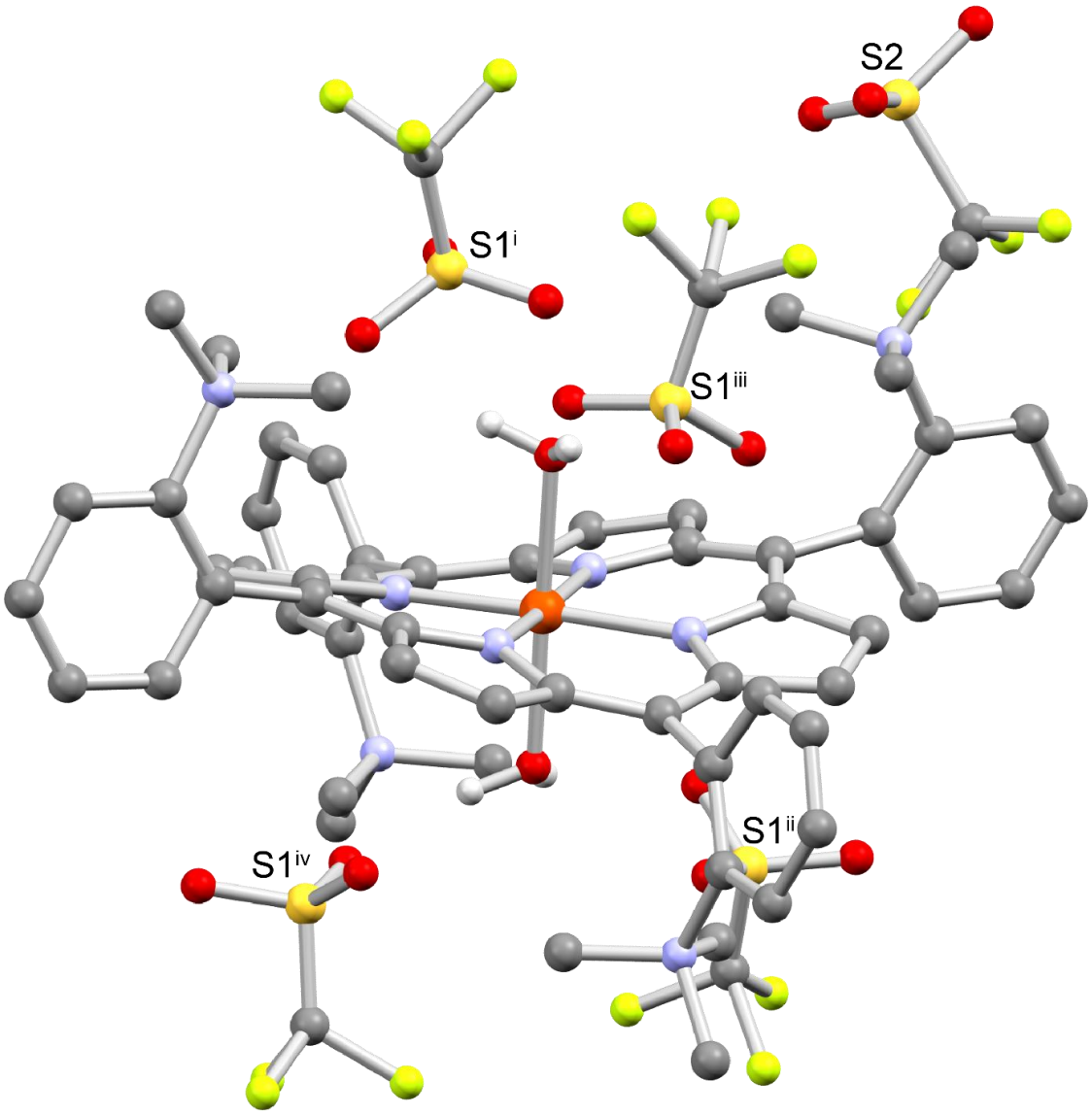

Figure B38. The complete X-ray model of [Fe(*o*-TMA)•2H$_2$O]OTf$_5$ represented with balls and sticks. Most of the hydrogen atoms have been omitted for clarity. The sulfur atoms are labeled, where the superscript notations highlight positions that are equivalent by symmetry. The operators are i: x, y, z; ii: $-\frac{1}{2}+y, \frac{1}{2}-x, \frac{1}{2}-z$; iii: $-x, 1-y, z$; iv: $\frac{1}{2}-y, \frac{1}{2}+x, \frac{1}{2}-z$.

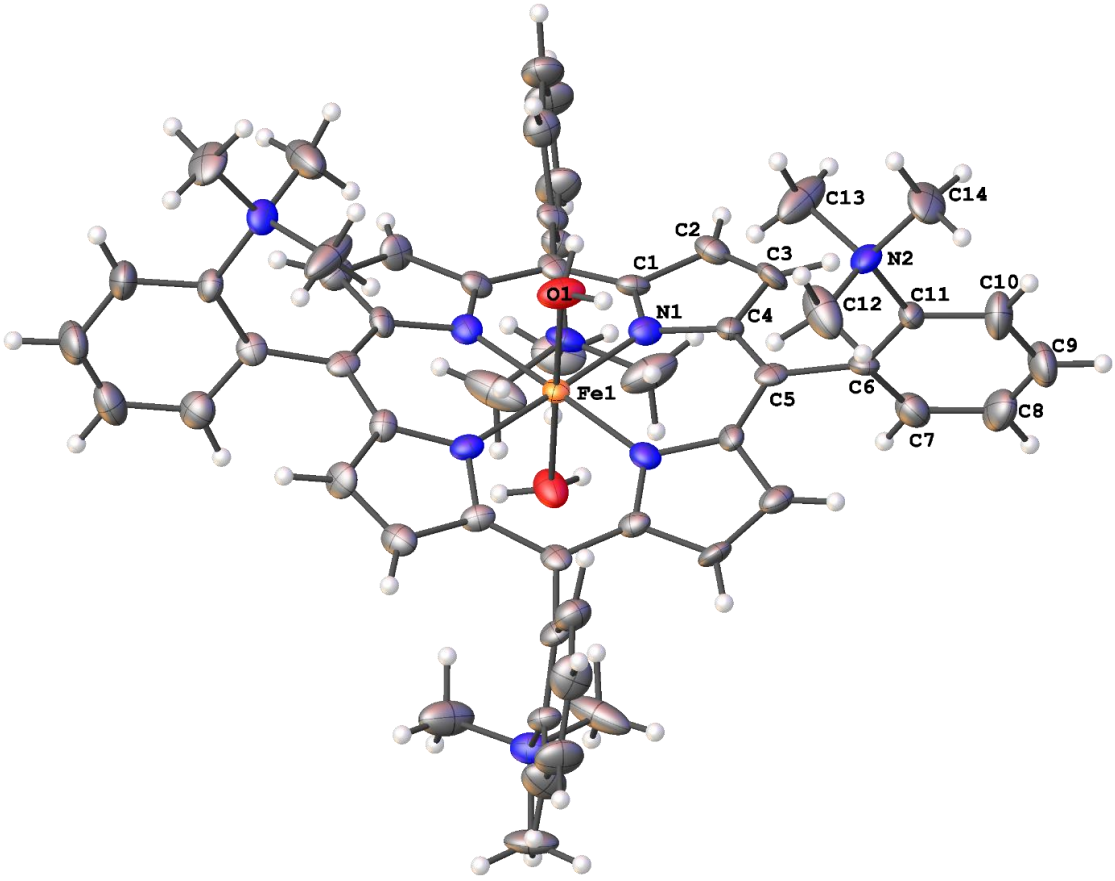

Figure B39. The complete numbering scheme of the cation-only portion of [Fe(*o*-TMA)•2H_2O]OTf_5 with 50% thermal ellipsoid probability levels. Only the asymmetric unit is labeled. The hydrogen atoms are shown as circles for clarity. The symmetry equivalent water protons and the triflate counter ions are omitted for clarity.

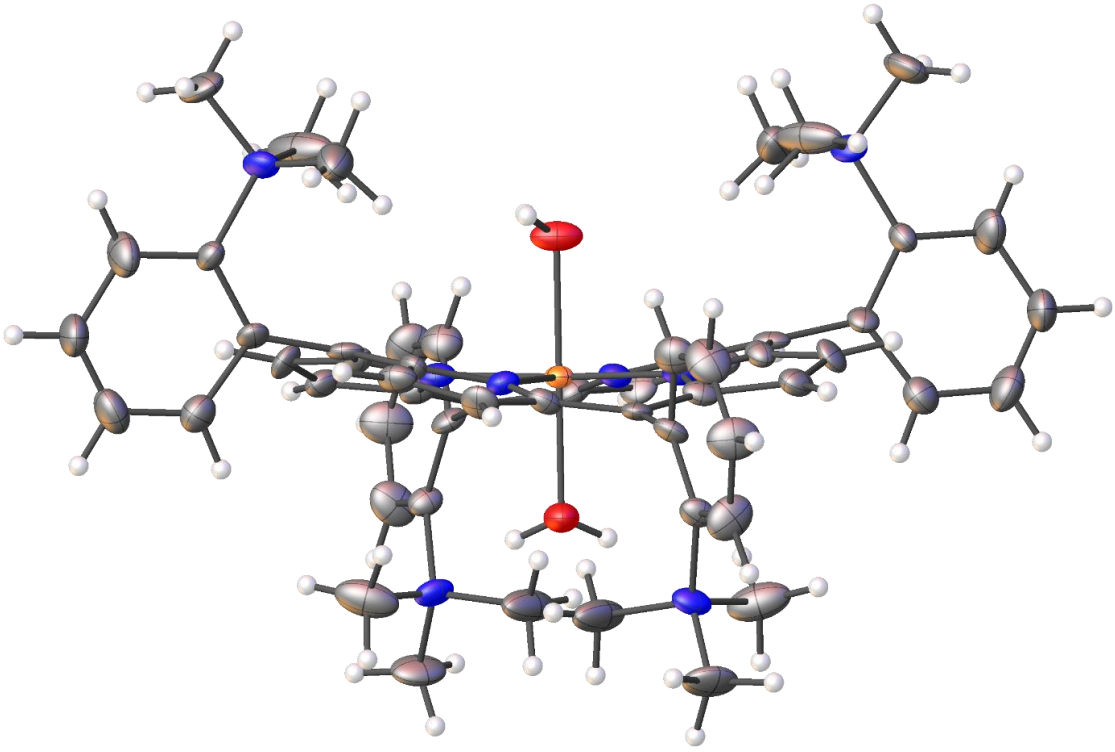

Figure B40. The complete numbering scheme of the cation-only portion of [Fe(*o*-TMA)•2H_2O]OTf_5 with 50% thermal ellipsoid probability levels. Only the asymmetric unit is labeled. The hydrogen atoms are shown as circles for clarity. The symmetry equivalent water protons and the triflate counter ions are omitted for clarity.

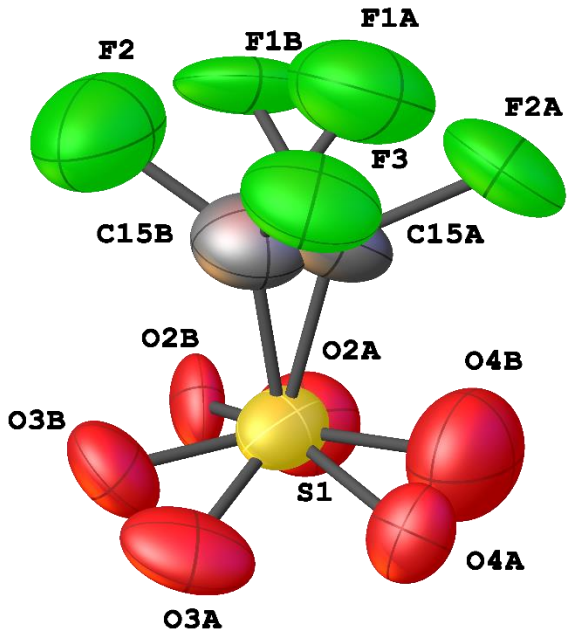

Figure B41. The complete numbering of the disordered triflate at a general position in the model of [Fe(*o*-TMA)•2H_2O]OTf_5 with 50% thermal ellipsoid probability levels. The other portions of the model are omitted for clarity.

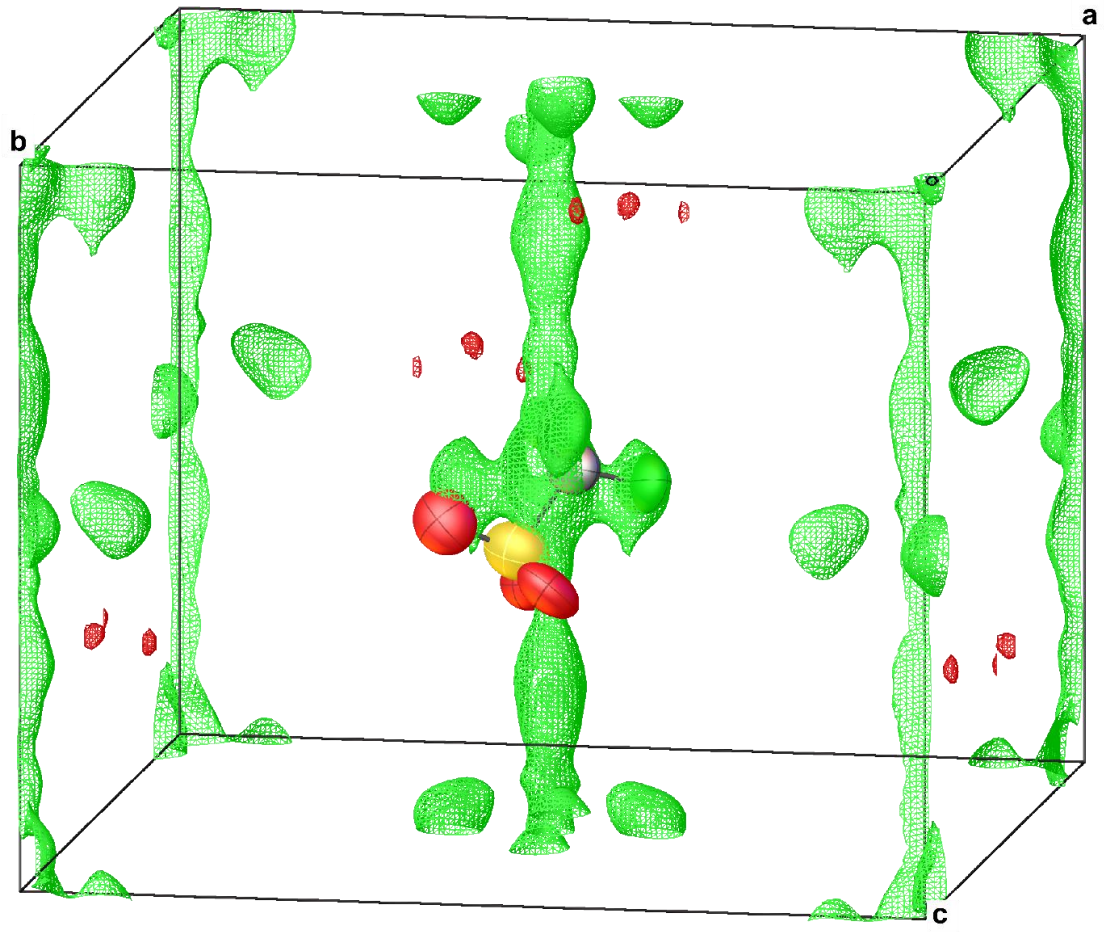

Figure B42. The unit cell of [Fe(*o*-TMA)•2H_2O]OTf_5, with a surface that represents a level of 1.5 e/Å^3. A single orientation of the disordered triflate near the $\bar{4}$ special position is shown. The other portions of the model are omitted for clarity.

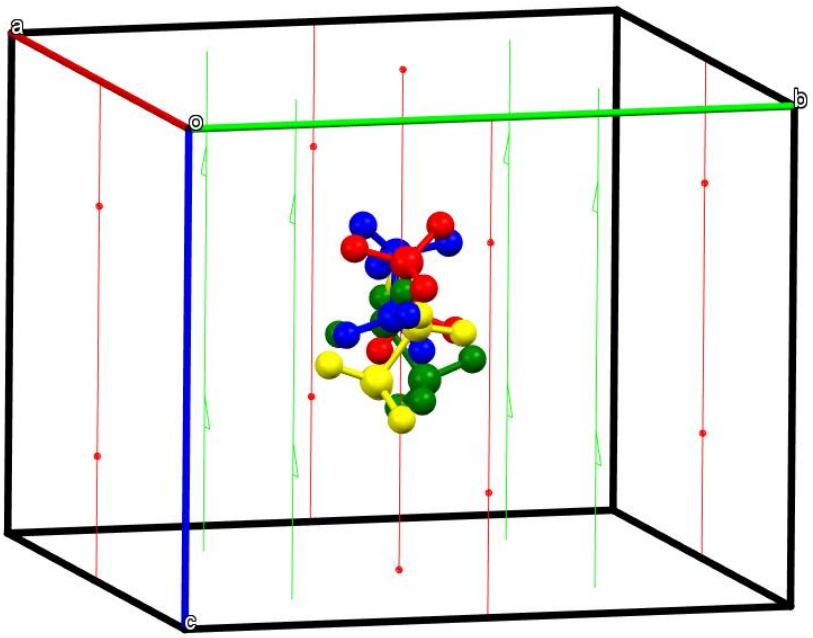

Figure B43. All orientations of the disordered triflate are shown in relation to the $\bar{4}$ rotation axis, represented with red lines. The models are distinguished by grouping the atoms in arbitrary colors: red, blue, yellow, green. The 2_1 screw axes are shown with green lines.

Table B6. Crystal data and structure refinement for [Fe(*o*-TMA)•2H_2O]OTf_5.

Identification code	007b-17062	
Empirical formula	C61 H64 F15 Fe N8 O17 S5	
Formula weight	1682.35	
Temperature	93(2) K	
Wavelength	1.54184 Å	
Crystal system	Tetragonal	
Space group	I-4	
Unit cell dimensions	a = 16.9175(2) Å	α= 90°.
	b = 16.9175(2) Å	β= 90°.
	c = 13.5620(2) Å	γ = 90°.
Volume	3881.47(11) $Å^3$	
Z	2	
Density (calculated)	1.439 Mg/m^3	
Absorption coefficient	3.730 mm^{-1}	
F(000)	1726	
Crystal size	0.100 x 0.040 x 0.020 mm^3	
Crystal color and habit	black block	
Diffractometer	Rigaku Saturn 944+ CCD	
Theta range for data collection	3.695 to 66.755°.	
Index ranges	-20<=h<=20, -20<=k<=19, -16<=l<=16	
Reflections collected	69870	
Independent reflections	3447 [R(int) = 0.0388]	
Observed reflections (I > 2sigma(I))	3447	
Completeness to theta = 66.755°	99.9 %	
Absorption correction	Semi-empirical from equivalents	
Max. and min. transmission	1.00000 and 0.54233	
Solution method	SHELXT-2014/5 (Sheldrick, 2014)	
Refinement method	SHELXL-2014/7 (Sheldrick, 2014)	
Data / restraints / parameters	3447 / 208 / 332	
Goodness-of-fit on F^2	1.058	
Final R indices [I>2sigma(I)]	R1 = 0.0857, wR2 = 0.2351	
R indices (all data)	R1 = 0.0857, wR2 = 0.2351	
Absolute structure parameter	0.418(16)	
Extinction coefficient	0.0041(7)	
Largest diff. peak and hole	1.469 and -0.700 $e.Å^{-3}$	

B.10 References

1. Azcarate, I.; Costentin, C.; Robert, M.; Savéant, J. M., Through-Space Charge Interaction Substituent Effects in Molecular Catalysis Leading to the Design of the Most Efficient Catalyst of CO_2-to-CO Electrochemical Conversion. *J. Am. Chem. Soc.* **2016,** *138* (51), 16639-16644.
2. Lexa, D.; Rentien, P.; Savéant, J. M.; Xu, F., Methods for Investigating the Mechanistic and Kinetic Role of Ligand Exchange Reactions in Coordination Electrochemistry. *J. Electroanal. Chem.* **1985,** *191* (2), 253-279.
3. Fang, M.; Engelhard, M. H.; Zhu, Z.; Helm, M. L.; Roberts, J. A. S., Electrodeposition from Acidic Solutions of Nickel Bis(benzenedithiolate) Produces a Hydrogen-Evolving Ni–S Film on Glassy Carbon. *ACS Catal.* **2014,** *4* (1), 90-98.
4. Artero, V.; Fontecave, M., Solar fuels generation and molecular systems: is it homogeneous or heterogeneous catalysis? *Chem. Soc. Rev.* **2013,** *42* (6), 2338-2356.
5. Walker, F. A.; Simonis, U., Iron Porphyrin Chemistry. John Wiley & Sons, Ltd: Chichester, UK, 2006.
6. Appel, A. M.; Helm, M. L., Determining the Overpotential for a Molecular Electrocatalyst. *ACS Catal.* **2014,** *4* (2), 630-633.
7. Roberts, J. A. S.; Bullock, R. M., Direct Determination of Equilibrium Potentials for Hydrogen Oxidation/Production by Open Circuit Potential Measurements in Acetonitrile. *Inorg. Chem.* **2013,** *52* (7), 3823-3835.
8. Fourmond, V.; Jacques, P.-A.; Fontecave, M.; Artero, V., H_2 Evolution and Molecular Electrocatalysts: Determination of Overpotentials and Effect of Homoconjugation. *Inorg. Chem.* **2010,** *49* (22), 10338-10347.
9. McCarthy, B. D.; Martin, D. J.; Rountree, E. S.; Ullman, A. C.; Dempsey, J. L., Electrochemical reduction of brønsted acids by glassy carbon in acetonitrile-implications for electrocatalytic hydrogen evolution. *Inorg. Chem.* **2014,** *53* (16), 8350-61.
10. Helm, M. L.; Stewart, M. P.; Bullock, R. M.; DuBois, M. R.; DuBois, D. L., A Synthetic Nickel Electrocatalyst with a Turnover Frequency Above 100,000 s^{-1} for H_2 Production. *Science* **2011,** *333* (6044), 863-866.
11. Stewart, M. P.; Ho, M.-H.; Wiese, S.; Lindstrom, M. L.; Thogerson, C. E.; Raugei, S.; Bullock, R. M.; Helm, M. L., High Catalytic Rates for Hydrogen Production Using Nickel Electrocatalysts with Seven-Membered Cyclic Diphosphine Ligands Containing One Pendant Amine. *J. Am. Chem. Soc.* **2013,** *135* (16), 6033-6046.
12. Rountree, E. S.; McCarthy, B. D.; Eisenhart, T. T.; Dempsey, J. L., Evaluation of Homogeneous Electrocatalysts by Cyclic Voltammetry. *Inorg. Chem.* **2014,** *53* (19), 9983-10002.
13. Costentin, C.; Savéant, J.-M., Multielectron, Multistep Molecular Catalysis of Electrochemical Reactions: Benchmarking of Homogeneous Catalysts. *ChemElectroChem* **2014,** *1* (7), 1226-1236.
14. Costentin, C.; Drouet, S.; Robert, M.; Savéant, J.-M., Turnover Numbers, Turnover Frequencies, and Overpotential in Molecular Catalysis of Electrochemical Reactions. Cyclic Voltammetry and Preparative-Scale Electrolysis. *J. Am. Chem. Soc.* **2012,** *134* (27), 11235-11242.
15. Pegis, M. L.; McKeown, B. A.; Kumar, N.; Lang, K.; Wasylenko, D. J.; Zhang, X. P.; Raugei, S.; Mayer, J. M., Homogenous Electrocatalytic Oxygen Reduction Rates Correlate with Reaction Overpotential in Acidic Organic Solutions. *ACS Cent. Sci.* **2016,** *2* (11), 850-856.
16. Costentin, C.; Savéant, J.-M., Homogeneous Molecular Catalysis of Electrochemical Reactions: Manipulating Intrinsic and Operational Factors for Catalyst Improvement. *J. Am. Chem. Soc.* **2018,** *140* (48), 16669-16675.
17. Pegis, M. L.; Roberts, J. A. S.; Wasylenko, D. J.; Mader, E. A.; Appel, A. M.; Mayer, J. M., Standard Reduction Potentials for Oxygen and Carbon Dioxide Couples in Acetonitrile and *N*,*N*′-Dimethylformamide. *Inorg. Chem.* **2015,** *54* (24), 11883-11888.
18. Kütt, A.; Leito, I.; Kaljurand, I.; Sooväli, L.; Vlasov, V. M.; Yagupolskii, L. M.; Koppel, I. A., A Comprehensive Self-Consistent Spectrophotometric Acidity Scale of Neutral Brønsted Acids in Acetonitrile. *J. Org. Chem.* **2006,** *71* (7), 2829-2838.

19. Kolthoff, I. M.; Chantooni, M. K.; Bhowmik, S., Titration of bases in acetonitrile. *Anal. Chem.* **1967,** *39* (13), 1627-1633.
20. Pegis, M. L.; Wise, C. F.; Koronkiewicz, B.; Mayer, J. M., Identifying and Breaking Scaling Relations in Molecular Catalysis of Electrochemical Reactions. *J. Am. Chem. Soc.* **2017,** *139* (32), 11000-11003.
21. Pegis, M. L.; Martin, D. J.; Wise, C. F.; Brezny, A. C.; Johnson, S. I.; Johnson, L. E.; Kumar, N.; Raugei, S.; Mayer, J. M., Mechanism of Catalytic O_2 Reduction by Iron Tetraphenylporphyrin. *J. Am. Chem. Soc.* **2019,** *141*, 8315-8326.
22. Carver, C. T.; Matson, B. D.; Mayer, J. M., Electrocatalytic Oxygen Reduction by Iron Tetra-arylporphyrins Bearing Pendant Proton Relays. *J. Am. Chem. Soc.* **2012,** *134* (12), 5444-5447.
23. Wang, Y.-H.; Schneider, P. E.; Goldsmith, Z. K.; Mondal, B.; Hammes-Schiffer, S.; Stahl, S. S., Brønsted Acid Scaling Relationships Enable Control Over Product Selectivity from O_2 Reduction with a Mononuclear Cobalt Porphyrin Catalyst. *ACS Cent. Sci.* **2019,** *5* (6), 1024-1034.
24. Passard, G.; Dogutan, D. K.; Qiu, M.; Costentin, C.; Nocera, D. G., Oxygen Reduction Reaction Promoted by Manganese Porphyrins. *ACS Catal.* **2018,** *8* (9), 8671-8679.
25. Hooe, S. L.; Machan, C. W., Dioxygen Reduction to Hydrogen Peroxide by a Molecular Mn Complex: Mechanistic Divergence between Homogeneous and Heterogeneous Reductants. *J. Am. Chem. Soc.* **2019,** *141* (10), 4379-4387.

C Supporting Information for Chapter 4

Adapted from Martin, D. J.; Johnson, S. I.; Mercado, B. Q.; Simoné, R.; Mayer, J. M. "Intramolecular Electrostatic Effects on O_2, CO_2, and Acetate Binding to a Cationic Iron Porphyrin." *Inorg. Chem*. **2020**. DOI: 10.1021/acs.inorgchem.0c02703.

C.1 General Considerations

C.1.1 Instrumentation

High-resolution mass spectrometry was performed using a Waters Xevo GS-XS QTof mass spectrometer. ^{1}H NMR were recorded on an Agilent 500 MHz spectrometer and were referenced to proteo solvent impurities. Clark electrode measurements were recorded on a YSI 5300A Biological Oxygen Monitor. Ultraviolet-visible (UV-vis) measurements performed in the glovebox were recorded on a Cary 5000 spectrophotometer using fiber optic cables leading to a cell holder. UV-vis measurements recorded outside the glovebox and requiring temperature control were recorded on an Agilent 8452 diode-array spectrophotometer equipped with a Unisoku Unispeks cryostat. Stopped-flow measurements were performed on a TgK Scientific CryoStopped-Flow System (SF-61DX2) equipped with a diode array detector. All optical spectra were collected using 1 cm pathlengths. Details of individual measurements are described below.

C.1.2 Chemicals & Materials

Ferrocene (Sigma-Aldrich, >98%), decamethylferrocene (Sigma-Aldrich, >95%), 2-nitrobenzaldehyde (Sigma-Aldrich, >95%), acetic acid (Sigma-Aldrich, >99.9%), tin(II) chloride (Sigma-Aldrich, >99%), hydrochloric acid (36-38% wt), formaldehyde (Sigma-Aldrich, 37% wt, containing 10-15% methanol as stabilizer), sodium cyanoborohydride (Acros, >98%), iron (II) bromide (Sigma-Aldrich, >98%), 2,6-lutidine (Sigma-Aldrich, ReagentPlus® >98%), methyltrifluoromethylsulfonate (Sigma-Aldrich, >98%), 2,6-ditertbutylpyridine (Sigma-Aldrich, >97%), neutral aluminum oxide (Sigma-Aldrich, >99%), silica (Sigma-Aldrich, >99%), sodium chloride (Sigma-Aldrich, >99%), sodium bicarbonate (Sigma-Aldrich, >99%), ammonium hydroxide solution (Sigma-Aldrich, 35% wt), zinc granules (20 mesh, Sigma-Aldrich, >98%), mercury (II) chloride (Sigma-Aldrich, >99%), anthracene (Sigma-Aldrich, >98.5%), sodium metal (Sigma-Aldrich, >99.9%), tetrabutylammonium acetate (Sigma-Aldrich, >99%), and meso-

tetraphenylporphine (Frontier Scientific, chlorin free) were all used as received. The aryl aminium oxidant, $[N(Ar\text{-}OMe)_3][PF_6]$ was prepared as reported elsewhere.[1]

Tetrahydrofuran, dimethylformamide, acetonitrile, and diethyl ether were all degassed with argon and dried using a Pure Process Technology solvent system prior to use. *n*-Butyronitrile (Sigma-Aldrich, >99%) was sparged with dry N_2 for 12h before being passed over activated neutral alumina and stored over activated 3 Å sieves for 3-5 days in the glovebox. Trimethylphosphate (Sigma-Aldrich, >97%) was degassed and stored in the glovebox over 3 Å sieves. Tetrabutylammonium hexafluorophosphate (TCI, >99%) was recrystallized 5x from hot ethanol before being dried at 70 ^oC under vacuum for 2-3 days. Pyrrole (Acros, 99%) was freshly distilled immediately before use. Dioxygen (Airgas, Ultra High Purity) and argon (Airgas, Ultra High Purity) were used as received. Iron tetraphenylporphyrin chloride was synthesized according to the literature.[2]

C.1.3 Electrochemical Methods

The general methods for cyclic voltammetry are described in **Chapter 4.2**. Rotating disk electrochemistry was conducted using a BASi Epsilon potentiostat and a Pine instruments rotator. For these experiments, the working electrode was a 5 mm glassy carbon disk embedded in a PTFE shroud. The reference and auxiliary electrodes were the same as those described in **Chapter 4.2**.

C.1.4 Solubility of O_2 in n-butyronitrile

To our knowledge, the solubility of O_2 in PrCN has not been reported. Three different methods were used to measure the concentration of O_2 in PrCN (some used 1 atm O_2 while others used dry air from a cylinder and assumed 0.21 atm O_2): O_2-sensitive Clark electrode measurements following literature precedent,[3] digital simulations of the reversible $O_2/O_2^{\bullet-}$ cyclic voltammogram in PrCN, and a Levich analysis of rotating disk voltammetry measurements. All three methods are detailed below (**Table C3**). These three methods yielded an average value of the O_2-solubility of 5.5 ± 0.4 mM atm^{-1} in PrCN at 20 °C. The O_2 content of air-saturated butyronitrile (1.1 ± 0.1 mM) was calculated based on dry air containing 0.21 atm O_2.

C.1.5 Sparging Solutions with Gas

For experiments that required sparging solutions with dioxygen, dry air, or argon, the respective gas was first plumbed through a Drierite column and a solvent bubbler (filled with acetonitrile or butyronitrile, respectively) before reaching the sample. This method minimizes water contamination, solvent evaporation, and accompanying changes in temperature. The only exception to this was for the Clark electrode measurements, for which compressed air was used as-is and bubbled directly into the solution of water.

C.2 Synthesis and Characterization

C.2.1 Synthesis of Fe^{II}(TPP)

In a N_2 glovebox, Fe^{III}(TPP)(Cl) (50 mg, 1.0 equiv) was dissolved in 5 mL THF. While stirring, 0.35 mL of a stock solution of sodium anthracenide (1.0 equiv, ref [4]) was added dropwise. The solution was stirred for 30 minutes, filtered to remove NaCl, layered with pentanes and left to crystallize. After three days, small purple crystals of Fe^{II}(TPP) were collected and dried (40 mg, 84% yield). ^{1}H NMR matches reported spectrum (**Figure C1**).[2]

C.2.2 Synthesis of $[Fe^{III}(o\text{-TMA})](OTf)_5$

The synthesis of [Fe(*o*-TMA)]OTf_5 was adapted from literature.[5] The free-base αβαβ-5,10,15,20-tetra(ortho-*N*,*N*-dimethylaminophenyl)porphyrin was synthesized as reported but was metallated using $FeBr_2$ and lutidine at 20 °C and for only 4h (rather than at 45 °C for 24 h, ref [5]) to avoid rotamerization. After chromatography on silica and alumina, the yield was 40% (lower than reported). The final methylation reaction was performed at 20 °C for 12h in trimethylphosphate solvent using methyl triflate (MeOTf, 20 equivalents) and with the addition of 1-2 drops 2,6-ditertbutylpyridine, following a method used for methylating similar complexes.[6] After quenching excess MeOTf with methanol, the penta-triflate salt was precipitated by slowly adding the reaction mixture to rapidly stirring diethyl ether. The product was recrystallized from acetonitrile/diethyl ether in the glovebox with comparable yields to the original report (>90%) and identical HRMS. HRMS (*m*/*z*): ($[M]^{5+}$ + 4OTf^-) calcd for $C_{56}H_{60}FeN_8(CF_3SO_3)_4$ 1496.2373; found 1496.2493. ($[M]^{5+}$ + 3OTf^-) calcd for $C_{56}H_{60}FeN_8(CF_3SO_3)_3$ 673.6426; found 673.6395.

C.2.3 Synthesis of Zn(Hg) Amalgam

The amalgam was prepared according to literature (Note 2 in ref [7]). $HgCl_2$ (3.0 g) was dissolved in 25 mL of 6 M HCl (aq). Stirring quickly, Zn granules (20 mesh, 16.5 g) were added quickly to the solution and stirred for 5 minutes. The solid amalgam was filtered, washed with dilute HCl solution, ethanol, and diethyl ether before being dried and stored under N_2 in the glovebox. The amalgamation is quantitative in mercury salts; however, we advise disposing of the filtrates in a separate waste stream.

C.2.4 Synthesis of [Fe^{II}(o-TMA)](OTf)$_4$

To a 4 mL vial in the glovebox was added [Fe^{III}(*o*-TMA)](OTf)$_5$ (30.6 mg, 1 equiv.), Zn(Hg) amalgam (0.31 g, large excess), and ~1 mL acetonitrile. The solution was stirred vigorously for 1h, during which the solution color changes from red-brown to cherry-red. The solution was pipetted into a secondary container and the amalgam was rinsed using minimal MeCN. The product was slowly crystallized from the colored solution by vapor diffusion, which yielded large (1-2 mm) block crystals suitable for single-crystal XRD. ^{1}H NMR (CD_3CN, ppm): 8.56 (s, 8H), 8.54 (d, 4H), 8.24 (d, 4H), 8.09 (t, 4H), 7.99 (t, 4H), and 3.05 (s, 36H); spectrum shown in **Figure C2**. UV-vis spectrum in MeCN [λ_{max}, nm (ε, M^{-1} cm^{-1})]: 434 ((2.5 ± 0.1) × 10^5), 538 (2.6 ± 0.1) × 10^4). UV-vis spectrum in PrCN [λ_{max}, nm (ε, M^{-1} cm^{-1})]: 435 ((2.6 ± 0.1) × 10^5), 538 ((2.6 ± 0.1) × 10^4).

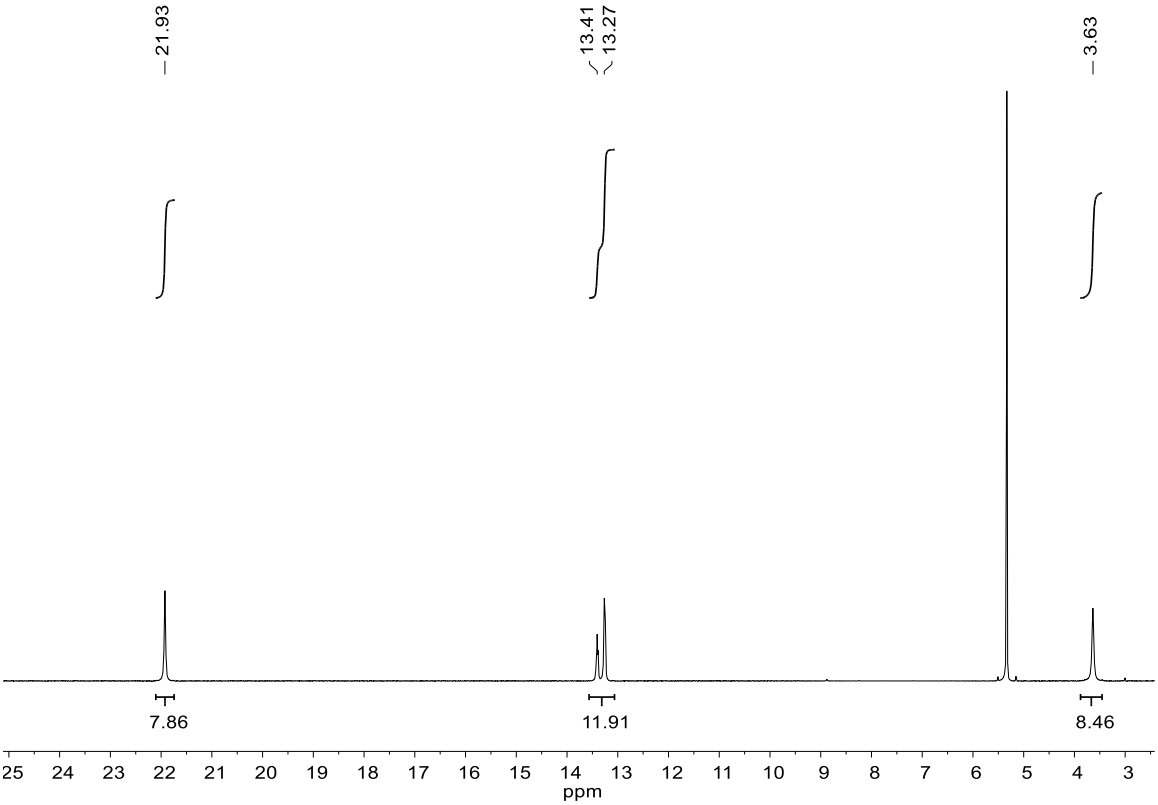

Figure C1. ^{1}H NMR spectrum of Fe^{II}(TPP) in CD_2Cl_2. This spectrum matches the literature report.[2]

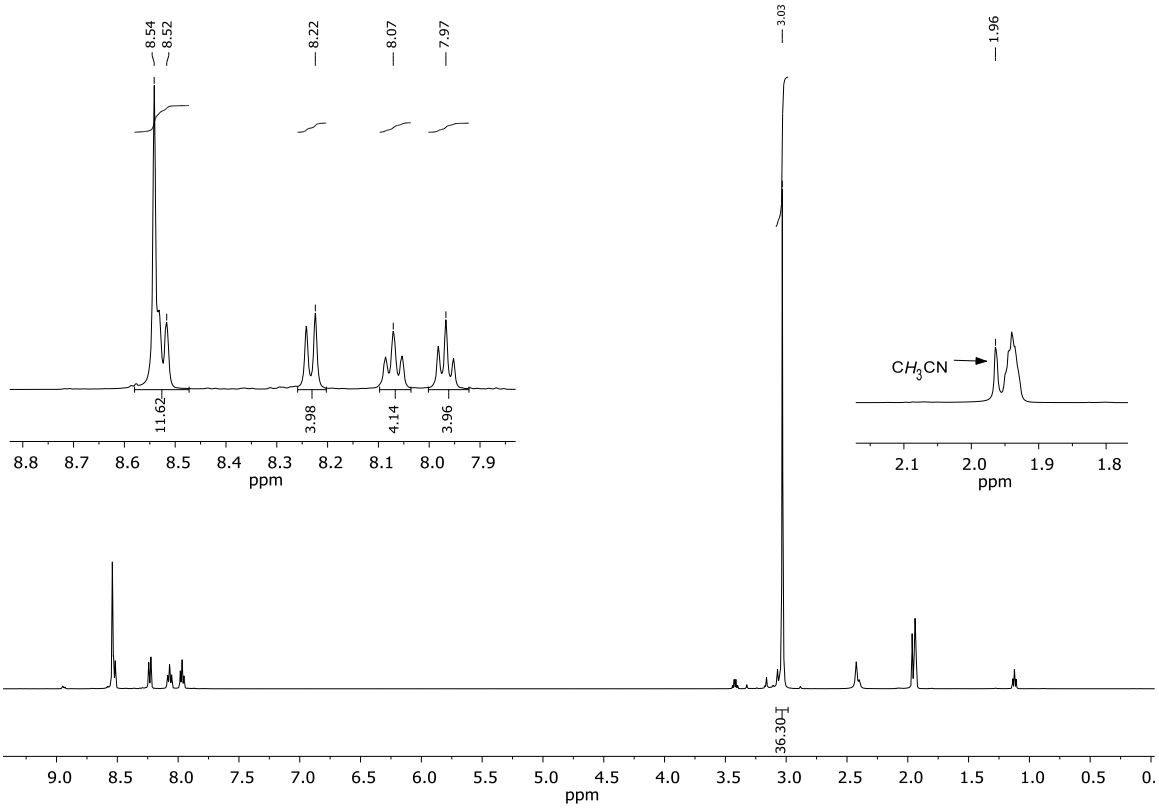

Figure C2. ^{1}H NMR spectrum of [Fe^{II}(*o*-TMA)]OTf$_4$ crystals in CD_3CN. The resonance at 1.96 is a result of the two C*H*$_3$CN ligands present in the crystals.

C.3 Acetate Binding Measurements

C.3.1 UV-vis Spectra and Job Plot for Acetate Titrations to [Fe^{II}(o-TMA)]$^{4+}$

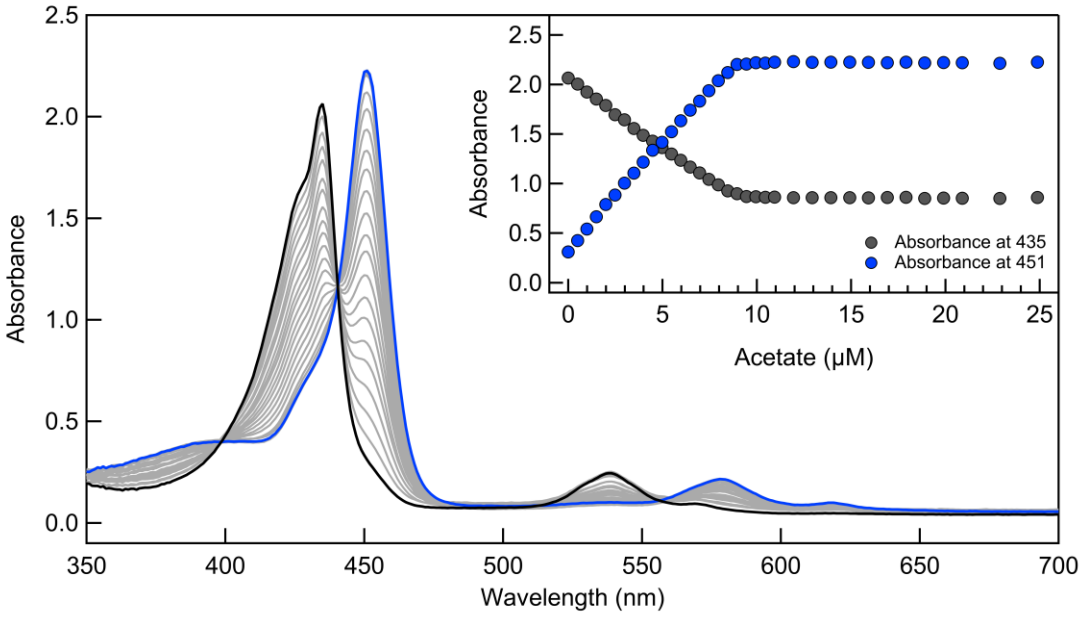

Figure C3. UV-vis spectra of a 8 μM solution of [Fe^{II}(*o*-TMA)]OTf$_4$ in PrCN with additions of [^{n}Bu$_4$N][AcO]. Acetate concentrations match values in inset. Inset: Plot of absorbance at the Soret maximums versus total acetate concentration.

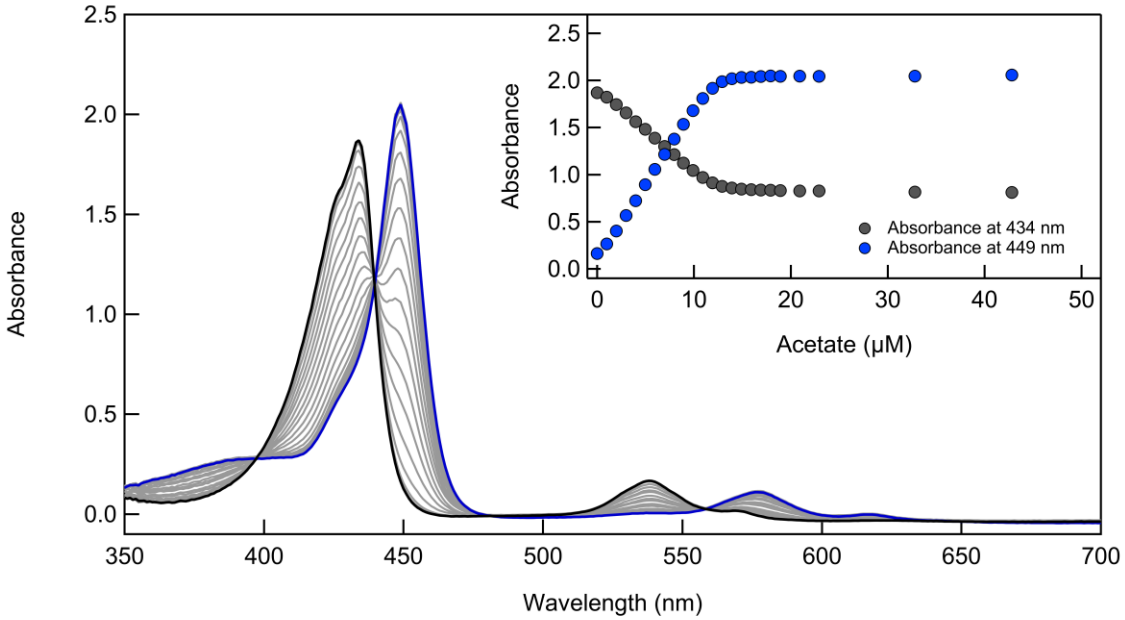

Figure C4. UV-vis spectra of a 8 μM solution of [Fe^{II}(*o*-TMA)]OTf$_4$ in MeCN with additions of [^{n}Bu$_4$N][AcO]. Acetate concentrations match values in inset. Inset: Plot of absorbance at the Soret maximums versus total acetate concentration.

Using stock solutions of [^{n}Bu$_4$N][AcO] (4.5 mM) and [Fe^{II}(*o*-TMA)]$^{4+}$ (5.4 mM), ten solutions were prepared such that the mole fraction [Fe^{II}(*o*-TMA)]$^{4+}$ was between 0 and 1. UV-vis spectra were collected for these solutions, shown below (**Figure C5**). The absorbance at 451 nm was used as a proxy for the concentration of [Fe^{II}(*o*-TMA)(AcO)]$^{3+}$ (451 nm is the Soret maximum in PrCN, see **Figure C3**). The ε of [Fe^{II}(*o*-TMA)]$^{4+}$ at this wavelength is conveniently small, though these absorbance contributions can be subtracted (blue circles, **Figure C6**). The Job plot[8] was made by plotting the absorbance values at 451 nm versus the mole fraction [Fe^{II}(*o*-TMA)]$^{4+}$, **Figure C6**.

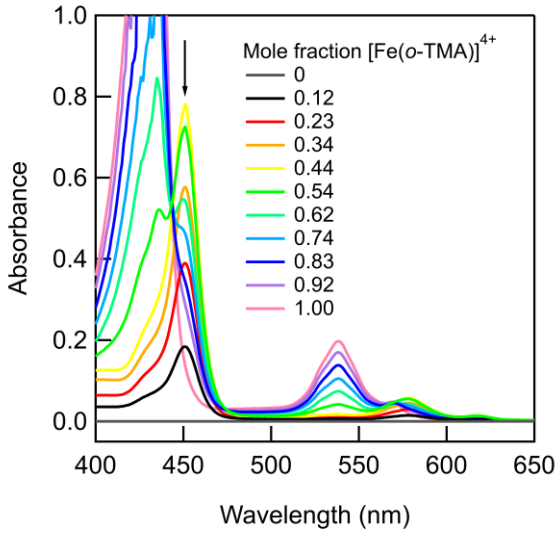

Figure C5. UV-vis spectra of the ten PrCN solutions used to prepare the Job plot for acetate binding to [Fe^{II}(*o*-TMA)]$^{4+}$. Absorbance at 451 nm is labeled with an arrow.

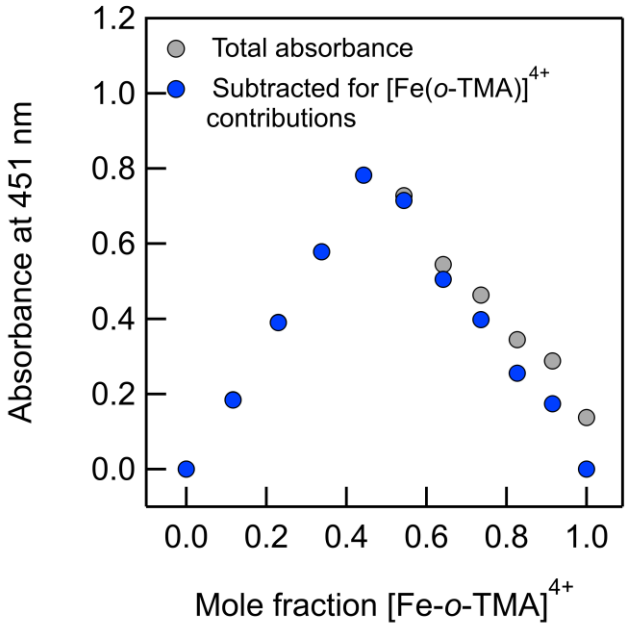

Figure C6. Job plot for acetate binding to $[Fe^{II}(o\text{-TMA})]^{4+}$ in PrCN. The sharp maximum at 0.5 mole fraction shows that the acetate-to-porphyrin ratio is 1:1. (Grey) Total absorbance at 451 nm; (Blue) absorbance values after subtracting contributions from uncomplexed $[Fe^{II}(o\text{-TMA})]^{4+}$.

C.3.2 UV-vis Spectra and Job Plot for Acetate Titrations to Fe^{II}(TPP)

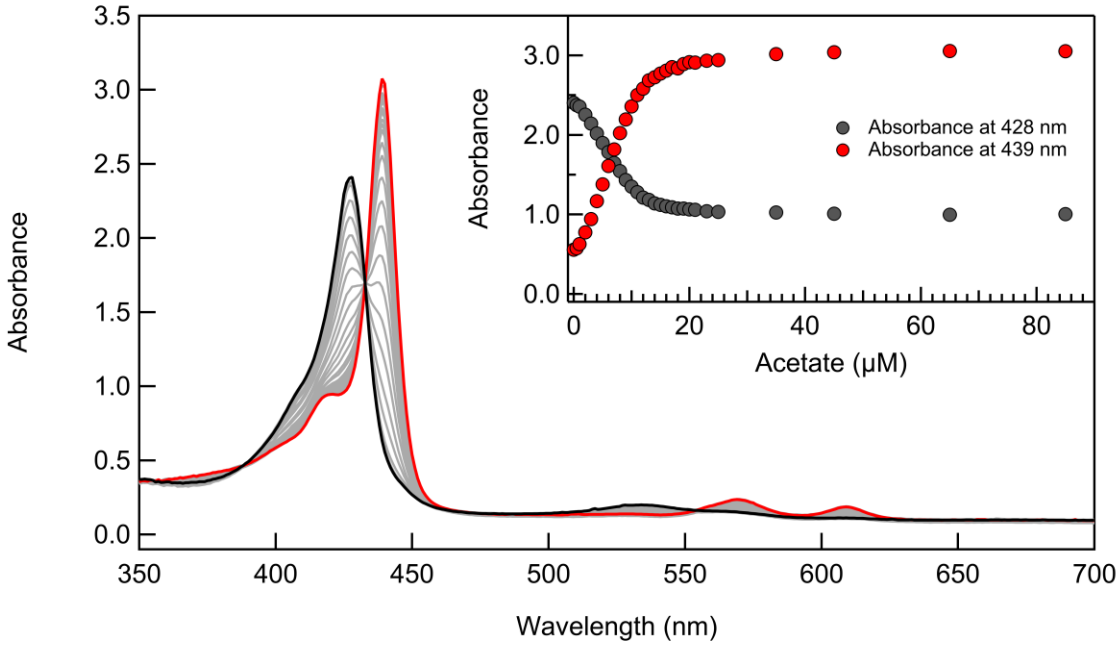

Figure C7. UV-vis spectra of a 7 μM solution of Fe^{II}(TPP) in PrCN with additions of [$^{n}Bu_4N$][AcO]. Acetate concentrations match values in inset. Inset: Plot of absorbance at the Soret maximums versus total acetate concentration.

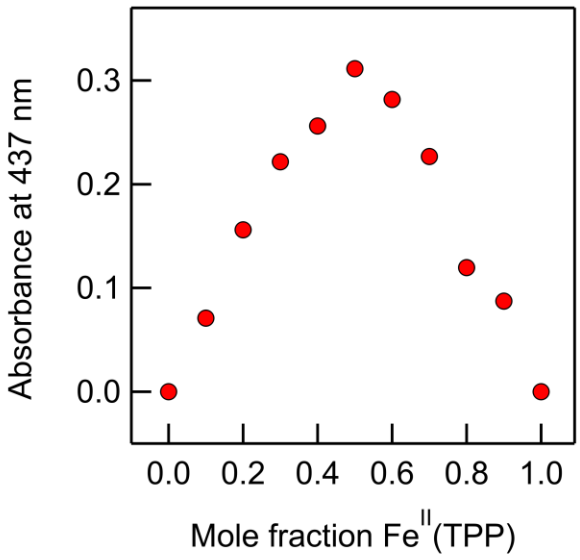

Figure C8. Job plot for acetate binding to Fe^{II}(TPP) in PrCN. The sharp maximum at 0.5 mole fraction shows that the acetate-to-porphyrin ratio is 1:1. Absorbance values measured after subtracting contributions from unbound Fe^{II}(TPP), see method description above **Figure C5**.

C.3.3 Stoichiometry of Acetate Binding to [Fe^{III}(o-TMA)]$^{5+}$

Acetate binding to [Fe^{III}(*o*-TMA)]$^{5+}$ could not be studied directly due to slow decomposition reactions. However, indirect measurements were still able to reveal the stoichiometry of acetate-to-ferric porphyrin in the electrochemically generated species (**Figure 4.3** in Chapter 4). These measurements were performed optically by monitoring the oxidation of [Fe^{II}(*o*-TMA)]$^{4+}$ in PrCN containing various amounts of [^{n}Bu$_4$N][AcO], using an aryl aminium oxidant, [N(Ar-OMe)$_3$]$^{\bullet+}$ ($E_{1/2}$ = 0.16 V vs. Fc$^+$/Fc in MeCN).[1]

Two solutions of [Fe(*o*-TMA)]$^{4+}$ were prepared (~8 μM and ~6 μM). To the first solution was added 4 equivalents acetate, enough to quantitatively form the [Fe^{II}(*o*-TMA)(AcO)]$^{3+}$ complex and still have acetate remaining in solution (**Figure C9**). This solution was titrated with [N(Ar-OMe)$_3$]$^{\bullet+}$. Monitoring by UV-vis spectroscopy showed stoichiometric conversion of [Fe(*o*-TMA)(AcO)]$^{3+}$ to an oxidized product with a spectrum that was different from that of [Fe^{III}(*o*-TMA)](OTf)$_5$. To the second solution was added 0.9 equivalents of acetate, so that no free acetate remained in solution. As before, this solution was oxidized and monitored by UV-vis. The spectra were very similar except for curvature in the titration data after 0.8 equivalents of [N(Ar-OMe)$_3$]$^{\bullet+}$ had been added. The data indicate complete oxidation of the [Fe^{II}(*o*-TMA)(AcO)]$^{3+}$ present followed by an equilibrium electron transfer reaction between remaining [Fe^{II}(*o*-TMA)]$^{4+}$ ($E_{1/2}$ = 0.067 V vs. Fc$^+$/Fc) and the oxidant.

A final solution of [Fe^{III}(*o*-TMA)](OTf)$_5$ (~8 μM) was prepared in PrCN containing 0.1 M [^{n}Bu$_4$N][PF$_6$], to which 20 equivalents of [^{n}Bu$_4$N][AcO] was added (to mirror electrochemical conditions, **Figure 4.3**, Chapter 4). The product spectrum of this mixture matched the spectra generated using the aminium oxidant under both sets of conditions. Together, these data demonstrate that the stoichiometry of the ferric o-TMA-acetate complex is [Fe^{III}(*o*-TMA)(AcO)]$^{4+}$.

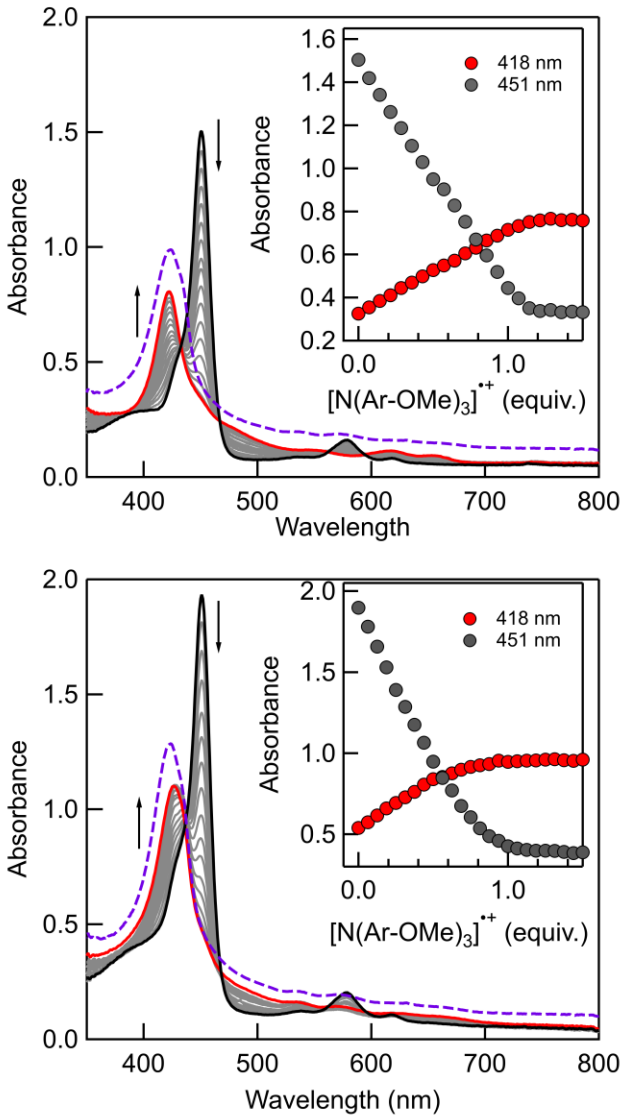

Figure C9. (Top) UV-vis spectra of a 7 μM solution of $[Fe^{II}(o\text{-TMA})]^{4+}$ containing 28 μM $[^{n}Bu_4N][AcO]$ in PrCN (black) with additions of $[N(Ar\text{-}OMe)_3][PF_6]$ aminium oxidant.[1] The reduced form of the oxidant, $N(Ar\text{-}OMe)_3$, is colorless and does not appear in the UV-vis spectrum. Inset shows absorbance at select wavelengths to monitor oxidation of the ferrous porphyrin. (Bottom) Identical experiment starting from a 9 μM solution of $[Fe^{II}(o\text{-TMA})]^{4+}$ containing 8 μM $[^{n}Bu_4N][AcO]$. Inset shows absorbance values used to monitor oxidation and shows expected curvature due to equilibrium electron transfer between the oxidant and $[Fe^{II}(o\text{-TMA})]^{4+}$ not bound to acetate. Dotted purple spectra (offset from baseline for clarity) is reference spectrum for $[Fe^{III}(o\text{-TMA})](OTf)_5$ in PrCN containing 0.1 M $[^{n}Bu_4N][PF_6]$ and 20 equivalents $[^{n}Bu_4N][AcO]$.

C.3.4 Acetate Binding Curves, Fitting Methods, and Equilibrium Constants

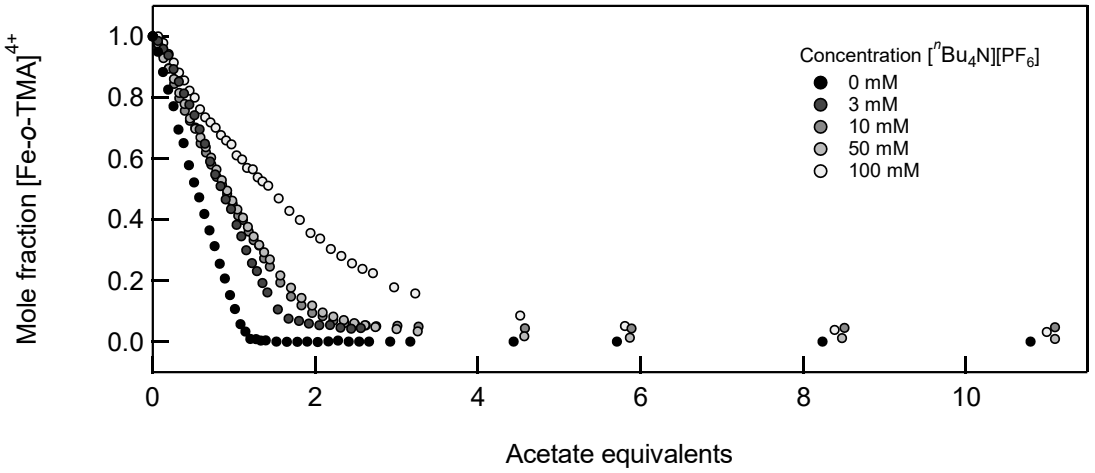

Figure C10. Mole fraction $[Fe(o\text{-TMA})]^{4+}$ versus acetate equivalents in PrCN containing various concentrations of supporting electrolyte. Mole fractions obtained using the method described in the text.

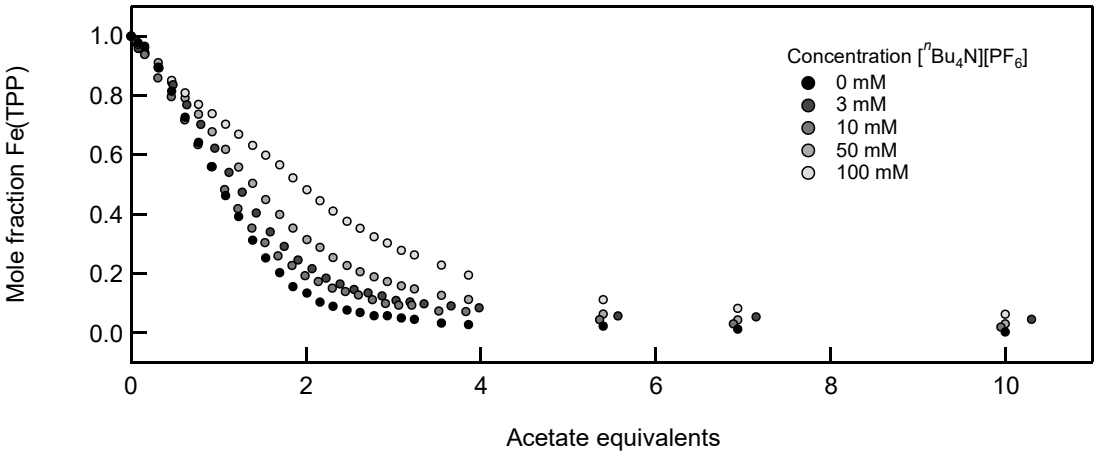

Figure C11. Mole fraction Fe(TPP) versus acetate equivalents in PrCN containing various concentrations of supporting electrolyte. Mole fractions obtained using the method described in the text.

In order to measure acetate binding constants (K_{AcO}), the ratio of acetate-bound to unbound porphyrin complexes (generically written as $[Fe(P)]^n$ and $[Fe(P)(AcO)]^{n-1}$) was determined by globally fitting the UV-vis spectra collected at each acetate concentration to a linear combination of the genuine bound and unbound spectra ($[Fe^{II}(o\text{-TMA})(AcO)]^{3+}$/$[Fe^{II}(o\text{-TMA})]^{4+}$ and $[Fe^{II}(TPP)]$/$[Fe^{II}(TPP)(AcO)]^-$, respectively). The total concentration of porphyrin was known, and—as shown above—sharp isosbestic points indicate mass-balance. Thus, eq C.1 can be written.

$$[Fe(P)]_{total} = [Fe(P)]^n + [Fe(P)(AcO)]^{n-1} \quad \text{(eq C.1)}$$

The total concentration of acetate titrated into solution is also known $[AcO^-]_{total}$. Using this value and the concentration of acetate-bound porphyrin ($[Fe(P)(AcO)]^{n-1}$, determined from above), the concentration of acetate remaining in solution after equilibrium is established, $[AcO^-]_{eq}$, was determined using eq C2.

$$[AcO^-]_{total} = [AcO^-]_{eq} + [Fe(P)(AcO)]^{n-1} \quad \text{(eq C.2)}$$

The equilibrium and equilibrium constant for acetate binding are described by eq C.3 and eq C.4, respectively. For the data shown below, eq C.4 was rearranged so that the ratio of acetate bound to unbound porphyrins could be plotted against $[AcO^-]_{eq}$ (eq C.5). From eq C.1 and eq C.2, above, all of the terms in eq C.5 could be determined from known concentrations ($[AcO^-]_{total}$ and $[Fe(P)]_{total}$) and from the ratio of acetate bound to unbound porphyrins.

$$[Fe(P)]^n + [AcO^-]_{eq} \rightleftharpoons [Fe(P)(AcO)]^{n-1} \quad \text{(eq C.3)}$$

$$K_{AcO}(M^{-1}) = \frac{[Fe(P)(AcO)]^{n-1}}{[Fe(P)]^n[AcO^-]_{eq}} \quad \text{(eq C.4)}$$

$$[AcO^-]_{eq} K_{AcO}(M^{-1}) = \frac{[Fe(P)(AcO)]^{n-1}}{[Fe(P)]^n} \quad \text{(eq C.5)}$$

Plotting the titration data using eq C.5 linearizes the titration to the form y = *m*x, where the slope of the data yields K_{AcO} (eq C.5). An example of the fit where the data was linear and had zero intercept is shown below in **Figure C12**. All data and fits are shown in **Figure C13**, **Figure C14**, and **Table C1**. Not all fits were perfectly linear or had zero intercept; however, and curvature was sometimes seen at low $[AcO^-]_{eq}$ values (in **Figure C13** at 0.1 M $[^nBu_4N][PF_6]$, for instance). To account for the error introduced from some of these deviations, the linearized titration data was fit

to two different expressions, y = *m*x + b and y = *m*x, where the intercept was set to zero. The difference in slopes was typically small (< 50%), and the uncertainty reported in **Table C1** captures the significance of this error.

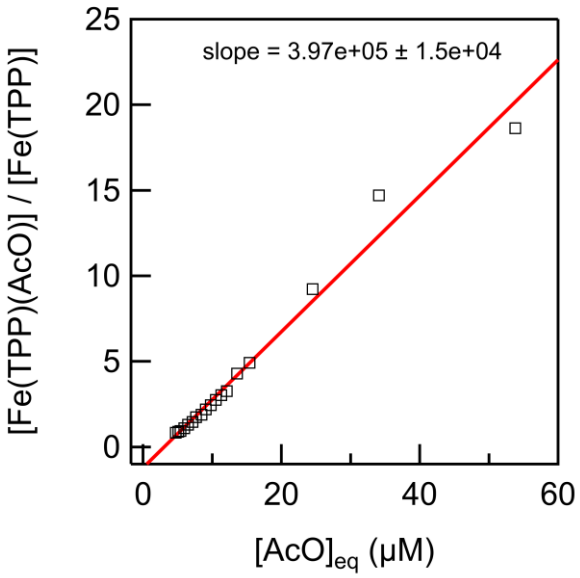

Figure C12. Plot showing the ratio of $[Fe(TPP)(AcO)]^-$ to [Fe(TPP)] versus the concentration of free acetate remaining in solution. Data collected for acetate titration into PrCN containing 7 μM Fe(TPP) and no electrolyte. The data were fit using a linear regression (the slope and one standard deviation are shown above).

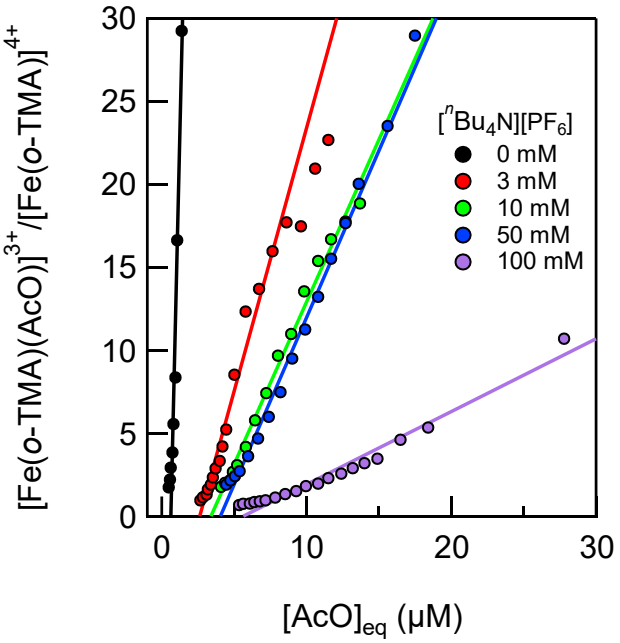

Figure C13. Plot showing the ratio of $[Fe^{II}(o\text{-TMA})(AcO)]^{3+}$ to $[Fe(o\text{-TMA})]^{4+}$ versus the concentration of free acetate remaining in solution at four different electrolyte concentrations. The data were fit using linear regressions to yield equilibrium constants, see **Table C1**.

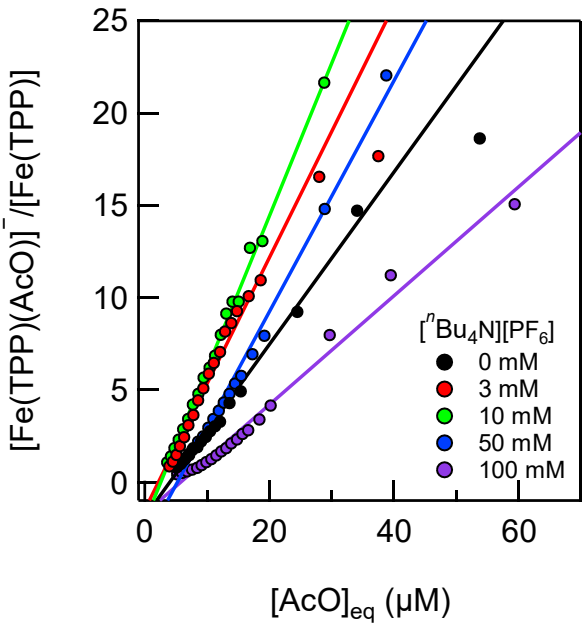

Figure C14. Plot showing the ratio of $[Fe(TPP)(AcO)]^-$ to [Fe(TPP)] versus the concentration of free acetate remaining in solution at various electrolyte concentrations. The data were fit using linear regressions to yield equilibrium constants, see **Table C1**.

Table C1. Acetate binding constants and conditions

Metalloporphyrin	Solvent	[^{n}Bu$_4$N][PF$_6$] (mM) [a]	K_{AcO} (M^{-1})	log(K_{AcO}) (M^{-1})
[Fe^{II}(*o*-TMA)]$^{4+}$	PrCN	0 [b]	(1.6−6.3) × 10^7	7.5 ± 0.3
[Fe^{II}(*o*-TMA)]$^{4+}$	PrCN	3	(2.1−8.3) × 10^6	6.6 ± 0.3
[Fe^{II}(*o*-TMA)]$^{4+}$	PrCN	10	(1.1−4.5) × 10^6	6.4 ± 0.3
[Fe^{II}(*o*-TMA)]$^{4+}$	PrCN	50	(0.8−3.2) × 10^6	6.2 ± 0.3
[Fe^{II}(*o*-TMA)]$^{4+}$	PrCN	100	(3.3−13.2) × 10^5	5.8 ± 0.3
[Fe^{II}(*o*-TMA)]$^{4+}$	MeCN	0	(1.0−4.0) × 10^6	6.3 ± 0.3
[Fe^{II}(*o*-TMA)]$^{4+}$	MeCN	10	(1.7−6.6) × 10^5	5.5 ± 0.3
[Fe^{II}(*o*-TMA)]$^{4+}$	MeCN	100	(3.8−15.2) × 10^4	4.9 ± 0.3
Fe(TPP)	PrCN	0	(2.3−9.4) × 10^5	5.7 ± 0.3
Fe(TPP)	PrCN	3	(3.4−13.5) × 10^5	5.8 ± 0.3
Fe(TPP)	PrCN	10	(4.2−16.6) × 10^5	5.9 ± 0.3
Fe(TPP)	PrCN	50	(3.1−12.3) × 10^5	5.8 ± 0.3
Fe(TPP)	PrCN	100	(2.5−10.0) × 10^5	5.5 ± 0.3

[a] These values are nearly equal to the ionic strength of the solutions unless otherwise indicated. [b] The ionic strength is 80 μM for this solution, which contained 8 μM [Fe^{II}(*o*-TMA)](OTf)$_4$.

C.4 Reference Potential of Fc* vs. Fc in PrCN

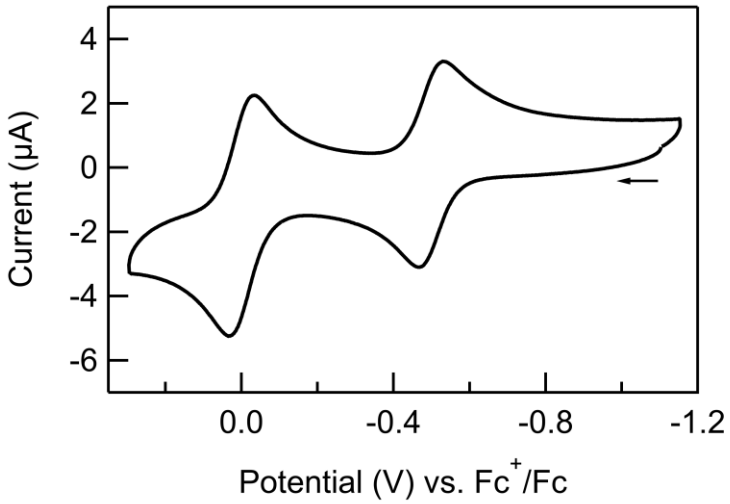

Figure C15. Cyclic voltammogram of 0.1 mM ferrocene (Fc) and 0.1 mM decamethylferrocene (Fc*) in PrCN containing 0.1 M [^{n}Bu$_4$N][PF$_6$]. Voltammogram collected at 0.1 V s^{-1}. The potential of Fc*$^{+}$/Fc* is −0.499 V vs. Fc^{+}/Fc under these conditions.

C.5 Cyclic Voltammograms of Fe(TPP) in PrCN and Tabulated $E_{1/2}$ Values

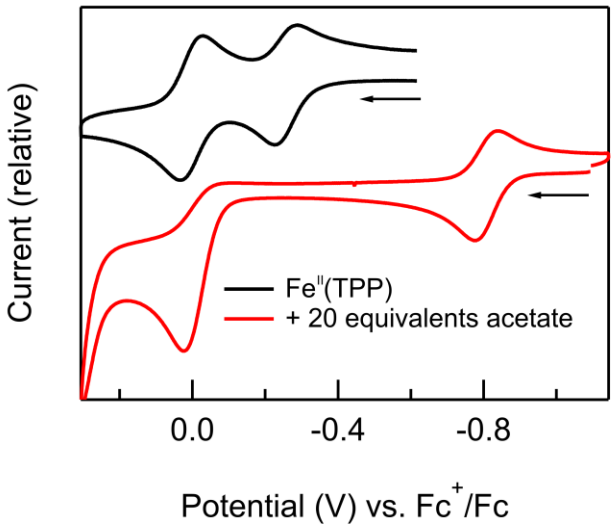

Figure C16. Cyclic voltammogram of 0.1 mM Fe^{II}(TPP) and 0.1 mM ferrocene in PrCN containing 0.1 M [^{n}Bu$_4$N][PF_6] before (black) and after (red) adding 2.0 mM [^{n}Bu$_4$N][AcO]. Voltammograms collected at 0.1 V s^{-1}. The irreversible feature in the red trace near 0.0 V vs. Fc^+/Fc is the decomposition reaction between ferrocenium (generated during the oxidative sweep) and excess acetate. This decomposition is well-known, as discussed elsewhere.[9]

Table C2. Experimental $E_{1/2}$ values of Fe^{III}/Fe^{II} redox couples with and without added acetate.[a]

Reduction reaction	$E_{1/2}$ (V) vs. Fc^+/Fc
$[Fe^{III}(o\text{-TMA})]^{5+} + e^- \rightarrow [Fe^{II}(o\text{-TMA})]^{4+}$	0.061
$[Fe^{III}(o\text{-TMA})(AcO)]^{4+} + e^- \rightarrow [Fe^{II}(o\text{-TMA})(AcO)]^{4+}$	−0.807
$[Fe^{III}(TPP)]^{+} + e^- \rightarrow [Fe^{II}(TPP)]$	−0.259
$[Fe^{III}(TPP)(AcO)] + e^- \rightarrow [Fe^{II}(TPP)(AcO)]^-$	−0.809

[a] All voltammograms collected in PrCN containing 0.1 M [^{n}Bu$_4$N][PF_6] at 0.1 V s^{-1}. Acetate-bound complexes generated in-situ using 20 equiv. [^{n}Bu$_4$N][AcO].

C.6 Solubility of O_2 in PrCN

To our knowledge, the concentration of dissolved O_2 at 1 atm O_2 has not yet been reported in *n*-butyronitrile. We determined an average value from three different methods (1−3). The experimental methods for each of these measurements are individually detailed below. The solubility values are summarized in **Table C3**).

Methods of measuring O_2 solubility in PrCN

1. Using a Clark electrode and the method described in reference [3].
2. Simulating experimental cyclic voltammograms of the reversible $1e^-$ oxygen/superoxide couple ($O_2/O_2^{\bullet-}$) and the reversible $1e^-$ ferrocenium/ferrocene couple (Fc^+/Fc).
3. Analyzing the limiting current of rotating disk voltammetry experiments using the Levich equation.

Table C3. Measurements for the molar solubility of dissolved O_2 in PrCN.

Method	Description	Concentration dissolved O_2 (M) [a]
1	Clark electrode	5.43 ± 0.22
2	Cyclic voltammetry [b]	5.3 ± 0.1
3	Rotating disk voltammetry [b]	5.90 ± 0.67
	Average solubility	5.5 ± 0.4

[a] Defined at 20 °C and 1 atm O_2. [b] PrCN solutions contained 0.1 M [^{n}Bu$_4$N][PF$_6$].

C.6.1 Method 1: Clark Electrode

These measurements were made following the method described in reference [3]. In a custom, water-jacketed (20.0 °C) cell with a side-arm was added 10 mL of Millipore water and a small stir bar. The water was sparged with lab air for 15 minutes before a Clark electrode was submerged in solution. The Clark electrode made an air-tight seal with the cell and no headspace remained. The potential was recorded for several minutes while stirring to obtain a baseline (**Figure C17**; left, black trace).

Using a long hypodermic needle, 0.1 mL of an O_2 sparged solution of PrCN was slowly added into solution. The added volume displaced an equal volume of water in the side-arm of the cell. The potential at the Clark electrode spiked and slowly equilibrated within a few minutes. After the change in potential was < 5 mV/minute, another 0.1 mL of PrCN was added. This addition and equilibration was performed four times.

Given the known concentration of [O_2] at 20.0 °C in water under 1 atm air (0.284 mM O_2), the "equilibrated" potentials were converted to units of moles/L [O_2] in the bulk solution. Using the total volume of the solution after each addition, these concentrations were converted to units of μmoles O_2 in the total solution and were plotted against the added volumes of PrCN (**Figure C17**). The slope of this line gives the concentration of [O_2] in PrCN under 1 atm O_2 at 20 °C.

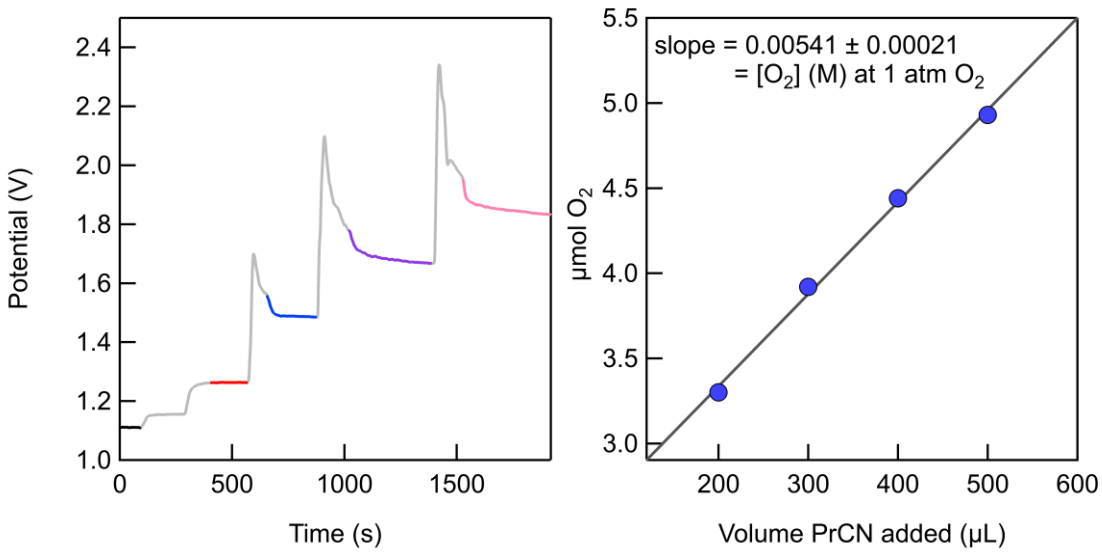

Figure C17. (Left) Potential versus time responses recorded at the Clark electrode with additions of PrCN containing dissolved O_2. Colored traces indicate equilibration periods after each addition. Grey trace is of raw data. (Right) Relationship between total moles dissolved O_2 versus volume of added PrCN. Slope of the line is equal to the concentration of dissolved O_2 in PrCN under 1 atm O_2 at 20 °C.

C.6.2 Method 2: Simulating Cyclic Voltammograms

Cyclic voltammograms were collected using the three-electrode set-up described above in a water-jacked cell at 20.0 °C and by first passing the O_2 stream through an initial bubbler of PrCN (to minimize solvent evaporation). The solution was saturated with O_2 by gently bubbling with dry O_2 (1 atm) for 20 minutes before a CV was collected ($E_{1/2}[O_2/O_2^{\bullet-}]$ = −1.42 V vs. Fc^+/Fc). The solution was then bubbled with argon for 20 minutes before 8.65 mM ferrocene was added using a stock solution and a second CV was collected. The same glassy carbon electrode was used for both voltammograms and was polished in-between scans.

The two voltammograms were simulated and fit using DigiSim as reversible 1e^- couples (parameters and mechanism summarized in **Table C4**). The fits are good, as shown by the accuracy of the simulated ferrocene concentration ($[Fc]_{sim}$ = $[Fc]_{exp}$). The heterogeneous rate constant and diffusion constants for O_2 and $O_2^{\bullet-}$ were assumed to be equal to those reported in acetonitrile.[10-11]

Table C4. Fitting parameters for simulated cyclic voltammograms of ferrocene and dissolved O_2 butyronitrile.

Parameter	Value (Fc^+/Fc)	Value ($O_2/O_2^{\bullet-}$)
Reaction Mechanism	A + e = B	A + e = B
Estart (V)	−0.3285	−0.3285
Erev (V)	0.4765	−1.9235
Eend (V)	−0.3285	−0.3285
v (V/s)	0.1	0.1
Cycles	1	1
Ru (Ohm)	140	140
Cdl (F)	0	0
Temp. (K)	293	293
Geometry	Planar	Planar
Area (cm^2)	0.09	0.09
Diffusion	Semi-Infinite	Semi-Infinite
[A] (M)	0.00865	0.0053
Type	BV	BV
E_0 (V)	0.0000	−1.4050
α (eV)	0.5	0.5
k_s (cm/s)	1E4	0.0088 [a]
D (analyte A, cm^2/s)	1E-5	9.2E-5 [b]
D (analyte B, cm^2/s)	1E-5	2.3E-5 [b]
Expanding grid factor	0.5	0.5
X_{max}/SQRT(Dt)	6	6
Potential steps (V)	0.005	0.005
Gauss-Newton Iterations	1	1
Noise Level (A)	0	0

[a] Heterogeneous electron transfer rate constant for $O_2/O_2^{\bullet-}$ using glassy carbon in acetonitrile containing 0.1 M electrolyte (reference [10]). [b] Diffusion coefficients reported for O_2 and $O_2^{\bullet-}$ in acetonitrile containing 0.1 M electrolyte (reference [11]).

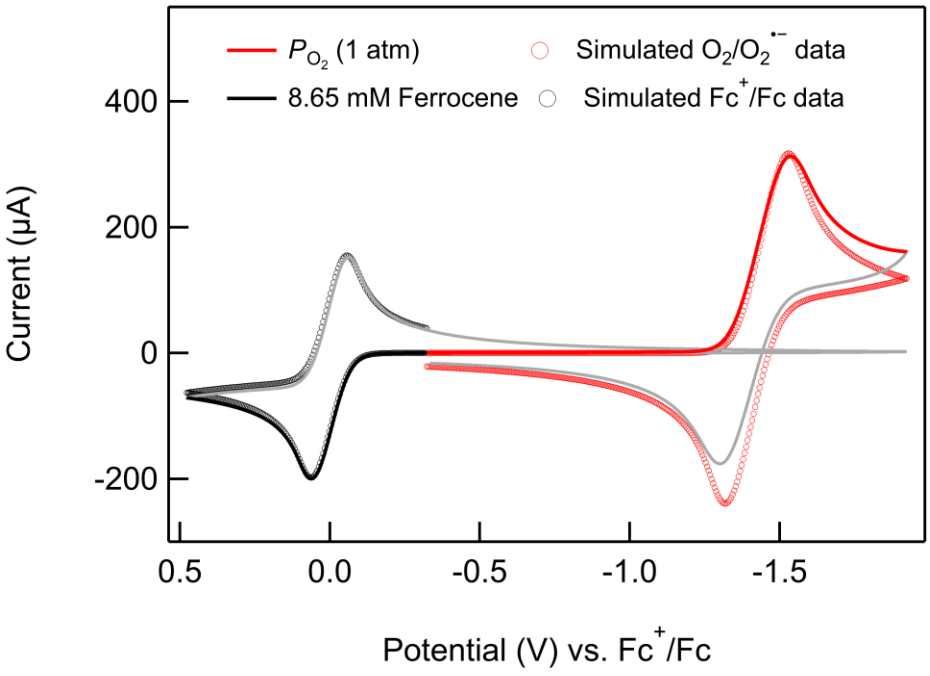

Figure C18. Cyclic voltammograms of $O_2/O_2^{\bullet-}$ (1 atm O_2) and of ferrocene/ferrocenium in PrCN containing 0.1 M [^{n}Bu$_4$N][PF_6]. Voltammograms collected at 0.1 V s^{-1}. Forward sweeps for each couple highlighted in red and black. Simulated voltammograms shown as open circles.

C.6.3 Method 3: Rotating Disk Voltammetry

Rotating disk voltammetry experiments were performed using a three-electrode set-up. Unlike the above experiments, however, the working electrode was a 5mm glassy carbon disk embedded in a PTFE shroud and was attached to a Pine Instruments rotator. Similar to the experiments described above, the solution was aerated by bubbling with 1 atm air for 20 minutes, which was first passed through Drierite and a PrCN bubbler.

Linear sweep voltammograms were collected between −0.3 V and −1.8 V vs. Fc^+/Fc at varying scan rates and rotation rates. In all cases the currents reached mass-transport plateaus at potentials negative of the $O_2/O_2^{\bullet-}$ couple (**Figure C19**). These limiting currents were analyzed using the Levich equation to obtain the concentration of [O_2] at 20 °C under 1 atm air (eq C.6). As before, the diffusion coefficient for O_2 in PrCN was assumed to be equal to the reported constant in acetonitrile (9.2E-5 cm^2/s).[11] A representative example of the linear sweep voltammograms is shown in **Figure C19**. A summary of the conditions, currents, and calculated [O_2] concentrations is reported in **Table C5**.

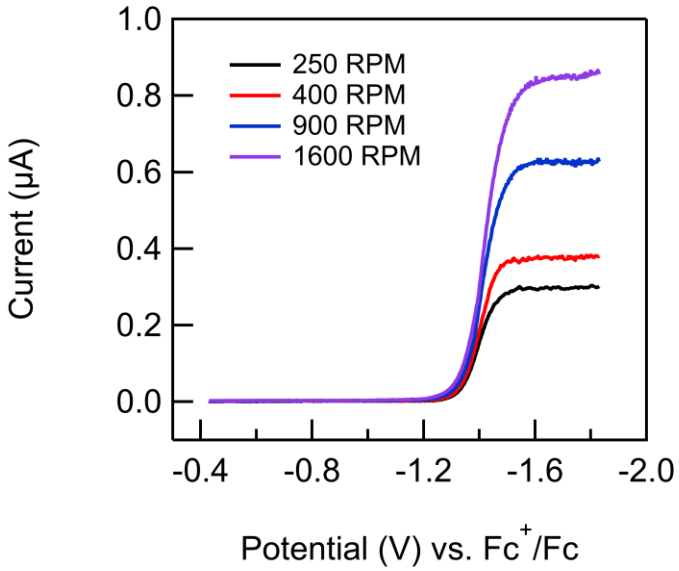

Figure C19. Linear sweep voltammograms for the reduction of O_2 to $O_2^{\bullet-}$ at various rotation rates in PrCN containing 0.1 M [^{n}Bu$_4$N][PF_6]. All voltammograms collected at 0.025 V s^{-1} and under 1 atm air.

$$I_L = 0.620nFAD^{2/3}\omega^{1/2}\upsilon^{-1/6}C_0 \quad \text{(eq C.6)}$$

I_L = limiting current (A)
n = number of electrons
F = Faraday's constant (C mol^{-1})
A = Electrode surface area (cm^2)
D = diffusion coefficient (cm^2 s^{-1})
ω = angular momentum (rad s^{-1})
υ = scan rate (V s^{-1})
C_0 = analyte concentration (mol cm^{-3})

Table C5. Summary of rotating disk voltammetry conditions and measured O_2 concentrations.

#	I_L (A)	n	F (C mol^{-1})	A (cm^2)	D (cm^2 s^{-1})	ω (rad s^{-1})	υ (V s^{-1})	C_0 (mol cm^{-3})	$[O_2]$ (mM) [a]	$[O_2]$ (mM) [b]
1	2.99E-04	1	96485	0.25	9.2E-05	26.175	0.025	1.04E-06	1.04	4.98
2	3.78E-04	1	96485	0.25	9.2E-05	41.88	0.025	1.04E-06	1.04	4.98
3	6.24E-04	1	96485	0.25	9.2E-05	94.23	0.025	1.14E-06	1.14	5.48
4	8.51E-04	1	96485	0.25	9.2E-05	167.52	0.025	1.17E-06	1.17	5.61
5	2.95E-04	1	96485	0.25	9.2E-05	26.175	0.050	1.15E-06	1.15	5.53
6	3.75E-04	1	96485	0.25	9.2E-05	41.88	0.050	1.15E-06	1.15	5.54
7	6.03E-04	1	96485	0.25	9.2E-05	94.23	0.050	1.24E-06	1.24	5.95
8	8.60E-04	1	96485	0.25	9.2E-05	167.52	0.050	1.32E-06	1.32	6.37
9	2.99E-04	1	96485	0.25	9.2E-05	26.175	0.100	1.31E-06	1.31	6.28
10	3.76E-04	1	96485	0.25	9.2E-05	41.88	0.100	1.30E-06	1.30	6.24
11	6.10E-04	1	96485	0.25	9.2E-05	94.23	0.100	1.40E-06	1.40	6.75
12	8.61E-04	1	96485	0.25	9.2E-05	167.52	0.100	1.49E-06	1.49	7.15
Average ± standard deviation									1.23 ± 0.14	5.91 ± 0.67

[a] Concentration O_2 under 1 atm air (20.8% O_2). [b] Concentration O_2 under 1 atm O_2.

C.7 O_2 Binding Measurements

C.7.1 UV-vis Spectra of O_2-Bound and Unbound Complexes

UV-vis spectra were recorded on an Agilent 8452 diode-array spectrophotometer equipped with a Unisoku Unispeks cryostat. The spectra only show the Q-band portion of the porphyrin absorbance features.

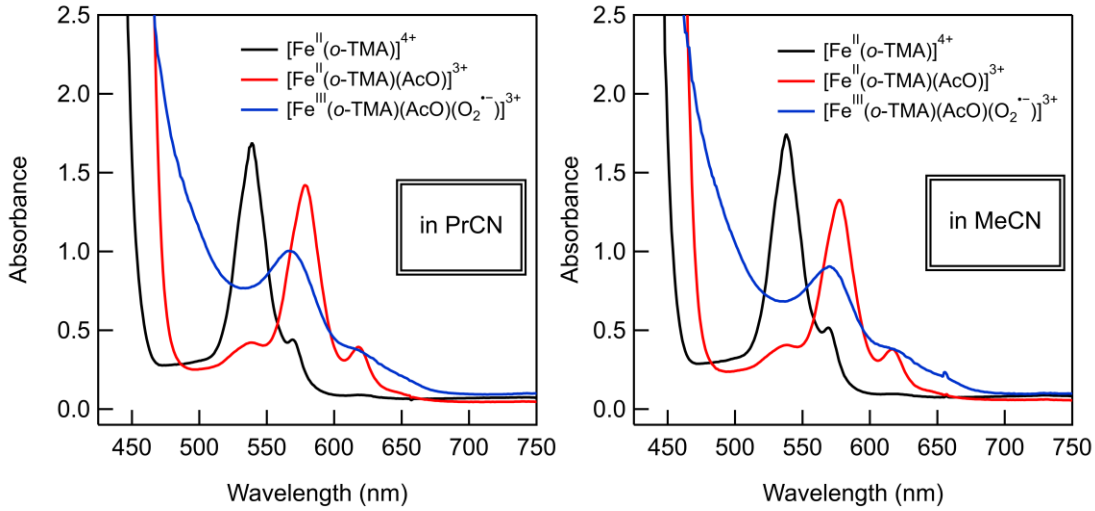

Figure C20. (Left) UV-vis spectra of $[Fe^{II}(o\text{-TMA})]^{4+}$, $[Fe^{II}(o\text{-TMA})(AcO)]^{3+}$, and $[Fe^{III}(o\text{-TMA})(AcO)(O_2^{\bullet-})]^{3+}$ in PrCN, all concentrations are 67 μM. (Right) UV-vis spectra of the same complexes in MeCN. Spectra of $[Fe^{III}(o\text{-TMA})(AcO)(O_2^{\bullet-})]^{3+}$ were recorded after sparging with pure O_2 for 60 s at −80 °C and −40 °C (in PrCN and MeCN, respectively).

C.7.2 Reversible O_2 Binding

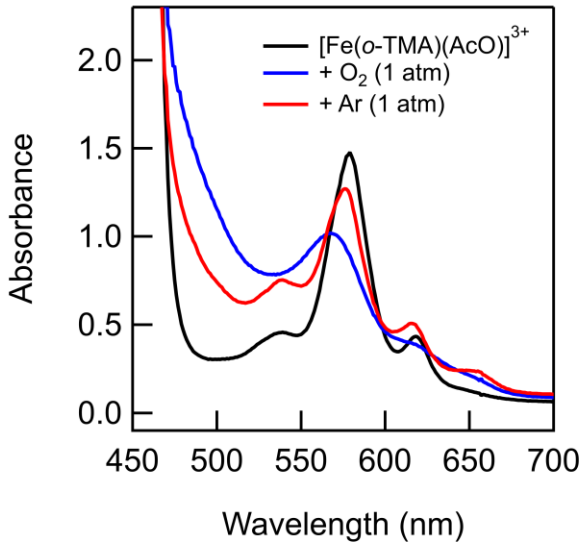

Figure C21. UV-vis spectra of a 67 μM solution of $[Fe^{II}(o\text{-TMA})(AcO)]^{3+}$ in PrCN at −60 °C. Solution was prepared under N_2 (black), bubbled with pure O_2 (1 minute, blue), and then sparged with argon (5 minutes, red). Complete reversibility was limited due to decomposition of the superoxide over long time scales (see stopped flow data below).

C.7.3 Stopped-flow O_2 Binding Measurements

O_2 binding measurements were performed using a TgK Scientific CryoStopped-Flow System (SF-61DX2) equipped with a diode array detector. In a typical experiment, two solutions (A and B) were prepared either in acetonitrile or butyronitrile (depending on the experiment) and loaded into gas-tight syringes. Upon mixing these two solutions in the stopped-flow, all concentrations were halved.

Solution A was prepared in a N_2 glovebox and contained ~0.1 mM $[Fe^{II}(o\text{-TMA})](OTf)_4$ and varying concentrations of $[^nBu_4N][PF_6]$. Solution B was prepared by first dissolving ~1.0 mM $[^nBu_4N][AcO]$ in either MeCN or PrCN and then sparging the solution with air that had passed through a Drierite column and a secondary bubbler of the respective solvent for 20 minutes. Using this method *i*) avoids changes in $[O_2]$ for experiments performed using different ionic strengths and *ii*) generates the O_2-sensitive complex *in situ* when the two solutions are mixed.

Upon mixing the two solutions, optical spectra were rapidly collected every 1-2 milliseconds. Below −30 °C the spectra typically stopped changing within 0.5 s (**Figure C22**). At warmer temperatures this occurred within 20-40 ms (**Figure C23**). For both cases the final spectrum could be well-fit to a combination of the $[Fe^{II}(o\text{-TMA})(AcO)]^{3+}$ and $[Fe^{III}(o\text{-TMA})(AcO)(O_2^{\bullet-})]^{3+}$ spectra (**Figure C20**). At longer timescales (120 s) the mixed solution slowly oxidized and the spectra could no longer be fit (**Figure C24**).

Using linear combinations of the $[Fe^{II}(o\text{-TMA})(AcO)]^{3+}$ and $[Fe^{III}(o\text{-TMA})(AcO)(O_2^{\bullet-})]^{3+}$ spectra (**Figure C20**) and the known concentration of $[O_2]$ originally dissolved in solution B (**Table C3**), the equilibrium spectra collected at each temperature were fit to yield O_2 binding constants. These constants and conditions are reported in **Table C6**.

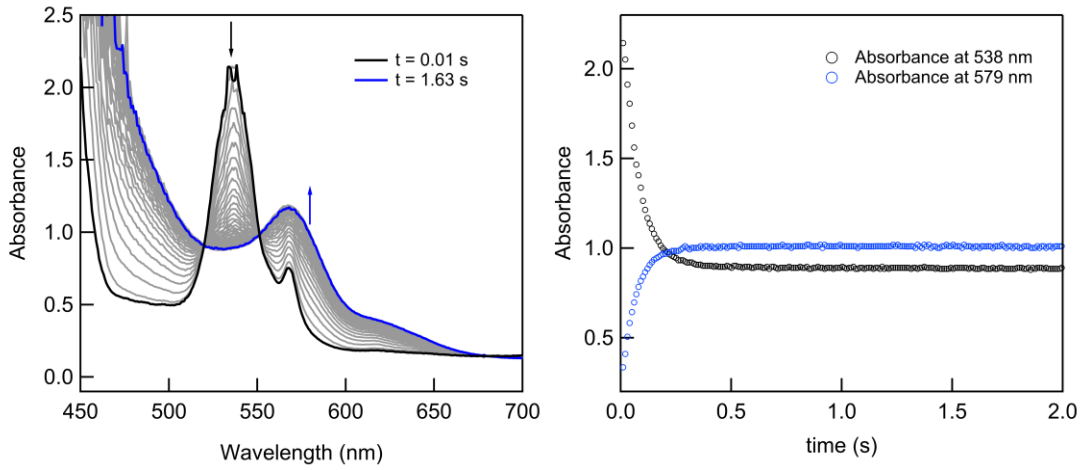

Figure C22. (Left) Stopped-flow UV-vis spectra for the reaction of $[Fe^{II}(o\text{-TMA})]^{4+}$ (60 μM) with acetate (0.6 mM) and O_2 (1.4 mM) in PrCN at −50 °C. (Right). Absorbance versus time plots for noted wavelengths (also indicated with arrows on the spectra). Equilibrium is reached within 0.5 s. Reported concentrations are after mixing.

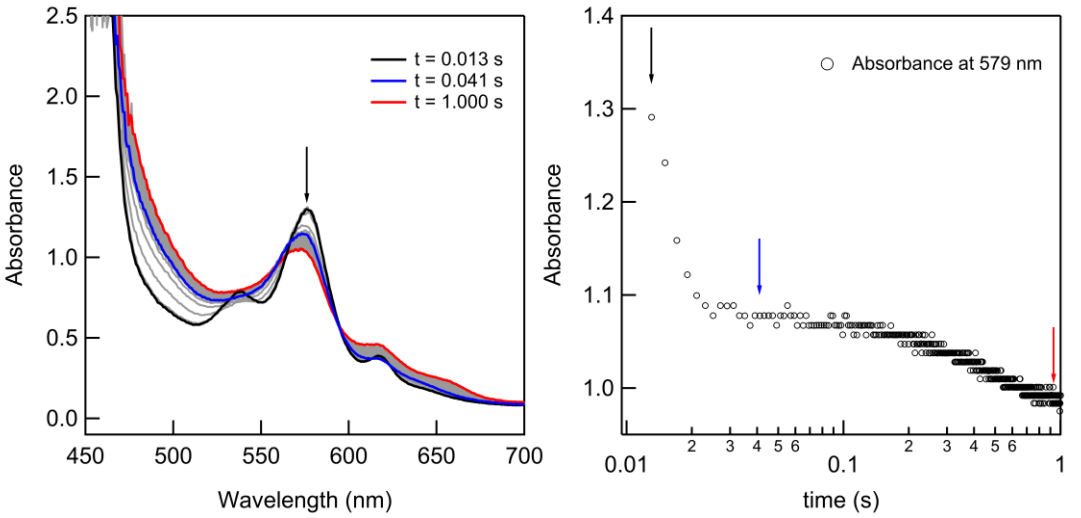

Figure C23. (Left) Stopped-flow UV-vis spectra for the reaction of $[Fe^{II}(o\text{-TMA})]^{4+}$ (60 μM) with acetate (0.6 mM) and O_2 (1.4 mM) in PrCN at −10 °C. Note that the initial spectra is of $[Fe^{II}(o\text{-TMA})(AcO)]^{3+}$, which is formed within the mixing time. (Right). Absorbance versus time plot at 579 nm (indicated with arrows on the spectra), plotted using a logarithmic time-axis. Note that there is a fast-component during which O_2-binding equilibrium is reached (blue) and a longer-component due to slow oxidation (red). Reported concentrations are after mixing.

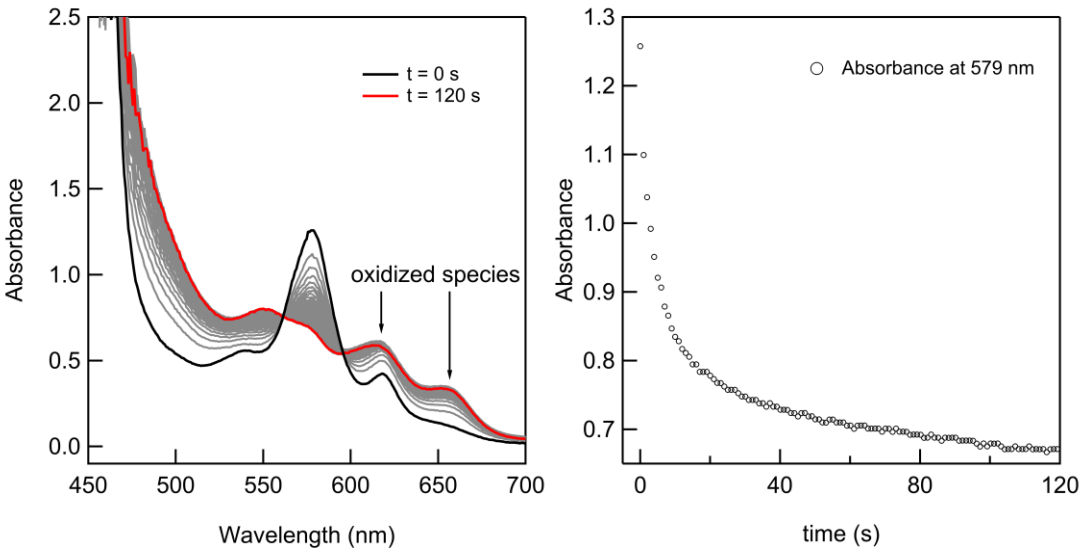

Figure C24. (Left) Stopped-flow UV-vis spectra for a 120s reaction of $[Fe^{II}(o\text{-TMA})]^{4+}$ (60 μM) with acetate (0.6 mM) and O_2 (1.4 mM) in PrCN at 20 °C, showing decomposition and formation of oxidized products at 620 nm and 655 nm. Note that the initial spectra is almost exclusively $[Fe^{II}(o\text{-TMA})(AcO)]^{3+}$ (Right). Absorbance versus time plots for noted wavelengths. Reported concentrations are after mixing.

C.7.4 O_2 Binding van 't Hoff Plots and Equilibrium Constants

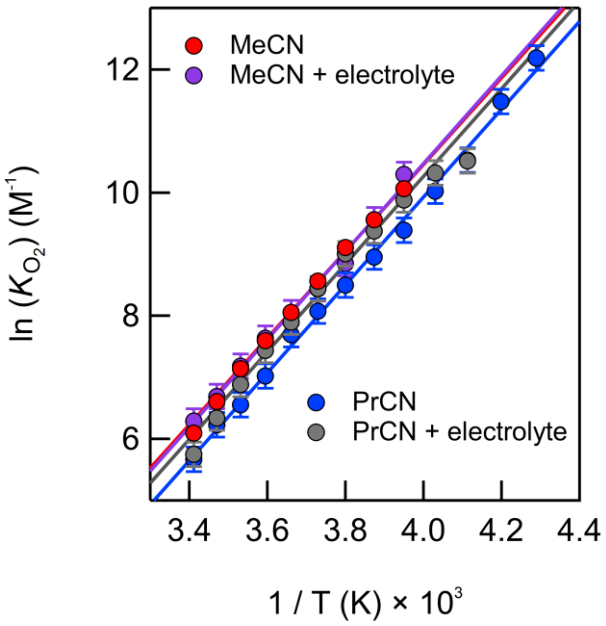

Figure C25. van 't Hoff plots for O_2 binding to $[Fe^{II}(o\text{-TMA})(AcO)]^{3+}$ in PrCN and MeCN containing various concentrations of $[^nBu_4N][PF_6]$ supporting electrolyte.

Table C6. Tabulated values of K_{O2} for O_2 binding to $[Fe^{II}(o\text{-TMA})(AcO)]^{3+}$.[a]

Solvent	T (K)	without added electrolyte		with 0.1 M $[^nBu_4N][PF_6]$	
		K_{O2} (M^{-1})	ln(K_{O2} / M^{-1})	K_{O2} (M^{-1})	ln(K_{O2} / M^{-1})
PrCN	233	(1.6−2.4) × 10^5	12.2 ± 0.2		
	238	(0.8−1.2) × 10^5	11.5 ± 0.2		
	243	(3.0−4.0) × 10^4	10.5 ± 0.2	(3.0−4.4) × 10^4	10.5 ± 0.2
	248	(1.8−2.7) × 10^4	10.0 ± 0.2	(2.4−3.6) × 10^4	10.3 ± 0.2
	253	(1.0−1.5) × 10^4	9.4 ± 0.2	(1.6−2.4) × 10^4	9.9 ± 0.2
	258	(6.6−9.9) × 10^3	9.0 ± 0.2	(1.0−1.5) × 10^4	9.4 ± 0.2
	263	(4.0−6.0) × 10^3	8.5 ± 0.2	(6.6−9.9) × 10^3	9.0 ± 0.2
	268	(2.7−4.0) × 10^3	8.1 ± 0.2	(3.6−5.4) × 10^3	8.4 ± 0.2
	273	(1.8−2.7) × 10^3	7.7 ± 0.2	(2.2−3.3) × 10^3	7.9 ± 0.2
	278	(0.9−1.3) × 10^3	7.0 ± 0.2	(1.3−2.0) × 10^3	7.4 ± 0.2
	283	(6.0−9.0) × 10^2	6.6 ± 0.2	(0.8−1.2) × 10^3	6.9 ± 0.2
	288	(4.0−6.0) × 10^2	6.2 ± 0.2	(4.5−6.7) × 10^2	6.3 ± 0.2
	293	(2.5−3.7) × 10^2	5.7 ± 0.2	(2.5−3.7) × 10^2	5.7 ± 0.2
MeCN	253	(2.0−3.0) × 10^4	10.1 ± 0.2	(2.4−3.6) × 10^4	10.3 ± 0.2
	258	(1.2−1.8) × 10^4	9.6 ± 0.2	(1.2−1.8) × 10^4	9.6 ± 0.2
	263	(0.7−1.1) × 10^4	9.1 ± 0.2	(5.4−8.1) × 10^3	8.8 ± 0.2
	268	(4.9−7.3) × 10^3	8.7 ± 0.2	(3.6−5.4) × 10^3	8.4 ± 0.2
	273	(3.0−4.5) × 10^3	8.2 ± 0.2	(2.7−4.0) × 10^3	8.1 ± 0.2
	278	(1.6−2.4) × 10^3	7.6 ± 0.2	(1.6−2.4) × 10^3	7.6 ± 0.2
	283	(1.1−1.6) × 10^3	7.2 ± 0.2	(1.1−1.6) × 10^3	7.2 ± 0.2
	288	(6.0−9.0) × 10^2	6.6 ± 0.2	(6.7−9.9) × 10^2	6.7 ± 0.2
	293	(3.7−5.5) × 10^2	6.1 ± 0.2	(4.5−6.7) × 10^2	6.3 ± 0.2

[a] Uncertainties were limited to the accuracy of the ratio between $[Fe^{II}(o\text{-TMA})(AcO)]^{3+}$ and $[Fe^{III}(o\text{-TMA})(AcO)(O_2^{\bullet-})]^{3+}$. These were typically within 5%, based on fitting of the equilibrium spectra, and contributed to a maximum error of ca. 20% in K_{O2}.

C.7.5 Porphyrin Abbreviations used in Table 4.5

F_8TPP = tetra(*o*,*o'*-difluorophenyl)porphyrin
Piv_3(5ClmP)P = *α*,*β*,*γ*-tris(*o*-pivalamidophenyl)-*δ*-[*o*-3-*N*-imidazolylvaleramido)phenyl]porphyrin
Piv_3(4ClmP)P = *α*,*β*,*γ*-tris(*o*-pivalamidophenyl)-*δ*-[*o*-3-*N*-imidazolylbutyramido)phenylporphyrin
T_{piv}PP = tetra(*o*-pivalamidophenyl)porphyrin
durene-4/4 = durene-capped porphyrin
C_2-cap = pyromellitoyl(tetrakis(*o*-oxyethoxyphenyl))porphyrin
C_3-cap = pyromellitoyl(tetrakis(*o*-oxypropoxyphenyl))porphyrin
1,2-Me_2Im = 1,2-dimethylimidazole
DcIm = 1,5-dicyclohexylimidazole
1-MeIm = *N*-methylimidazole
Me_2Im = 1,2-methylimidazole

C.8 Computations

Table C7. Free energies and spins of calculated compounds. Open shell singlets are denoted by OSS.

Molecule	G (kcal mol^{-1})	Spin (S)
$[Fe^{II}(o\text{-TMA})]^{4+}$	−1711397.5	3
$[Fe^{II}(o\text{-TMA})(AcO)]^{3+}$	−1854684.5	1
$[Fe^{II}(o\text{-TMA})(AcO)_2]^{2+}$	−1997957.9	1
$Fe^{II}(TPP)$	−1276208.2	3
$[Fe^{II}(TPP)(AcO)]^{-}$	−1419488.6	5
$[Fe^{II}(TPP)(AcO)_2]^{2-}$	−1562754.7	1
$[Fe^{III}(o\text{-TMA})]^{5+}$	−1711292.1	4
$[Fe^{III}(o\text{-TMA})(AcO)]^{4+}$	−1854594.8	6
$[Fe^{III}(o\text{-TMA})(AcO)_2]^{3+}$	−1997881.0	2
$[Fe^{II}(o\text{-TMA})(MeCN)]^{4+}$	−1794586.3	3
$[Fe^{III}(o\text{-TMA})(MeCN)]^{5+}$	−1794478.9	2
$[Fe^{II}(o\text{-TMA})(MeCN)_2]^{4+}$	−1877773.0	1
$[Fe^{III}(o\text{-TMA})(MeCN)_2]^{5+}$	−1877663.3	2
$[Fe^{II}(o\text{-TMA})(MeCN)(AcO)]^{3+}$	−1937869.8	1
$[Fe^{III}(o\text{-TMA})(MeCN)(AcO)]^{4+}$	−1937778.4	6
$[Fe^{III}(o\text{-TMA})(O_2^{\bullet-})]^{4+}$ (towards charge)	−1805650.3	OSS
$[Fe^{III}(o\text{-TMA})(AcO)(O_2^{\bullet-})]^{3+}$ (towards charge)	−1948938.8	OSS
$[Fe^{III}(o\text{-TMA})(O_2^{\bullet-})]^{4+}$ (away from charge)	−1805649.0	OSS
$[Fe^{III}(o\text{-TMA})(AcO)(O_2^{\bullet-})]^{3+}$ (away from charge)	−1948937.7	OSS
O_2	−94247.7	3
AcO^{-}	−143269.4	1

Table C8. Low-spin and high-spin atom charges (q) from natural population analysis for CO_2 and O_2 bound adducts of Fe(*o*-TMA) and Fe(TPP). Extended **Table 4.4** from Chapter 4.

	CO_2 radical anion complex 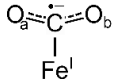	q(Fe)	q(C)	q(O_a)[a]	q[O_a + O_b]	q[C + O_a + O_b]
	Singlet state					
1	[(Fe^{I}(*o*-TMA)($CO_2^{\bullet-}$)]$^{2+}$ [b]	1.514	0.620	−0.661	−1.322	–0.702
2	[Fe^{I}(TPP)($CO_2^{\bullet-}$)]$^{2-}$	1.514	0.417	−0.528	−1.056	–0.639
3	Δq (line 1 – line 2) [c]	0.000	0.203	−0.133	−0.266	−0.064
	Quintet state					
4	[(Fe^{I}(*o*-TMA)($CO_2^{\bullet-}$)]$^{2+}$ [b]	1.409	0.577	−0.534	−1.068	–0.491
5	[Fe^{I}(TPP)($CO_2^{\bullet-}$)]$^{2-}$	1.388	0.629	−0.522	−1.044	–0.415
6	Δq (line 4 – line 5) [c]	0.021	−0.052	−0.012	−0.023	−0.074
	O_2 radical anion complex 	q(Fe)	q(O_p)[d]	q(O_d)[d]	Δq[O_d]	q[O_d + O_p]
	Singlet state					
7	[(Fe^{III}(*o*-TMA)($O_2^{\bullet-}$)]$^{4+}$ [b]	1.718	−0.254	−0.107		–0.361
8	[Fe^{III}(TPP)($O_2^{\bullet-}$)]	1.706	−0.262	−0.093		–0.355
9	Δq (line 7 – line 8) [c]	0.012	0.008	−0.014	−0.014	−0.006
	Quintet state					
10	[(Fe^{III}(*o*-TMA)($O_2^{\bullet-}$)]$^{4+}$ [b]	1.487	−0.252	−0.156		−0.408
11	[Fe^{III}(TPP)($O_2^{\bullet-}$)]	1.484	−0.245	−0.142		−0.387
12	Δq (line 10 – line 11) [c]	0.003	−0.007	−0.014	−0.014	−0.021

[a] O_a and O_b are symmetry equivalent. [b] Rotamer where bound substrate is oriented towards the trimethylanilinium group. [c] Δq is the difference in the charges between similar atoms in complexes with different porphyrin ligands, Δq = q(TMA) – q(TPP). [d] O_p and O_d are the proximal and distal oxygen atoms, respectively.

C.9 Single Crystal X-ray Structure

Low-temperature diffraction data (ω-scans) were collected on a Rigaku MicroMax-007HF diffractometer coupled to a Saturn994+ CCD detector with Cu Kα (λ = 1.54178 Å) for the structure of $[Fe^{II}(o\text{-TMA})\bullet 2CH_3CN](OTf)_4$. The diffraction images were processed and scaled using Rigaku Oxford Diffraction software. The structure was solved with SHELXT and was refined against F^2 on all data by full-matrix least squares with SHELXL.[12] All non-hydrogen atoms were refined anisotropically. Hydrogen atoms were included in the model at geometrically calculated positions and refined using a riding model. The isotropic displacement parameters of all hydrogen atoms were fixed to 1.2 times the U value of the atoms to which they are linked (1.5 times for methyl groups). Two of the four triflate groups are disordered in equal population. Each of the disordered triflates occupies two crystallographically distinct positions. The chemically equivalent C-S, S-O, C-F distances were restrained to be similar. The thermal ellipsoids were restrained to be similar and the disordered groups were restrained to behave as rigid groups. The program SQUEEZE was used to compensate for the contribution of disordered solvents contained in voids within the crystal lattice from the diffraction intensities. This procedure was applied to the data file and the submitted model is based on the solvent removed data. Based on the total electron density found in the voids (252 e/$Å^3$), it is likely that ~8 acetonitrile molecules are present in the unit cell. See "_platon_squeeze_details" in the .cif for more information. The full numbering scheme of compound $[Fe^{II}(o\text{-TMA})\bullet 2CH_3CN](OTf)_4$ can be found in the full details of the X-ray structure determination (CIF), which is included as Supporting Information. CCDC number 2016355 ($[Fe^{II}(o\text{-TMA})\bullet 2CH_3CN](OTf)_4$) contains the supplementary crystallographic data for this paper. These data can be obtained free of charge from The Cambridge Crystallographic Data Center via www.ccdc.cam.ac.uk/data_request/cif.

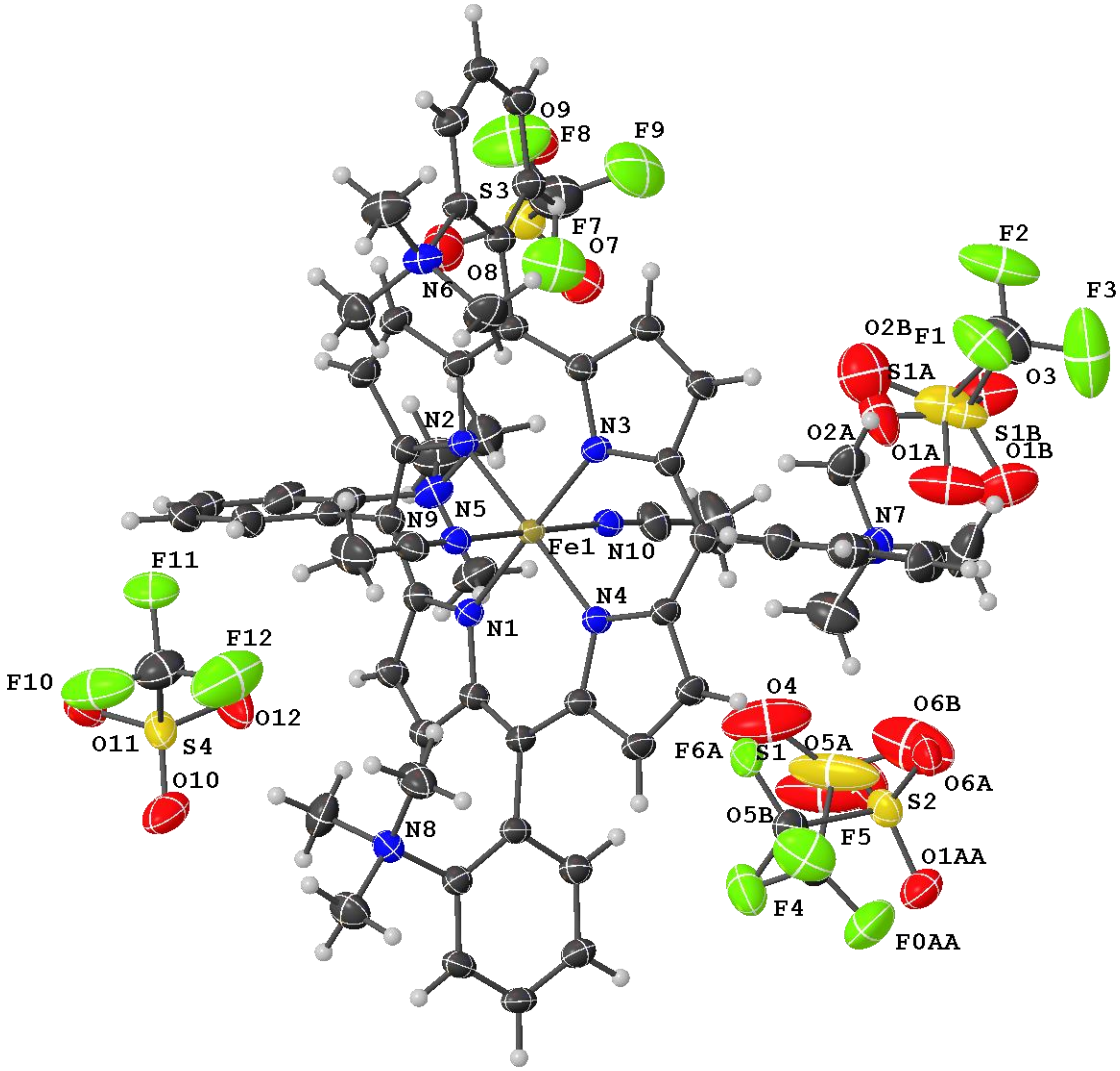

Figure C26. A partial numbering scheme of [Fe^{II}(*o*-TMA)•2CH_3CN](OTf)$_4$ with 50% thermal ellipsoid probability levels. The hydrogen atoms are shown as circles for clarity.

Table C9. Crystal data and structure refinement for $[Fe^{II}(o\text{-TMA})\bullet 2CH_3CN](OTf)_4$.

Identification code	007b-20007	
Empirical formula	C64 H66 F12 Fe N10 O12 S4	
Formula weight	1579.35	
Temperature	93(2) K	
Wavelength	1.54184 Å	
Crystal system	Triclinic	
Space group	P-1	
Unit cell dimensions	a = 13.1045(3) Å	α= 89.445(2)°.
	b = 14.3224(3) Å	β= 84.162(2)°.
	c = 23.0804(4) Å	γ = 73.490(2)°.
Volume	4130.93(15) $Å^3$	
Z	2	
Density (calculated)	1.270 Mg/m^3	
Absorption coefficient	3.148 mm^{-1}	
F(000)	1628	
Crystal size	0.200 x 0.200 x 0.080 mm^3	
Crystal color and habit	Black Block	
Diffractometer	Rigaku Saturn 944+ CCD	
Theta range for data collection	1.924 to 66.598°.	
Index ranges	-15<=h<=15, -16<=k<=17, -27<=l<=27	
Reflections collected	143393	
Independent reflections	14367 [R(int) = 0.0348]	
Observed reflections (I > 2sigma(I))	13900	
Completeness to theta = 66.598°	98.4 %	
Absorption correction	Semi-empirical from equivalents	
Max. and min. transmission	1.00000 and 0.63456	
Solution method	SHELXT-2014/5 (Sheldrick, 2014)	
Refinement method	SHELXL-2014/7 (Sheldrick, 2014)	
Data / restraints / parameters	14367 / 161 / 1025	
Goodness-of-fit on F^2	1.031	
Final R indices [I>2sigma(I)]	R1 = 0.0712, wR2 = 0.1967	
R indices (all data)	R1 = 0.0726, wR2 = 0.1980	
Extinction coefficient	0.0050(2)	
Largest diff. peak and hole	1.383 and -0.756 $e.Å^{-3}$	

C.10 References

1. Darcy, J. W.; Kolmar, S. S.; Mayer, J. M., Transition State Asymmetry in C-H Bond Cleavage by Proton-Coupled Electron Transfer. *J. Am. Chem. Soc.* **2019,** *141* (27), 10777-10787.
2. Pegis, M. L.; Martin, D. J.; Wise, C. F.; Brezny, A. C.; Johnson, S. I.; Johnson, L. E.; Kumar, N.; Raugei, S.; Mayer, J. M., Mechanism of Catalytic O_2 Reduction by Iron Tetraphenylporphyrin. *J. Am. Chem. Soc.* **2019,** *141*, 8315-8326.
3. Karlin, K. D.; Wei, N.; Jung, B.; Kaderli, S.; Niklaus, P.; Zuberbuehler, A. D., Kinetics and thermodynamics of formation of copper-dioxygen adducts: oxygenation of mononuclear copper(I) complexes containing tripodal tetradentate ligands. *J. Am. Chem. Soc.* **1993,** *115* (21), 9506-9514.
4. Lexa, D.; Rentien, P.; Savéant, J. M.; Xu, F., Methods for Investigating the Mechanistic and Kinetic Role of Ligand Exchange Reactions in Coordination Electrochemistry. *J. Electroanal. Chem.* **1985,** *191* (2), 253-279.
5. Azcarate, I.; Costentin, C.; Robert, M.; Savéant, J. M., Through-Space Charge Interaction Substituent Effects in Molecular Catalysis Leading to the Design of the Most Efficient Catalyst of CO_2-to-CO Electrochemical Conversion. *J. Am. Chem. Soc.* **2016,** *138* (51), 16639-16644.
6. La, T.; Richards, R.; Miskelly, G. M., Synthesis and Characterization of the Cationic Porphyrin Meso-Tetrakis(2,3,5,6-Tetrafluoro-*N*,*N*,*N*-Trimethyl-4-Aniliniumyl)Porphyrin. *Inorg. Chem.* **1994,** *33* (14), 3159-3163.
7. Caesar, P. D., 1,5-Naphthalenedithiol. *Org. Synth.* **1953,** *33* (September), 47.
8. Renny, J. S.; Tomasevich, L. L.; Tallmadge, E. H.; Collum, D. B., Method of Continuous Variations: Applications of Job Plots to the Study of Molecular Associations in Organometallic Chemistry. *Angew. Chem. Int. Ed.* **2013,** *52* (46), 11998-12013.
9. Waidmann, C. R.; Miller, A. J. M.; Ng, C.-W. A.; Scheuermann, M. L.; Porter, T. R.; Tronic, T. A.; Mayer, J. M., Using combinations of oxidants and bases as PCET reactants: thermochemical and practical considerations. *Energy Environ. Sci.* **2012,** *5* (7), 7771-7780.
10. Vasudevan, D.; Wendt, H., Electroreduction of oxygen in aprotic media. *J. Electroanal. Chem.* **1995,** *392* (1-2), 69-74.
11. Li, Q.; Batchelor-McAuley, C.; Lawrence, N. S.; Hartshorne, R. S.; Compton, R. G., Anomalous solubility of oxygen in acetonitrile/water mixture containing tetra-n-butylammonium perchlorate supporting electrolyte; the solubility and diffusion coefficient of oxygen in anhydrous acetonitrile and aqueous mixtures. *J. Electroanal. Chem.* **2013,** *688*, 328-335.
12. Sheldrick, G. M., A short history of SHELX. *Acta Crystallogr. Sect. A: Found. Crystallogr.* **2008,** *64* (1), 112-122.

D Supporting Information for Chapter 5

Adapted from Martin, D. J.; Mercado, B. Q.; Mayer, J. M. "All Four Atropisomers of the Polycationic Iron(III) and Iron(II) Tetra(*o*-*N*,*N*,*N*-trimethylanilinium)porphyrin." *Unsubmitted work*.

D.1 General Considerations

D.1.1 Materials

Acetic acid (Sigma-Aldrich, >99%), 2-nitrobenzaldehyde (Sigma-Aldrich, >95%), tin (II) chloride (Sigma-Aldrich, >99%), hydrochloric acid (36-38% wt), ammonium hydroxide (Sigma-Aldrich, 35% wt), sodium cyanoborohydride (Acros, >98%), formaldehyde (Sigma-Aldrich, 37% wt, containing 10-15% methanol as stabilizer), methyl trifluoromethylsulfonate (methyl triflate; Sigma-Aldrich, >98%), 2,6-ditertbutylpyridine (Sigma-Aldrich, >97%), ammonium hexafluorophosphate (Sigma-Aldrich, >99%), trimethylsilyl triflate (Sigma-Aldrich, >98%) zinc granules (20 mesh, Sigma-Aldrich, >98%), mercury (II) chloride (Sigma-Aldrich, >99%), ferrocene (Sigma-Aldrich, >98%), decamethylferrocene (Sigma-Aldrich, >95%), sodium bicarbonate (Sigma-Aldrich, >99%), sodium chloride (Sigma-Aldrich, >99%), silica (Sigma-Aldrich, >99%), neutral aluminum oxide (Sigma-Aldrich, >99%), and basic alumina (Sigma-Aldrich, >99%) were all purchased and used without further purification.

Acetonitrile and diethylether were degassed with argon and purified using a Pure Process Technology solvent system. Pyrrole (Acros, >99%) was distilled immediately prior to use. Lithium bis(trimethylsilyl)amide was gifted by the Holland Lab. Iron(II) bromide was gifted by the Hazari Lab as the bis-tetrahydrofuran adduct, which had been prepared following a reported procedure.[1] The zinc mercury amalgam [Zn(Hg)] was prepared following a reported procedure[2] and stored in the glovebox. Deuterated NMR solvents, *n*-butyronitrile (Sigma-Aldrich, >99%), and trimethylphosphate (Sigma-Aldrich, >97%) were degassed and stored in the glovebox over 3Å molecular sieves. Tetrabutylammonium hexafluorophosphate (TCI, >99%) was recrystallized from ethanol (3×), dried at 70°C for 48 h, and stored in the glovebox. Tetrabutylammonium tetrafluoroborate (Acros, >98%) was purchased in high purity and stored in a desiccator without additional purification. The synthesized porphyrins were stored as solids in the glovebox and are indefinitely stable under these conditions.

D.1.2 Electrochemical Methods

Cyclic voltammograms were collected using a CH Instruments model 600 D potentiostat using a three-electrode set-up in a N_2 glovebox. Glassy carbon (CH Instruments, 3 mm) was used as the working electrode, platinum wire as the auxiliary electrode, and a silver wire pseudoreference as the reference electrode. The silver wire pseudoreference was prepared following a method described elsewhere.[3] The working electrode was polished before each voltammogram using 0.05 µm alumina (CH Instruments, containing no agglomerating agents) on a Buhler polishing pad. All voltammograms were internally referenced to ferrocene or decamethylferrocene and were corrected for uncompensated resistance (< 100 Ω).

D.1.3 Instrumentation

^{1}H NMR were collected on Agilent 400 and 500 MHz spectrometers. High-resolution mass spectrometry was collected on a Waters Xevo GS-XS QToF mass spectrometer. Single-crystal X-ray diffraction methods and instrumentation described below.

D.2 Synthesis and Purification

D.2.1 5,10,15,20-tetra(o-nitrophenyl)porphyrin

The preparation of tetra(*o*-nitrophenyl)porphyrin followed literature.[4] First, 2-nitrobenzaldehyde (35.0 g, 0.23 mol) was dissolved in 500 mL glacial acetic acid. The solution was brought to gentle reflux and pyrrole (14.7 mL, 0.23 mol) was slowly added. Take caution, as the addition of pyrrole is slightly exothermic. The mixture was allowed to reflux in open air for 20 minutes before being removed from heat. To avoid tarry byproducts, chloroform (100 mL) was added to the mixture once the solution cooled to 60 °C. The solution was filtered at 40 °C, and the lustrous purple solid was washed with $CHCl_3$ and MeOH. Yield: 7.0 g (ca. 15%).

D.2.2 5,10,15,20-tetra(o-aminophenyl)porphyrin, H_2(o-AMP)

The reduction of tetra(*o*-nitrophenyl)porphyrin to the tetra(*o*-aminophenyl)porphyrin form followed literature.[4] First, the corresponding tetra(*o*-nitrophenyl)porphyrin (5.0 g, 6.3 mmol) was dissolved in 170 mL HCl (conc.) in a large, 2L beaker. Solid $SnCl_2(H_2O)_2$ (15.0 g, 66 mmol) was added, and the mixture was quickly brought to 80 °C for 20 minutes. Caution, the reaction foams around ca. 70 °C. At the end of the heating period, crushed ice was added to the reaction, followed by the slow addition of 150 mL NH_4OH (conc.) to quench the bulk acid. The solution was then brought to neutral pH using a bicarbonate solution.* The porphyrin was separated using CH_2Cl_2, dried using $MgSO_4$, and was brought to dryness under vacuum. Crude yield: 3.8 g (89%). The individual atropisomers were purified by chromatography on silica gel using the method/eluent mixtures described in Chapter 5.

*Higher pH solutions resulted in the precipitation of SnO_x sponges, which were troublesome to separate.

D.2.3 5,10,15,20-tetra(o-N,N-dimethylaminophenyl)porphyrin, H_2(o-DMA)

Each of the H_2(*o*-AMP) atropisomers were methylated using conditions adapted from the literature. While the following describes the methylation of the $\alpha\alpha\alpha\alpha$ atropisomer, all others were prepared in an identical fashion and with comparable yields. To a round bottom flask containing MeCN/CH_2Cl_2 (60 mL/30 mL) was added $\alpha\alpha\alpha\alpha$ H_2(*o*-AMP) (1.0 g, 1.5 mmol), formaldehyde (5.25 mL, 37% wt, 65 mmol) and $NaBH_3CN$ (0.7 g, 11 mmol). The mixture was cooled to 0 °C before

slowly adding glacial acetic acid (30 mL). The reaction was stirred for 0.5 h at 0 °C before being warmed to 15 °C for an additional 2 h. After removing the solvent, the solid was basified with a bicarbonate solution and separated with CH_2Cl_2. After repeated brine washes, the organics were separated and pumped to dryness under vacuum. The solid was purified on silica gel using a Et_2O/CH_2Cl_2 (20/80) mixture.* Yield: 0.75 g (64%).

*Eluent mixtures (Et_2O/CH_2Cl_2) for the other atropisomers: $\alpha\beta\alpha\beta$ (10/90), $\alpha\alpha\beta\beta$ (10/90), $\alpha\alpha\alpha\beta$ (15/85). Over-reduced products (e.g. chlorin) tended to elute after the target molecules and were easily spotted by green discoloration in the eluent.

D.2.4 Iron(III) chloride tetra(o-N,N-dimethylaminophenyl)porphyrin, FeCl(o-DMA)

While the following describes the methylation of the $\alpha\alpha\alpha\alpha$ atropisomer, all others were prepared in an identical fashion and with comparable yields. In a N_2 glovebox, $\alpha\alpha\alpha\alpha$ H_2(*o*-DMA) (0.75 g, 0.95 mmol) and Li(HMDS) (0.35 g, 2.1 mmol) were dissolved in dry THF (100 mL). The mixture was stirred for 0.5 h, during which the color changed from red to green. Solid $FeBr_2(THF)_2$ (0.36 g, 2.1 mmol) was then added, which caused the green solution to rapidly become red again. After stirring for an additional hour under N_2, the mixture was opened to air. The solvent was removed, and the solid was dissolved in 1M HCl. After stirring for 0.5 h, the pH was brought to neutral with a bicarbonate solution, and the black solid was filtered by suction. The crude product was purified first on silica gel. Unreacted H_2(*o*-DMA) was eluted first using Et_2O/CH_2Cl_2 (20/80), and the metallated product was eluted using $MeOH/CH_2Cl_2$ (10/90). After removing the solvent, the metalloporphyrin was purified again on alumina using Et_2O/CH_2Cl_2 (20/80) eluent. Yield: 0.50 g (60%).

D.2.5 Iron(III) tetra(o-N,N,N-trimethylanilinium)porphyrin pentatriflate,

The $\alpha\beta\alpha\beta$, $\alpha\alpha\beta\beta$, and $\alpha\alpha\alpha\beta$ [Fe^{III}(*o*-TMA)](OTf)$_5$ products were all prepared using the same method and in similar yields. First, the FeCl(*o*-DMA) (100 mg, 0.12 mmol) precursor was converted to the hydroxo- form by dissolving the solid in CH_2Cl_2 (50 mL) and stirring for 1 h with an equal volume of 1M NaOH. The organics were separated, washed with water (2 × 50 ml), and brought to dryness under a vacuum (12h) to yield a black, powdery-solid. In a glovebox, the solid was dissolved in PO_4Me_3 (4.0 mL) containing MeOTf (0.3 mL, 2.7 mmol) and 2,6-di-*tert*-butylpyridine

(0.3 mL, 1.8 mmol). The mixture was stirred at room temperature for 12 h before precipitating the target porphyrin from rapidly stirring Et_2O. After repeated precipitations from MeCN/Et_2O mixtures, the brown solid was collected and dried. Yield:185 mg (98%)

The $\alpha\alpha\alpha\alpha$ isomer followed a similar method. Upon stirring with 1M NaOH, $\alpha\alpha\alpha\alpha$ FeCl(*o*-DMA) (100 mg, 0.12 mmol) dimerized to form the corresponding μ-oxo complex. The dimer was purified on basic alumina, using CH_2Cl_2 as the eluent.* After the solvent was removed, the green-black solid was dried under vacuum. The same methylation conditions were used as above, and the porphyrin was precipitated from Et_2O as the dimer-form. A series of salt metatheses (below) were then performed to cleave the dimer and purify the product.

i) The solid was dissolved in 1 M HCl before the solution was basified using NH_4OH.

ii) The dimer was precipitated using NH_4PF_6 (xs.) and was centrifuged/washed (3×) with pH 7 water.

iii) The PF_6-salt was acidified with 2 M HCl, which re-solubilized the solid and cleaved the dimer.

iv) Under these acidified conditions, the monomer was precipitated with NH_4PF_6 (xs.) and was repeatedly centrifuged/washed with pH 7 water.

v) After drying, the [Fe^{III}(*o*-TMA)Cl]$(PF_6)_4$ salt (not characterized) was dissolved in MeCN and was precipitated using [*n*-Bu_4N][Cl] (xs.) to yield the penta-chloride salt, [Fe^{III}(*o*-TMA)Cl]Cl_4. Yield: 54 mg (43%).

vi) In the glovebox, the [Fe^{III}(*o*-TMA)Cl]Cl_4 solid (30 mg, 0.028 mmol) was suspended in a small amount of MeCN (3 mL). While stirring, TMS(OTf) (0.106 mL, 0.58 mmol) was added, which caused the porphyrin to immediately solubilize. After stirring for 20 min, all the volatiles were removed under vacuum and the remaining solid was recrystallized from MeCN/Et_2O mixtures. Yield: 44 mg (98%).

*Using neutral or activated alumina caused the dimer to decompose on the column.

D.2.6 Iron (II) tetra(o-N,N,N-trimethylanilinium)porphyrin tetratriflate$_4$

All four atropisomers were prepared using the same method and in similar yields. In a glovebox, the corresponding [Fe^{III}(*o*-TMA)](OTf)$_5$ salt (25 mg) was stirred over solid Zn(Hg) in a minimal amount of MeCN. After 1-2 h, the solution had lightened in color and the amalgam was separated. The colored solution was recrystallized from Et_2O to yield the reduced, [Fe^{II}(*o*-TMA)](OTf)$_4$ products. Yield: 23 mg (*quant*.).

D.3 High-resolution Mass Spectra

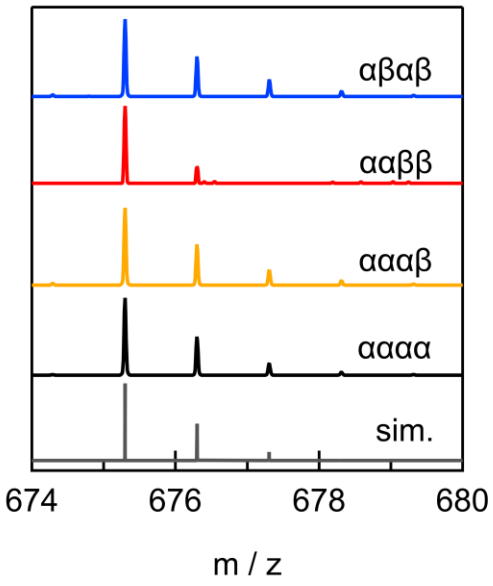

Figure D1. High resolution mass spectra for H_2(*o*-AMP) atropisomers. Mass corresponds to the protonated cation, $[C_{44}H_{35}N_8]^+$.

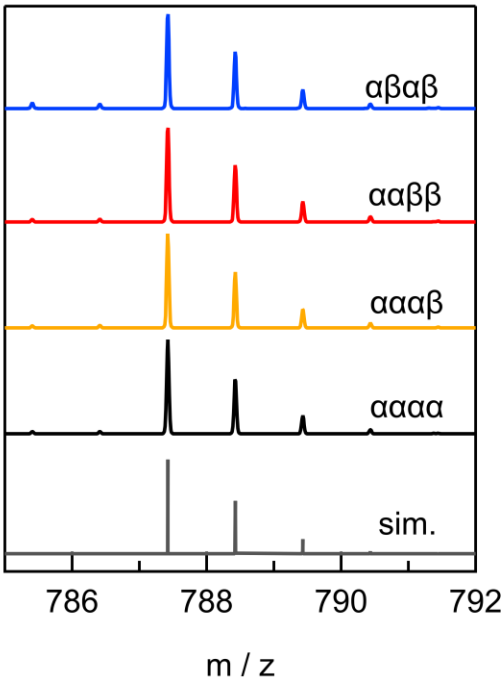

Figure D2. High resolution mass spectra for H_2(*o*-DMA) atropisomers. Mass corresponds to the protonated cation, $[C_{52}H_{51}N_8]^+$.

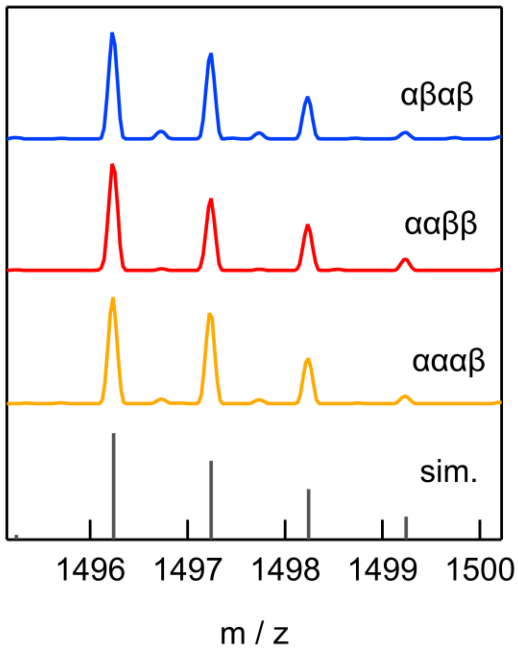

Figure D3. High resolution mass spectra for αβαβ, ααββ, and αααβ [Fe^{III}(*o*-TMA)](OTf)$_5$ atropisomers. Mass corresponds to the ferric, tetra-triflate cation [Fe^{III}(*o*-TMA)](OTf)$_4^+$, [$C_{60}H_{60}N_8FeF_{12}S_4O_{12}]^+$.

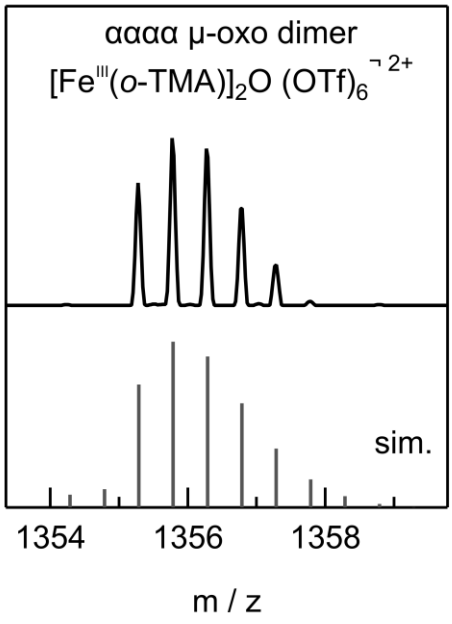

Figure D4. High resolution mass spectra for the αααα [Fe^{III}(*o*-TMA)](OTf)$_5$ complex. Mass corresponds to the μ-oxo dimer di-cation: [Fe^{III}(*o*-TMA)]$_2$O(OTf)$_6^{2+}$, [$C_{118}H_{120}N_{16}Fe_2F_{18}S_6O_{19}]^{2+}$, which is the highest m/z peak in the spectrum.

D.4 ^{1}H NMR Spectra

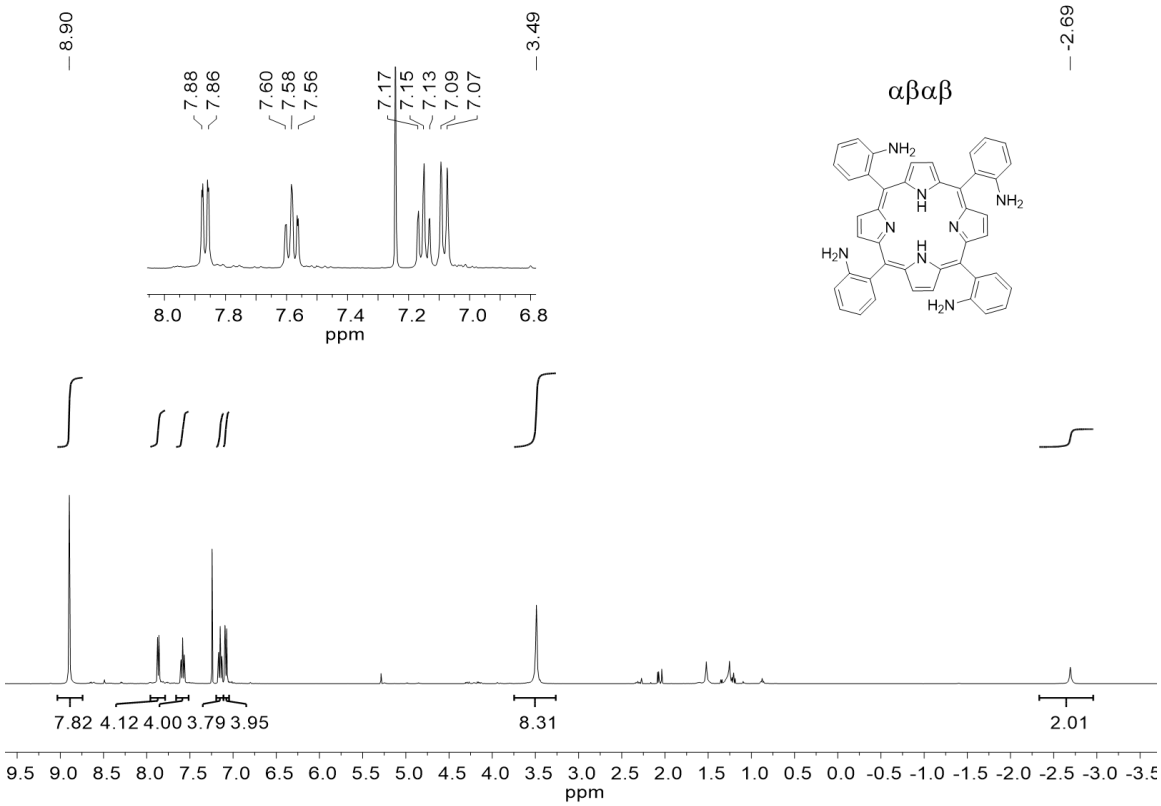

Figure D5. ^{1}H NMR of αβαβ H_2(*o*-AMP) in $CDCl_3$. Inset details aromatic region. Chemical shifts (ppm) match reported values.[5-7]

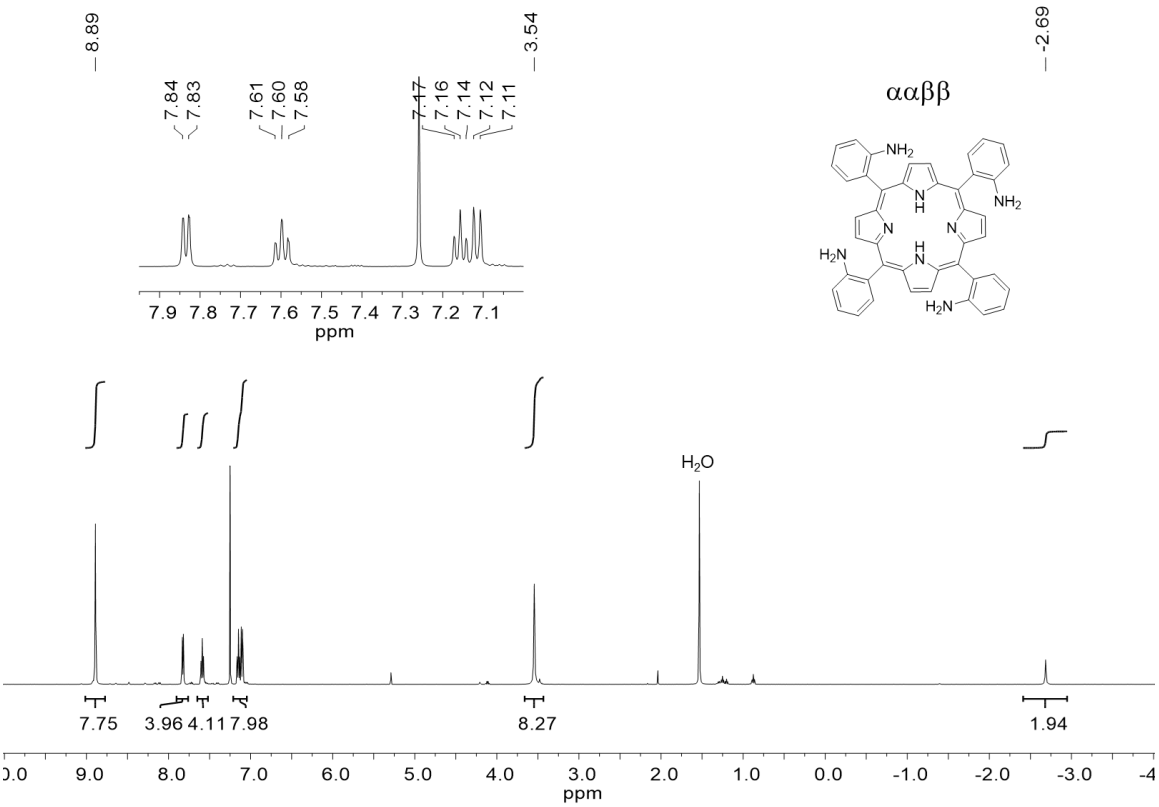

Figure D6. ^{1}H NMR of αααββ H_2(*o*-AMP) in $CDCl_3$. Inset details aromatic region. Chemical shifts (ppm) match reported values.[8]

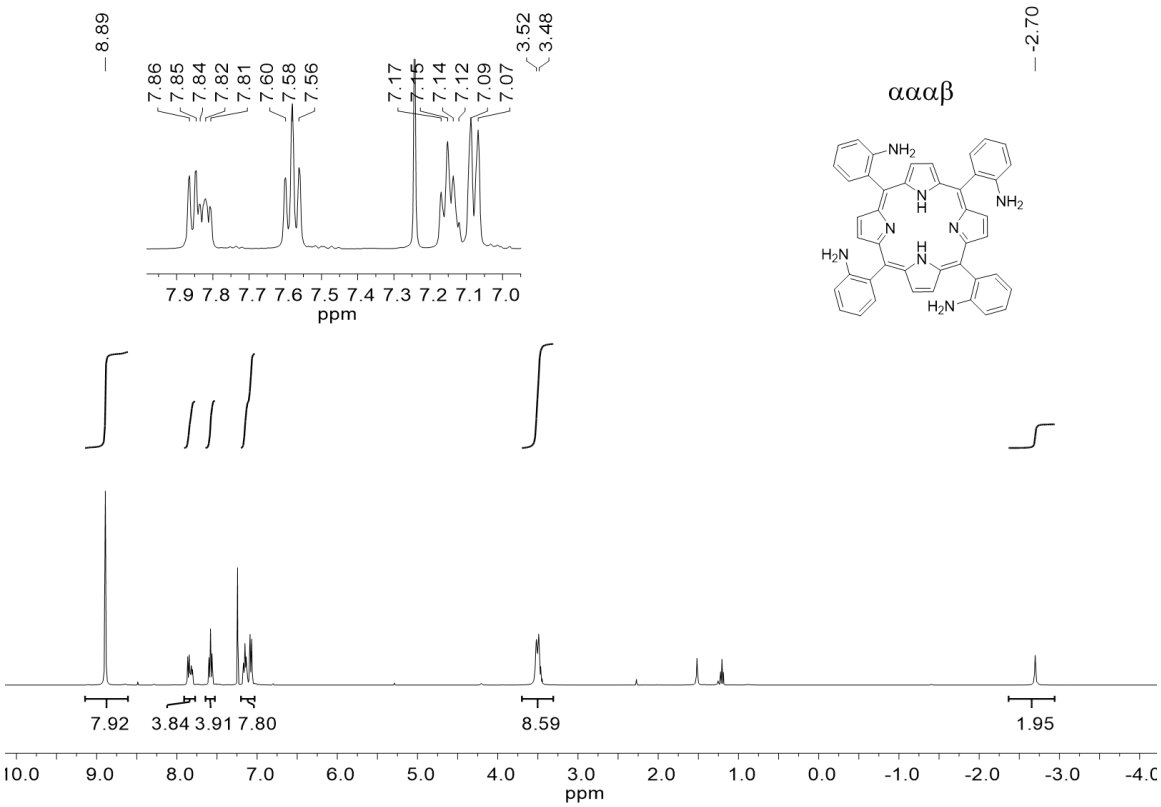

Figure D7. ^{1}H NMR of αααβ H_2(*o*-AMP) in $CDCl_3$. Inset details aromatic region. Chemical shifts (ppm) match reported values.[6]

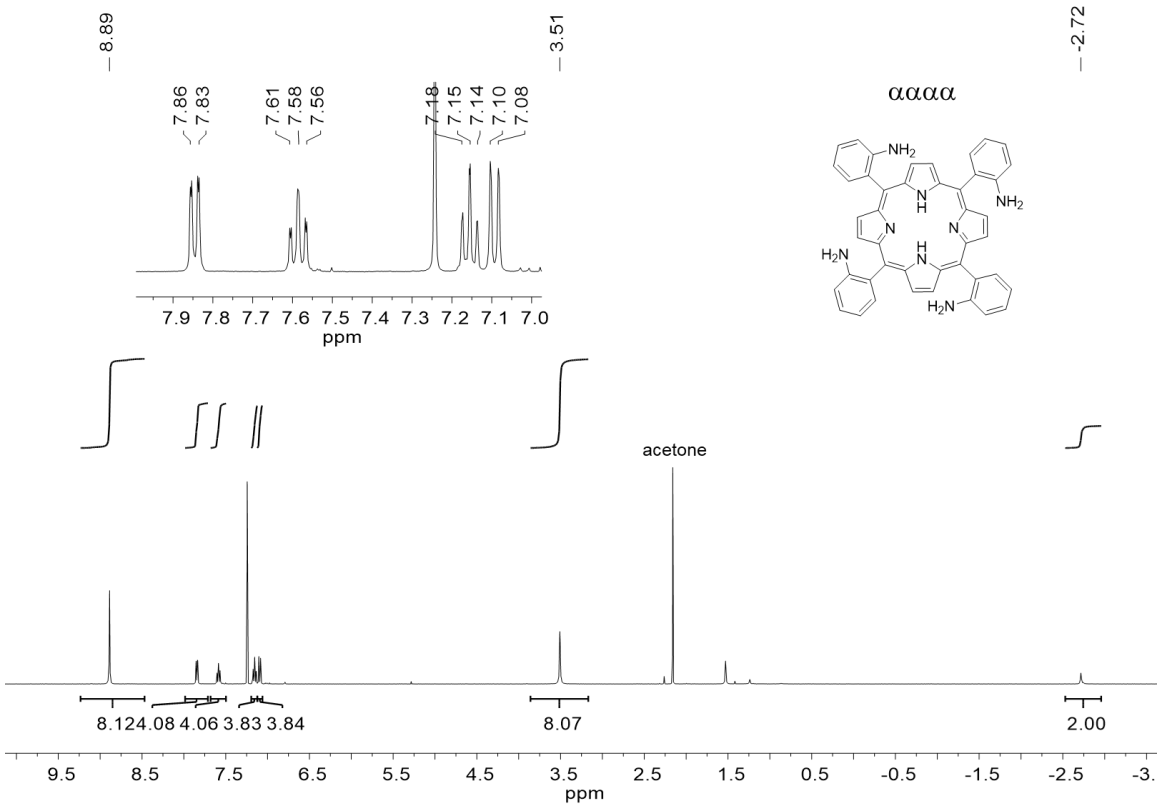

Figure D8. ^{1}H NMR of αααα H_2(*o*-AMP) in $CDCl_3$. Inset details aromatic region. Chemical shifts (ppm) match reported values.[4,9]

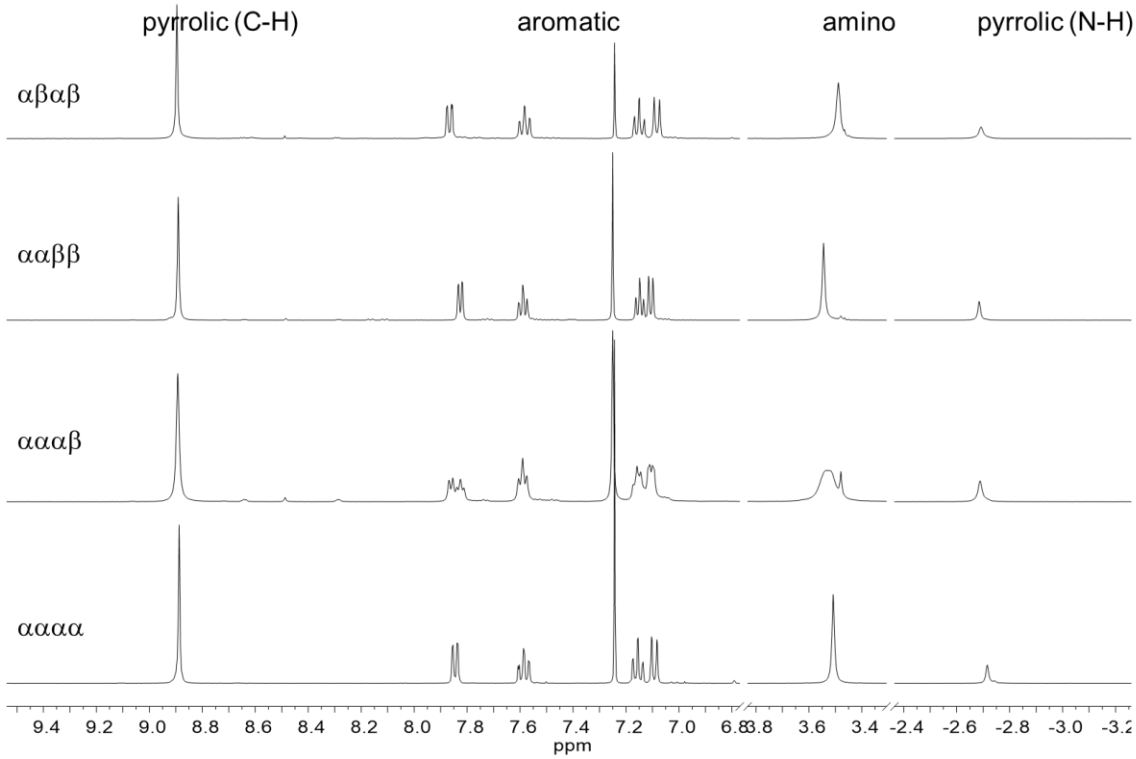

Figure D9. Stacked, partial ^{1}H NMR spectra of the four atropisomers of H_2(*o*-AMP) in $CDCl_3$. The four spectra are very similar, with the most notable differences being additional complexity in the aromatic region of the αααβ spectrum.

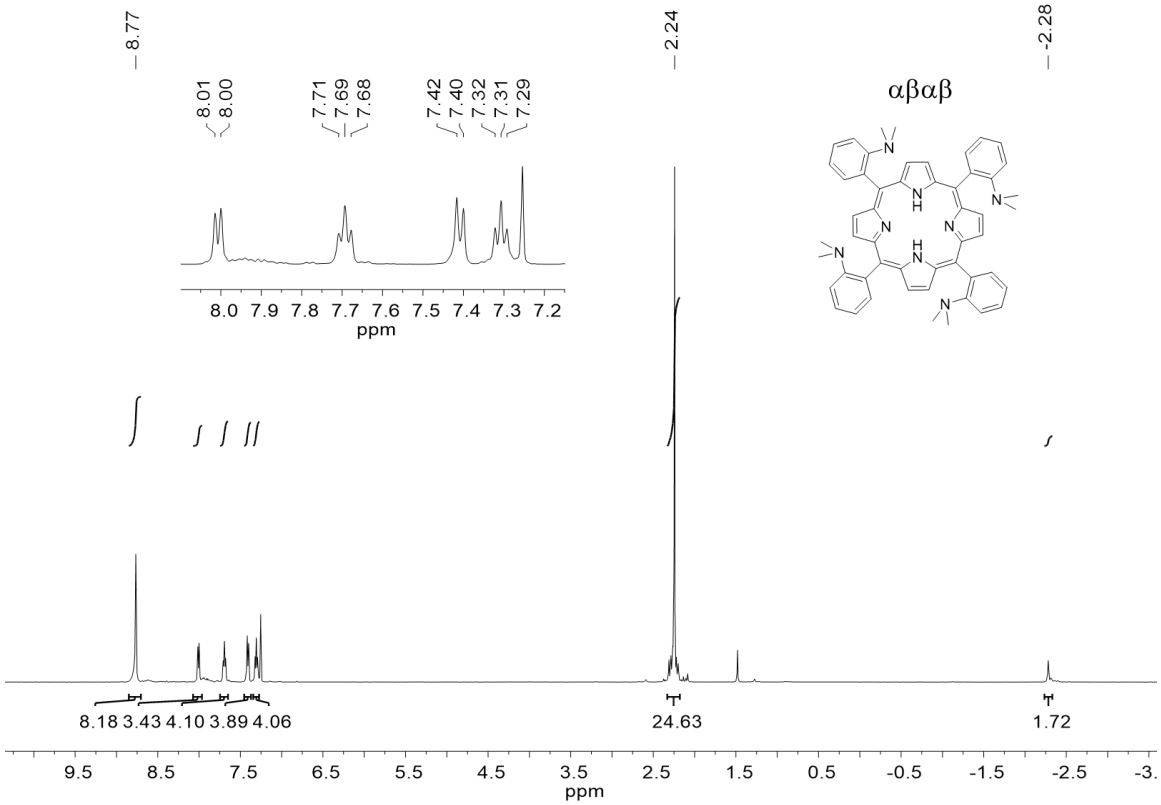

Figure D10. ^{1}H NMR of αβαβ H_2(*o*-DMA) in $CDCl_3$. Inset details aromatic region. Chemical shifts (ppm) match reported values.[7]

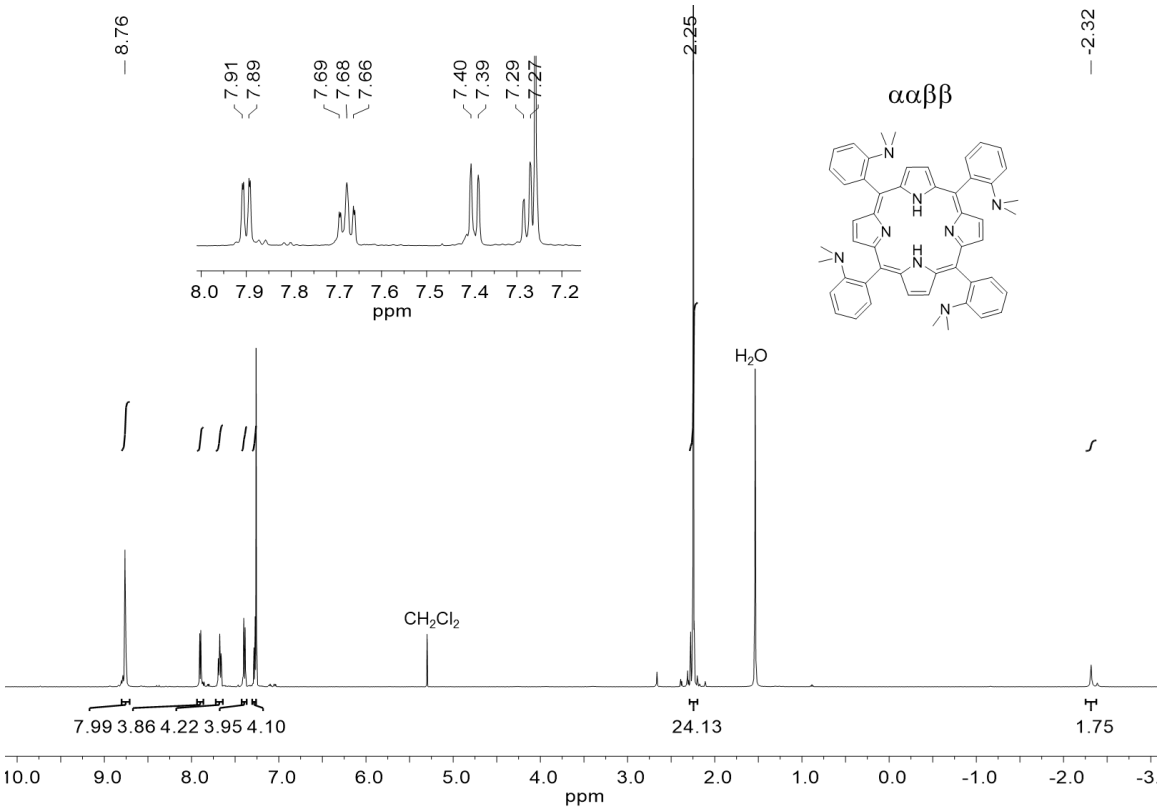

Figure D11. ^{1}H NMR of αααββ H_2(*o*-DMA) in $CDCl_3$. Inset details aromatic region.

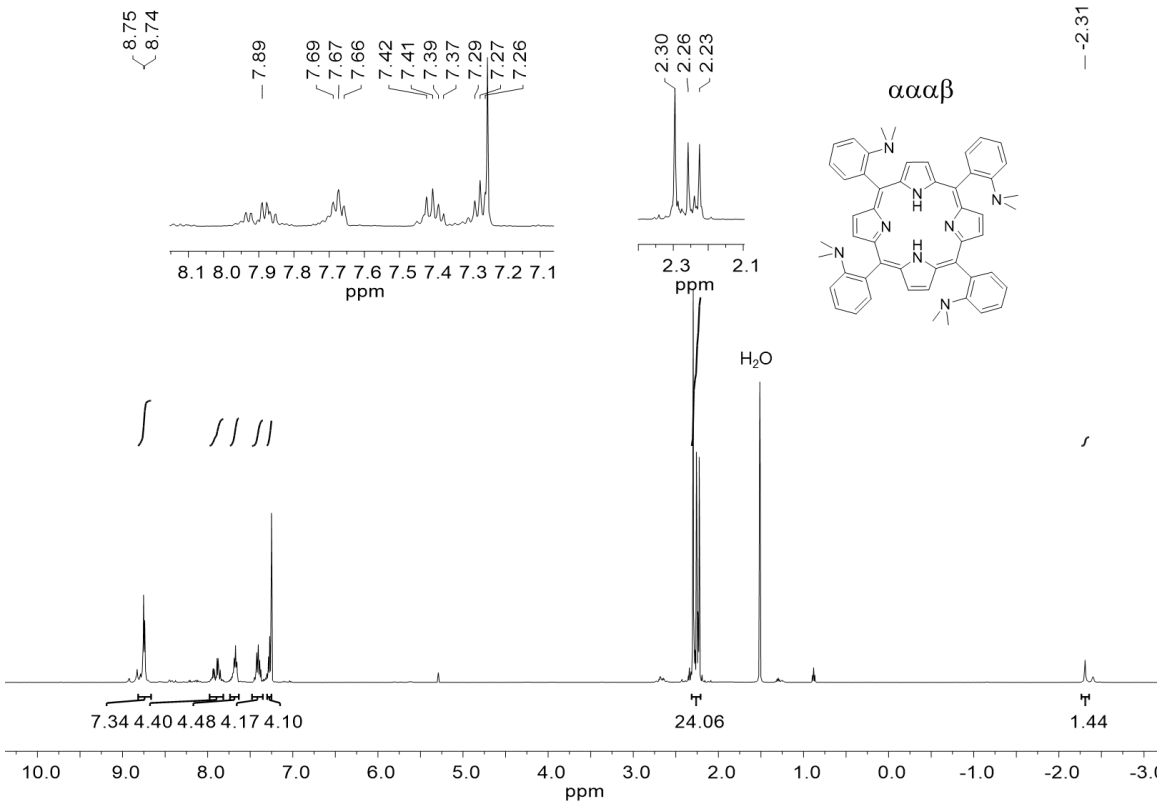

Figure D12. ^{1}H NMR of αααβ H_2(*o*-DMA) in $CDCl_3$. Left inset details aromatic region. Right inset details 1:1:2 ratio of dimethylamino residues. Small features in baseline represent undermethylated species that could not be separated by chromatography.

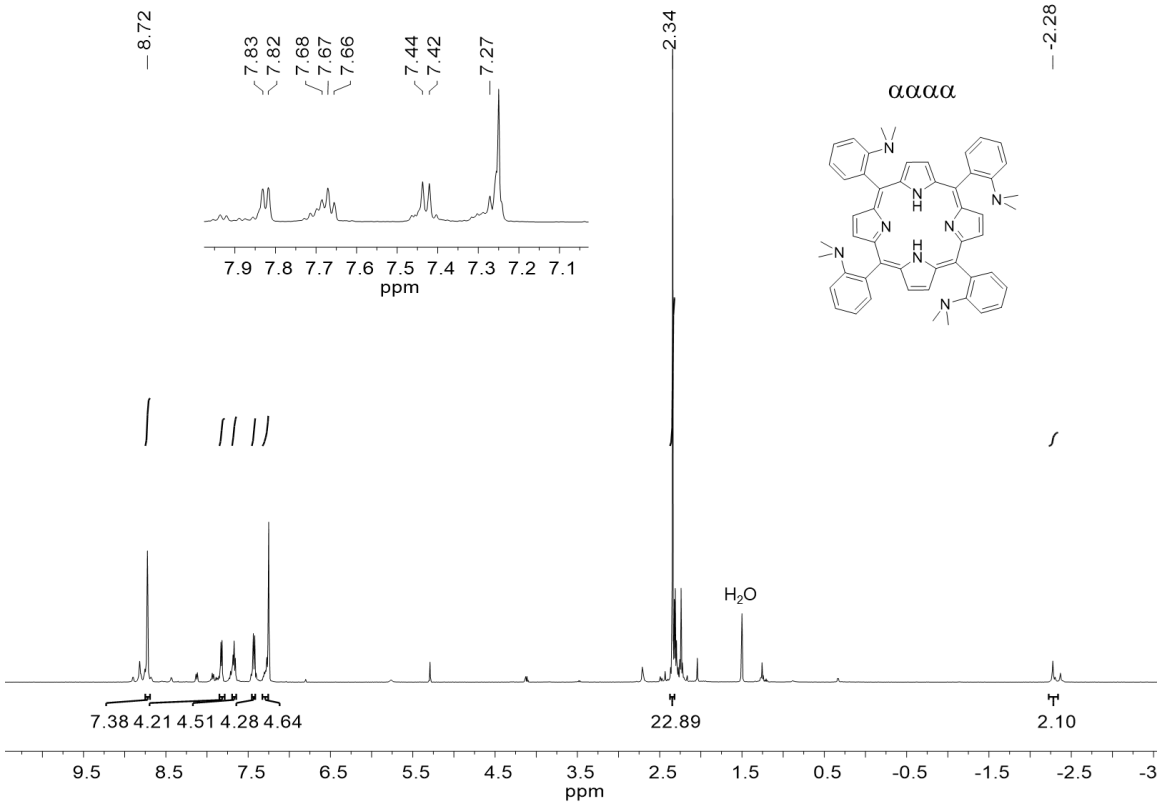

Figure D13. ^{1}H NMR of αααα H_2(*o*-DMA) in $CDCl_3$. Inset details aromatic region. Small features in baseline represent undermethylated species that could not be separated by chromatography.

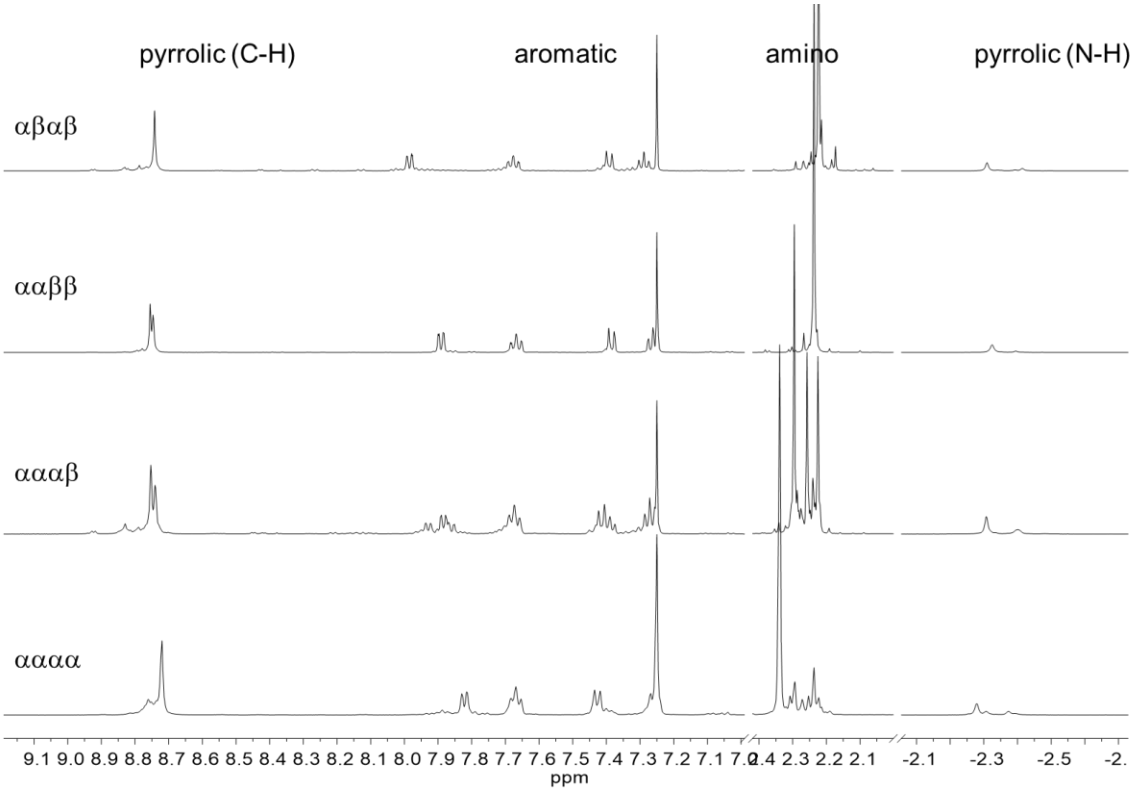

Figure D14. Stacked, partial ^{1}H NMR spectra of the four atropisomers of H_2(*o*-DMA) in $CDCl_3$. The four spectra are more different than the *o*-amino derivatives shown in **Figure D9**. The most significant differences are the chemical shifts of the dimethylamino residues (and set of peaks for the αααβ isomer).

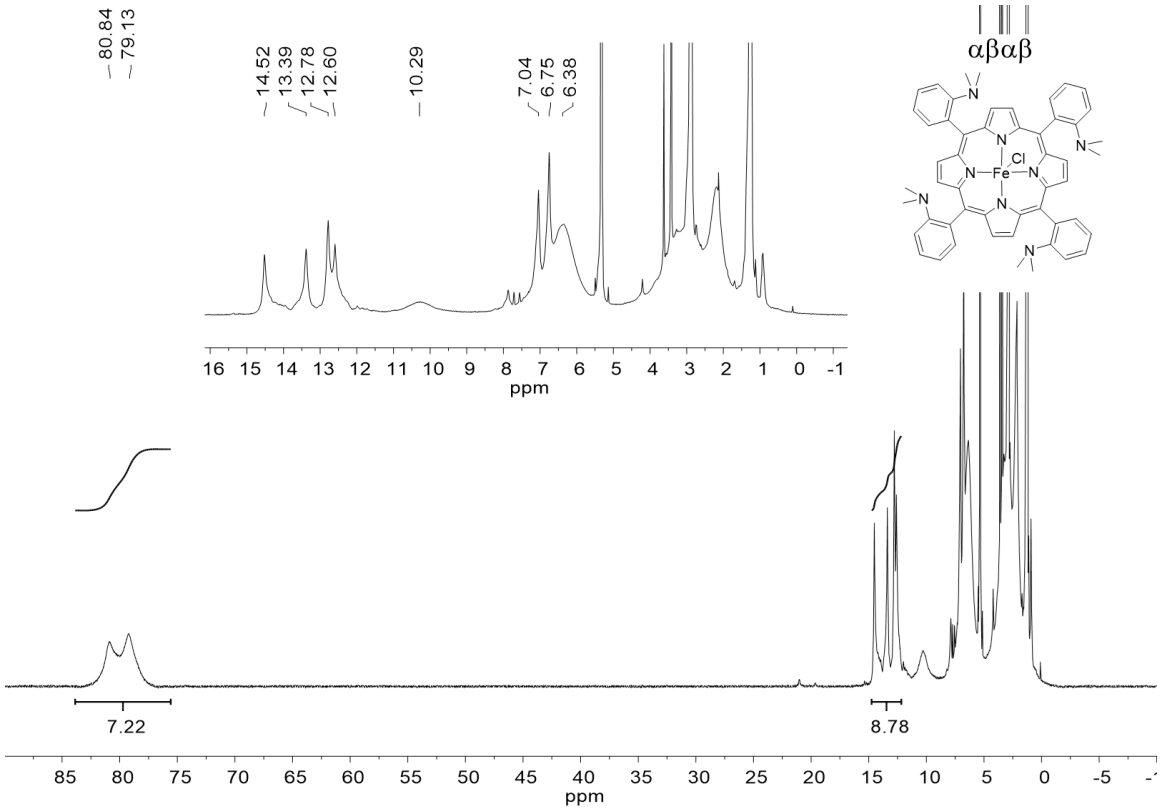

Figure D15. ^{1}H NMR of αβαβ FeCl(*o*-DMA) in CD_2Cl_2. Inset details upfield region of the spectrum. The aromatic protons appear as sets of singlets due to asymmetry introduced by chloride binding. Integrations show that the total number of pyrrolic protons (8*H*) are proportional to two of the more resolved sets of aromatic singlets (8*H*).

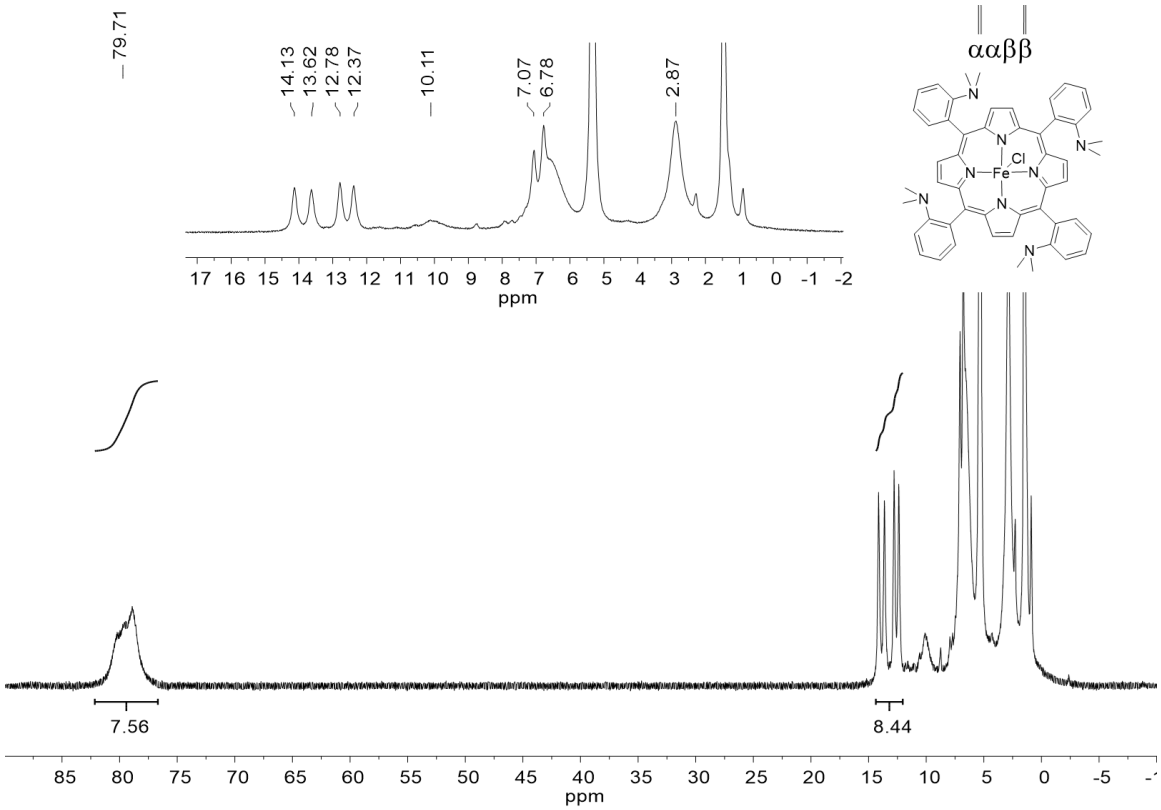

Figure D16. ^{1}H NMR of αααββ FeCl(*o*-DMA) in CD_2Cl_2. Inset details upfield region of the spectrum. The aromatic protons appear as sets of singlets due to asymmetry introduced by chloride binding. Integrations show that the total number of pyrrolic protons (8*H*) are proportional to two of the more resolved sets of aromatic singlets (8*H*). This spectrum was collected using a crystalline sample of the metalloporphyrin.

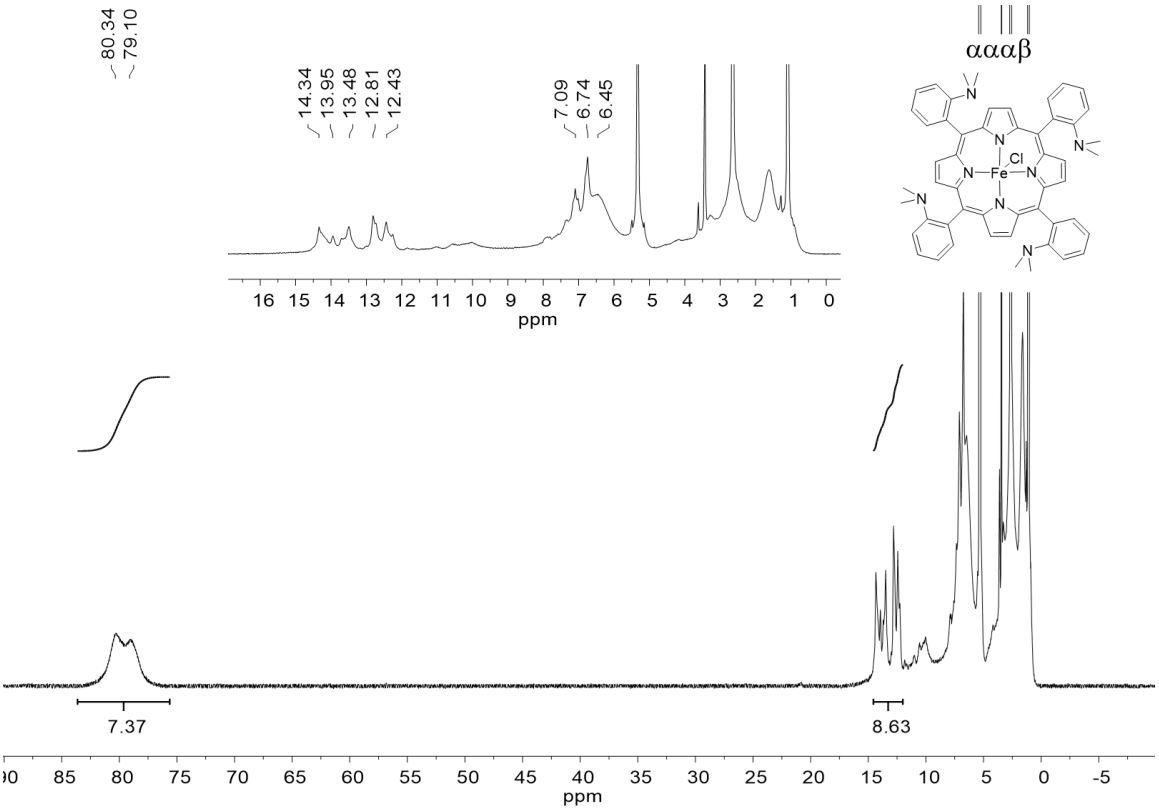

Figure D17. ^{1}H NMR of αααβ FeCl(*o*-DMA) in CD_2Cl_2. Inset details upfield region of the spectrum. The aromatic protons appear as a complicated set of multiplets due to asymmetry of the αααβ atropisomer and additional asymmetry introduced by chloride binding. Integrations show that the total number of pyrrolic protons (8*H*) are proportional a more resolved aromatic region (8*H*) following the model used in **Figure D15** and **Figure D16**, above.

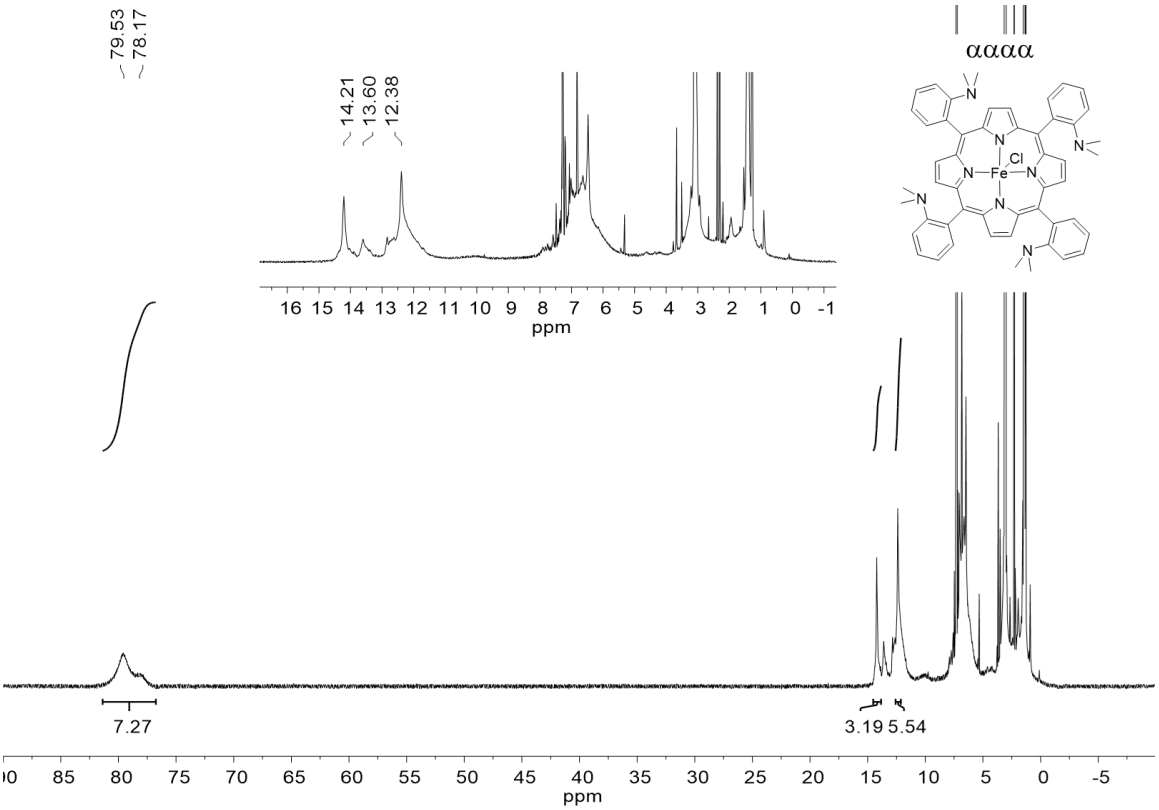

Figure D18. ^{1}H NMR of αααα FeCl(*o*-DMA) in $CDCl_3$. Inset details upfield region of the spectrum. The pyrrolic and aromatic protons appear as a set of singlets due to asymmetry introduced by chloride binding inequivalently to the α and β faces. Integrations show that the total number of pyrrolic protons (8*H*) are proportional a more resolved aromatic region (8*H*) following the model used in **Figure D15** and **Figure D16**, above.

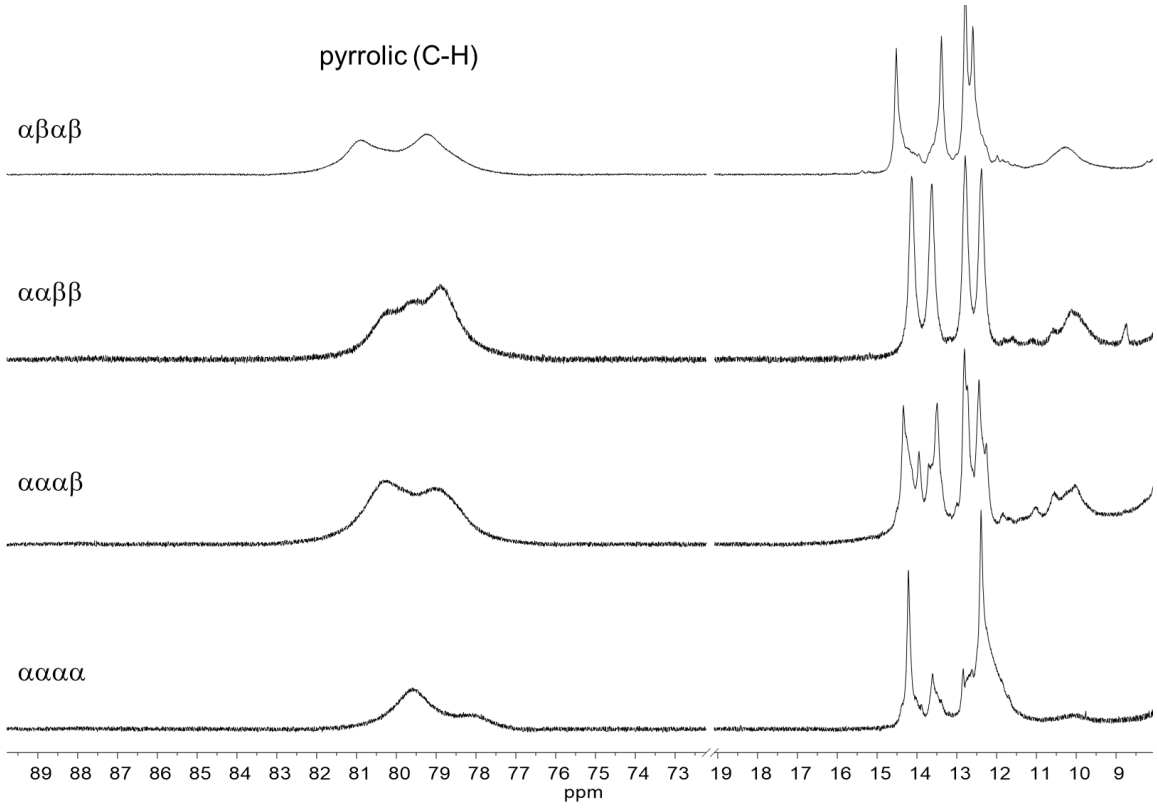

Figure D19. Stacked, partial ^{1}H NMR spectra of the four atropisomers of FeCl(*o*-DMA) in CD_2Cl_2 or $CDCl_3$. The four spectra are unique. Chloride binding to the αβαβ and ααββ atropisomers break the degeneracy of the α and β faces, resulting in sets of singlets in the aromatic region. Chloride binding to the αααα and αααβ atropisomers—which already have non-degenerate α and β faces—result in different molecules altogether.

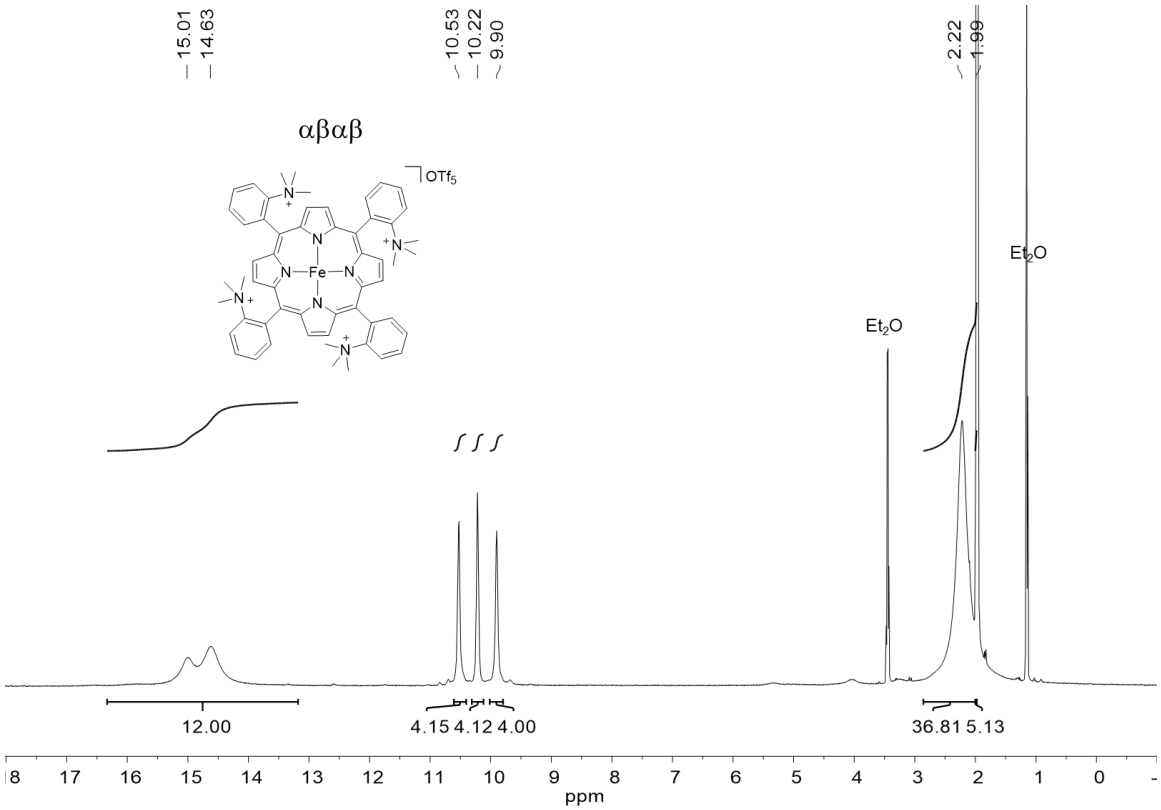

Figure D20. ^{1}H NMR of αβαβ [Fe(*o*-TMA)](OTf)$_5$ in CD_3CN. Sample prepared from crystals.

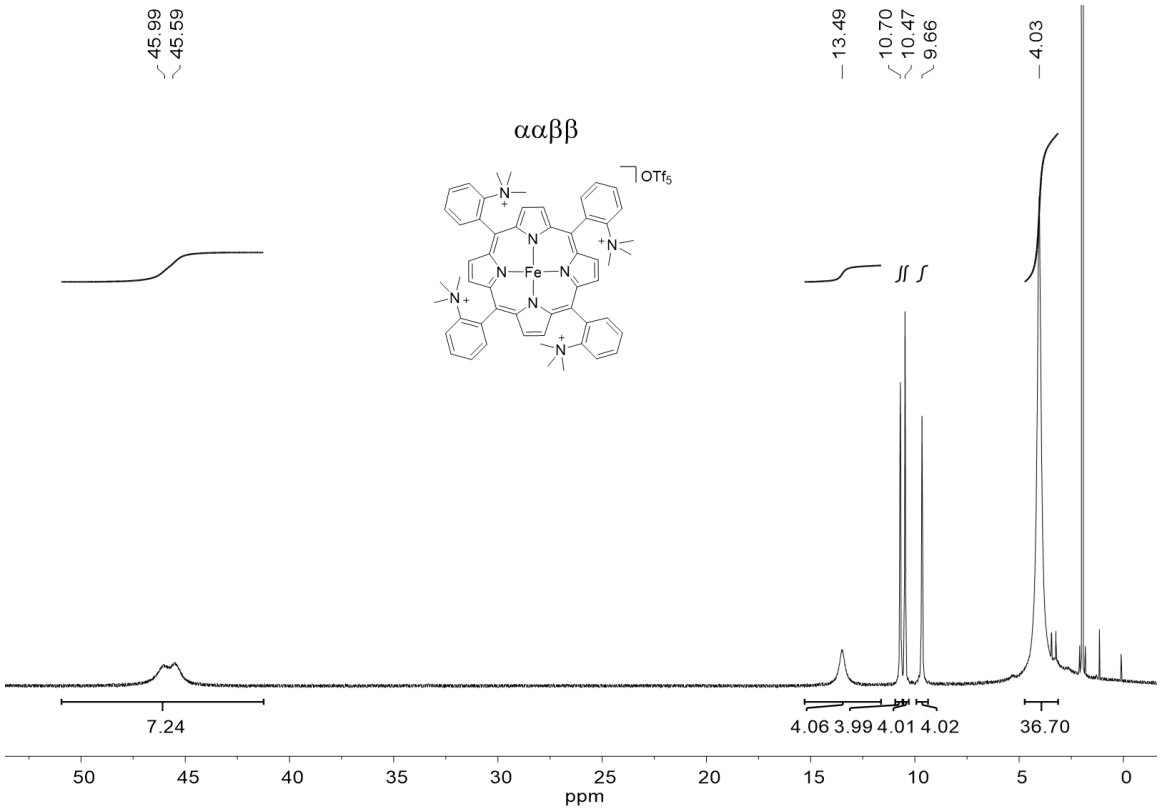

Figure D21. ^{1}H NMR of αααββ [Fe(*o*-TMA)](OTf)$_5$ pentatriflate in CD_3CN. Sample prepared from crystals.

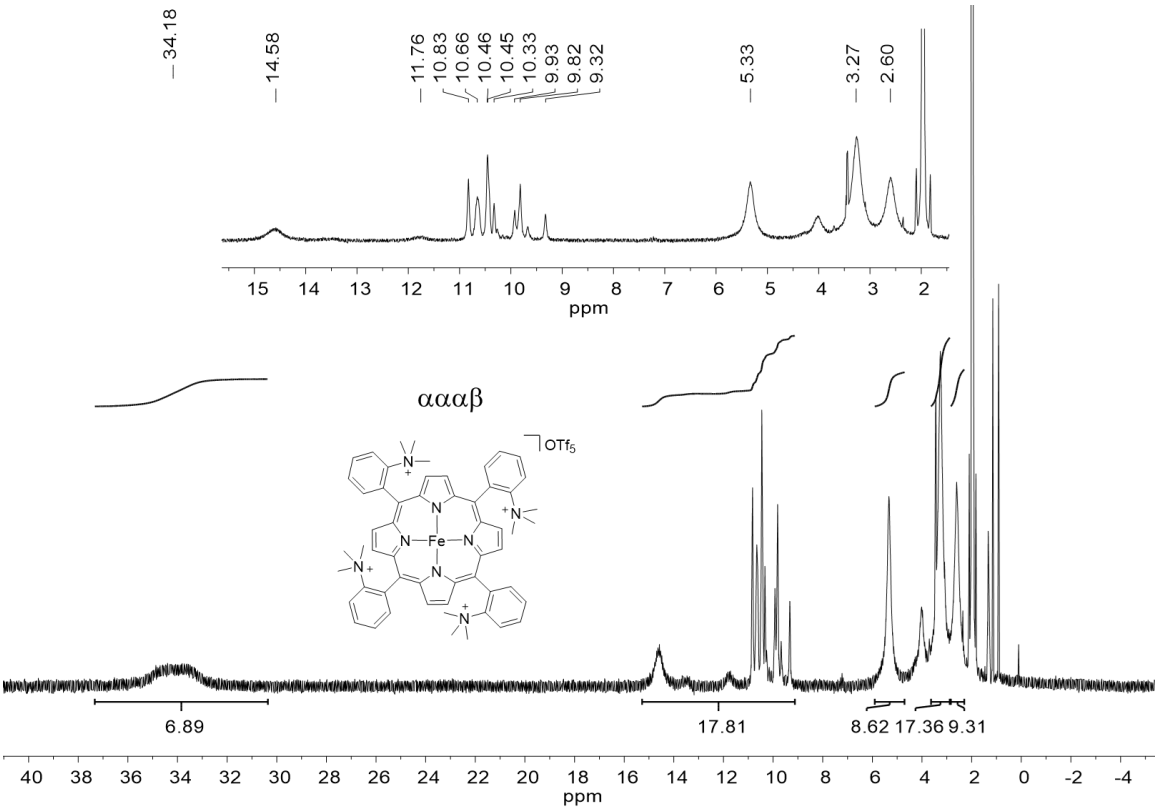

Figure D22. ^{1}H NMR of αααβ [Fe(*o*-TMA)](OTf)$_5$ in CD_3CN.

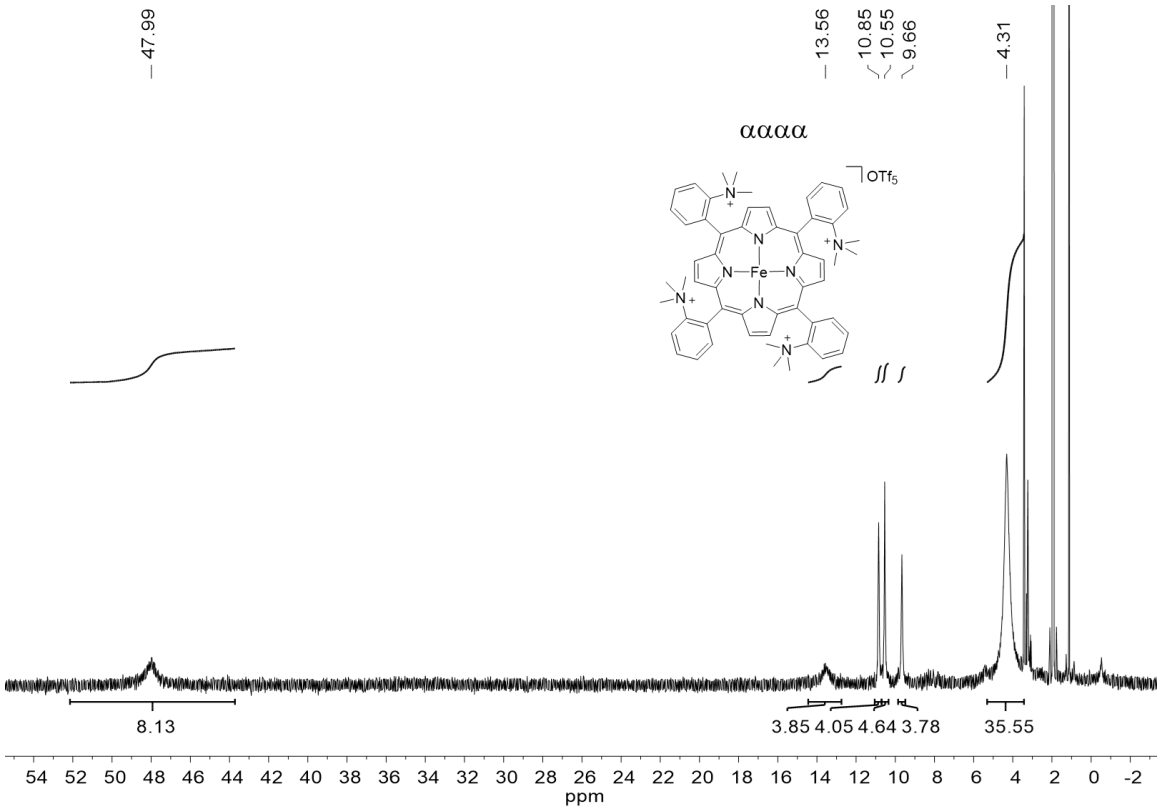

Figure D23. ^{1}H NMR of αααα [Fe(*o*-TMA)](OTf)$_5$ pentatriflate in CD_3CN. Sample prepared from crystals.

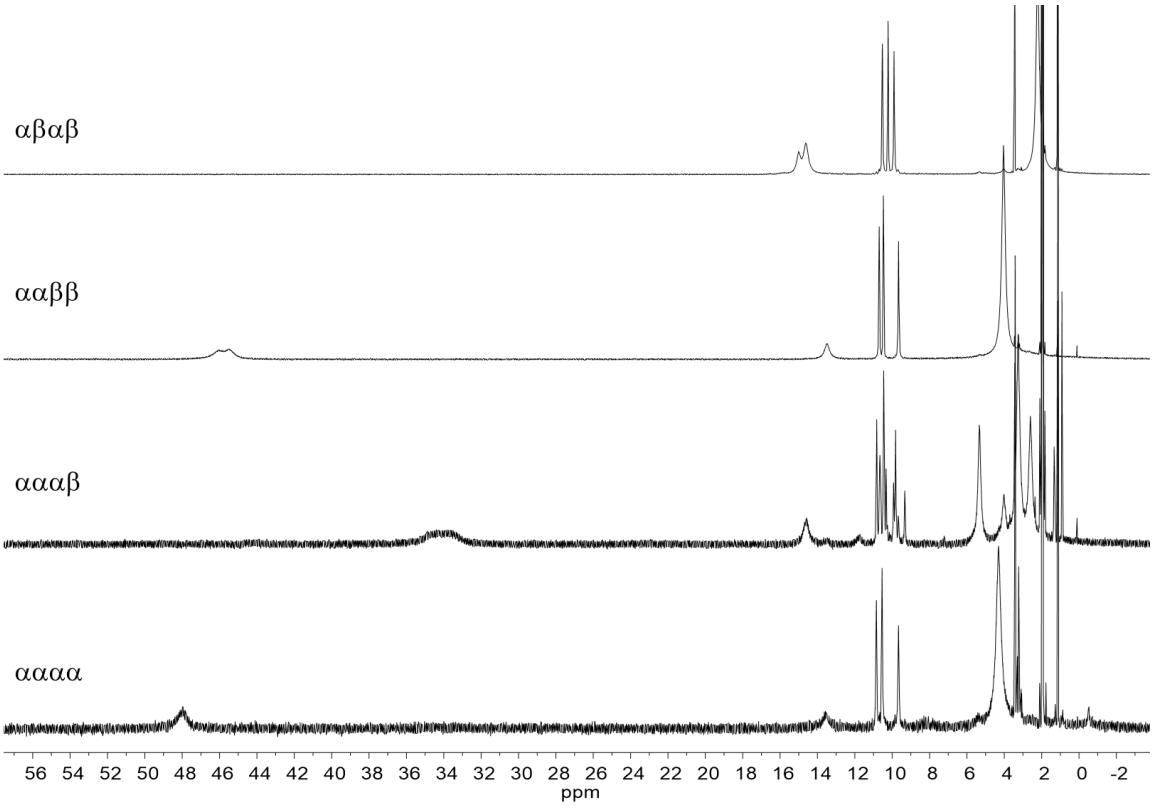

Figure D24. Stacked ^{1}H NMR spectra of the four atropisomers of [Fe(*o*-TMA)](OTf)$_5$. The four spectra are unique. Partial spectra are shown below in **Figure D25** and **Figure D26**.

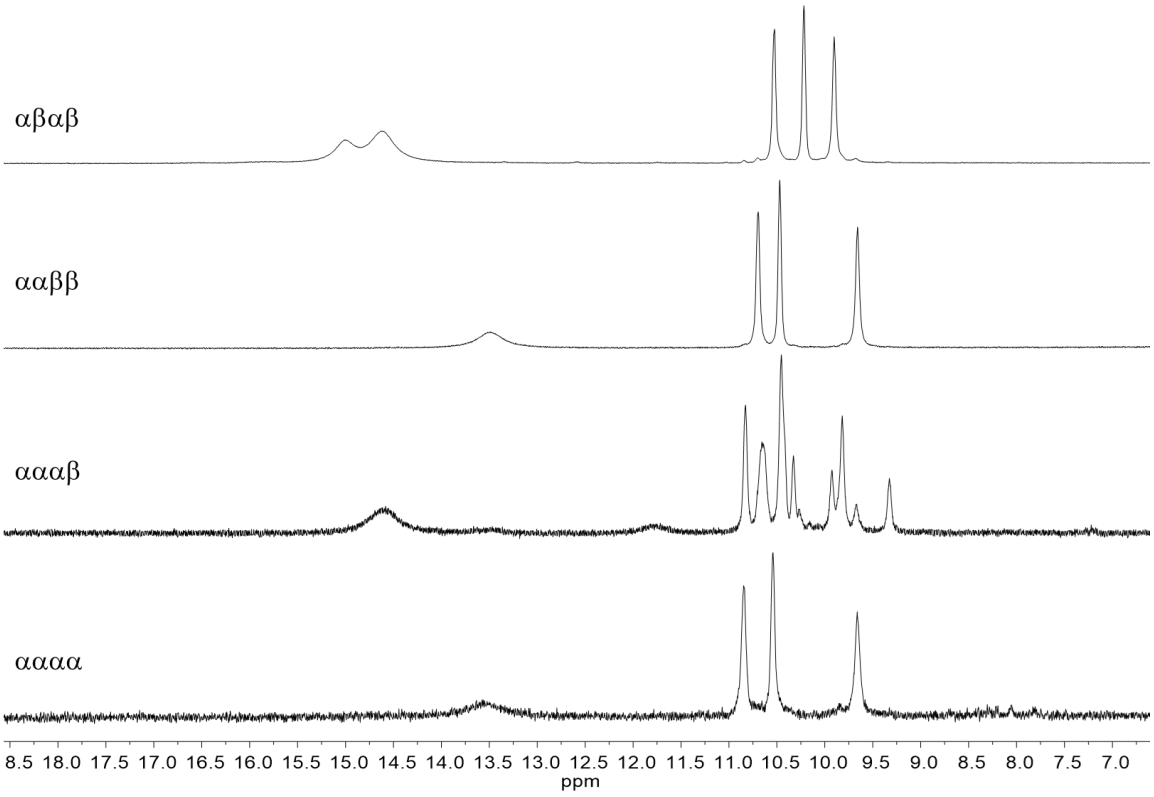

Figure D25. Stacked, partial ^{1}H NMR spectra of the four atropisomers of [Fe(*o*-TMA)](OTf)$_5$ in CD_3CN. Region shown highlights uniqueness of aromatic protons. The αααβ atropisomer contains <10% of the ααββ isomer as a contaminant.

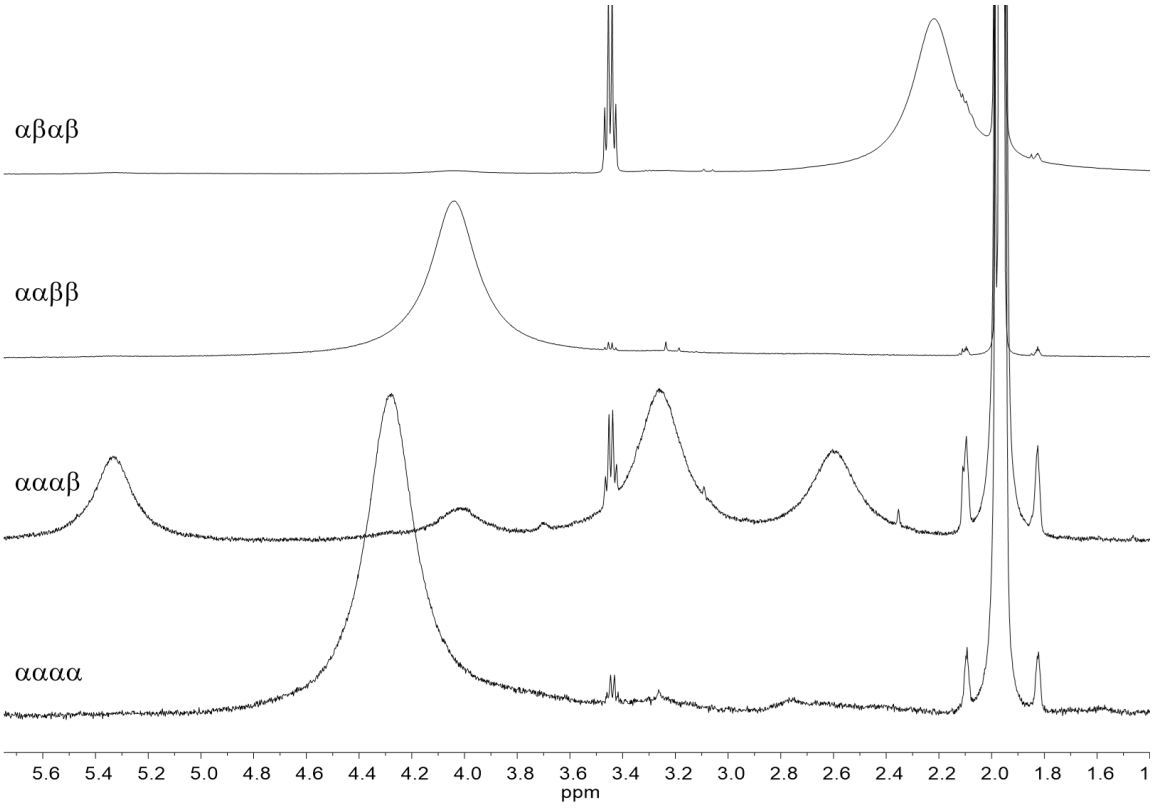

Figure D26. Stacked, partial ^{1}H NMR spectra of the four atropisomers of [Fe(*o*-TMA)](OTf)$_5$ in CD_3CN. Region shown highlights uniqueness of trimethylanilinium protons. The $\alpha\alpha\alpha\beta$ atropisomer contains <10% of the $\alpha\alpha\beta\beta$ isomer as a contaminant, as shown by the feature at ca. 4.0 ppm.

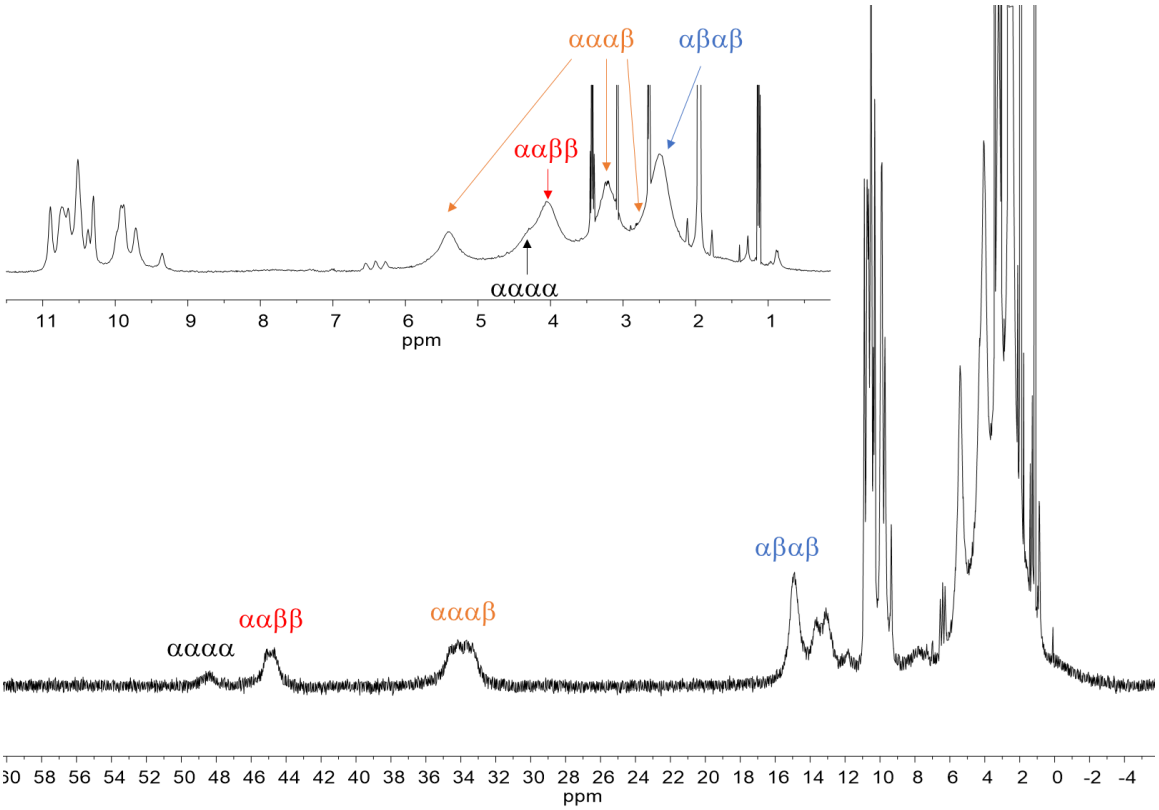

Figure D27. ^{1}H NMR spectrum of the product obtained using the conditions reported in reference [7]. The product contains all four atropisomers of [Fe(*o*-TMA)](OTf)$_5$. Both the pyrrolic protons and trimethylanilinium protons (inset) are identified for each of the various isomers.

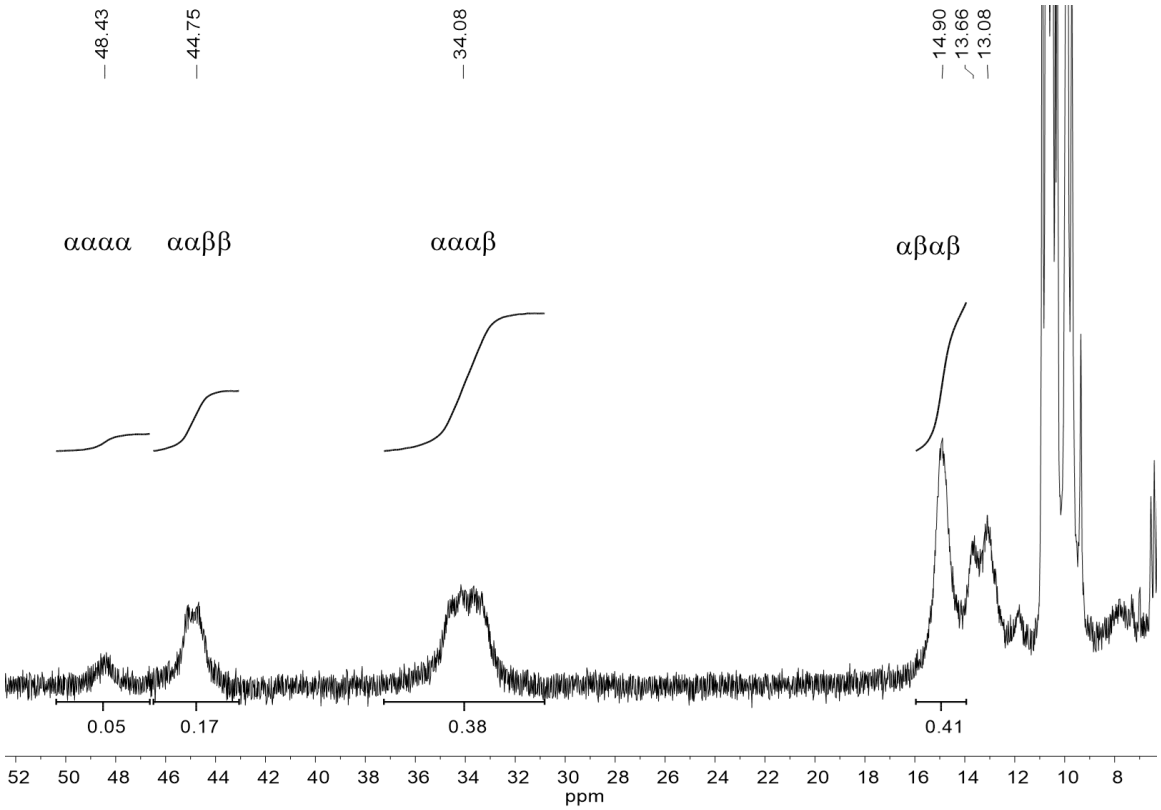

Figure D28. Partial spectrum of the atropisomeric mixture obtained from the synthesis reported in reference [7]. Fitted regions show relative integrations for the four isomers, the sum of which is equal to 1.0. Error on integrated values is <0.05.

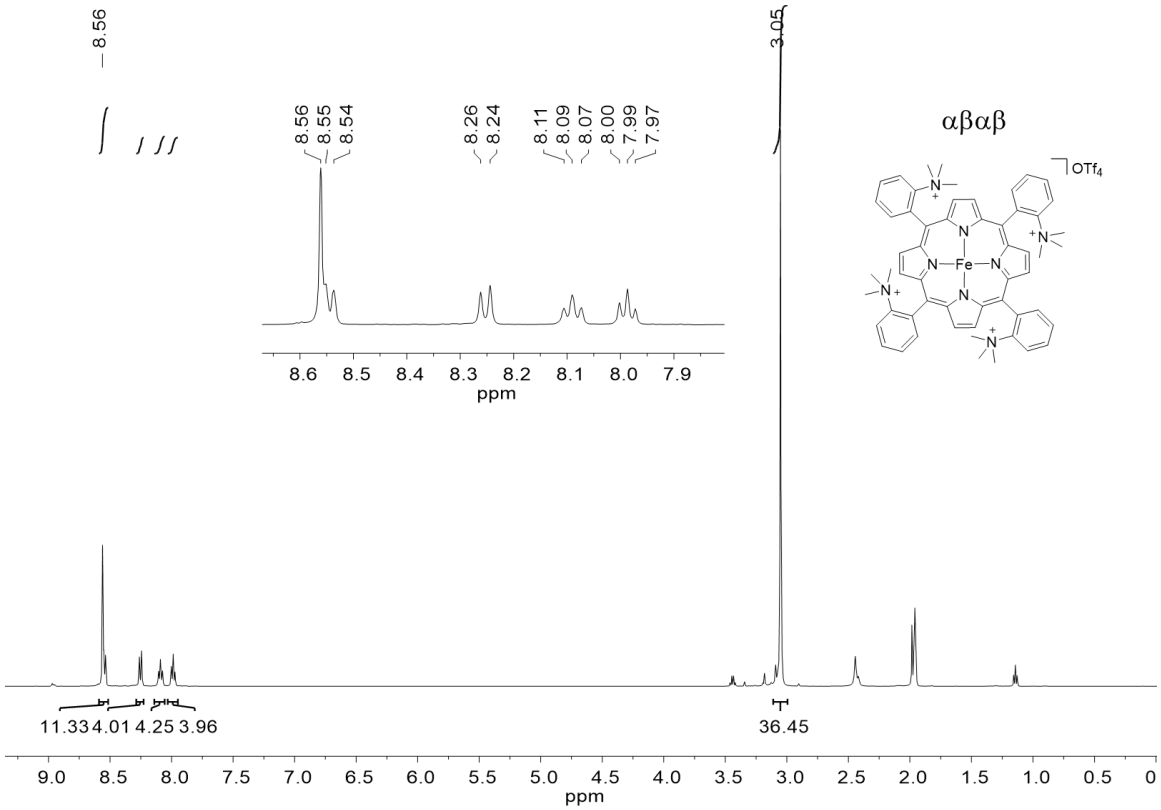

Figure D29. ^{1}H NMR of αβαβ [Fe(*o*-TMA)](OTf)$_4$ in CD_3CN. Spectrum previously reported in reference [2].

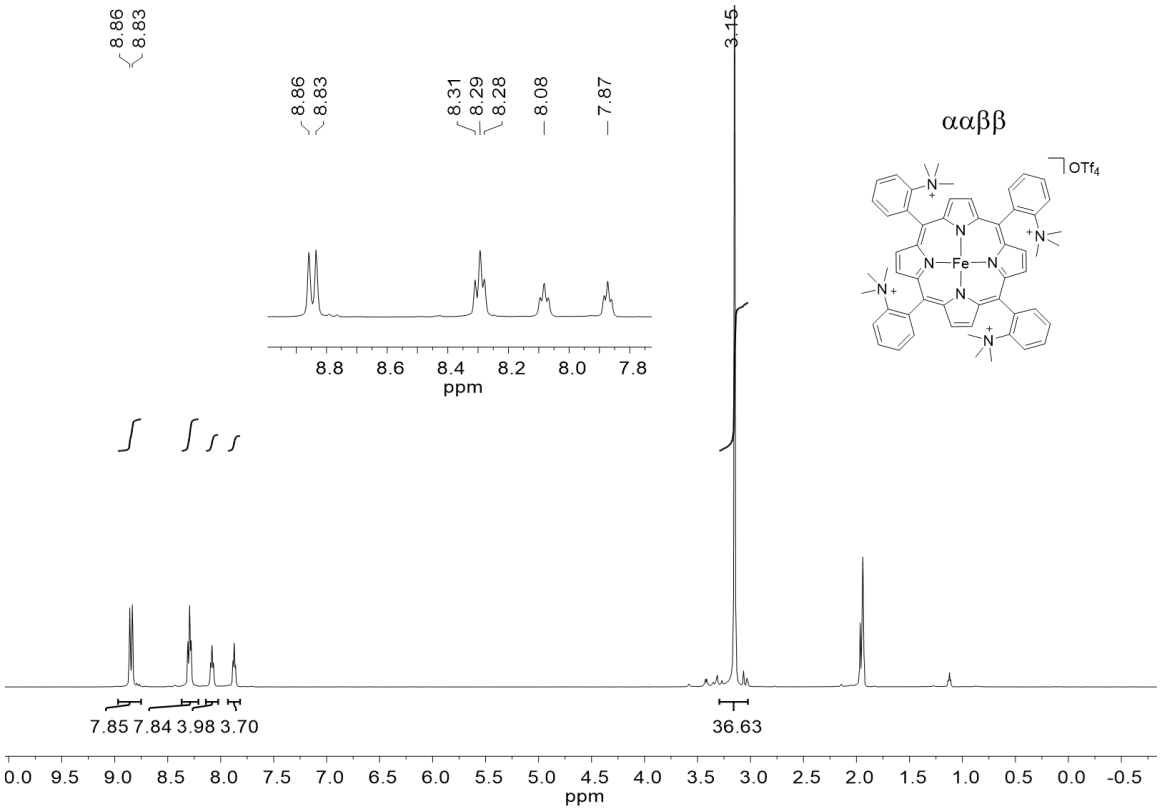

Figure D30. ^{1}H NMR of αααββ [Fe(*o*-TMA)](OTf)$_4$ in CD_3CN.

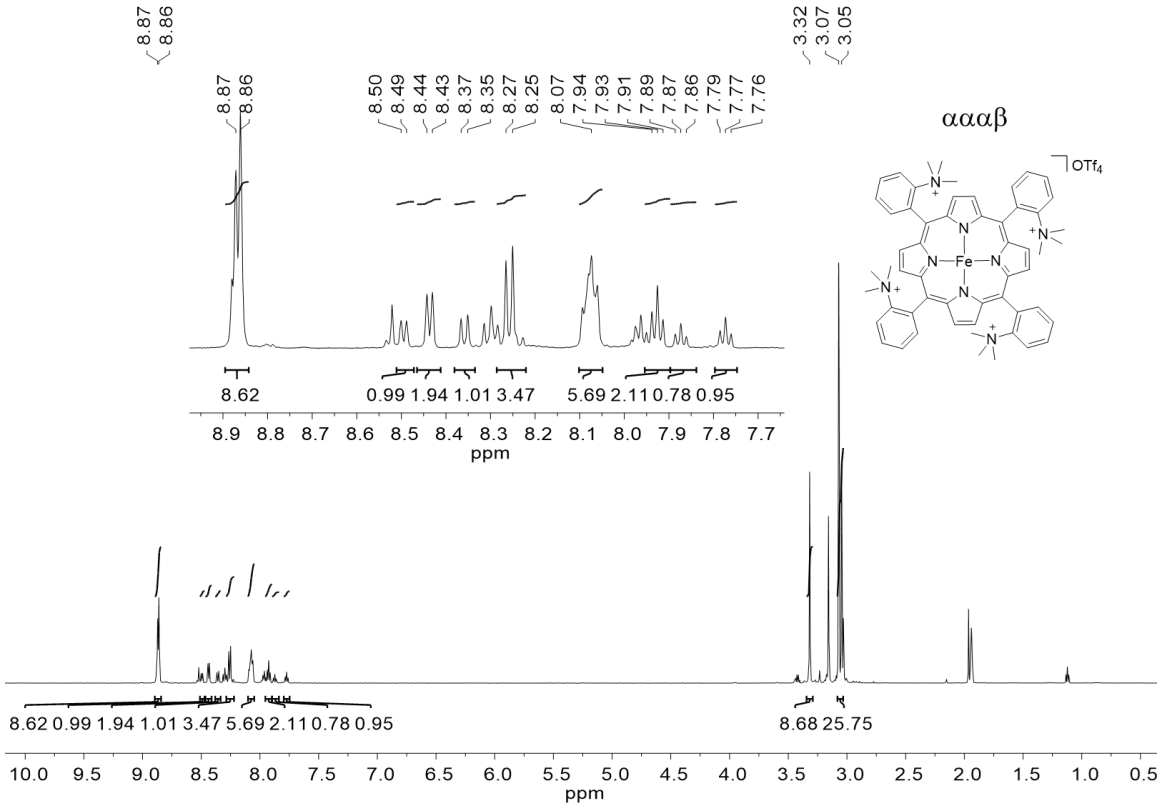

Figure D31. ^{1}H NMR of αααβ [Fe(*o*-TMA)](OTf)$_4$ in CD_3CN.

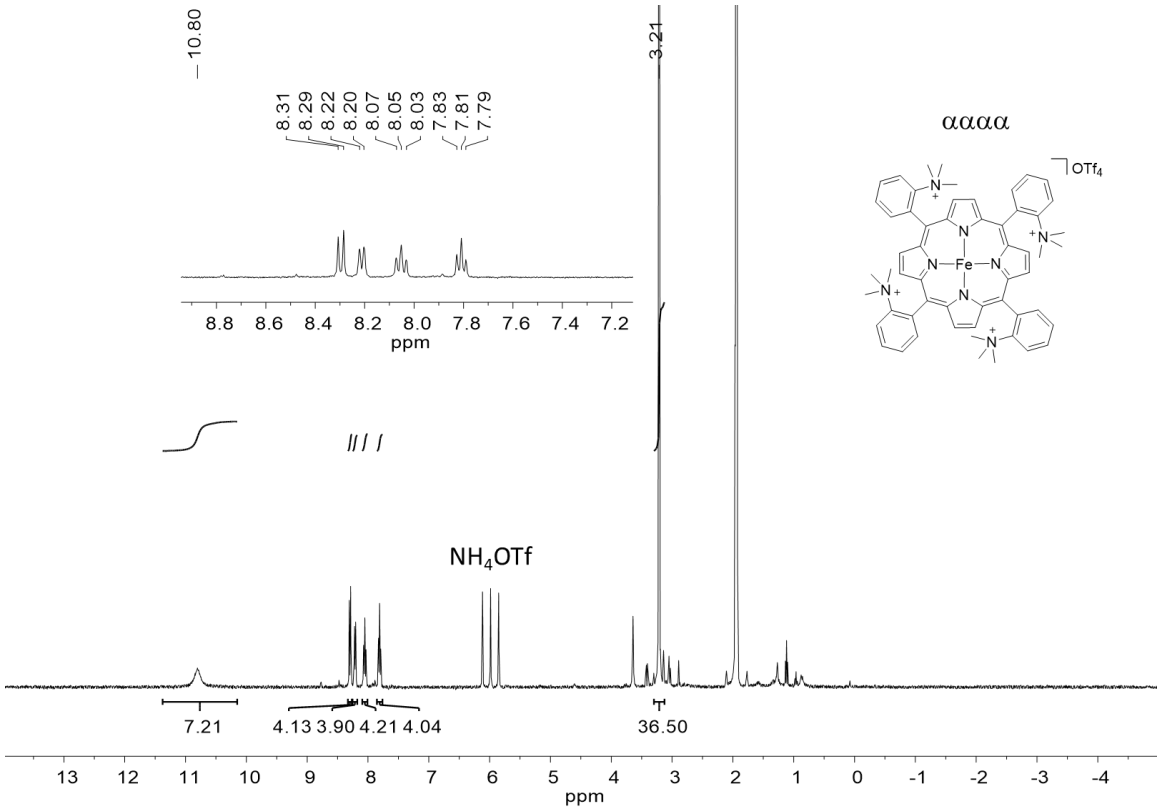

Figure D32. ^{1}H NMR of αααα [Fe(*o*-TMA)](OTf)$_4$ in CD_3CN. Ammonium triflate was an impurity from the synthesis.

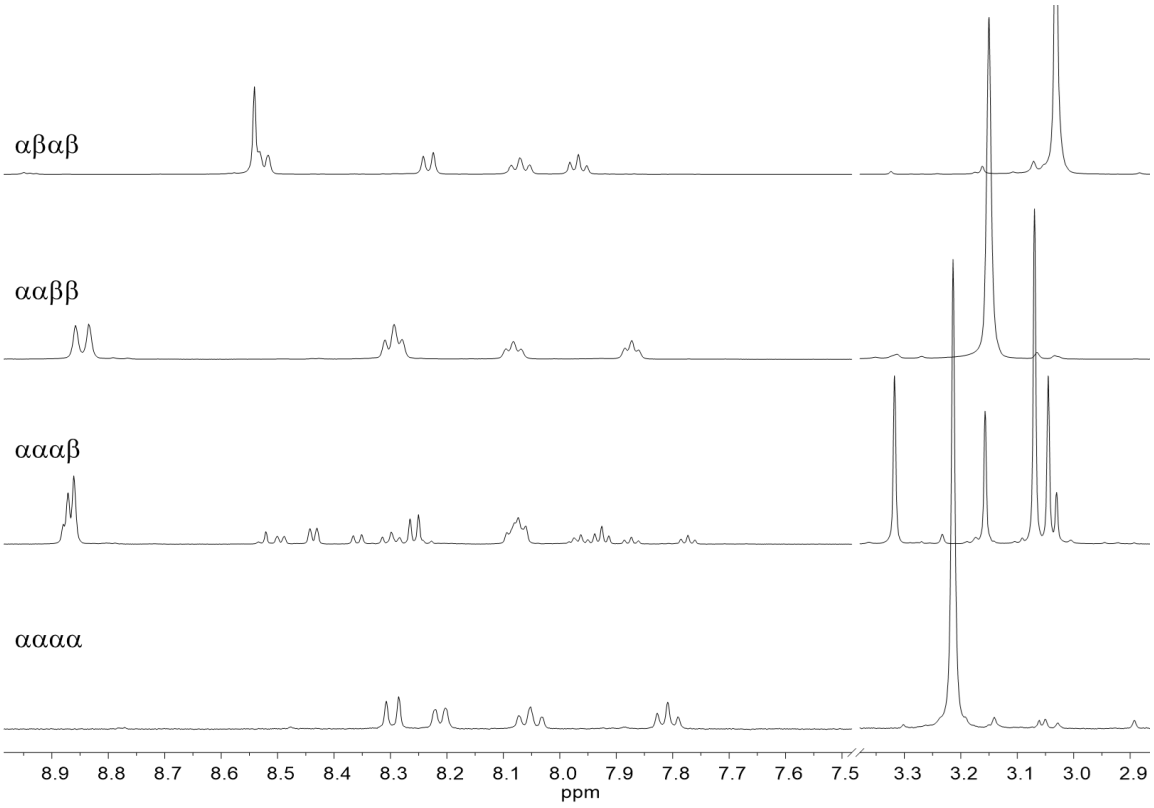

Figure D33. Stacked, partial ^{1}H NMR spectra of the four atropisomers of [Fe(*o*-TMA)](OTf)$_4$ in CD_3CN. Region shown highlights uniqueness of aromatic and trimethylanilinium protons. The αααβ atropisomer contains <10% of the ααββ isomer as a contaminant.

D.5 Thermal Rotamerization

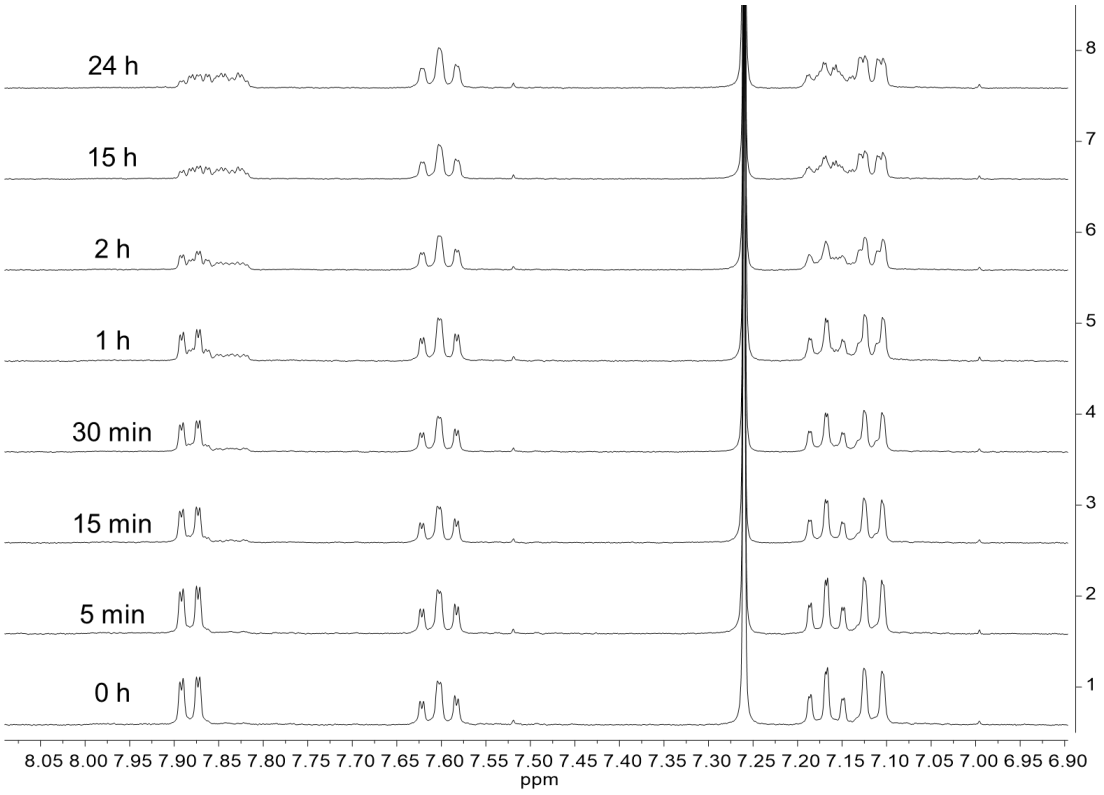

Figure D34. ^{1}H NMR timecourse for the rotamerization of αβαβ H_2(*o*-AMP). Only the aromatic region is shown. Sample was heated for 24 h at 80 °C (various timepoints) in $CDCl_3$.

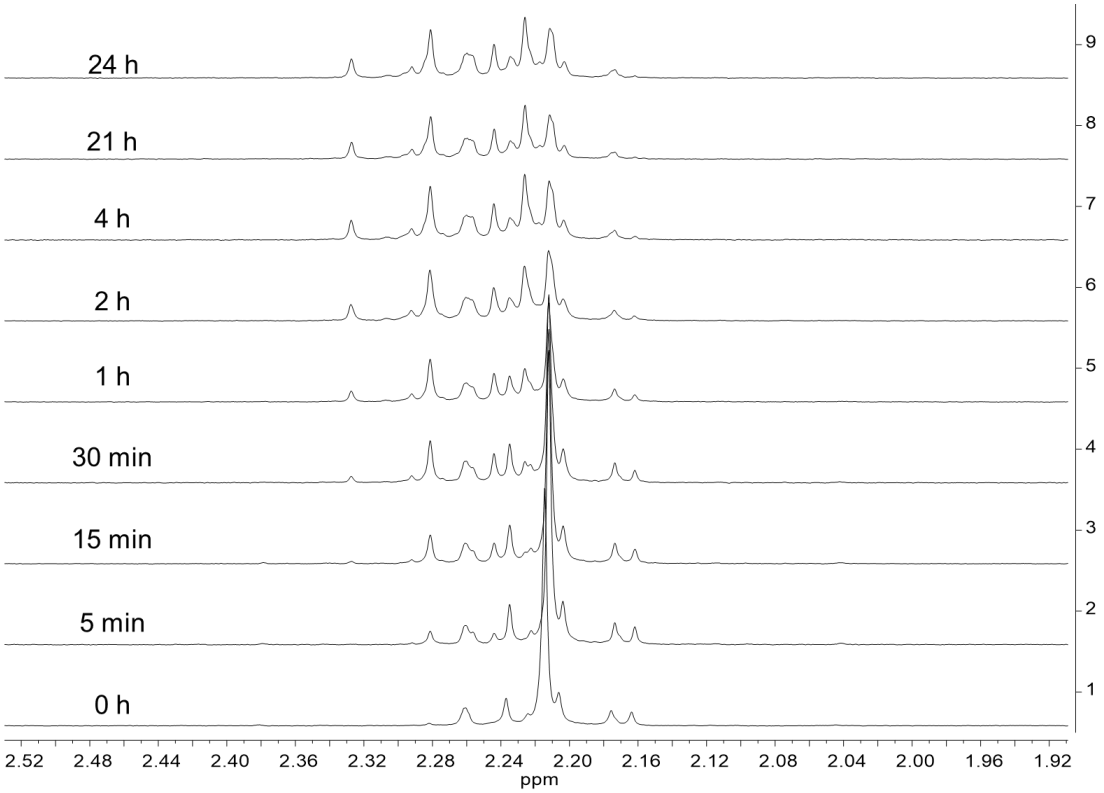

Figure D35. ^{1}H NMR timecourse for the rotamerization of αβαβ H_2(*o*-DMA). Only the *o*-($N(CH_3)_2$) protons are shown. Sample was heated for 24 h at 80 °C (various timepoints) in $CDCl_3$.

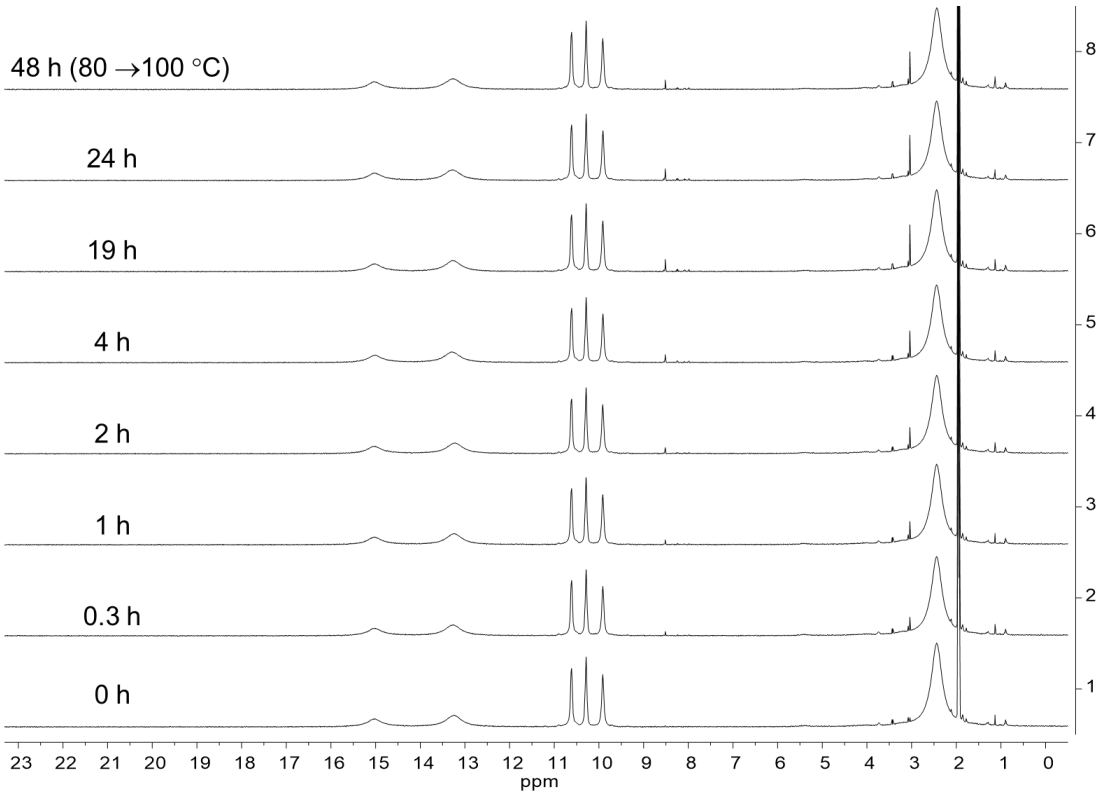

Figure D36. ^{1}H NMR timecourse for the rotamerization of αβαβ [Fe^{III}(*o*-TMA)](OTf)$_5$. Sample was heated for 24 h at 80 °C (various timepoints) in CD_3CN. After the 24 h mark, the temperature was increased to 100 °C for an additional 24 h.

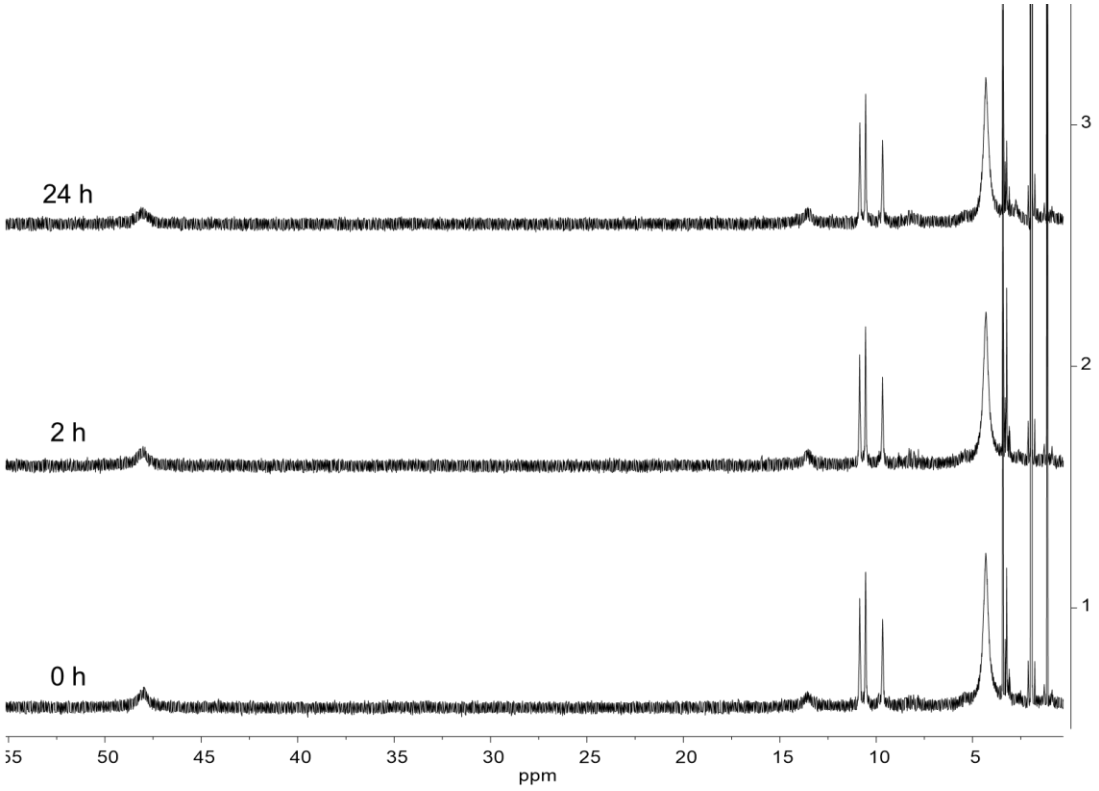

Figure D37. ^{1}H NMR timecourse for the rotamerization of αααα [Fe^{III}(*o*-TMA)](OTf)$_5$. Sample was heated for 24 h at 80 °C (various timepoints) in CD_3CN.

D.6 Single Crystal X-ray Diffraction Methods

Low-temperature diffraction data (ω-scans) were collected on a Rigaku MicroMax-007HF diffractometer coupled to a Saturn994+ CCD detector with Cu Kα (λ = 1.54178 Å). The diffraction images were processed and scaled using Rigaku Oxford Diffraction software (CrysAlisPro; Rigaku OD: The Woodlands, TX, 2015). The structure was solved with SHELXT and was refined against F^2 on all data by full-matrix least squares with SHELXL (Sheldrick, G. M. Acta Cryst. 2008, A64, 112–122). All non-hydrogen atoms were refined anisotropically. Hydrogen atoms were included in the model at geometrically calculated positions and refined using a riding model. The isotropic displacement parameters of all hydrogen atoms were fixed to 1.2 times the U value of the atoms to which they are linked (1.5 times for methyl groups).

D.6.1 αβαβ [Fe^{III}(o-TMA)•H_2O•OTf](OTf)$_4$

General instrument and modeling conditions described above.

The 1,3 distances of the water protons and iron center were restrained to be similar. Two of the five triflates are disordered. The model with S5 is disordered over two, equally occupied positions. All chemically equivalent 1,2 distances were restrained to be similar. The disordered groups were restrained to behave as rigid groups. The thermal parameters with a disordered group were restrained to have similar values. O14 is shared between both models. Atom sites F16 and O15A are in the same crystallographic position and were constrained to have identical thermal parameters. The same is true for F17 and O16A. In the triflate with atom S4, the fluorine atoms F10, F11, and F12 are disordered over two positions. The occupancy splits are ~0.60/0.40. The minor component positions are distinguished with "B" suffixes.

The program SQUEEZE (see A.L.Spek, J. Appl. Cryst. 2015, C71, 9-18) was used to compensate for the contribution of disordered solvents contained in voids within the crystal lattice from the diffraction intensities. This procedure was applied to the data file and the submitted model is based on the solvent removed data. Based on the total electron density found in the voids (644 e/Å^3), it is likely that ~29 MeCN, ~64 water or some combination of these molecules are present in the unit cell. See "_platon_squeeze_details" in the .cif for more information. The full numbering scheme of compound 007c-20038 can be found in the full details of the X-ray structure determination (CIF). These data can be obtained free of charge from The Cambridge Crystallographic Data Center via www.ccdc.cam.ac.uk/data_request/cif.

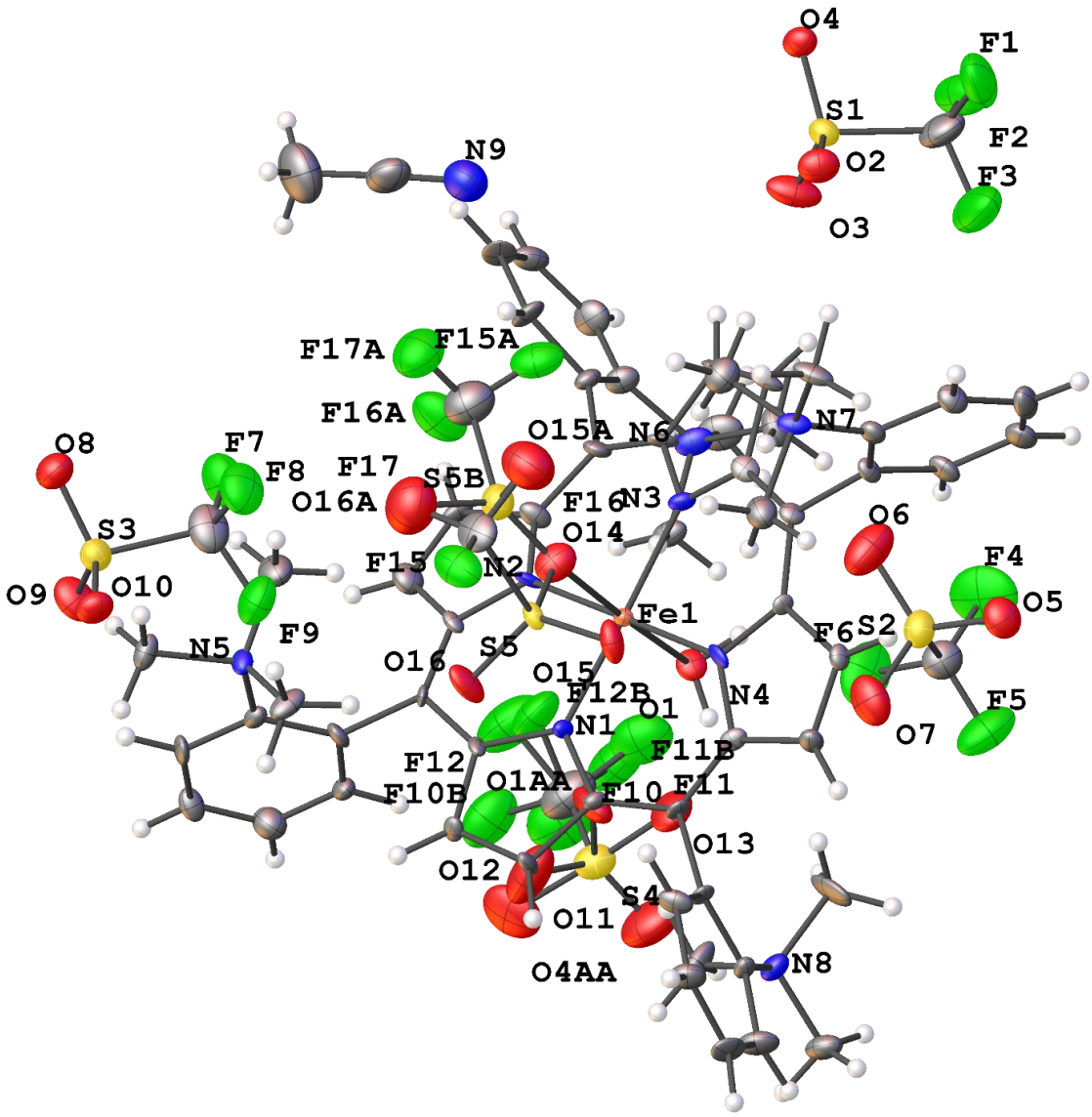

Figure D38. A partial numbering scheme of αβαβ [Fe^{III}(*o*-TMA)•H_2O•OTf](OTf)$_4$ with 50% thermal ellipsoid probability levels. The hydrogen atoms are shown as circles for clarity.

Table D1. Crystal data and structure refinement for αβαβ [Fe^{III}(*o*-TMA)•H_2O•OTf](OTf)$_4$.

Identification code	007c-20038	
Empirical formula	C63 H65 F15 Fe N9 O16 S5	
Formula weight	1705.39	
Temperature	93(2) K	
Wavelength	0.71073 Å	
Crystal system	Monoclinic	
Space group	Cc	
Unit cell dimensions	a = 22.3718(6) Å	α= 90°.
	b = 15.9396(3) Å	β= 110.154(3)°.
	c = 25.1710(6) Å	γ = 90°.
Volume	8426.3(4) $Å^3$	
Z	4	
Density (calculated)	1.344 Mg/m^3	
Absorption coefficient	0.398 mm^{-1}	
F(000)	3500	
Crystal size	0.100 x 0.080 x 0.050 mm^3	
Crystal color and habit	Black Block	
Diffractometer	Dectris Pilatus 3R	
Theta range for data collection	3.007 to 27.485°.	
Index ranges	-27<=h<=29, -20<=k<=20, -32<=l<=32	
Reflections collected	77576	
Independent reflections	18214 [R(int) = 0.0872]	
Observed reflections (I > 2sigma(I))	17106	
Completeness to theta = 25.242°	99.9 %	
Absorption correction	Semi-empirical from equivalents	
Max. and min. transmission	1.00000 and 0.63547	
Solution method	SHELXT-2014/5 (Sheldrick, 2014)	
Refinement method	SHELXL-2014/7 (Sheldrick, 2014)	
Data / restraints / parameters	18214 / 436 / 1085	
Goodness-of-fit on F^2	1.049	
Final R indices [I>2sigma(I)]	R1 = 0.1159, wR2 = 0.2937	
R indices (all data)	R1 = 0.1194, wR2 = 0.2963	
Absolute structure parameter	0.17(4)	
Largest diff. peak and hole	2.091 and -0.943 e.$Å^{-3}$	

D.6.2 αααββ [Fe^{III}(o-TMA)•OTf](OTf)$_4$

General instrument and modeling conditions described above.

The triflates in the asymmetric unit are disordered. The final model required that the minor component triflate models be placed in the difference map as rigid groups (see Guzei, I. A. (2014). J. Appl. Crystallogr. 47, 806-809). The site occupancies of the disordered groups were freely refined as linked variables. The population distribution converged at 0.81/0.19 for the triflate set with atoms S1/S6. A similar approach resulted in a distribution of 0.67/0.33 for the triflate set S2/S5; 0.56/0.44 for S3/S4. The thermal parameters were restrained to also behave as a ridged group. Additionally, several atoms required there thermal parameters be constrained to neighboring atoms, due to proximity to one another. Finally, 1,2 and 1,3 distance restraints were required for the major occupancy triflate S1. The full numbering scheme of compound αααββ [Fe^{III}(*o*-TMA)•OTf](OTf)$_4$ can be found in the full details of the X-ray structure determination (CIF). These data can be obtained free of charge from The Cambridge Crystallographic Data Center via www.ccdc.cam.ac.uk/data_request/cif.

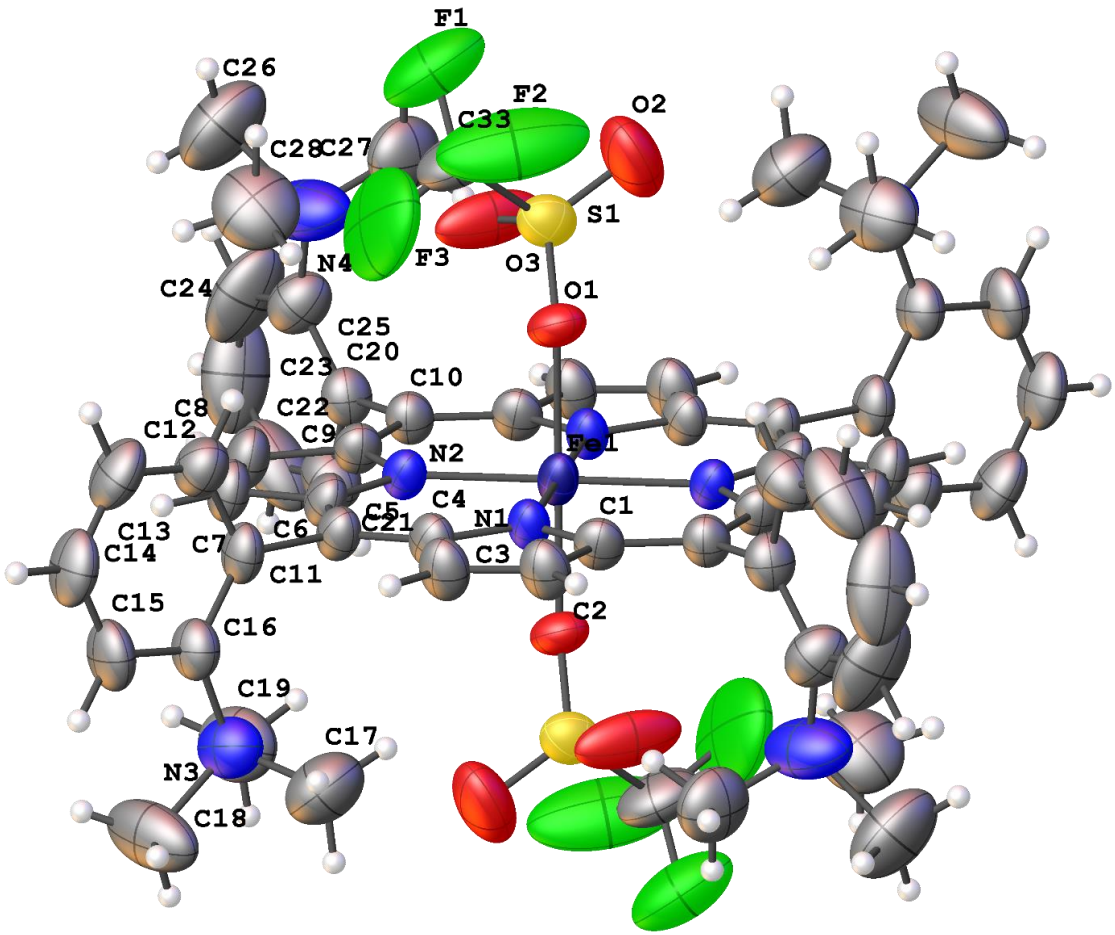

Figure D39. The complete numbering scheme of αααββ [Fe^{III}(*o*-TMA)•OTf](OTf)$_4$ with 50% thermal ellipsoid probability levels. The hydrogen atoms are shown as circles for clarity.

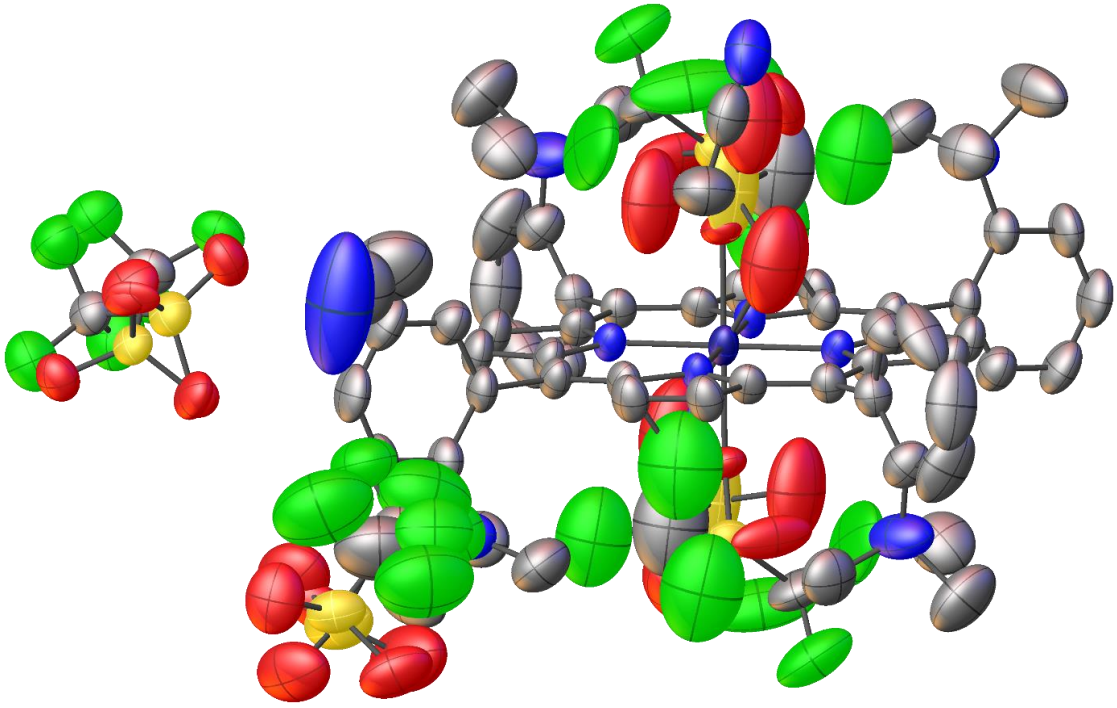

Figure D40. The complete model of αααββ [Fe^{III}(*o*-TMA)•OTf](OTf)$_4$.

Table D2. Crystal data and structure refinement for αβαβ [Fe^{III}(*o*-TMA)•H_2O•OTf](OTf)$_4$.

Identification code	007c-19055	
Empirical formula	C69 H72 F15 Fe N12 O15 S5	
Formula weight	1810.53	
Temperature	93(2) K	
Wavelength	0.71073 Å	
Crystal system	Triclinic	
Space group	P-1	
Unit cell dimensions	a = 11.3411(15) Å	α= 97.616(9)°.
	b = 11.8660(16) Å	β= 101.268(9)°.
	c = 15.3572(14) Å	γ = 108.711(12)°.
Volume	1876.8(4) $Å^3$	
Z	1	
Density (calculated)	1.602 Mg/m^3	
Absorption coefficient	0.452 mm^{-1}	
F(000)	931	
Crystal size	0.200 x 0.180 x 0.020 mm^3	
Crystal color and habit	Black Plate	
Diffractometer	Rigaku Saturn 944+ CCD	
Theta range for data collection	2.958 to 27.624°.	
Index ranges	-14<=h<=14, -15<=k<=13, -19<=l<=19	
Reflections collected	35319	
Independent reflections	8514 [R(int) = 0.0591]	
Observed reflections (I > 2sigma(I))	5495	
Completeness to theta = 25.242°	99.8 %	
Absorption correction	Semi-empirical from equivalents	
Max. and min. transmission	1.00000 and 0.46106	
Solution method	SHELXT-2014/5 (Sheldrick, 2014)	
Refinement method	SHELXL-2014/7 (Sheldrick, 2014)	
Data / restraints / parameters	8514 / 286 / 708	
Goodness-of-fit on F^2	1.040	
Final R indices [I>2sigma(I)]	R1 = 0.1112, wR2 = 0.3075	
R indices (all data)	R1 = 0.1498, wR2 = 0.3370	
Largest diff. peak and hole	1.258 and -0.716 $e.Å^{-3}$	

D.6.3 αααβββ [Fe^{II}(o-TMA)•2(CH$_3$CN)](OTf)$_4$

General instrument and modeling conditions described above.

The triflates in the asymmetric unit are disordered. The final model required that the minor component triflate models be placed in the difference map as rigid groups (see Guzei, I. A. (2014). J. Appl. Crystallogr. 47, 806-809). The site occupancies of the disordered groups were freely refined as linked variables. The population distribution converged at 0.64/0.36 for the triflate set with atoms S1/S1B. A similar approach resulted in a distribution of 0.52/0.48 for the trflate set S2/S2B. The thermal parameters were restrained to also behave as a ridged group. Finally, 1,2 and 1,3 distance restraints were required for the major occupancy triflate S1. The full numbering scheme of αααβββ [Fe^{II}(*o*-TMA)•(CH$_3$CN)](OTf)$_4$ can be found in the full details of the X-ray structure determination (CIF). These data can be obtained free of charge from The Cambridge Crystallographic Data Center via www.ccdc.cam.ac.uk/data_request/cif.

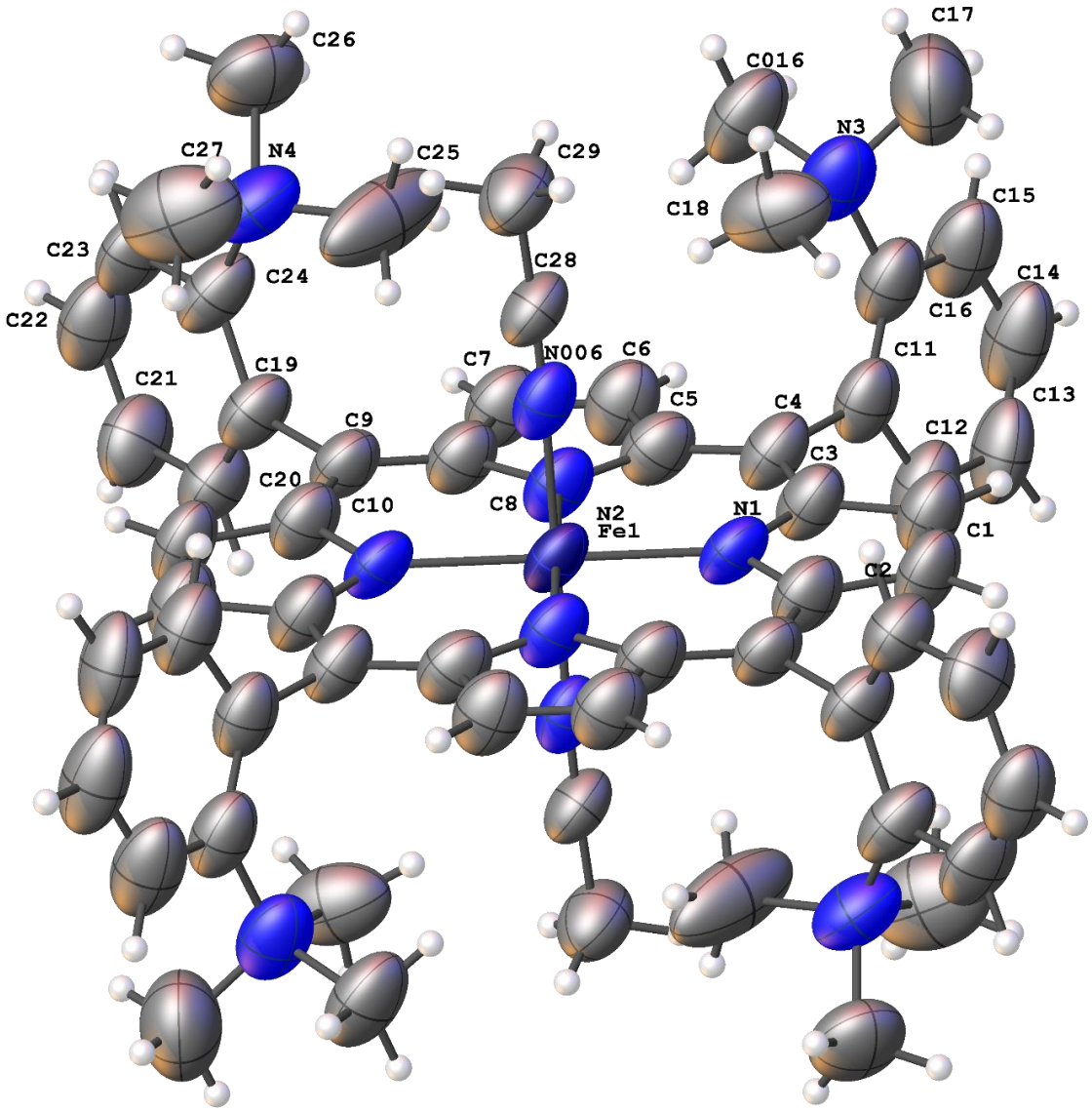

Figure D41. The complete porphyrin numbering scheme of αααββ [Fe^{II}(*o*-TMA)•(CH_3CN)]($OTf)_4$with 50% thermal ellipsoid probability levels. The hydrogen atoms are shown as circles for clarity.

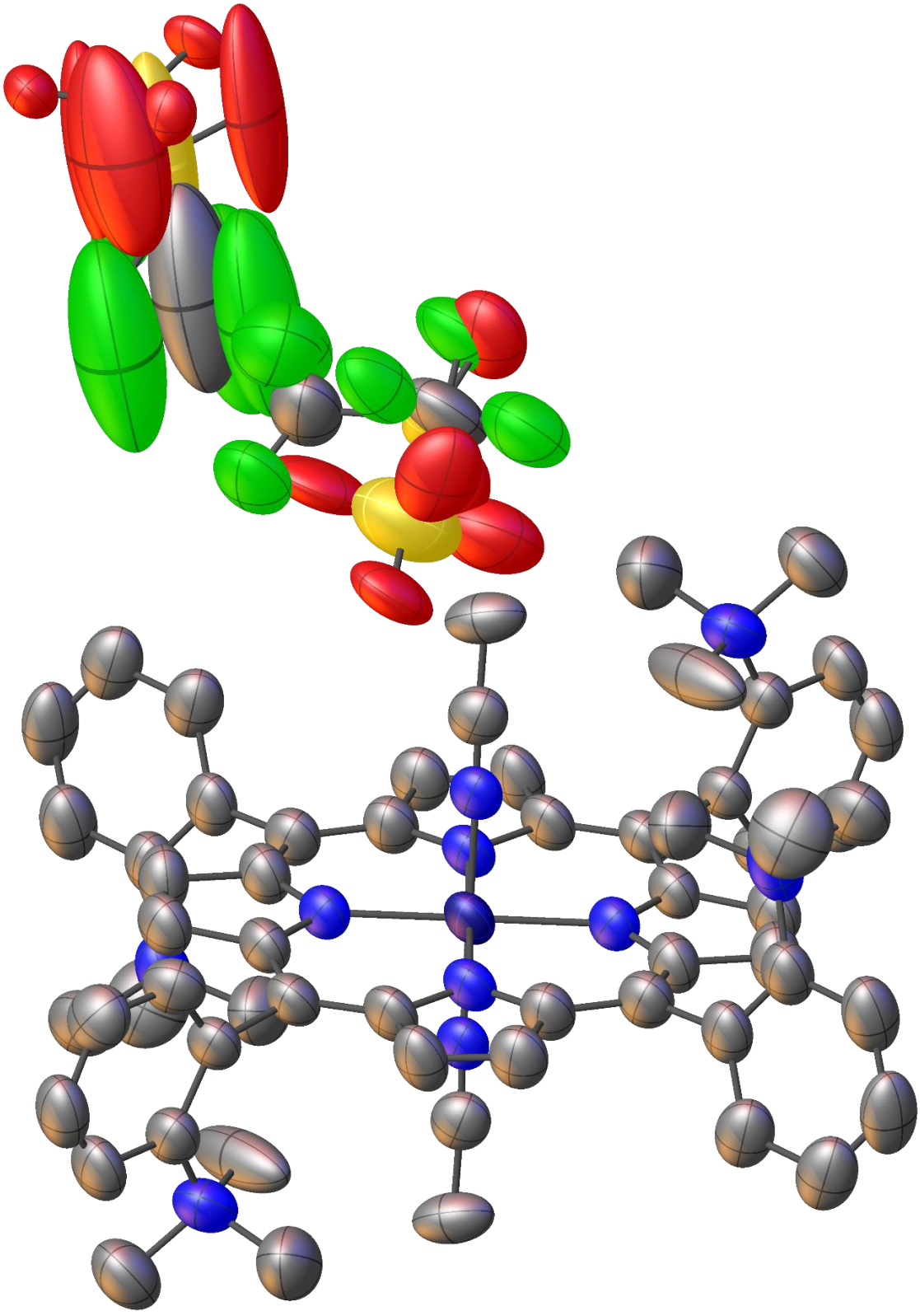

Figure D42. The complete model of αααββ [Fe^{II}(*o*-TMA)•(CH_3CN)]($OTf)_4$.

Table D3. Crystal data and structure refinement for αααββ [Fe^{II}(*o*-TMA)•(CH_3CN)]($OTf)_4$.

Identification code	007b-20028	
Empirical formula	C64 H66 F12 Fe N10 O12 S4	
Formula weight	1579.35	
Temperature	93(2) K	
Wavelength	1.54184 Å	
Crystal system	Triclinic	
Space group	P-1	
Unit cell dimensions	a = 11.0358(11) Å	α= 109.205(8)°.
	b = 13.0320(10) Å	β= 91.523(8)°.
	c = 13.0544(12) Å	γ = 96.561(7)°.
Volume	1757.2(3) $Å^3$	
Z	1	
Density (calculated)	1.492 Mg/m^3	
Absorption coefficient	3.701 mm^{-1}	
F(000)	814	
Crystal size	0.140 x 0.080 x 0.060 mm^3	
Crystal color and habit	Black Block	
Diffractometer	Rigaku Saturn 944+ CCD	
Theta range for data collection	3.594 to 66.535°.	
Index ranges	-13<=h<=13, -15<=k<=15, -15<=l<=14	
Reflections collected	53954	
Independent reflections	6078 [R(int) = 0.1232]	
Observed reflections (I > 2sigma(I))	3960	
Completeness to theta = 66.535°	98.2 %	
Absorption correction	Semi-empirical from equivalents	
Max. and min. transmission	1.00000 and 0.54771	
Solution method	SHELXT-2014/5 (Sheldrick, 2014)	
Refinement method	SHELXL-2014/7 (Sheldrick, 2014)	
Data / restraints / parameters	6078 / 231 / 583	
Goodness-of-fit on F^2	1.043	
Final R indices [I>2sigma(I)]	R1 = 0.1420, wR2 = 0.3597	
R indices (all data)	R1 = 0.1779, wR2 = 0.3915	
Largest diff. peak and hole	0.822 and -1.264 e.$Å^{-3}$	

D.6.4 $\alpha\alpha\alpha\beta$ *[Fe^{II}(o-TMA)•2(CH$_3$CN)](OTf)$_4$*

General instrument and modeling conditions described above.

Several methyl groups on the porphyrin are disordered. The disordered sites are extremely close to each other. The best refinement model was obtained when a single methyl site was used. The thermal parameters of the carbon atoms were restrained to be similar to the neighboring methyls, and the chemically equivalent C-N distances were restrained to be similar. The program SQUEEZE (see A.L.Spek, J. Appl. Cryst. 2015, C71, 9-18) was used to compensate for the contribution of disordered solvents contained in voids within the crystal lattice from the diffraction intensities. This procedure was applied to the data file and the submitted model is based on the solvent removed data. Based on the total electron density found in the voids (1258 e/Å^3), it is likely that ~17 triflate molecules are present in the unit cell (~4 per porphyrin). There may be some voids which also contain partially occupied acetonitrile. See "_platon_squeeze_details" in the .cif for more information. The four triflate sites are clearly visable in the difference map, but are incredibly disordered. After numerous restraints and constraints, the best R1-value obtained was ~20%. The general positions parameters below are the likely locations of the triflates.

S1x	5	0.90768	0.82006	0.37135
F1x	4	0.89580	0.90115	0.28628
F2x	4	0.88024	1.01075	0.33542
F3x	4	0.97603	0.96098	0.34610
O1x	3	0.94856	0.74155	0.36323
O2x	3	0.93088	0.86610	0.41906
O3x	3	0.83973	0.79811	0.35107
C1x	1	0.91529	0.92845	0.33294
S2x	5	0.56254	1.17016	0.33911
F4x	4	0.48510	1.01974	0.33246
F5x	4	0.58774	0.98005	0.33448
F6x	4	0.58053	1.05557	0.40621
O4x	3	0.63021	1.17318	0.34755
O5x	3	0.54965	1.17152	0.28685
O6x	3	0.52305	1.24019	0.35137
C2x	1	0.55271	1.06030	0.35186
S3x	5	0.86269	0.20336	0.47550
F7x	4	0.86526	0.28350	0.55684
F8x	4	0.83726	0.38683	0.49900
F9x	4	0.94014	0.33273	0.53546
O7x	3	0.90178	0.11911	0.50185
O8x	3	0.88594	0.25293	0.44231
O9x	3	0.79946	0.18251	0.46703
C3x	1	0.87772	0.30577	0.51843
S4x	5	0.62406	0.34417	0.59695
F10x	4	0.72806	0.31450	0.57948

F11x	4	0.70878	0.46507	0.58625
F12x	4	0.74369	0.38684	0.63928
O10x	3	0.63067	0.23669	0.61720
O11x	3	0.59967	0.33777	0.54679
O12x	3	0.62159	0.37691	0.63775
C4x	1	0.69078	0.38067	0.59865

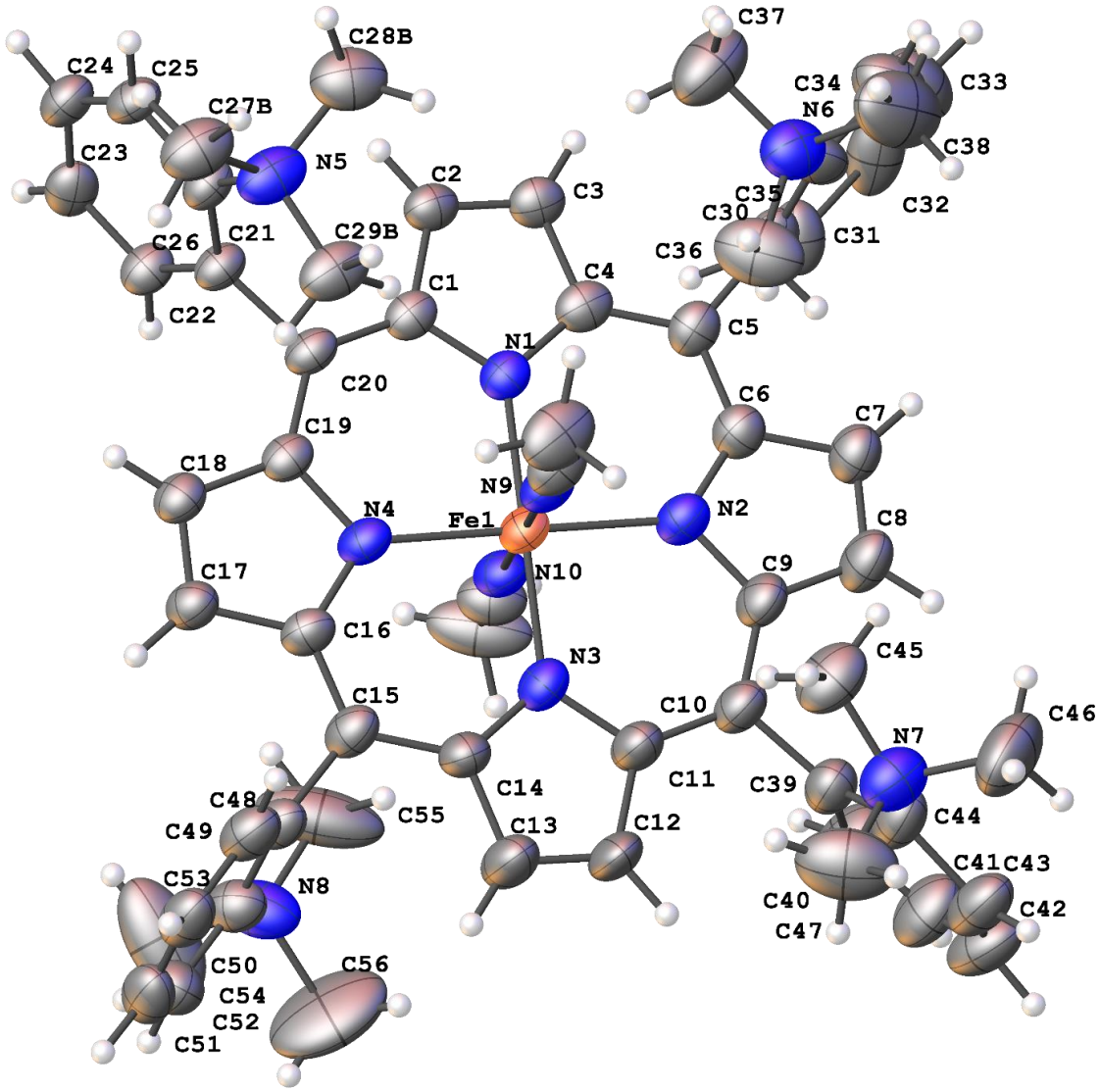

Figure D43. The complete model of αααβ [Fe^{II}(*o*-TMA)•2(CH_3CN)]$(OTf)_4$ with 50% thermal ellipsoid probability levels. The hydrogen atoms are shown as circles for clarity.

Table D4. Crystal data and structure refinement for αααβ [Fe^{II}(*o*-TMA)•2(CH_3CN)]($OTf)_4$.

Identification code	007b-20060	
Empirical formula	C60 H66 Fe N10	
Formula weight	983.07	
Temperature	93(2) K	
Wavelength	1.54184 Å	
Crystal system	Monoclinic	
Space group	$P2_1/n$	
Unit cell dimensions	a = 22.4622(4) Å	α= 90°.
	b = 12.88579(13) Å	β= 111.7405(19)°.
	c = 29.7586(5) Å	γ = 90°.
Volume	8000.8(2) $Å^3$	
Z	4	
Density (calculated)	0.816 Mg/m^3	
Absorption coefficient	1.758 mm^{-1}	
F(000)	2088	
Crystal size	0.200 x 0.190 x 0.020 mm^3	
Crystal color and habit	? ?	
Diffractometer	Rigaku Saturn 944+ CCD	
Theta range for data collection	2.129 to 66.593°.	
Index ranges	-26<=h<=26, -15<=k<=15, -35<=l<=35	
Reflections collected	283655	
Independent reflections	14129 [R(int) = 0.1781]	
Observed reflections (I > 2sigma(I))	9361	
Completeness to theta = 66.593°	99.9 %	
Absorption correction	Semi-empirical from equivalents	
Max. and min. transmission	1.00000 and 0.71814	
Solution method	SHELXT-2014/5 (Sheldrick, 2014)	
Refinement method	SHELXL-2014/7 (Sheldrick, 2014)	
Data / restraints / parameters	14129 / 30 / 652	
Goodness-of-fit on F^2	1.079	
Final R indices [I>2sigma(I)]	R1 = 0.1411, wR2 = 0.3842	
R indices (all data)	R1 = 0.1746, wR2 = 0.4122	
Largest diff. peak and hole	0.899 and -0.613 $e.Å^{-3}$	

D.6.5 αααα [Fe^{III}(o-TMA)•H_2O•OTf](OTf)$_4$

General instrument and modeling conditions described above.

The axially coordinated triflate is disordered over with respect to the crystallographic 4-fold axis. The special position constraints were suppressed and the site occupancy was constrained to 0.25. The triflate not directly coordinated to the porphyrin was modeled as disordered over two positions. The site occupancies were freely refined to a distribution of 0.72/0.28. All disordered thermal parameters were restrained to be similar to those in their disordered group and behave as a rigid group. All chemically equivalent C-C, C-F, S-C, and S-O distances were restrained to be similar. The program SQUEEZE was used to compensate for the contribution of disordered solvents contained in voids within the crystal lattice from the diffraction intensities. This procedure was applied to the data file and the submitted model is based on the solvent removed data. Based on the total electron density found in the voids (210 e/A^3), it is likely that ~3 triflates, 21 waters or some combination of these molecules are present in the unit cell. See "_platon_squeeze_details" in the .cif for more information. The full numbering scheme of compound can be found in the full details of the X-ray structure determination (CIF). These data can be obtained free of charge from The Cambridge Crystallographic Data Center via www.ccdc.cam.ac.uk/data_request/cif.

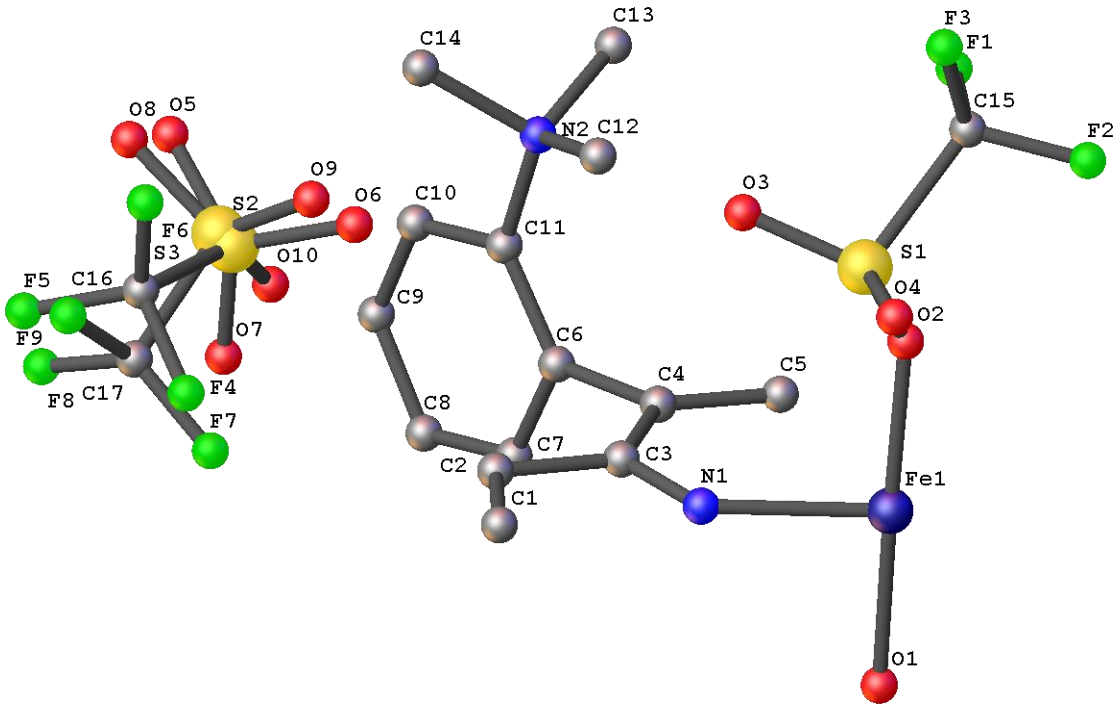

Figure D44. The complete numbering scheme of αααα [Fe^{III}(*o*-TMA)•H_2O•OTf](OTf)$_4$ with ball and sticks representing the atoms. Only the asymmetric unit is shown. The hydrogen atoms are omitted for clarity.

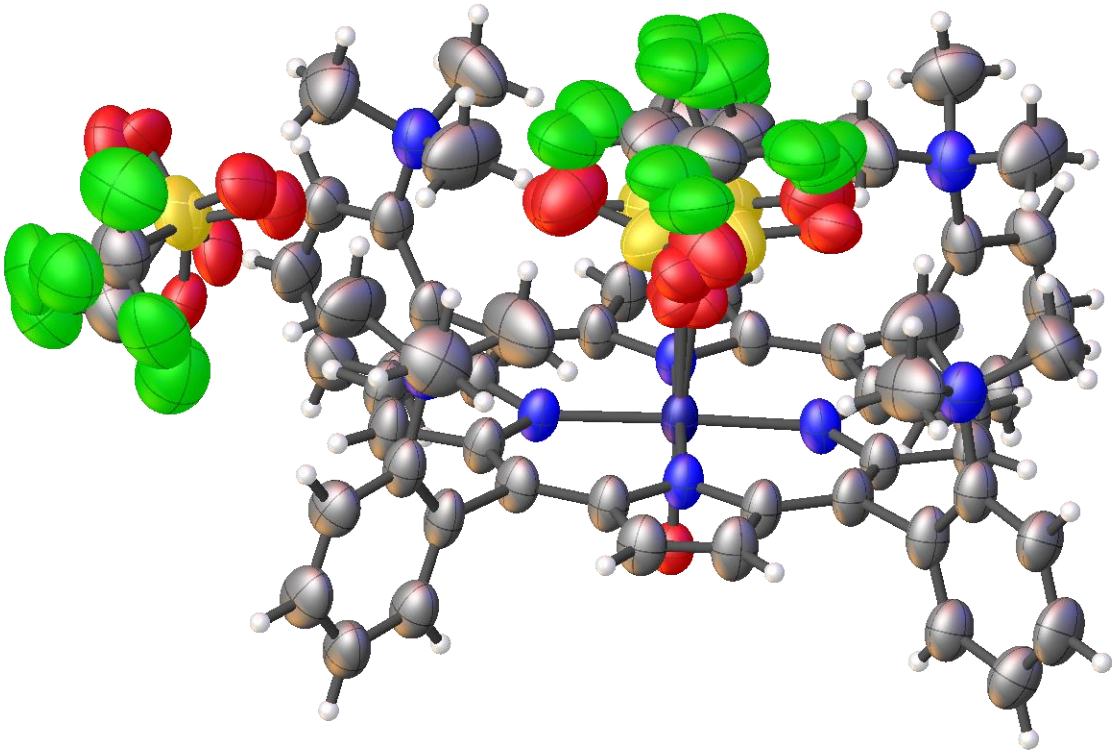

Figure D45. The complete model of αααα [Fe^{III}(*o*-TMA)•H_2O•OTf](OTf)$_4$ with 50% thermal ellipsoid probability levels. The hydrogen atoms are shown as circles for clarity.

Table D5. Crystal data and structure refinement for αααα [Fe^{III}(*o*-TMA)•H_2O•OTf](OTf)$_4$.

Identification code	007b-19125	
Empirical formula	C61 H60 F15 Fe N8 O16 S5	
Formula weight	1662.32	
Temperature	93(2) K	
Wavelength	1.54184 Å	
Crystal system	Tetragonal	
Space group	P4/n	
Unit cell dimensions	a = 16.4548(3) Å	α= 90°.
	b = 16.4548(3) Å	β= 90°.
	c = 14.9753(6) Å	γ = 90°.
Volume	4054.7(2) $Å^3$	
Z	2	
Density (calculated)	1.362 Mg/m^3	
Absorption coefficient	3.556 mm^{-1}	
F(000)	1702	
Crystal size	0.200 x 0.100 x 0.020 mm^3	
Crystal color and habit	black block	
Diffractometer	Rigaku Saturn 944+ CCD	
Theta range for data collection	2.951 to 66.982°.	
Index ranges	-19<=h<=19, -19<=k<=19, -17<=l<=17	
Reflections collected	142217	
Independent reflections	3617 [R(int) = 0.2018]	
Observed reflections (I > 2sigma(I))	2458	
Completeness to theta = 66.982°	99.7 %	
Absorption correction	Semi-empirical from equivalents	
Max. and min. transmission	1.00000 and 0.72402	
Solution method	SHELXT-2014/5 (Sheldrick, 2014)	
Refinement method	SHELXL-2014/7 (Sheldrick, 2014)	
Data / restraints / parameters	3617 / 334 / 347	
Goodness-of-fit on F^2	1.057	
Final R indices [I>2sigma(I)]	R1 = 0.0891, wR2 = 0.2612	
R indices (all data)	R1 = 0.1211, wR2 = 0.2923	
Extinction coefficient	n/a	
Largest diff. peak and hole	0.500 and -0.910 e.$Å^{-3}$	

D.6.6 αααα [Fe^{II}(o-TMA)•OTf](OTf)$_3$

General instrument and modeling conditions described above.

Two of the four triflates are disordered. The site occupancies of all disordered sites were freely refined as linked pairs. All chemically equivalent 1,2 and 1,3 distances within the disordered models were restrained to be similar. Due to the low quality of the diffraction data, a model required the whole model be restrained with rigid bond restraints. The full numbering scheme of compound 007b-20045 can be found in the full details of the X-ray structure determination (CIF). These data can be obtained free of charge from The Cambridge Crystallographic Data Center via www.ccdc.cam.ac.uk/data_request/cif.

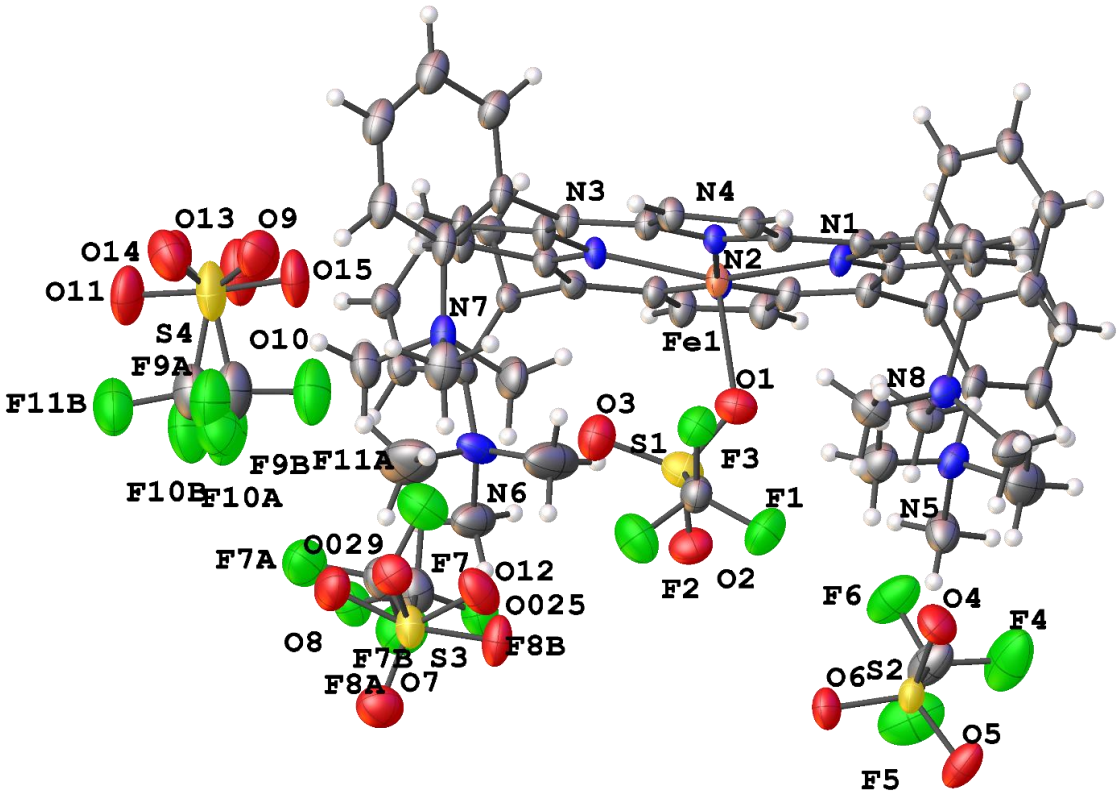

Figure D46. The complete numbering scheme of αααα [Fe^{II}(*o*-TMA)•OTf](OTf)$_3$ with 50% thermal ellipsoid probability levels. The hydrogen atoms are shown as circles for clarity.

Table D6. Crystal data and structure refinement for αααα [Fe^{II}(*o*-TMA)•OTf](OTf)$_3$.

Identification code	007b-20045	
Empirical formula	C60 H60 F12 Fe N8 O12 S4	
Formula weight	1497.25	
Temperature	93(2) K	
Wavelength	1.54184 Å	
Crystal system	Monoclinic	
Space group	$P2_1/c$	
Unit cell dimensions	a = 15.4857(6) Å	α= 90°.
	b = 30.6674(11) Å	β= 117.370(5)°.
	c = 15.1369(6) Å	γ = 90°.
Volume	6383.9(5) $Å^3$	
Z	4	
Density (calculated)	1.558 Mg/m^3	
Absorption coefficient	4.030 mm^{-1}	
F(000)	3080	
Crystal size	0.350 x 0.020 x 0.020 mm^3	
Crystal color and habit	Red Needle	
Diffractometer	Rigaku Saturn 944+ CCD	
Theta range for data collection	2.882 to 66.590°.	
Index ranges	-18<=h<=17, -36<=k<=36, -18<=l<=18	
Reflections collected	184244	
Independent reflections	11200 [R(int) = 0.3567]	
Observed reflections (I > 2sigma(I))	5432	
Completeness to theta = 66.590°	99.4 %	
Absorption correction	Semi-empirical from equivalents	
Max. and min. transmission	1.00000 and 0.30496	
Solution method	SHELXT-2014/5 (Sheldrick, 2014)	
Refinement method	SHELXL-2014/7 (Sheldrick, 2014)	
Data / restraints / parameters	11200 / 1025 / 996	
Goodness-of-fit on F^2	1.015	
Final R indices [I>2sigma(I)]	R1 = 0.1152, wR2 = 0.2704	
R indices (all data)	R1 = 0.2078, wR2 = 0.3341	
Largest diff. peak and hole	0.926 and -0.678 e.$Å^{-3}$	

D.7 References

1. Inorganic Syntheses. Wold, A.; Ruff, J. K., Eds. John Wiley & Sons, Inc.: Hoboken, 1973; pp 102-103.
2. Martin, D. J.; Johnson, S. I.; Mercado, B. Q.; Raugei, S.; Mayer, J. M., Intramolecular Electrostatic Effects on O_2, CO_2, and Acetate Binding to a Cationic Iron Porphyrin. *Inorg. Chem.* **2020,** *59* (23), 17402-17414.
3. Elgrishi, N.; Rountree, K. J.; McCarthy, B. D.; Rountree, E. S.; Eisenhart, T. T.; Dempsey, J. L., A Practical Beginner's Guide to Cyclic Voltammetry. *J. Chem. Educ.* **2018,** *95* (2), 197-206.
4. Collman, J. P.; Gagne, R. R.; Reed, C. A.; Halbert, T. R.; Lang, G.; Robinson, W. T., "Picket fence porphyrins." Synthetic models for oxygen binding hemoproteins. *J. Am. Chem. Soc.* **1975,** *97* (6), 1427-39.
5. Nishino, N.; Kobata, K.; Mihara, H.; Fujimoto, T., Efficient Preparation of αβαβ-Atropisomer ofmeso-Tetra(o-aminophenyl)porphyrin. *Chem. Lett.* **1992,** *21* (10), 1991-1994.
6. Rose, E.; Quelquejeu, M.; Pochet, C.; Julien, N.; Kossanyi, A.; Hamon, L., Large-scale preparation of α,β,α,β atropisomer of meso-Tetrakis(o-aminophenyl)porphyrin. *J. Org. Chem.* **1993,** *58* (19), 5030-5031.
7. Azcarate, I.; Costentin, C.; Robert, M.; Savéant, J. M., Through-Space Charge Interaction Substituent Effects in Molecular Catalysis Leading to the Design of the Most Efficient Catalyst of CO_2-to-CO Electrochemical Conversion. *J. Am. Chem. Soc.* **2016,** *138* (51), 16639-16644.
8. Rose, E.; Cardonpilotaz, A.; Quelquejeu, M.; Bernard, N.; Kossanyi, A.; Desmazieres, B., Efficient Preparation of the α,α,β,β-Atropoisomer of meso-Tetrakis(o-aminophenyl)porphyrin. *J. Org. Chem.* **1995,** *60* (12), 3919-3920.
9. Lindsey, J., Increased Yield of a Desired Isomer by Equilibria Displacement on Binding to Silica-Gel, Applied to Meso-Tetrakis(*o*-aminophenyl)Porphyrin. *J. Org. Chem.* **1980,** *45* (25), 5215-5215.

E Supporting Information for Chapter 6

Adapted from Martin, D. J. and Mayer, J. M. "Spatial Electrostatic Effects on O_2 and CO_2 Reduction by a Cationic Iron Porphyrin." *Unsubmitted work*.

E.1 General Considerations

E.1.1 Materials

Acetic acid (Sigma-Aldrich, >99%), tetrabutylammonium acetate (Sigma-Aldrich, >99%), ferrocene (Sigma-Aldrich, >98%), decamethylferrocene (Sigma-Aldrich, >95%), dimethylformamide (anhydrous; Sigma-Aldrich >99.9%), and acetonitrile (anhydrous; Honeywell, >99.9%), argon (Airgas, Ultra High Purity), O_2 (Airgas, Ultra High Purity), and CO_2 (Airgas, Ultra High Purity) were all purchased and used without further purification. Phenol (Sigma-Aldrich, >99%) was distilled and stored in a glovebox, away from light sources. Tetrabutylammonium hexafluorophosphate (TCI, >99%) was recrystallized from ethanol (3×), dried at 70°C for 48 h, and stored in the glovebox. Argon (Airgas, Ultra High Purity), O_2 (Airgas, Ultra High Purity), and CO_2 (Airgas, Ultra High Purity) were used without further purification. The porphyrins used in this work were prepared as previously reported and were also stored as solids in the glovebox.[1-2]

E.1.2 Electrochemical Methods

Cyclic voltammograms were collected using a CH Instruments model 600 D potentiostat using a three-electrode set-up. Glassy carbon (CH Instruments, 3 mm or 1 mm) was used as the working electrode, platinum wire as the auxiliary, and a silver wire pseudoreference as the reference electrode. A silver wire pseudoreference was prepared for both the MeCN and DMF solvents following a method described elsewhere.[3] The working electrode was polished before each voltammogram using 0.05 μm alumina (CH Instruments, containing no agglomerating agents) on a Buhler polishing pad. All voltammograms were internally referenced to ferrocene or decamethylferrocene. Unless otherwise noted, all voltammograms were corrected for uncompensated resistance (< 200 Ω) using the values provided by the potentiostat.

E.2 O_2 Reduction

All cyclic voltammetry data for O_2 reduction were collected using the same solution conditions and at 0.1 V s^{-1} scan rates. Solutions of MeCN were prepared to contain 0.1 M acetic acid, 0.1 M [*n*-Bu_4N][AcO], 0.1 M [H_2O], and 0.1 M [*n*-Bu_4N][PF_6]. Voltammograms were internally referenced to decamethylferrocene ($E_{1/2}$ = −0.48 V vs. Fc^+/Fc), which was added at the end of each experiment to avoid confounding the foot-of-the-wave analysis.

E.2.1 Cyclic Voltammetry

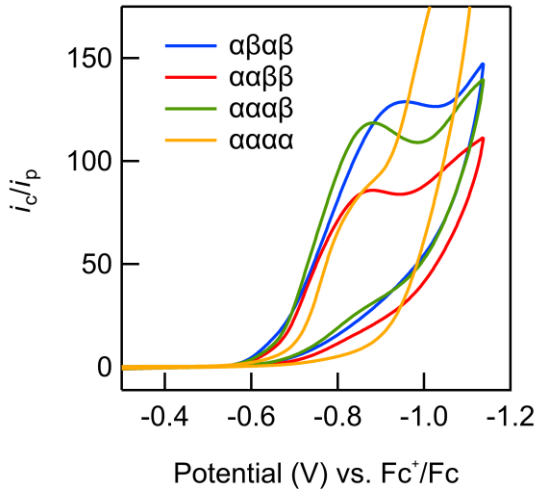

Figure E1. Cyclic voltammograms of the Fe(*o*-TMA) atropisomers under 1 atm O_2. Conditions described above.

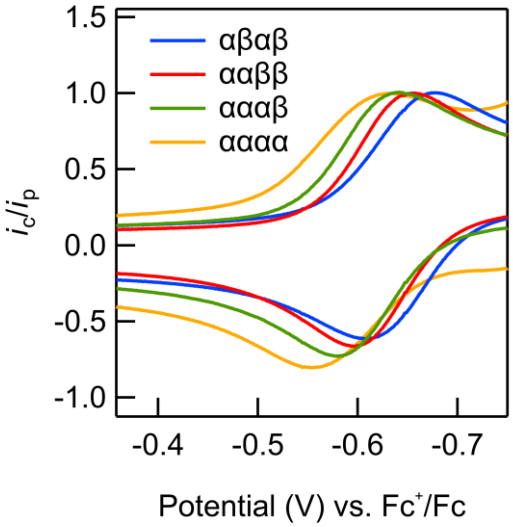

Figure E2. Cyclic voltammograms of the Fe(*o*-TMA) atropisomers under 1 atm Ar. Conditions described above.

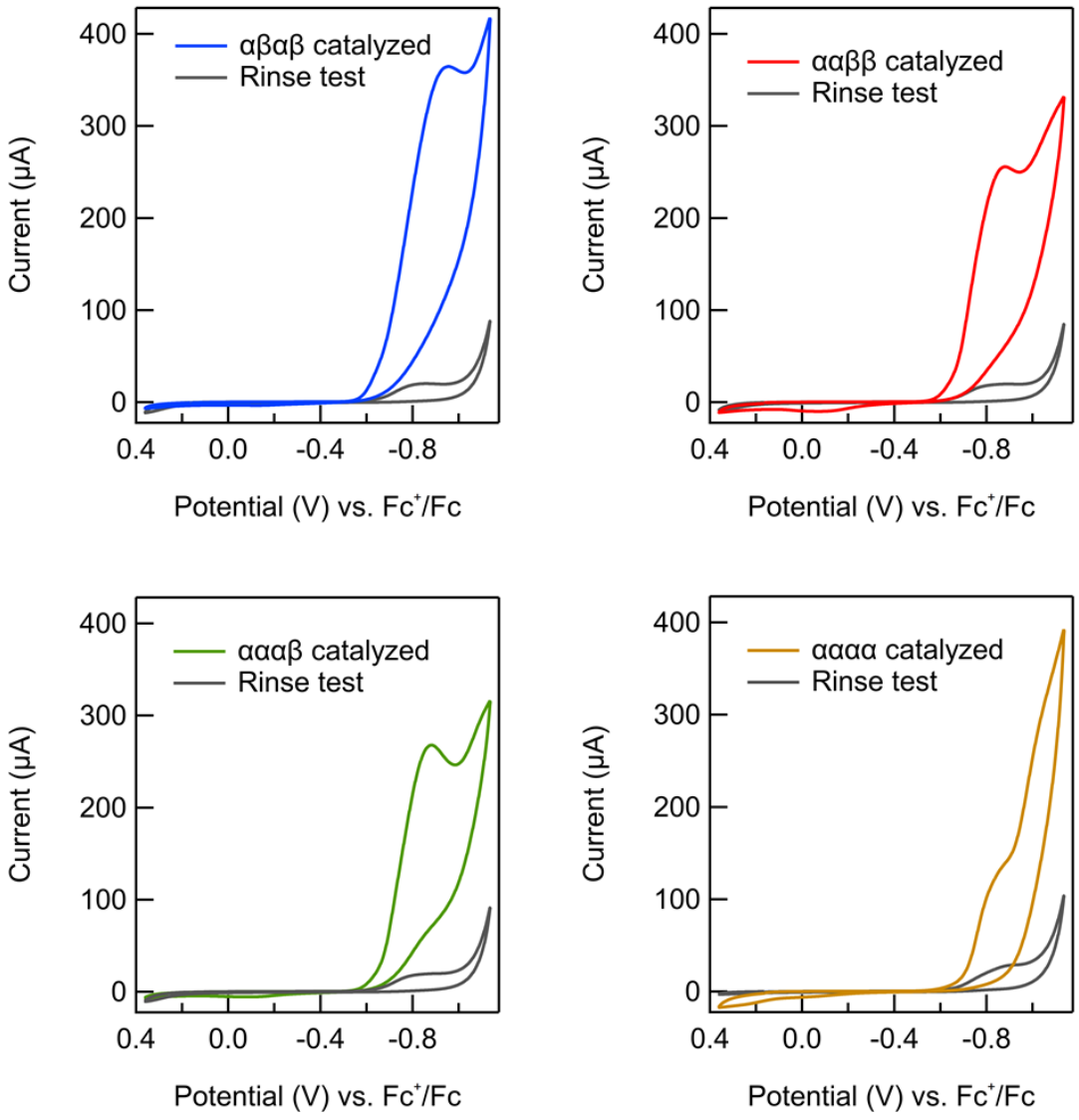

Figure E3. Rinse tests for the Fe(*o*-TMA) atropisomers.

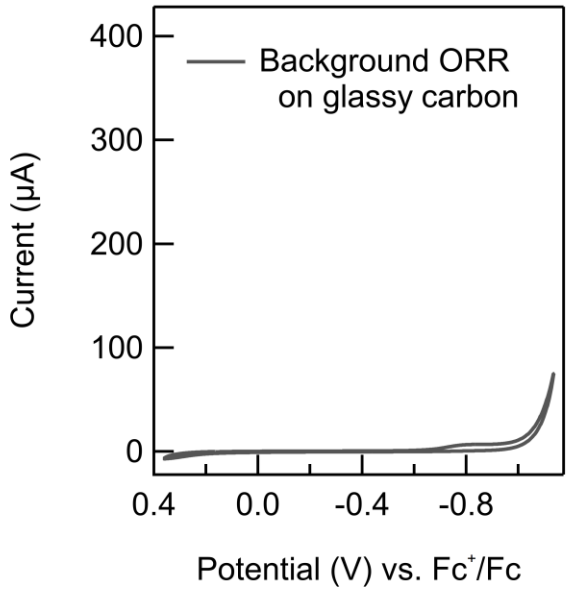

Figure E4. Background O_2 reduction on glassy carbon using the same conditions described above.

E.2.2 Foot of the Wave Analysis

Following the methods detailed in references [4-6], Foot-of-the-wave analysis (FOWA) was used to determine TOF_{max} for O_2 reduction by each of the atropisomers. This approach extrapolates TOF_{max} from the early part of the catalytic wave, a region where substrate depletion and side phenomena are small. As shown elsewhere, the FOWA equation (eq E1) derived for an *E*C′ is appropriate for O_2 reduction by Fe(*o*-TMA) under these conditions.[4-5]

$$\frac{i_c}{i_p} = \frac{2.24 n_{cat}^{\sigma} \sqrt{\frac{RT}{Fv} TOF_{max}}}{1 + \exp\left[\frac{F}{RT}(E - E_{1/2})\right]} \qquad \text{(eq E.1)}$$

i_c = current measured under catalytic conditions

i_p = current of the 1 e^- iron(III/II) redox couple

n_{cat} = number of electrons in one catalytic turnover, equal to 4 for O_2 to H_2O for the Fe(*o*-TMA) catalysts (reference [4])

σ = stoichiometric factor, assumed to be 1 to give the lower-limit estimate of TOF_{max} (reference [5])

ν = scan rate

$E_{1/2} = E_{1/2}(Fe^{III}/Fe^{II})$

E = applied potential

As shown in both Chapter 6 (**Figure 6.1**) and below in **Figure E5,** the voltammetry data from above was replotted as i_c/i_p vs. the denominator of equation E1. The slope of the linear region between i_c/i_p was fit between 1 and 4, which corresponds to the first catalytic turnover, or until $R^2 < 0.98$. From equation E1, the slope was used to determine the TOF_{max} reported in **Table 6.1**. See reference 4 Supporting Information document for related FOWA data under various substrate concentrations.

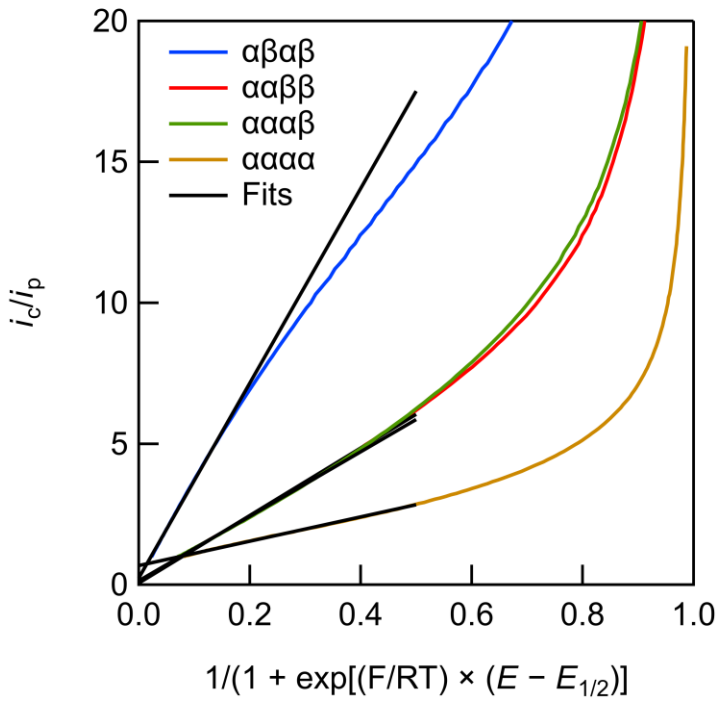

Figure E5. Foot-of-the-wave plots for all four atropisomers under identical conditions.

E.2.3 Effective Overpotential

Effective overpotential was determined using the same method as described in references [4-5,7]. In short, the effective overpotential is defined as the difference between the equilibrium potential of the four electron, four proton reduction of O_2 to $2H_2O$ under catalytic conditions (E_{ORR}) and the catalyst $E_{1/2}$ (equations E.2). The equilibrium potential is determined using the standard potential of O_2/H_2O in MeCN ($E_{ORR}°$) and the Nernst law (equations E.3).

$$\eta_{\text{eff}} = E_{\text{ORR}} - E_{1/2} \qquad \text{(eq E.2)}$$

$$\eta_{\text{eff}} = E^{\text{o}}_{\text{ORR}} - E_{1/2} - \frac{2.303\text{RT}}{n_{cat}\text{F}}\log\left(\frac{\left[\text{H}_2\text{O}\right]^2\left[\text{A}^-\right]^4}{P_{\text{O}_2}\left[\text{HA}\right]^4}\right) - (0.0592\text{V})\text{p}K_a \qquad \text{(eq E.3)}$$

η_{eff} = effective overpotential

E_{ORR} = equilibrium potential under catalytic conditions

$E_{1/2}$ = iron(III/II) reduction potential

$E_{ORR}°$ = standard potential of O_2 to H_2O; reference 8

n_{cat} = number of electrons in one turnover; n_{cat} = 4 for O_2/H_2O (see reference 4)

pK_a = pK_a of the proton donor (HA); pK_a(acetic acid) = 23.51 in MeCN[9]

Because all four solutions were prepared identically, the differences in effective overpotential values for the atropisomers reflect differences in $E_{1/2}(Fe^{III}/Fe^{II})$ values under catalytic conditions. We note that buffering the solution with a 1:1 ratio of acid to conjugate base is important, which minimizes the effect of homoconjugation on the reported η_{eff} values.[4,10] For estimating η_{eff}, the concentration of water was taken to be 0.1 M, which was deliberately added to solution. The native concentration of H_2O was 15 ± 10 mM, from Karl Fischer titrations, which introduces an error in η_{eff} of about 20 mV. This error is smaller than the width of the data points reported in the Chapter 6.

E.3 Acetate Binding

E.3.1 Acetate Titrations and Optical Spectra

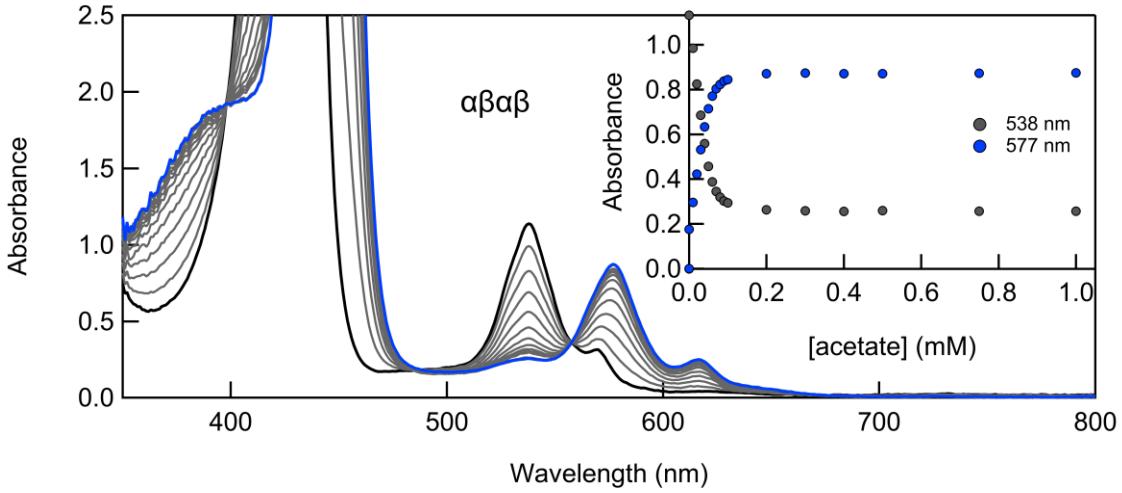

Figure E6. UV-vis spectra showing the titration of αβαβ $[Fe^{II}(o\text{-TMA})]^{4+}$ (43 μM) with [*n*-Bu_4N][AcO] at 20 °C. The sharp isosbestic points show that mass balance is preserved. Inset shows absorbance at 538 nm and 577 nm, the local maxima for $[Fe^{II}(o\text{-TMA})]^{4+}$ and $[Fe^{II}(o\text{-TMA})(AcO)]^{3+}$ respectively. Solution contained 0.1 M [*n*-Bu_4N][PF_6].

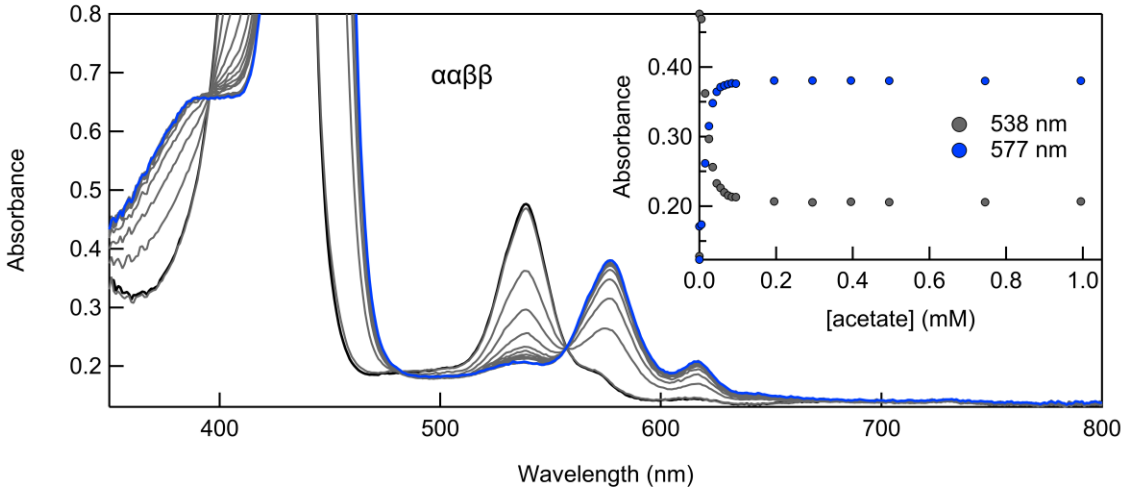

Figure E7. UV-vis spectra showing the titration of αααββ $[Fe^{II}(o\text{-TMA})]^{4+}$ (18 μM) with [*n*-Bu_4N][AcO] at 20 °C. The sharp isosbestic points show that mass balance is preserved. Inset shows absorbance at 538 nm and 577 nm, the local maxima for $[Fe^{II}(o\text{-TMA})]^{4+}$ and $[Fe^{II}(o\text{-TMA})(AcO)]^{3+}$ respectively. Solution contained 0.1 M [*n*-Bu_4N][PF_6].

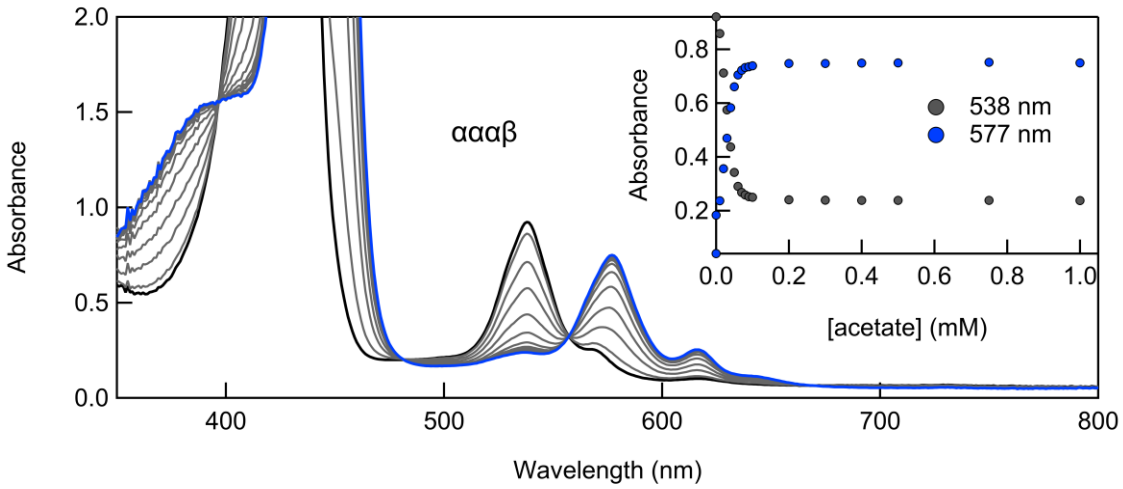

Figure E8. UV-vis spectra showing the titration of αααβ $[Fe^{II}(o\text{-TMA})]^{4+}$ (35 μM) with [*n*-Bu_4N][AcO] at 20 °C. The sharp isosbestic points show that mass balance is preserved. Inset shows absorbance at 538 nm and 577 nm, the local maxima for $[Fe^{II}(o\text{-TMA})]^{4+}$ and $[Fe^{II}(o\text{-TMA})(AcO)]^{3+}$ respectively. Solution contained 0.1 M [*n*-Bu_4N][PF_6].

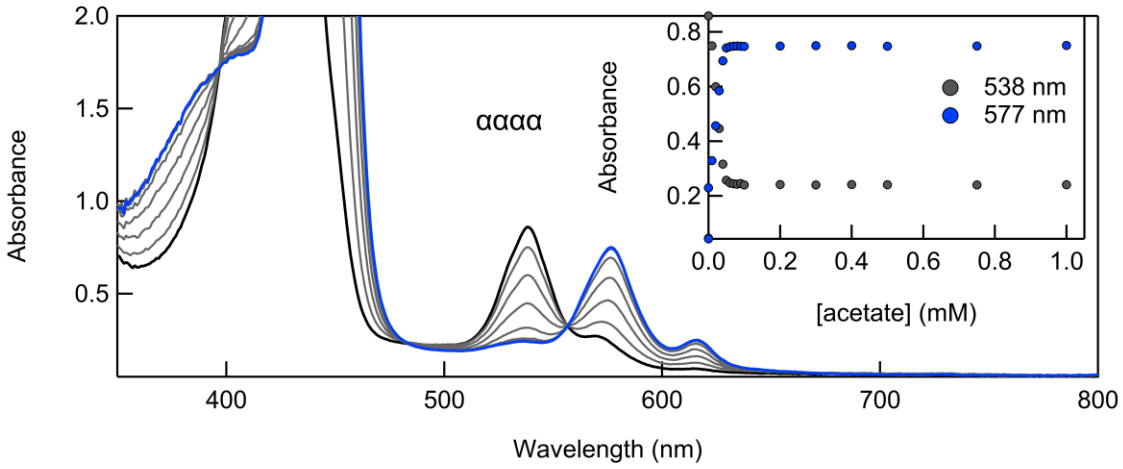

Figure E9. UV-vis spectra showing the titration of αααα $[Fe^{II}(o\text{-TMA})]^{4+}$ (33 μM) with [*n*-Bu_4N][AcO] at 20 °C. The sharp isosbestic points show that mass balance is preserved. Inset shows absorbance at 538 nm and 577 nm, the local maxima for $[Fe^{II}(o\text{-TMA})]^{4+}$ and $[Fe^{II}(o\text{-TMA})(AcO)]^{3+}$ respectively. Solution contained 0.1 M [*n*-Bu_4N][PF_6].

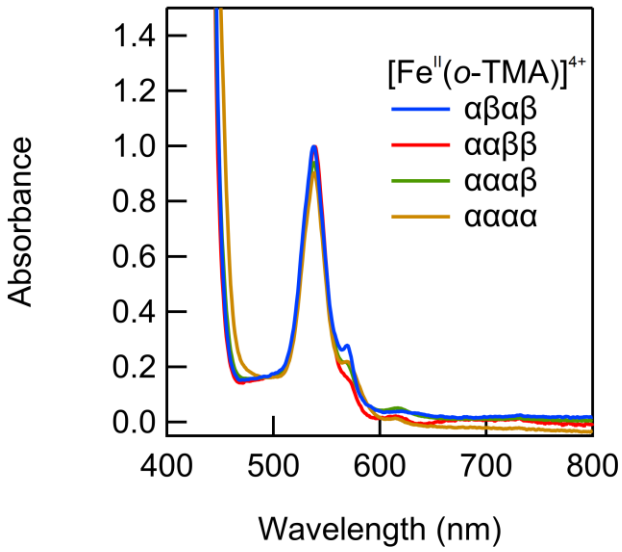

Figure E10. UV-vis spectra of the four [Fe^{II}(*o*-TMA)]$^{4+}$ atropisomers (~40 μM) in MeCN containing 0.1 M [*n*-Bu$_4$N][PF$_6$].

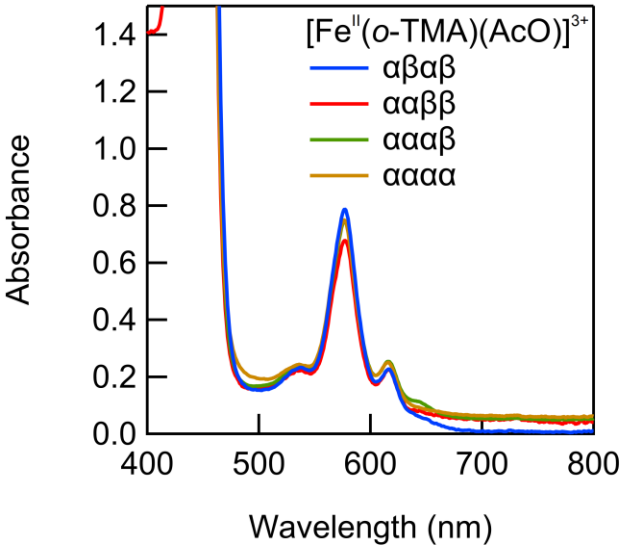

Figure E11. UV-vis spectra of the four [Fe^{II}(*o*-TMA)(AcO)]$^{3+}$ atropisomers (~40 μM) in MeCN containing 0.1 M [*n*-Bu$_4$N][PF$_6$] and 1.0 mM [*n*-Bu$_4$N][AcO].

E.3.2 Variable Temperature Acetate Binding

In a typical experiment, a small amount of $[Fe^{II}(o\text{-TMA})]^{4+}$ was combined with 1.0 mM [*n*-Bu_4N][AcO] in MeCN containing 0.1 M [*n*-Bu_4N][PF_6]. This mixture was loaded into a Kontes quarts cuvette in the glovebox before being placed in the cryostat. The sample was then cooled to −40 °C, with stirring, before a spectrum was collected. The sample was heated incrementally, with optical spectra being collected at several different temperatures. The optical spectra showed sharp isosbestic points, indicating mass balance.

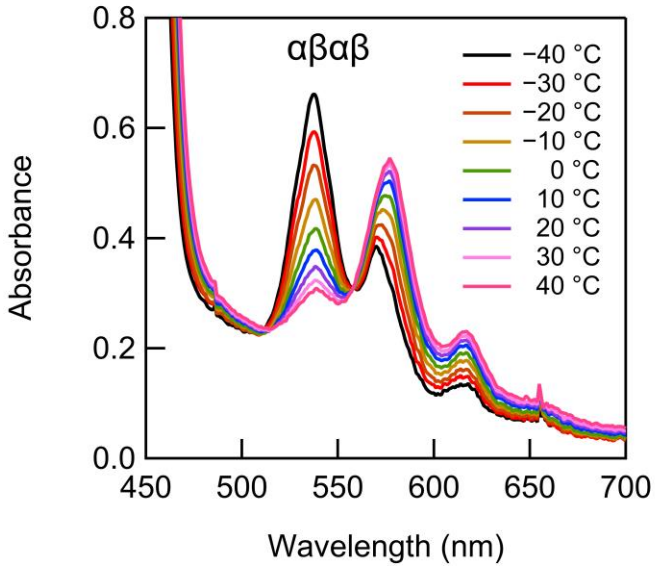

Figure E12. Variable temperature UV-vis spectra of 35μM αβαβ $[Fe^{II}(o\text{-TMA})]^{4+}$ + 1.0 mM [*n*-Bu_4N] [AcO] in MeCN containing 0.1 M [*n*-Bu_4N][PF_6]. Temperatures labeled in figure legend.

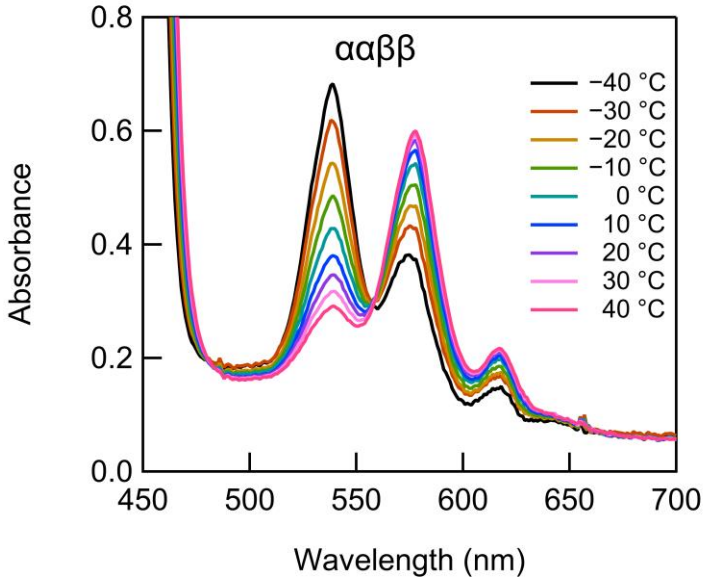

Figure E13. Variable temperature UV-vis spectra of 36 μM αααββ $[Fe^{II}(o\text{-TMA})]^{4+}$ + 1.0 mM [*n*-Bu_4N] [AcO] in MeCN containing 0.1 M [*n*-Bu_4N][PF_6]. Temperatures labeled in figure legend.

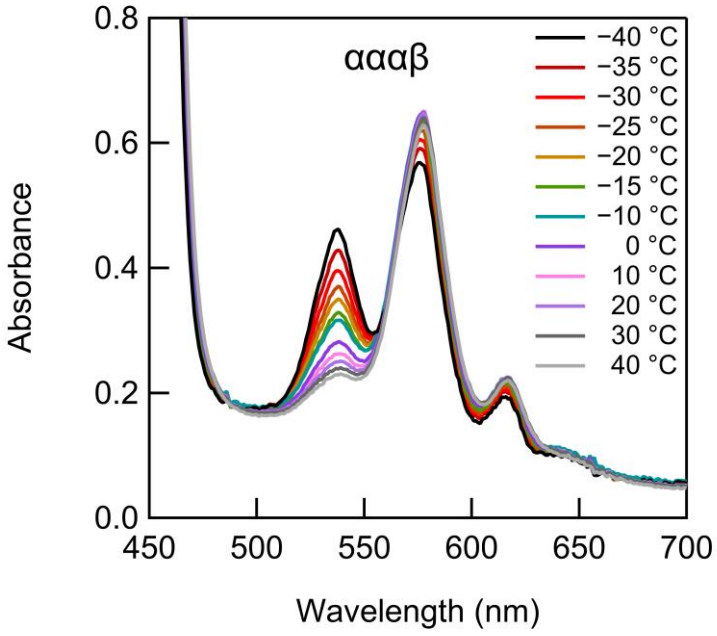

Figure E14. Variable temperature UV-vis spectra of 38 μM αααβ $[Fe^{II}(o\text{-TMA})]^{4+}$ + 1.0 mM [*n*-Bu_4N] [AcO] in MeCN containing 0.1 M [*n*-Bu_4N][PF_6]. Temperatures labeled in figure legend.

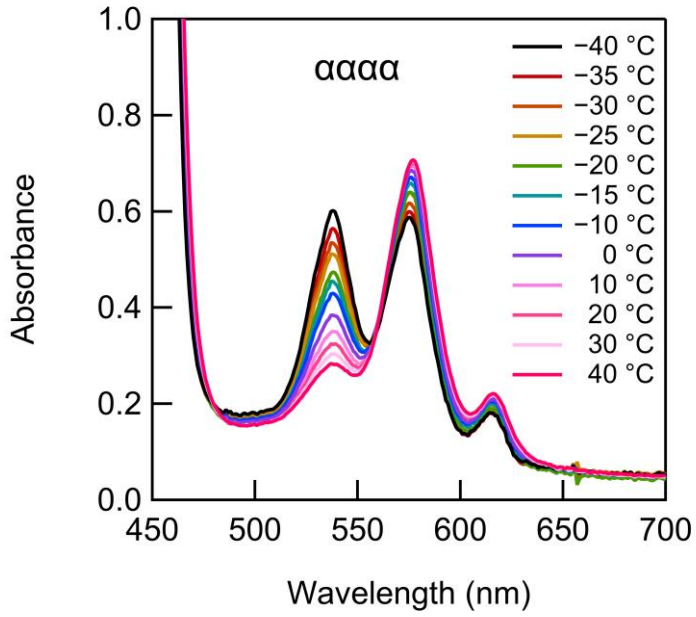

Figure E15. Variable temperature UV-vis spectra of 40 μM αααα $[Fe^{II}(o\text{-TMA})]^{4+}$ + 1.0 mM [*n*-Bu_4N] [AcO] in MeCN containing 0.1 M [*n*-Bu_4N][PF_6]. Temperatures labeled in figure legend.

Table E1. Acetate binding constants and conditions. [a]

Atropisomer	Temperature (°C)	K_{AcO} (M^{-1})	ln(K_{AcO}) (M^{-1})
αβαβ	−40	(4.1-7.4)×10^3	8.6 ± 0.3
αβαβ	−30	(0.6-1.1)×10^3	9.0 ± 0.3
αβαβ	−20	(0.9-1.6)×10^4	9.4 ± 0.3
αβαβ	−10	(1.2-2.3)×10^4	9.7 ± 0.3
αβαβ	0	(1.8-3.3)×10^4	10.1 ± 0.3
αβαβ	10	(2.6-4.7)×10^4	10.5 ± 0.3
αβαβ	20	(3.2-5.9)×10^4	10.7 ± 0.3
αβαβ	30	(4.5-8.2)×10^4	11.0 ± 0.3
αβαβ	40	(6.7-1.2)×10^5	11.4 ± 0.3
αααβ	−40	(0.6-1.0)×10^4	8.9 ± 0.3
αααβ	−30	(0.8-1.5)×10^4	9.3 ± 0.3
αααβ	−20	(1.2-2.3)×10^4	9.7 ± 0.3
αααβ	−10	(1.8-3.3)×10^4	10.1 ± 0.3
αααβ	0	(2.6-4.7)×10^4	10.5 ± 0.3
αααβ	10	(3.7-6.7)×10^4	10.8 ± 0.3
αααβ	20	(5.3-9.5)×10^4	11.2 ± 0.3
αααβ	30	(0.7-1.3)×10^5	11.5 ± 0.3
αααβ	40	(1.0-1.9)×10^5	11.8 ± 0.3
αααβ	−40	(2.0-3.6)×10^4	10.2 ± 0.3
αααβ	−35	(2.4-4.4)×10^4	10.4 ± 0.3
αααβ	−30	(3.0-5.5)×10^4	10.6 ± 0.3
αααβ	−25	(3.9-7.1)×10^4	10.9 ± 0.3
αααβ	−20	(4.8-8.8)×10^4	11.1 ± 0.3
αααβ	−15	(0.6-1.0)×10^5	11.2 ± 0.3
αααβ	−10	(0.7-1.2)×10^5	11.4 ± 0.3
αααβ	0	(0.8-1.5)×10^5	11.6 ± 0.3
αααβ	10	(1.0-1.9)×10^5	11.8 ± 0.3
αααβ	20	(1.4-2.5)×10^5	12.1 ± 0.3
αααβ	30	(2.0-3.6)×10^5	12.5 ± 0.3
αααβ	40	(2.5-4.6)×10^5	12.7 ± 0.3
αααα	−40	(1.1-2.0)×10^4	9.6 ± 0.3
αααα	−35	(1.3-2.4)×10^4	9.8 ± 0.3
αααα	−30	(1.5-2.7)×10^4	9.9 ± 0.3
αααα	−25	(1.7-3.1)×10^4	10.0 ± 0.3
αααα	−20	(2.1-3.8)×10^4	10.2 ± 0.3
αααα	−15	(2.4-4.4)×10^4	10.4 ± 0.3
αααα	−10	(2.9-5.2)×10^4	10.6 ± 0.3
αααα	0	(3.6-6.7)×10^4	10.8 ± 0.3
αααα	10	(4.8-8.7)×10^4	11.1 ± 0.3
αααα	20	(0.6-1.1)×10^5	11.3 ± 0.3
αααα	30	(0.8-1.5)×10^5	11.6 ± 0.3
αααα	40	(1.0-1.8)×10^5	11.8 ± 0.3

[a] All data collected in MeCN containing 0.1 M [*n*-Bu_4N][PF_6]. The supporting electrolyte was added *i*) to minimize deviations due to changes in ionic strength and *ii*) to match electrochemical conditions. Error comes from fitting ratio of $[Fe^{II}(o\text{-TMA})]^{4+}$ and $[Fe^{II}(o\text{-TMA})(AcO)]^{3+}$.

E.4 CO_2 Reduction Cyclic Voltammetry

E.4.1 Voltammetry of Fe(o-TMA) Isomers

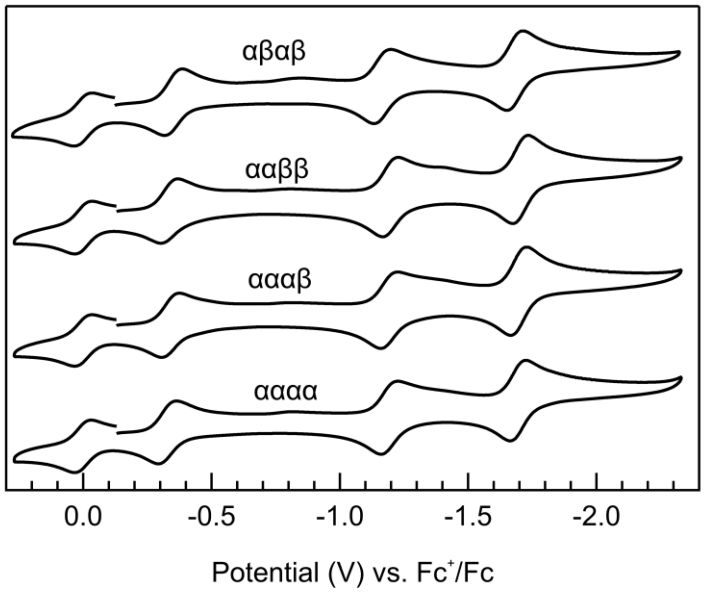

Figure E16. Cyclic voltammograms of the Fe(*o*-TMA) atropisomers (1 atm Ar) in DMF containing 0.1 M [*n*-Bu_4N][PF_6]. Sequential reductions correspond to Fe^{III}/Fe^{II}, Fe^{II}/Fe^{I}, and Fe^{I}/Fe^{0} redox couples. Ferrocene is the couple centered at 0.0 V. Data first reported in reference 2.

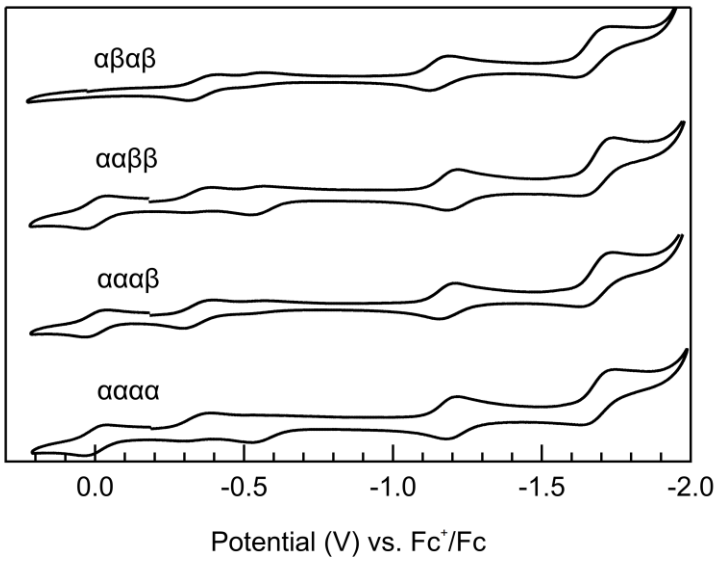

Figure E17. Cyclic voltammograms of the Fe(*o*-TMA) atropisomers (1 atm Ar) in DMF containing 0.1 M [*n*-Bu_4N][PF_6], 0.1 M H_2O, and 3.0 M PhOH. There are very small differences between the $E_{1/2}(Fe^{II}/Fe^{I})$ and $E_{1/2}(Fe^{I}/Fe^{0})$ values of the various atropisomers. There is more deviation in the Fe^{III}/Fe^{II} couple, which is known to engage in dynamic ligand binding.[11] Ferrocene is the couple centered at 0.0 V for the $\alpha\alpha\beta\beta$, $\alpha\alpha\alpha\beta$, and $\alpha\alpha\alpha\alpha$ samples.

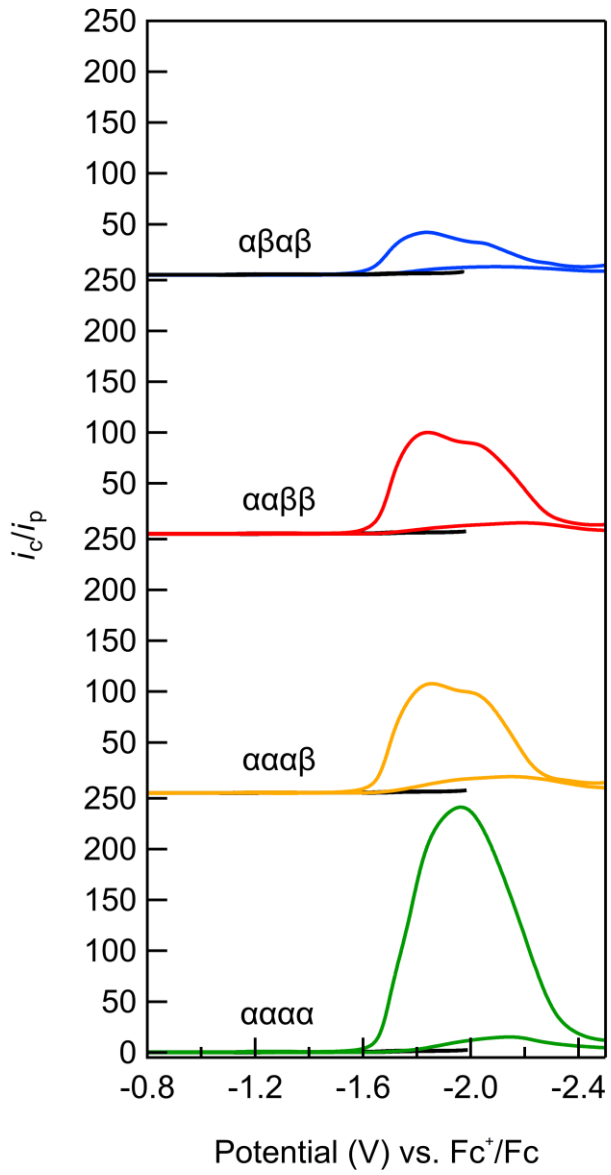

Figure E18. Cyclic voltammograms of the Fe(*o*-TMA) atropisomers (1 atm CO_2) in DMF containing 0.1 M [*n*-Bu_4N][PF_6], 0.1 M H_2O, and 3.0 M PhOH. Currents were divided by the noncatalytic peak current of the Fe^{II}/Fe^{I} couple, which is constant under both Ar and CO_2. Black traces are voltammograms collected under argon (see **Figure E17**).

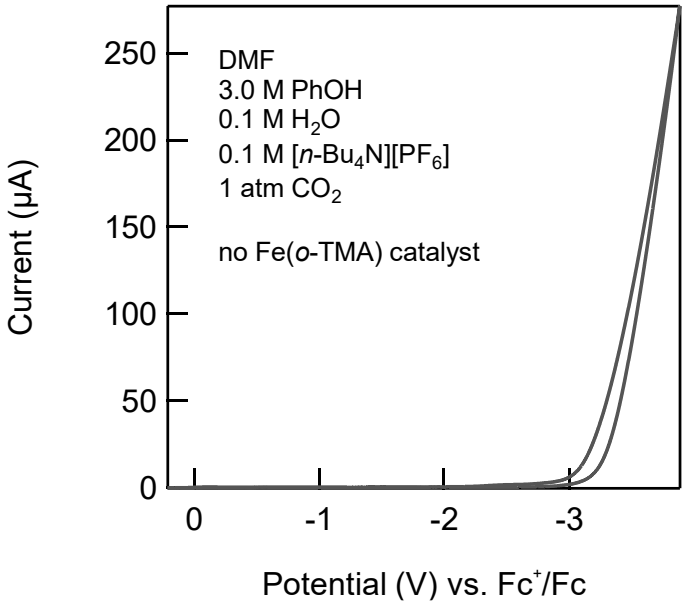

Figure E19. Cyclic voltammogram of a solution of DMF containing 0.1 M [*n*-Bu_4N][PF_6], 0.1 M H_2O, and 3.0 M PhOH under 1 atm CO_2. No catalyst was present. The large current at potentials more negative than −3.0 V corresponds to proton reduction on glassy carbon under these conditions.

E.4.2 Internal Resistance Measurements

The CO_2 voltammetry data collected at fast scan rates was corrected for internal resistance using the chronoamperometric method reported by Dempsey et al. in reference [12]. In short, this method measures the solution resistance by fitting the rapid current decay of a chronoamperogram, in which a polarized electrode (e.g. at −0.15 V vs. Fc^+/Fc) is jumped to another potential (ΔE). The current decay was fit to an exponential function to obtain the current at time zero (i_0), **Figure E20**-**Figure E21**. From Ohm's law, the uncompensated resistance can then be calculated using the values of i_0 and ΔE (**Table E2**).

As shown by Dempsey et al. using a dummy cell (a circuit used to mock up an electrochemical cell) this method yields internal resistance values that are typically within 10% of the actual resistance.[12] On the CH Instruments potentiostat used in Chapter 6, these fits yield internal resistance values that are about 30% larger than those indicated by the potentiostat.

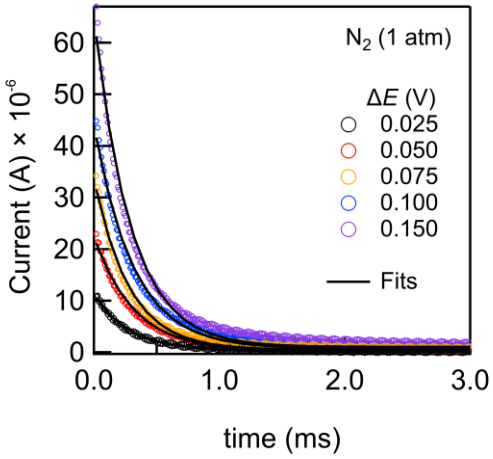

Figure E20. Chronoamperograms and exponential fits for several different values of ΔE. Data collected using the Ar-saturated solutions from **Figure E17**. Initial potential was held at −0.15 V, in a region where no faradaic process occurred.

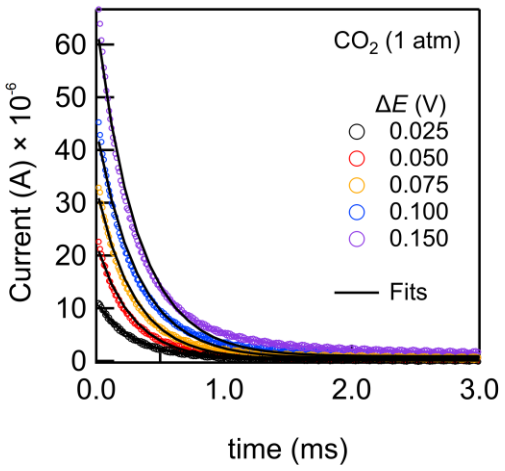

Figure E21. Chronoamperograms and exponential fits for several different values of ΔE. Data collected using the CO_2-saturated solutions from **Figure E18**. Initial potential was held at −0.15 V, in a region where no faradaic process occurred.

Table E2. Summary of internal resistance measurements [a]

Gas	Initial Potential (V)	ΔE (V)	y_0	A	i_0 (A)	Resistance (Ω)
Ar	−0.15	0.025	1.09×10^{-7}	1.11×10^{-5}	1.11×10^{-5}	2.26×10^{3}
Ar	−0.15	0.050	2.63×10^{-7}	2.22×10^{-5}	2.24×10^{-5}	2.23×10^{3}
Ar	−0.15	0.075	4.46×10^{-7}	3.34×10^{-5}	3.39×10^{-5}	2.21×10^{3}
Ar	−0.15	0.100	7.09×10^{-7}	4.36×10^{-5}	4.43×10^{-5}	2.26×10^{3}
Ar	−0.15	0.150	1.02×10^{-6}	6.46×10^{-5}	6.56×10^{-5}	2.29×10^{3}
				Average		$(2.25 \pm 0.05)\times10^{3}$
CO_2	−0.15	0.025	8.99×10^{-8}	1.10×10^{-5}	1.11×10^{-5}	2.26×10^{3}
CO_2	−0.15	0.050	1.95×10^{-7}	2.22×10^{-5}	2.23×10^{-5}	2.24×10^{3}
CO_2	−0.15	0.075	2.94×10^{-7}	3.27×10^{-5}	3.30×10^{-5}	2.27×10^{3}
CO_2	−0.15	0.100	4.88×10^{-7}	4.38×10^{-5}	4.42×10^{-5}	2.26×10^{3}
CO_2	−0.15	0.150	8.86×10^{-7}	6.40×10^{-5}	6.49×10^{-5}	2.31×10^{3}
				Average		$(2.27 \pm 0.05)\times10^{3}$

[a] All data collected in DMF containing 0.1 M [*n*-Bu_4N][PF_6], 3.0 M PhOH, and 0.1 M H_2O. Values come from fits to chronoamperometric data, **Figure E20**-**Figure E21**.

E.4.3 Fast Scan Rate Experiments

All of the following experiments refer to DMF solutions (1.0 atm CO_2) containing 3.0 M PhOH, 0.1 M H_2O, 0.1 M [*n*-Bu_4N][PF_6] and one of the four Fe(*o*-TMA) catalysts. In all cases, these voltammetry data were collected using a 1 mm glassy carbon working electrode, which was polished between scans.

Several steps were required to process the data and correct for internal resistance, capacitive currents, and non-catalytic, faradaic currents. The following pages show each stage of the data processing. All four isomers were treated identically.

The general workflow involved three steps:

i. *Correcting for* internal *resistance (**A** → **B** in the following Figures)*. The internal resistance was separately measured and determined using the method described above (**Figure E20**-**Figure E21**). The average uncompensated resistance was 2250 Ω. Using this value and Ohm's law (ΔE = i×R), the potentials for each voltammogram were first corrected for internal resistance. The resulting voltammograms are less broad and more closely resemble the canonical S-shaped behavior.

ii. *Fitting and subtracting capacitive currents (**B** → **C** in the following Figures*). Each of the iR corrected voltammograms were fit between −0.1 V and −0.4 V to yield the non-faradaic, capacitive current. This linear fit was subtracted from each of the respective voltammograms. The resulting data show only faradaic processes.

iii. *Subtracting non-catalytic, faradaic currents and normalizing to i_p (**C** → **D** in the following Figures)*. Neither the Fe^{III}/Fe^{II} or Fe^{II}/Fe^{I} reduction events contribute to catalysis and were thus subtracted from the voltammograms. Thus, the current obtained at −1.5 V [between $E_{1/2}(Fe^{II}/Fe^{I})$ and $E_{1/2}(Fe^{I}/Fe^{0})$] was subtracted from each of the voltammograms. The resulting data was then divided by the peak of the non-catalytic Fe^{II}/Fe^{I} redox couple, as described above.

The advantage of this workflow is that the reported plateau currents yield lower-limit estimations of TOF_{max}. The disadvantage of this approach is that error is introduced to the value of

η_{eff}, which depends on the accuracy of the internal resistance. As shown in **Table E2**, the error in the internal resistance is <10%. This corresponds to a maximum error in η_{eff} of ca. 60 mV for the highest current experiments ($\alpha\alpha\alpha\alpha$ at 300 V s^{-1}).

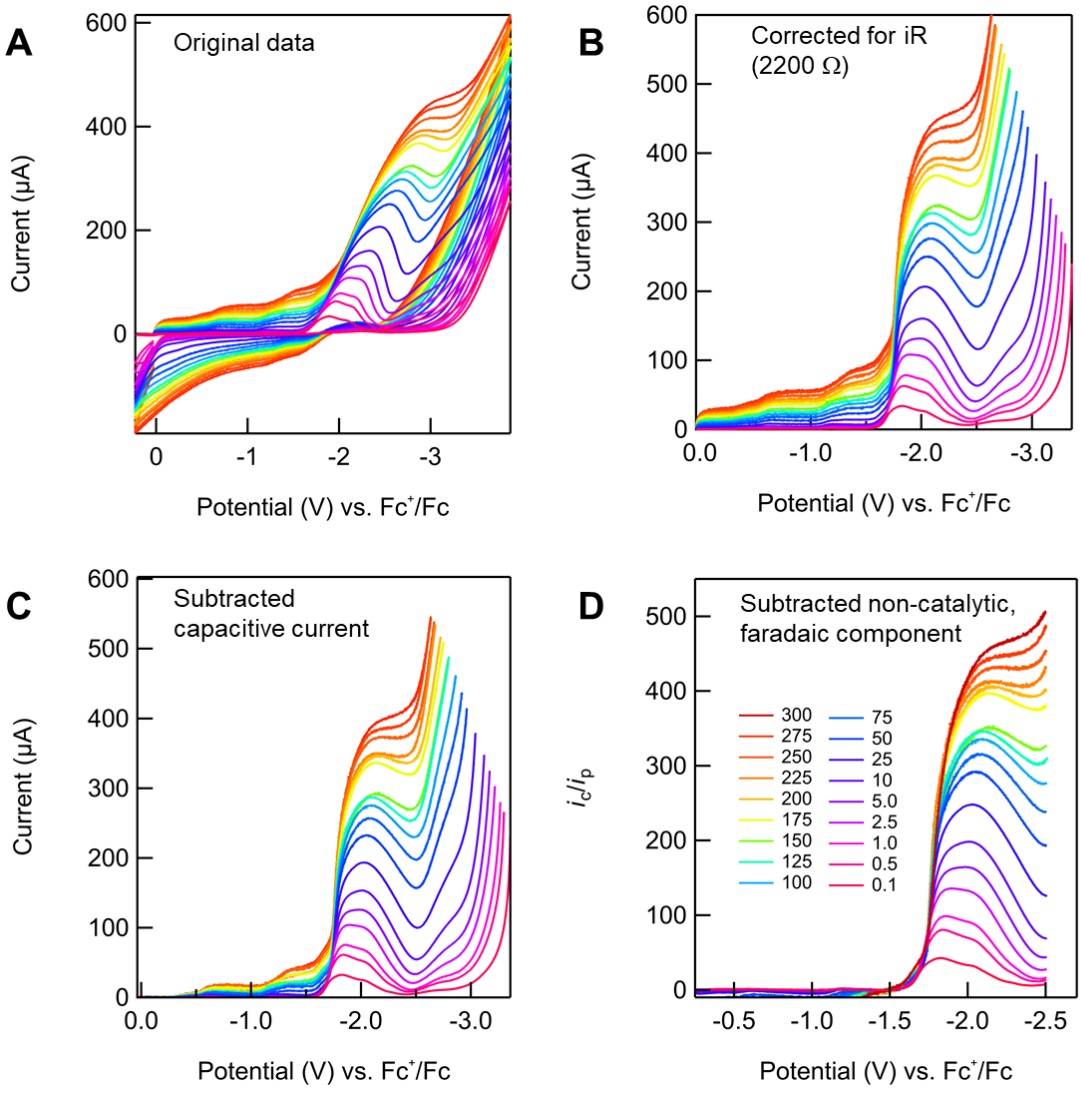

Figure E22. Cyclic voltammetry data for CO_2 reduction by $\alpha\beta\alpha\beta$ Fe(*o*-TMA). Conditions described above. Data processing: (**A**) raw data; (**B**) corrected for internal resistance (2200 Ω); (**C**) corrected for capacitive current; (**D**) subtracted currents due to Fe^{III}/Fe^{II} and Fe^{II}/Fe^{I} reduction and normalization of the data to i_p (Fe^{II}/Fe^{I} couple at 0.1 V s^{-1}).

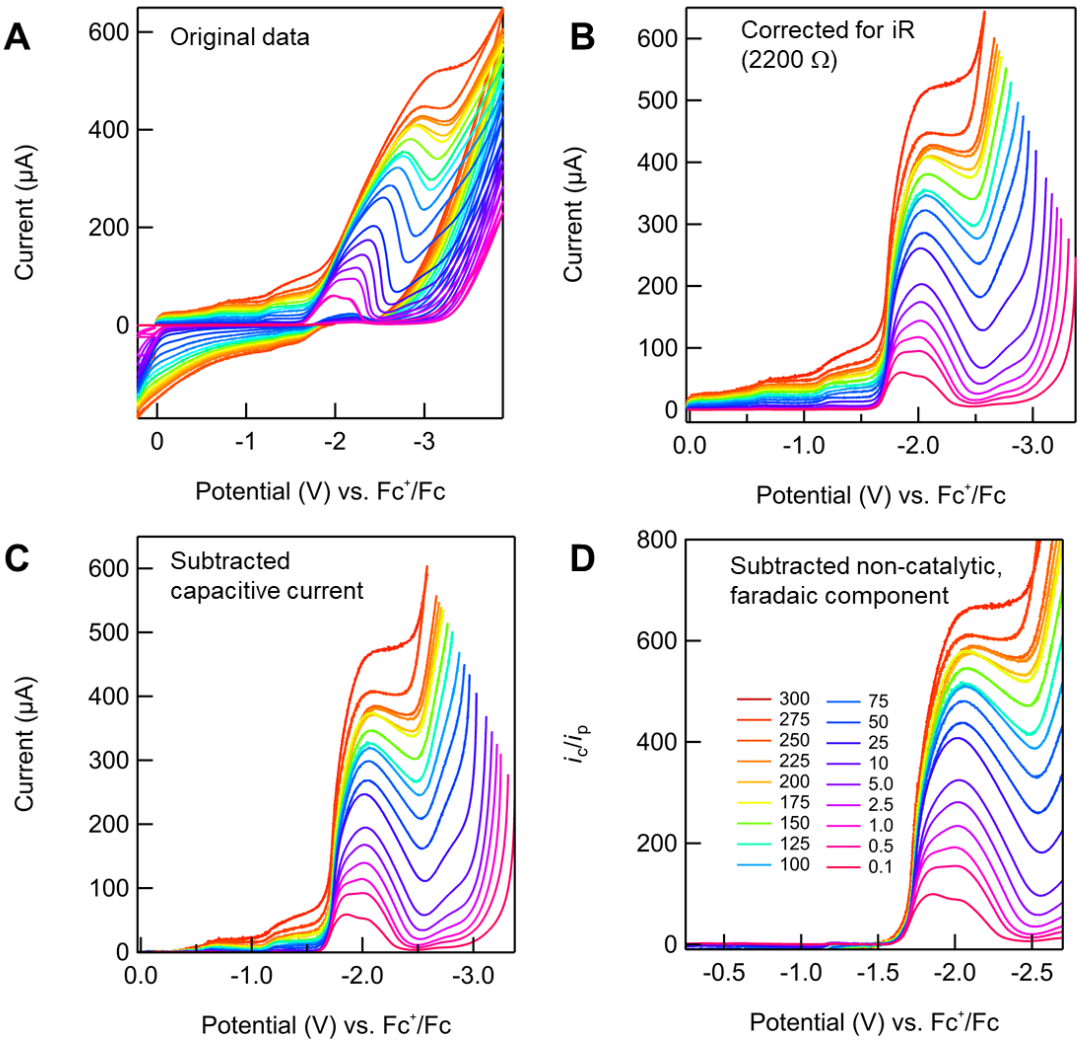

Figure E23. Cyclic voltammetry data for CO_2 reduction by αααββ Fe(*o*-TMA). Conditions described above. Data processing: (**A**) raw data; (**B**) corrected for internal resistance (2200 Ω); (**C**) corrected for capacitive current; (**D**) subtracted currents due to Fe^{III}/Fe^{II} and Fe^{II}/Fe^{I} reduction and normalization of the data to i_p (Fe^{II}/Fe^{I} couple at 0.1 V s^{-1}).

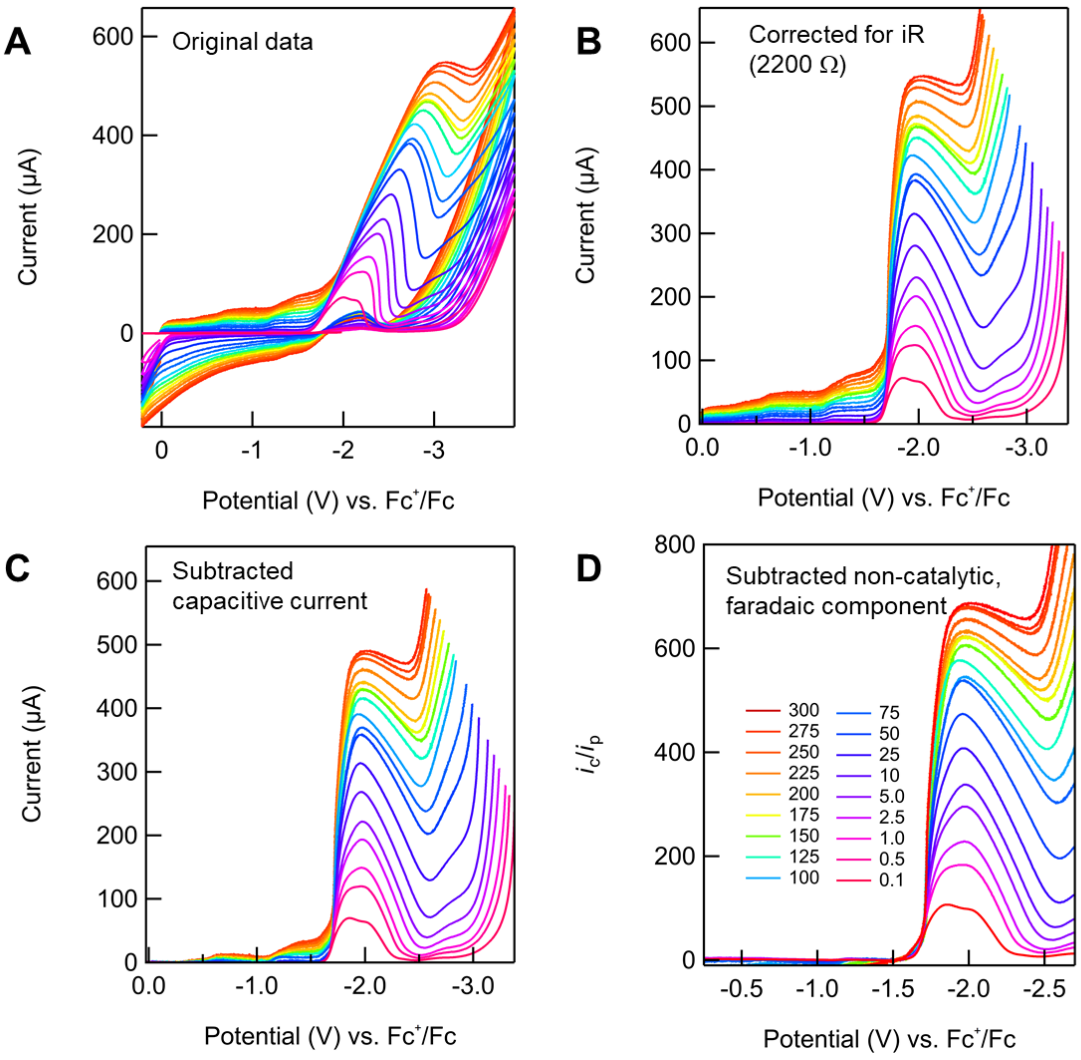

Figure E24. Cyclic voltammetry data for CO_2 reduction by αααβ Fe(*o*-TMA). Conditions described above. Data processing: (**A**) raw data; (**B**) corrected for internal resistance (2200 Ω); (**C**) corrected for capacitive current; (**D**) subtracted currents due to Fe^{III}/Fe^{II} and Fe^{II}/Fe^{I} reduction and normalization of the data to i_p (Fe^{II}/Fe^{I} couple at 0.1 V s^{-1}).

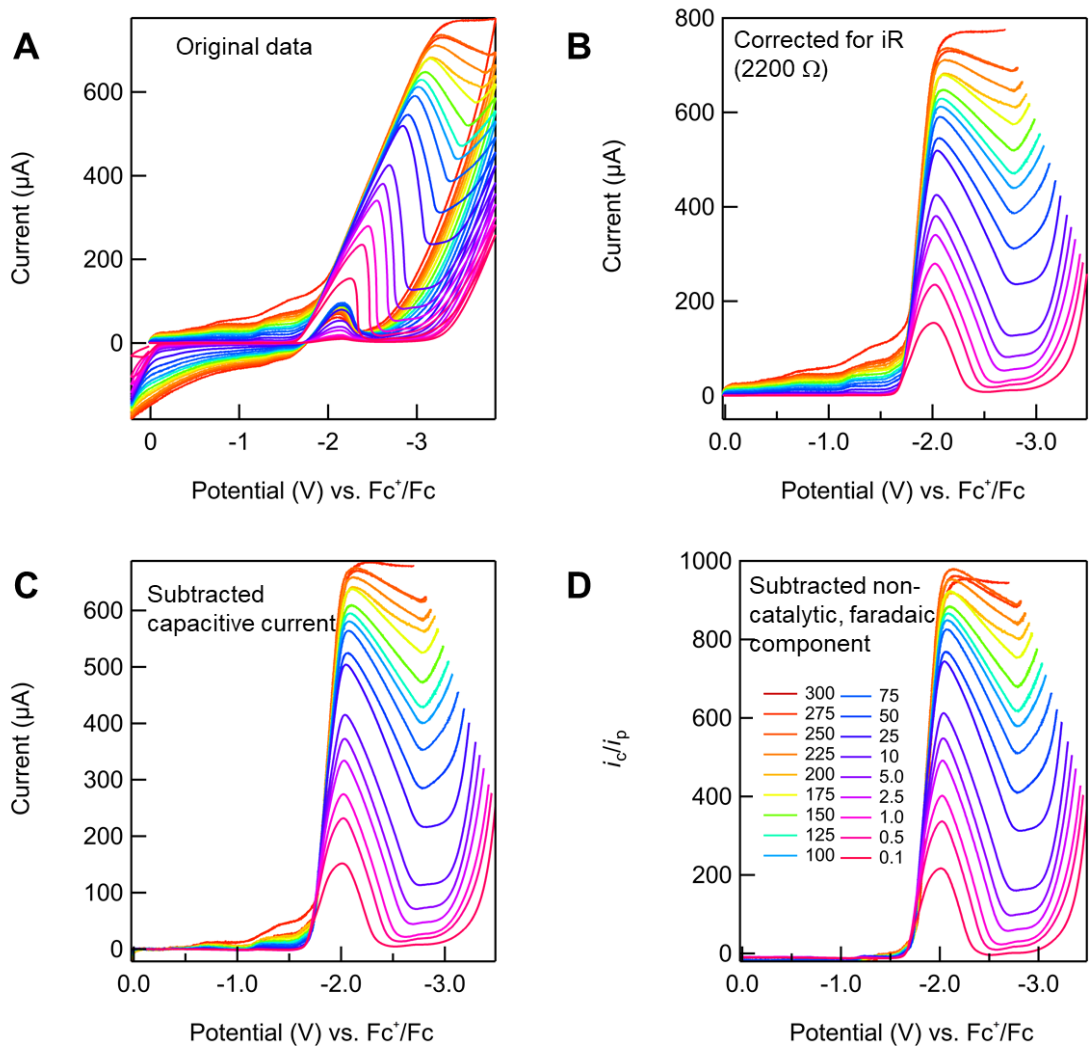

Figure E25. Cyclic voltammetry data for CO_2 reduction by αααα Fe(*o*-TMA). Conditions described above. Data processing: (**A**) raw data; (**B**) corrected for internal resistance (2200 Ω); (**C**) corrected for capacitive current; (**D**) subtracted currents due to Fe^{III}/Fe^{II} and Fe^{II}/Fe^{I} reduction and normalization of the data to i_p (Fe^{II}/Fe^{I} couple at 0.1 V s^{-1}).

E.4.4 Simulated Curves (Determining E_2)

Following the method of Costentin and Savéant, the value of E_2 for an E_1CE_2C' mechanism can be obtained by mathematically generating S-shaped current-potential responeses from the FOWA equation (eq E2, above) and overlaying them onto the experimental, catalytic voltammograms. Assuming that TOF_{max} is known, as was the case here, S-shaped waves were generated for each of the corresponding TOF_{max} values and atropisomers. The values of $E_{cat/2}$ were then varied by guess and check such that the mathematical current-potential responses were best aligned with the experimental voltammograms. A generous error of 40 mV was assumed using this fitting method to account for non-ideal shapes in the experimental voltammograms. Even with this error, however, relative values of E_2 are all close to one another for the series of atropisomers.

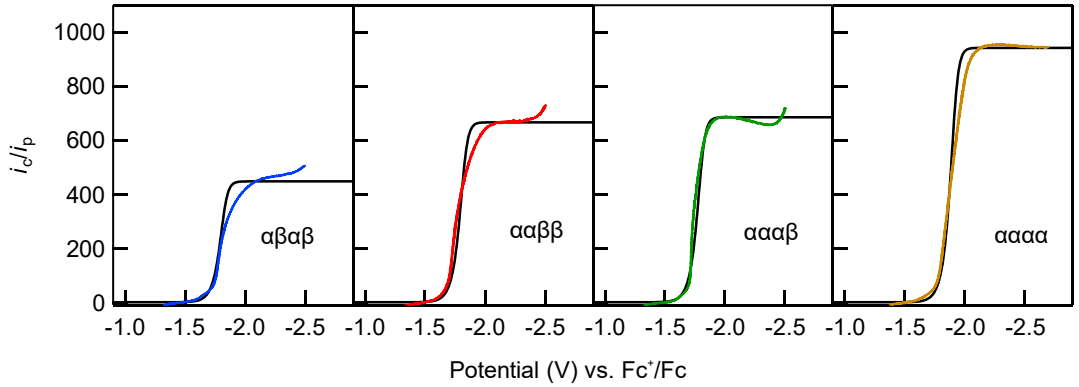

Figure E26. Experimental linear sweep voltammograms for CO_2 reduction by the Fe(*o*-TMA) atropisomers and simulated fits. Data collected at 300 V s^{-1} and corrected using the methods described above. Fits were simulated using TOF_{max} values (from plateaus) and the FOWA expression in **eq E1**, above. Potential at half-plateau current ($E_{pl/2}$) was taken to approximate $E°_{Q'/B}$ and thus E_2 (see Chapter 6).

E.4.5 CO_2 Reduction by Fe(o-TMA) at Various [PhOH]

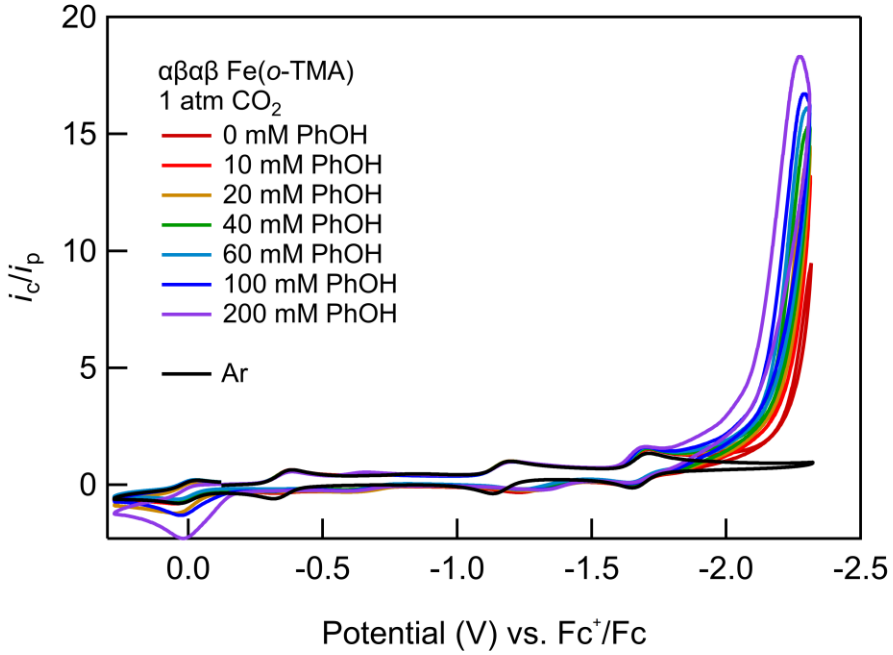

Figure E27. Cyclic voltammograms of CO_2 reduction by αβαβ Fe(*o*-TMA) in DMF containing 0.1 M H_2O, 0.1 M [*n*-Bu_4N][PF_6] and varying concentrations of phenol (indicated in legend).

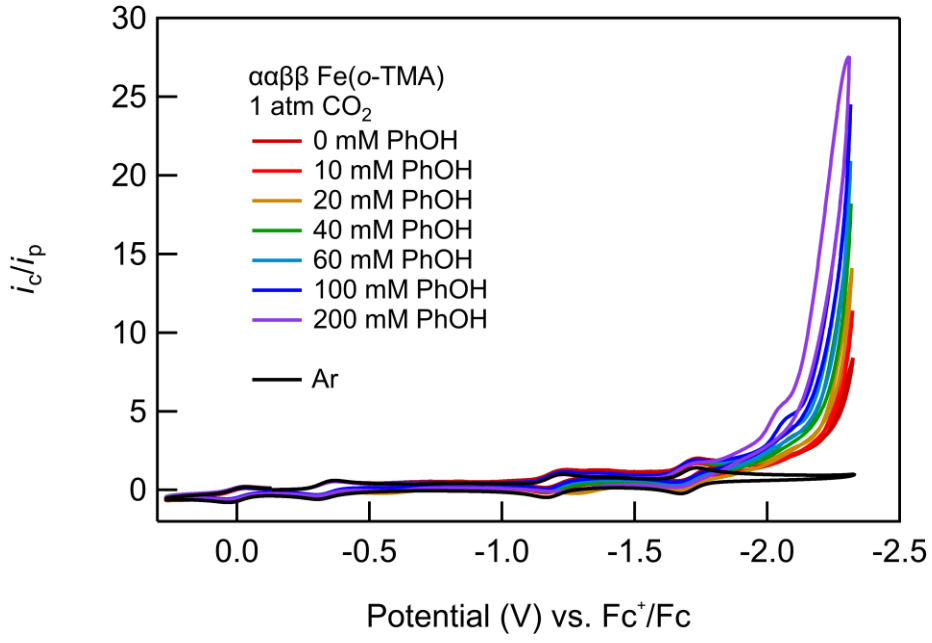

Figure E28. Cyclic voltammograms of CO_2 reduction by αααββ Fe(*o*-TMA) in DMF containing 0.1 M H_2O, 0.1 M [*n*-Bu_4N][PF_6] and varying concentrations of phenol (indicated in legend).

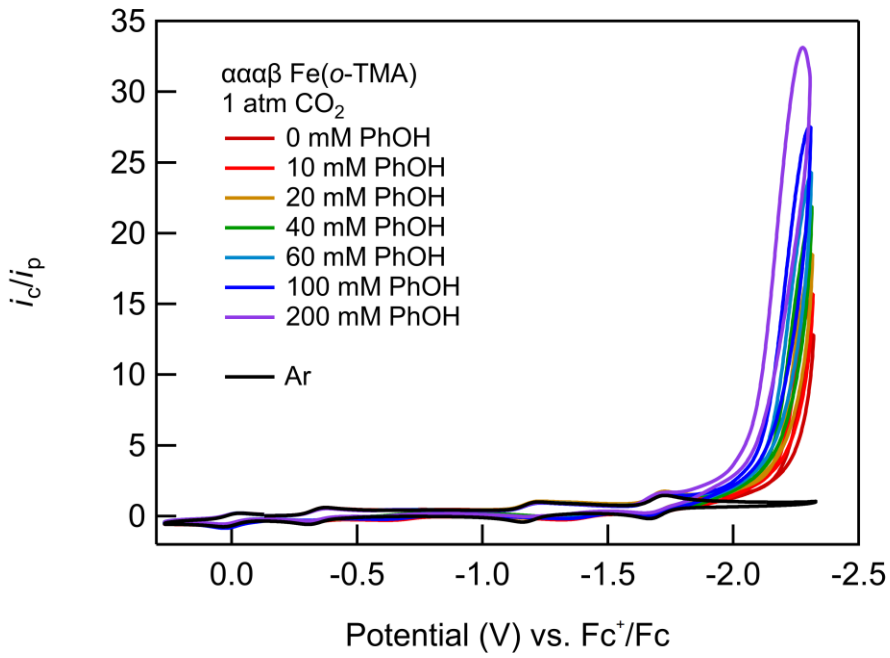

Figure E29. Cyclic voltammograms of CO_2 reduction by αααβ Fe(*o*-TMA) in DMF containing 0.1 M H_2O, 0.1 M [*n*-Bu_4N][PF_6] and varying concentrations of phenol (indicated in legend).

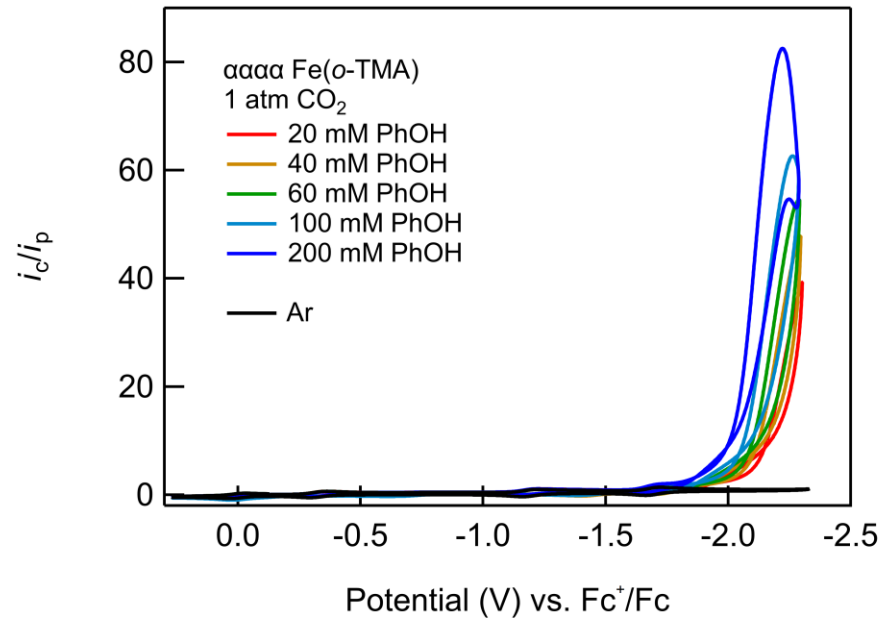

Figure E30. Cyclic voltammograms of CO_2 reduction by αααα Fe(*o*-TMA) in DMF containing 0.1 M H_2O, 0.1 M [*n*-Bu_4N][PF_6] and varying concentrations of phenol (indicated in legend).

E.5 References

1. Martin, D. J.; Johnson, S. I.; Mercado, B. Q.; Raugei, S.; Mayer, J. M., Intramolecular Electrostatic Effects on O_2, CO_2, and Acetate Binding to a Cationic Iron Porphyrin. *Inorg. Chem.* **2020,** *59* (23), 17402-17414.
2. Martin, D. J.; Mercado, B. Q.; Mayer, J. M., All Four Atropisomers of Iron(III) and Iron(II) Tetra(*o*-*N*,*N*,*N*-trimethylanilinium)porphyrin. In preparation.
3. Elgrishi, N.; Rountree, K. J.; McCarthy, B. D.; Rountree, E. S.; Eisenhart, T. T.; Dempsey, J. L., A Practical Beginner's Guide to Cyclic Voltammetry. *J. Chem. Educ.* **2018,** *95* (2), 197-206.
4. Martin, D. J.; Mercado, B. Q.; Mayer, J. M., Combining scaling relationships overcomes rate versus overpotential trade-offs in O_2 molecular electrocatalysis. *Sci. Adv.* **2020,** *6* (11), eaaz3318.
5. Pegis, M. L.; McKeown, B. A.; Kumar, N.; Lang, K.; Wasylenko, D. J.; Zhang, X. P.; Raugei, S.; Mayer, J. M., Homogenous Electrocatalytic Oxygen Reduction Rates Correlate with Reaction Overpotential in Acidic Organic Solutions. *ACS Cent. Sci.* **2016,** *2* (11), 850-856.
6. Pegis, M. L.; Martin, D. J.; Wise, C. F.; Brezny, A. C.; Johnson, S. I.; Johnson, L. E.; Kumar, N.; Raugei, S.; Mayer, J. M., Mechanism of Catalytic O_2 Reduction by Iron Tetraphenylporphyrin. *J. Am. Chem. Soc.* **2019,** *141*, 8315-8326.
7. Martin, D. J.; Wise, C. F.; Pegis, M. L.; Mayer, J. M., Developing Scaling Relationships for Molecular Electrocatalysis through Studies of Fe-Porphyrin-Catalyzed O_2 Reduction. *Acc. Chem. Res.* **2020,** *53* (5), 1056-1065.
8. Pegis, M. L.; Roberts, J. A. S.; Wasylenko, D. J.; Mader, E. A.; Appel, A. M.; Mayer, J. M., Standard Reduction Potentials for Oxygen and Carbon Dioxide Couples in Acetonitrile and *N*,*N*′-Dimethylformamide. *Inorg. Chem.* **2015,** *54* (24), 11883-11888.
9. Kütt, A.; Leito, I.; Kaljurand, I.; Sooväli, L.; Vlasov, V. M.; Yagupolskii, L. M.; Koppel, I. A., A Comprehensive Self-Consistent Spectrophotometric Acidity Scale of Neutral Brønsted Acids in Acetonitrile. *J. Org. Chem.* **2006,** *71* (7), 2829-2838.
10. Appel, A. M.; Helm, M. L., Determining the Overpotential for a Molecular Electrocatalyst. *ACS Catal.* **2014,** *4* (2), 630-633.
11. Lexa, D.; Rentien, P.; Savéant, J. M.; Xu, F., Methods for Investigating the Mechanistic and Kinetic Role of Ligand Exchange Reactions in Coordination Electrochemistry. *J. Electroanal. Chem.* **1985,** *191* (2), 253-279.
12. McCarthy, B. D.; Martin, D. J.; Rountree, E. S.; Ullman, A. C.; Dempsey, J. L., Electrochemical reduction of brønsted acids by glassy carbon in acetonitrile-implications for electrocatalytic hydrogen evolution. *Inorg. Chem.* **2014,** *53* (16), 8350-61.

F Supporting Information for Chapter 7

Adapted from Martin, D. J.; Mercado, B. Q.; Mayer, J. M. “Synthesis and Prior Misidentification of 4-*tert*-butyl-2,6-dinitrobenzadelhyde.” *J. Org. Chem*. **2019**, *84*, 12172-12176.

F.1 ^{1}H NMR and ^{13}C NMR Spectra

Each compound was separated onto its own page, below.

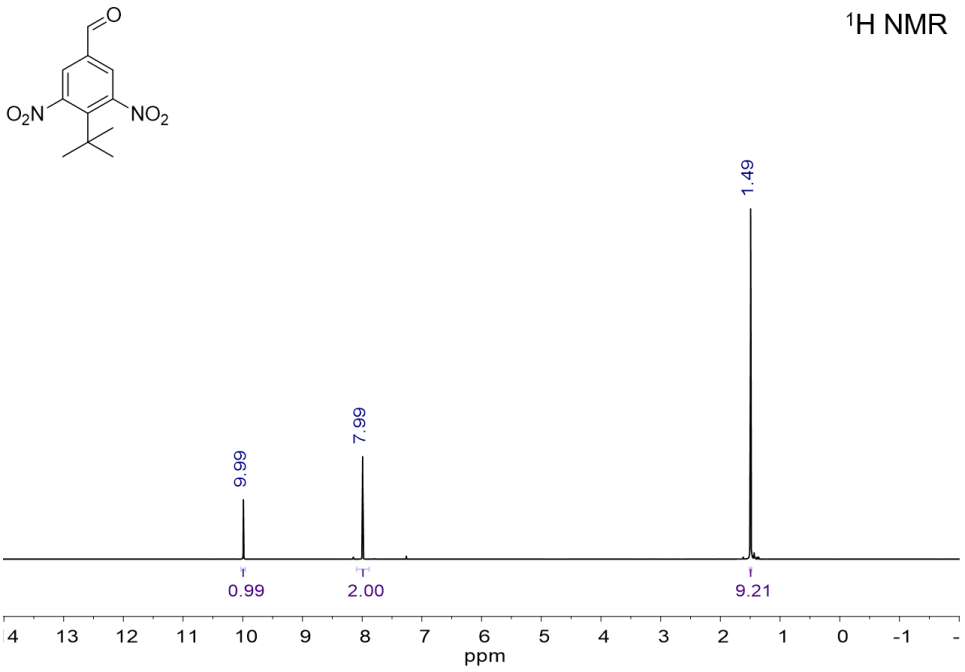

Figure F1. ^{1}H NMR of 4-*tert*-butyl-3,5-dinitrobenzaldehyde (**2**). Chemical shifts (ppm) match those reported and incorrectly assigned as the 4-*tert*-butyl-2,6-dinitrobenzaldehyde in reference.[1]

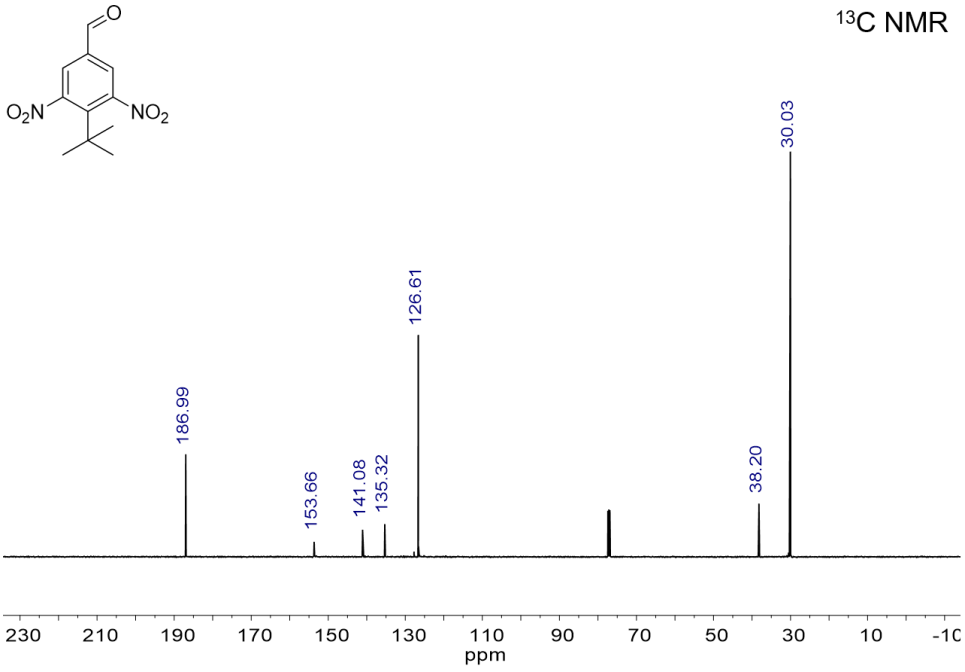

Figure F2. ^{13}C NMR of 4-*tert*-butyl-3,5-dinitrobenzaldehyde (**2**). Chemical shifts (ppm) match those reported and incorrectly assigned as the 4-*tert*-butyl-2,6-dinitrobenzaldehyde in reference.[1]

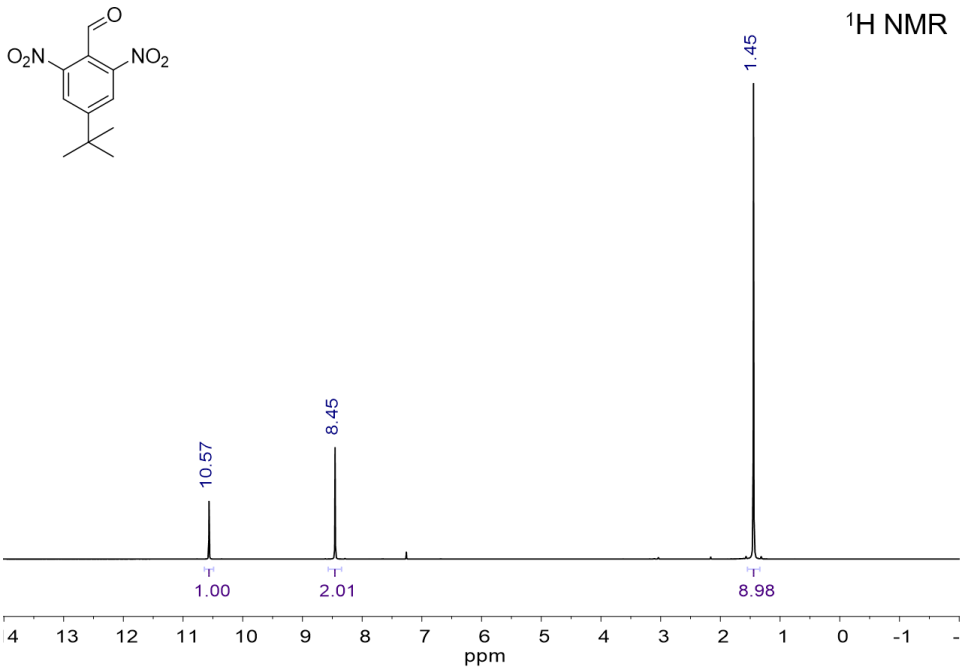

Figure F3. ^{1}H NMR of 4-*tert*-butyl-2,6-dinitrobenzaldehyde (**1**). Chemical shifts (ppm) match those reported in reference for 4-*tert*-butyl-2,6-dinitrobenzaldehyde.[2]

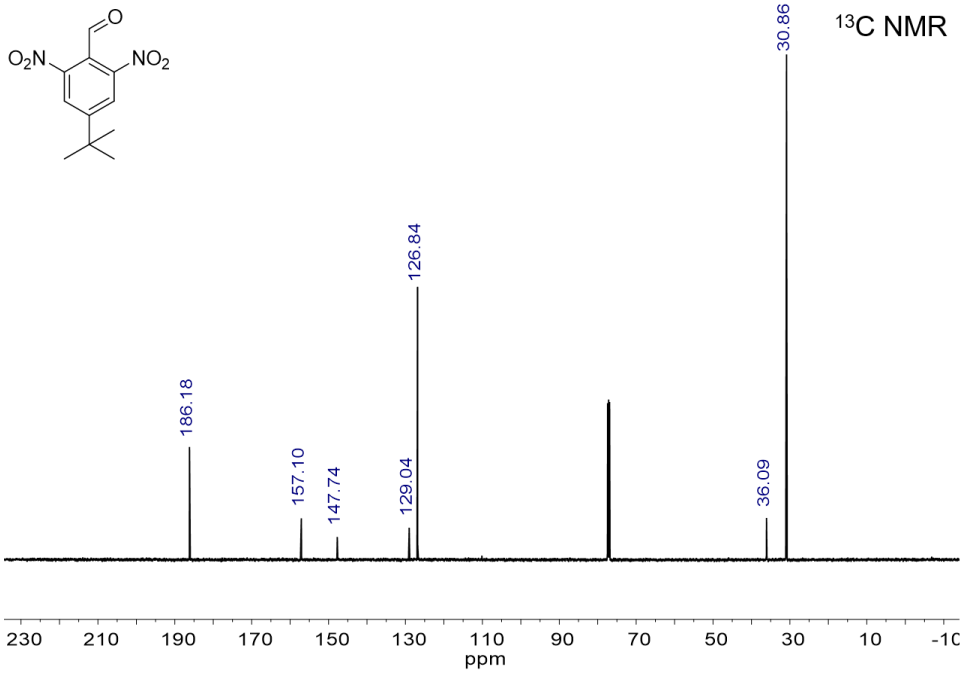

Figure F4. ^{13}C NMR of 4-*tert*-butyl-2,6-dinitrobenzaldehyde. Chemical shifts (ppm) match those reported in reference [3] for 4-*tert*-butyl-2,6-dinitrobenzaldehyde.[2]

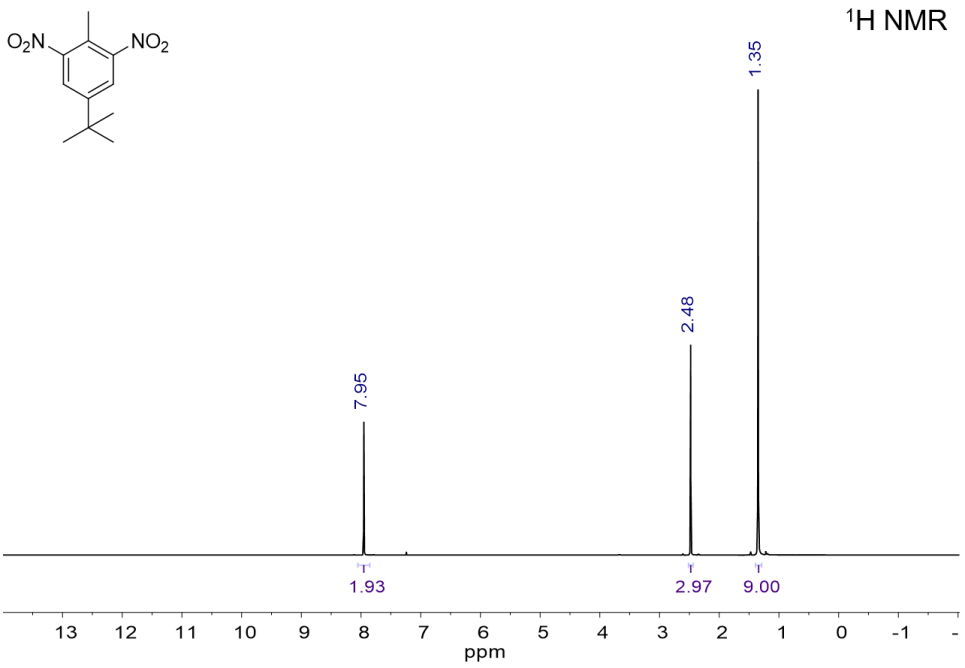

Figure F5. ^{1}H NMR of 4-*tert*-butyl-2,6-dinitrotoluene. Chemical shifts match reference.[2]

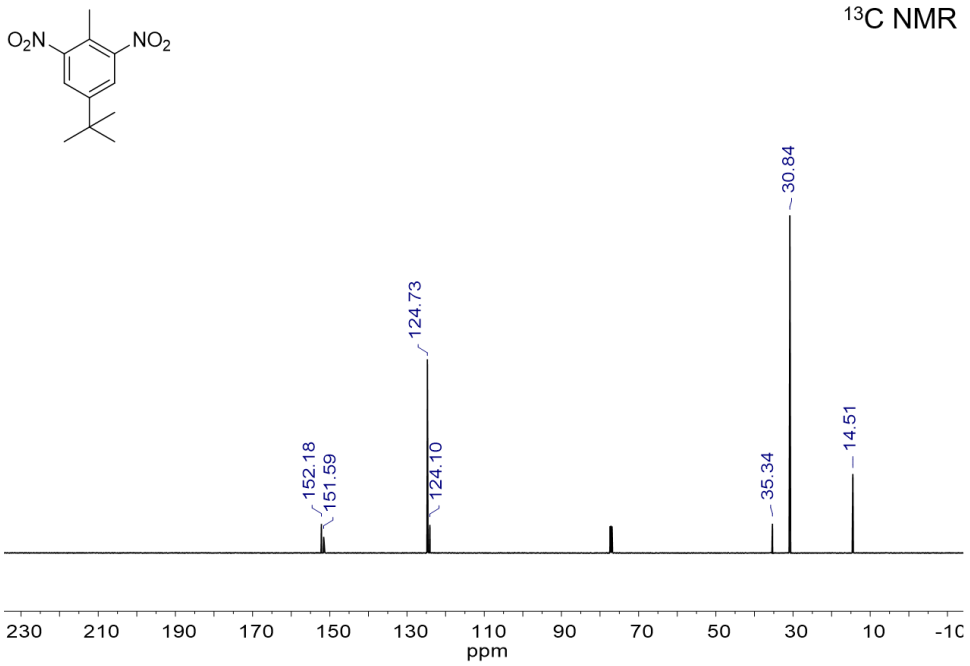

Figure F6. ^{13}C NMR of 4-*tert*-butyl-2,6-dinitrotoluene. Chemical shifts match reference.[2]

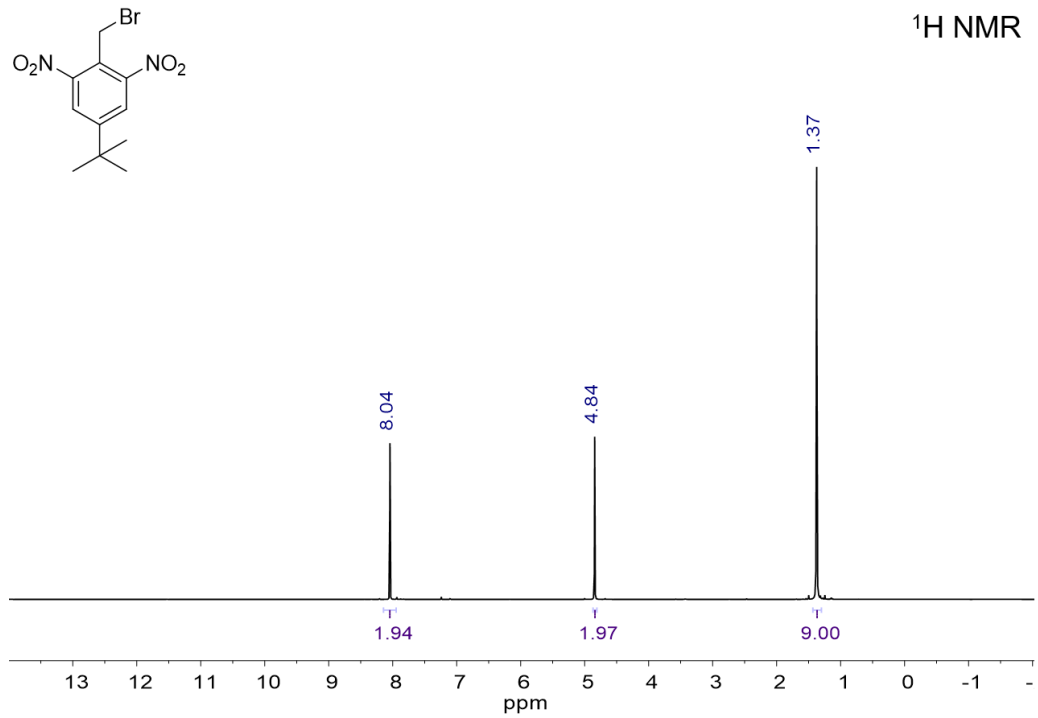

Figure F7. [1]H NMR of 4-*tert*-butyl-2,6-dinitrobenzylbromide. Chemical shifts match reference.[2]

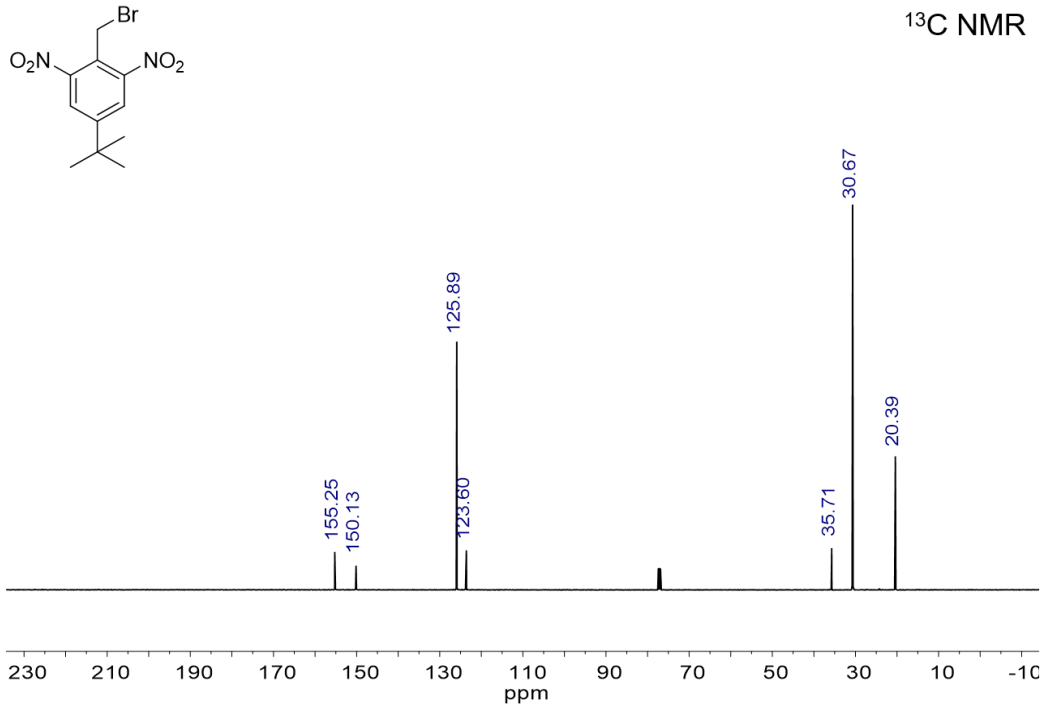

Figure F8. [13]C NMR of 4-*tert*-butyl-2,6-dinitrobenzylbromide. Chemical shifts match reference.[2]

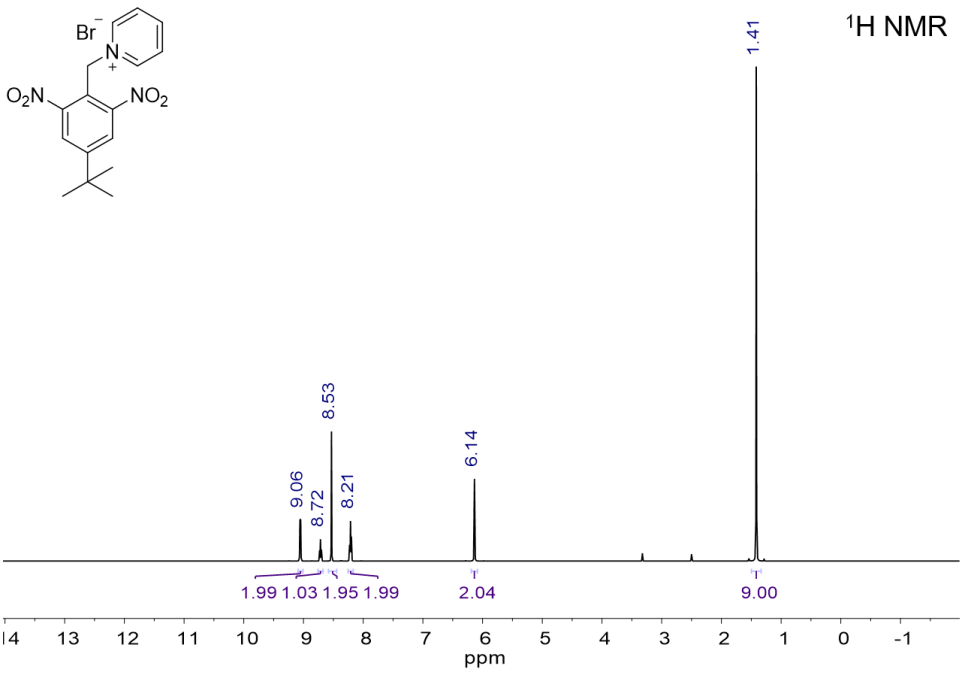

Figure F9. ^{1}H NMR of 4-*tert*-butyl-2,6-dinitrobenzylpyridinium bromide.

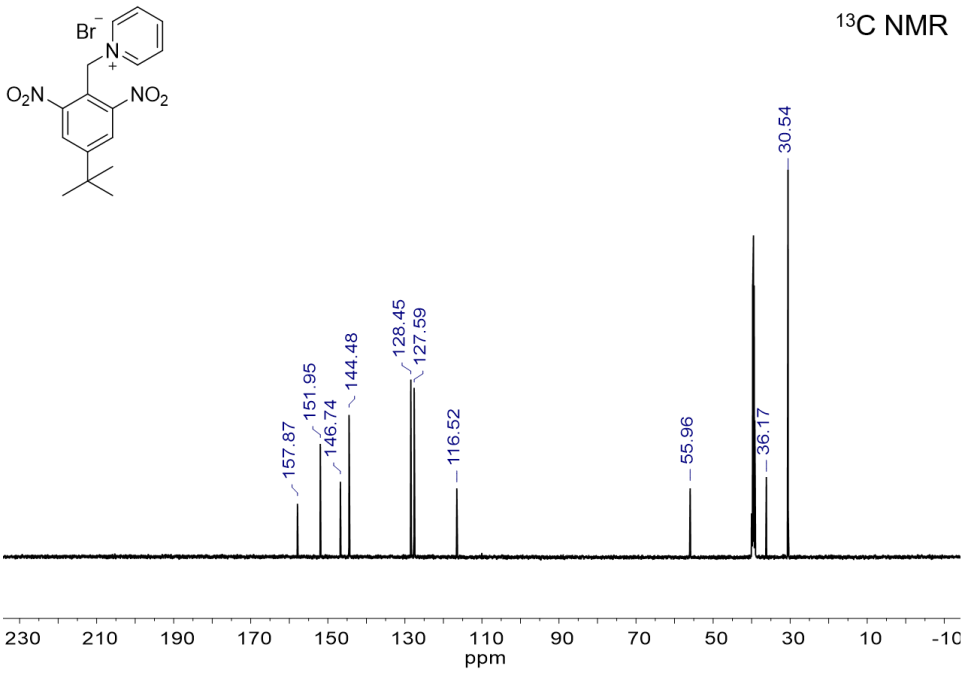

Figure F10. ^{13}C NMR of 4-*tert*-butyl-2,6-dinitrobenzylpyridinium bromide.

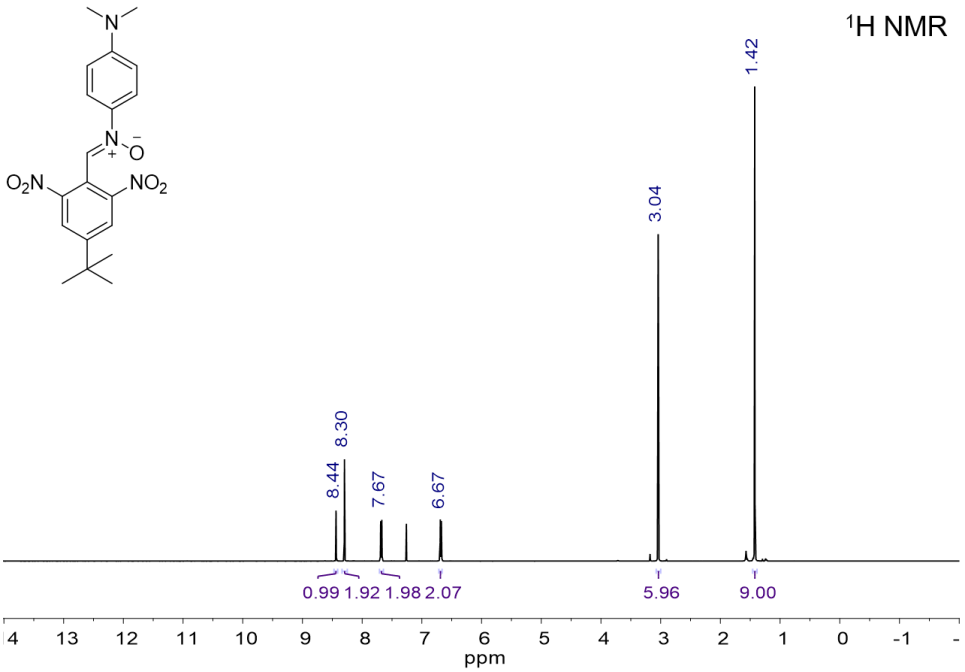

Figure F11. ^{1}H NMR of *N*-(4-dimethylaminophenyl)-α-(4-*tert*-butyl-2,6-dinitrophenyl)nitrone.

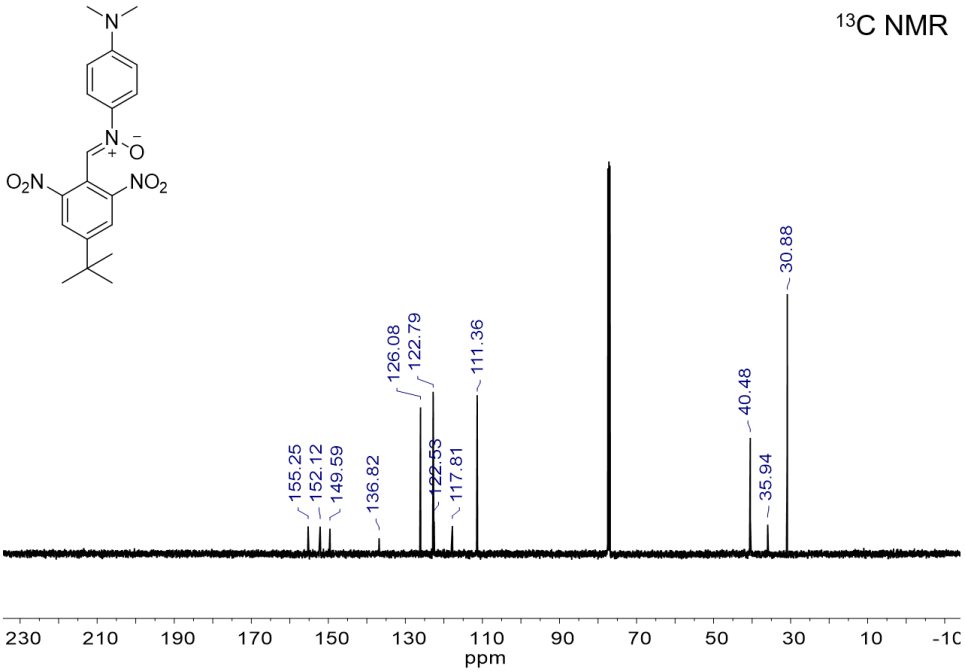

Figure F12. ^{13}C NMR of *N*-(4-dimethylaminophenyl)-α-(4-*tert*-butyl-2,6-dinitrophenyl)nitrone.

F.2 Photographs of Products

Figure F13. Photo of 4-*tert*-butyl-2,6-dinitrotoluene crystals (flakes).

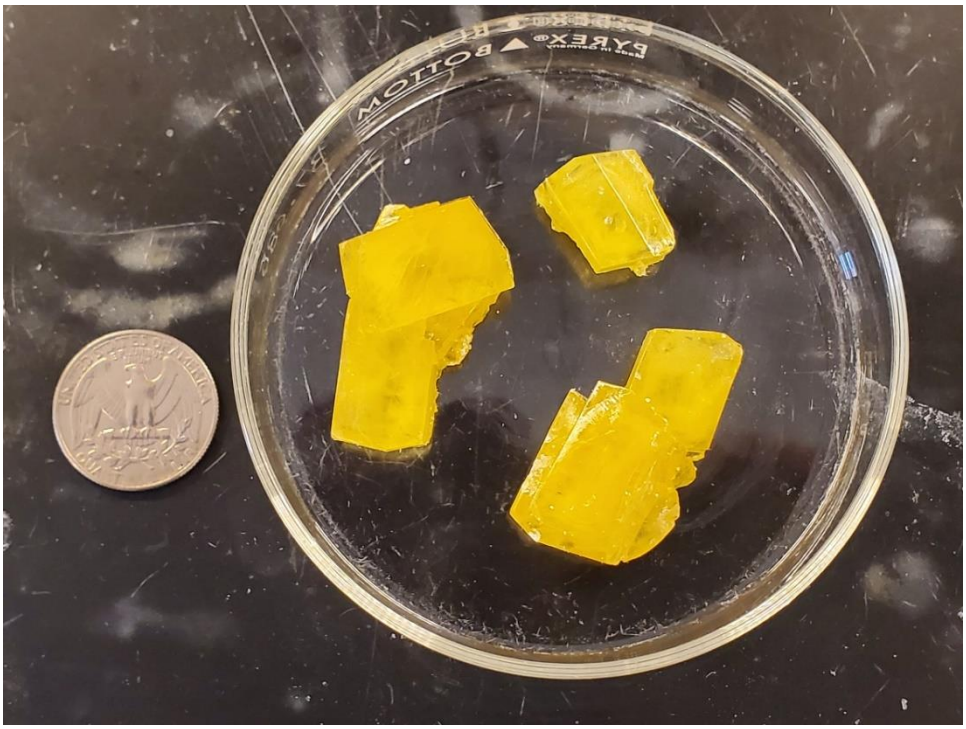

Figure F14. Photo of 4-*tert*-butyl-2,6-dinitrobenzylbromide crystals (large prisms).

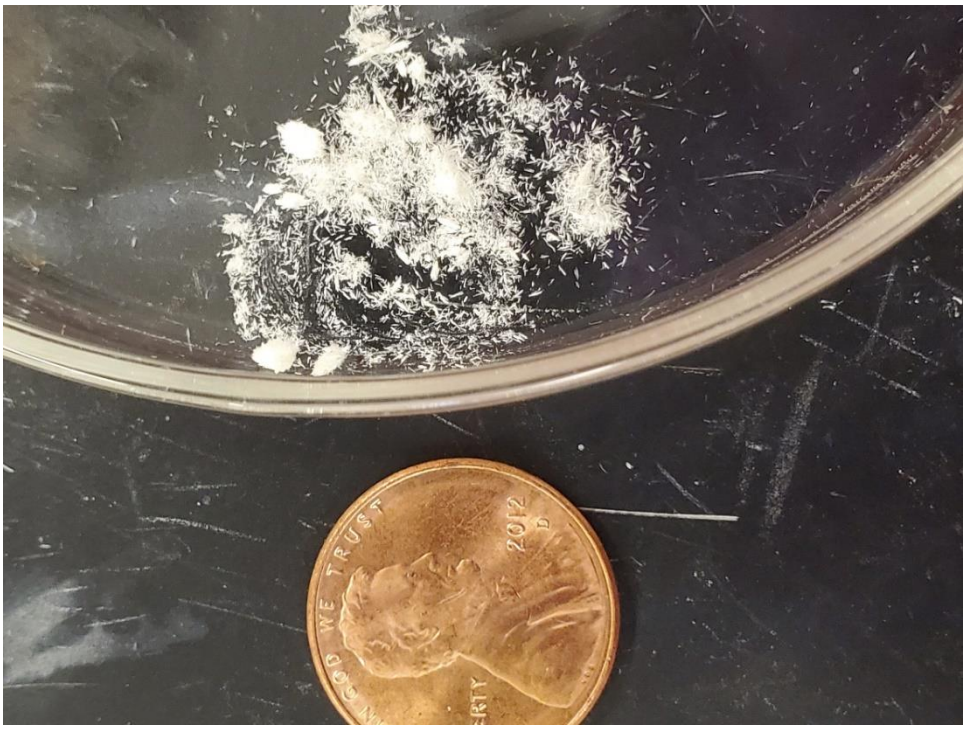

Figure F15. Photo of 4-*tert*-butyl-2,6-dinitrobenzylpyridinium bromide crystals (needles).

Figure F16. Photo of *N*-(4-dimethylaminophenyl)-α-(4-*tert*-butyl-2,6-dinitrophenyl)nitrone (powder).

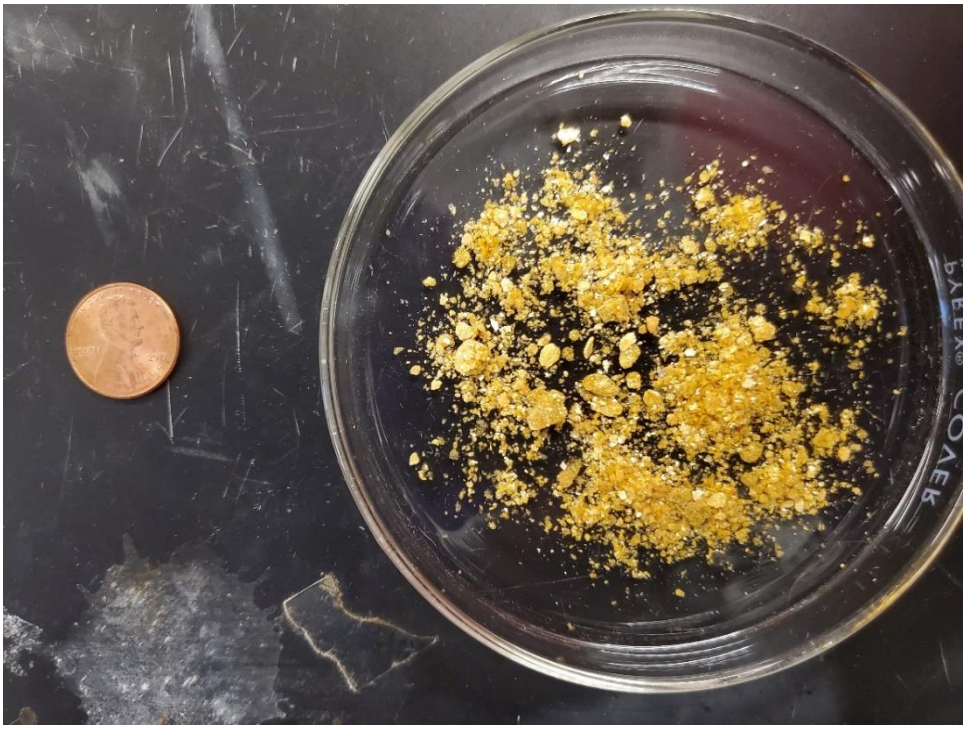

Figure F17. Photo of 4-*tert*-butyl-2,6-dinitrobenzaldehyde crystals (flakes).

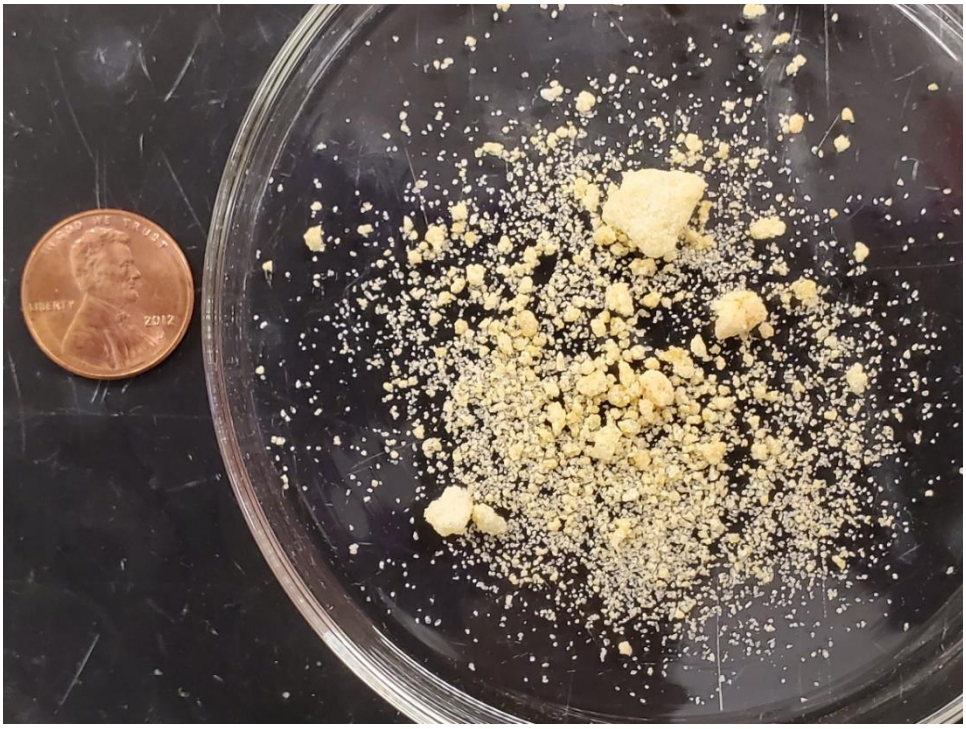

Figure F18. Photo of 4-*tert*-butyl-3,5-dinitrobenzaldehyde crystals (cubes/blocks).

F.3 Single Crystal X-ray Data

*F.3.1 4-tert-butyl-3,5-dinitrobenzaldehyde (**2**)*

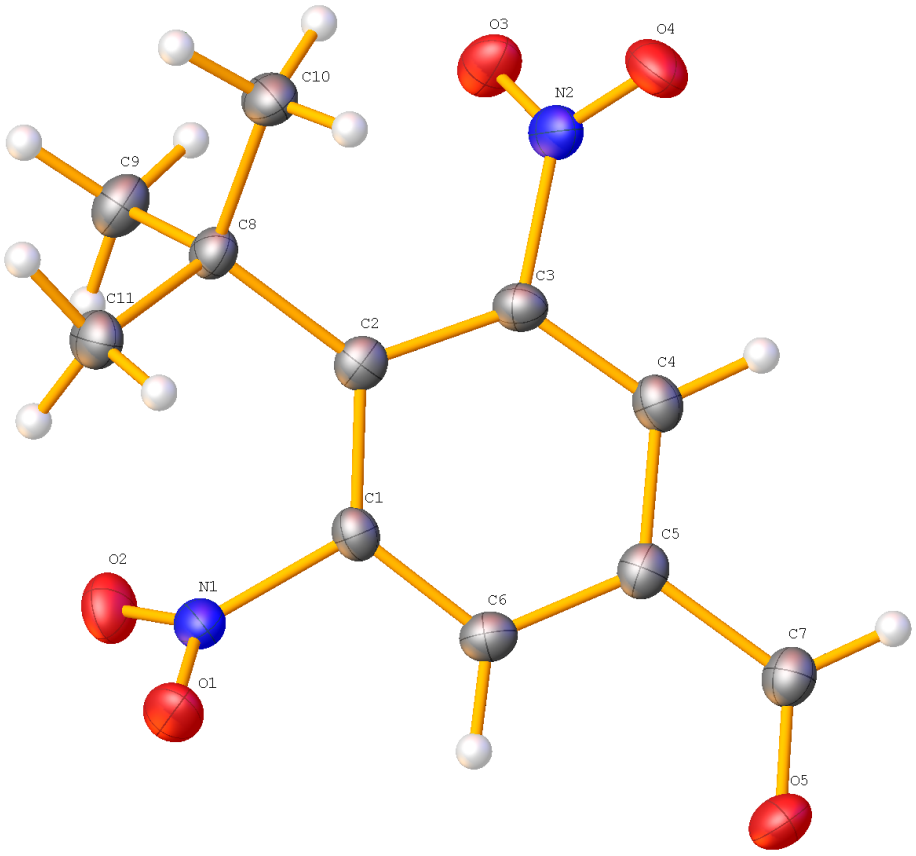

Figure F19. The complete numbering scheme of **2** with 50% thermal ellipsoid probability levels. The hydrogen atoms are shown as white shaded spheres of arbitrary size for clarity.

Table F1. Crystal data and structure refinement for **2**.

Identification code	mini-18069	
Empirical formula	C11 H12 N2 O5	
Formula weight	252.23	
Temperature	93(2) K	
Wavelength	0.71073 Å	
Crystal system	Monoclinic	
Space group	$P2_1/c$	
Unit cell dimensions	a = 9.4352(10) Å	α= 90°
	b = 8.4152(9) Å	β= 97.276(11)°
	c = 14.7368(17) Å	γ = 90°
Volume	1160.7(2) $Å^3$	
Z	4	
Density (calculated)	1.443 Mg/m^3	
Absorption coefficient	0.116 mm^{-1}	
F(000)	528	
Crystal size	0.300 x 0.200 x 0.100 mm^3	
Crystal color and habit	Colorless Block	
Diffractometer	Rigaku Mercury275R CCD	
Theta range for data collection	2.787 to 25.279°.	
Index ranges	-11<=h<=11, -10<=k<=10, -17<=l<=17	
Reflections collected	4525	
Independent reflections	4525 [R(int) = 0.1062]	
Observed reflections (I > 2sigma(I))	3732	
Completeness to theta = 25.242°	98.5 %	
Absorption correction	Semi-empirical from equivalents	
Max. and min. transmission	1.00000 and 0.64665	
Solution method	SHELXT-2014/5 (Sheldrick, 2014)	
Refinement method	SHELXL-2014/7 (Sheldrick, 2014)	
Data / restraints / parameters	4525 / 0 / 167	
Goodness-of-fit on F^2	1.030	
Final R indices [I>2sigma(I)]	R1 = 0.0532, wR2 = 0.1443	
R indices (all data)	R1 = 0.0629, wR2 = 0.1497	
Largest diff. peak and hole	0.304 and -0.216 $e.Å^{-3}$	

*F.3.2 4-tert-butyl-2,6-dinitrobenzaldehyde (**1**)*

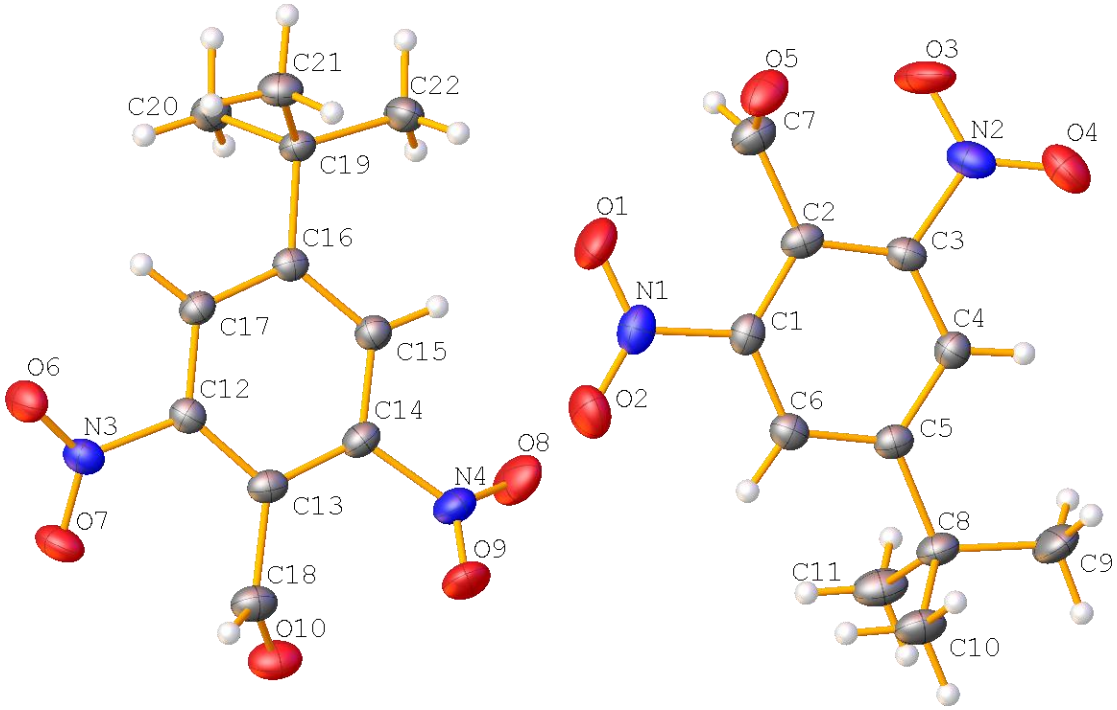

Figure F20. The complete numbering scheme for **1**, with 50% thermal ellipsoid probability levels. The unit cell contained two chemically identical, crystallographically distinct molecules of **1** (Z' = 2). The hydrogen atoms are shown as white shaded spheres of arbitrary size for clarity.

Table F2. Crystal data and structure refinement for **1**.

Identification code	mini-18070	
Empirical formula	C11 H12 N2 O5	
Formula weight	252.23	
Temperature	93(2) K	
Wavelength	0.71073 Å	
Crystal system	Monoclinic	
Space group	$P2_1/c$	
Unit cell dimensions	a = 18.7889(11) Å	α= 90°
	b = 10.5423(6) Å	β= 91.857(5)°
	c = 11.6936(7) Å	γ = 90°
Volume	2315.0(2) $Å^3$	
Z	8	
Z′	2	
Density (calculated)	1.447 Mg/m^3	
Absorption coefficient	0.116 mm^{-1}	
F(000)	1056	
Crystal size	0.300 x 0.230 x 0.200 mm^3	
Crystal color and habit	Colorless Block	
Diffractometer	Rigaku Mercury275R CCD	
Theta range for data collection	2.215 to 27.482°.	
Index ranges	-24<=h<=24, -13<=k<=13, -15<=l<=15	
Reflections collected	39134	
Independent reflections	5315 [R(int) = 0.0594]	
Observed reflections (I > 2sigma(I))	3971	
Completeness to theta = 25.242°	100.0 %	
Absorption correction	Semi-empirical from equivalents	
Max. and min. transmission	1.00000 and 0.52213	
Solution method	SHELXT-2014/5 (Sheldrick, 2014)	
Refinement method	SHELXL-2014/7 (Sheldrick, 2014)	
Data / restraints / parameters	5315 / 0 / 331	
Goodness-of-fit on F^2	1.045	
Final R indices [I>2sigma(I)]	R1 = 0.0484, wR2 = 0.1078	
R indices (all data)	R1 = 0.0724, wR2 = 0.1204	
Largest diff. peak and hole	0.312 and -0.227 $e.Å^{-3}$	

F.4 References

1. Peters, M. V.; Stoll, R. S.; Goddard, R.; Buth, G.; Hecht, S., On the Illusive Nature of o-Formylazobenzenes: Exploiting the Nucleophilicity of the Azo Group for Cyclization to Indazole Derivatives. *J. Org. Chem.* **2006,** *71* (20), 7840-7845.
2. Rose, E.; Kossanyi, A.; Quelquejeu, M.; Soleilhavoup, M.; Duwavran, F.; Bernard, N.; Lecas, A., Synthesis of Biomimetic Heme Precursors: The "Double Picket Fence" 5,10,15,20-Tetrakis(2′,6′-dinitro-4′-tert-butylphenyl)porphyrin. *J. Am. Chem. Soc.* **1996,** *118* (6), 1567-1568.

G Tidbits

Problem-solving at the bench has been known to topple even the most well-planned experiments. The purpose of this final appendix is to offer anecdotal advice and lab lore that may help others troubleshoot common problems. Most of these bullets were derived from my own experiences; however, some lessons were kindly learned from peers, acknowledged below.

G.1 Rules of Thumb

- One of the best panaceas for unknown bench problems is to just walk away. You would be surprised at how many problems resolve themselves if given some time. Unless there is an obvious problem with a clear fix, fussing with unknown problems typically makes things worse.
- Trust in your chemicals. A lot of problems are caused by user-error and not some mysterious unknown. This tidbit can be hard to follow, especially for perfectionists, and it takes a significant amount of resolve not to bin your sample if "something went wrong."
- Never take short cuts to avoid trivial problems. When something inevitably goes wrong or unexpected happens, it is important to have minimized sources of error/contamination. Get a new pipette if you dropped the old one on the glovebox floor. The extra 30 seconds is well worth it, especially if the alternative is unintentionally adding nanomolar amounts of rhodamine and an extra three hours of work to remove the colored impurity [B. McCarthy and B. Groff].
- When it comes to cleanliness, trust no one – especially yourself.
- There is merit to performing same-day experiments. To be able to say "same day, same instrument, same sample" can be very powerful.
- Take a few minutes and make stock solutions day-of. Many folks have been burned by leaky caps or slow decomposition in solution [E. Rountree].

G.2 General Electrochemistry

- For simple homogeneous voltammetry experiments, the optimal analyte range is ~1-2 mM. This concentration range offers good balance between material conservation, contributions from capacitive current, and minimizing internal resistance issues associated with larger concentrations. Lower analyte concentrations (50-100μM) can be used effectively so long as the sample has a well-behaved electrochemical response.
- It is not trivial to polish electrodes in a glovebox. When planning glovebox electrochemistry experiments, always polish and pump in an extra electrode or two. Glassy carbon tends to foul, especially when it is least convenient.
- It is always possible to add more ferrocene. It is very hard to remove it.
- Mechanical polishing is not always the be-all, end-all form of electrode cleaning. If low-current or low-concentration experiments are required, electrochemically conditioning the electrode (cycling to the electrochemical solvent window) can remove troublesome and persistent material.
- Cross-contamination between users can most often be traced to poorly cleaned reference electrodes, especially those that contain a fritted capillary. Soaking the capillary before and after use in a separate solvent/electrolyte matched solution is typically sufficient for removing soluble contaminants (e.g. ferrocene).
- Polishing pads should be replaced regularly. The adhesive on the back of the felt pads is water-resistant but will eventually desorb and can mar the electrode surface. It is also possible to polish using EtOH or ^{i}PrOH instead of water, though the same considerations apply [E. Nichols].

G.3 Electrochemistry – Nonaqueous Reference Electrodes

- Nonaqueous solutions should be referenced using an internal standard like ferrocene or using a pseudo reference electrode (e.g. Ag^{+}/Ag) and later referenced to an internal standard. An aqueous reference electrode should *never* be used in a nonaqueous solution. Anecdotally, saturated calomel electrodes are used by the Paris electrochemistry group in

DMF; however, potentials measured with this reference should be taken with caution. [M. Robert, C. Tard].

- Although ferrocene is popular, the (old) literature is not standardized to nonaqueous references. The conversion chart, below, is generally useful for comparing voltammograms reported using different reference electrodes. Values obtained from this conversion chart should be taken with great caution [M. Pegis].
- When separated from bulk solution with a capillary, the Ag^+/Ag pseudoreference electrode holds a relatively stable potential and will drift less than 5 mV per hour.

Reference Electrode Redox Potentials for silver nitrate (ANE) and silver perchlorate (APE) electrodes made in acetonitrile solutions versus normal hydrogen (NHE), saturated calomel (SCE), saturated sodium chloride (SSCE) and standard hydrogen (SHE) electrodes in acetonitrile at 25 C.

From\To	*ANE1*[a]	*ANE2*[b]	*ANE3*[c]	*APE*[d]	*Fc*$^{+/0}$ [e]	*NHE*[f]	*SCE*[g]	*SSCE*[h]	*SHE*[i]
ANE1	0	45	97	47	-37	593	343	347	587
ANE2	-45	0	52	2	-87	548	298	302	542
ANE3	-97	-52	0	-50	-133	496	246	250	490
APE	-47	-2	50	0	-83	546	296	300	540
Fc$^{+/0}$	37	87	133	83	0	630	380	384	624
NHE	-593	-548	496	-546	-630	0	-250	246	-6
SCE	-343	-298	-246	-296	-380	250	0	4	244
SSCE	-347	-302	-250	-300	-384	246	-4	0	235
SHE	-587	-542	-490	-540	-624	6	-244	-240	0

[a] Ag/Ag^+, 0.1 M $AgNO_3$, 0.1M $[N(Et)_3][ClO_4]$, CH_3CN. [b] Ag/Ag^+, 0.01 M $AgNO_3$, 0.1M $[N(Et)_3][ClO_4]$, CH_3CN. [c] Ag/Ag^+, 0.001 M $AgNO_3$, 0.1M $[N(Et)_3][ClO_4]$, CH_3CN. [d] Ag/Ag^+, 0.01 M $AgClO_4$, 0.1M $[N(Et)_3][ClO_4]$, CH_3CN. [e] Internal standard. [f] H^+/H_2, 1 N $HClO_4$, 1 atm H_2, H_2O. [g] $HgCl_2$/Hg, sat. KCl , H_2O. [h] $HgCl_2$/Hg, sat NaCl, H_2O. [i] H^+/H_2, extrapolated from infinite dilution to 1 M H^+, 1 atm H_2, H_2O.

G.4 Electrochemistry – Internal Resistance

- Internal resistance (a.k.a. “ohmic drop” or “IR drop”) can result in broadness for simple one-electron reactions and becomes far more problematic when large amounts of current are passed (e.g. during electrocatalysis).
- Average internal resistance values in conventional three-electrode set-ups containing 0.1 M supporting electrolyte depend most significantly on the solvent and working electrode material. On glassy carbon, typical values for: water (15-20 Ω), acetonitrile (60-80 Ω), dimethylformamide (80-200 Ω), dichloromethane (ca. 200 Ω) [K. Fisher]. These values can be much larger for ethereal solvents like tetrahydrofuran (500-2000 Ω).

- Many potentiostats will correct for internal resistance; however, the estimates are almost always far lower than the actual resistance (e.g. 80/200 Ω). If this becomes an issue (e.g. electrocatalysis), the internal resistance should be manually set as high as possible (190/200 Ω). When the internal resistance is set *above* the actual resistance (210/200 Ω), the potentiostat will return an oscillating pattern in the voltammogram [M. Robert].
- Decreased analyte loading, increased supporting electrolyte concentration, and changing to a metal working electrode all improve internal resistance.

G.5 Electrochemistry – Molecular Electrocatalysis

- Ideal S-shaped voltammograms are tricky to obtain. Raising the scan rate is the recommended textbook solution; however, a far simpler and (often) more effective solution is to drop the catalyst loading.
- Foot-of-the-wave analysis is almost common practice in today's molecular electrocatalysis literature. Unfortunately, many literature examples use it incorrectly. It is important to i) use the correct version of the FOWA expression, which depends on the operative mechanism, and to ii) fit between n = 1 and n = #e^- in one complete turnover (e.g. 1-4 for $4H^+ + 4e^- + O_2 \rightarrow 2H_2O$; or 1-2 for $2H^+ + 2e^- \rightarrow H_2$) to obtain an accurate turnover frequency. This second parameter is often ignored (e.g. a fit between n = 0.05 and 0.15) and can result in estimates for maximum turnover frequency that far exceed the true values.

G.6 General Synthesis

- Textbooks are not the only forms of learning media. There are many online video resources that demonstrate common synthesis and workup methods. Some of the best video resources are prepared by 'at home' chemists, who are actively motivated to circumvent challenging workups (e.g. chromatography) and decrease chemical waste (e.g. high yielding or solvent-less reactions). NileRed is among my favorites, because the focus is on the chemistry rather than on the "wow factor."
- Always make more than you will need, because inevitably something will go wrong. Having to backtrack several steps in the synthesis to prepare starting material can be very painful [B. Koronkiewicz].

- The idiom “A bird in the hand is worth two in the bush” very much applies to product purity.
- Do not start columns after 5:00 pm, it is never worth it.

G.7 Iron Porphyrin Synthesis and Chromatography

- Iron porphyrins that do not contain sterically bulky substituents are often prone to μ-oxo dimerization. A good rule of thumb is that ortho-ortho substituted porphyrins do not typically dimerize, but meta-meta or para-substituted systems are still capable of doing so. For instance, *o*,*o*-difluorophenylporphyrin will not dimerize (although the F-atoms are small), but 3,4,5-trimethoxyphenylporphyrin will readily do so [H. Nedzbala].
- The formation of μ-oxo dimers is most easily detected spectrophotometrically. Solutions of these molecules are often green-brown and are unpleasant to look at. A single, symmetric peak around 14 ppm is also a typical tell-tale indicator in the ^{1}H NMR, which corresponds to the sixteen pyrrolic protons of the dimer.
- μ-oxo dimers will decompose into the monomeric forms in the presence of strong acids. This allows for the convenient synthesis of the corresponding conjugate base complexes (e.g. adding HX forms Fe(X)P). The solutions must remain acidified in order to avoid forming Fe(OH)P complexes, which will re-dimerize.
- Column chromatography of non-metallated porphyrins or “free-base” porphyrins not containing charged groups tend to run well on silica. The corresponding iron porphyrins will aggressively stick to silica. The difference in these behaviors allows for convenient separation of metallated and unmetallated products.
- Once metallated, column chromatography becomes far less effective for separating different porphyrin products. Alumina is the preferred solid phase if separation is required for metallated porphyrins, but separation is often still poor.
- Unlike columns of most other organic products, almost all the eluent will be colored during a porphyrin column. Do not fall into the trap of collecting *every* colored fraction or attempting to “flush” with solvent until the eluent is clear – it will never happen. The eluent will become intensely colored when the porphyrin elutes, so much so that it is often impossible to see through the fractions.

- Nitrophenylporphyrins are frustratingly insoluble in everything except hot acid [E. Nichols]. This can be used advantageously if side products (e.g. polypyrroles or other oligomers) need to be removed.
- Many free base and metallated porphyrins can be conveniently crystallized on the rotovap using a combination of DCM/MeOH [K. Fisher]. Slowly removing the DCM increases the relative concentration of MeOH, which will typically precipitate the porphyrin as a matte, microcrystalline product.

G.8 Metalloporphyrin Colors

- Differences between these colors are most easily detected by eye and in the 0.05-1.0 mM concentration range. Contributions from the Q-bands are more significant in this concentration range. It is more difficult to tell porphyrins apart at lower concentrations because the Soret dominates the UV-vis spectrum and everything looks yellow.
- In general, the UV-vis spectra of free-base and metallporphyrins are more sensitive to changes in coordination environment than in porphyrin substitution differences. This is not always the case but is often a good rule of thumb.
- Changes in the UV-vis spectra due to ligand binding are often more dramatic for binding to iron (II) porphyrins than to iron (III) porphyrins.
- $(Fe^{III}P)_2O$: green-brown and sewage colored; two Soret peaks
- $Fe^{III}(Cl)P$ or $Fe^{III}(Br)P$: brown and earthy colored
- $Fe^{III}(OTf)P$: red-brown and cherry colored
- $Fe^{II}(Cl)P$ or $Fe^{II}(Br)P$: red-brown, often slightly browned version of free base
- $Fe^{II}(OTf)P$: lustrous red and pinkish in MeCN/PrCN
- $Zn^{II}P$: red-orange, with more highly symmetric Soret and Q-band features
- $Fe^{II}(AcO)P$: red-green and nearly bichromic
- H_2P: most often ruby red or cabernet colored, but purple hues are sometimes present
- $[H(H_2P)]^+$: sprite green and yellow if dilute
- Li_2P: deep forest green

G.9 Crystallization and Recrystallization Methods

The following examples summarize the various conditions and successes that I had in graduate school for crystallization of organic and inorganic products. Many additional purification-by-recrystallization methods can be found in “Purification of Laboratory Chemicals” (10.1016/C2009-0-26589-5)

- In my experience, layering and vapor diffusion result in crystals within a similar time frame and with similar quality crystals. Using combinations of MeCN and Et_2O, precipitation is almost complete between 24-36 hours at 20 °C. Longer times are required at colder temperature (7-10 days in at −20 °C). In my hands, the quality of the crystals does not improve using the slower precipitation method.
- (Evaporation) [DCM]: 2-nitrophenylporphyrin
- (Thermal) [EtOH; 60 to 0 °C]: 4-*tert*-butyl-2,6-dinitro-toluene; 4-*tert*-butyl-2,6-dinitro-benzaldehyde; 4-*tert*-butyl-3,5-dinitrobenzaldehyde
- (Thermal) [Et_2O; 40 to 0 °C, watch for spontaneous ignition]: 2,6-dinitro-4-*tert*-butylbenzylbromide
- (Thermal) [$(CH_3)_2CO$; 50 °C]: 4-*tert*-butyl-2,6-dinitro-benzylpyridinium bromide
- (Thermal) [CH_3COOH; 110 to 20 °C]: 2-nitrophenylporphyrin
- (Thermal) [H_2O; 80 to 20 °C]: 4-methylpyridylporphyrin tetratriflate
- (Layering) [DCM/MeOH]: general conditions for precipitating tetra-arylporphyrins
- (Layering) [DCM/Pentanes]: 2-aminophenylporphyrin atropisomers
- (Layering) [DCM/Et_2O]: 2-aminophenylporphyrin atropisomers
- (Layering) [Toluene/Pentanes]: iron(II) tetraphenylporphyrin
- (Layering) [THF/Pentanes]: iron(II) tetraphenylporphyrin
- (Vapor diffusion) [MeCN/Et_2O]: iron(III/II) 2-*N,N,N*-trimethylaniliniumporphyrin triflate atropisomers; iron(III) 2,6-*N,N,N*-trimethylammoniumphenylporphyrin triflate